Complexity

Reinforcement Learning and Adaptive Optimisation of Complex Dynamic Systems and Industrial Applications

Lead Guest Editor: Shuping He
Guest Editors: Xiaoli Luan, Vladimir Stojanovic, and Guangchen Zhang

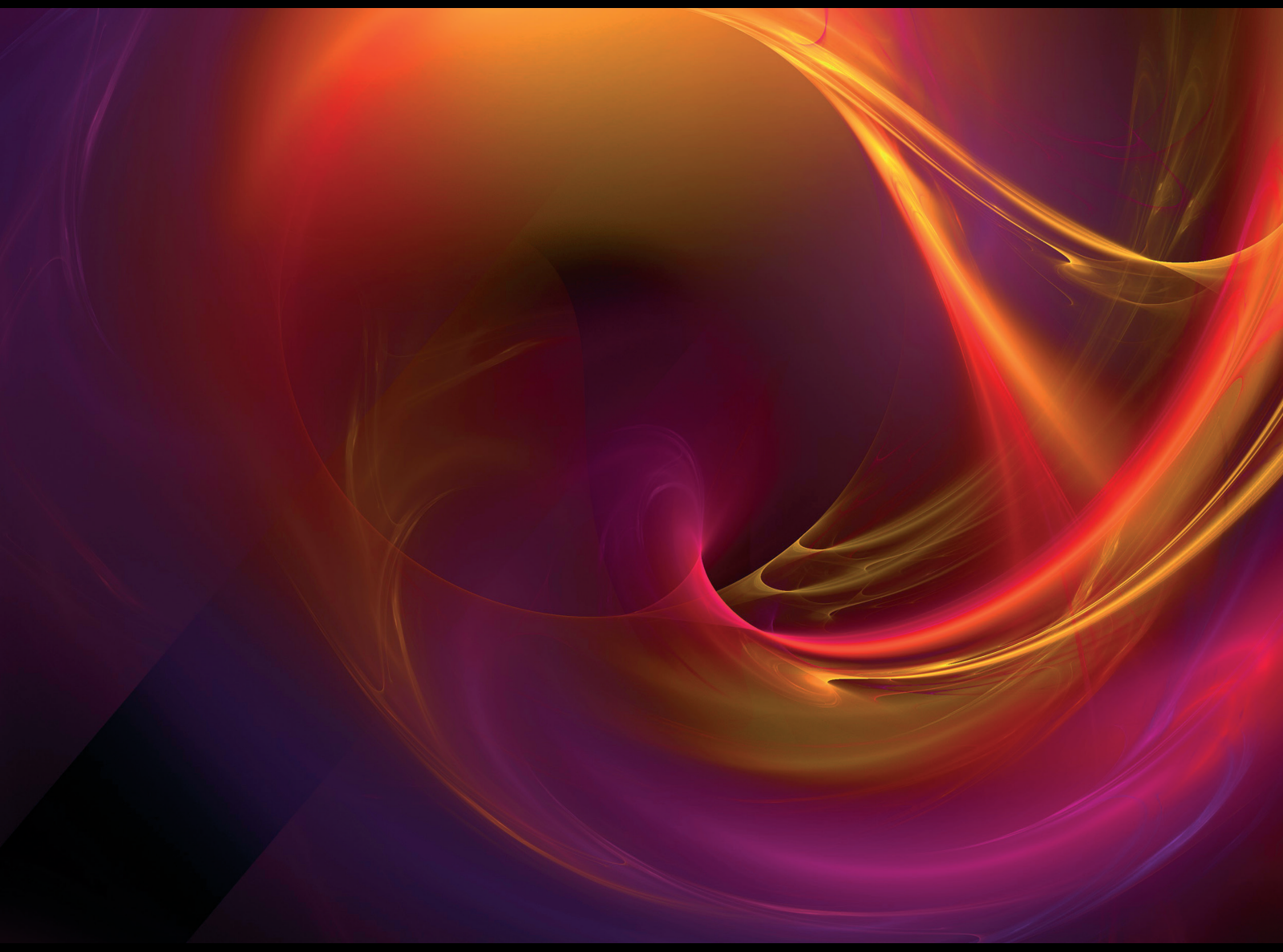

Reinforcement Learning and Adaptive Optimisation of Complex Dynamic Systems and Industrial Applications

Complexity

Reinforcement Learning and Adaptive Optimisation of Complex Dynamic Systems and Industrial Applications

Lead Guest Editor: Shuping He
Guest Editors: Xiaoli Luan, Vladimir Stojanovic, and Guangchen Zhang

Contents

Contents

Hindawi
Complexity
Volume 2021, Article ID 4527878, 1 page
https://doi.org/10.1155/2021/4527878

Erratum

Erratum to "Finite-Time Asynchronous Stabilization for Nonlinear Hidden Markov Jump Systems with Parameter Varying in Continuous-Time Case"

Lianjun Xiao,[1] Xiaofeng Wang,[2] and Lingling Gao[1]

[1]*School of Artificial Intelligence and Big Data, Hefei University, Hefei 230601, China*
[2]*Anhui Provincial Engineering Laboratory of Big Data Technology Application for Urban Infrastructure, School of Artificial Intelligence and Big Data, Hefei University, Hefei 230601, China*

Correspondence should be addressed to Xiaofeng Wang; xfwang@hfuu.edu.cn

Received 6 February 2021; Accepted 6 February 2021; Published 19 February 2021

In the article titled "Finite-Time Asynchronous Stabilization for Nonlinear Hidden Markov Jump Systems with Parameter Varying in Continuous-Time Case" [1], the Acknowledgments section was mistakenly omitted from the published article and should be added as follows.

Acknowledgments

This work was supported in part by the National Nature Science Foundation of China (Grant Nos. 61672204 and 61806068), the grant of Major Science and Technology Project of Anhui Province (No. 17030901026), the Natural Science Foundation of Anhui Provincial (Nos. 1908085MF184 and 2008085MF202), the Outstanding Young Talent Visiting and Research Foundation of Anhui Province University (No. gxgnfx2019060), and the Talent Foundation of Hefei University (No. 18–19RC28).

References

[1] L. Xiao, X. Wang, and L. Gao, "Finite-time asynchronous stabilization for nonlinear hidden Markov jump systems with parameter varying in continuous-time case," *Complexity*, vol. 2020, Article ID 1208951, 12 pages, 2020.

Hindawi
Complexity
Volume 2021, Article ID 5964540, 6 pages
https://doi.org/10.1155/2021/5964540

Research Article

Positive Periodic Solutions for a Class of Strongly Coupled Differential Systems with Singular Nonlinearities

Ruipeng Chen, Guangchen Zhang, and Jiayin Liu

Department of Mathematics, North Minzu University, Yinchuan 750021, China

Correspondence should be addressed to Ruipeng Chen; ruipengchen@163.com

Received 13 June 2020; Revised 1 October 2020; Accepted 28 December 2020; Published 16 January 2021

Academic Editor: Dan Selisteanu

This article studies the existence of positive periodic solutions for a class of strongly coupled differential systems. By applying the fixed point theory, several existence results are established. Our main findings generalize and complement those in the literature studies.

1. Introduction

In this paper, we are concerned with the existence of positive periodic solutions of the strongly coupled differential systems:

$$L_i x_i = f_i(t, x_1, x_2) + e_i(t), \quad i = 1, 2, \tag{1}$$

where $L_i x_i = x_i'' + p_i(t)x_i' + q_i(t)x_i$ is a linear differential operator with $p_i, q_i \in L^1(\mathbb{R}/T\mathbb{Z}, \mathbb{R})$. In addition, we assume $e_i \in L^1(\mathbb{R}/T\mathbb{Z}, \mathbb{R})$ and $f_i \in \mathrm{Car}(\mathbb{R}/T\mathbb{Z} \times (0, \infty) \times (0, \infty), \mathbb{R})$, that is, $f_i|_{[0,T]}$: $[0, T] \times (0, \infty) \times (0, \infty) \longrightarrow \mathbb{R}$ is a L^1-Caratheodory function, and it is singular at $(x_1, x_2) = (0, 0)$.

During the past few decades, the fixed point theory has been widely adopted to investigate the nonperiodic coupled differential systems, and researchers have mainly concentrated on the existence and multiplicity of positive solutions [1–3]. Meanwhile, the periodic equations and systems with singular nonlinearities have been dealt via some classical fixed point theorems, such as Schauder's fixed point theorem and fixed point theorems in cones [4–12]. What is worth mentioning is the results obtained in [5, 6, 11, 12], where the authors show, under some circumstances, weak singularities are helpful to seek out periodic solutions for not only singular equations [5] but also singular coupled systems [11]. Especially, in [10], Li and Zhang considered the singular equation

$$x'' + a(t)x = f(t, x) + c(t), \tag{2}$$

where $a, c \in L^1[0, T]$ and $f \in \mathrm{Car}([0, T] \times (0, \infty), \mathbb{R})$. By employing a fixed point theorem in cones, they established several existence theorems under the following basic assumption.

$(\widetilde{H})$ There exist $b>0, \widehat{b}>0$, and $\lambda > 0$ such that

$$0 \le \frac{\widehat{b}(t)}{x^\lambda} \le f(t, x) \le \frac{b(t)}{x^\lambda}, \quad \forall x > 0, \text{a.e. } t \in [0, T], \tag{3}$$

and pointed out they have not limited themselves to the weak singularities; see [10], Section 3, for more details. Besides, the case $a(t) \equiv 0$ (the resonant case) has also been studied in [10], Theorem 4.1. For other research works related to the resonant case of (2), one may refer to [13–15] and references therein.

To our knowledge, however, so far, the existing results on strongly coupled periodic singular systems are relatively few. Therefore, motivated by the aforementioned papers, we shall establish the existence of positive periodic

solutions of system (1) in the present paper to further improve and complement those in the literature studies. To demonstrate our new results, we choose the following differential systems:

$$\begin{cases} x_1'' + p_1(t)x_1' + q_1(t)x_1 = \dfrac{1}{(x_1 + x_2)^{\alpha_1}} + e_1(t), \\ x_2'' + p_2(t)x_2' + q_2(t)x_2 = \dfrac{1}{(x_1 + x_2)^{\alpha_2}} + e_2(t), \end{cases} \tag{4}$$

where $p_i, q_i, e_i \in L^1(\mathbb{R}/T\mathbb{Z}, \mathbb{R})$ and $\alpha_i > 0, i = 1, 2$. Here, $\alpha_i > 0$ means we need not restrict ourselves to the weak force conditions in our results.

The rest of the paper is arranged as follows. In Section 2, we give some required preliminaries and notations. In Section 3, we shall state and prove the existence results for (1) in the nonresonant case. Finally, in Section 4, an existence theorem will be proved for (1) in the resonant case $L_i x_i = x_i'', i = 1, 2$.

2. Preliminaries

The linear boundary value problem

$$x'' + p(t)x' + q(t)x = 0, \tag{5}$$

$$x(0) = x(T), \quad x'(0) = x'(T), \tag{6}$$

is called nonresonant if its unique solution is the trivial one. When (5) and (6) are nonresonant, the well-known Fredholm's alternative ensures the nonhomogeneous equation

$$x'' + p(t)x' + q(t)x = l(t) \tag{7}$$

admits a unique T-periodic solution, which can be expressed as

$$x(t) = \int_0^T K(t, s)l(s)\mathrm{d}s, \tag{8}$$

where $K(t, s)$ is Green's function associated to (5) and (6).

For given $\xi \in L^1[0, T]$, we denote by ξ_* and ξ^*, respectively, the essential infimum and supremum of ξ. $\xi > 0$ means $\xi \geq 0$ for a.e. $t \in [0, T]$, and it is positive on a set with positive measures. Moreover, if (7) has a unique periodic solution x_l for any $l \in C(\mathbb{R}/T\mathbb{Z})$ and x_l is positive on $[0, T]$ when $l > 0$, then we say (5) satisfies the antimaximum principle. Recently, Hakl and Torres [16] established an explicit criterion to guarantee the antimaximum principle holds for (5). For the sake of convenience, set

$$\begin{aligned} \sigma(p)(t) &= e^{\int_0^t p(s)\mathrm{d}s}, \\ \sigma_1(p)(t) &= \sigma(p)(T)\int_0^t \sigma(p)(s)\mathrm{d}s + \int_t^T \sigma(p)(s)\mathrm{d}s. \end{aligned} \tag{9}$$

Lemma 1 (see [16]). *If $q \equiv 0$ and*

$$\int_0^T q(s)\sigma(p)(s)\sigma_1(-p)(s) \geq 0, \tag{10}$$

$$\sup_{0 \leq t \leq T} \left\{ \int_t^{t+T} \sigma(-p)(s)\mathrm{d}s \cdot \int_t^{t+T} [q(s)]_+ \sigma(p)(s)\mathrm{d}s \right\} \leq 4, \tag{11}$$

then (5) satisfies the antimaximum principle, where $[q(s)]_+ = \max\{q(s), 0\}$, whereafter Chu et al. [17] pointed out if (5) admits the antimaximum principle, then $K(t, s) \geq 0$ on $[0, T] \times [0, T]$. In addition, they obtained the following.

Lemma 2. *If $q \equiv 0$ and (11) holds, then the distance between two consecutive zeroes of a nontrivial solution of (5) is greater than T.*

Obviously, Lemma 2 implies $K(t, s)$ does not vanish. As a consequence of Lemmas 1 and 2, Chu et al. established the following.

Lemma 3. *If $q \equiv 0$ and (10) and (11) hold, then $K(t, s) > 0$ on $[0, T] \times [0, T]$.*

Note that Lemma 3 plays an important role in the application of the classical fixed point theorems. Indeed, by Lemma 3, the positivity of some completely continuous operators could be easily obtained.

Remark 1. Clearly, if $p(t) \equiv 0$ (without damping terms), then (10) and (11) reduce, respectively, to

$$\int_0^T q(s)\mathrm{d}s > 0, \quad \left\| [q(s)]_+ \right\|_1 < \frac{4}{T}, \tag{12}$$

which are conditions used to guarantee the positivity of Green's function corresponds to (5) and (6); see [18] for more details.

Throughout the paper, we always suppose $p_i, q_i, e_i \in L^1(\mathbb{R}/T\mathbb{Z}; \mathbb{R})$ and $f_i \in \mathrm{Car}(\mathbb{R}/T\mathbb{Z} \times (0, \infty) \times (0, \infty), \mathbb{R})$. Furthermore,

(H1) The linear equation $L_i x_i = 0$ is nonresonant, and corresponding Green's function $K_i(t, s) > 0$ on $[0, T] \times [0, T], i = 1, 2$.

(H2) There are $b_i > 0, \widehat{b}_i > 0$, and $\alpha_i > 0$ so that, for a.e. $t \in [0, T]$,

$$0 \leq \frac{\widehat{b}_i(t)}{(x_1 + x_2)^{\alpha_i}} \leq f_i(t, x_1, x_2) \leq \frac{b_i(t)}{(x_1 + x_2)^{\alpha_i}}, \quad \forall x_1 > 0, x_2 > 0, i = 1, 2. \tag{13}$$

It is not hard to see (H1) implies the antimaximum principle holds for $L_i x_i = 0$, and thus, $\sigma_i = (m_i/M_i) \in (0, 1)$, where

$$m_i = \min_{0 \leq t, s \leq T} K_i(t, s), M_i = \max_{0 \leq t, s \leq T} K_i(t, s), \quad i = 1, 2. \tag{14}$$

Hence,

$$\sigma := \min\{\sigma_1, \sigma_2\} \in (0,1). \tag{15}$$

Set $\mathbb{R}^n = \prod_{i=1}^n \mathbb{R}, \mathbb{R}_+^n = \prod_{i=1}^n \mathbb{R}_+$, where $\mathbb{R} = (-\infty, +\infty)$ and $\mathbb{R}_+ = [0, +\infty)$. For $\mathbf{x} = (x_1, \ldots, x_n) \in \mathbb{R}^n$, we write $\|\mathbf{x}\| = \sum_{i=1}^n |u_i|$. Let

$$E = \Big\{\mathbf{x}(t) = \big(x_1(t), x_2(t)\big) \in C\big(\mathbb{R}, \mathbb{R}^2\big) \colon x_i(t+T) = x_i(t), t \in \mathbb{R}, i = 1,2\Big\} \tag{16}$$

be the Banach space equipped with the norm

$$\|\mathbf{x}\| = \|x_1\|_\infty + \|x_2\|_\infty, \quad \mathbf{x} = (x_1, x_2) \in E. \tag{17}$$

Here, $\|x_i\|_\infty = \sup_{t\in[0,T]} |x_i(t)|, i = 1,2$.

A vector function $(x_1(t), x_2(t)) \in E$ is called a positive T-periodic solution of (1) if it satisfies (1) and $x_i > 0$ on $[0,T]$, $i = 1,2$. Let

$$K = \Big\{\mathbf{x} = (x_1, x_2) \in E \colon x_i(t) \geq \sigma_i \|x_i\|_\infty, t \in [0,T], i = 1,2\Big\}. \tag{18}$$

Then, it is not difficult to check K is a positive cone in E, and for any $\mathbf{x} = (x_1, x_2) \in E$, we get by (15) that

$$x_1(t) + x_2(t) \geq \sigma \|\mathbf{x}\|. \tag{19}$$

For $r > 0$, let $\Omega_r = \{\mathbf{x} \in K \colon \|\mathbf{x}\| < r\}$; then, $\partial\Omega_r = \{\mathbf{x} \in K \colon \|\mathbf{x}\| = r\}$.

Lemma 4 (see [19]). *Let E be a Banach space and $K \subseteq E$ a cone. Suppose $\Omega_1, \Omega_2 \subseteq E$ are open bounded subsets satisfying $0 \in \Omega_1, \overline{\Omega}_1 \subseteq \Omega_2$. If $\mathscr{A} \colon K \cap (\overline{\Omega}_2 \backslash \Omega_1) \longrightarrow K$ is completely continuous and satisfies*

there is $\psi \in K\backslash\{0\}$ such that $u \neq \mathscr{A}u + \lambda\psi$ for $u \in K \cap \partial\Omega_1$ and $\lambda > 0$,

$\|\mathscr{A}u\| \leq \|u\|, \forall u \in K \cap \partial\Omega_2$,

or

there is $\psi \in K\backslash\{0\}$ such that $u \neq \mathscr{A}u + \lambda\psi$ for $u \in K \cap \partial\Omega_2$ and $\lambda > 0$,

$\|\mathscr{A}u\| \leq \|u\|, \forall u \in K \cap \partial\Omega_1$,

then $\mathscr{A}$ admits a fixed point in $K \cap (\overline{\Omega}_2 \backslash \Omega_1)$.

3. The Nonresonant Systems

This section is devoted to establishing the existence results for system (1) in the nonresonant case. To this end, we define

$$\begin{aligned} \gamma_i(t) &= \int_0^T K_i(t,s) e_i(s)\mathrm{d}s, \quad i = 1,2, \\ B_i(t) &= \int_0^T K_i(t,s) b_i(s)\mathrm{d}s, \widehat{B}_i(t) \\ &= \int_0^T K_i(t,s)\widehat{b}_i(s)\mathrm{d}s, \quad i = 1,2. \end{aligned} \tag{20}$$

Theorem 1. *Assume (H1) and (H2) hold. Let*

$$\begin{aligned} R_i &= \left(\frac{\widehat{b}_{i*}}{|e_{i*}|}\right)^{(1/\alpha_i)}, \\ R_0 &= \min\{R_1, R_2\}. \end{aligned} \tag{21}$$

(i) If $e_{i*} < 0$, $\widehat{b}_{i*} > 0$, and

$$\sum_{i=1}^2 \gamma_i^* \leq R_0 - \sum_{i=1}^2 \frac{B_i^*}{(\sigma R_0)^{\alpha_i}}, \tag{22}$$

then (1) has a positive T-periodic solution.

(ii) If $e_{i*} \geq 0\,(i = 1,2)$, then (1) has a positive T-periodic solution.

Proof

(i) Let $\mathscr{A} \colon E \longrightarrow E$ be an operator defined by $\mathscr{A} = (\mathscr{A}_1, \mathscr{A}_2)$ with

$$(\mathscr{A}_i\mathbf{x})(t) = \int_0^T K_i(t,s) f_i\big(s, x_1(s), x_2(s)\big)\mathrm{d}s + \gamma_i(t), \quad i = 1,2. \tag{23}$$

Then, $\mathscr{A} \colon E \longrightarrow E$ is completely continuous, and a T-periodic solution of (1) is equivalent to a fixed point of $\mathscr{A}$.

We shall divide the proof of the case into three steps as follows.

Step 1: if we choose $r \ll 1$, then for $\psi = (1,1) \in K$,

$$\mathbf{x} \neq \mathscr{A}\mathbf{x} + \lambda\psi, \quad \forall \mathbf{x} \in K \cap \partial\Omega_r, \lambda > 0. \tag{24}$$

Or else, if there are $\mathbf{x}_0 = (x_{10}, x_{20}) \in K \cap \partial\Omega_r$ and $\lambda_0 > 0$ so that $\mathbf{x}_0 = \mathscr{A}\mathbf{x}_0 + (\lambda_0, \lambda_0)$, then by the definition of K and (15), we get

$$\sigma r = \sigma\|\mathbf{x}_0\| \leq x_{10} + x_{20} \leq \|\mathbf{x}_0\| = r. \tag{25}$$

This together with (H2) implies

$$\begin{aligned} x_{i0}(t) &= (\mathscr{A}_i\mathbf{x}_0)(t) + \lambda_0 \\ &= \int_0^T K_i(t,s) f_i\big(s, x_{10}(s), x_{20}(s)\big)\mathrm{d}s + \gamma_i(t) + \lambda_0 \\ &\geq \int_0^T K_i(t,s) \frac{\widehat{b}_i(s)}{\big(x_{10}(s) + x_{20}(s)\big)^{\alpha_i}}\mathrm{d}s + \gamma_{i*} + \lambda_0 \\ &\geq \frac{\widehat{B}_{i*}}{r^{\alpha_i}} + \gamma_{i*} + \lambda_0 > r, \quad i = 1,2, \end{aligned} \tag{26}$$

which contradicts $\|\mathbf{x}_0\| = r$ since $r \ll 1$.

Step 2: for R: $= R_0 > r$, $\mathscr{A}$ maps $K \cap (\overline{\Omega}_R \backslash \Omega_r)$ into K.

Since $R = R_0$, for any $(x_1, x_2) \in (0,\infty) \times (0,\infty)$ satisfying $x_1 + x_2 \in (0, R]$ and a.e. $t \in [0,T]$, we can deduce from (H2) that

$$f_i(t,x_1,x_2)+e_i(t)\geq\frac{\widehat{b}_i(t)}{(x_1+x_2)^{\alpha_i}}+e_i(t)\geq\frac{\widehat{b}_{i*}}{(x_1+x_2)^{\alpha_i}}+e_{i*}\geq 0,\quad i=1,2, \tag{27}$$

and subsequently, for $\mathbf{x}\in K\cap(\overline{\Omega}_R\setminus\Omega_r)$,

$$\begin{aligned}(\mathscr{A}_i\mathbf{x})(t)&=\int_0^T K_i(t,s)\left(f_i(s,x_1(s),x_2(s))+e_i(s)\right)\mathrm{d}s\\&\geq m_i\int_0^T\left(f_i(s,x_1(s),x_2(s))+e_i(s)\right)\mathrm{d}s\\&=\sigma_i\int_0^T M_i\left(f_i(s,x_1(s),x_2(s))+e_i(s)\right)\mathrm{d}s\\&\geq\sigma_i\left\|\mathscr{A}_i\mathbf{x}\right\|_\infty,\quad i=1,2,\end{aligned} \tag{28}$$

which means $\mathscr{A}$ maps $K\cap(\overline{\Omega}_R\setminus\Omega_r)$ into K.

Step 3: we shall show

$$\|\mathscr{A}\mathbf{x}\|\leq\|\mathbf{x}\|,\quad\forall\mathbf{x}\in K\cap\partial\Omega_R. \tag{29}$$

Recall that $R=R_0$. For any $\mathbf{x}\in K\cap\partial\Omega_R$, we have $\sigma R=\sigma\|\mathbf{x}\|\leq x_1+x_2\leq\|\mathbf{x}\|=R$, and then by (27), (H1), and (H2), we can obtain

$$\begin{aligned}0\leq(\mathscr{A}_i\mathbf{x})(t)&=\int_0^T K_i(t,s)\left(f_i(s,x_1(s),x_2(s))+e_i(s)\right)\mathrm{d}s\\&\leq\int_0^T K_i(t,s)\frac{b_i(s)}{(x_1(s)+x_2(s))^{\alpha_i}}\mathrm{d}s+\gamma_i^*\\&\leq\frac{B_i^*}{(\sigma R)^{\alpha_i}}+\gamma_i^*,\quad i=1,2,\end{aligned} \tag{30}$$

which yields $\|\mathscr{A}_i\mathbf{x}\|_\infty\leq(B_i^*/(\sigma R)^{\alpha_i})+\gamma_i^*, i=1,2$. This together with (22) shows

$$\|\mathscr{A}\mathbf{x}\|=\left\|\mathscr{A}_1\mathbf{x}\right\|_\infty+\left\|\mathscr{A}_2\mathbf{x}\right\|_\infty\leq R=\|\mathbf{x}\|. \tag{31}$$

And accordingly, Lemma 4 ensures (1) admits a positive T-periodic solution.

(ii) To deal with this case, we only need to show (24)–(29) are still satisfied. Indeed, if we choose $r\ll 1$, then we can easily prove by (H2) that (24) holds true. Moreover, since $e_{i*}\geq 0$, $R\gg 1$ could be chosen so that (27) and (29) are all satisfied. Consequently, Lemma 4 yields (1) has a positive T-periodic solution. □

Remark 2. Obviously, (H2) reduces to $(\widetilde{H})$ under some special circumstances; hence, Theorem 1 generalizes [10], Theorem 3.1.

Remark 3. When $p_i(t)\equiv 0$, $f_1(t,x_1,x_2)\equiv f_1(t,x_2)$, and $f_2(t,x_1,x_2)\equiv f_2(t,x_1)$, system (1) becomes

$$\begin{cases}x_1''+q_1(t)x_1=f_1(t,x_2)+e_1(t),\\x_2''+q_2(t)x_2=f_2(t,x_1)+e_2(t).\end{cases} \tag{32}$$

In [11], several existence theorems have been established for (32) via Schauder's fixed point theorem, where f_i satisfies only the weak force conditions. However, we do not restrict ourselves here to weak singularities, and Theorem 1 is still valid for (32) with strong singularities.

Theorem 2. *Assume (H1) and (H3) There are $b_i>0, \widehat{b}_i>0, d_i>0$, and $\alpha_i,\eta_i>0$ such that, for a.e. $t\in[0,T]$,*

$$0\leq\frac{\widehat{b}_i(t)}{(x_1+x_2)^{\alpha_i}}\leq f_i(t,x_1,x_2)\leq\frac{b_i(t)}{(x_1+x_2)^{\alpha_i}}+d_i(t)(x_1+x_2)^{\eta_i},\quad\forall x_1,x_2>0. \tag{33}$$

Then, the following results hold true:

(i) If $e_{i*}<0$, $\widehat{b}_{i*}>0$, and

$$\sum_{i=1}^2\gamma_i^*\leq R_0-\sum_{i=1}^2\frac{B_i^*}{(\sigma R_0)^{\alpha_i}}-\sum_{i=1}^2 D_i^*R_0^{\eta_i}, \tag{34}$$

then (1) has a positive T-periodic solution.

(ii) If $e_{i*}\geq 0\,(i=1,2)$, then (1) has a positive T-periodic solution.

Here, R_0 is defined as in Theorem 1.

Proof

(i) Choose $r\ll 1$ and set $R=R_0$. By (H3) and an argument similar to the proof of Theorem 1 (i), we can get (24) and (27). To apply Lemma 4, we just need to show

$$\|\mathscr{A}\mathbf{x}\|\leq\|\mathbf{x}\|,\quad\forall\mathbf{x}\in K\cap\partial\Omega_R. \tag{35}$$

In fact, for any $\mathbf{x}=(x_1,x_2)\in K\cap\partial\Omega_R$, it follows from (27) and (H3) that

$$\begin{aligned}0\leq(\mathscr{A}_i\mathbf{x})(t)&=\int_0^T K_i(t,s)f_i(s,x_1(s),x_2(s))\mathrm{d}s+\gamma_i(t)\\&\leq\int_0^T K_i(t,s)\frac{b_i(s)}{(x_1(s)+x_2(s))^{\alpha_i}}\mathrm{d}s\\&\quad+\int_0^T K_i(t,s)d_i(s)(x_1(s)+x_2(s))^{\eta_i}\mathrm{d}s+\gamma_i^*\\&\leq\frac{B_i^*}{(\sigma R)^{\alpha_i}}+D_i^*R^{\eta_i}+\gamma_i^*,\quad i=1,2,\end{aligned} \tag{36}$$

and then (34) yields $\|\mathscr{A}\mathbf{x}\|=\|\mathscr{A}_1\mathbf{x}\|_\infty+\|\mathscr{A}_2\mathbf{x}\|_\infty\leq R=\|\mathbf{x}\|$. Therefore, Lemma 4 implies (1) has a positive T-periodic solution.

(ii) Using Lemma 4 and similar to the proof of Theorem 1 (ii), we can easily get the conclusions. □

Remark 4. Jiang et al. [4] studied the singular equation

$$u'' + a(t)u = \frac{b(t)}{u^{\alpha}} + d(t)u^{\eta} + c(t), \tag{37}$$

where $\alpha, \eta > 0$ are constants, $b(t), d(t) \in C[0,T]$ are nonnegative, and $c(t) \in C[0,T]$. For the positone case, they supposed $c(t) \geq 0$, which means $c_* \geq 0$, and for the semipositone case, a strong force condition was required. See [4], Corollaries 3.2 and 4.3. Evidently, Theorem 2 generalizes [10], Theorem 3.2, and the corresponding ones in [4].

4. The Resonant Systems

Let us consider the singular systems

$$\begin{cases} x_1'' = f_1(t, x_1, x_2) + e_1(t), \\ x_2'' = f_2(t, x_1, x_2) + e_2(t). \end{cases} \tag{38}$$

Theorem 3. *Assume (H2) and (H4) There are $k_1, k_2 \in (0, (\pi/T))$ so that, for any $(x_1, x_2) \in \mathbb{R}_+^2 \backslash \{(0,0)\}$ and a.e. $t \in [0,T]$,*

$$f_i(t, x_1, x_2) + e_i(t) + k_i^2 x_i \geq 0, \quad i = 1, 2. \tag{39}$$

If $\widehat{b}_{i*} > 0$ and $e_i^* < 0$, then (38) has a positive T-periodic solution.

Proof.

Let us take into account the auxiliary systems

$$\begin{cases} x_1'' + k_1^2 x_1 = f_1(t, x_1, x_2) + e_1(t) + k_1^2 x_1, \\ x_2'' + k_2^2 x_2 = f_2(t, x_1, x_2) + e_2(t) + k_2^2 x_2, \end{cases} \tag{40}$$

where $k_1, k_2 \in (0, (\pi/T))$ are constants introduced as in (H4). Clearly, a solution of (40) is just a solution of original system (38), and vice versa. Therefore, to complete the proof, it is enough to show (40) has a positive T-periodic solution.

Let $K_i(t,s)$ be Green's function of Hill's equation $x_i'' + k_i^2 x_i = 0, i = 1, 2$. Then, a solution of (40) is equivalent to a fixed point of completely continuous operator $\mathscr{A}: E \longrightarrow E$ with components $(\mathscr{A}_1, \mathscr{A}_2)$:

$$\begin{aligned} (\mathscr{A}_i \mathbf{x})(t) = \int_0^T K_i(t,s) \big(& f_i(s, x_1(s), x_2(s)) \\ & + k_i^2 x_i(s) + e_i(s) \big) \mathrm{d}s, \quad i = 1, 2. \end{aligned} \tag{41}$$

Moreover, let m_i and M_i denote the minimum and maximum of $K_i(t,s)$, respectively; then, $\sigma_i = (m_i/M_i) = \cos(k_i T/2) \in (0,1)$, and so, $\sigma := \min\{\sigma_1, \sigma_2\} \in (0,1)$. For $\sigma_i = \cos(k_i T/2)$, we denote again by K, introduced in (18), the positive cone in E.

Choose $R \gg (1/\sigma)$ sufficiently large and define $\Omega_R = \{\mathbf{x} \in E: \|\mathbf{x}\| < R\}$. Since $e_i^* < 0$, we have for $\mathbf{x} \in K \cap \partial\Omega_R$,

$$\int_0^T K_i(t,s) \left(\frac{b_i(s)}{(x_1 + x_2)^{\alpha_i}} + e_i(s) \right) \mathrm{d}s \leq \int_0^T K_i(t,s) \left(\frac{b_i(s)}{(\sigma R)^{\alpha_i}} + e_i(s) \right) \mathrm{d}s < 0, \tag{42}$$

and subsequently, by (H4),

$$\begin{aligned} 0 \leq (\mathscr{A}_i \mathbf{x})(t) &= \int_0^T K_i(t,s) \big(k_i^2 x_i(s) + f_i(s, x_1(s), x_2(s)) + e_i(s) \big) \mathrm{d}s \\ &\leq \int_0^T K_i(t,s) \left(\frac{b_i(s)}{(x_1 + x_2)^{\alpha_i}} + e_i(s) + k_i^2 x_i(s) \right) \mathrm{d}s \\ &< k_i^2 \|x_i\|_{\infty} \int_0^T K_i(t,s) \mathrm{d}s = k_i^2 \frac{1}{k_i^2} \|x_i\|_{\infty} = \|x_i\|_{\infty}, \quad i = 1, 2, \end{aligned} \tag{43}$$

this yields $\|\mathscr{A}\mathbf{x}\| \leq \|\mathbf{x}\|, \forall \mathbf{x} \in K \cap \partial\Omega_R$.

By (H2) and $\widehat{b}_{i*} > 0$, there exists $r < R$ small enough such that, for any $\mathbf{x} = (x_1, x_2)$ satisfying $\sigma r \leq x_1 + x_2 \leq r$,

$$f_i(t, x_1, x_2) + e_i(t) \geq \frac{\widehat{b}_i(t)}{(x_1 + x_2)^{\alpha_i}} + e_i(t) \geq \frac{\widehat{b}_{i*}}{r^{\alpha_i}} + e_{i*} \geq 0, \tag{44}$$

which implies

$$f_i(t, x_1, x_2) + e_i(t) + k_i^2 x_i \geq k_i^2 x_i, \quad \sigma r \leq x_1 + x_2 \leq r. \tag{45}$$

Let $\Omega_r = \{\mathbf{x} \in E: \|\mathbf{x}\| < r\}$ and $\psi \equiv (1,1)^T \in K$; then,

$$\mathbf{x} \neq \mathscr{A}\mathbf{x} + \lambda\psi, \quad \forall \mathbf{x} \in K \cap \partial\Omega_r, \lambda > 0. \tag{46}$$

Otherwise, if there are $\mathbf{x}_0 = (x_{10}, x_{20}) \in K \cap \partial\Omega_r$ and $\lambda_0 > 0$ such that $\mathbf{x}_0 = \mathscr{A}\mathbf{x}_0 + \lambda_0\psi$, then from (45), it follows

$$\begin{aligned} x_{i0}(t) &= (\mathscr{A}_i \mathbf{x}_0)(t) + \lambda_0 \\ &= \int_0^T K_i(t,s) f_i\big(s, x_{10}(s), x_{20}(s) + e_i(s) + k_i^2 x_{i0}(s)\big) \mathrm{d}s + \lambda_0 \\ &\geq \int_0^T K_i(t,s) k_i^2 x_{i0}(s) \mathrm{d}s + \lambda_0. \end{aligned} \tag{47}$$

Setting $\Upsilon = \min_{t \in [0,T]} x_{i0}(t)$, we obtain from (47) that $\Upsilon \geq \Upsilon + \lambda_0$, which contradicts $\lambda_0 > 0$.

To apply Lemma 4, it remains to verify

$$\mathscr{A}\left(K \cap \left(\overline{\Omega}_R \backslash \Omega_r\right)\right) \subseteq K. \tag{48}$$

Using (H4), we can easily get

$$\begin{aligned} \|\mathscr{A}_i \mathbf{x}\|_{\infty} \leq M_i \int_0^T K_i(t,s) \big(& f_i(s, x_1(s), x_2(s)) + e_i(s) \\ & + k_i^2 x_i(s) \big) \mathrm{d}s, \quad i = 1, 2, \end{aligned} \tag{49}$$

and thus,

$$\begin{aligned}\left(\mathscr{A}_i\mathbf{x}\right)(t) &\geq m_i \int_0^T \left(f_i\left(s, x_1(s), x_2(s)\right) + e_i(s) + k_i^2 x_i(s)\right)\mathrm{d}s \\ &= \sigma_i M_i \int_0^T \left(f_i\left(s, x_1(s), x_2(s)\right) + e_i(s) + k_i^2 x_i(s)\right)\mathrm{d}s \\ &= \sigma_i \left\|\mathscr{A}_i\mathbf{x}\right\|_\infty, \quad i = 1, 2,\end{aligned} \tag{50}$$

which means (48) holds true.

Consequently, Lemma 4 ensures (40) has a positive T-periodic solution, and accordingly, system (38) admits a positive T-periodic solution. □

Remark 5. Many authors have paid their attention to the optimal control of the nonlinear systems, and a number of excellent results have been established. See, for instance, [20–23] and the references therein. For the optimal control of nonlinear system (1), we shall deal in the forthcoming paper.

Data Availability

Data sharing is not applicable to this article as no datasets were generated or analysed during the current study.

Conflicts of Interest

The authors declare that they have no conflicts of interest.

Acknowledgments

The corresponding author was supported by the National Natural Science Foundation of China (no. 61761002) and the NSF of Ningxia Hui Autonomous Region of China (nos. 2020AAC03232 and 2020AAC03234).

References

[1] R. P. Agarwal and D. O'Regan, "A coupled system of boundary value problems," *Applicable Analysis*, vol. 69, no. 3, pp. 381–385, 1998.

[2] R. P. Agarwal and D. O'Regan, "Multiple solutions for a coupled system of boundary value problems," *Dynamics of Continuous, Discrete and Impulsive Systems*, vol. 7, pp. 97–106, 2000.

[3] H. Lu, H. Yu, and Y. Liu, "Positive solutions for singular boundary value problems of a coupled system of differential equations," *Journal of Mathematical Analysis and Applications*, vol. 302, pp. 14–29, 2005.

[4] D. Jiang, J. Chu, and M. Zhang, "Multiplicity of positive periodic solutions to superlinear repulsive singular equations," *Journal of Differential Equations*, vol. 211, no. 2, pp. 282–302, 2005.

[5] P. J. Torres, "Weak singularities may help periodic solutions to exist," *Journal of Differential Equations*, vol. 232, no. 1, pp. 277–284, 2007.

[6] J. Chu and P. J. Torres, "Applications of schauder's fixed point theorem to singular differential equations," *Bulletin of the London Mathematical Society*, vol. 39, no. 4, pp. 653–660, 2007.

[7] J. Chu and M. Li, "Positive periodic solutions of hill's equations with singular nonlinear perturbations," *Nonlinear Analysis: Theory, Methods & Applications*, vol. 69, no. 1, pp. 276–286, 2008.

[8] A. Fonda and R. Toader, "Periodic orbits of radially symmetric keplerian-like systems: a topological degree approach," *Journal of Differential Equations*, vol. 244, no. 12, pp. 3235–3264, 2008.

[9] D. Franco and P. J. Torres, "Periodic solutions of singular systems without the strong force condition," *Proceedings of the American Mathematical Society*, vol. 136, pp. 1229–1236, 2008.

[10] X. Li and Z. Zhang, "Periodic solutions for second-order differential equations with a singular nonlinearity," *Nonlinear Analysis: Theory, Methods & Applications*, vol. 69, no. 11, pp. 3866–3876, 2008.

[11] Z. Cao and D. Jiang, "Periodic solutions of second order singular coupled systems," *Nonlinear Analysis: Theory, Methods & Applications*, vol. 71, no. 9, pp. 3661–3667, 2009.

[12] R. Ma, R. Chen, and Z. He, "Positive periodic solutions of second-order differential equations with weak singularities," *Applied Mathematics and Computation*, vol. 232, pp. 97–103, 2014.

[13] M. del Pino, R. Manásevich, and A. Montero, "T-periodic solutions for some second order differential equations with singularities," *Proceedings of the Royal Society of Edinburgh: Section A Mathematics*, vol. 120, no. 3, pp. 231–243, 1992.

[14] I. Rachunková, M. Tvrdý, and I. Vrkoc, "Existence of nonnegative and nonpositive solutions for second order periodic boundary value problems," *Journal of Differential Equations*, vol. 176, pp. 445–469, 2001.

[15] D. Bonheure and C. De Coster, "Forced singular oscillators and the method of lower and upper solutions," *Topological Methods in Nonlinear Analysis*, vol. 22, no. 2, pp. 297–317, 2003.

[16] R. Hakl and P. J. Torres, "Maximum and antimaximum principles for a second order differential operator with variable coefficients of indefinite sign," *Applied Mathematics and Computation*, vol. 217, no. 19, pp. 7599–7611, 2011.

[17] J. Chu, N. Fan, and P. J. Torres, "Periodic solutions for second order singular damped differential equations," *Journal of Mathematical Analysis and Applications*, vol. 388, no. 2, pp. 665–675, 2012.

[18] A. Cabada and J. Á. Cid, "On the sign of the green's function associated to hill's equation with an indefinite potential," *Applied Mathematics and Computation*, vol. 205, no. 1, pp. 303–308, 2008.

[19] K. Deimlimg, *Nonlinear Functional Analysis*, Springer, Berlin, Germany, 1985.

[20] S. He, H. Fang, M. Zhang, F. Liu, and Z. Ding, "Adaptive optimal control for a class of nonlinear systems: the online policy iteration approach," *IEEE Transactions on Neural Networks and Learning Systems*, vol. 31, no. 2, pp. 549–558, 2020.

[21] S. He, H. Fang, M. Zhang, F. Liu, X. Luan, and Z. Ding, "Online policy iterative-based H∞ optimization algorithm for a class of nonlinear systems," *Information Sciences*, vol. 495, pp. 1–13, 2019.

[22] S. He, M. Zhang, H. Fang, F. Liu, X. Luan, and Z. Ding, "Reinforcement learning and adaptive optimization of a class of Markov jump systems with completely unknown dynamic information," *Neural Computing and Applications*, vol. 32, no. 18, Article ID 14311, 2019.

[23] C. Wang, H. Fang, and S. He, "Adaptive optimal controller design for a class of LDI-based neural network systems with input time-delays," *Neurocomputing*, vol. 385, pp. 292–299, 2020.

Hindawi
Complexity
Volume 2020, Article ID 7643812, 10 pages
https://doi.org/10.1155/2020/7643812

Research Article

Fractional-Order Modeling and Analysis of a Variable Structure Hybrid Energy Storage System for EVs

Jianlin Wang,[1] **Dan Xu**,[2] **Jiahui Zhou**,[2] **and Jinlu Mao**[2]

[1]*School of Electrical Information Engineering, North Minzu University, Yinchuan, NingXia, China*
[2]*School of Mechanical Engineering, Xi'an Jiaotong University, Xi'an, Shaanxi, China*

Correspondence should be addressed to Dan Xu; xudan@xjtu.edu.cn

Received 16 June 2020; Revised 12 November 2020; Accepted 25 November 2020; Published 9 December 2020

Academic Editor: Shuping He

Hybrid energy storage system has been widely studied as an important technology for electric vehicles. Since the hybrid energy storage system is a nonlinear and complex system, the modeling of the system and the high-precision nonlinear control strategy are technical difficulties for research. The establishment of a high-precision mathematical model of the hybrid energy storage system is the basis for the study of high-quality nonlinear control algorithms. Fortunately, the theory of fractional calculus can help build accurate mathematical models of hybrid energy storage systems. In order to obtain the high-quality nonlinear control strategy of this complex system, this paper, respectively, carried out fractional-order modeling and analysis on the three basic equivalent working states of the hybrid energy storage system of electric vehicles. Among them, the fractional-order average state space model is carried out for the equivalent Buck and Boost mode. Also, the steady-state analysis of the equivalent Dual-Boost mode is carried out by combining the fractional-order calculus theory with the equivalent small parameter variable method. Finally, the effectiveness and precision of the fractional-order model are proved by simulation and experiment.

1. Introduction

The hybrid energy storage system (HESS) of electric vehicles, that is, the composite power supply technology, is a combination of two or more energy sources to form a power system for electric vehicles [1, 2] . Generally, the overall performance of electric vehicles is improved by complementing the advantages of various energy sources, which is a relatively advanced technology in the field of electric vehicles. As we all know, the hybrid energy storage system contains two or more power supplies, and there are also multiple DC-DC converters with strong nonlinear characteristics, which make the design of the control strategy for the hybrid energy storage system difficult. In order to be able to design high-performance control strategies, it is necessary to carry out topology design and high-precision system modeling for hybrid energy storage systems.

The topology of a HESS is generally passive, semiactive, active, or cascaded. It is all well known, and each topology of HESS has obvious advantages and disadvantages [3]. In order to integrate the advantages of various topologies, a new variable structure HESS has been proposed, which can realize the function of battery/supercapacitor (SC) semiactive structure, SC/battery semiactive structure, and fully active structure. The topology of the new variable structure HESS is shown in Figure 1. It mainly has three working states; that is, it works in the Buck mode when the SC absorbs the braking energy; it works in the Boost mode when the SC or the battery is outputting separately; and it works in the Dual-Boost mode when the SC and the battery are outputting together.[4, 5].

The control problem of this nonlinear complex system is a difficult point, but there are some research results that can be used. For example, the sliding mode control method is used to control the DC-DC converter to implement power distribution, and the convergence time of the positive Markov neural network is optimized [6–8], and the fractional calculus theory is used to perform fractional control to obtain high performance [9]. However, the accuracy of these control strategies needs to be based on a high-precision

system model, and the design of HESS for electric vehicles is diverse so that there are relatively few studies on the modeling of variable structure HESS for electric vehicles.

An accurate mathematical model for the equivalent DC-DC converter system corresponding to each working state is the basis for applying the variable structure HESS use in electric vehicles. Considering the nondualities of commercial inductors, it is difficult to describe such circuit components with long-memory characteristics using conventional integer-order calculus. Fortunately, the fractional-order theory is gradually maturing, and in the past decade, fractional-order calculus has been applied in almost all fields of science, engineering, and mathematics. Concepts from fractional-order circuits and systems have attracted much attention from the electrical engineering community. Some research results prove that the fractional-order model has higher precision than the integer-order model in mathematical modeling of nonlinear circuit systems, and the integer-order model is a special case of the fractional-order model [10]. Therefore, this article focuses on the fractional-order modeling research on the three working states of the variable structure HESS.

The volt-ampere characteristics of fractional inductor and capacitor shown in Figure 1 can be described as

$$v_{L1} = L\frac{d^{\alpha} i_{L1}}{\mathrm{d}t^{\alpha}},$$
$$v_{L2} = L\frac{d^{\beta} i_{L2}}{\mathrm{d}t^{\beta}}, \tag{1}$$
$$i_C = C\frac{d^{\gamma} v_C}{\mathrm{d}t^{\gamma}},$$

where α is the order of the fractional inductor L_1, β is the order of the fractional inductor L_2, and γ is the order of the fractional capacitor C, respectively [11].

In this article, the fractional-order modeling of equivalent DC-DC converters corresponding to the three working states of the variable structure HESS is mainly based on the fractional-order characteristics of inductors and capacitors. The rest of this manuscript is organized as follows: Section 2 introduces the fractional-order modeling of the equivalent Buck converter for braking energy recovery. Section 3 introduces the fractional-order modeling of the equivalent Boost converter for power output. Section 4 introduces the steady-state analysis of the dual-Boost output mode based on the fractional-order equivalent small parameter variable method. In Section 5, simulations and experiments are performed to verify the fractional-order mode. Finally, conclusions are given in Section 6.

2. Fractional-Order Modeling of Equivalent Buck Converter for Braking Energy Recovery

From the working principle of the variable structure HESS, it is known that when the electric vehicle brakes to produce energy, it is absorbed by the SC alone. In this mode of operation, the equivalent Buck converter of the variable structure HESS is shown in Figure 2. The input voltage is

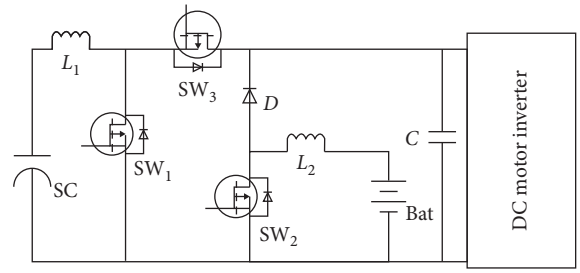

Figure 1: Topology of the variable structure HESS.

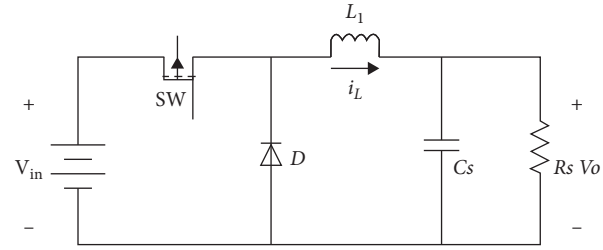

Figure 2: Equivalent Buck converter of the variable structure HESS.

equivalent to the voltage of the motor inverter, the load is the internal resistance of the SC, and the capacitance is the equivalent capacitance of the SC.

The equivalent Buck converter has two main operating states. The operating state 1 is that the switch SW is closed; that is, the capacitor is charged; the operating state 2 is that the switch SW is open; that is, the capacitor is discharged. Throughout one duty cycle period, the inductor voltage can be defined as

$$v_L = \begin{cases} v_{\mathrm{in}} - v_o, & 0 < t < \mathrm{d}T, \\ -v_o, & \mathrm{d}T < t < T. \end{cases} \tag{2}$$

The average current of the inductor current over the entire period can be described as

$$\langle i_{L1}(t,\alpha)\rangle_T = \frac{1}{T}\int_t^{t+T} i_{L1}(\tau,\alpha)\mathrm{d}\tau. \tag{3}$$

The average inductor current also can be converted into a form by fractional-order calculation as follows:

$$\frac{d^{\alpha}\langle i_{L1}(t,\alpha)\rangle_T}{\mathrm{d}t^{\alpha}} = \frac{1}{T}\int_t^{t+T}\left(\frac{d^{\alpha} i_{L1}(t,\alpha)}{\mathrm{d}\tau^{\alpha}}\right)\mathrm{d}\tau = \langle\frac{d^{\alpha} i_{L1}(t,\alpha)}{\mathrm{d}t^{\alpha}}\rangle, \tag{4}$$

where $\langle i_{L1}(t,\alpha)\rangle$ is the superposition of the AC component under the influence of the DC component and the high-frequency switching harmonics. Similarly, the input voltage, output voltage, inductor current, and switching duty cycle in an equivalent Buck converter can be considered as a superposition of the DC component and the interference component [12, 13].

Assume that the equivalent capacitance of the SC also has a fractional-order characteristic, and the order is defined

as ρ. A fractional-order average state space model can be established for equivalent Buck converter.

When $t \in [0, \mathrm{d}T]$, the equation of state for the equivalent Buck converter is

$$\begin{aligned} \frac{d^{\alpha}\langle i_{L1}\rangle}{\mathrm{d}t^{\alpha}} &= \frac{1}{L_1}\left(\langle v_{in}\rangle - \langle v_o\rangle\right), \\ \frac{d^{\rho}\langle v_o\rangle}{\mathrm{d}t^{\rho}} &= \frac{1}{C_s}\left(\langle i_{L1}\rangle - \frac{\langle v_o\rangle}{R_s}\right). \end{aligned} \tag{5}$$

When $t \in [dT, T]$, the equation of state for the equivalent Buck converter is

$$\begin{aligned} \frac{d^{\alpha}\langle i_{L1}\rangle}{\mathrm{d}t^{\alpha}} &= -\frac{1}{L_1}\left(\langle v_o\rangle\right), \\ \frac{d^{\rho}\langle v_o\rangle}{\mathrm{d}t^{\rho}} &= \frac{1}{C_s}\left(\langle i_{L1}\rangle - \frac{\langle v_o\rangle}{R_s}\right). \end{aligned} \tag{6}$$

Introducing the duty cycle function in equations (5) and (6), the fractional-order average state model of the equivalent Buck circuit is obtained, as

$$\begin{bmatrix} \dfrac{d^{\alpha}\langle i_{L1}\rangle}{\mathrm{d}t^{\alpha}} \\ \dfrac{d^{\rho}\langle v_o\rangle}{\mathrm{d}t^{\rho}} \end{bmatrix} = \begin{bmatrix} 0 & -\dfrac{1}{L_1} \\ \dfrac{1}{C_s} & -\dfrac{1}{R_sC_s} \end{bmatrix} \begin{bmatrix} \langle i_{L1}\rangle \\ \langle v_o\rangle \end{bmatrix} + \begin{bmatrix} \dfrac{\langle d\rangle}{L_1} \\ 0 \end{bmatrix} \langle v_{\mathrm{in}}\rangle. \tag{7}$$

Based on the fractional-order Laplace transform method [6], the Laplace transform of equation (7) is obtained:

$$\begin{bmatrix} s^{\alpha}\langle i_{L1}(s)\rangle \\ s^{\rho}\langle v_o(s)\rangle \end{bmatrix} = \begin{bmatrix} 0 & -\dfrac{1}{L_1} \\ \dfrac{1}{C_s} & -\dfrac{1}{R_sC_s} \end{bmatrix} \begin{bmatrix} \langle i_{L1}(s)\rangle \\ \langle v_o(s)\rangle \end{bmatrix} + \begin{bmatrix} \dfrac{\langle d(s)\rangle}{L_1} \\ 0 \end{bmatrix} \langle v_{\mathrm{in}}(s)\rangle. \tag{8}$$

The transfer function of the output voltage to the input voltage is obtained by equation (8) as

$$G_V(s) = \frac{v_o(s)}{v_{\mathrm{in}}(s)}\Big|_{\widehat{d}(s)=0} = \frac{(D/L_1C_S)}{s^{\alpha\rho} + (1/R_SC_S)s^{\alpha} + (1/L_1C_S)}. \tag{9}$$

Assuming that the input and output voltages are constant during the cycle, we can obtain the input and output energies as

$$\begin{aligned} E_{\mathrm{in}} &= v_{\mathrm{in}} \int_0^{\mathrm{d}T} i_{L1}(\tau, \alpha)\mathrm{d}\tau, \\ &= v_{\mathrm{in}}\left[\mathrm{d}T i_R + \frac{(v_{\mathrm{in}} - v_o)}{L_1\Gamma(\alpha+1)}T^{\alpha+1}d\left(d^{\alpha} - d\right)\right], \\ E_o &= v_o\left(\int_0^{\mathrm{d}T} i_{L1}(\tau, \alpha)\mathrm{d}\tau + \int_{\mathrm{d}T}^{T} i_{L2}(\tau, \alpha)\mathrm{d}\tau\right), \\ &= v_o\left[T i_R + \frac{\left(d^{\alpha+1} - d\right)v_{in} + (1-d)^{\alpha}}{L_1\Gamma(\alpha+2)}T^{\alpha+1}\right]. \end{aligned} \tag{10}$$

At steady state, the average energy efficiency is

$$\eta = \frac{E_o}{E_m} = \frac{d}{\left(1-(1-d)^{\alpha}\right)i_R}\left[i_R - \frac{v_{\mathrm{in}}T^{\alpha}(1-d)^{\alpha}\left(d^{\alpha} - d\right)}{L_1\Gamma(\alpha+2)}\right]. \tag{11}$$

3. Fractional-Order Modeling of Equivalent Boost Converter for Power Output

When the power demand of the electric vehicle is positive, the variable structure HESS works in the Boost mode and boosts the voltage of the battery or the SC for output. In this working state, the equivalent Boost converter of the variable structure HESS is shown in Figure 3. The input voltage v_{in} is equivalent to the voltage of the battery or SC, and the load is the motor inverter. In this section, the battery boost output is chosen as an example to illustrate the fractional-order modeling and analysis of the Boost mode.

Similar to the equivalent Buck converter, the equivalent Boost converter also contains two operating states. In one duty cycle, the inductor voltage can be described as

$$v_L = \begin{cases} v_{\mathrm{in}}, & 0 < t < \mathrm{d}T, \\ v_{\mathrm{in}} - v_o, & \mathrm{d}T < t < T. \end{cases} \tag{12}$$

When $t \in [0, \mathrm{d}T]$, the equation of state for the equivalent Boost converter is

$$\begin{aligned} \frac{d^{\beta}\langle i_{L2}\rangle}{\mathrm{d}t^{\beta}} &= \frac{1}{L_2}\langle v_{\mathrm{in}}\rangle, \\ \frac{d^{\gamma}\langle v_o\rangle}{\mathrm{d}t^{\gamma}} &= \frac{1}{RC}\langle v_o\rangle. \end{aligned} \tag{13}$$

When $t \in [\mathrm{d}T, T]$, the equation of state for the equivalent Boost converter is

$$\begin{aligned} \frac{d^{\beta}\langle i_{L2}\rangle}{\mathrm{d}t^{\beta}} &= \frac{1}{L_2}\left(\langle v_{in}\rangle - \langle v_o\rangle\right), \\ \frac{d^{\gamma}\langle v_o\rangle}{\mathrm{d}t^{\gamma}} &= \frac{1}{C}\left(\langle i_{L2}\rangle - \frac{\langle v_o\rangle}{R}\right). \end{aligned} \tag{14}$$

Introducing the duty cycle function in equations (13) and (14), the fractional-order average state model of the equivalent Buck circuit is obtained, as

$$\begin{bmatrix} \dfrac{d^{\beta}\langle i_L\rangle}{\mathrm{d}t^{\beta}} \\ \dfrac{d^{\gamma}\langle v_o\rangle}{\mathrm{d}t^{\gamma}} \end{bmatrix} = \begin{bmatrix} 0 & -\dfrac{1-\langle d\rangle}{L_2} \\ \dfrac{1-\langle d\rangle}{C} & -\dfrac{1}{RC} \end{bmatrix} \begin{bmatrix} \langle i_{L2}\rangle \\ \langle v_o\rangle \end{bmatrix} + \begin{bmatrix} \dfrac{1}{L_2} \\ 0 \end{bmatrix} \langle v_{\mathrm{in}}\rangle. \tag{15}$$

Based on the fractional-order Laplace transform method, the Laplace transform of equation (15) is obtained:

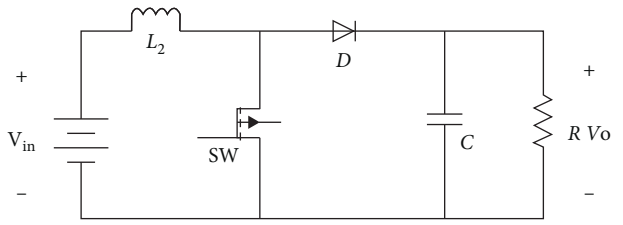

Figure 3: Equivalent Boost converter of the variable structure HESS.

$$\begin{bmatrix} s^{\beta}\langle i_{L2}(s)\rangle \\ s^{\gamma}\langle v_o(s)\rangle \end{bmatrix} = \begin{bmatrix} 0 & -\dfrac{1-\langle d(s)\rangle}{L_2} \\ \dfrac{1-\langle d(s)\rangle}{C} & -\dfrac{1}{RC} \end{bmatrix} \begin{bmatrix} \langle i_{L2}(s)\rangle \\ \langle v_o(s)\rangle \end{bmatrix} + \begin{bmatrix} \dfrac{1}{L_2} \\ 0 \end{bmatrix} \{\langle v_{in}(s)\}. \tag{16}$$

The transfer function of the output voltage to the input voltage is obtained by equation (16) as

$$G_V(s) = \frac{\langle v_o(s)\rangle}{\langle v_{in}(s)\rangle}\Big|_{\widehat{d}(s)=0} = \frac{\left(1 - D/L_2C\right)}{s^{\beta+\gamma} + (1/RC)s^{\beta} + \left((1-D)^{\beta}/LC\right)}. \tag{17}$$

Assuming that the input and output voltages are constant during the cycle, we can obtain the input and output energies as

$$\begin{aligned} E_{in} &= v_{in}\left[\int_0^{dT} i'_{L2}(\tau,\beta)d\tau + \int_{aT}^{T} i''_{L2}(\tau,\beta)d\tau\right], \\ &= \frac{v_{in}T}{1-d}\left[i_R - \frac{v_{in}T^{\beta}\left(1-d+d^2-d^{\beta+1}\right) - v_oT^{\beta}(1-d)^{\beta+1}}{L_2\Gamma(\beta+2)}\right], \\ E_o &= v_o\int_{aT}^{T} i''_{L2}(\tau,\beta)d\tau = v_oi_RT = \frac{v_{in}i_RT}{1-d^{\beta}}. \end{aligned} \tag{18}$$

At steady state, the average energy efficiency is

$$\eta = \frac{E_o}{E_{in}} = \frac{1-d^{\beta}}{1-d}\left[1 - \frac{v_{in}T^{\beta}\left(1-d+d^2-d^{\beta+1}\right) - v_o(1-d)^{\beta+1}}{L_2\Gamma(\beta+2)i_R}\right]. \tag{19}$$

4. Fractional-Order Modeling and Steady-State Analysis for Dual-Boost Output Mode

When the state of the battery and the SC are not in an extreme state, the variable structure HESS is often operating in a common output mode. In this mode, the switch SW3 is turned off, and the variable structure HESS can be equivalent to the dual-Boost parallel output. The equivalent DC-DC converter is shown in Figure 4. Such a parallel output circuit system has high requirements for the design of the control algorithm and the implementation of the power allocation strategy.

The state space averaging has many advantages in modeling, but not enough precision. It cannot perform steady-state analysis of this type of circuitry, especially ripple analysis. The equivalent small parameter variable method is a high-precision symbol analysis method combining the disturbance analysis method and the harmonic balance method [4]. This method does not need to introduce small parameter quantities, which has certain advantages for the ripple analysis of nonlinear high-order systems [14, 15].

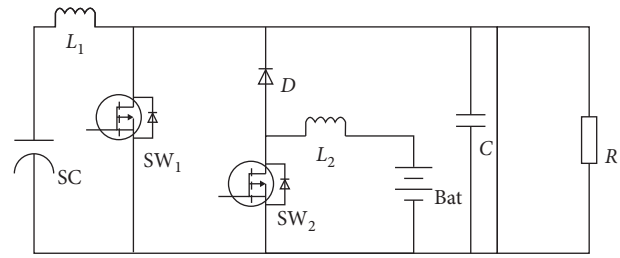

Figure 4: Equivalent dual-Boost converter of variable structure HESS.

Considering the fractional-order characteristics of the capacitor and inductor in the circuit system shown in Figure 4, the results of the circuit analysis are

$$\begin{cases} \dfrac{d^{\alpha}i_{L1}}{dt^{\alpha}} = \dfrac{V_{SC}}{L_1} - \dfrac{v_C}{L_1}, \\ \dfrac{d^{\beta}i_{L2}}{dt^{\beta}} = \dfrac{V_{Bat}}{L_2} - \dfrac{v_C}{L_2}, \\ \dfrac{d^{\gamma}v_C}{dt^{\gamma}} = \dfrac{\left(i_{L_1} + i_{L_2}\right)}{C} - \dfrac{v_C}{R}. \end{cases} \tag{20}$$

The state equation of the dual-PWM switch Boost equivalent circuit system is described as

$$G_0\left(p^{\alpha} \quad p^{\beta} \quad p^{\gamma}\right)x + G_1f^{(1)}(x) + G_2f^{(2)}(x) = U, \tag{21}$$

where $x = [i_{L1}\, i_{L2}\, v_C]^T$, $G_0 = \begin{bmatrix} p^{\alpha} & 0 & (1/L_1) \\ 0 & p^{\beta} & (1/L_2) \\ -(1/C) & -(1/C) & p^{\gamma} + (1/RC) \end{bmatrix}$, $G_1 = \begin{bmatrix} 0 & 0 & -(1/L_1) \\ 0 & 0 & 0 \\ (1/C) & 0 & 0 \end{bmatrix}$, $G_2 = \begin{bmatrix} 0 & 0 & 0 \\ 0 & 0 & -(1/L_2) \\ 0 & (1/C) & 0 \end{bmatrix}$, $U = \begin{bmatrix} (V_{SC}/L_1) \\ (V_{Bat}/L_2) \\ 0 \end{bmatrix}$, $p^{\alpha} = D^{\alpha}$ is fractional calculus operator, $f^{(1)}(x) = \delta^{(1)}(t)x$, $f^{(2)}(x) = \delta^{(2)}(t)x$, and $\delta(t)$ is the pulse function.

State variable x and $\delta(t)$ pulse function are, respectively, expanded into a series form of a sum of a main component and a small component, that is,

$$x = x_0 + \sum_{i=1}^{\infty} \varepsilon^i x_i, \tag{22}$$

$$\delta^{(n)}(t) = \delta_0^{(n)} + \sum_{i=1}^{\infty} \varepsilon^i \delta_i^{(n)}. \tag{23}$$

Substituting equations (22) and (23) into equation (21), we get

$$f^{(n)}\left(\delta^{(n)}, x\right) = f_0^{(n)} + \sum_{i=1}^{\infty} \varepsilon^i f_i^{(n)}, \tag{24}$$

where i is the order of the harmonics and x_i, δ_i, and f_i are the i-th order components of x, $\delta(x)$, and $f(x)$. ε is a small component symbol, which only means that x_i is much smaller than x.

The Fourier series of x_0 and $x_{i(i\geq 1)}$ are expanded to

$$\begin{aligned} x_0 &= \sum_{k\in E_0} x_{k0} = a_{00}, \\ x_i &= \sum_{k\in E_{ir}} x_{kj} = a_{0i} + \sum_{k\in E_{ir}} \left[a_{ki} e^{jk\tau} + \overline{a}_{ki} e^{-jk\tau}\right], \end{aligned} \tag{25}$$

where $\tau = \omega t = (2\pi t/T)$, a_{0t} is the DC component of x_i, and a_{ki} is the k-th order amplitude of the i-th harmonic. $\{E_0\}$ is the spectrum set of the state vector x_0, and $\{E_{ir}\}$ is the spectrum set of the correction x_i during the iterative calculation.

Furthermore, the Fourier series expansion of the $\delta_0^{(n)}$ and $\delta_{i(i\geq 1)}^{(n)}$ is

$$\begin{aligned} \delta_0^{(n)} &= b_0^{(n)} + b_1^{(n)} e^{jr} + \overline{b}_1^{(n)} e^{-jt}, \\ \delta_i^{(n)} &= b_{2i}^{(n)} e^{j2i\tau} + b_{2i+1}^{(n)} e^{j(2i+1)\tau} + \overline{b}_{2i}^{(n)} e^{-j2i\tau} + \overline{b}_{2i+1}^{(n)} e^{-j(2i+1)\tau}, \end{aligned} \tag{26}$$

where $b_0^{(n)} = 1/T \int_0^T \delta^{(n)}(t)\mathrm{d}t = d^{(n)}$ and $b_i^{(n)} = 1/2\,(a_i^{(n)} - j\beta_i^{(n)})$.

Furthermore, equation (20) can be rewritten as

$$\begin{cases} f_0^{(n)} = \delta_0^{(n)} x_0, \\ f_1^{(n)} = \delta_0^{(n)} x_1 + \delta_1^{(n)} x_0, \\ f_2^{(n)} = \delta_0^{(n)} x_2 + \delta_1^{(n)} x_1 + \delta_2^{(n)} x_0, \\ \cdots. \end{cases} \tag{27}$$

Expand the function $f_i^{(n)}(x)$ into the series form of the sum of the main and small components, which can be expressed as

$$f_i^{(n)} = f_{i=1}^{(n)} + \varepsilon R_{i+1}, \quad (i = 0, 1, 2, \ldots,). \tag{28}$$

When $i = 0$, $f_{0m}^{(n)}$ is the main component of $f_0^{(n)}$, which is the same as the spectrum of x_0, and R_1 is the remaining high-order small components. According to the spectrum of R_1, the frequency set of can be determined. Similarly, the frequency set of $f_{0m}^{(n)}$ can be determined according to the spectrum of $f_{im}^{(n)}$. $f_{0m}^{(n)}$, $f_{im}^{(n)}$, and R_i in equation (28) are

$$\begin{aligned} f_{0m}^{(n)} &= h_{00} + \sum_{k\in E_0} \left(h_{\Sigma 0} e^{jk\tau} + \overline{h}_{k0} e^{-jkz}\right), \\ f_{im}^{(n)} &= h_{0i} + \sum_{k\in E_{ir}} \left(h_{ki} e^{jkr} + \overline{h}_{ki} e^{-jk\tau}\right), \\ R_i &= g_{0i} + \sum_{k\in E_{ir}} \left(g_{ki} e^{jk\tau} + \overline{g}_{ki} e^{-jk\tau}\right), \end{aligned} \tag{29}$$

where h_{00}, h_{0i}, and g_{0i} are all DC components. Substitute the above equation into equation (28) to get the following equation:

$$f^{(n)} = \left(f_{0m}^{(n)} + \varepsilon f_{1m}^{(n)} + \varepsilon^2 f_{2m}^{(n)} + \ldots\right) + \left(\varepsilon R_1 + \varepsilon^2 R_2 + \ldots\right). \tag{30}$$

According to the above analysis, the principal component of the steady-state solution is DC, and the principal component of the state variable is defined as

$$x_0 = a_{00} = \left[\, I_{L_1 00} I_{L_2 00} V_{C00} \,\right]^T. \tag{31}$$

Considering that there is no derivative change in the DC component of the system, let $G_{00} = G_0\left(\, 0^{\alpha} \;\; 0^{\beta} \;\; 0^{\gamma} \,\right)$, and we can get

$$\begin{bmatrix} 0 & 0 & \dfrac{1-d^{(1)}}{L_1} \\ 0 & 0 & \dfrac{1-d^{(2)}}{L_2} \\ -\dfrac{1-d^{(1)}}{C} & -\dfrac{1-d^{(2)}}{C} & \dfrac{1}{RC} \end{bmatrix} \cdot \begin{bmatrix} I_{L_1\infty} \\ I_{L_2 00} \\ V_{C00} \end{bmatrix} = \begin{bmatrix} \dfrac{V_{SC}}{L_1} \\ \dfrac{V_{\mathrm{Bat}}}{L_2} \\ 0 \end{bmatrix}. \tag{32}$$

Solving equation (32) can obtain the steady-state solution of the main oscillation component, and we can get

$$\begin{cases} V_{C00} = \dfrac{V_{SC}}{1-d^{(1)}} = \dfrac{V_{\mathrm{Bat}}}{1-d^{(2)}}, \\ I_{L,00} = \dfrac{V_{SC}}{2R\left(1-d^{(1)}\right)^2}, \\ I_{L_2 00} = \dfrac{V_{\mathrm{Bat}}}{2R\left(1-d^{(2)}\right)^2}. \end{cases} \tag{33}$$

The first-order correction contains only the fundamental component, so suppose

$$x_1 = a_{11} e^{j\tau} + \overline{a}_{11} e^{-j\tau}, \tag{34}$$

where $a_{11} = \left[\, I_{L_1 11} \;\; I_{L_2 11} \;\; V_{C11} \,\right]^T$ and $I_{L_1 11}$, $I_{L_2 11}$, and V_{C11} are the first-order amplitude small components of the first harmonics of $i_{L_1 11}$, $i_{L_2 11}$, and v_{C11}, respectively. Substituting equation (34) into equation (30), we get

$$\begin{aligned} f_{1m}^{(1)} &= b_0^{(1)}\left(a_{11} e^{j\tau} + \overline{a}_{11} e^{-j\tau}\right), \\ f_{1m}^{(2)} &= b_0^{(2)}\left(a_{11} e^{j\tau} + \overline{a}_{11} e^{-j\tau}\right), \\ R_1^{(1)} &= a_{11}\left(b_1^{(1)} e^{j\tau} + \overline{b}_1^{(1)} e^{-j\tau}\right), \\ R_1^{(2)} &= a_{11}\left(b_1^{(2)} e^{j\tau} + \overline{b}_1^{(2)} e^{-j\tau}\right). \end{aligned} \tag{35}$$

According to the calculation principle of fractional calculus, $p^{\alpha}e^{j\omega t} = (j\omega)^{\alpha}e^{j\omega t}$, $p^{\beta}e^{j\omega t} = (j\omega)^{\beta}e^{j\omega t}$, and $p^{\gamma}e^{j\omega t} = (j\omega)^{\gamma}e^{j\omega t}$. [16] The first-order correction amount that can be calculated is

$$\begin{cases} V_{C11} \approx \dfrac{b_1\left((j\omega)^{\alpha}L_1 I_{L,00} + (j\omega)^{\beta}L_2 I_{L_2 00} - (1-d\prime)V_{C00}\right)}{\Delta(j\omega)}, \\ I_{L_{11}} = \dfrac{b_1 V_{C00} - \left(1-d^{(1)}\right)V_{C11}}{(j\omega)^{\alpha}L_1}, \\ I_{L_2 11} = \dfrac{b_1 V_{C00} - \left(1-d^{(2)}\right)V_{C11}}{(j\omega)^{\beta}L_2}. \end{cases} \tag{36}$$

According to the above calculation principle, $E_{ir} = \{0, 2, 3\}$ is known; then, we suppose

$$x_2 = a_{02} + \left(a_{22}e^{j2\tau} + \overline{a}_{22}e^{-j2\tau} + a_{32}e^{j3\tau} + \overline{a}_{32}e^{-j3\tau}\right), \tag{37}$$

where $a_{02} = \left[\, I_{L_1 02} \;\; I_{L_2 02} \;\; V_{C02} \,\right]^T$ is the second-order correction of the DC component and $a_{22} = \left[\, I_{L_1 22} \;\; I_{L_2 22} \;\; V_{C22} \,\right]^T$ and $a_{32} = \left[\, I_{L_1 32} \;\; I_{L_2 32} \;\; V_{C32} \,\right]^T$ are the higher-order components of the second harmonic, respectively.

Substituting equation (37) into equation (30), after ignoring the high-order small component of the second harmonic, we can get

$$\begin{aligned} f_{2m}^{(1)} &\approx b_0^{(1)}a_{02} + \left(b_0^{(1)}a_{22} + b_3^{(1)}\overline{a}_{11}\right)e^{j2\tau} \\ &\quad + \left(b_0^{(1)}a_{32} + b_1^{(1)}a_{22} + b_2^{(1)}a_{11}\right)e^{j3t} + c.c, \\ f_{2m}^{(2)} &\approx b_0^{(2)}a_{02} + \left(b_0^{(2)}a_{22} + b_3^{(2)}\overline{a}_{11}\right)e^{j2t} \\ &\quad + \left(b_0^{(2)}a_{32} + b_1^{(2)}a_{22} + b_2^{(2)}a_{11}\right)e^{j3t} + c.c. \end{aligned} \tag{38}$$

Furthermore, the second-order correction of the DC component and the higher-order component of the second-order harmonic can be obtained:

$$\begin{cases} V_{C02} = \dfrac{\left(\overline{b}_1 V_{C11} + b_1 \overline{V}_{C11}\right)}{(1-d')}, \\ I_{L_1 02} = \dfrac{V_{C02}}{2R\left(1-d^{(1)}\right)}, \\ I_{L_2 02} = \dfrac{2V_{C02}}{2R\left(1-d^{(2)}\right)}, \end{cases}$$

$$\begin{cases} V_{C22} = \dfrac{(1-d)\left(b_1 V_{C11} + b_2 V_{C00} + b_3 \overline{V}_{C11}\right)}{\Delta(j2\omega)} - \\ \dfrac{(j2\omega)^{\alpha}L_1\left(b_1 I_{L_1 11} + b_2 I_{L_1 00} + b_3 \overline{I}_{L_1 11}\right) + (j2\omega)^{\beta}L_2\left(b_1 I_{L_2 11} + b_2 I_{L_2 00} + b_3 \overline{I}_{L_2 11}\right)}{\Delta(j2\omega)}, \\ I_{L_1 22} = \dfrac{\left(b_1 V_{C11} + b_2 V_{C00} + b_3 \overline{V}_{C11}\right) - \left(1-d^{(1)}\right)V_{C22}}{(j2\omega)^{\alpha}L_1}, \\ I_{L_2 22} = \dfrac{\left(b_1 V_{C11} + b_2 V_{C00} + b_3 \overline{V}_{C11}\right) - \left(1-d^{(2)}\right)V_{C22}}{(j2\omega)^{\beta}L_2}, \end{cases} \tag{39}$$

$$\begin{cases} V_{C32} = \dfrac{(1-d)\left(b_1 V_{C22} + b_2 V_{C11} + b_3 \overline{V}_{C00}\right)}{\Delta(j3\omega)} - \\ \dfrac{(j3\omega)^{\alpha}L_1\left(b_1 I_{L_1 22} + b_2 I_{L_1 11} + b_3 \overline{I}_{L_1 00}\right) + (j3\omega)^{\beta}L_2\left(b_1 I_{L_2 22} + b_2 I_{L_2 11} + b_3 \overline{I}_{L_2 00}\right)}{\Delta(j3\omega)}, \\ I_{L_1 32} = \dfrac{\left(b_1 V_{C22} + b_2 V_{C11} + b_3 \overline{V}_{C00}\right) - \left(1-d^{(1)}\right)V_{C23}}{(j3\omega)^{\alpha}L_1}, \\ I_{L_2 32} = \dfrac{\left(b_1 V_{C22} + b_2 V_{C11} + b_3 \overline{V}_{C00}\right) - \left(1-d^{(2)}\right)V_{C23}}{(j3\omega)^{\beta}L_2}. \end{cases}$$

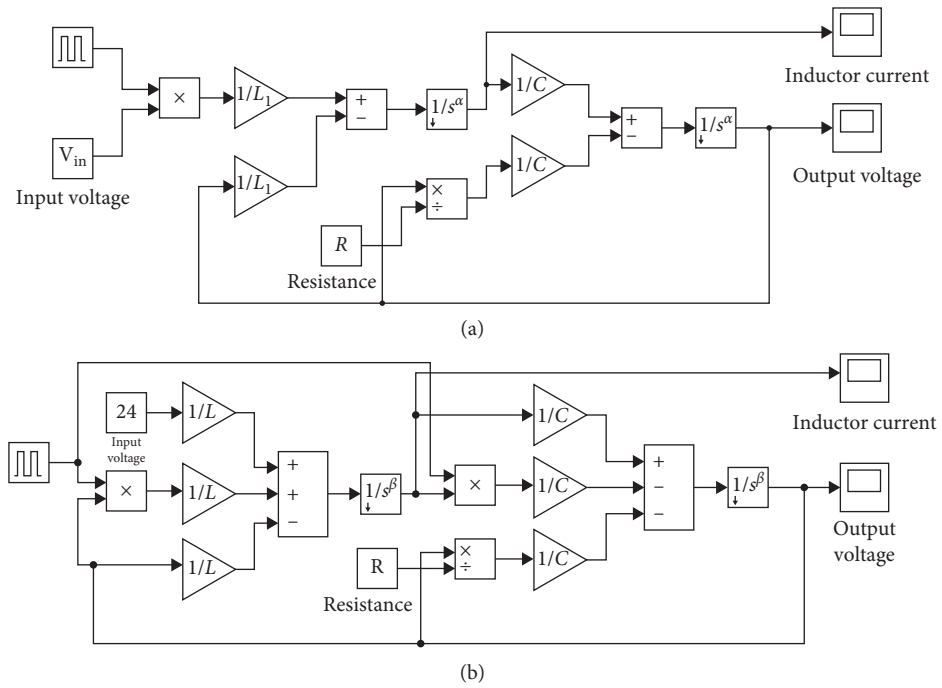

Figure 5: Fractional-order simulation of equivalent DC-DC converter: (a) Buck converter; (b) Boost converter.

Using the principle of harmonic balance, it is possible to approximate $a_{00}, a_{11}, a_{02}, a_{22}, a_{32}$. Thereby, a steady-state periodic solution of the system of equation (25) is obtained, which includes a DC solution and a ripple solution, as

$$\begin{aligned} i_{L_1} &\approx I_{L_100} + I_{L_102} + 2\big(\mathrm{Re}I_{L_111}\cos\tau - \mathrm{Im}I_{L_111}\sin\tau, \\ &\quad + \mathrm{Re}I_{L_122}\cos\tau - \mathrm{Im}I_{L_122}\sin\tau, \\ &\quad + \mathrm{Re}I_{L_132}\cos\tau - \mathrm{Im}I_{L_132}\sin\tau, \\ i_{L_2} &\approx I_{L_200} + I_{L_202} + 2\big(\mathrm{Re}I_{L_211}\cos\tau - \mathrm{Im}I_{L_211}\sin\tau, \\ &\quad + \mathrm{Re}I_{L_222}\cos\tau - \mathrm{Im}I_{L_222}\sin\tau, \\ &\quad + \mathrm{Re}I_{L_232}\cos\tau - \mathrm{Im}I_{L_232}\sin\tau, \\ v_C &\approx V_{C00} + V_{C02} + 2\big(\mathrm{Re}V_{C11}\cos\tau - \mathrm{Im}V_{C11}\sin\tau, \\ &\quad + \mathrm{Re}V_{C22}\cos\tau - \mathrm{Im}V_{C22}\sin\tau, \\ &\quad + \mathrm{Re}V_{C32}\cos\tau - \mathrm{Im}V_{C32}\sin\tau. \end{aligned} \tag{40}$$

5. Simulation

In order to verify the validity and accuracy of the fractional-order average state space model and the fractional-order equivalent small parameter variable method, simulation studies are implemented in MATLAB2018b [17]. The values of the main parameters of the variable structure HESS L_1, L_2, C, and R are set to 100μH, 100μH, 470μF, and 10Ω, respectively.

According to the fractional average state space model of the equivalent Buck converter and the equivalent Boost converter, the corresponding mathematical simulation models were established in MATLAB2018b/Simulink, as shown in Figure 5. In the open-loop simulation of the equivalent buck converter fractional-order model, the input voltage is set to 24V, the duty cycle is set to 0.7, and the order is chosen to be 0.8, 0.9, and 1, respectively. The simulation results are shown in Figure 6(a) and Figure 6(b). In the open-loop simulation of the equivalent Boost converter fractional-order model, the input voltage is set to 24V, the duty cycle is set to 0.5, and the order is chosen to be 0.8, 0.9, and 1, respectively. The simulation results are shown in Figure 6(c) and Figure 6(d). In addition, experiments were carried out on the Buck mode and Boost mode, respectively. It was found that the experiment results of output voltage are close to the simulation results with the order of 0.95. This shows that the inductor and capacitor used in the circuit have fractional-order characteristics, and the order is close to 0.95.

In order to verify the effectiveness of the fractional-order small parameter variable method for the steady-state analysis of the equivalent dual-switch converter, a simulation program of the fractional-order small parameter variable method was written in MATLAB2018b. The calculation process of programming can be divided into the following 5 parts:

① Establish the fractional-order state equation based on the equivalent circuit and determine the sign row vector.

② Calculate the Fourier series of the single pulse function.

③ Calculate the DC component a_{00}.

④ Calculate the ripple components $a_{11}, a_{02}, a_{22}, a_{32}$.

⑤ Get the steady-state periodic solution of the equivalent circuit.

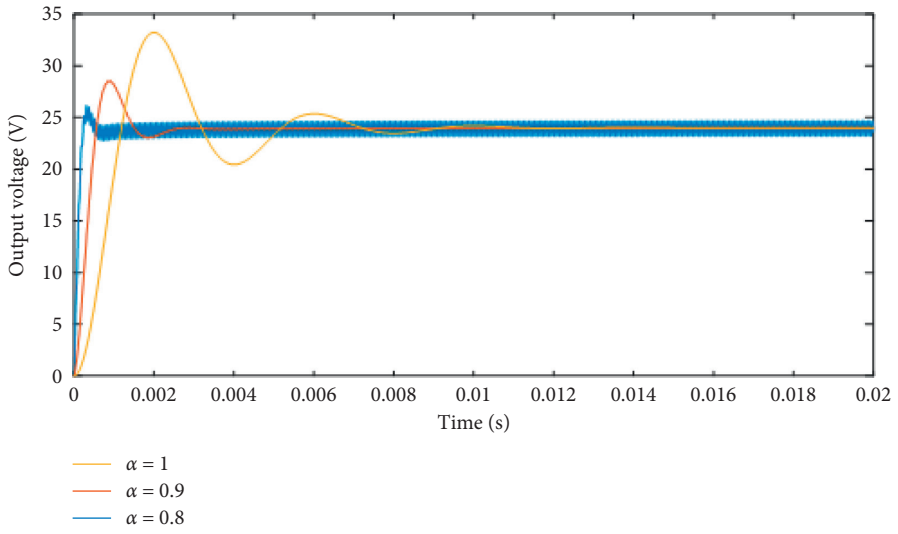

(a)

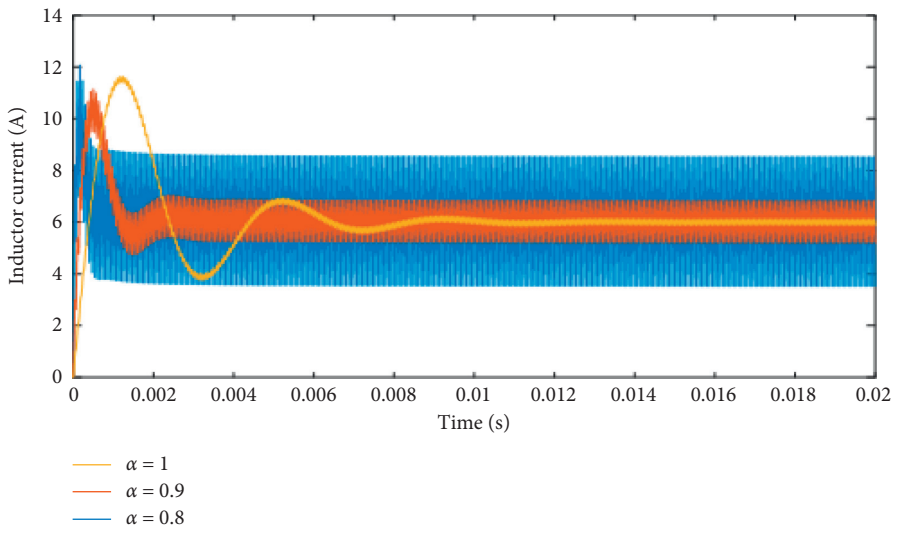

(b)

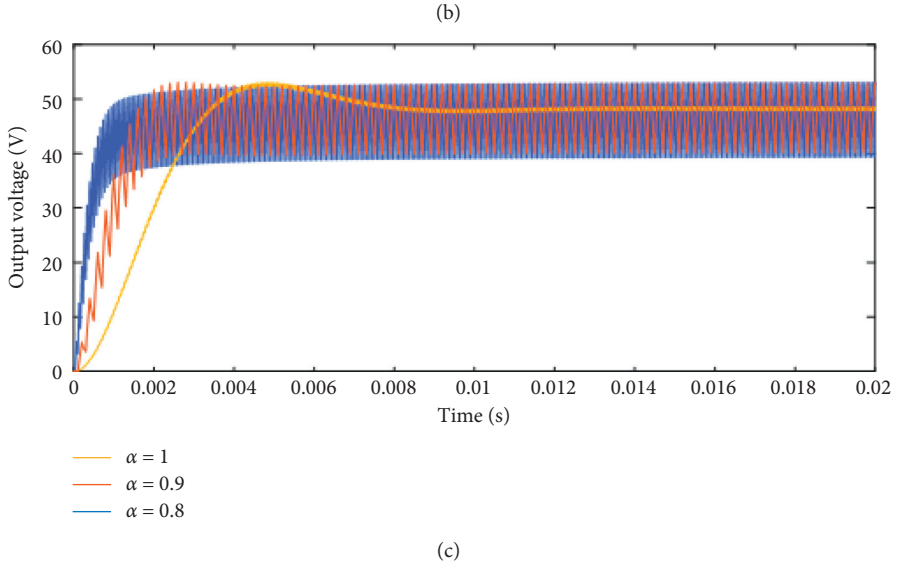

(c)

Figure 6: Continued.

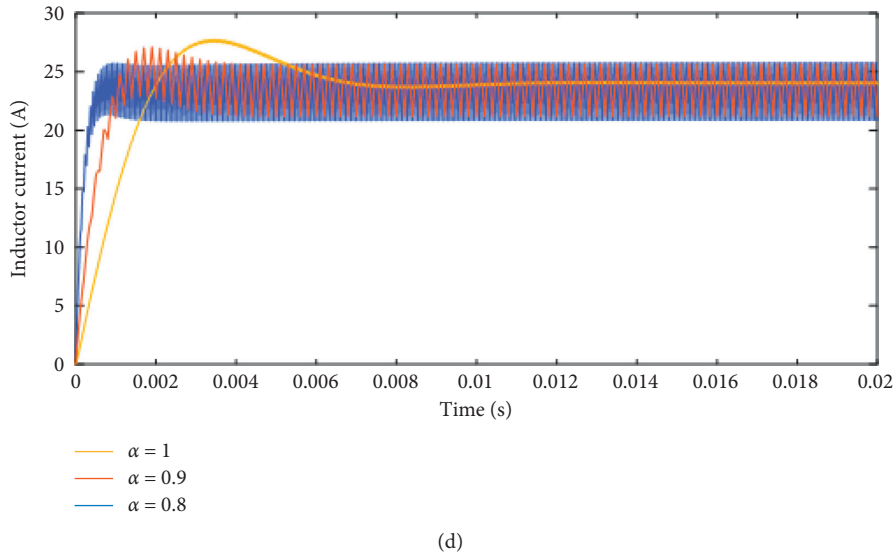

(d)

Figure 6: Simulation results of fractional-order model of equivalent DC-DC converter: (a) output voltage of fractional-order model of equivalent Buck converter; (b) inductor current of fractional-order model of equivalent Buck converter; (c) output voltage of fractional-order model of equivalent Boost converter; (d) inductor current of fractional-order model of equivalent Boost converter.

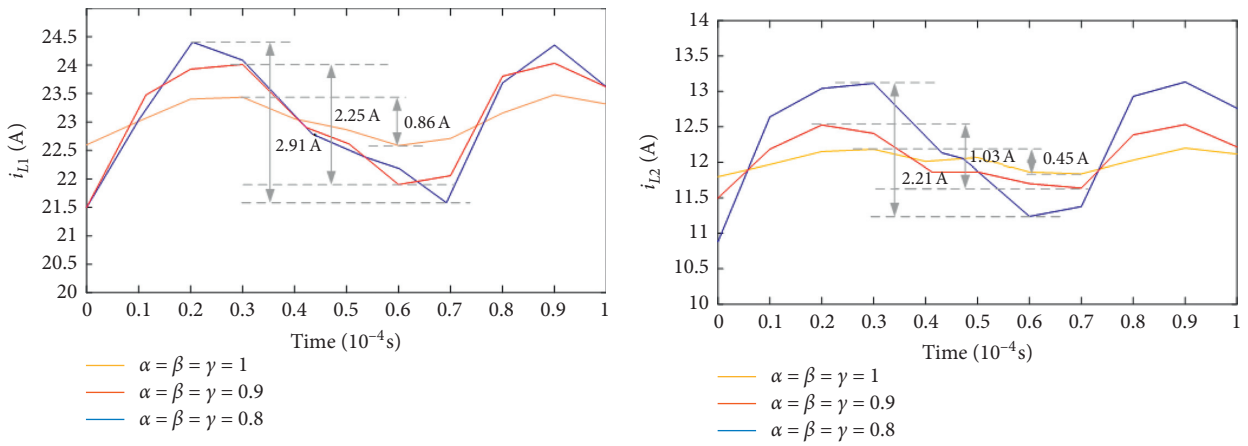

(a)

(b)

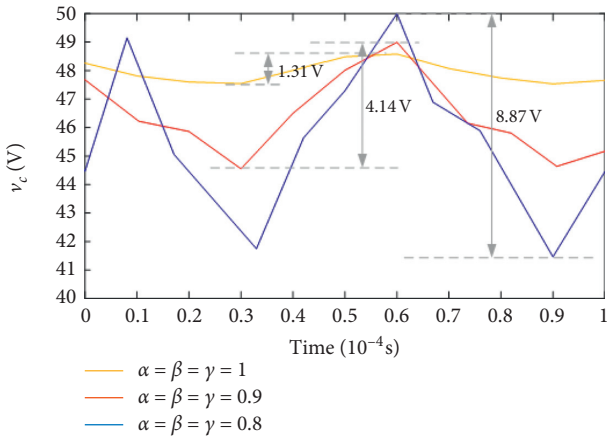

(c)

Figure 7: Simulation result of fractional-order model of equivalent dual-switch Boost converter: (a) inductor L1 current; (b) inductor L2 current; (c) output voltage.

Write ②-⑤ as a subprogram, the main program entry is the circuit parameter matrix and duty cycle row vector, and the exit is the steady-state periodic solution of the circuit. In the simulation process, the SC voltage is set to 38 V, the lithium battery voltage is 24 V, and the duty cycle of SW_1 and SW_2 is set to 0.4 and 0.5 (synchronously boosted to 48 V output). The calculation results are obtained in the time domain, and the steady-state waveforms that generate the inductor current and output voltage are shown in Figure 7.

From the simulation results, it can be seen that the fractional-order model of the equivalent DC-DC converter has more freedom to choose when describing the DC-DC operating characteristics. As the fractional-order decreases, the overshoot of the dynamic characteristics decreases. The amount of ripple in the steady-state characteristic increases. In practical applications, the voltage response of the equivalent Boost converter of the variable structure HESS has a certain degree of ripple component. However, the ripple of the steady-state characteristics described by the integer-order model is very small, which is obviously in error with the actual situation, and it also shows that the accuracy of integer-order modeling is insufficient. That is to say, when the order of the fractional model is selected to an appropriate value, the dynamic and steady-state characteristics of the DC-DC converter can be accurately described.

6. Conclusions

As an important technology for electric vehicles, hybrid energy storage systems have been extensively studied. However, there are still many problems, and this technology cannot be made mature and widely used. Especially the high-precision modeling and control strategy for this complex system is the bottleneck of this technology. In this paper, a fractional-order modeling of a variable structure HESS is carried out. For the three working modes of variable structure HESS, different fractional modeling methods are used to perform fractional modeling and analysis. The effectiveness and precision of the fractional-order model are proved by simulation and experiment.

Data Availability

The data used to support the findings of this study are available from the corresponding author upon request.

Conflicts of Interest

The authors declare that they have no conflicts of interest.

Authors' Contributions

Jianlin Wang and Dan Xu wrote the main manuscript text. Jiahui Zhou and Jinglu Mao assisted in the design of HESS topology and model building. All authors reviewed the manuscript.

References

[1] M. Sabri, K. Danapalasingam, and M. Rahmat, "A review on hybrid electric vehicles architecture and energy management strategies," *Renewable and Sustainable Energy Reviews*, vol. 53, pp. 1433–1442, 2016.

[2] J. Cao and A. Emadi, "A new battery/UltraCapacitor hybrid energy storage system for electric, hybrid, and plug-in hybrid electric vehicles," *IEEE Transactions on Power Electronics*, vol. 27, pp. 122–132, 2012.

[3] Z. Song, H. Hofmann, J. Li, X. Han, X. Zhang, and M. Ouyang, "A comparison study of different semi-active hybrid energy storage system topologies for electric vehicles," *Journal of Power Sources*, vol. 274, pp. 400–411, 2015.

[4] H. S. Das, C. W. Tan, and A. H. M. Yatim, "Fuel cell hybrid electric vehicles: a review on power conditioning units and topologies," *Renewable and Sustainable Energy Reviews*, vol. 76, pp. 268–291, 2017.

[5] M. B. Camara, H. Gualous, F. Gustin, A. Berthon, and B. Dakyo, "DC/DC converter design for supercapacitor and battery power management in hybrid vehicle applications-polynomial control strategy," *IEEE Transactions on Industrial Electronics*, vol. 57, no. 2, pp. 587–597, 2010.

[6] C. Ren, X. S. He, and H. R. F. KarimiLiu, "Finite-time L_2-Gain asynchronous control for continuous-time positive hidden Markov jump systems via T-S fuzzy model approach," *IEEE Transactions on Cybernetics*, vol. 99, pp. 1–11, 2020.

[7] C. Ren and S. He, "Finite-time stabilization for positive Markovian jumping neural networks," *Applied Mathematics and Computation*, vol. 365, Article ID 124631, 2020.

[8] C. Ren, R. Nie, and S. He, "Finite-time positiveness and distributed control of Lipschitz nonlinear multi-agent systems," *Journal of the Franklin Institute*, vol. 356, no. 15, pp. 8080–8092, 2019.

[9] A. Davoudi and J. Jatskevich, "Realization of parasitics in state-space average-value modeling of PWM DC-DC converters," *IEEE Transactions on Power Electronics*, vol. 21, no. 4, pp. 1142–1147, 2017.

[10] J. Wang, D. Xu, H. Zhou, and A. Bai, "High-performance fractional order terminal sliding mode control strategy for DC-DC Buck converter," *PLoS One*, vol. 12, no. 10, Article ID e0187152, 2017.

[11] C. Wu, G. Si, Y. Zhang, and N. Yang, "The fractional-order state-space averaging modeling of the Buck-Boost DC/DC converter in discontinuous conduction mode and the performance analysis," *Nonlinear Dynamics*, vol. 79, no. 1, pp. 689–703, 2015.

[12] H. Komurcugil, "Adaptive terminal sliding-mode control strategy for DC-DC buck converters," *ISA Transactions*, vol. 51, no. 6, pp. 673–681, 2012.

[13] G.-C. Wu, D. Baleanu, and W.-H. Luo, "Lyapunov functions for Riemann-Liouville-like fractional difference equations," *Applied Mathematics and Computation*, vol. 314, pp. 228–236, 2017.

[14] I. M. Filanovsky and S. S. Shui-Sheng Qiu, "Harmonic analysis of PWM converters," *IEEE Transactions on Circuits and Systems I: Fundamental Theory and Applications*, vol. 47, no. 9, pp. 1340–1349, 2000.

[15] A. G. Radwan, A. A. Emira, A. M. Abdelaty et al., "Modeling and analysis of fractional order DC-DC converter," *ISA Transactions*, vol. 82, pp. 184–199, 2017.

[16] X. Chen, Y. F. Chen, B. Zhang et al., "A method of modeling and analysis for fractional-order DC-DC converters," *IEEE Transactions on Power Electronics*, vol. 99, 2016.

[17] J. L. Wang, L. Zhang, J. L. Mao et al., "Fractional order equivalent circuit model and SOC estimation of supercapacitors for use in HESS," *Digital Object Identifier*, vol. 10, Article ID 2912221, 2019.

Hindawi
Complexity
Volume 2020, Article ID 7913050, 16 pages
https://doi.org/10.1155/2020/7913050

Research Article

Stochastically Globally Exponential Stability of Stochastic Impulsive Differential Systems with Discrete and Infinite Distributed Delays Based on Vector Lyapunov Function

Xiaoyan Liu[1,2] **and Quanxin Zhu**[1]

[1]*MOE-LCSM, School of Mathematics and Statistics, Hunan Normal University, Changsha, Hunan 410081, China*
[2]*School of Information Science and Engineering, Chengdu University, Chengdu 610106, China*

Correspondence should be addressed to Quanxin Zhu; zqx22@126.com

Received 23 July 2020; Revised 19 September 2020; Accepted 25 September 2020; Published 1 December 2020

Academic Editor: Shuping He

This paper deals with stochastically globally exponential stability (SGES) for stochastic impulsive differential systems (SIDSs) with discrete delays (DDs) and infinite distributed delays (IDDs). By using vector Lyapunov function (VLF) and average dwell-time (ADT) condition, we investigate the unstable impulsive dynamics and stable impulsive dynamics of the suggested system, and some novel stability criteria are obtained for SIDSs with DDs and IDDs. Moreover, our results allow the discrete delay term to be coupled with the nondelay term, and the infinite distributed delay term to be coupled with the nondelay term. Finally, two examples are given to verify the effectiveness of our theories.

1. Introduction

During the past few years, stochastic differential systems (SDSs) have been paid a great deal of attention in various fields. For example, there have been a number of works on the stability of SDSs (e.g., see [1–6]), and such a topic is of great significance in many practical applications. On the other hand, delay problems are often encountered in the chemical industry system, neural network system, and other systems. As a result, the stability analysis problem of SDSs with delays was studied in [2–12], where the delays were divided into constant delays, time-varying delays, and distributed delays. For a kind of SDSs with DDs and IDDs, there are many researchers to pay much attention on this topic, SDSs with DDs and IDDs were applied to study neural network systems [13–15], especially. However, these modes do not include some dynamic phenomena with impulses even if they are indeed important in practice.

Systems with impulses have been widely applied in practice. For instance, they are often used to describe dynamic processes that mutate at successive times [7, 8, 11, 12, 16–20]. In the past few decades, addressed system was studied extensively (e.g., see [16, 19]) and it was found that impulsive systems can contribute the exponential stability of SDSs (e.g., see [8, 11, 12]). The impulse one can not only cause complex dynamic behaviors such as instability, but also stabilize the unstable dynamic system. How to use the appropriate impulse control to stabilize the unstable SDSs or let impulses play a negative role on the stable system is of great significance. This paper aims to study these interesting topics for SIDSs with DDs and IDDs.

In order to deal with the stability of systems with DDs and IDDs, there have appeared many methods such as the fixed point theory, Lyapunov-Krasovskii function or the scalar Lyapunov function. For example, the Lyapunov -Krasovskii function and matrix inequality method were used in [13]; Chen et al. in [15] employed the fixed point theorem; Huang and Cao in [14] applied the Lyapunov functional method and the semimartingale convergence theorem. However, until now, there have been essentially no results to deal with SIDSs with DDs and IDDs by using the vector Lyapunov method. To investigate the stability issue,

two new methods were recently proposed: the VLF method [9, 12, 19–23] and the ADT method [18, 24]. The ADT effectively limits the impulse and could promote the stability of the system. By using VLF, inequality techniques, and impulse conditions, some useful exponential stability criteria are obtained. As a feasible alternative to scalar Lyapunov function, VLF has attracted more and more attention in recent years (e.g., see [9]). In [25], VLF was first introduced and widely used in various fields owing to its outstanding advantages. In terms of construction, the theory of VLF provides a more flexible method for dealing with the complexity of SIDSs (e.g., see [19, 26]). The real reason is that the theory of VLF can reduce the dimension and reduce the requirement of system component (e.g., see [26]). Therefore, there are many related results reported on the vector Lyapunov function method (e.g., see [9, 12, 19–23]). However, the joint system with IDDs of stochastic impulsive and DDs has not been solved, which greatly limits the effectiveness of VLF.

Motivated by the above discussions, we study SGES of SIDS with DDs and IDDs by using ADT condition and VLF. We consider two cases: unstable impulse dynamics and stable impulsive dynamics. For these two cases, some sufficient conditions are established for SIDS with DDs and IDDs based on the strength of VLF and ADT condition. Moreover, the results show that continuous SDSs with DDs and IDDs are stable and the impulsive one is unstable, according to the relationship between ADT and impulse, a lower bound of ADT is given to the mixed system is exponential stability. When continuous SIDS with DDs and IDDs are not stable, the impulsive effect can stabilize the system successfully under the upper bound condition of the given ADT.

There are three contributions to the paper. (1) To the best of our knowledge, there have been no studies on the stability of SIDS with DDs and IDDs by VLF. (2) The discrete delay term is coupled with the nondelay term and the infinitely distributed delay term is coupled with the nondelay term. It should be mentioned that the comparison principle was used [19, 20, 23] and the components of VLF were separate, but the coupling of distributed delay term with nondelay term was not considered in [9, 12]. (3) The third is infinitely distributed delay: due to its infinite nature, we deal with it by the construction formula $\sum_{j=1}^{n}\int_0^{\infty}k_{ij}(s)\exp(\eta_i s)\alpha_j \mathrm{d}s$ and $\sum_{j=1}^{n}\int_0^{\infty}k_{ij}(s)\exp(-\eta_i s)\alpha_j \mathrm{d}s$. Thus, our results are innovative than those in [9, 19, 20, 23].

The remainder of this paper is organized as follows. In the second part, the model and the preliminary knowledge are introduced. Two novel stability criteria are established for the stochastic impulsive systems with DDs and IDDs in the third part. In the fourth part, two examples are given to verify the correctness of our results.

2. Preliminaries

Through the paper, no special instructions, we will use the following instructions.

$w(t)$ is an $\mathbb{R}^m$-valued Brownian motion defined on a complete probability space $(\Omega, \mathscr{F}, \{\mathscr{F}_t\}_{t\geq t_0}, P)$. $N_{>0}$ represents the set of positive integer and $\mathbb{R}$ denotes the real number. For a give $t_0 \geq 0$, let $\mathbb{R}_{\geq t_0} \coloneqq (t_0, +\infty]$. Given a, $b \in \mathbb{R}^n$, $a > b$ if $a_i > b_i$, for all $i \in \iota = \{1, \ldots, n\}$. Define $(a, b) \coloneqq (a^T, b^T)^T$. Given a vector or matrix C, its transpose is denoted by C^{T}. $A \backslash D \coloneqq \{z\colon z \in A, z \in D\}$ for two given sets A with D. $tr[B]$ represents the trace of the matrix B, where $B = B^T \in \mathbb{R}^{n\times n}$. Let $|.|$ be the Euclidean norm and E present the vector that all the components are 1. I means identity matrix. For a given function $p\colon \mathbb{R}_{\geq t_0} \longrightarrow \mathbb{R}^n$ and the initial time $-\infty < t \leq t_0$, define $\|p\|_{\infty} \coloneqq \sup_{t\leq s\leq t_0}|p(t)|$. Given a function $g\colon \mathbb{R} \longrightarrow \mathbb{R}$, denote $g(t^-) \coloneqq \limsup_{s\longrightarrow 0^-} g(t+s)$. A function $\alpha\colon \mathbb{R}_{\geq 0} \longrightarrow \mathbb{R}_{\geq 0}$ is of class $\mathscr{CK}_{\infty}$ if it is of class $\mathscr{K}_{\infty}$ and concave. A function $\gamma\colon \mathbb{R}_{\geq 0} \times \mathbb{R}_{\geq 0} \longrightarrow \mathbb{R}_{\geq 0}$ is of class $\mathscr{KL}$, if $\gamma(s,t)$ is of class $\mathscr{K}$ for each fixed $t \geq 0$ and decreases to zero as $t \longrightarrow \infty$ for each fixed $s \geq 0$. The inverse of the function β is denoted by β^{-1}.

We will consider the following SIDSs with DDs and IDDs:

$$\begin{cases} \mathrm{d}x(t) = f\left(t, x_t, \int_0^{\infty} k(s)x(t-s)\mathrm{d}s\right)\mathrm{d}t + g\left(t, x_t, \int_0^{\infty} k(s)x(t-s)\mathrm{d}s\right)\mathrm{d}w(t), & t \in \mathbb{R}_{\geq} t_0 \backslash \mathscr{T}, \\ \Delta x(t)/_{t=t_k} = x(t_k) - x(t_k^-) = h_k(t_k, x(t_k^-)), & t \in \mathscr{T}, k \in N_{>0}, \\ x(t) = \xi(t), \quad t \in (-\infty, t_0], \end{cases} \tag{1}$$

where $x(t) \in \mathbb{R}^n$ is the system state, $x_t \coloneqq x(t-\tau)$, τ is a bounded and positive constant. $\mathscr{T} \coloneqq \{t_0, t_1, \ldots, t_n\}$ is a impulsive time sequence satisfying $0 \leq t_0 \leq t_1 \leq \cdots \leq t_n$. The initial function $\xi\colon [-\infty, t_0] \longrightarrow \mathbb{R}^n$ is a $\mathscr{F}_{t_0^-}$ adapted continuous stochastic variable with finite $\mathbb{E}[\|\xi\|_{\tau}^p]$. For all $k \in N_{>0}$, the function $f\colon \mathbb{R}_{\geq t_0} \times \mathbb{R}^n \times \mathbb{R}^n \longrightarrow \mathbb{R}^n$, $g\colon \mathbb{R}_{\geq t_0} \times \mathbb{R}^n \times \mathbb{R}^n \longrightarrow \mathbb{R}^{n\times m}$, and $h_k\colon \mathbb{R}_{\geq t_0} \times \mathbb{R}^n \longrightarrow \mathbb{R}^n$ are assumed to be Lipschitz and Borel measurable. For the aim of stability, we assume that $f(t,0,0) \equiv 0$ and $g(t,0,0) \equiv 0$, and thus $x(t) \equiv 0$ is a trivial solution of system (1). As a usual, we assume with no emphasis on conditions that there exists a unique global solution $x(t,\xi)$ for the initial value ξ.

In this paper, we always assume that $K \coloneqq [\int_0^{\infty} k_{ij}\mathrm{d}s]_{n\times n}$ is meaningful. That is, the delay kernels $k_{ij}\colon [0, +\infty) \to [0, +\infty)$ are real-valued nonnegative continuous functions and satisfy $\int_0^{\infty} e^{\mu s}k_{ij}(s)\mathrm{d}s < \infty$, where μ is a positive number.

Definition 1 (see [6]): For arbitrary $\varepsilon \in (0,1)$, if there is $\varrho \in \mathscr{KL}$, $x(t_0) \in \mathbb{R}^n$, $t \in \mathbb{R}_{\geq t_0}$, $M \geq 0$, $b > 0$ such that

$$P\{|x(t)| \le \varrho(|x(t_0)|, t - t_0)\} \ge 1 - \varepsilon. \tag{2}$$

Then, system (1) is stochastically globally asymptotically stable. Furthermore, if $\varrho(a,t) := Ma^2e^{-bt}$, then system (1) is stochastically globally exponentially stable (SGES).

Definition 2 (see [11, 24]): For an impulsive sequence $\{t_k\}_{k\in N}$, $N(t,s)$ shows the number of impulses that occur in the half-open interval $(s,t]$. If

$$\frac{t-s}{\tau_c} - N_0 \le N(t,s) \le \frac{t-s}{\tau_c} + N_0, \tag{3}$$

for $N_0 > 0$, $\tau_c > 0$, then τ_c and N_0 are called the average dwell-time (ADT) and the elasticity number, respectively.

Definition 3 (see [9]): Let $\mathscr{C}^{1,2}$ denote the family of the nonnegative functions $V_i(t,x)$: $\mathbb{R}_{\ge 0} \times \mathbb{R}^n \longrightarrow \mathbb{R}_{\ge 0}$ that are continuously twice differentiable in x and once in t, n is bounded. Then, for any $\mathscr{C}^{1,2}$, the operator of $\mathscr{L}V_i(t, x_t, \int_0^\infty k(s)x(t-s)\mathrm{d}s)$: $\mathbb{R}_{\ge 0} \times \mathbb{R}^n \times \mathbb{R}^n \longrightarrow \mathbb{R}_{\ge 0}$, $i \in \iota$ is defined as

$$\begin{aligned}\mathscr{L}V_i\left(t, x_t, \int_0^\infty k(s)x(t-s)\mathrm{d}s\right) &= \frac{\partial V_i(t,x(t))}{\partial t} + \frac{\partial V_i(t,x(t))}{\partial x} f\left(t, x_t, \int_0^\infty k(s)x(t-s)\mathrm{d}s\right) \\ &+ \frac{1}{2} tr\left[g^T\left(t, x_t, \int_0^\infty k(s)x(t-s)\mathrm{d}s\right) \frac{\partial V_i(t,x(t))}{\partial x^2} g\left(t, x_t, \int_0^\infty k(s)x(t-s)\mathrm{d}s\right)\right].\end{aligned} \tag{4}$$

Define $V(t,x(t)) := (V_1(t,x(t)), \ldots, V_n(t,x(t)))$. In particular, if $n = 1$, then V becomes a scalar.

Let Ψ: $\mathbb{R}_{\ge t_0} \longrightarrow \mathbb{R}_{\ge t_0}$ be a continuous function. Then, the upper Dini derivative of $\Psi(t)$ is defined as $D^+\Psi(t) := \limsup_{s \longrightarrow 0^+} \Psi(t+s) - \Psi(t)/s$. In particular, if $\mathbb{E}[\mathscr{L}V_i(t,x(t),x_t)]$ is continuous, then it follows from [27] that $\mathbb{E}[\mathscr{L}V_i(t,x(t),x_t)] = D^+[\mathbb{E}V_i(t,x(t),x_t)]$.

Definition 4 (see [28]) Let off-diagonal elements of the matrix $A = (a_{ij})_{n\times n}$ be nonpositive. If each of the following statements holds, then A is a nonsingular M-matrix.

(1) If the diagonal elements of A are all positive, then there exists a positive vector a such that $Aa > 0$ or $A^{\mathrm{T}}a > 0$.

(2) $A = C - M$, $\rho(C^{-1}M) < 1$, where $M \ge 0$, $C = \mathrm{diag}\{c_1, c_2, \ldots, c_n\}$ and $\rho(\cdot)$ is the spectral radius of the matrix $(\cdot)$.

For a nonsingular M-matrix A, it can denote $\Omega_M(A) \triangleq \{z \in R^n | Az > 0, z > 0\}$.

3. Main Results

In this section, we will establish the SGES of system (1) with destabilizing impulses.

Theorem 1. *For system (1), assume that there is locally Lipschitz Lyapunov function V_i: $\mathbb{R}_{\ge 0} \times \mathbb{R}^n \longrightarrow \mathbb{R}_{\ge 0}$, $i \in \iota$, $r > 1$, $\zeta E \ge E$, $\nu \in \mathscr{K}_\infty$, $\varsigma \in \mathscr{C}\mathscr{K}_\infty$, positive matrices $\mu := diag(\mu_1, \mu_2, \ldots, \mu_n)$, $\zeta := diag(\zeta_1, \zeta_2, \ldots, \zeta_n)$ and nonnegative matrices $P := [p_{ij}]_{n\times n}$, $Q := [q_{ij}]_{n\times n}$, $O := [o_{ij}]_{n\times n}$, where $K := [\int_0^\infty k_{ij}(s)ds]_{n\times n}$ is continuous function and $k_{ij}(s) \ge 0$ such that the following conditions:*

(i) $i \in \iota$, $t \in \mathbb{R}_{\ge t_0}$, $\nu(|x(t)|) \le V_i(t) \le \varsigma(|x(t)|)$.

(ii) $i \in \iota$, $t \in \mathbb{R}_{\ge t_0} \backslash \mathscr{T}$,

$$\begin{aligned}\mathscr{L}V_i\left(t, x(t), x_t, \int_0^\infty k(s)x(t-s)\mathrm{d}s\right) \le & -\mu_i V_i(t) + \sum_{j=1}^n p_{ij}(V_i(t))^{1/r'}\left(V_j(t)\right)^{1/r} + \sup_{-\tau\le\theta\le 0} \sum_{j=1}^n q_{ij}(V_i(t))^{1/r'}\left(V_j(t+\theta)\right)^{1/r} \\ &+ \sum_{j=1}^n \int_0^\infty k_{ij}(s)\left(V_i(t)\right)^{1/r'}\left(V_j(t-s)\right)^{1/r}\mathrm{d}s,\end{aligned} \tag{5}$$

where $\mu - P - Q - K$ is a nonsingular M-matrix, $\theta \in [-\tau, 0]$, $r' = (1 - r^{-1})^{-1}$.

(iii) $i \in \iota$ and $k \in N_{>0}$,

$$V_i(t_k) \le \zeta_i V_i(t_k^-) + \left(\sum_{j=1}^n o_{ij}\right)(V_i(t_k^-))^{1/r'}\left(V_j(t_k^-)\right)^{1/r}. \tag{6}$$

(iv) $\tau_c > \max \ln(\zeta_i + \sum_{j=1}^{n} o_{ij})/\lambda$, *where* $\lambda \in (0, \overline{\lambda})$, $V_i(t) \overset{i\in\iota}{=} V_i(t, x(t))$,

$$\overline{\lambda} := \max\left\{\eta_i > 0 : r\alpha_i\eta_i - \mu_i\alpha_i + \sum_{j=1}^{n} p_{ij}\alpha_j + \sum_{j=1}^{n} q_{ij}\alpha_j \exp(\tau\eta_i) + \sum_{j=1}^{n}\int_0^{\infty} k_{ij}(s)\exp(\eta_i s)\alpha_j \mathrm{d}s < 0\right\}, \tag{7}$$

where $i \in \iota$, $\alpha \in \Omega_M(\mu - P - Q - K)$, *with* $\min_{1\le i\le n}\{\alpha_i\} \ge 1$, $\overline{\alpha} = \max\{\alpha_i\}$.

Then, system (1) is SGES.

Proof. By taking expectation on both sides of (5) and (6) and using Holder inequality in [6], we have

$$\begin{aligned}\mathbb{E}\mathscr{L}V_i\left(t, x(t), x_t, \int_0^{\infty} k(s)x(t-s)\mathrm{d}s\right) \le & -\mu_i\mathbb{E}V_i(t) + \sum_{j=1}^{n} p_{ij}\left(\mathbb{E}V_i(t)\right)^{1/r'}\left(\mathbb{E}V_j(t)\right)^{1/r} + \sup_{-\tau\le\theta\le 0}\sum_{j=1}^{n} q_{ij}\left(\mathbb{E}V_i(t)\right)^{1/r'}\left(\mathbb{E}V_j(t+\theta)\right)^{1/r} \\ & + \sum_{j=1}^{n}\int_0^{\infty} k_{ij}(s)\left(\mathbb{E}V_i(t)\right)^{1/r'}\left(\mathbb{E}V_j(t-s)\right)^{1/r}\mathrm{d}s, \quad i \in \iota, t \in \mathbb{R}_{\ge t_0}\backslash\mathscr{T}.\end{aligned} \tag{8}$$

$$\mathbb{E}V_i(t_k) \le \zeta_i\mathbb{E}V_i(t_k^-) + \left(\sum_{j=1}^{n} o_{ij}\right)\left(\mathbb{E}V_i(t_k^-)\right)^{1/r'}\left(\mathbb{E}V_j(t_k^-)\right)^{1/r}, \quad i \in \iota \text{ and } k \in N_{>0}. \tag{9}$$

Next, we divide the proof into three steps.

Step 1. We first prove the existence of λ.

If $\mu - P - Q - K$ is a nonsingular M-matrix, there is $\alpha \in \Omega_M(\mu - P - Q - K)$ with $\min_{1\le i\le n}\{\alpha_i\} \ge 1$ such that

$$\mu_i\alpha_i - \sum_{j=1}^{n} p_{ij}\alpha_j - \sum_{j=1}^{n} q_{ij}\alpha_j - \sum_{j=1}^{n}\int_0^{\infty} k_{ij}(s)\alpha_j \mathrm{d}s > 0, \quad i \in \iota. \tag{10}$$

For any given i, let

$$H_i(\eta) = -r\alpha_i\eta + \mu_i\alpha_i - \sum_{j=1}^{n} p_{ij}\alpha_j - \sum_{j=1}^{n} q_{ij}\alpha_j \exp(\tau\eta) - \sum_{j=1}^{n}\int_0^{\infty} k_{ij}(s)\exp(\eta s)\alpha_j \mathrm{d}s. \tag{11}$$

Obviously, it follows from (11) that $H_i(0) > 0$ and $H_i(\infty) = -\infty$, where $\eta \longrightarrow \infty$. On the other hand, we have

$$H_i'(\eta) = -r\alpha_i - \tau\sum_{j=1}^{n} q_{ij}\alpha_j \exp(\tau\eta) - \sum_{j=1}^{n}\int_0^{\infty} s k_{ij}(s)\exp(\eta s)\alpha_j \mathrm{d}s < 0 \tag{12}$$

Thus, there is a unique constant $\eta_i > 0$ such that $H_i(\eta_i) = 0$. Letting $\overline{\lambda} = \max_{1\le i\le n}\eta_i > 0$, there is a constant λ such that $\lambda \in (0, \overline{\lambda})$.

Step 2. Next, we need to prove that for $i \in \iota$ and $\lambda \in (0, \overline{\lambda})$,

$$\mathbb{E}[V_i(t)] \le \mathbb{E}[V(t_0)]\overline{\mu}^{rN(t,t_0)}\overline{\alpha}^r \exp(-r\lambda(t - t_0)), \tag{13}$$

where $V(t_0) = \sum_{i=1}^{n} V_i(t_0)$, $\overline{\mu} = \max_{i\in\iota}\left\{\zeta_i + \sum_{j=1}^{n} o_{ij}\right\}$ and $\overline{\alpha} := \max_{i\in\iota}\alpha_i$. Clearly, (13) holds for $t = t_0$.

For simplicity, let $W_i(t - t_0) = [\mathbb{E}V(t_0)]^{1/r}\ \overline{\mu}^{N(t,t_0)}\alpha_i$ $\exp(-\lambda(t - t_0))$, $U_i(t) = [\mathbb{E}V_i(t)]^{1/r}$.

It is easy to check that (13) is equivalent to the following:

$$[\mathbb{E}V_i(t)]^{1/r} \le \max_{i\in\iota}\left\{[\mathbb{E}V(t_0)]^{1/r}\overline{\mu}^{N(t,t_0)}\alpha_i \exp(-\lambda(t-t_0))\right\} =: \max_{i\in\iota}\{W_i(t-t_0)\}. \tag{14}$$

Now suppose that (13) is not valid in some interval, then there are two cases:

Case 1. (13) is not true at the nonimpulse point of the certain interval;

Case 2. (13) does not hold at the impulse point of the certain interval.

For Case 1, there exists a k such that $U_i(t) \le W_i(t-t_0)$ holds for all $t \in [t_0, t_k]$ and $i \in \iota$, and $U_i(t) \le W_i(t-t_0)$ is not true for $i \in \iota$ and $t \in (t_k, t_{k+1})$. Define

$$t^* := \inf\{t \in (t_k, t_{k+1}): U_i(t) > W_i(t-t_0)\}. \tag{15}$$

Noting that $U_i(t)$ and $W_i(t-t_0)$ are continuous for $t \in \mathbb{R}_{\ge t_0}\backslash\mathscr{T}$, there exist $\bar{i}$ and t^* such that

$$U_{\bar{i}}(t^*) = W_{\bar{i}}(t^*-t_0), \tag{16}$$

$$U_i(t) > W_i(t-t_0), \quad t \in (t^*, t^*+\Delta t), \tag{17}$$

where $\Delta t > 0$ is arbitrarily small. Hence, it follows from (16) and (17) that

$$D^+U_{\bar{i}}(t^*) > D^+W_{\bar{i}}(t^*-t_0). \tag{18}$$

$$D^+W_{\bar{i}}(t^*-t_0) = -\lambda\alpha_{\bar{i}}\overline{\mu}^{N(t^*,t_0)}[\mathbb{E}V(t_0)]^{1/r}\exp(-\lambda(t^*-t_0)). \tag{19}$$

By the definition of λ, we have

$$-\lambda\alpha_i > \frac{1}{r}\left(-\mu_i\alpha_i + \sum_{j=1}^{n} p_{ij}\alpha_j + \sum_{j=1}^{n} q_{ij}\alpha_j \exp(\tau\lambda) + \sum_{j=1}^{n}\int_0^\infty k_{ij}(s)\exp(\lambda s)\alpha_j \mathrm{d}s\right), \tag{20}$$

which together with (19) yields

$$\begin{aligned}
D^+W_{\bar{i}}(t^*-t_0) &> \frac{1}{r}\left(-\mu_{\bar{i}}\alpha_{\bar{i}} + \sum_{j=1}^{n} p_{\bar{i}j}\alpha_j + \sum_{j=1}^{n} q_{\bar{i}j}\alpha_j \exp(\tau\lambda) + \sum_{j=1}^{n}\int_0^\infty k_{\bar{i}j}(s)\exp(\lambda s)\alpha_j \mathrm{d}s\right)\\
&\quad\times \overline{\mu}^{N(t^*,t_0)}[\mathbb{E}V(t_0)]^{1/r}\exp(-\lambda(t^*-t_0))\\
&= \frac{1}{r}\left(-\mu_{\bar{i}}\alpha_{\bar{i}}\right)\overline{\mu}^{N(t^*,t_0)}[\mathbb{E}V(t_0)]^{1/r}\exp(-\lambda(t^*-t_0))\\
&\quad+\frac{1}{r}\sum_{j=1}^{n} p_{\bar{i}j}\alpha_j\overline{\mu}^{N(t^*,t_0)}[\mathbb{E}V(t_0)]^{1/r}\exp(-\lambda(t^*-t_0))\\
&\quad+\frac{1}{r}\sum_{j=1}^{n} q_{\bar{i}j}\alpha_j\exp(\tau\lambda)\overline{\mu}^{N(t^*,t_0)}[\mathbb{E}V(t_0)]^{1/r}\exp(-\lambda(t^*-t_0))\\
&\quad+\frac{1}{r}\sum_{j=1}^{n}\int_0^\infty k_{\bar{i}j}(s)\exp(\lambda s)\alpha_j\mathrm{d}s\overline{\mu}^{N(t^*,t_0)}[\mathbb{E}V(t_0)]^{1/r}\exp(-\lambda(t^*-t_0))\\
&\ge \frac{1}{r}\left(-\mu_{\bar{i}}\mathbb{E}V_{\bar{i}}(t^*)\right)^{1/r} + \sum_{j=1}^{n} p_{\bar{i}j}\left(\mathbb{E}V_{\bar{j}}(t^*)\right)^{1/r}\\
&\quad+\sum_{j=1}^{n} q_{\bar{i}j}\sup_{-\tau\le\theta\le 0}\exp(\lambda(\tau+\theta))\overline{\mu}^{N(t^*,t^*,t_0)}\left(\mathbb{E}V_{\bar{i}}(t^*)\right)^{1/r}\\
&\quad+\sum_{j=1}^{n}\int_0^\infty k_{\bar{i}j}(s)\left(\mathbb{E}V_{\bar{j}}(t^*-s)\right)^{1/r}\mathrm{d}s\Bigg).
\end{aligned} \tag{21}$$

Due to $U_i(t) = [\mathbb{E}V_i(t)]^{1/r}$, then $\mathbb{E}V_i(t) = [U_i(t)]^r$, for $i \in \iota$. By virtue of Dini-derivation, (8), and the Itô formula, we obtain

$$\begin{aligned} D^+\mathbb{E}V_i(t) &= r[U_i(t)]^{r-1}D^+U_i(t) \\ &\le -\mu_i[U_i(t)]^r + \sum_{j=i}^{n} p_{ij}[(U_i(t))]^{r/r'}U_j(t) + \sum_{j=i}^{n} q_{ij}\sup_{-\tau\le\theta\le 0}[(U_i(t))]^{r/r'}U_j(t+\theta) \\ &\quad + \sum_{j=i}^{n}\int_0^{\infty} k_{ij}(s)[(U_i(t))]^{r/r'}U_j(t-s)\mathrm{d}s. \end{aligned} \tag{22}$$

Then, it follows from (22) that

$$D^+U_i(t) \le \frac{1}{r}\left(-\mu_i U_i(t) + \sum_{j=i}^{n} p_{ij}\big(U_j(t)\big) + \sum_{j=i}^{n} q_{ij}\sup_{-\tau\le\theta\le 0}\big(U_j(t+\theta)\big) + \sum_{j=i}^{n}\int_0^{\infty} k_{ij}(s)\big(U_j(t-s)\big)\mathrm{d}s\right). \tag{23}$$

Combining (21) and (23), we get $D^+U_{\bar{i}}(t^*) \le D^+W_{\bar{i}}(t^* - t_0)$, which contradicts with (18). Thus, $U_i(t) \le W_i(t - t_0)$ holds for all $t \in (t_k, t_{k+1})$. That is, (13) holds for all $t \in (t_k, t_{k+1})$.

For Case 2, we have that (13) holds for all $t \in [t_0, t_k)$ and does not hold at t_k. Thus, for some $i \in \iota$,

$$\mathbb{E}[V_i(t_k)] > \mathbb{E}[V(t_0)]\overline{\mu}^{rN(t,t_0)}\overline{\alpha}^r \exp(-r\lambda(t - t_0)). \tag{24}$$

Then, it follows from (9) that at the time instance t_k,

$$\begin{aligned} \mathbb{E}[V_i(t_k)] &\le \zeta_i\mathbb{E}V_i(t_k^-) + \left(\sum_{j=1}^{n} o_{ij}\right)(\mathbb{E}V_i(t_k^-))^{1/r}\big(\mathbb{E}V_j(t_k^-)\big)^{1/r} \\ &\le \zeta_i\mathbb{E}[V(t_0)]\overline{\mu}^{rN(t_k^-,t_0)}\overline{\alpha}^r \exp(-r\lambda(t_k^- - t_0)) \\ &\quad + \left(\sum_{j=1}^{n} o_{ij}\right)\times\Big(\mathbb{E}[V(t_0)]\overline{\mu}^{rN(t_k^-,t_0)}\overline{\alpha}^r \exp(-r\lambda(t_k^- - t_0))\Big)^{1/r'}\Big(\mathbb{E}[V(t_0)]\overline{\mu}^{rN(t_k^-,t_0)}\overline{\alpha}^r \exp(-r\lambda(t_k^- - t_0))\Big)^{1/r} \\ &\le \left(\zeta_i + \sum_{j=1}^{n} o_{ij}\right)\mathbb{E}[V(t_0)]\overline{\mu}^{rN(t_k^-,t_0)}\overline{\alpha}^r \exp(-r\lambda(t_k^- - t_0)) \\ &\le \mathbb{E}[V(t_0)]\overline{\mu}^{rN(t_k^-,t_0)}\overline{\alpha}^r \exp(-r\lambda(t_k^- - t_0)), \end{aligned} \tag{25}$$

which contradicts with (24). Therefore, (13) holds for $t = t_k$.

Therefore, by using the mathematical induction, we see that (13) is satisfied for all $t \in [t_0, \infty)$.

Step 3. Finally, we will prove that system (1) is SGES. In fact, it follows from condition (i) and Jensen's inequality in [29] that

$$\begin{aligned} &\mathbb{E}[V(t_0)]\overline{\mu}^{rN(t,t_0)}\overline{\alpha}^r \exp(-r\lambda(t - t_0)) \\ &\le \mathbb{E}[V(t_0)]\overline{\mu}^{rN_0 + r(t-t_0)/\tau_c}\overline{\alpha}^r \exp(-r\lambda(t - t_0)) \\ &= \mathbb{E}[V(t_0)]\overline{\mu}^{rN_0}\overline{\alpha}^r \exp\big((-r\lambda + r/\tau_c\ln\overline{\mu})(t - t_0)\big) \\ &\le \varsigma\mathbb{E}[\|\xi\|_\tau]\overline{\mu}^{rN_0}\overline{\alpha}^r n \exp\big((-r\lambda + r/\tau_c\ln\overline{\mu})(t - t_0)\big). \end{aligned} \tag{26}$$

According to (iv), we obtain $-r\lambda + (r/\tau_c)\ln\overline{\mu} < 0$. This fact together with and (26) gives

$$\mathbb{E}[V_i(t)] \le \varsigma\mathbb{E}[\|\xi\|_\tau]\overline{\mu}^{rN_0}\overline{\alpha}^r n\exp\left((-r\lambda + r/\tau_c \times \ln\overline{\mu})(t-t_0)\right). \tag{27}$$

By using Markov inequality in [29] and (27), we have that for arbitrary $\varepsilon \in (0,1)$ and $i \in \iota$, $P\{V_i(t) \le \varepsilon^{-1}\varsigma\mathbb{E}[\|\xi\|_\tau]\overline{\mu}^{rN_0}\overline{\alpha}^r n\exp((-r\lambda + r/\tau_c \times \ln\overline{\mu})(t-t_0))\} \ge 1-\varepsilon$, which together with (i) yields

$$P\{|x(t)| \le \varrho(\mathbb{E}[\|\xi\|_\tau], t-t_0)\} \ge 1-\varepsilon, \tag{28}$$

where $\varrho(a, t) = \nu^{-1}[\varepsilon^{-1}\varsigma(a)\mathbb{E}[\|\xi\|_\tau]\overline{\mu}^{rN_0}\overline{\alpha}^r n\exp((-r\lambda + r/\tau_c \times \ln\overline{\mu})t)]$. This verifies that system (1) is SGES. □

Corollary 1. *For system (1), assume that there is locally Lipschitz Lyapunov function V_i: $\mathbb{R}_{\ge 0} \times \mathbb{R}^n \longrightarrow \mathbb{R}_{\ge 0}$, $i \in \iota$, $r = 1$, $\zeta E \ge E$, $\nu \in \mathcal{K}_\infty$, $\varsigma \in \mathcal{CK}_\infty$, positive matrices $\mu := diag(\mu_1, \mu_2, \ldots, \mu_n)$, $\zeta := diag(\zeta_1, \zeta_2, \ldots, \zeta_n)$, and non-negative matrices $P := [p_{ij}]_{n\times n}$, $Q := [q_{ij}]_{n\times n}$, $O := [o_{ij}]_{n\times n}$, where $K := [\int_0^\infty k_{ij}(s)ds]_{n\times n}$ is continuous function and $k_{ij}(s) \ge 0$ such that the following conditions hold.*

(A): $i \in \iota$, $t \in \mathbb{R}_{\ge t_0}$, $\nu(|x(t)|) \le V_i(t) \le \varsigma(|x(t)|)$;

(B): $i \in \iota$, $t \in \mathbb{R}_{\ge t_0}\backslash\mathcal{T}$.

$$\begin{aligned}&\mathscr{L}V_i\left(t, x_t, \int_0^\infty k(s)x(t-s)\mathrm{d}s\right)\\ &\le -\mu_i V_i(t) + \sum_{j=1}^n p_{ij}V_j(t) + \sup_{-\tau\le\theta\le 0}\sum_{j=1}^n q_{ij}V_j(t+\theta) + \sum_{j=1}^n\int_0^\infty k_{ij}(s)V_j(t-s)\mathrm{d}s,\end{aligned} \tag{29}$$

where $\mu - P - Q - K$ is a nonsingular M-matrix, $\theta \in [-\tau, 0]$.

(C): $i \in \iota$ and $k \in N_{>0}$,

$$V_i(t_k) \le \zeta_i V_i(t_k^-) + \left(\sum_{j=1}^n o_{ij}\right)V_j(t_k^-). \tag{30}$$

(D): $\tau_c > \max_{i\in\iota} ln(\zeta_i + \sum_{j=1}^n o_{ij})/\lambda$, where $\lambda \in (0, \overline{\lambda})$, $V_i(t) = V_i(t, x(t))$.

$$\overline{\lambda} := \sup\left\{\eta > 0:\ \alpha_i\eta - \mu_i\alpha_i + \sum_{j=1}^n p_{ij}\alpha_j + \sum_{j=1}^n q_{ij}\alpha_j\exp(\tau\eta) + \sum_{j=1}^n\int_0^\infty k_{ij}(s)\exp(\eta s))\alpha_j\mathrm{d}s < 0\right\}, \tag{31}$$

where $i \in \iota$, $\alpha \in \Omega_M(\mu - P - Q - K)$, with $\min_{1\le i\le n}\{\alpha_i\} \ge 1$, $\overline{\alpha} = \max\{\alpha_i\}$.

Then, system (1) is SGES.

Remark 1. In Theorem 1, a difficulty is that condition $\zeta E > E$ destabilizes system (1). To overcome this difficulty, we give a lower bound by using the relation between the ADT and impulses, and it may guarantee that the number of destabilizing impulses can be reduced. As a consequence, we can prove that system (1) is SGES.

The next theorem will show that the impulses can promote the stability of system (1) even if system (1) without impulses may be unstable.

Theorem 2. *For system (1), assume that that there exist locally Lipschitz Lyapunov function V_i: $\mathbb{R}_{\ge 0} \times \mathbb{R}^n \longrightarrow \mathbb{R}_{\ge 0}$, for all $i \in \iota$, $r > 1$, $\nu \in \mathcal{K}_\infty$, $\varsigma \in \mathcal{CK}_\infty$, positive matrices $\mu := diag(\mu_1, \mu_2, \ldots, \mu_n)$, $\zeta := diag(\zeta_1, \zeta_2, \ldots, \zeta_n)$, and non-negative matrices $P := [p_{ij}]_{n\times n}$, $Q := [q_{ij}]_{n\times n}$, $O := [o_{ij}]_{n\times n}$, where $K := [\int_0^\infty k_{ij}(s)ds]_{n\times n}$ be continuous function, $k_{ij}(s) \ge 0$ and $(\zeta + O)E < E$:*

(A1) $i \in \iota$, $t \in \mathbb{R}_{\geq t_0}$, $\nu(|x(t)|) \leq V_i(t) \leq \varsigma(|x(t)|)$;

(A2) $i \in \iota$, $t \in \mathbb{R}_{\geq t_0} \backslash \mathscr{T}$.

$$\begin{aligned}\mathbb{E}\mathscr{L}V_i\left(t, x_t, \int_0^\infty k(s)x(t-s)\mathrm{d}s\right) \leq \mu_i \mathbb{E}V_i(t) &+ \sum_{j=1}^n p_{ij}\left(\mathbb{E}V_i(t)\right)^{1/r^r}\left(\mathbb{E}V_j(t)\right)^{1/r} \\ &- \sup_{-\tau\leq\theta\leq 0}\sum_{j=1}^n q_{ij}\left(\mathbb{E}V_i(t)\right)^{1/r^r}\left(\mathbb{E}V_j(t+\theta)\right)^{1/r} \\ &+ \sum_{j=1}^n \int_0^\infty k_{ij}(s)\left(\mathbb{E}V_i(t)\right)^{1/r^r}\left(\mathbb{E}V_j(t-s)\right)^{1/r}\mathrm{d}s,\end{aligned} \tag{32}$$

where $\mu + P - Q + K$ *is a nonsingular M-matrix,* $\theta \in [-\tau, 0], r = (1-r')^{-1}$.

(A3) $i \in \iota$ *and* $k \in N_{>0}$,

$$V_i(t_k) \leq \zeta_i V_i(t_k^-) + \sum_{j=1}^n o_{ij}\left(V_i(t_k^-)\right)^{1/r^r}\left(V_j(t_k^-)\right)^{1/r}. \tag{33}$$

(A4) $\tau_c < \min_{i\in\iota}\ln(\zeta_i + \sum_{j=1}^n o_{ij})/-\lambda$, *where* $\lambda > \overline{\lambda}$ *and* $V_i(t) = V_i(t, x(t))$.

$$\overline{\lambda} := \inf\left\{\omega > 0: \ -r\pi_i\omega + \mu_i\pi_i + \sum_{j=1}^n p_{ij}\pi_j - \sum_{j=1}^n q_{ij}\pi_j \exp(\tau\omega) + \sum_{j=1}^n \int_0^\infty k_{ij}(s)\exp(-\omega s)\pi_j \mathrm{d}s < 0\right\}. \tag{34}$$

where $i \in \iota$, $\pi \in \Omega_M(\mu + P - Q + K)$, $\min_{1\leq i\leq n}\{\pi_i\} \geq 1$, $\overline{\lambda} = \max_{i\in\iota}\omega_i$, $\overline{\pi} = \max\{\pi_i\}$.

Then, system (1) is SGES.

Proof. Like the proof of Theorem 1, we divide the proof into three steps.

Step 1. We first prove the existence of $\overline{\lambda}$. Since $\mu + P - Q + K$ is a nonsingular M-matrix, there is $\pi \in \Omega_M(\mu + P - Q + K)$, where $\min_{1\leq i\leq n}\{\pi_i\} \geq 1$, such that

$$\mu_i\pi_i + \sum_{j=1}^n p_{ij}\pi_j - \sum_{j=1}^n q_{ij}\pi_j + \sum_{j=1}^n \int_0^\infty k_{ij}(s)\pi_j \mathrm{d}s > 0, \quad i \in \iota. \tag{35}$$

For any given i, set

$$\overline{H}_i(\omega) = -r\pi_i\omega + \mu_i\pi_i + \sum_{j=1}^n p_{ij}\pi_j - \sum_{j=1}^n q_{ij}\pi_j \exp(\tau\omega) + \sum_{j=1}^n \int_0^\infty k_{ij}(s)\exp(-\omega s)\pi_j \mathrm{d}s. \tag{36}$$

Obviously, it follows from (36) that $\overline{H}_i(0) > 0$ and $\overline{H}_i(\infty) = -\infty$, where $\omega \longrightarrow \infty$. On the other hand, we have

$$\begin{aligned}\overline{H}_i'(\omega) &= -r\pi_i - \tau\sum_{j=1}^n q_{ij}\pi_j \exp(\tau\omega) \\ &\quad - \sum_{j=1}^n \int_0^\infty s k_{ij}(s)\exp(-\omega s)\pi_j \mathrm{d}s.\end{aligned} \tag{37}$$

Then $\overline{H}_i'(\omega) < 0$, and so there is a unique constant $\omega_i > 0$ such that $\overline{H}_i(\omega_i) = 0$. Setting $\overline{\lambda} = \min_{1\leq i\leq n}(\omega_i)$, it is clear that there exists a constant $\lambda > \overline{\lambda} > 0$.

Step 2. Next, for $i \in \iota$ and $\lambda > \overline{\lambda}$, then $(\zeta + O)E < E$, we need to prove that

$$\mathbb{E}[V_i(t)] \leq \mathbb{E}[V(t_0)]\overline{\mu}^{rN(t,t_0)}\overline{\pi}^r \exp(r\lambda(t-t_0)), \tag{38}$$

where $V(t_0) = \sum_{i=1}^{n} V_i(t_0)$, $\overline{\mu} = \max_{i\in\iota}\{\zeta_i + \sum_{j=1}^{n} o_{ij}\}$, and $\overline{\pi} := \max_{i\in\iota}(\pi_i)$. Clearly, (38) holds for $t = t_0$.

For convenience, define $W_i(t-t_0) = [\mathbb{E}V(t_0)]^{1/r}\overline{\mu}^{N(t,t_0)}\pi_i \exp(\lambda(t-t_0))$, $U_i(t) = [\mathbb{E}V_i(t)]^{1/r}$. It is easy to check that (38) is equivalent to the following:

$$[\mathbb{E}V_i(t)]^{1/r} \le \max_{i\in\iota}\left\{[\mathbb{E}V(t_0)]^{1/r}\overline{\mu}^{N(t,t_0)}\pi_i \exp(\lambda(t-t_0))\right\} =: \max_{i\in\iota}\{W_i(t-t_0)\}. \tag{39}$$

Now suppose that (38) is not true in some interval, then there are two cases:

Case 1. (38) is not true at the non-impulsive time of certain interval;

Case 2. (38) is not true at the impulsive time of certain interval.

For Case 1, there exists a k such that $U_i(t) \le W_i(t-t_0)$ holds for all $t \in [t_0, t_k]$ and $i \in \iota$, and $U_i(t) \le W_i(t-t_0)$ is not true for $i \in \iota$ and $t \in (t_k, t_{k+1})$. Define

$$t^* := \inf\{t \in (t_k, t_{k+1}): U_i(t) > W_i(t-t_0)\}. \tag{40}$$

Since $U_i(t)$ and $W_i(t-t_0)$ are continuous for $t \in \mathbb{R}_{\ge t_0}\backslash\mathscr{T}$, there exist $\bar{i}$ and t^* such that

$$U_{\bar{i}}(t^*) = W_{\bar{i}}(t^* - t_0), \tag{41}$$

$$U_i(t) > W_i(t-t_0), t \in (t^*, t^* + \Delta t). \tag{42}$$

where $\Delta t > 0$ is arbitrarily small. Therefore, it follows from (41) and (42) that

$$D^+U_{\bar{i}}(t^*) > D^+W_{\bar{i}}(t^* - t_0), \tag{43}$$

$$D^+W_{\bar{i}}(t^* - t_0) = \lambda\pi_{\bar{i}}\overline{\mu}^{N(t^*,t_0)}[\mathbb{E}V(t_0)]^{1/r}\exp(\lambda(t^* - t_0)). \tag{44}$$

By the definition of λ, we have

$$\begin{aligned}\lambda\pi_i > \frac{1}{r}\Bigg(&\mu_i\pi_i + \sum_{j=1}^{n} p_{ij}\pi_j - \sum_{j=1}^{n} q_{ij}\pi_j \exp(\tau\lambda)\\ &+ \sum_{j=1}^{n}\int_0^{\infty} k_{ij}(s)\exp(-\lambda s)\pi_j \mathrm{d}s\Bigg),\end{aligned} \tag{45}$$

which together with (44) yields

$$\begin{aligned}D^+W_{\bar{i}}(t^* - t_0) &> \frac{1}{r}\left(\mu_{\bar{i}}\pi_{\bar{i}} + \sum_{j=1}^{n} p_{\bar{i}j}\pi_j - \sum_{j=1}^{n} q_{\bar{i}j}\pi_j \exp(\tau\lambda) + \sum_{j=1}^{n}\int_0^{\infty} k_{\bar{i}j}(s)\exp(-\lambda s)\pi_j \mathrm{d}s\right)\\ &\quad\times \overline{\mu}^{N(t^*,t_0)}[\mathbb{E}V(t_0)]^{1/r}\exp(\lambda(t^* - t_0))\\ &= \frac{1}{r}(\mu_{\bar{i}}\pi_{\bar{i}})\overline{\mu}^{N(t^*,t_0)}[\mathbb{E}V(t_0)]^{1/r}\exp((\lambda(t^* - t_0)))\\ &\quad+ \frac{1}{r}\sum_{j=1}^{n} p_{\bar{i}j}\pi_j\overline{\mu}^{N(t^*,t_0)}[\mathbb{E}V(t_0)]^{1/r}\exp(\lambda(t^* - t_0))\\ &\quad- \frac{1}{r}\sum_{j=1}^{n} q_{\bar{i}j}\pi_j \exp(\tau\lambda)\overline{\mu}^{N(t^*,t_0)}[\mathbb{E}V(t_0)]^{1/r}\exp(\lambda(t^* - t_0))\\ &\quad+ \frac{1}{r}\sum_{j=1}^{n}\int_0^{\infty} k_{\bar{i}j}(s)\exp(-\lambda s)\pi_j \mathrm{d}s\overline{\mu}^{N(t^*,t_0)}[\mathbb{E}V(t_0)]^{1/r}\exp(\lambda(t^* - t_0))\\ &\ge \frac{1}{r}\left(\mu_{\bar{i}}\left(\mathbb{E}V_{\bar{i}}(t^*)\right)^{1/r} + \sum_{j=1}^{n} p_{\bar{i}j}\left(\mathbb{E}V_j(t^*)\right)^{1/r}\right)\\ &\quad- \frac{1}{r}\sum_{j=1}^{n} q_{\bar{i}j}\sup_{-\tau\le\theta\le 0}\left(\mathbb{E}V_j(t^* + \theta)\right)^{1/r}\\ &\quad+ \frac{1}{r}\sum_{j=1}^{n}\int_0^{\infty} k_{\bar{i}j}(s)\left(\mathbb{E}V_j(t^* - s)\right)^{1/r}\mathrm{d}s.\end{aligned} \tag{46}$$

Due to $U_i(t) = [\mathbb{E}V_i(t)]^{1/r}$, then $\mathbb{E}V_i(t) = [U_i(t)]^r$, for $i \in \iota$. By virtue of Dini-derivation and the Itô formula, we obtain $D^+\mathbb{E}V_i(t) = \mathbb{E}\mathscr{L}V_i$ and

$$\begin{aligned} D^+\mathbb{E}V_i(t) &= r[U_i(t)]^{r-1}D^+U_i(t) \le \mu_i[U_i(t)]^r + \sum_{j=i}^{n} p_{ij}[(U_i(t))]^{r/r'}U_j(t) \\ &\quad - \sum_{j=i}^{n} q_{ij} \sup_{-\tau\le\theta\le 0}[(U_i(t))]^{r/r'}U_j(t+\theta) + \sum_{j=i}^{n}\int_0^{\infty} k_{ij}(s)[(U_i(t))]^{r/r'}U_j(t-s)\mathrm{d}s. \end{aligned} \tag{47}$$

Therefore, it follows from (47) that

$$D^+U_i(t) \le \frac{1}{r}\left(\mu_i U_i(t) + \sum_{j=i}^{n} p_{ij}\big(U_j(t)\big) - \sum_{j=i}^{n} q_{ij} \sup_{-\tau\le\theta\le 0}\big(U_j(t+\theta)\big) + \sum_{j=i}^{n}\int_0^{\infty} k_{ij}(s)\big(U_j(t+s)\big)\mathrm{d}s\right). \tag{48}$$

Combining (46) and (48), we get $(\mathbb{E}V_{\bar{i}}(t^*))^{1/r} = D^+U_{\bar{i}}(t^*) \le D^+W_{\bar{i}}(t^* - t_0))$, which contradicts with (39). In the end, $U_i(t) \le W_i(t - t_0)$ holds for all $t \in (t_k, t_{k+1})$. In other words, (38) holds for all $t \in (t_k, t_{k+1})$.

For Case 2, (38) holds for all $t \in [t_0, t_k)$ and dose not hold at t_k. Then, for some $i \in \iota$.

$$\mathbb{E}[V_i(t_k)] > \mathbb{E}[V(t_0)]\overline{\mu}^{rN(t_k,t_0)}\overline{\pi}^r \exp(r\lambda(t_k - t_0)). \tag{49}$$

By taking expectation and using the Holder inequality, it follows from (A3) that at the impulsive instant t_k,

$$\begin{aligned} \mathbb{E}[V_i(t_k)] &\le \zeta_i\mathbb{E}V_i(t_k^-) + \left(\sum_{j=1}^{n} o_{ij}\right)(\mathbb{E}V_i(t_k^-))^{1/r'}\big(\mathbb{E}V_j(t_k^-)\big)^{1/r} \\ &\le \zeta_i\mathbb{E}[V(t_0)]\overline{\mu}^{rN(t_k^-,t_0)}\overline{\pi}^r \exp(r\lambda(t_k^- - t_0)) + \left(\sum_{j=1}^{n} o_{ij}\right) \\ &\quad \times\Big(\mathbb{E}[V(t_0)]\overline{\mu}^{rN(t_k^-,t_0)}\overline{\pi}^r \exp(r\lambda(t_k^- - t_0))\Big)^{1/r'}\Big(\mathbb{E}[V(t_0)]\overline{\mu}^{rN(t_k^-,t_0)}\overline{\pi}^r \exp(r\lambda(t_k^- - t_0))\Big)^{1/r} \\ &\le \left(\zeta_i + \sum_{j=1}^{n} o_{ij}\right)\mathbb{E}[V(t_0)]\overline{\mu}^{rN(t_k^-,t_0)}\overline{\pi}^r \exp(r\lambda(t_k^- - t_0)) \\ &\le \mathbb{E}[V(t_0)]\overline{\mu}^{rN(t_k,t_0)}\overline{\pi}^r \exp(r\lambda(t_k - t_0)), \end{aligned} \tag{50}$$

which contradicts with (49). This verifies that (38) holds for $t = t_k$. Therefore, by using the mathematical induction, we see that (38) is valid for all $t \in [t_0, \infty)$.

Step 3. Finally, we will prove that system (1) is SGES. According to $(A1)$ and Jensen's inequality, we have

$$\begin{aligned} &\mathbb{E}[V(t_0)]\overline{\mu}^{rN(t,t_0)}\overline{\pi}^r \exp(r\lambda(t - t_0)) \\ &\le \mathbb{E}[V(t_0)]\overline{\mu}^{rN_0 + r(t-t_0)/\tau_c}\overline{\pi}^r \exp(r\lambda(t - t_0)) \\ &= \mathbb{E}[V(t_0)]\overline{\mu}^{rN_0}\overline{\pi}^r \exp\big((r\lambda + r/\tau_c \ln\overline{\mu})(t - t_0)\big) \\ &\le \varsigma\mathbb{E}[\|\xi\|_\tau]\overline{\mu}^{rN_0}\overline{\pi}^r \exp\big((r\lambda + r/\tau_c \ln\overline{\mu})(t - t_0)\big). \end{aligned} \tag{51}$$

It follows from condition (A4) that $r\lambda + (r/\tau_c)\ln\overline{\mu} < 0$. The rest of the proof is similar to that in Theorem 1, and thus we omit it here. This completes the proof. □

Corollary 2. *For system (1), assume that there is locally Lipschitz Lyapunov function* $V_i: \mathbb{R}_{\geq 0} \times \mathbb{R}^n \longrightarrow \mathbb{R}_{\geq 0}$, $i \in \iota$, $r = 1$, $(\zeta + O)E < E$, $\nu \in \mathcal{K}_\infty$, $\varsigma \in \mathcal{CK}_\infty$, *positive matrices* $\mu \coloneqq diag(\mu_1, \mu_2, \ldots, \mu_n)$, $\zeta \coloneqq diag(\zeta_1, \zeta_2, \ldots, \zeta_n)$, *and nonnegative matrices* $P \coloneqq [p_{ij}]_{n\times n}$, $Q \coloneqq [q_{ij}]_{n\times n}$, $O \coloneqq [o_{ij}]_{n\times n}$. *Where* $K \coloneqq [\int_0^\infty k_{ij}(s)ds]_{n\times n}$ *is continuous function and* $k_{ij}(s) \geq 0$ *such that the following conditions hold:*

(A): $i \in \iota$, $t \in \mathbb{R}_{\geq t_0}$, $\nu(|x(t)|) \leq V_i(t) \leq \varsigma(|x(t)|)$;

(B): $i \in \iota$, $t \in \mathbb{R}_{\geq t_0} \backslash \mathcal{T}$,

$$\mathcal{L}V_i\left(t, x_t, \int_0^\infty k(s)x(t-s)\mathrm{d}s\right) \leq \mu_i V_i(t) + \sum_{j=1}^n p_{ij}V_j(t) - \sup_{-\tau\leq\theta\leq 0}\sum_{j=1}^n q_{ij}V_j(t+\theta) + \sum_{j=1}^n \int_0^\infty k_{ij}(s)V_j(t-s)\mathrm{d}s, \tag{52}$$

where $\mu + P - Q + K$ *is a nonsingular M-matrix,* $\theta \in [-\tau, 0]$;

(C): $i \in \iota$ *and* $k \in N_{>0}$,

$$V_i(t_k) \leq \zeta_i V_i(t_k^-) + \left(\sum_{j=1}^n o_{ij}\right)V_j(t_k^-). \tag{53}$$

(D): $\lambda + (1/\tau_c)ln\overline{\mu} < 0$, *where* $\overline{\mu} = \max_{i\in\iota}\left\{\zeta_i + \sum_{j=1}^n o_{ij}\right\}$ *and* $\lambda > \overline{\lambda}$ *and* $V_i(t) = V_i(t, x(t))$.

$$\overline{\lambda} \coloneqq \inf\left\{\omega > 0: \ -\pi_i\omega + \mu_i\pi_i + \sum_{j=1}^n p_{ij}\pi_j - \sum_{j=1}^n q_{ij}\pi_j \exp(\tau\omega) + \sum_{j=1}^n \int_0^\infty k_{ij(s)\exp(-\omega s)\pi_j}\mathrm{d}s < 0\right\}, \tag{54}$$

where $i \in \iota$, $\pi \in \Omega_M(\mu + P - Q + K)$, *with* $\min_{1\leq i\leq n}\{\pi_i\} \geq 1$, $\overline{\pi} = \max\{\pi_i\}$.

Then, system (1) is SGES.

Remark 2. In Theorem 2, the condition $(\zeta + O)E < E$ shows that the impulses can do the contribution of the stability of system (1). Although system (1) may not be stable, we can give an upper bound by using the relation between ADT and impulses and prove that SIDSs with DDs and IDDs are SGES.

Remark 3. When $k_{ij} = 0$, $r = 2$, Theorems 1 and 2 will be reduced to the case of stochastic differential systems with only DDS, which was studied in [12]. It should be mentioned that [12] only considered time-delay terms coupled with nondelay terms. However, we consider the effect of mixed delay terms including the DDs item and IDDs item coupled with delay-free item, which also appears in the $\mathcal{L}V$-operator differential inequality. Thus, our results not only avoid to use elementary inequality to analyze crossterm problem but also is more representative.

Remark 4. Conditions (ii) and (A2) are the vector version of the Halandy inequality in [9], which is an important tool in the stability analysis of SDSs. Especially, they also play an important role in discussing stochastically perturbed neural networks and stochastically generalized ecological systems.

4. Two Examples

In this section, two numerical examples are used to check the validity of our theories.

Consider a two-neuron stochastically perturbed neural network with impulsive control.

$$\begin{cases} \mathrm{d}x(t) = \left[Ax(t) + Bf(x(t)) + Cf(x_t) + Df\left(\int_0^6 k(s)x(t-s)\mathrm{d}s\right)\right]\mathrm{d}t \\ +\sigma(t, x(t))\mathrm{d}\omega(t), t \in \mathbb{R}_{\geq} t_0 \backslash \mathcal{T}, \\ x(t_k) = hx(t_k^-), \quad t_k \in \mathcal{T}, k = 1, 2, \ldots n, \end{cases} \tag{55}$$

where $x(t) \in \mathbb{R}^2$, $\mathcal{T}$ is a given impulsive time sequence. Define $f(x) = (f_1(x_1), f_2(x_2)) = (0.05 * \tanh(x_1), 0.05 * \tanh(x_2))$, $x_t := (x_1(t-\tau), x_2(t-\tau))$, then we have

$$0 \le (f_i(z_1) - f_i(z_2))/(z_1 - z_2) \le 0.05, \tag{56}$$

for all $z_1, z_2 \in \mathbb{R}$ and $i = 1, 2$.

4.1. Example I. Set

$$\begin{aligned} A &= \begin{bmatrix} -2.4 & 0 \\ 0 & -2.8 \end{bmatrix}, \\ B &= \begin{bmatrix} 1.6 & 3.5 \\ 0.3 & 0.4 \end{bmatrix}, \\ C &= \begin{bmatrix} 0.1 & 0.6 \\ 0.4 & 0.1 \end{bmatrix}, \\ D &= \begin{bmatrix} 0.4 & 0.5 \\ 0.3 & 0.1 \end{bmatrix}, \\ \sigma &= \begin{bmatrix} 0.2 * x_1(t) & 0 \\ 0 & 0.2 * x_2(t) \end{bmatrix}, \\ h &= \begin{bmatrix} 1.5 & 0 \\ 0 & 1.5 \end{bmatrix}, \end{aligned} \tag{57}$$

where $k(s) = e^{-s}/1 - e^{-6}$.

Define $V(t, x(t)) = (V_1(t, x(t)), V_2(t, x(t)))$ with $V_i(t, x(t)) = |x_i(t)|^p, i = 1, 2\,(p > 1)$. Applying the Itô formula, we get

$$\begin{aligned} \mathscr{L}V_1(t, x_t) \le{}& \left(-2.32p + 0.02\left(p^2 - p\right)\right)\left|x_1(t)\right|^p \\ &+ 0.175p\left|x_1(t)\right|^{p-1}\left|x_2(t)\right| + 0.05p\left|x_1(t)\right|^{p-1}\left|x_1(t-\tau)\right| \\ &+ 0.03p\left|x_1(t)\right|^{p-1}\left|x_2(t-\tau)\right| + 0.02p\left|x_1(t)\right|^{p-1}\int_0^6 \frac{e^{-s}}{1-e^{-6}}\left|x_1(t-s)\right|\mathrm{d}s \\ &+ 0.025p\left|x_1(t)\right|^{p-1}\int_0^6 \frac{e^{-s}}{1-e^{-6}}\left|x_2(t-s)\right|\mathrm{d}s, \\ \mathscr{L}V_2(t, x_t) \le{}& \left(-2.78p + 0.02\left(p^2 - p\right)\right)\left|x_2(t)\right|^p \\ &+ 0.015p|x_2(t)|^{p-1}\left|x_1(t)\right| + 0.02p\left|x_2(t)\right|^{p-1}\left|x_1(t-\tau)\right| \\ &+ 0.005p\left|x_2(t)\right|^{p-1}\left|x_2(t-\tau)\right| + 0.015p\left|x_2(t)\right|^{p-1}\int_0^6 \frac{e^{-s}}{1-e^{-6}}\left|x_1(t-s)\right|\mathrm{d}s \\ &+ 0.005p\left|x_2(t)\right|^{p-1}\int_0^6 \frac{e^{-s}}{1-e^{-6}}\left|x_2(t-s)\right|\mathrm{d}sV_i(t_k) \le 1.5V_i\left(t_k^-\right)(i = 1, 2). \end{aligned} \tag{58}$$

Then, we can easily obtain

$$\mu = \begin{bmatrix} 2.32p - 0.02\left(p^2 - p\right) & 0 \\ 0 & 2.78p - 0.02\left(p^2 - p\right) \end{bmatrix},$$
$$P = \begin{bmatrix} 0 & 0.175p \\ 0.015p & 0 \end{bmatrix},$$
$$Q = \begin{bmatrix} 00.05p & 0.03p \\ 0.02p & 0.05p \end{bmatrix},$$
$$K = \begin{bmatrix} 0.02p & 0.025p \\ 0.015p & 0.005p \end{bmatrix},$$
$$\zeta = \begin{bmatrix} 1.5 & 0 \\ 0 & 1.5 \end{bmatrix}. \tag{59}$$

Thus, we have that $\mu - P - Q - K$ is a nonsingular M-matrix, for any $p \in (1, 112.4376)$. In particular, when $p = 4$, $\alpha_1 = 1$, $\alpha_2 = 1.5$, $\tau = 1$, we can calculate $\overline{\lambda} = 0.5453$ and $\tau_c > 2.9743$, which verifies that all the conditions of Theorem 1 are satisfied. Thus, system (1) is SGES. Choosing $\tau_c = 6$ and a proper $\mathscr{T}$, the initial state $x_0 = (0.7, -0.6)$, the sample path of solution is given in Figure 1.

4.2. Example II. Set

$$A = \begin{bmatrix} -0.04 & 0 \\ 0 & -0.01 \end{bmatrix},$$
$$B = \begin{bmatrix} 1.6 & 3.5 \\ 0.5 & 0.4 \end{bmatrix},$$
$$C = \begin{bmatrix} -0.1 & -0.6 \\ -0.4 & -0.1 \end{bmatrix},$$
$$D = \begin{bmatrix} 1 & 0 \\ 0 & 1 \end{bmatrix},$$
$$\sigma = \begin{bmatrix} 2 * x_1(t) & 0 \\ 0 & 2 * x_2(t) \end{bmatrix},$$
$$h = \begin{bmatrix} 0.75 & 0 \\ 0 & 0.75 \end{bmatrix}, \tag{60}$$

where $k(s) = e^{-s}/1 - e^{-6}$.

Define $V(t, x(t)) = (V_1(t, x(t)), V_2(t, x(t)))$, where $V_i(t, x(t)) = |x_i(t)|^p, i = 1, 2\,(p > 1)$. Applying the Itô formula, we get

$$\begin{aligned}
\mathscr{L}V_1(t, x_t) \le{}& \left(0.04p + 2\left(p^2 - p\right)\right)\left|x_1(t)\right|^p + 0.175p\left|x_1(t)\right|^{p-1}\left|x_2(t)\right| \\
&- 0.005p\left|x_1(t)\right|^{p-1}\left|x_1(t-\tau)\right| - 0.03p\left|x_1(t)\right|^{p-1}\left|x_2(t-\tau)\right| \\
&+ 0.05p\left|x_1(t)\right|^{p-1}\int_0^6 \frac{e^{-s}}{1-e^{-6}}\left|x_1(t-s)\right|\mathrm{d}s, \\
\mathscr{L}V_2(t, x_t) \le{}& \left(0.01p + 2\left(p^2 - p\right)\right)\left|x_2(t)\right|^p + 0.025p\left|x_2(t)\right|^{p-1}\left|x_1(t)\right| \\
&- 0.02p\left|x_2(t)\right|^{p-1}\left|x_1(t-\tau)\right| - 0.005p\left|x_2(t)\right|^{p-1}\left|x_2(t-\tau)\right| \\
&+ 0.05p\left|x_2(t)\right|^{p-1}\int_0^6 \frac{e^{-s}}{1-e^{-6}}\left|x_2(t-s)\right|\mathrm{d}s.
\end{aligned} \tag{61}$$

By taking expectation on both sides of the inequality and using the *Hölder* inequality, we have

$$\begin{aligned}
\mathbb{E}\mathscr{L}V_1(t, x_t) \le{}& \left(0.04p + 2\left(p^2 - p\right)\right)\mathbb{E}V_1(t) + 0.175p\left(\mathbb{E}V_1(t)\right)^{p-1/p}\left(\mathbb{E}V_2(t)\right)^{1/p} \\
&- 0.005p\left(\mathbb{E}V_1(t)\right)^{p-1/p}\left(\mathbb{E}V_1(t-\tau)\right)^{1/p} - 0.03p\left(\mathbb{E}V_1(t)\right)^{p-1/p}\left(\mathbb{E}V_2(t-\tau)\right)^{1/p} \\
&+ 0.05p\left(\mathbb{E}V_1(t)\right)^{p-1/p}\int_0^6 \frac{e^{-s}}{1-e^{-6}}\left(\mathbb{E}V_1(t-s)\right)^{1/p}\mathrm{d}s, \\
\mathbb{E}\mathscr{L}V_2(t, x_t) \le{}& \left(0.01p + 2\left(p^2 - p\right)\right)\mathbb{E}V_2(t) + 0.025p\left(\mathbb{E}V_2(t)\right)^{p-1/p}\left(\mathbb{E}V_1(t)\right)^{1/p} \\
&- 0.02p\left(\mathbb{E}V_2(t)\right)^{p-1/p}\left(\mathbb{E}V_1(t-\tau)\right)^{1/p} - 0.005p\left(\mathbb{E}V_2(t)\right)^{p-1/p}\left(\mathbb{E}V_2(t-\tau)\right)^{1/p} \\
&+ 0.05p\left(\mathbb{E}V_2(t)\right)^{p-1/p}\int_0^6 \frac{e^{-s}}{1-e^{-6}}\left(\mathbb{E}V_2(t)\right)^{1/p}\mathrm{d}s, \\
\mathbb{E}V_i(t_k) \le{}& 0.75\mathbb{E}V_i\left(t_k^-\right)\ (i = 1, 2).
\end{aligned} \tag{62}$$

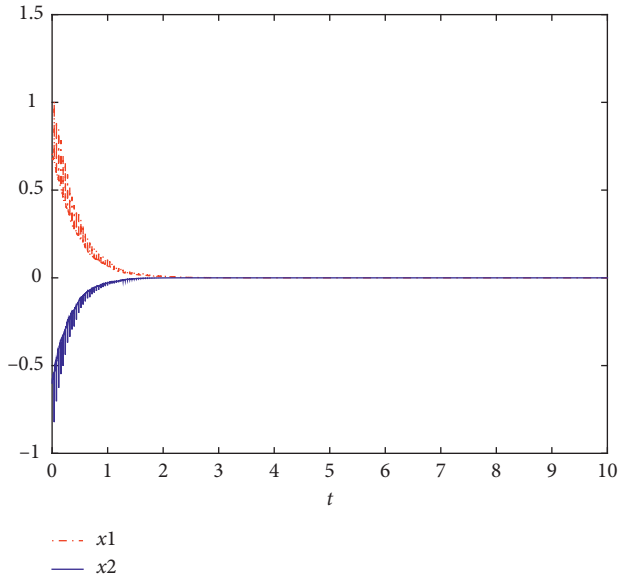

Figure 1: The solution of $\tau = 1$, $\tau_c = 6$ in example I.

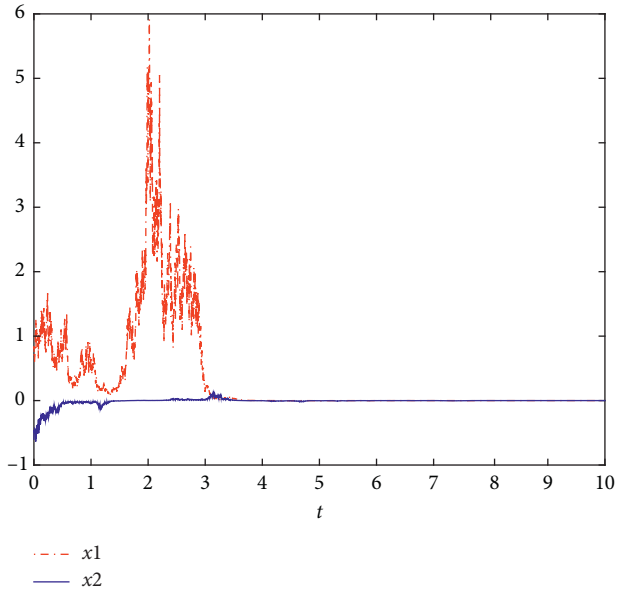

Figure 2: The solution of $\tau = 1$, $\tau_c = 0.16$ in example II.

Then, it follows that

$$\mu = \begin{bmatrix} 0.04p + 2\left(p^2 - p\right) & 0 \\ 0 & 0.01p + 2\left(p^2 - p\right) \end{bmatrix},$$
$$P = \begin{bmatrix} 0 & 0.175p \\ 0.025p & 0 \end{bmatrix},$$
$$Q = \begin{bmatrix} 0.005p & 0.03p \\ 0.02p & 0.005p \end{bmatrix}, \quad (63)$$
$$K = \begin{bmatrix} 0.05p & 0 \\ 0 & 0.05p \end{bmatrix},$$
$$\zeta = \begin{bmatrix} 0.75 & 0 \\ 0 & 0.75 \end{bmatrix}.$$

Then, we see that $\mu + P - Q + K$ is a nonsingular M-matrix for any $p \in (1, +\infty)$. Specially, when $p = 2$, $\pi_1 = 1$, $\pi_2 = 1.5$, $\tau = 1$, we can calculate $\bar{\lambda} = 1.9695$ and $\tau_c < 0.1661$. Thus, all the conditions of Theorem 2 are true, which verifies that (1) is SGES. Choosing $\tau_c = 0.16$ and a proper T, the initial state $x_0 = (0.7, -0.6)$, the sample path of solution is presented in Figure 2.

5. Conclusion

In this paper, we have used the ADT condition and VLF to study SGES of SIDSs with DDs and IDDs under two cases: unstable impulse dynamics situation and stable impulse dynamics situation. By using VLF and ADT conditions, two sufficient stability criteria are established. One is that the lower bound of the mixed system relative to the average dwell-time is SGES when continuous SIDSs with DDs and IDDs is stable and the impulsive effect is unstable. The other is that the impulses can stabilize the system successfully under the upper bound condition of the given average dwell-time when continuous SIDSs with DDs and IDDs could not stochastic stable. Finally, two examples are provided to verify the effectiveness of our results. In future, we will consider apply our method to neural networks [30, 31] and semi-Markov switching systems [32–34].

Data Availability

No data were used to support this study.

Conflicts of Interest

The authors declare that they have no conflicts of interest.

Acknowledgments

This work was jointly supported by the National Natural Science Foundation of China (61773217), the Natural

Science Foundation of Hunan Province (2020JJ4054), the Hunan Provincial Science and Technology Project Foundation (2019RS1033), and the Scientific Research Fund of Hunan Provincial Education Department (18A013).

References

[1] S. E. A. Mohammed, *Stochastic Functional Differential Equations*, Longman Scientific and Technical, London, UK, 1984.

[2] Q. Zhu, "Stability analysis of stochastic delay differential equations with Lévy noise," *Systems & Control Letters*, vol. 118, pp. 62–68, 2018.

[3] Q. Zhu and T. Huang, "Stability analysis for a class of stochastic delay nonlinear systems driven by G-Brownian motion," *Systems & Control Letters*, vol. 140, Article ID 104699, 2020.

[4] Q. Zhu, "Stabilization of stochastic nonlinear delay systems with exogenous disturbances and the event-triggered feedback control," *IEEE Transactions on Automatic Control*, vol. 64, no. 9, pp. 3764–3771, 2019.

[5] W. Ma, X. Luo, and Q. Zhu, "Practical exponential stability of stochastic age-dependent capital system with Lévy noise," *Systems & Control Letters*, vol. 144, Article ID 104759, 2020.

[6] X. Mao, *Stochastic Differential Equations and Their Applications*, Elsevier, Amsterdam, Netherlands, 2nd edition, 2007.

[7] M. S. Alwan, X. Liu, and W.-C. Xie, "Existence, continuation, and uniqueness problems of stochastic impulsive systems with time delay," *Journal of the Franklin Institute*, vol. 347, no. 7, pp. 1317–1333, 2010.

[8] L. Gao, Z. Cao, M. Zhang, and Q. Zhu, "Input-to-state stability for hybrid delayed systems with admissible edge-dependent switching signals," *Journal of the Franklin Institute*, vol. 357, no. 13, pp. 8823–8850, 2020.

[9] L. Liu, "New criteria on exponential stability for stochastic delay differential systems based on vector Lyapunov function," *IEEE Transactions on Systems, Man, and Cybernetics: Systems*, vol. 47, no. 11, pp. 2985–2993, 2017.

[10] M. S. Ali, M. Usha, Q. Zhu, and S. Shanmugam, "Synchronization analysis for stochastic T-S fuzzy complex networks with Markovian jumping parameters and mixed time-varying delays via impulsive control," *Mathematical Problems in Engineering*, vol. 2020, Article ID 9739876, , 2020.

[11] W. Hu and Q. Zhu, "Stability analysis of impulsive stochastic delayed differential systems with unbounded delays," *Systems & Control Letters*, vol. 136, Article ID 104606, 2020.

[12] W. Ren and J. Xiong, "Exponential stability of stochastic impulsive switched delayed systems based on vector lyapunov functions," in *Proceeding of the 2017 11th Asian Control Conference (ASCC)*, pp. 1888–1893, Gold Coast, Australia, December 2017.

[13] P. Balasubramaniam and R. Rakkiyappan, "Global asymptotic stability of stochastic recurrent neural networks with multiple discrete delays and unbounded distributed delays," *Applied Mathematics and Computation*, vol. 204, no. 2, pp. 680–686, 2008.

[14] C. Huang and J. Cao, "Almost sure exponential stability of stochastic cellular neural networks with unbounded distributed delays," *Neurocomputing*, vol. 72, no. 13-15, pp. 3352–3356, 2009.

[15] G. Chen, D. Li, L. Shi, O. van Gaans, and S. Verduyn Lunel, "Stability results for stochastic delayed recurrent neural networks with discrete and distributed delays," *Journal of Differential Equations*, vol. 264, no. 6, pp. 3864–3898, 2018.

[16] W. M. Haddad, V. Chellaboina, and S. G. Nersesov, "Impulsive and hybrid dynamical systems: stability, dissipativity and control: stability, dissipativity, and control," in *Princeton Series in Applied Mathematics*, Princeton University Press, Princeton, NJ, USA, 2014.

[17] W.-H. Chen and W. X. Zheng, "Input-to-state stability and integral input-to-state stability of nonlinear impulsive systems with delays," *Automatica*, vol. 45, no. 6, pp. 1481–1488, 2009.

[18] J. P. Hespanha, D. Liberzon, and A. R. Teel, "Lyapunov conditions for input-to-state stability of impulsive systems," *Automatica*, vol. 44, no. 11, pp. 2735–2744, 2008.

[19] S. G. Nersesov and W. M. Haddad, "Control vector Lyapunov functions for large-scale impulsive dynamical systems," *Nonlinear Analysis: Hybrid Systems*, vol. 1, no. 2, pp. 223–243, 2007.

[20] I. M. Stamova, "Vector Lyapunov functions for practical stability of nonlinear impulsive functional differential equations," *Journal of Mathematical Analysis and Applications*, vol. 325, no. 1, pp. 612–623, 2007.

[21] W. Ren and J. Xiong, "Stability and stabilization of switched stochastic systems under asynchronous switching," *Systems & Control Letters*, vol. 97, pp. 184–192, 2016.

[22] H. Ros, L. Hetel, and D. Efimov, "Vector Lyapunov function based stability for a class of impulsive systems," in *Proceedings of the 2015 54th IEEE Conference on Decision and Control*, pp. 2247–2251, Osaka, Japan, December 2015.

[23] I. Karafyllis and Z.-P. Jiang, "Global stabilization of nonlinear systems based on vector control Lyapunov functions," *IEEE Transactions on Automatic Control*, vol. 58, no. 10, pp. 2550–2562, 2013.

[24] J. P. Hespanha and A. S. Morse, "Stability of switched systems with average dwell-time," in *Proceedings of the 38th IEEE Conference on Decision and Control*, pp. 2655–2660, Phoenix, AZ, USA, December 1999.

[25] R. Bellman, "Vector Lyapunov functions," *Journal of the Society for Industrial and Applied Mathematics Series A Control*, vol. 1, no. 1, pp. 32–34, 1962.

[26] V. Lakshmikantham, V. M. Matrosov, and S. Sivasundaram, *Vector Lyapunov Functions and Stability Analysis of Nonlinear Systems*, Springer Science and Business Media, Berlin, Germany, 2013.

[27] P. Zhao, W. Feng, and Y. Kang, "Stochastic input-to-state stability of switched stochastic nonlinear systems," *Automatica*, vol. 48, no. 10, pp. 2569–2576, 2012.

[28] H. Wang, J. Tan, T. Huang, and S. Duan, "Impulsive delayed integro-differential inequality and its application on IMNNs with discrete and distributed delays," *Neurocomputing*, vol. 341, pp. 99–106, 2019.

[29] L. Rogers and D. Williams, *Diffusions, Markov Processes and Martingales: Volume 2, Itô Calculus*, Cambridge University Press, Cambridge, UK, 2000.

[30] Z. Zeng, J. Wang, and X. Liao, "Global exponential stability of a general class of recurrent neural networks with time-varying delays," *IEEE Transactions on Circuits and Systems I: Fundamental Theory and Applications*, vol. 50, no. 10, pp. 1353–1358, 2003.

[31] Z. Zeng and J. Wang, "Improved conditions for global exponential stability of recurrent neural networks with time-varying delays," *IEEE Transactions on Neural Networks*, vol. 17, no. 3, pp. 623–635, 2006.

[32] J. Cheng, J. H. Park, J. Cao, and W. Qi, "A hidden mode observation approach to finite-time SOFC of Markovian

switching systems with quantization," *Nonlinear Dynamics*, vol. 100, no. 1, pp. 509–521, 2020.

[33] J. Cheng, D. Zhang, W. Qi, J. Cao, and K. Shi, "Finite-time stabilization of T-S fuzzy semi-Markov switching systems: a coupling memory sampled- data control approach," *Journal of The Franklin Institute*, vol. 357, no. 16, pp. 11265–11280, 2020.

[34] B. Wang and Q. Zhu, "Stability analysis of semi-Markov switched stochastic systems," *Automatica*, vol. 94, pp. 72–80, 2018.

Hindawi
Complexity
Volume 2020, Article ID 1659103, 19 pages
https://doi.org/10.1155/2020/1659103

Research Article

An Air Traffic Controller Action Extraction-Prediction Model Using Machine Learning Approach

Duc-Thinh Pham, Sameer Alam, and Vu Duong

Air Traffic Management Research Institute, School of Mechanical and Aerospace Engineering, Nanyang Technological University, Singapore

Correspondence should be addressed to Duc-Thinh Pham; dtpham@ntu.edu.sg

Received 9 July 2020; Revised 21 October 2020; Accepted 26 October 2020; Published 18 November 2020

Academic Editor: Vladimir Stojanovic

In air traffic control, the airspace is divided into several smaller sectors for better management of air traffic and air traffic controller workload. Such sectors are usually managed by a team of two air traffic controllers: planning controller (*D*-side) and executive controller (*R*-side). *D*-side controller is responsible for processing flight-plan information to plan and organize the flow of traffic entering the sector. *R*-side controller deals with ensuring safety of flights in their sector. A better understanding and predictability of *D*-side controller actions, for a given traffic scenario, may help in automating some of its tasks and hence reduce workload. In this paper, we propose a learning model to predict *D*-side controller actions. The learning problem is modeled as a supervised learning problem, where the target variables are *D*-side controller actions and the explanatory variables are the aircraft 4D trajectory features. The model is trained on six months of ADS-B data over an en-route sector, and its generalization performance was assessed, using crossvalidation, on the same sector. Results indicate that the model for vertical maneuver actions provides highest prediction accuracy (99%). Besides, the model for speed change and course change action provides predictability accuracy of 80% and 87%, respectively. The model to predict the set of all the actions (altitude, speed, and course change) for each flight achieves an accuracy of 70% implying for 70% of flights; *D*-side controller's action can be predicted from trajectory information at sector entry position. In terms of operational validation, the proposed approach is envisioned as ATCO assisting tool, not an autonomous tool. Thus, there is always ATCO discretion element, and as more ATCO actions are collected, the models can be further trained for better accuracy. For future work, we will consider expanding the feature set by including parameters such as weather and wind. Moreover, human in the loop simulation will be performed to measure the effectiveness of the proposed approach.

1. Introduction

The primary purpose of Air Traffic Control (ATC) worldwide is to prevent collisions, organize and expedite the flow of air traffic, and provide information and other support for pilots [1]. In regions, where the Air Traffic Management (ATM) system is well developed, three types of control facilities play a critical role during the successive phase of a typical flight: (1) the airport traffic control tower (aerodrome control), (2) the terminal airspace control center (approach control), and (3) the en-route control center (area control) [2]. The en-route airspace is organized vertically and horizontally according to local air structure, and traffic flows into a smaller area called "sectors." A sector is generally considered as a fundamental "unit" of airspace volume from the ATM point of view. The en-route sector is usually managed by a team of two air traffic controllers: planning controller (*D*-side) and executive controller (*R*-side) [3].

Both *D*-side and *R*-side air traffic controllers (ATCOs) are responsible for airspace monitoring, conflict detection, and resolution, along with managing route or altitude modification requests from the aircraft. The difference between the two roles lies in the strategic and tactical levels of intervention. The *D*-side controller is primarily responsible for processing flight-plan information to plan, coordinate, and organize the flow of air traffic entering into a sector. The

D-side controller uses the flight-plan information and employs Medium Term Conflict Detection (MTCD) tool [4] to predict aircraft trajectories in a 20 minute look-ahead time window. *D*-side controller employs a variety of strategies/actions, i.e., combination of altitude, speed, course change, hold maneuvers, etc. to maintain an orderly flow of the incoming traffic in a sector. Thus, it minimizes crossings events which may lead to loss of separation. This ensures, at a tactical level, a minimum intervention is required from the *R*-side controller while managing the air traffic in a given sector. The *R*-side controller uses the Short Term Conflict Alert (STCA) tool [5] to predict any loss of separation in a 4 to 8 minutes look-ahead time window. The *R*-side controller is mainly concerned with tactical interventions to maintain safe separation between flights.

The *D*-side controller receives flight plan information of the flight before it enters the sector (transfer of communication). At this point, the aircraft is in contact with both, the previous sector *D*-side controller as well as the next sector *D*-side controller. The *D*-side controller then negotiates with the aircraft regarding entry flight level, entry speed, and entry way-point depending upon the strategic situation in his/her sector at a certain look-ahead time. The primary objective of this planning is to maintain an orderly flow of traffic and to minimize crossings which may lead to a loss of separation (LOS) scenario for an *R*-Side controller to intervene. Once the aircraft enters the sector boundaries (transfer of control), the *D*-side hands off the aircraft to the *R*-side controller who then provides ATC services via radio communication. In some circumstances (e.g., bad weather), the aircraft may need to be handed off differently than the letter of agreement. In those cases, the *D*-side controller must coordinate with the other sector controller to ask for approval for another route which is not specified in the letter of agreement before the aircraft cross the boundary.

As ATC is becoming increasingly complex and dynamic, the role of ATCOs in an ATC system is getting more and more challenging [6]. Within the safety-critical domain of ATC, workload remains a dominant consideration in improving ATC system performance. Since the main responsibility of the *D*-side controller is to manage and organize traffic flow such that the tactical flight interventions from the *R*-side controller are minimized, it is desirable to automate the *D*-side controller tasks such that its task load is reduced. A possible way is to develop a mechanism that can learn and predict *D*-side controller's traffic management strategies for a given traffic scenario.

The contribution of this paper is modeling the learning problem by extracting the *D*-side controller's actions. The novelty is in formulating the problem as predicting a quantitative response for an observation, i.e., classifying that observation, since it involves assigning the observation to a class. Thus, we have approached the classical simulation-modeling problem as a data-driven problem where controller's strategies are learned from the natural behavior of a human *D*-side controller, the way he/she handles different traffic scenarios. This task requires visualizing, analysing, and understanding 6-month traffic trajectory data for formulating a reasonable and solvable question. Besides, another contribution of this paper is on learning mechanisms that may offer better predictability for planning controllers under different traffic scenarios. We have adopted tree-based ensemble methods for learning ATCO's actions in a complex air traffic environment on a real dataset. The method involves segmenting the predictor space into several simple regions, and then in order to make a prediction from a given observation, a mean or mode of the training observations in the region, to which it belongs, is used. Such set of splitting rules were then used to segment the predictor space and then summarized in the form of a tree. Such multiple trees can then be combined to yield an accurate consensus [7]. Furthermore, we have demonstrated that tree-based methods can closely mirror human decision-making than other classification approaches [8]. Even though the used learning models are well-known ones, preparing the analytical dataset for training them are challenging because of the noises and missing in trajectories. Besides, detecting and removing outliers such as holding or incomplete trajectories under those conditions is also another challenge.

This paper is organized as follows. Section 2 introduces the background for this research question especially focusing on successful applications of machine learning and tree-based ensemble learning in air traffic management. Section 3 describes the overview of the proposed approach for predicting planning controller's action including data preparation steps. Section 4 discusses in detail our data analysis and data processing steps for extracting ATCO's action from trajectory data. Section 5 introduces our methodology for developing predictive models using two different ensemble learning techniques: Random Forest and Extreme Gradient Boosting. Section 6 describes our predictive models for predicting controller decision and taxi time for departure flights and introduces our experimental setup for evaluating the predictive models as well as the discussion and analysis of the results. Section 7 is a discussion section on the implementation for ATCO command from our predicted results. Finally, Section 8 presents our conclusions and future work.

2. Background

The quest of understanding and learning opponent's strategies in games such as Chess, Backgammon, and Game of Go and be able to predict the next move of an opponent, is well known in literature [9–12]. Machine learning methods such as deep neural networks, tree-search methods, and Bayesian reinforcement learning have recently been quite successful in learning game strategies and outperforming world champions [13–16]. However, a major assumption in such machine learning algorithms is that the training and future data must be in the same feature space and have the same distribution [17].

In air traffic, the feature space (airspace structure including its airways and way points) and the data distribution (aircraft trajectory points) varies significantly. Since every airspace is unique, thus every air traffic scenario has a different data distribution. Furthermore, traffic flow

management relies almost exclusively on the judgment of air traffic controllers for decisions [18]. Previous research studies into identifying air traffic controller's strategies from traffic data have found some interesting insights, but they were generic in nature and lack any predictability of ATCO actions given a traffic scenario. For example, in [19], it was found that, in the presence of conflict between a few aircraft, the velocity variation strategy seems to cost more (in terms of the time of flight) than the course angle deviation strategy. In [4], the authors developed an evolutionary computation framework to identify air traffic maneuvers that may expose a traffic scenario to loss of separation but fall short of generalizing it to a range of traffic scenarios. In [20], authors predicted air traffic controller workload from past sector merge and split actions but could not generalize the learning to new sectors due to overfitting of the training data. In [21], the authors proposed using game theory for conflict resolution in en-route airspace. Apart from en-route airspace, machine learning methods have also been applied in terminal airspace. For example, in [22], a simulator was designed which can simulate control of air traffic and landing clearance and departure by using backpropagation network based on various controlling parameters, but for single-runway only.

With the availability of aviation data and the significant advancements in computational power, data-driven and machine-learning-based methods have recently become a very promising approach to many challenging problems in air traffic management, such as taxi-out time prediction [23, 24], aircraft sequencing [25], aircraft performance parameter predicting [26], air traffic flow extraction [27], flight delay prediction [28, 29], and aircraft trajectory prediction [30, 31]. However, to the best of authors' knowledge, there has not been any study to extract controller actions or decision as well as learn controller strategy from real data.

In this study, we consider tree-based ensemble learning as our learning algorithm which has been applied in a variety of field, including transportation [32], energy [33, 34], networking [35–37], and air traffic management [38, 39]. It is popular for not only being able to achieve high accuracy levels [32, 40] but also enabling the interpretation of the importance of features used in the predictions. In human-centric and safety-critical domain such as air traffic control, this is a critical property to provide ATCO understanding of proposed models and solutions [41, 42]. Moreover, tree-based ensembles require minimum data preprocessing and are capable of fitting highly nonlinear data and handling big data.

3. Overview

The proposed learning process is demonstrated in Figure 1, which contains preprocessing data, extracting ATCO actions, and building Learning Models. The 4D trajectories points for individual flights are constructed directly from ADS-B raw data and the spatial information about the sector is collected and processed from Aeronautical Information Publication (AIP). Then, preprocessing techniques are applied to clean data and remove noises and outliers trajectories from the raw data. Two points from each flight (first and last points in terms of *timestamp*) were used to identify the new flight trajectory upon entering the sector, which reflects the main course of the trajectory inside the sector. Only simple actions are extracted by comparing the above result with flight information (speed, altitude, and course) at the exiting point. Those can be seen as the changes in *Speed*, *Course*, and *Altitude*, which need to be applied for each flight to reach the exit point at the given 4D position (latitude, longitude, altitude, and time). Up to this point, two sets are generated: action values (continuous) and actions ([−1, 0, 1]) which are related to Ground Speed Rate, Vertical Speed, and Δ Course for each flight. Finally, using the information at entry points as the input and the mentioned two sets as targets, we build two groups of random forest models: regression and classification models. Outputs of those models are the changes or applied actions for each given flight at its entry point.

Noting that, in the scope of this work, only three mentioned groups of actions are considered, and actions such as holding or more complex actions will be studied in future work. Besides, in future work, more traffic information will be included to increase the accuracy of prediction.

3.1. Selected Sector. For this research purpose, we have identified Sector 2E, an en-route area within Kuala Lumpur Flight Information Region (FIR), managed by Singapore Area Control Center (ACC), for providing air traffic service from flight level FL120 (12,000 *feet*) to flight level FL360 (36,000 *feet*) inclusive. We have chosen Sector 2E in Singapore FIR as this is the main feeder sector into the Singapore TMA, having interface with three FIR boundaries HO CHI MINH FIR, BANGKOK FIR, and KUALA LUMPUR FIR. This sector has a high degree of flight vectoring and tactical trajectory management making it a natural choice for the Controller Action Prediction problem. Figure 2 depicts the spatial characteristics of the selected sector. It takes about on average 5 minutes for a typical flight to cross sector. The sector contains 8 way-points and is crossed by 8 Air Traffic Service (ATS) Route. There is one crossing in the sector and one convergence point in the south of the sector (way-point VMR).

3.2. Dataset and Data Preparation. The ADS-B data is collected for the South-East Asian region for six-month period (from September 2016 to February 2017). The dataset contains three main weather conditions in Singapore: southwest monsoon season, intermonsoon period, and northeast monsoon season (Table 1) which are different in both the strength and the direction of winds. The dataset is sufficient for this study as it captures all the main weather and traffic cycles in Singapore airspace. Each sample of data contains features, as shown in Table 2, and an example of one-row sample of 4D trajectory data is shown in Table 3. Even though our dataset is not available for public, similar ADS-B data for European airspace (from OpenSky Network

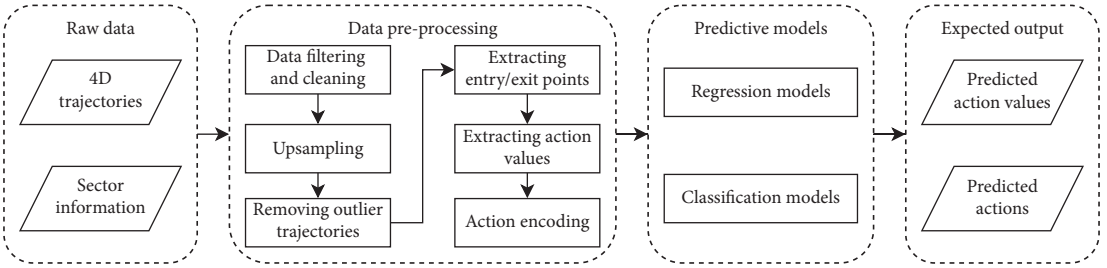

Figure 1: The illustration of our approach for building predictive models.

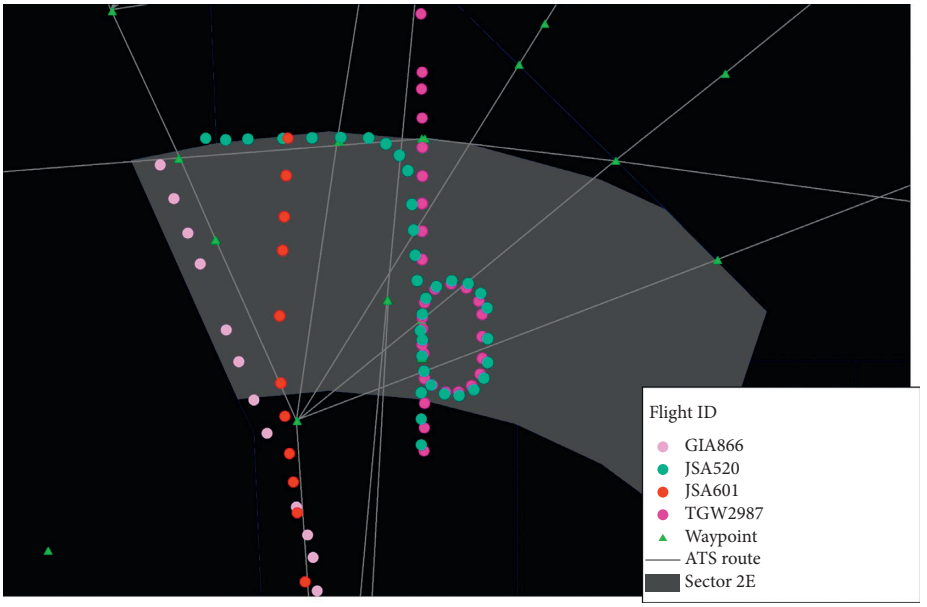

Figure 2: An example of four different flight trajectories reflecting speed, heading change, and hold maneuver in the sample data for sector 2E.

Table 1: Singapore seasonal information of the dataset.

Seasons	Dataset	Description
Southwest monsoon	09/2016	Southeasterly to southerly wind
Intermonsoon	10-11/2016	Lighter and more variable wind
Northeast monsoon	12/2016, 01/2017	Northeast monsoon-wet phase
	02/2017	Northeast monsoon-dry phase

Table 2: 4D trajectory data features.

Feature	Description
Position	Latitude (decimal degrees), longitude (decimal degrees), altitude (ft)
Ground speed	Horizontal speed relative to the ground (knots)
Rate of climb	Altitude change (feet per minute)
Course	Aircraft course relative to north (decimal degrees)
Flight ID	Unique serial number represents each flight
Time	Time (UTC) that data been recorded

Table 3: One row sample of 4D trajectory data.

Field name	Value
Flight ID	CDG4963-1482966600-schedule-0000
Time (UTC)	12/31/2016 00 : 58 : 14
Latitude (dec. deg)	34.29153
Longitude (dec. deg)	108.5708
Groundspeed (kts)	182
Altitude (ft)	3900
Rate (fps)	−514
Course (deg)	18

or ADS-B Exchange) are available for applying our proposed approach.

Each group of records represents trajectories of flights, carrying the status of the flight spatially throughout time. Figure 2 illustrates trajectories of 4 different flights passing through the sector. Sample points with the same color belong to the same flight and the time interval between each point is ≈ 15 seconds.

The original ADS-B dataset is a large dataset with noises and missing data points. Moreover, with the given spatial information of the sector 2E, only a subset of trajectories should be considered and investigated. Thus, some preprocessing steps need to be applied:

(1) Because each sector is defined as a three dimension volume, thus we apply a 3D spatial-filtering to filter out all trajectories which do not pass the through the sector. In this step, we filter out using both lateral (sector boundary) and vertical (FL120 to FL360) conditions. For example, we found that there were 12,141 flights that pass through the 2E sector in December 2016 data.

(2) The second 3D spatial-filtering (similar conditions) is applied to filter out trajectory segments outside of the selected sector. It is separated from the first step just for flexibility in manipulating the filtering criteria.

(3) Outlier trajectories are detected and removed from the dataset, in which trajectories that do not pass the sector's lateral boundary or have significantly long travel distance and time are all considered as outliers. In the context of our research problem, holding trajectories are also treated as outliers. They are rare events that only contribute less than 1.7% of whole data but may affect the predictive models significantly.

(4) To deal with missing data points, we first remove all the flight trajectories which have less than four data points in the sector. After this step, the working dataset contains $\approx 75\%$ of flights from original data. The remaining dataset still has missing data which makes the time interval become inconsistent. Furthermore, for later processing, we aim to extract the entry and exit position of flights on the sector's boundary; then, a dense and consistent time interval in the dataset is required. Therefore, to achieve that the remaining trajectories are up-sampling (interval = 1 second) using interpolation techniques.

4. ATCO Action Extraction

In a practical scenario, pilots communicate with the *D*-side controller while entering the sector and with the *R*-side controller once inside the sector. An aircraft trajectory bears signatures of both *R*-side and *D*-side controller actions. However, *D*-side controller actions can be identified in the trajectory data by observing the trajectory prior to entering a sector.

To better understand the relationship between controller actions and air traffic trajectory data derived from ADS-B, we first visualized the 4D data with GIS. The observing airspace is visualized discretely by grids with 3 nautical miles in length and width, action in the same grid will be summed up, and every grid will be classified into 5 classes using the Jenks Natural Breaks Classification method [43], which is a data clustering method designed to reduce the variance within classes and maximize the variance between them. The color of the grid from yellow to red means the higher frequency of certain features appears in the position, and the first class was not set to visualize. Figures 3 and 4 show the spatial density of entering points and exit points of the aircraft of sector 2E, while Figures 5–7 show spatial distribution of ACT actions in the sector. These figures indicate that there are patterns in ATCO actions.

4.1. Extracting Flight Change/Action Values. Observing from flight trajectories as in Figure 2, there are multiple changes in trajectories of aircraft when flies over the sector. However, the flight usually enters the sector at a specific region and should be directed to follow the designed ATS routes and way-points which means all the changes should be applied for aircraft to reach a specific region to exit the sector. Figure 8 presents some examples for trajectories passing Sector 2E of Singapore FIR. Flights with the same flight' identification will share their flight plans, reflecting by the pattern in their trajectories. However, in terms of sector entry and exit positions, they show a significant dispersion. The dispersion may come from multiple factors such as weather or controller's decisions. Besides, another interesting observation is the consistent relation between flights' entry and exit positions for the demonstrated sector. The assumption is that ATCO has its own pattern or strategy in handling traffic of a given sector. Then, the flights which enter the sector at a specific region will be navigated to similar region for exiting the sector. Thus, instead of using flight plan information for prediction, we mainly focus on using entry and exit positions relation to capture and validate ATCO's actions. This approach can capture the major changes of the flight in the sector. Three values will be extracted from those pairs of points:

4.1.1. Ground Speed Rate. While cruising inside sector 2E, flight speed usually varies. However, because of the nature of this sector, three common and simple trends can be observed

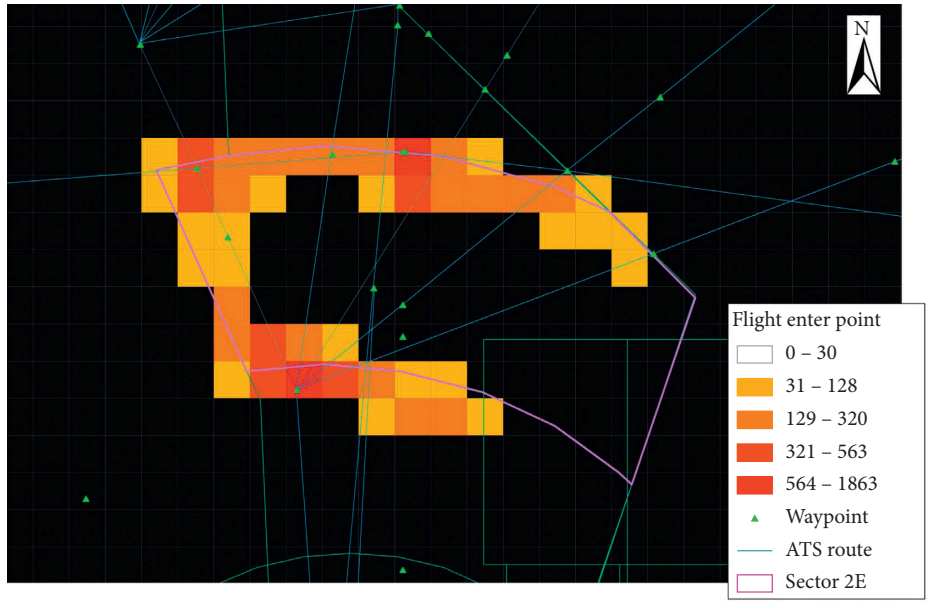

Figure 3: Distribution of entry points in sector 2E.

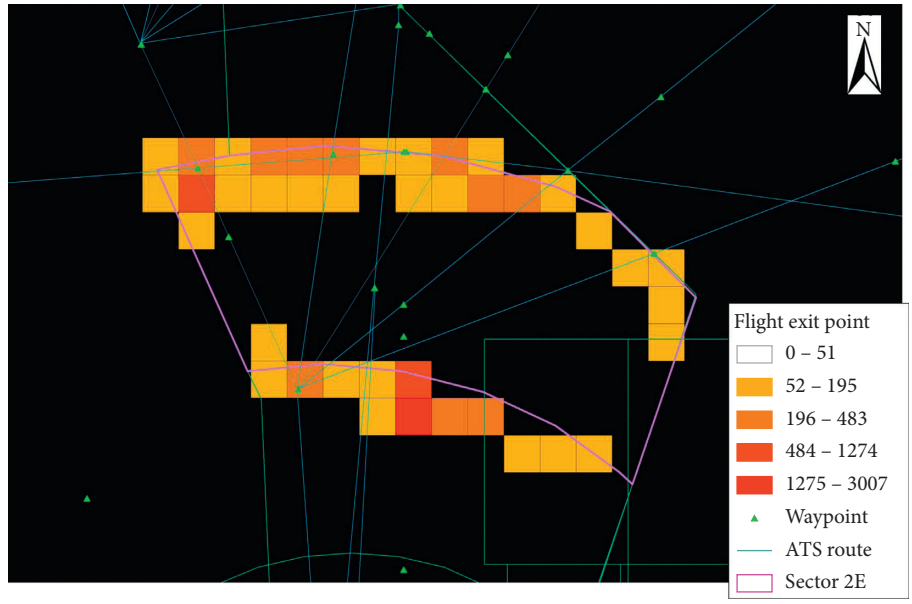

Figure 4: Distribution of exit points in sector 2E.

from data: maintaining speed, increasing (speed up), and decreasing (slow down), see in Figure 9. It indicates that the rate of ground speed change is quite stable and can be used as an action of flight. From that observation, the rate of change is extracted and considered for the next learning steps. In detail, it is computed based on estimating the required rate for a flight with a given speed at the entry point to travel to the exit point. In the case of unstable ground speed, the estimated rate of change in ground speed can be considered as the average rate of change:

$$\begin{aligned} \text{Distance} = \overline{v}.T &= \int_0^T v_t \mathrm{d}t = \int_0^T (v_0 + a.t)\mathrm{d}t \\ \overline{v}.T &= v_0.T + \frac{1}{2}a.T^2 \\ a &= \frac{2(\overline{v} - v_0)}{T}, \end{aligned} \tag{1}$$

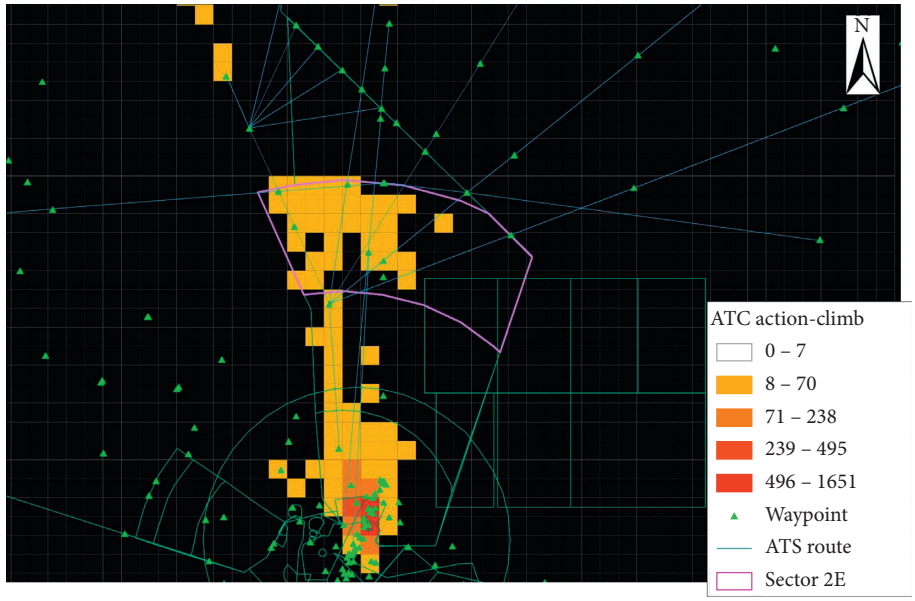

Figure 5: Distribution of ATCO action-climb.

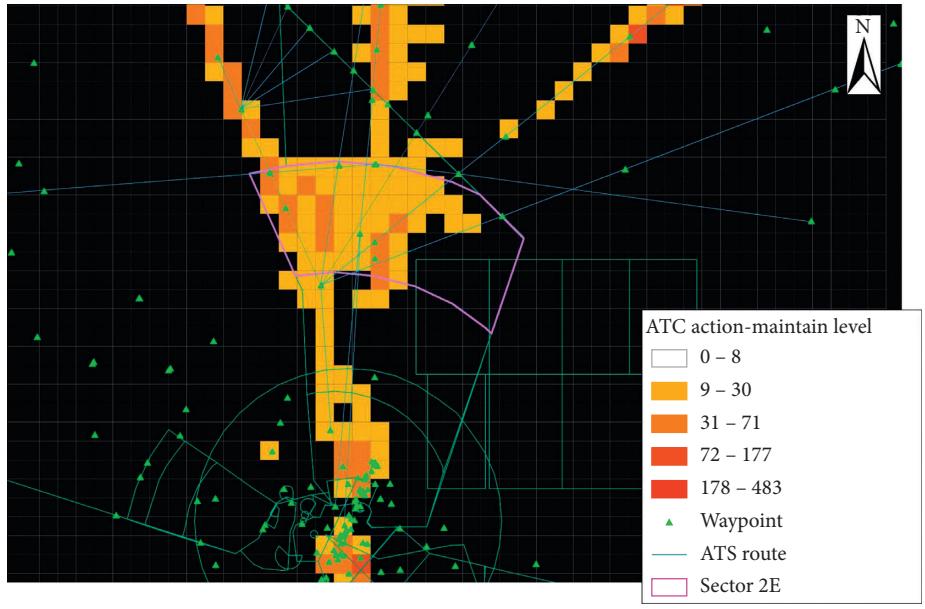

Figure 6: Distribution of ATCO action-maintain.

where $\overline{v}$ is the average speed of aircraft through the sector, T is the total travel duration, v_0 is the speed at entry point, and a is the acceleration (ground speed rate).

4.1.2. Vertical Speed. The actions related to vertical speed: similar to Ground Speed Rate, we also observe some common trends in altitude changes from data. The vertical speed is used as the vertical actions and computed simply based on the ratio of difference in altitude between entry and exit points and the travel duration.

4.1.3. ΔCourse. It is the difference between course at the entry point and "course in sector." Since course of the flight varies throughout the sector and course at exit point also does not reflect the travel direction, we simplify the definition for "course in sector" as the direction from entry and exit points which is the expected direction for flight to travel through our sector. We use the Δ Course instead of "course in sector" because it reflects the turning actions of flights after entering sector.

The detail of action extraction algorithm from entry and exit points is illustrated in Algorithm 1.

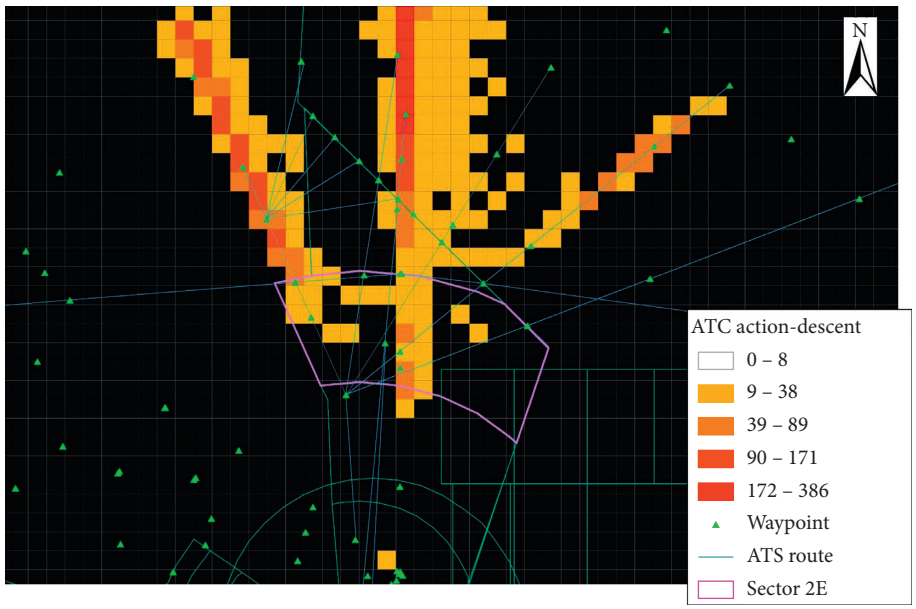

Figure 7: Distribution of ATCO action-descend.

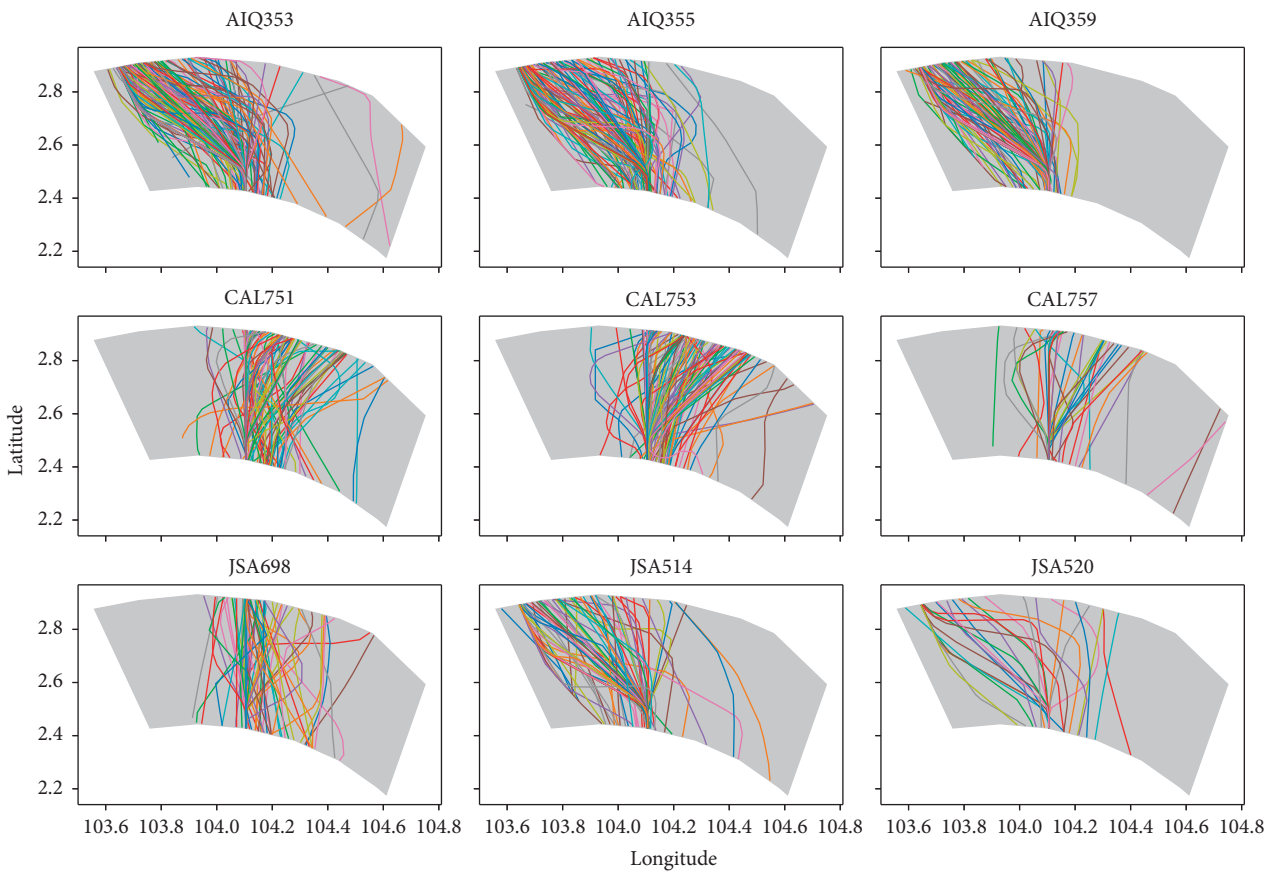

Figure 8: Each subplot is an example of multiple trajectories of the same flight's identification passing sector 2E for landing at Singapore Changi Airport in our dataset. The flows come from the North to the South with various entry points and exit point.

4.2. Encoding ATCO Actions from Action Values. As the requirement for supervised learning, we need a set of actions as labels for building classification models. Thus, for each flight, the set of actions should be converted from extracted action values. Figure 10 displays idea on how the labels are encoded from values. There are three types of actions which

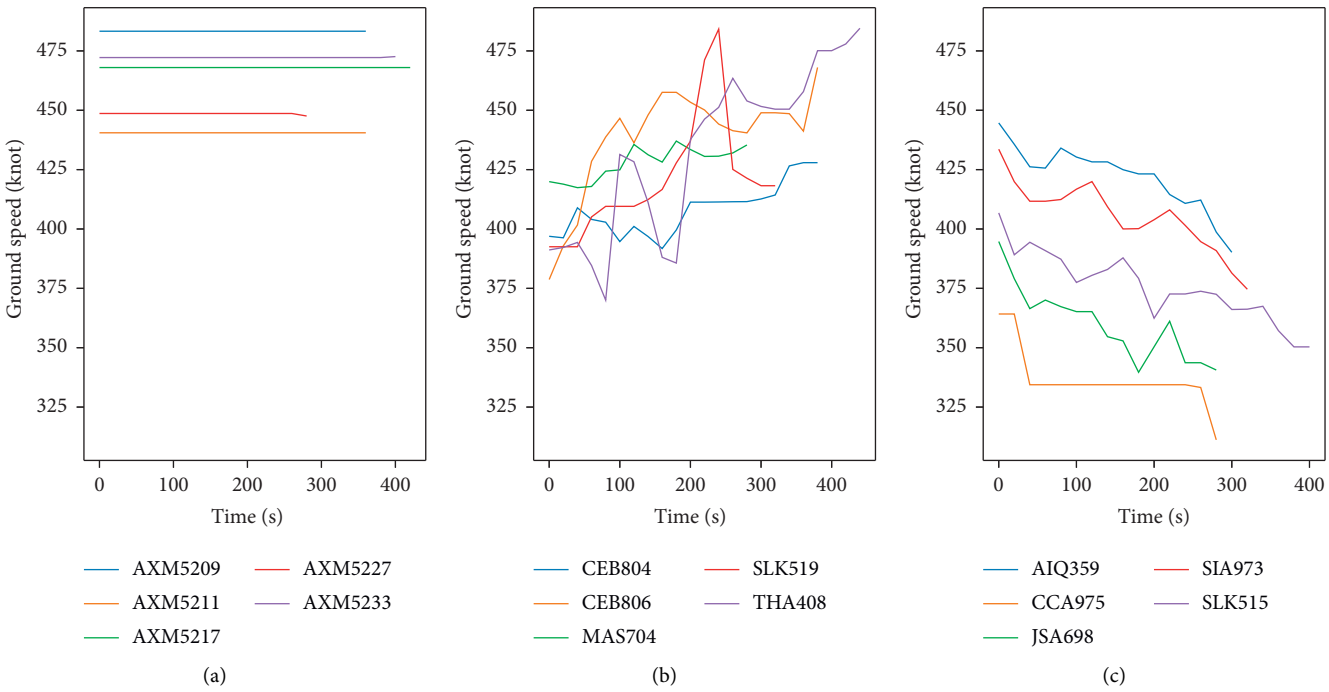

Figure 9: Example of trends in ground speed from real data. Three figures share the same y-axes which is the ground speed in *knot*. (a) Maintaining speed, (b) increasing speed, and (c) decreasing speed.

Input: Entry and Exit Points
Output: G Speed Rate, V Speed, Δ Course
  Travel_Distance = Euclidean_distance (Entry, Exit)
  Travel_Time = Exit.Time − Entry.Time
  Avg_GSpeed = Travel_Distance/Travel_Time
  GSpeed Rate = 2 ∗ Avg_G Speed − Entry.Speed/Travel_Time
  VSpeed = Exit.Alt − Entry.Alt/Travel_Time
  $\theta = a\tan 2(\text{Exit.Lat} - \text{Entry.Lat}/\text{Exit.Lng} - \text{Entry.Lng}) \in (-\pi, \pi]$
  if $\theta \geq 0$ **then**
    Course_in_Sector = θ
  else
    Course_in_Sector = $2\pi + \theta$
  end if
  ΔCourse = Course_in_Sector − Entry.Course
  return G Speed Rate, V Speed, Δ Course

Algorithm 1: Action extraction from entry and exit points.

are related to ground speed rate, vertical speed, and delta course. Each of them is encoded into 3 actions: −1, 0, and 1 based on the thresholds selected as follows:

Speed Action: the ± 10 knots variance in the cruising speed of an aircraft can be considered as maintaining speed since those changes can happen without the need of permission from ATCO. In our work, we assume that any change of cruising speed more than 10 knots is considered as applied speed control. Thus, if the absolute change of speed between exit and entry points is less than 10 knots, we consider it as maintaining speed. Besides the expected travel time of the sector is 5 mins. From both of that, threshold_sr = $\pm 0.017\,(\text{m/s}^2)$ is selected.

Vertical Action: due to the altimetry system error for aircraft in en-route phase, the recorded altitudes may have some dispersion with its true values. In [44], for safety reason, the authors have specified those errors are less than 2 flight level (200 ft). Inspired from that, in this work, if the absolute change in altitude between two points is less than 100 feet, we consider it as maintaining flight level. Besides the expected travel time of the sector is 5 mins. Thus, threshold_vs = $\pm 20\,(\text{feet/minute})$ is selected. The *climb* and *descend* actions are mainly

distributed corresponding to south and north of the sector which will have a strong influence in building predictive model given entry information of a flight.

Course Action: due to the errors in the navigation system, wind, or several other factors, even though the aircraft is maintaining its course, the recorded course may also have some variations. From analysing the data and considering the reasonable values for course error, we have selected ± 3 degrees as the error threshold for this action. Then, if the absolute of delta course is less than 3 degrees, we consider it as maintaining course. threshold_dc = ± 3(degree) is selected for course action encoding.

Figure 11 illustrates the distribution of all extracted actions. The distributions of speed actions and course actions have bell shapes (in (a) and (c)). From (c) and (d), we conclude that course action has balanced distribution. However, the mean of ground speed rate is positive; therefore, there are more *speed up* actions than others in speed action. It is confirmed by (b): around 86% of speed action in this sector is *speed up*. However, since every action is equivalently considered, we do not solve unbalanced problem in the learning model. In (e), the changes in vertical speed can be seen as two separated normal distributions. Then, there are only two major actions: *climb* and *descend* corresponding to two distributions. The maintain level is kept, but there are limited samples for this action, as seen in (f).

5. Methodology

In this part, we will describe our approach for predicting the next actions of flight after entering the sector. The training data includes features of flight at the entry point and the extracted actions from real data as the targets. Table 4 mentions list of features and all targets. We propose Random Forest Method [45] and Extreme Gradient Boosting (XGBoost) [46] for building predictive models of ATCO actions.

5.1. Tree-Based Ensemble Learning Method. The tree-based ensemble learning method is used for building our predictive models for both classification and regression tasks. In general, it constructs multiple decision trees which are trained and combined together to reduce the variance of the model (illustrated in Figure 12). It is used in different domains and predictive problems as it provides high accuracy with simple implementation. It is highly robust since it can deal with outliers/noises without skewing the prediction results and avoids overfitting due to the diversity of trees. One of the key advantages of tree-based ensemble learning method which suits our problem is its capability to handle unbalanced datasets and able to work with different types of features and range of feature values. Furthermore, the 4D trajectories are derived from ADS-B data which usually contains noisy data points and the input features have different meanings and scales. Moreover, the interpret ability of the model is also considered for understanding the important factors for predicting actions; thus, tree-based ensemble learning method is found suitable for this purpose. In this study, the two algorithms which we considered are Random Forest (RF) and XGBoost-Extreme Gradient Boosting (XGB).

Random Forest [45]. It applies a bagging technique to decision trees. To train the model, it creates a large number of trees by resampling the given data and combines them (using averages or voting technique) at the end of the process.

XGBoost-Extreme Gradient Boosting [46, 47]. Among tree-based ensemble algorithms, Gradient Tree Boosting [48] has shown its success in many applications and provided state-of-the-art results on many standard classification benchmarks [49]. It applies a boosting technique to decision trees. It also creates and combines a large number of trees; however, instead of combining them at the end, it starts the process at the beginning. The algorithm will train each subsequent tree using the residuals (the difference between the predicted and true values) of previous ones. In this work, we use a scalable machine learning system for tree boosting, called XGBoost. It has been widely used in a number of machine learning and data mining challenges with real-life data in Kaggle and KDDCup. Besides all advantages of tree boosting algorithms, the most important factor behind success of XGBoost is its scalability in all scenarios.

5.2. Building Predictive Models. There are two levels of prediction that should be investigated: whether we can predict the abstract action or the magnitude of each action. Each kind of setting can answer different questions. The first can support the analysis of controller strategy, while the second one can support for understanding and studying details of controller behaviors. However, they are useful and have strong relations; thus, in this work, we introduce both kinds of prediction using Random Forest and XGBoost Regression and Random Forest and XGBoost Classification models (illustrated in Figure 13). Because each dimension of actions (Speed, Vertical, and Course) has a different range of values and can be affected by different features, we build separated models for each action. Six regression models and six classification models are developed to predict the value for each kind of action. However, for classification, two 3-actions models using Random Forest (RF) and XGBoost (XGB) are also developed to explore the potential of combining three models into one for action prediction. These models are considered for the completeness of our approach rather than the practical requirements, since in practice, the controller usually performs only one kind of action/decision in handling traffic.

(1) Regression models (RF, XGB):

Model RR1/XR1: predict ground speed rate
Model RR2/XR2: predict vertical speed
Model RR3/XR3: predict Δ Course

We use R^2 score as performance metric for this group of models.

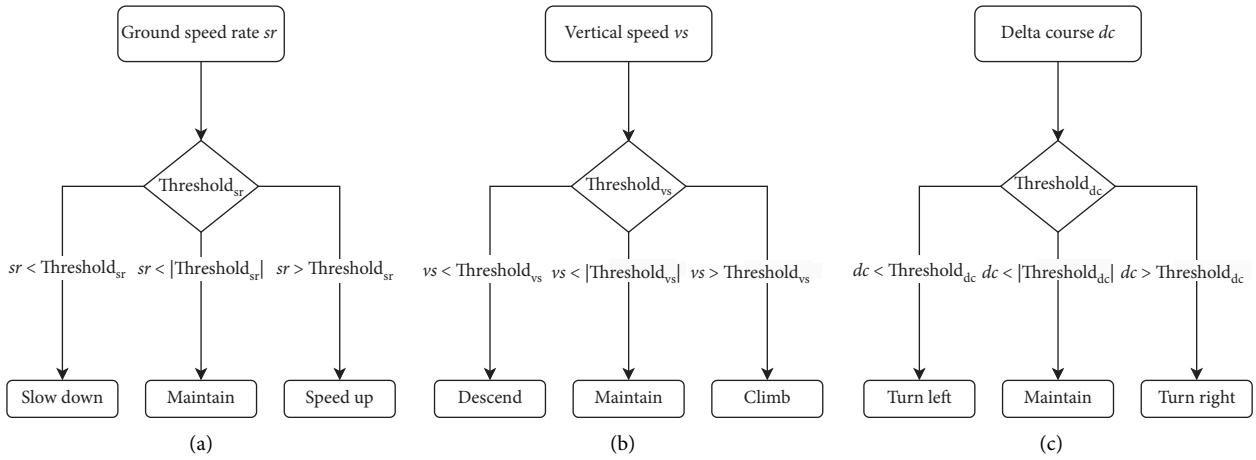

Figure 10: The illustration of the encoding step for extracting speed and vertical and course actions from continuous action values.

(2) Classification models (RF, XGB):

Model RC1/XC1: predict speed action
Model RC2/XC2: predict vertical action
Model RC3/XC3: predict course action
Model RC4/XC4: predict all 3-Actions.

We use Accuracy = Number of correct predictions/Total number of predictions as performance metric for this group of models.

6. Experiments and Results

As mentioned, we use RF and XGB methods to build both groups of predictive models. For both groups, we apply the same experiment setup:

The models are trained and tested with all 6-month of data.

Using flight information at the entry points as the input for the predictive model, the targets are extracted actions (mentioned in Table 4).

Parameter tuning: the range of hyperparameters for both types of models is manually selected to cover the optimal hyperparameter sets.

For regression models: number of estimatorsruns from 50 to 300 with the step is 50 (6 values) while max_depth of forest varies from 6 to 58, step 2 (27 values).
For classification models: number of estimators runs from 50 to 300 with the step is 50 (6 values) while max_depth of forest varies from 6 to 58 with the step is 2 (27 values).

The k-fold crossvalidation ($k = 10$) technique is used for evaluating and the performance is averaged to select best set of parameters. It is popular for handling the overfitting issue in machine learning. The dataset is split into ten folds in which, for each fold, it is used for testing, and the remaining ones are used for training models. The computed errors are averaged to estimate the model performance in general.

Experiment results for parameter tuning of RF regression models are shown in Figure 14. This heatmap shows the $R^2 \pm$ Score for RF regression models with each pair of parameters. The lighter the color is, the higher the score of the model is; thus, the result indicates that the number of estimators (≥ 150) does not affect the performance of models, instead, Max_Depth plays a more important role. Max_Depth ≥ 10 makes all three models stable with small variance. Another interesting observation is the significant improvement of Model RR3 (ΔCourse) when we increase the Max_Depth of the trees from 6 to 20. It emphasizes the importance of this parameter tuning step for selecting suitable hyperparameters for our models. Thus, all RF Regression Models are trained with [Estimator = 150, Max_Depth = 10]. Similar phenomena can be observed during the parameter tuning process of XGB Regression models. As a result, a common set of parameters [Estimator = 100, Max_Depth = 8] is selected for all XGB regression models.

Table 5 presents the performance of regression models for each kind of action. Note that R^2score is best at 1 and worst at 0. All six models can predict action values for each given flight with a high value of R^2score. Model performance is reported for each month as well as the overall performance. The overall performance of models is a little higher in intermonsoon period (October and November) and is the highest in February which is the dry phase of northeast monsoon season. As we observe, the performance of models for December is lower than other months. Since December is the transition month in which winds and weather conditions are unstable, the accurate predictions are more challenging. Comparing models from two learning methods, we can see that XGB models outperform RF models generally for vertical speed and ΔCourse. While for ground speed rate, they vary with different datasets.

For models which are built on whole six-month dataset (all data), the models for ground speed rate have the lowest performance with the overall R^2 scores as 0.667 for RF and 0.677 for XGB. The models achieve high performance (RF:

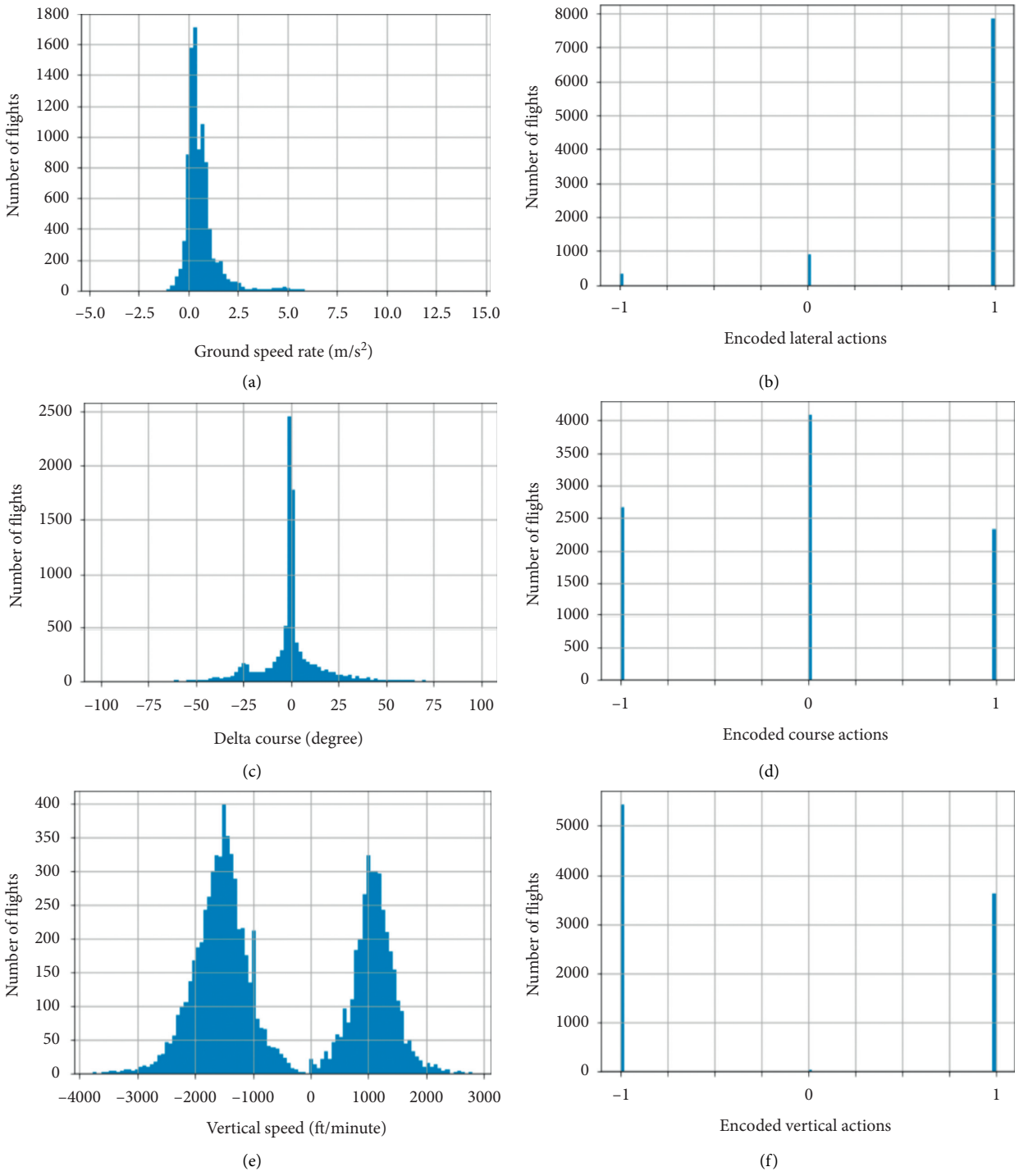

Figure 11: (a), (c), and (e) are distributions of computed trajectories' changes (actions) from ADS-B data. (b), (d), and (f) are distributions of encoded actions.

0.793, XGB: 0.858) for Δ Course and (RF: 0.835, XGB: 0.870) for vertical speed. The XGB models have shown better performance in prediction comparing to RF models. Besides, as we can observe from Figure 15, the group of black dots in the bottom of the figure is close to each other, while their corresponding red dots are spatially diverse which is overcome by considering features on origin and destination of the flight.

As mentioned, the tree-based models can provide the feature importance information which reflects the contribution of each feature in those models. The list of top-10 features that have the most contribution for three RF regression models is shown in Table 6. The two features which have most contributions (> 66%) for predicting Ground Speed Rate (Model RR1) are Entry_Speed and Destination_WSSS. In Model RR2 (Vertical), there is only one

Table 4: Flight information (features) at entry point and actions and their values.

Features	Action values	Actions
Longitude	Ground speed rate	(1) speed up
Latitude	Vertical speed	(0) maintain speed
Altitude	Δ Course	(−1) slow down
Ground speed		(1) cimb
Vertical speed		(0) maintain level
Course		(−1) descent
Destination		(1) turn right
Origin		(0) maintain course
Month of year		(−1) turn left
Day of week		
Hour of day		
Flight ident		

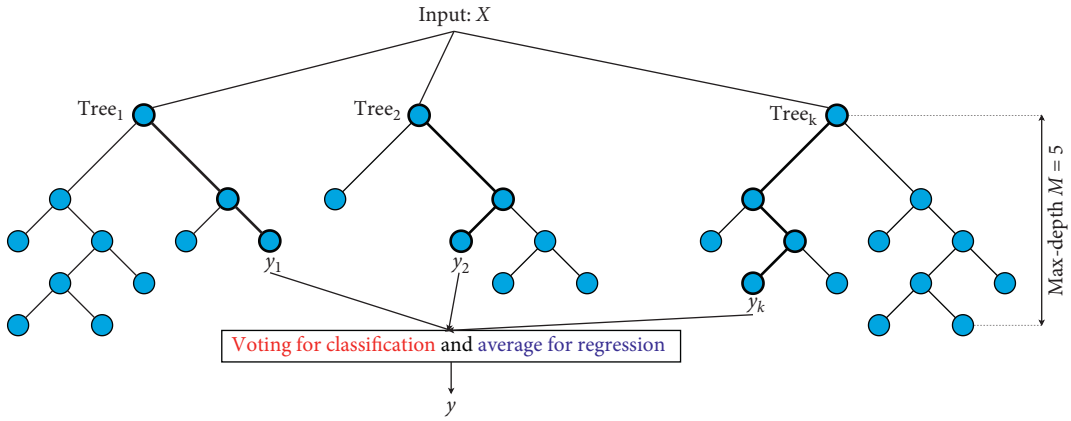

Figure 12: The illustration of tree-based ensemble learning method. The model contains k tree with maximum depth of each tree is $M = 5$. For each input vector X each tree will predict one target value. The predicted values of all the trees then are combined to the final prediction y.

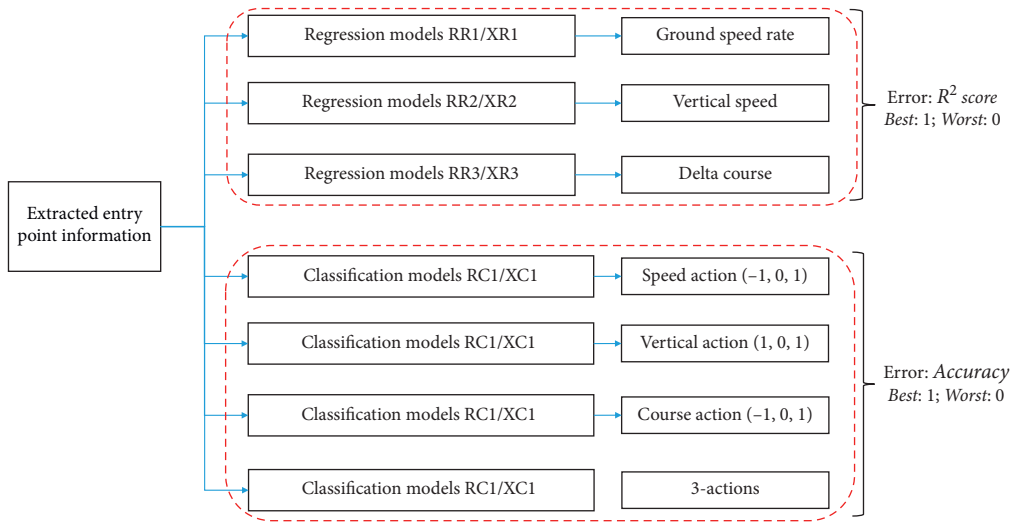

Figure 13: Illustration of developed predictive models: regression models of Random Forest (RR) and XGBoost (XR) and classification models of Random Forest (RC) and XGBoost (XC). R^2 score is used as metric for regression models, while Accuracy is the metric for classification models.

dominant feature (> 82%) which is Destination_WSSS. For Model RR3 (Course), the entry position and course of the flight have a significant impact on the course through the selected sector (> 86%) in which course and longitude are more important than Latitude. Features for date and time information of the flight, such as Hour Of Day, Day of Week,

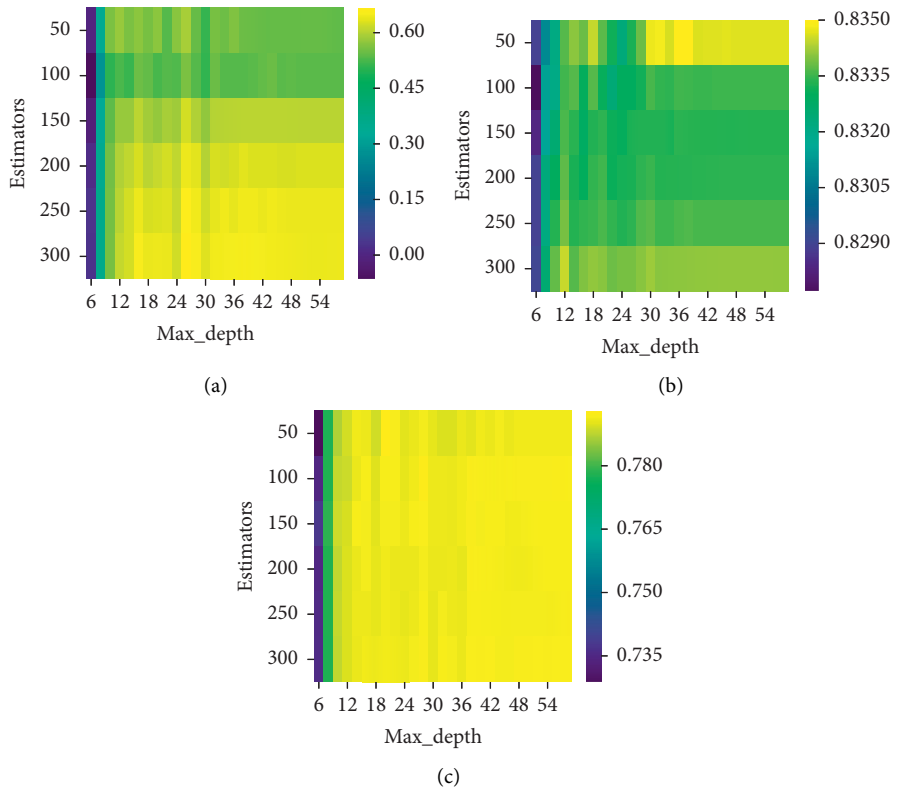

Figure 14: Parameter tuning for regression models. Estimators are [50 : 300, step 50] and Max_Depth are [6 : 58, step 2]. (a) GSpeed Rate, (b) *V*Speed, and (c) ΔCourse.

Table 5: Experiment results for predicting actions in R^2 score.

Dataset	GSpeed rate		Vertical speed		Δ Course	
	RF	XGB	RF	XGB	RF	XGB
Sep-16	0.617 ± 0.037	**0.666** ± 0.046	0.838 ± 0.015	**0.859** ± 0.020	0.804 ± 0.042	**0.828** ± 0.049
Oct-16	**0.666** ± 0.042	0.622 ± 0.037	**0.846** ± 0.023	0.836 ± 0.023	0.758 ± 0.042	**0.796** ± 0.029
Nov-16	0.664 ± 0.048	**0.690** ± 0.055	**0.882** ± 0.013	0.859 ± 0.017	0.831 ± 0.029	**0.855** ± 0.020
Dec-16	0.614 ± 0.046	**0.637** ± 0.051	0.806 ± 0.021	**0.853** ± 0.013	**0.733** ± 0.030	0.724 ± 0.026
Jan-17	**0.649** ± 0.060	0.633 ± 0.030	0.828 ± 0.016	**0.87**3 ± 0.012	0.804 ± 0.021	**0.824** ± 0.023
Feb-17	**0.693** ± 0.048	0.654 ± 0.040	0.839 ± 0.016	**0.902** ± 0.013	**0.914** ± 0.043	0.877 ± 0.044
All data	0.667 ± 0.016	**0.677** ± 0.018	0.835 ± 0.006	**0.870** ± 0.007	0.793 ± 0.007	**0.858** ± 0.011

and Month of Year, have a small contribution in the trained models, which also implies that the season does not have a strong impact on our predictive models.

The parameter tuning for classification models show similar characteristics as regression models. An example of tuning process for RF models can be observed in Figure 16. For each value of the number of estimators, the model performance will vary and become stable with Max_Depth ≥ 24. The number of estimators (≥50) does not affect the performance of classification models. Thus, all RF classification models are trained with [Estimator = 50, Max_Depth = 24] and all XGB Classification Models are trained with [Estimator = 250, Max_Depth = 8].

Table 7 shows the performances of classification models. Eight predictive models are developed and evaluated in this study. Their performances are quite stable for different months. The overall performances are accessed by training these models with whole six-month dataset. As a result, the models for vertical actions provide the highest prediction accuracy (> 99.0%). Two models for speed action achieve approximately 80% in accuracy while the XGB model for course action can achieve up to 86.5% accuracy. The best model to predict the set of all the actions (altitude, speed, and course change) for each flight is the XGB model, and it achieves an accuracy 70% implying that, for 70% of flights, *D*-side controller's actions can be predicted from trajectory information at sector entry position. The 3-action model has lower performance comparing to the individual action model due to the increase in complexity of the output with 3 dimensions and 27 possible labels.

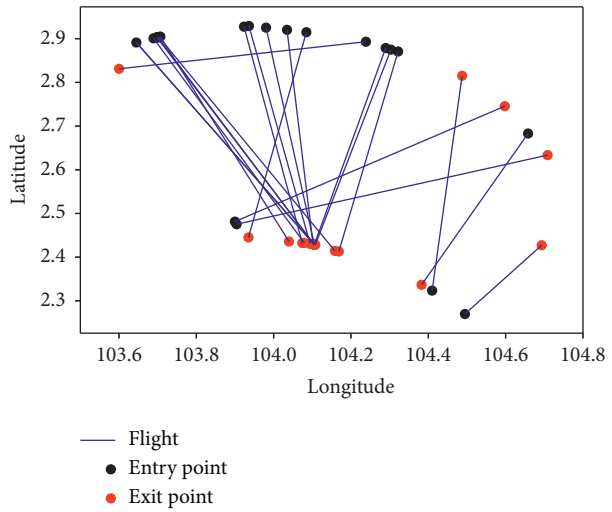

Figure 15: Example for flight direction. Black dots are entry points and red dots are exit points.

Table 6: Feature importance of random forest models for action value prediction.

Model RR1	FI_RR1 (%)	Model RR2	FI_RR2 (%)	Model RR3	FI_RR3 (%)
Speed	34.2	*D*_WSSS	82.7	Course	46.6
*D*_WSSS	32.1	*V*_Speed	5.2	Longitude	30.1
Altitude	6.3	Altitude	4.0	Latitude	10.4
*T*_Remain	5.0	*T*_Remain	2.7	*D*_RPLL	1.7
*V*_Speed	3.2	Speed	0.8	*T*_Remain	1.6
Longitude	2.9	Course	0.8	Altitude	1.4
Course	2.8	Longitude	0.6	*D*_WSSS	1.1
Latitude	2.1	Latitude	0.5	*V*_Speed	0.9
Hour	1.7	Hour	0.4	Speed	0.9
Month	1.5	Month	0.3	Hour	0.8

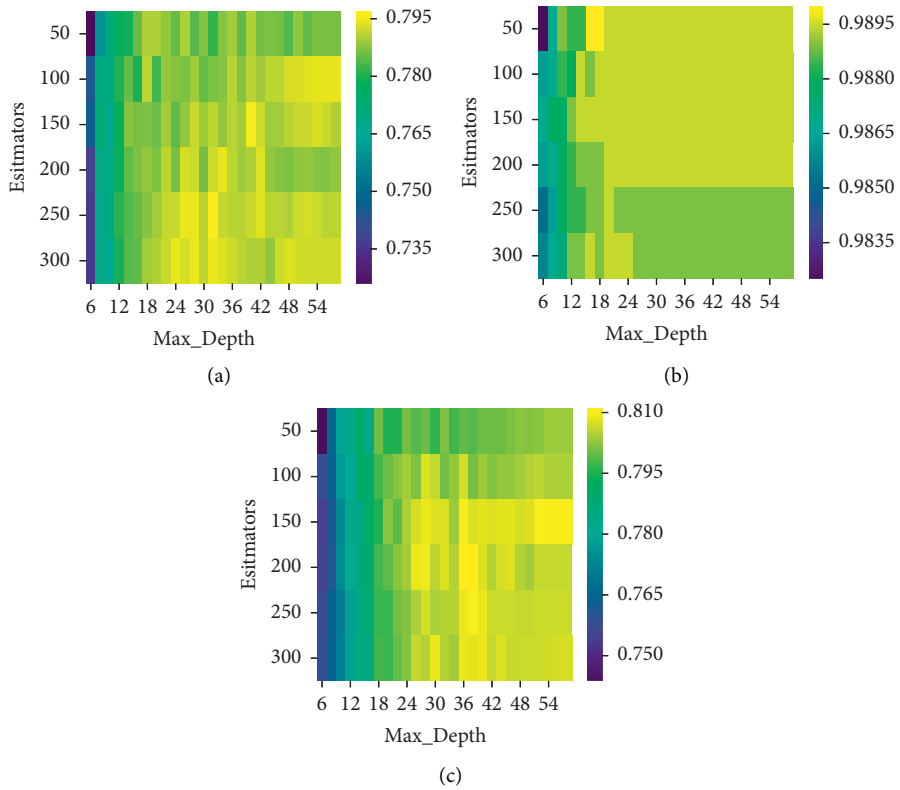

Figure 16: Illustration for parameter tuning process for classification models. Estimators are [50 : 300, step 50] and Max_Depth are [6 : 58, step 2]. (a) Speed action, (b) vertical action, and (c) course action.

Table 7: Predictive accuracy of predictive models: speed action, vertical action, course action, and 3-action.

Dataset	S_Action		V_Action		C_Action		3-action	
	RF	XGB	RF	XGB	RF	XGB	RF	XGB
09-2016	75.7% ± 1.9%	80.3% ± 3.0%	99.3% ± 0.5%	98.9% ± 0.9%	80.4% ± 3.3%	87.1% ± 2.2%	66.0% ± 2.5%	71.0% ± 2.5%
10-2016	78.4% ± 1.6%	76.8% ± 2.2%	98.7% ± 0.5%	98.4% ± 0.6%	76.4% ± 2.3%	84.4% ± 2.2%	63.9% ± 2.5%	65.2% ± 2.3%
11-2016	81.8% ± 2.2%	82.7% ± 3.0%	99.2% ± 0.4%	99.7% ± 0.6%	77.9% ± 2.8%	85.2% ± 1.2%	68.7% ± 1.6%	70.6% ± 1.7%
12-2016	78.6% ± 1.5%	75.5% ± 2.5%	99.1% ± 0.4%	99.7% ± 0.6%	76.1% ± 2.7%	82.0% ± 1.4%	67.3% ± 1.8%	70.4% ± 2.3%
01-2017	78.7% ± 2.8%	73.6% ± 1.7%	99.3% ± 0.5%	99.0% ± 0.3%	80.3% ± 2.9%	84.2% ± 1.8%	68.3% ± 2.3%	63.8% ± 1.9%
02-2017	77.9% ± 1.8%	76.8% ± 1.8%	99.0% ± 0.5%	99.2% ± 0.3%	86.5% ± 2.0%	90.0% ± 1.8%	74.1% ± 1.5%	69.7% ± 1.7%
All data	79.7% ± 1.5%	78.5% ± 2.0%	99.0% ± 0.2%	99.2% ± 0.3%	81.1% ± 1.2%	86.5% ± 1.1%	67.2% ± 1.45%	69.5% ± 0.7%

Table 8: Feature importance of random forest models for action prediction.

RC1	FI1 (%)	RC2	FI2 (%)	RC3	FI3 (%)	RC4	FI4 (%)
Speed	14	Latitude	17	Course	19	Latitude	17
*V*_Speed	10	*V*_Speed	15	Longitude	16	Course	13
*T*_Remain	10	*T*_Remain	15	Latitude	14	Longitude	10
Latitude	8	*O*_WSSS	14	Altitude	8	*T*_Remain	9
Course	7	*D*_WSSS	8	*T*_Remain	5	*V*_Speed	9
Altitude	7	Course	4	Speed	4	Speed	7
Longitude	7	*D*_VTBS	3	*V*_Speed	4	Altitude	6
Month	4	Altitude	3	*O*_RKSI	2	*D*_WSSS	4
Day	4	Longitude	3	Month	2	*O*_WSSS	3
Hour	3	Hour	2	Day	2	Month	3

Though predictive models for individual action achieve good performance with high accuracy, the performance of 3-action models is presented for completeness of the results. It is highly unlikely that the controller will issue three actions together for the same flight. In terms of operational validation, the proposed approach is envisioned as ATCO assisting tool, not an autonomous tool. Thus, there is always ATCO discretion element, and as more ATCO actions are collected, the models can be further trained for better accuracy.

Table 8 shows feature importance for four RF classification models. Different from RF regression models where a few features have a significant contribution, the feature importance or features' contributions of all RF classification models are scattered. The feature importance of 3-action RF Model has highlighted the impact of features such as location, speed, course, and vertical speed of entry point, datetime information, and the relation of this flight with Changi Airport (WSSS) as its origin or destination.

This proposed learning mechanism also has an advantage for scalability. The two selected tree-based ensemble techniques are well known for their low computational cost with parallel computing option. Moreover, XGBoost is specially designed for handling big data. In terms of running time, the training time of the selected model varies from 40 to 50 seconds for the input with 25,000 samples. All the experiments are performed on a desktop with Processor Intel Xeron W-2123 CPU 3.6 Hz and RAM 32 GB.

7. Implementation of ATCO's Command

For the complex and stochastic environment of ATC, the tasks and required actions of planning controllers are more than what are covered in the scope of this work. However, as we target the most fundamental actions of ATCO, the predicted results are useful in predicting the ATCO action to form appropriated commands. Some examples of ATCO's command for pilot regarding speed control, vectoring, and vertical speed are presented in Table 9.

Table 9: Examples for basic ATCO's command for speed control, vectoring, and vertical speed.

Speed control
Maintain 350 knots or greater
Reduce speed 250 knots or less for sequencing
Increase speed mach .83 or greater for the next 5 minutes
Vectoring
Continue present heading
Fly heading (three digits)
Turn (left/right) heading (three digits)
Turn (left/right) (number of degrees) degrees
Vertical speed
PRE078 descend FL 120 at 1500 feet per minute or less
EKR365 climb FL 370 at 1000 feet per minute or greater

The process to convert our results into similar ATCO's commands can be observed in the flow diagram in Figure 17. The aircraft information at the entry point such as airspeed, ground speed (or wind speed), heading, course (or wind vector), and flight level is necessary input to generate the command. By combining the input with the predicted actions, we can estimate the target values of airspeed, heading, and flight level for the given aircraft. Then, by using a list of predefined command templates, we can generate the expected command.

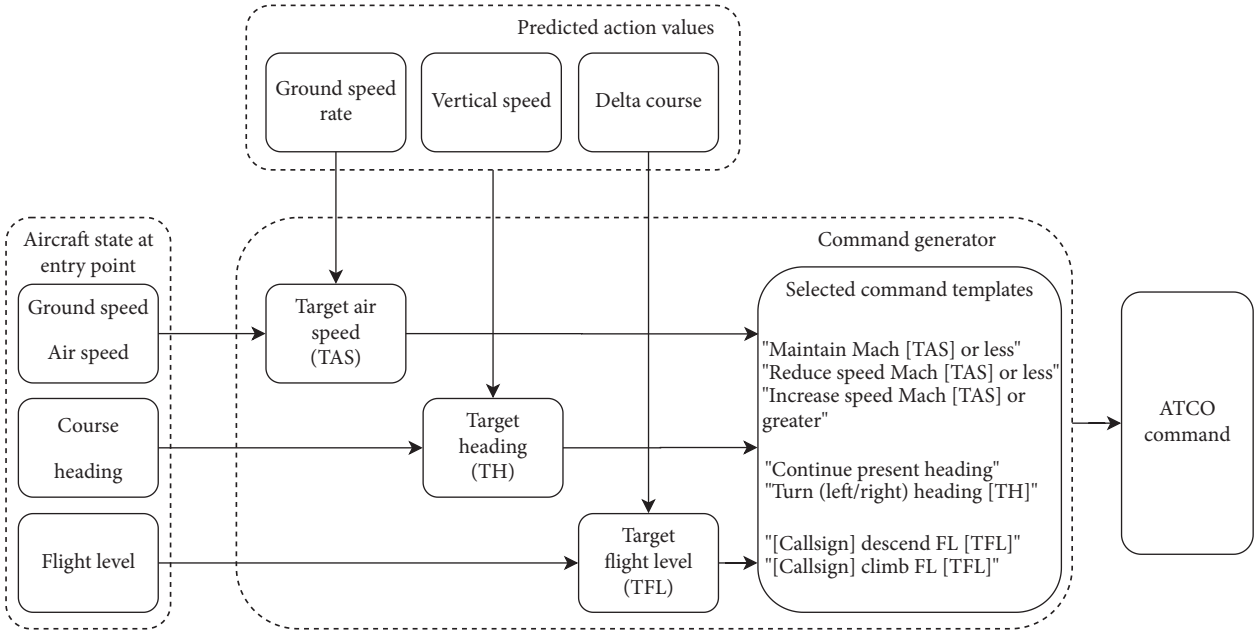

Figure 17: The flow diagram for converting from predicted results into ATCO's command.

8. Conclusions

In this paper, we have looked into learning and predicting the *D*-side controller's action for a given traffic scenario in a sector using two tree-based regression and classification method known as Random Forest and XGBoost. This learning problem was modeled as a classification problem where the target variable is *D*-side controller actions and the explanatory variables are the aircraft 4D trajectory features prior to entering a sector. The air traffic trajectories constructed through ADS-B data are analyzed spatial-temporal with sector data to establish that patterns in *D*-side controllers exist. Two groups of models were developed, one to predict the actions and the other to predict the associate action value. We used flight information at the sector entry point as the input for the predictive model and the targets are extracted actions. The model for vertical action provided the highest accuracy with 99%, whereas models for speed and course action provide predictability accuracy of 80% and 87%, respectively. This was attributed to highly complex sector entry and exit point configuration that makes learning challenging. The high prediction accuracy of altitude change maneuvers by the ATCO is significant as the airspace sector used in this research is a Transition Sector (Sector 2E in the Singapore ACC). The transition sector is typically where the flights are climbing to their cruise flight level or descending from the cruise flight level to terminal airspace. In such sectors, ATCO actions concerning altitude change are quite important, as there is a significant number of climbing and descending maneuvers happening in the sector. The model that predicts the set of all 3 kinds of actions (multiple-output) for each flight achieved an accuracy of 70%. This means that, for 70% flights, ATCO actions can be predicted on all actions by using flight information at the sector entry position. The lower predictability can be due to an imbalance of the training data for the controller's actions, leading to poor generalization performance. The noise and low quality of ADS-*B* data can be another area of improvement as the model is as good as the data used to train it. Besides, as mentioned, this work only focuses on predicting simple actions from individual flight entry information.

The results and findings of this research can be used in several ways, in terms of application. For example,

> The set of predicted maneuvers can be organized into patterns to derive and understand ATCO strategies, for traffic management, in a given sector
>
> The results can also provide an insight into any biases ATCOs might have in managing traffic in a given sector, which can be addressed

For future work, we will apply clustering models to identify clusters of loss of separation events in spatial-temporal plane. Detected events can be used to evaluate the model performance in term of conflict solving. Then, some clustering methods will be applied over whole trajectories to detect and extract more complex actions from ADS-B data. Finally, more features from sector and traffic will be considered for learning and predicting to improve the practical of those models. Expanding the feature set by including parameters such as weather and wind could be useful; however, in the absence of meteorological information at that flight level makes that challenging. However, we will try to approximate the wind data by extrapolating the surface winds (available from METAR Data) to a higher altitude as our future work. We will also conduct Human in the Loop simulation to measure the effectiveness of the proposed

algorithm as well as comparing it with traditional tools used by Air Traffic Controllers for Aircraft Trajectory Prediction to better understand the predictability of ATCO's actions.

There can be several practical implications and difficulties in implementing the results of the research. Even though, the proposed approach is envisioned as ATCO assisting tool, not an autonomous tool. The biggest challenge is the acceptance of such machine learning-based tool by the controllers and the safety regulators. The design of such a tool will be also a challenge in an already overcrowded ATCO's working environment. There are issues of trust with such automation/advisory systems, where ATCOs do not fully accept the proposed solutions/advisories generated by the system. Thus, there will be a need of a human factor study and safety validation scenarios, to realize the benefits of such research. Eventually, this research may help develop an AI Agent, which can augment a *D*-side controller to manage and coordinate strategic traffic flow within and beyond sectors, thereby managing their workload.

Nomenclature

ACC:	Area control center
ADS – *B*:	Automatic-dependent surveillance-broadcast
AIP:	Aeronautical information publication
ATC:	Air traffic control
ATCO (*s*):	Air traffic controller (*s*)
ATM:	Air traffic management
ATS:	Air traffic service
FIR:	Flight information region
LOS:	Loss of separation
METAR:	Meteorological aerodrome reports
MTCD:	Medium term conflict detection
RF:	Random forest (machine learning technique)
STCA:	Short term conflict alert
TMA:	Terminal control area
XGB:	Extreme gradient boosting or xgboost (machine learning technique).

Data Availability

The used ADS-B data, or flight trajectories, belong to ATMRI and NTU, with a restriction on publicly sharing the dataset.

Disclosure

Any opinions, findings, and conclusions or recommendations expressed in this material are those of the authors and do not reflect the views of National Research Foundation, Singapore, and the Civil Aviation Authority of Singapore. Part of this research is published as a PhD thesis of first author.

Conflicts of Interest

The authors declare that they have no conflicts of interest.

Acknowledgments

This research was supported by the National Research Foundation, Singapore, and the Civil Aviation Authority of Singapore, under the Aviation Transformation Programme.

References

[1] ICAO, *Pans, Air Traffic Management. Doc-4444*, ICAO, Montreal, Canada, 2007.

[2] M. Nolan, *Fundamentals of Air Traffic Control*, Cengage Learning, Boston, MA, USA, 2010.

[3] D. McNally, H. Erzberger, R. Bach, and W. Chan, "A controller tool for transition airspace," in *Proceedings of the Guidance, Navigation, and Control Conference and Exhibit*, p. 4298, Portland, OR, USA, August 1999.

[4] S. Alam, A. Ha, C. J. Lokan, M. Ellejmi, and S. Kirby, "Computational red teaming to investigate failure patterns in medium term conflict detection," in *Proceedings of the 8th Eurocontrol Innovation Research Workshop, Eurocontrol Experimental Center*, Brtigny-sur-Orge, France, December 2009.

[5] A. Shakarian and A. Haraldsdottir, "Required total system performance and results of a short term conflict alert simulation study," in *Proceedings of the 4th US/Europe Air Traffic Management R & D Seminar*, pp. 1–9, Sante Fe, NM, USA, December 2001.

[6] M. Strohmeier, M. Schafer, V. Lenders, and I. Martinovic, "Realities and challenges of nextgen air traffic management: the case of ads-b," *IEEE Communications Magazine*, vol. 52, no. 5, pp. 111–118, 2014.

[7] G. James, D. Witten, T. Hastie, and R. Tibshirani, *An Introduction to Statistical Learning*, Vol. 112, Springer, Berlin, Germany, 2013.

[8] J. Friedman, T. Hastie, and R. Tibshirani, *The elements of Statistical Learning*, Vol. 1, Springer Series in Statistics, New York, NY, USA, 2001.

[9] D. B. Fogel, T. J. Hays, S. L. Hahn, and Q. James, "A self-learning evolutionary chess program," *Proceedings of the IEEE*, vol. 92, no. 12, pp. 1947–1954, 2004.

[10] D. Cannel and S. Markovitch, "Learning Models of Opponent's Strategy Game Playing," in *Proceedings of the 1993 AAAI Fall Symposium on Games: Learning and Planning*, pp. 140–147, AAAI Press Technical Report FS93-02, Menlo Park, CA, USA, 1993.

[11] J. B. Pollack and A. D. Blair, "Co-evolution in the successful learning of backgammon strategy," *Machine Learning*, vol. 32, no. 3, pp. 225–240, 1998.

[12] J. Fürnkranz, "Machine learning in computer chess: the next generation," *ICGA Journal*, vol. 19, no. 3, pp. 147–161, 1996.

[13] D. Silver, A. Huang, C. J. Maddison et al., "Mastering the game of go with deep neural networks and tree search," *Nature*, vol. 529, no. 7587, pp. 484–489, 2016.

[14] T. Dyster, S. A. Sheth, and G. M. McKhann, "Ready or not, here we go," *Neurosurgery*, vol. 78, no. 6, pp. N11–N12, 2016.

[15] H. Sethy, A. Patel, and V. Padmanabhan, "Real time strategy games: a reinforcement learning approach," *Procedia Computer Science*, vol. 54, pp. 257–264, 2015.

[16] D. Bloembergen, K. Tuyls, D. Hennes, and M. Kaisers, "Evolutionary dynamics of multi-agent learning: a survey," *Journal of Artificial Intelligence Research*, vol. 53, pp. 659–697, 2015.

[17] K. Weiss, T. M. Khoshgoftaar, and D. D. Wang, "A survey of transfer learning," *Journal of Big Data*, vol. 3, no. 1, p. 9, 2016.

[18] A. R. Odoni, "The flow management problem in air traffic control," in *Flow Control of Congested Networks*, pp. 269–288, Springer, Berlin, Germany, 1987.

[19] L. Pallottino, E. M. Feron, and A. Bicchi, "Conflict resolution problems for air traffic management systems solved with mixed integer programming," *IEEE Transactions on Intelligent Transportation Systems*, vol. 3, no. 1, pp. 3–11, 2002.

[20] D. Gianazza, "Learning air traffic controller workload from past sector operations," in *Proceedings of the ATM Seminar, 12th USA/Europe Air Traffic Management R&D Seminar*, Seattle, WC, USA, June 2017.

[21] T. Wu and W. Du, "A distributed approach to aircraft conflict resolution based on satisficing game theory," in *Advances in Intelligent Systems and Computing, Foundations of Intelligent Systems*, pp. 383–393, Springer, Berlin, Germany, 2014.

[22] V. B. Kulkarni, "Intelligent air traffic controller simulation using artificial neural networks," in *Proceedings of the 2015 International Conference on Industrial Instrumentation and Control (ICIC)*, pp. 1027–1031, IEEE, Pune, India, May 2015.

[23] S. Ravizza, J. Chen, J. A. D. Atkin, P. Stewart, and E. K. Burke, "Aircraft taxi time prediction: comparisons and insights," *Applied Soft Computing*, vol. 14, pp. 397–406, 2014.

[24] H. Lee, W. Malik, and Y. C. Jung, "Taxi-out time prediction for departures at charlotte airport using machine learning techniques," in *Proceedings of the 16th AIAA Aviation Technology, Integration, and Operations Conference*, p. 3910, Washington, DC, USA, June 2016.

[25] M. Ahmed, S. Alam, and M. Barlow, "A cooperative co-evolutionary optimisation model for best-fit aircraft sequence and feasible runway configuration in a multi-runway airport," *Aerospace*, vol. 5, no. 3, p. 85, 2018.

[26] R. Alligier, D. Gianazza, and N. Durand, "Machine learning and mass estimation methods for ground-based aircraft climb prediction," *IEEE Transactions on Intelligent Transportation Systems*, vol. 16, no. 6, pp. 3138–3149, 2015.

[27] M. C. R. Murca, R. J. H. Richard DeLaura, R. Jordan, T. Reynolds, and H. Balakrishnan, "Trajectory clustering and classification for characterization of air traffic flows," in *Proceedings of the 16th AIAA Aviation Technology, Integration, and Operations Conference*, p. 3760, Washington, DC, USA, June 2016.

[28] N. Takeichi, R. Kaida, A. Shimomura, and T. Yamauchi, "Prediction of delay due to air traffic control by machine learning," in *Proceedings of the AIAA Modeling and Simulation Technologies Conference*, p. 1323, Grapevine, TX, USA, January 2017.

[29] C. Sun, Y. J. Kim, B. Simon, and D. Mavris, "Prediction of weather-induced airline delays based on machine learning algorithms," in *Proceedings of the 2016 IEEE/AIAA 35th Digital Avionics Systems Conference (DASC)*, pp. 1–6, IEEE, Sacramento, CA, USA, September 2016.

[30] H. Georgiou, S. Karagiorgou, Y. Kontoulis et al., "Moving objects analytics: survey on future location & trajectory prediction methods," 2018, https://arxiv.org/abs/1807.04639.

[31] R. Wu, G. Luo, J. Shao, L. Tian, and C. Peng, "Location prediction on trajectory data: a review," *Big Data Mining and Analytics*, vol. 1, no. 2, pp. 108–127, 2018.

[32] Y. Zhang and A. Haghani, "A gradient boosting method to improve travel time prediction," *Transportation Research Part C: Emerging Technologies*, vol. 58, pp. 308–324, 2015.

[33] S. Papadopoulos, E. Azar, W.-L. Woon, and C. E. Kontokosta, "Evaluation of tree-based ensemble learning algorithms for building energy performance estimation," *Journal of Building Performance Simulation*, vol. 11, no. 3, pp. 322–332, 2018.

[34] Y. Li and Z. Yang, "Application of eos-elm with binary jaya-based feature selection to real-time transient stability assessment using PMU data," *IEEE Access*, vol. 5, pp. 23092–23101, 2017.

[35] A. Pescape, A. Montieri, G. Aceto, and D. Ciuonzo, "Anonymity services tor, i2p, jondonym: classifying in the dark (web)," *IEEE Transactions on Dependable and Secure Computing*, vol. 17, no. 3, pp. 662–675, 2018.

[36] V. F. Taylor, R. Spolaor, M. Conti, and I. Martinovic, "Appscanner: automatic fingerprinting of smartphone apps from encrypted network traffic," in *Proceedings of the 2016 IEEE European Symposium on Security and Privacy (EuroS&P)*, pp. 439–454, IEEE, Saarbrucken, Germany, March 2016.

[37] G. Aceto, D. Ciuonzo, A. Montieri, and A. Pescapé, "Multi-classification approaches for classifying mobile app traffic," *Journal of Network and Computer Applications*, vol. 103, pp. 131–145, 2018.

[38] J. J. Rebollo and H. Balakrishnan, "Characterization and prediction of air traffic delays," *Transportation Research Part C: Emerging Technologies*, vol. 44, pp. 231–241, 2014.

[39] P. Monmousseau, D. Delahaye, A. Marzuoli, and E. Feron, "Predicting and analyzing us air traffic delays using passenger-centric data-sources," in *Proceedings of the Thirteenth USA/Europe Air Traffic Management Research and Development Seminar (ATM2019)*, Vienna, Austria, June, 2019.

[40] R. Caruana and A. Niculescu-Mizil, "An empirical comparison of supervised learning algorithms," in *Proceedings of the 23rd International Conference on Machine Learning*, pp. 161–168, Pittsburgh, PA, USA, June 2006.

[41] X. Zhang and S. Mahadevan, "Ensemble machine learning models for aviation incident risk prediction," *Decision Support Systems*, vol. 116, pp. 48–63, 2019.

[42] A.-D. Nguyen, D.-T. Pham, N. Lilith, and S. Alam, "Model generalization in arrival runway occupancy time prediction by feature equivalences," in *Proceedings of the 9th International Conference for Research in Air Transportation (ICRAT)*, Tampa, FL, USA, September 2020.

[43] G. F. Jenks and F. C. Caspall, "Error on choroplethic maps: definition, measurement, reduction," *Annals of the Association of American Geographers*, vol. 61, no. 2, pp. 217–244, 1971.

[44] S. Alam, C. Lokan, and H. Abbass, "What can make an airspace unsafe? characterizing collision risk using multi-objective optimization," in *Proceedings of the 2012 IEEE Congress on Evolutionary Computation*, pp. 1–8, IEEE, Brisbane, Australia, June 2012.

[45] A. Liaw and M. Wiener, "Classification and regression by randomforest," *R News*, vol. 2, no. 3, pp. 18–22, 2002.

[46] T. Chen, H. Tong, M. Benesty, V. Khotilovich, and Y. Tang, *Xgboost: Extreme Gradient Boosting. R Package version 0.4-2*, NYC Data Science Academy, New York, Ny, USA, 2015.

[47] T. Chen and C. Guestrin, "Xgboost: a scalable tree boosting system," in *Proceedings of the 22nd Acm Sigkdd International Conference on Knowledge Discovery and Data Mining*, pp. 785–794, San Francisco, CA, USA, August 2016.

[48] J. H. Friedman, "Greedy function approximation: a gradient boosting machine," *Annals of Statistics*, vol. 29, no. 5, pp. 1189–1232, 2001.

[49] P. Li, "Robust logitboost and adaptive base class (ABC) logitboost," 2012, https://arxiv.org/abs/1203.3491.

[50] D.-T. Pham, *Machine learning-based flight trajectories prediction and air traffic conflict resolution advisory*, PhD Thesis, PSL Research University, Paris, France, 2019.

Hindawi
Complexity
Volume 2020, Article ID 1208951, 12 pages
https://doi.org/10.1155/2020/1208951

Research Article

Finite-Time Asynchronous Stabilization for Nonlinear Hidden Markov Jump Systems with Parameter Varying in Continuous-Time Case

Lianjun Xiao,[1] **Xiaofeng Wang**,[2] **and Lingling Gao**[1]

[1]*School of Artificial Intelligence and Big Data, Hefei University, Hefei 230601, China*
[2]*Anhui Provincial Engineering Laboratory of Big Data Technology Application for Urban Infrastructure, School of Artificial Intelligence and Big Data, Hefei University, Hefei 230601, China*

Correspondence should be addressed to Xiaofeng Wang; xfwang@hfuu.edu.cn

Received 12 July 2020; Revised 2 September 2020; Accepted 25 September 2020; Published 28 October 2020

Academic Editor: Shuping He

The finite-time asynchronous stabilization problem has received great attention because of the wide application of actual engineering. In this paper, we consider the problem of finite-time asynchronous stabilization for nonlinear hidden Markov jump systems (HMJSs) with linear parameter varying. Compared with the existing research results on Markov jump systems, this paper considers the HMJSs which contain both the hidden state and the observed state in continuous-time case. Moreover, we consider the parameters of the systems are time varying. The aim of the paper is to design a proper observation-mode-based asynchronous controller such that the closed-loop HMJSs with linear parameter varying be stochastically finite-time bounded with H_∞ performance (SFTB-H_∞). Then, we give some sufficient conditions to solve the SFTB-H_∞ asynchronous controller by considering the stochastic Lyapunov–Krasovskii functional (SLKF) methods. Finally, a numerical example is used to show the validity of the main results.

1. Introduction

In recent years, hybrid systems have attracted the great attention and research due to their wide application in the industrial control field. Moreover, with the continuous upgrading and changes in the industrial environment, how to model and control hybrid systems in complex environments has become a major research hotspot in the control field. As a kind of special hybrid systems, Markov jump systems (MJSs) have received researchers' great attention and many constructive results have been made. It should be noted that the synchronous controllers are always considered in many existing results when it comes to the stabilization problem of Markov jump systems. That means the controller of the systems can always track the information of the model of the system in real time. However, such a situation is always impossible to achieve in a Markov jump system with a complex environment. Therefore, the asynchronous characteristic between the system modal and the controller has attracted the attention of many researchers and they began to focus on the various characteristics of the HMJSs. The static output constrained control [1], the output feedback control [2], and the observer-based asynchronous fault detection [3] problems of the HMJSs with the discrete-time state are studied by the authors, respectively. In [4], the resilient asynchronous H_∞ control problem of the discrete-time HMJSs with singularly perturbed was considered. For the nonlinear HMJSs, the quantized control [5] and the finite-time L_2-gain asynchronous control [6] problems by using T-S fuzzy model approach are studied, respectively. Moreover, many researchers also have carried out some work for the continuous-time HMJSs. The asynchronous H_2-controller design and the asynchronous filter design problems are studied for the continuous-time HMJSs in [7, 8], respectively. For more particulars of HMJSs, the interested readers can read references [9, 10].

It should be pointed out that many results of the MJSs assume that the parameter matrices are constant matrices or

uncertain matrices that satisfy some given known conditions. In actual control systems, the system parameters may have the characteristics of convex polygonal linear parameters varying due to the sensor and actuator failures. For the control systems with such a special situation, it is necessary to design the corresponding nonlinear parameter time-varying controller to stabilization of the systems. Thus, many researchers proposed the linear parameter-varying control methods which laid a solid theoretical foundation for the design of nonlinear parameter time-varying controller. For a kind of parameter-varying system [11], an adaptive algorithm was proposed to achieve the active vibration control by using a new online secondary path estimation method. For bounded parameter variation linear parameter-varying systems, the LMI-based filter design problem is studied in [12]. The robust fault estimation [13] and set-membership fault estimation [14] problem is studied for parameter time-varying systems. For more particulars of parameter-varying systems, the interested readers can read references [15–18].

In the abovementioned references, the system analysis and/or some control method were concerned only over an infinite-time interval, which portrayed the asymptotic properties of the HMJSs and parameter-varying systems. However, the transient characteristics in a given finite-time interval is significant in many control systems [19–21] and should be considered simultaneously. For a class of nonlinear systems, the authors studied the finite-time adaptive fuzzy control problem in [22, 23], respectively. In [24], a finite-time control approach was used to solve the problem of accurate trajectory tracking for disturbed surface vehicles. Moreover, many researchers also combine the finite-time control scheme with the networked switched systems [25], nonlinear systems [26, 27], and quadrotors control [28] and have carried out lots of excellent works. The authors studied the design and implementation of bounded finite-time control algorithm problem for the speed regulation of permanent magnet synchronous motor in [29]. By using the state-dependent switching method, the adaptive fuzzy finite-time control of switched nonlinear systems is studied in [30]. The problem of fuzzy finite-time control for switched systems via adding a barrier power integrator is considered in [31]. For more particulars of HMJSs, the interested readers can read references [32–34].

However, few results have been reported regarding research on finite-time asynchronous control of HMJSs based on the parameter varying, which is the motivation of this work. Different from some existing results on the finite-time control problem [35, 36], the problem of SFTB-H_∞ asynchronous control is studied for continuous-time HMJSs via parameter varying in this paper. Compared with the existing results of asynchronous control for discrete-time HMJSs [37–40], this paper mainly consists of the following threefold contributions:

(1) The asynchronous characteristic between the controller modes and the system modes is characterized by the hidden Markov dynamics. Moreover, we firstly consider the asynchronous stabilization problem for the continuous-time HMJSs with parameter varying models.

(2) Some sufficient conditions will be given to solve the SFTB-H_∞ observation-mode-based asynchronous controller by considering the SLKF methods and introducing some auxiliary variables.

(3) Considering the parameter time-varying, the methods of gridding technique and approximate basis function will be used in order to change the infinite LMIs into finite LMIs which can be solved by MATLAB LMI toolbox to get the finite-time asynchronous controller gain directly.

The organization of this paper is made of five parts. In Section 1, the background of the HMJSs, the parameter time-varying systems, finite-time control scheme, and the notation meaning of this paper are introduced and given. Section 2 introduces the system description of the parameter varying hidden Markov jump systems (PV-HMJSs) and designs a suitable asynchronous controller for the studied systems. Moreover, the main definitions and lemmas are also given in this part. Section 3 gives some sufficient conditions to solve the SFTB-H_∞ observation-mode-based asynchronous controller. In Section 4, the simulation experiment of HMJSs via parameter varying with two subsystems is carried out, only to find that the closed-loop HMJSs via parameter varying fulfill the condition of SFTB-H_∞ under the action of the designed asynchronous controller. The conclusion and future research work follow in Section 5.

Notation: the notation meaning throughout this paper is shown in Table 1. Furthermore, we assume that the matrices and notations in this paper are standard with compossible dimensions.

2. System Formulation

2.1. System Description. We consider the nonlinear parameter varying hidden Markov jump systems (PV-HMJSs) defined on the probability space $(\Gamma, \Delta, \mathrm{Prob}(\cdot))$:

$$\begin{cases} \begin{bmatrix} \dot{x}(t) \\ y(t) \end{bmatrix} = f^{p(t)}_{H(t)}(x(t), \omega(t)) + g^{p(t)}_{H(t)} u(t), \\ x(t) = x_0, \\ p(t) = p_0, \\ H(t) = H_0, \\ t = 0, \end{cases} \tag{1}$$

where $H(t) = (h_1(t), h_2(t))$ and $p(t) = [p_1(t), p_2(t), \ldots, p_m(t)]^{\mathrm{T}}$. The notations of the PV-HMJSs (1) are given in Table 2.

The right-continuous hidden Markov chain $H(t)$ is composed of the hidden state $h_1(t)$ in the finite set $\mathscr{M} := \{1, 2, \ldots, M\}$ and the observation state $h_2(t)$ in the finite set $\mathscr{M} := \{1, 2, \ldots, N\}$. Furthermore, the hidden Markov chain $H(t) \in \mathscr{M} \times \mathscr{M}$ can be seen as a homogeneous Markov process which satisfies

Table 1: Symbol notations.

Notation	Denotes
$\mathbb{R}^n$	n-dimensional Euclidean space
$\mathbb{R}^{n\times m}$	$n\times m$ real matrices
$*$	symmetric matrix
$\mathfrak{J}V$	The weak infinitesimal operator of V
I	Unit matrix
A^{T}	Matrix transpose
A^{-1}	Matrix inverse
0	Zero matrix
$\|*\|$	Euclidean vector norm
$\mathbf{Her}(A)$	$A+A^{\mathrm{T}}$
$\lambda_{\max}(P)$	Maximum eigenvalue of P
$\lambda_{\min}(P)$	Minimum eigenvalue of P
diag$\{AB\}$	The block-diagonal matrix of A and B
Γ	The sample space
Δ	The algebra of events
$\mathbb{P}(\cdot)$	The probability measure which defined on Δ

$$\mathbb{P}(H(t+\tau)=(\mathcal{J},\mathcal{L})\mid H(t)=(\mathcal{I},\mathcal{K}))=\begin{cases}\mathcal{R}_{(\mathcal{I},\mathcal{K}),(\mathcal{J},\mathcal{L})}\tau+o(\tau), & (\mathcal{I},\mathcal{K})\neq(\mathcal{J},\mathcal{L}),\\ 1+\mathcal{R}_{(\mathcal{I},\mathcal{K}),(\mathcal{J},\mathcal{L})}\tau+o(\tau), & (\mathcal{I},\mathcal{K})=(\mathcal{J},\mathcal{L}),\end{cases}\tag{2}$$

where $\mathcal{R}_{(\mathcal{J},\mathcal{K}),(\mathcal{J},\mathcal{L})}\geq 0$, $\forall(\mathcal{I},\mathcal{K})\neq(\mathcal{J},\mathcal{L})$ is the transition rate with $\sum_{(\mathcal{J},\mathcal{K})\neq(\mathcal{J},\mathcal{L})}\mathcal{R}_{(\mathcal{J},\mathcal{K}),(\mathcal{J}\mathcal{L})}=-r_{(\mathcal{J},\mathcal{K})}$ and for any $\mathcal{L},\mathcal{K}\in\mathcal{M},\mathcal{I},\mathcal{J}\in\mathcal{M}$, which satisfies

$$\mathcal{R}_{(\mathcal{J},\mathcal{K}),(\mathcal{I},\mathcal{L})}=\begin{cases}\alpha^{\mathcal{K}}_{\mathcal{J}\mathcal{L}}\pi_{\mathcal{J}\mathcal{I}}, & \mathcal{I}\neq\mathcal{J},\\ q^{\mathcal{J}}_{\mathcal{K}\mathcal{L}}, & \mathcal{L}\neq\mathcal{K},\ \mathcal{J}=\mathcal{I},\\ \pi_{\mathcal{J}\mathcal{J}}+q^{\mathcal{J}}_{\mathcal{K}\mathcal{K}}, & \mathcal{J}=\mathcal{I},\ \mathcal{K}=\mathcal{L}\\ 0, & \text{otherwise},\end{cases}\tag{3}$$

in which $\sum_{\mathcal{L}=1}^{N}\alpha^{\mathcal{K}}_{\mathcal{J}\mathcal{L}}=1$, $\Pi=[\pi_{\mathcal{J}\mathcal{J}}]$ is the transition rate matrix and satisfies $\pi_{\mathcal{J}\mathcal{J}}\geq 0$ for $\forall\mathcal{I}\neq\mathcal{J}$, $\aleph^{\mathcal{J}}=[q^{\mathcal{J}}_{\mathcal{K}\mathcal{L}}]$ is the Π-dependent conditional probability matrix and satisfies $q^{\mathcal{J}}_{\mathcal{K}\mathcal{L}}\geq 0$ for $\forall\mathcal{K}\neq\mathcal{L}$, $\pi_{\mathcal{J}\mathcal{J}}=-\sum_{\mathcal{I}\neq\mathcal{J}}\pi_{\mathcal{J}\mathcal{I}}$, and $q_{\mathcal{K}\mathcal{K}}=-\sum_{\mathcal{L}\neq\mathcal{K}}q^{\mathcal{J}}_{\mathcal{K}\mathcal{L}}$.

Remark 1. From relation (3), we can summarize that the same state will be visited of the hidden state $h_1(t)$ and the observation state $h_2(t)$ if $\mathcal{M}=\mathcal{M}$, $\alpha^{\mathcal{K}}_{\mathcal{J}\mathcal{L}}=0$ with $\mathcal{J}\neq\mathcal{L}$, and $\alpha^{\mathcal{K}}_{\mathcal{J}\mathcal{J}}=1$ with $\mathcal{J}=\mathcal{L}$. In this case, the full information of the hidden state $h_1(t)$ will be provided for the detector. If $\alpha^{\mathcal{K}}_{\mathcal{J}\mathcal{L}}=1$ and $\alpha^{\mathcal{L}}_{\mathcal{J}\mathcal{L}}=0$ with $\mathcal{K}\neq\mathcal{L}$, only one jump will occur between the hidden state $h_1(t)$ and the observation state $h_2(t)$. Moreover, the observer will not provide any information if $\mathcal{M}=\{1\}$, $q^{\mathcal{J}}_{\mathcal{K}\mathcal{L}}=0$, and $\alpha^{1}_{\mathcal{J}1}=1$ and the observation state is $h_2(t)=1$. For more specific details of the relationship between the hidden state $h_1(t)$ and the observation state $h_2(t)$, we can refer to [3, 6, 35, 36].

In actual engineering applications, we often encounter situations where the system mode information accessible by the controller/observer is usually inaccurate. In other words, the actual model of the system cannot be observed by the controller, which makes the information between the controller mode and the system mode asynchronous. Therefore, a new controller mode $h_2(t)$ related to the system mode $h_1(t)$ needs to be introduced.

The PV-HMJSs (1) can be rewritten as the following PV-HMJSs:

$$\begin{cases}\begin{bmatrix}\dot{x}(t)\\ y(t)\end{bmatrix}=\mathbf{F}^{p(t)}_{h_1(t)}\mathbf{G}[x(t),u(t),\omega(t)],\\ x(t)=x_0,\\ p(t)=p_0,\\ h_1(t)=h_{10},\\ t=0,\\ h_1(t)\in\mathcal{M},\end{cases}\tag{4}$$

where

$$\mathbf{F}^{p(t)}_{h_1(t)}=\begin{bmatrix}A^{p(t)}_{h_1(t)} & B^{p(t)}_{h_1(t)} & W^{p(t)}_{1h_1(t)} & F^{p(t)}_{h_1(t)}\\ C^{p(t)}_{h_1(t)} & D^{p(t)}_{h_1(t)} & W^{p(t)}_{2h_1(t)} & 0\end{bmatrix}.\tag{5}$$

$\mathbf{G}[x(t),u(t),\omega(t)]=\mathrm{col}[x(t),u(t),\omega(t),f(x(t),t)]$, $A^{p(t)}_{H(t)}$ is the time-varying parameter-depende nt matrix, and $f(x(t),t)$ is the unknown nonlinear function.

We use $A^{p(t)}_{\mathcal{J}}$, $B^{p(t)}_{\mathcal{J}}$, $W^{p(t)}_{1\mathcal{J}}$, $F^{p(t)}_{\mathcal{J}}$, $C^{p(t)}_{\mathcal{J}}$, $D^{p(t)}_{\mathcal{J}}$, and $W^{p(t)}_{2\mathcal{J}}$ to denote $A^{p(t)}_{h_1(t)}$, $B^{p(t)}_{h_1(t)}$, $W^{p(t)}_{1h_1(t)}$, $F^{p(t)}_{h_1(t)}$, $C^{p(t)}_{h_1(t)}$, $D^{p(t)}_{h_1(t)}$, and $W^{p(t)}_{2h_1(t)}$, when $h_1(t)=\mathcal{J}$, $\mathcal{J}\in\mathcal{M}$, respectively.

For any $n=1,2,\ldots,m$, the time-varying parameter matrix $p(t)$ and its variation rate $\dot{p}(t)$ are both assumed bounded, i.e., $p_n(t)\in\left[\underline{p}_1\ \overline{p}_1\right]$ and $\dot{p}_n(t)\in\left[\underline{p}_2\ \overline{p}_2\right]$. Moreover, the time-varying parameter matrix $p(t)$ is also measurable and affine parameter dependent in real time. That means the following equations hold:

Table 2: The notations of the PV-HMJSs (1).

Notation	Denotes
$x(t) \in \mathbb{R}^n$	The systems state
$y(t) \in \mathbb{R}^m$	The controlled output
$u(t) \in \mathbb{R}^p$	The controlled input
$\omega(t) \in \mathbb{R}^q$	The disturbance input
$p(t)$	The time-varying parameter matrix
$H(t)$	A right-continuous hidden Markov chain
x_0	The initial state of the systems
p_0	The initial time-varying parameter matrix
H_0	The initial hidden Markov process

$$
\begin{aligned}
A_{\mathcal{F}}^{p} &= A_0 + \sum_{\mathcal{F}=1}^{m} A_{\mathcal{F}} p_{\mathcal{F}},\\
B_{\mathcal{F}}^{p} &= B_0 + \sum_{\mathcal{F}=1}^{m} B_{\mathcal{F}} p_{\mathcal{F}},\\
W_{1,\mathcal{F}}^{p} &= W_{10} + \sum_{\mathcal{F}=1}^{m} W_{1,\mathcal{F}} p_{\mathcal{F}},\\
C_{\mathcal{F}}^{p} &= C_0 + \sum_{\mathcal{F}=1}^{m} C_{\mathcal{F}} p_{\mathcal{F}},\\
D_{\mathcal{F}}^{p} &= D_0 + \sum_{\mathcal{F}=1}^{m} D_{\mathcal{F}} p_{\mathcal{F}},\\
W_{2,\mathcal{F}}^{p} &= W_{20} + \sum_{\mathcal{F}=1}^{m} W_{2,\mathcal{F}} p_{\mathcal{F}},\\
F_{\mathcal{F}}^{p} &= F_0 + \sum_{\mathcal{F}=1}^{m} F_{\mathcal{F}} p_{\mathcal{F}},
\end{aligned}
\tag{6}
$$

where $A_{\mathcal{F}}$, $B_{\mathcal{F}}$, $W_{1,\mathcal{F}}$, $F_{\mathcal{F}}$, $C_{\mathcal{F}}$, $D_{\mathcal{F}}$, and $W_{2,\mathcal{F}}$ with $\mathcal{F} = 0, 1, \ldots, m$ are known matrices.

We suppose the system states of the PV-HMJSs (9) be available, we design the following $h_2(t)$-dependent asynchronous controller:

$$
u(t) = K_{h_2(t)}^{p(t)} x(t), \quad h_2(t) \in \mathcal{M}, \tag{7}
$$

where $K_{h_2(t)}^{p(t)}$ is the h_2-dependent controller gain which will be solved in Theorem 3.

Submitting the $h_2(t)$-dependent controller (7) into the PV-HMJSs (5), we can get the following closed-loop PV-HMJSs if $h_1(t) = \mathcal{F}$ and $h_2(t) = \mathcal{K}$, $\mathcal{F} \in \mathcal{M}$, $\mathcal{K} \in \mathcal{M}$:

$$
\begin{cases}
\begin{bmatrix} \dot{x}(t) \\ y(t) \end{bmatrix} = \begin{bmatrix} \overline{A}_{\mathcal{F}\mathcal{K}}^{p} & W_{1,\mathcal{F}}^{p} & F_{\mathcal{F}}^{p} \\ \overline{C}_{\mathcal{F}\mathcal{K}}^{p} & W_{2,\mathcal{F}}^{p} & 0 \end{bmatrix} \begin{bmatrix} x(t) \\ \omega(t) \\ f(x(t),t) \end{bmatrix},\\
x(0) = x_0,\\
\mathcal{F}(0) = \mathcal{F}_0,\\
\mathcal{K}(0) = \mathcal{K}_0,
\end{cases}
\tag{8}
$$

where $\overline{A}_{\mathcal{F}\mathcal{K}}^{p} = A_{\mathcal{F}}^{p} + B_{\mathcal{F}}^{p} K_{\mathcal{K}}^{p}$ and $\overline{C}_{\mathcal{F}\mathcal{K}}^{p} = C_{\mathcal{F}}^{p} + D_{\mathcal{F}}^{p} K_{\mathcal{K}}^{p}$.

2.2. Main Definitions and Lemmas

Definition 1 (see [32]). Given two positive constants $0 < \mathcal{J}_1 < \mathcal{J}_2$, a weighting matrix $R_{\mathcal{F}\mathcal{K}} > 0$, and a finite-time interval $[0 \ T]$, the closed-loop PV-HMJSs (8) with $\omega(t) \equiv 0$ is SFTS within $(\mathcal{J}_1 \ \mathcal{J}_2 \ T \ R_{\mathcal{F}\mathcal{K}})$ if, for any initial condition $x_0^T R_{\mathcal{F}\mathcal{K}} x_0 \le \mathcal{J}_1$, we have

$$
\mathbf{E}\left\{x(t)^T R_{\mathcal{F}\mathcal{K}} x(t)\right\} \le \mathcal{J}_2, \quad t \in [0 \ T]. \tag{9}
$$

Definition 2 (see [32]). Given two positive constants $0 < \mathcal{J}_1 < \mathcal{J}_2$, a weighting matrix $R_{\mathcal{F}\mathcal{K}} > 0$, and a finite-time interval $[0 \ T]$, the closed-loop PV-HMJSs (12) is stochastically finite-time bounded (SFTB) within $(\mathcal{J}_1 \ \mathcal{J}_2 \ T \ R_{\mathcal{F}\mathcal{K}})$ if, for any initial condition $x_0^T R_{\mathcal{F}\mathcal{K}} x_0 \le \mathcal{J}_1$, we have $\mathbf{E}\left\{x(t)^T R_{\mathcal{F}\mathcal{K}} x(t)\right\} \le \mathcal{J}_2$, $t \in [0 \ T]$.

Definition 3 (see [6]). Under zero initial condition, the $h_2(t)$-dependent controller (9) is said to be a SFTB-H_∞ controller of the PV-HMJSs (7) if there exists a $h_2(t)$-dependent controller gain $K_{\mathcal{K}}^{p}$, $\mathcal{K} \in \mathcal{M}$ such that the closed-loop PV-HMJSs (10) be SFTB and satisfies the following H_∞-gain performance index:

$$
\mathbf{E}\left\{\int_0^T y^T(\tau) y(\tau) \mathrm{d}\tau\right\} < \varphi \mathbf{E}\left\{\int_0^T \omega^T(\tau) \omega(\tau) \mathrm{d}\tau\right\}. \tag{10}
$$

Lemma 1 (see [22]). *We have* $2E^T XYF \leqslant \beta E^T X^T XE + \beta^{-1} F^T Y^T YF$ *for any given proper dimensional matrices E and F, positive scalar* $\beta > 0$*, and matrices X and Y.*

Assumption 1. For any given positive scalars T and ϖ, the disturbance input $\omega(t)$ is bounded with $\int_0^T \omega^T(\tau)\omega(\tau)\mathrm{d}\tau \le \varpi$.

Assumption 2. For a given positive scalar $\vartheta > 0$, the unknown state-dependent nonlinear function $f(x(t), t)$ satisfies $\|f(x(t), t)\| \leqslant \vartheta \|x(t)\|$.

Remark 2. In this paper, the transient character in a given finite-time interval is considered for the stochastic linear parameter varying hidden HMJSs. For the given hidden HMJSs with initial conditions (or bounded disturbance input), we said such systems is stochastically finite-time stable (SFTS) (or stochastically finite-time bounded (SFTB)) if the systems' state does not exceed a given limit within a finite-time interval. The specific definitions of the SFTS and

SFTB are shown in Definitions 1 and 2. For more details of the SFTS and SFTB, we can refer to [31–33].

3. Main Results

In this section, we will give some sufficient conditions to solve the SFTB-H_∞ observation-mode-based asynchronous controller (11) and obtain the $h_2(t)$-dependent controller gain $K_{\mathscr{K}}^p$, $\mathscr{K} \in \mathscr{M}$. We aim the closed-loop PV-HMJSs (12) to fulfill the SFTB-H_∞ condition under the action of the observation-mode-based asynchronous controller (11).

Theorem 1. *Given four positive constants $\omega > 0$, $\mathscr{J}_1 > 0$, $\varpi > 0$, and $T > 0$, the closed-loop PV-HMJSs (12) is SFTB within $(\mathscr{J}_1\ \mathscr{J}_2\ T\ R_{\mathscr{J}\mathscr{K}}\ \varpi)$ if there exist positive constants $0 < \mathscr{J}_1 < \mathscr{J}_2$, $\overline{\lambda}_{P_{\mathscr{J}\mathscr{K}}'} > 0$, $\underline{\lambda}_{P_{\mathscr{J}\mathscr{K}}'} > 0$, $\varphi > 0$, and $H(t)$-dependent positive-definite symmetric matrices $P_{\mathscr{J}\mathscr{K}}$ and $R_{\mathscr{J}\mathscr{K}}$, where $(\mathscr{I}, \mathscr{K}) \in \mathscr{M} \times \mathscr{M}$, such that*

$$\begin{bmatrix} \Upsilon & P_{\mathscr{J}\mathscr{K}} W_{1\mathscr{J}}^p & F_{\mathscr{J}}^{p\mathrm{T}} P_{\mathscr{J}\mathscr{K}} & \Theta_{\mathscr{J}\mathscr{K}} \\ * & -\varphi I & 0 & 0 \\ * & * & -\beta^{-1} I & 0 \\ * & * & * & -\Psi_{\mathscr{J}\mathscr{K}} \end{bmatrix} < 0, \tag{11}$$

$$\left(\mathscr{J}_1 \overline{\lambda}_{P_{\mathscr{J}\mathscr{K}}'} + \varphi\varpi\right) e^{\omega T} < \mathscr{J}_2 \underline{\lambda}_{P_{\mathscr{J}\mathscr{K}}'}, \tag{12}$$

where

$$\begin{aligned} \Upsilon &= \mathbf{Her}\left(P_{\mathscr{J}\mathscr{K}}\ \overline{A}_{\mathscr{J}\mathscr{K}}^p\right) + \left(r_{(\mathscr{J},\mathscr{K})(\mathscr{J},\mathscr{K})} - \omega\right) P_{\mathscr{J}\mathscr{K}} + \beta^{-1}\vartheta I, \\ P_{\mathscr{J}\mathscr{K}}' &= R_{\mathscr{J}\mathscr{K}}^{-(1/2)} P_{\mathscr{J}\mathscr{K}} R_{\mathscr{J}\mathscr{K}}^{-(1/2)}, \\ \overline{\lambda}_{P_{\mathscr{J}\mathscr{K}}'} &= \max_{(\mathscr{J},\mathscr{K})\in\mathscr{R}} \lambda_{\max}\left(P_{\mathscr{J}\mathscr{K}}'\right), \\ \underline{\lambda}_{P_{\mathscr{J}\mathscr{K}}'} &= \min_{(\mathscr{J},\mathscr{K})\in\mathscr{R}} \lambda_{\min}\left(P_{\mathscr{J}\mathscr{K}}'\right), \\ \Psi_{\mathscr{J}\mathscr{K}} &= \mathrm{diag}\left\{P_{\nu_{(\mathscr{J},\mathscr{K})}^{(1)}}^{-1}, P_{\nu_{(\mathscr{J},\mathscr{K})}^{(2)}}^{-1}, \ldots, P_{\nu_{(\mathscr{J},\mathscr{K})}^{(h_{(\mathscr{J},\mathscr{K})})}}^{-1}\right\}, \\ \Theta_{\mathscr{J}\mathscr{K}} &= \left[\sqrt{\mathscr{R}_{(\mathscr{J},\mathscr{K})}\nu_{(\mathscr{J},\mathscr{K})}^{(1)}}\, I, \ldots, \sqrt{\mathscr{R}_{(\mathscr{J},\mathscr{K})}\nu_{(\mathscr{J},\mathscr{K})}^{(h_{(\mathscr{J},\mathscr{K})})}}\, I\right]. \end{aligned} \tag{13}$$

Proof. Select a SLKF candidate as follows:

$$V\left(x(t), H_t, t\right) = x^{\mathrm{T}}(t) P_{\mathscr{J}\mathscr{K}} x(t). \tag{14}$$

Recalling to the closed-loop PV-HMJSs (8), we can get the following weak infinitesimal operator of $V(x(t), H_t, t)$:

$$\begin{aligned} \mathfrak{J}V(x(t), H(t), t) &= \lim_{\tau\longrightarrow 0} \frac{1}{\tau}\left[\mathbf{E}\{V(x(t+\tau), H(t+\tau), t+\tau) | x(t), H(t)\}\right] - V(x(t), H(t), t) \\ &= x^T(t)\mathscr{P}_1 x(t) + \mathbf{Her}\left(x^T(t) P_{\mathscr{J}\mathscr{K}} W_{1,\mathscr{J}}^p \omega(t)\right) + \mathbf{Her}\left(x^T(t) P_{\mathscr{J}\mathscr{K}} F_{\mathscr{J}}^p f x(t), t\right), \end{aligned} \tag{15}$$

where

$$\mathscr{P}_1 = \left[\mathbf{Her}\left(P_{\mathscr{J}\mathscr{K}} \overline{A}_{\mathscr{J}\mathscr{K}}^p\right) + \sum_{(\mathscr{J},\mathscr{L})\in\mathscr{R}} \mathscr{R}_{(\mathscr{J},\mathscr{K})(j,l)} P_{\mathscr{J}\mathscr{L}}\right], \tag{16}$$

in which

$$\begin{aligned} \sum_{(\mathscr{J},\mathscr{L})\in\mathscr{R}} \mathscr{R}_{(\mathscr{J},\mathscr{K})(\mathscr{J},\mathscr{L})} P_{\mathscr{J}\mathscr{L}} &= \sum_{(\mathscr{J},\mathscr{L})\mathscr{R}'} \mathscr{R}_{(\mathscr{J},\mathscr{K})(\mathscr{J},\mathscr{L})} P_{\mathscr{J}\mathscr{L}} \\ &\quad + r_{(\mathscr{J}\mathscr{K})(\mathscr{J}\mathscr{K})} P_{\mathscr{J}\mathscr{K}} \\ &= \Theta_{\mathscr{J}\mathscr{K}} \Psi_{\mathscr{J}\mathscr{K}}^{-1} \Theta_{\mathscr{J}\mathscr{K}}^{\mathrm{T}} \\ &\quad + r_{(\mathscr{J}\mathscr{K})(\mathscr{J}\mathscr{K})} P_{\mathscr{J}\mathscr{K}}, \end{aligned} \tag{17}$$

with

$$\begin{aligned} \mathscr{R}' &= \left\{\mathscr{R}_{(\mathscr{J},\mathscr{K})(\mathscr{J},\mathscr{L})\neq 0, (\mathscr{J},\mathscr{L})\in\mathscr{R}, (\mathscr{J},\mathscr{K})\neq(\mathscr{J},\mathscr{L})}\right\} \\ &= \left\{\nu_{(\mathscr{J},\mathscr{K})}^{(1)} r_{(\mathscr{J},\mathscr{K})}, \ldots, \nu_{(\mathscr{J},\mathscr{K})}^{(h_{(\mathscr{J},\mathscr{K})})} \mathscr{R}_{(\mathscr{J},\mathscr{K})}\right\}, \\ \Psi_{\mathscr{J},\mathscr{K}} &= \mathrm{diag}\left\{P_{\nu_{(\mathscr{J},\mathscr{K})}^{(1)}}^{-1}, P_{\nu_{(\mathscr{J},\mathscr{K})}^{(2)}}^{-1}, \ldots, P_{\nu_{(\mathscr{J},\mathscr{K})}^{(h_{(\mathscr{J},\mathscr{K})})}}^{-1}\right\}, \\ \Theta_{\mathscr{J},\mathscr{K}} &= \left[\sqrt{r_{(\mathscr{J},\mathscr{K})}\nu_{(\mathscr{J},\mathscr{K})}^{(1)}}\, I, \ldots, \sqrt{r_{(\mathscr{J},\mathscr{K})}\nu_{(\mathscr{J},\mathscr{K})}^{(h_{(\mathscr{J},\mathscr{K})})}}\, I\right]. \end{aligned} \tag{18}$$

Recalling to Lemma 1 and Assumption 2, we know that

$$\mathfrak{J}V(x(t), H(t), t) < x^T(t)\mathscr{P}_2 x(t) + \mathbf{Her}\left(x^T(t) P_{\mathscr{J}\mathscr{K}} W_{1i}^p \omega(t)\right), \tag{19}$$

where

$$\begin{aligned} \mathscr{P}_2 = \Bigg[&\mathbf{Her}\left(P_{\mathscr{J}\mathscr{K}} \overline{A}_{\mathscr{J}\mathscr{K}}^p\right) + \sum_{(\mathscr{J},\mathscr{L})\in r} r_{(\mathscr{J},\mathscr{K})(\mathscr{J},\mathscr{L})} P_{\mathscr{J}\mathscr{L}} \\ &+ \beta F_{\mathscr{J}}^{p\mathrm{T}} P_{\mathscr{J}\mathscr{K}} P_{\mathscr{J}\mathscr{K}} F_{\mathscr{J}}^p + \beta^{-1}\vartheta I\Bigg]. \end{aligned} \tag{20}$$

From $\mathfrak{J}V(x(t), H(t), t) < 0$, it follows that

$$\begin{bmatrix} x(t) \\ \omega(t) \end{bmatrix}^{\mathrm{T}} \begin{bmatrix} \psi & P_{\mathscr{J}\mathscr{K}} W_{1,\mathscr{J}}^p \\ * & 0 \end{bmatrix} \begin{bmatrix} x(t) \\ \omega(t) \end{bmatrix} < 0, \tag{21}$$

where

$$\begin{aligned} \psi = &\mathbf{Her}\left(P_{\mathscr{J}\mathscr{K}} \overline{A}_{\mathscr{J}\mathscr{K}}^p\right) + \sum_{(\mathscr{J},\mathscr{L})\in r} r_{(\mathscr{J},\mathscr{K})(\mathscr{J},\mathscr{L})} P_{\mathscr{J}\mathscr{L}} \\ &+ \beta F_{\mathscr{J}}^{p\mathrm{T}} P_{\mathscr{J}\mathscr{K}} P_{\mathscr{J}\mathscr{K}} F_{\mathscr{J}}^p + \beta^{-1}\vartheta I. \end{aligned} \tag{22}$$

Recalling to inequalities (11) and (18)–(21), we have the following inequality with positive constant $\omega > 0$:

$$\mathbf{E}\{\Im V(x(t),H(t),t)\} < \omega V(x(t),H(t),t) + \varphi\omega^T(t)\omega(t). \tag{23}$$

Then, we have the following relation by integrating both left and right sides of inequality (23) from 0 to t for $\forall t \in [\,0 \;\; T\,]$:

$$\begin{aligned}\mathbf{E}\{V(x(t),H(t),t)\} &- \mathbf{E}\{V(x(0),H(0))\} \\ &< \varphi\int_0^t \omega^T(\tau)\omega(\tau)\mathrm{d}\tau \\ &\quad + \omega\int_0^t \mathbf{E}\{V(x(t),H(t),\tau)\}\mathrm{d}\tau.\end{aligned} \tag{24}$$

Thus,

$$\mathbf{E}\{V(x(t),H(t),t)\} < \left(\mathscr{J}_1\overline{\lambda}_{P'_{\mathscr{J}\mathscr{K}}} + \varphi\varpi\right) + \omega\int_0^t \mathbf{E}\{V(x(t),H(t),\tau)\}\mathrm{d}\tau. \tag{25}$$

The above inequality can be rewritten as (26) by considering the Gronwall inequality:

$$\mathbf{E}\{V(x(t),H(t),t)\} < \left(\mathscr{J}_1\overline{\lambda}_{P'_{\mathscr{J}\mathscr{K}}} + \varphi\varpi\right)e^{\omega t} < \left(\mathscr{J}_1\overline{\lambda}_{P'_{\mathscr{J}\mathscr{K}}} + \varphi\varpi\right)e^{\omega T}. \tag{26}$$

From Rayleigh inequality, we know that $\mathbf{E}\{V(x(t),H(t),t)\} > \underline{\lambda}_{P_{\mathscr{J}\mathscr{K}}}\mathbf{E}\{x(t)^T R_{\mathscr{J}\mathscr{K}} x(t)\}$. Then, we have

$$\mathbf{E}\{x(t)^T R_{\mathscr{J}\mathscr{K}} x(t)\} < \frac{\left(\mathscr{J}_1\overline{\lambda}_{P'_{\mathscr{J}\mathscr{K}}} + \varphi\varpi\right)e^{\omega T}}{\underline{\lambda}_{P'_{\mathscr{J}\mathscr{K}}}}. \tag{27}$$

Thus, the $\mathbf{E}\{x(t)^T R_{\mathscr{J}\mathscr{K}} x(t)\} < \mathscr{J}_2$ for $\forall t \in [\,0 \;\; T\,]$ holds by inequality (12). This completes the proof.

In Theorem 1, we give some sufficient conditions to ensure the SFTB of the closed-loop PV-HMJSs (12). Then, the SFTB-H_∞ condition will be given in the following Theorem 2 on the basis of Theorem 1. □

Theorem 2. *Given four positive constants $\omega > 0$, $\mathscr{J}_1 > 0$, $T > 0$, and $\varpi > 0$ with $\int_0^t \omega^T(\tau)\omega(\tau)d\tau \le \varpi$, the SFTB-$H_\infty$ condition (10) of the closed-loop PV-HMJSs (8) will be satisfied within $(\mathscr{J}_1 \;\; \mathscr{J}_2 \;\; T \;\; R_{\mathscr{J}\mathscr{K}} \;\; \varpi)$ if there exist positive constants $0 < \mathscr{J}_1 < \mathscr{J}_1$, $\overline{\lambda}_{P'_{\mathscr{J}\mathscr{K}}} > 0$, $\underline{\lambda}_{P'_{\mathscr{J}\mathscr{K}}} > 0$, $\varphi > 0$, and $H(t)$-dependent positive-definite symmetric matrices $P_{\mathscr{J}\mathscr{K}}$ and $R_{\mathscr{J}\mathscr{K}}$, where $(\mathscr{I},\mathscr{K}) \in \mathscr{M}\times\mathscr{M}$, such that inequalities (12) and (28) hold:*

$$\begin{bmatrix} \varkappa & P_{\mathscr{J}\mathscr{K}}W^p_{1\mathscr{J}} + \overline{C}^{p\mathrm{T}}_{\mathscr{J}\mathscr{K}}W^p_{2\mathscr{J}} & F^{p\mathrm{T}}_{\mathscr{J}}P_{\mathscr{J}\mathscr{K}} & \Theta_{\mathscr{J}\mathscr{K}} \\ * & W^{p\mathrm{T}}_{2\mathscr{J}}W^p_{2\mathscr{J}} - \varphi I & 0 & 0 \\ * & * & -\beta^{-1}I & 0 \\ * & * & * & -\Psi_{\mathscr{J}\mathscr{K}} \end{bmatrix} < 0, \tag{28}$$

where $\varkappa = \Upsilon + e^{\omega T}\overline{C}^{pT}_{\mathscr{J}\mathscr{K}}\overline{C}^{p}_{\mathscr{J}\mathscr{K}}$.

Proof. The same SLKF is selected as in Theorem 1 and we introduce

$$\begin{aligned}\mathbf{E}\{\Im V(x(t),H(t),t)\} &- \omega V(x(t),H(t),t) \\ &< \varphi\omega^T(t)\omega(t) - e^{\omega t}\mathbf{E}\left\{y^T(t)y(t)\right\}.\end{aligned} \tag{29}$$

Inequality (28) guarantees that inequality (29) is established. Then, we use $e^{-\omega t}$ to multiply inequality (29) and integrate such inequality from 0 to T under zero initial condition, and it yields

$$e^{-\omega t}\mathbf{E}\{V(x(t),H(t),t)\} < \mathbf{E}\left\{\int_0^T \left(\varphi e^{-\omega\tau}\omega^T(\tau)\omega(\tau) - y^T(\tau)y(\tau)\right)\mathrm{d}\tau\right\}. \tag{30}$$

We can rewrite inequality (30) as the following inequality by considering $\mathbf{E}\{V(x(t),H(t),t)\} > 0$:

$$\begin{aligned}\mathbf{E}\left\{\int_0^T y^T((\tau)y(\tau))\mathrm{d}\tau\right\} &< \mathbf{E}\left\{\int_0^T \varphi e^{-\omega\tau}d^T(\tau)\mathrm{d}(\tau)\mathrm{d}\tau\right\} \\ &< \varphi\mathbf{E}\left\{\int_0^T \omega^T(\tau)\omega(\tau)\mathrm{d}\tau\right\}.\end{aligned} \tag{31}$$

Thus, we can obtain

$$\mathbf{E}\left\{\int_0^T y^T((\tau)y(\tau))\mathrm{d}\tau\right\} < \varphi\mathbf{E}\left\{\int_0^T \omega^T(\tau)\omega(\tau)\mathrm{d}\tau\right\}. \tag{32}$$

Recalling Definition 3, we can get the SFTB-H_∞ condition (10) of the closed-loop PV-HMJSs (8). This completes the proof.

Through the analysis of Theorem 2, we know that the state feedback controller gain matrix $K^{p(t)}_{h_2(t)}$ cannot be solved by Matlab LMI tools due to the nonlinear terms in inequality (28). In the following Theorem 3, some sufficient conditions will be given to obtain finite-time asynchronous controller gain $K^{p(t)}_{h_2(t)}$. □

Theorem 3. *Given four positive constants $\omega > 0$, $\mathscr{J}_1 > 0$, $T > 0$, and $\varpi > 0$ with $\int_0^t \omega^T(\tau)\omega(\tau)d\tau \le \varpi$, there exist a finite-time H_∞-gain asynchronous controller with h_2-dependent state feedback gain $K^p_{\mathscr{K}} = Z^p_{\mathscr{K}}S^{-1}_{\mathscr{K}}$ such that the SFTB-H_∞ condition (10) of the closed-loop PV-HMJSs (12) will be satisfied within $(\mathscr{J}_1 \;\; \mathscr{J}_2 \;\; T \;\; R_{\mathscr{J}\mathscr{K}} \;\; \varpi)$ if there exist positive scalars $0 < \mathscr{J}_1 < \mathscr{J}_2$, $\underline{\lambda}_1 > 0$, $\varphi > 0$, $\beta > 0$, $\mu_{\mathscr{J}} > 0$, $\varphi > 0$, $H(t)$-dependent positive-definite symmetric matrices $X_{\mathscr{J}\mathscr{K}}$, $R_{\mathscr{J}\mathscr{K}}$, where $\mathscr{I} \in \mathscr{M}$, $\mathscr{K} \in \mathscr{M}$, h_2-dependent positive-definite symmetric matrix $S_{\mathscr{K}}$, and h_2-dependent matrix $Z^p_{\mathscr{K}}$, such that*

$$\mathscr{L}^p_{1\mathscr{J}\mathscr{K}} + \mathscr{B}_{1\mathscr{J}\mathscr{K}} < 0, \tag{33}$$

$$\underline{\lambda}_1 R^{-1}_{\mathscr{J}\mathscr{K}} < X_{\mathscr{J}\mathscr{K}} < R^{-1}_{\mathscr{J}\mathscr{K}}, \tag{34}$$

$$\begin{bmatrix} \varphi\varpi - \dfrac{\mathscr{J}_2 e^{-\omega T}}{\overline{\lambda}_1} & \sqrt{\mathscr{J}_1} \\ \sqrt{\mathscr{J}_1} & -\underline{\lambda}_1 \end{bmatrix} < 0, \tag{35}$$

where

$$\mathscr{L}_{1\mathcal{J}\mathcal{K}}^{p}=\mathbf{Her}\left(\begin{bmatrix} A_{\mathcal{J}}^{p}L_{\mathcal{J}}S_{\mathcal{K}}+B_{\mathcal{J}}^{p}Z_{\mathcal{K}}^{p} \\ 0 \\ 0 \\ \left(C_{\mathcal{J}}^{p}L_{\mathcal{J}}S_{\mathcal{K}}+D_{\mathcal{J}}^{p}Z_{\mathcal{K}}^{p}\right)^{T} \\ e^{\omega T}\left(C_{\mathcal{J}}^{p}L_{\mathcal{J}}S_{\mathcal{K}}+D_{\mathcal{J}}^{p}Z_{\mathcal{K}}^{p}\right)^{T} \\ 0 \end{bmatrix}\begin{bmatrix} \mu_{\mathcal{J}}I \\ 0 \\ 0 \\ 0 \\ 0 \\ 0 \end{bmatrix}^{T}\right),$$

$$\mathscr{B}_{1\mathcal{J}\mathcal{K}}=\begin{bmatrix} \mathscr{B}'_{1\mathcal{J}\mathcal{K}} & \mathscr{B}'_{2\mathcal{J}\mathcal{K}} \\ * & \mathscr{R}'_{3\mathcal{J}\mathcal{K}} \end{bmatrix},$$

$$\mathscr{B}'_{1\mathcal{J}\mathcal{K}}=\begin{bmatrix} \mathscr{O}_{1\mathcal{J}\mathcal{K}} & W_{1\mathcal{J}}^{p}X_{\mathcal{J}\mathcal{K}} & X_{\mathcal{J}\mathcal{K}}F_{\mathcal{J}}^{p\mathrm{T}} \\ * & \Xi_{5\mathcal{J}} & 0 \\ * & * & -\beta^{-1}I \end{bmatrix},$$

$$\mathscr{B}'_{2\mathcal{J}\mathcal{K}}=\begin{bmatrix} 0 & 0 & X_{\mathcal{J}\mathcal{K}}\Theta_{\mathcal{J}\mathcal{K}} \\ 0 & X_{\mathcal{J}\mathcal{K}}W_{2\mathcal{J}}^{p\mathrm{T}} & 0 \\ 0 & 0 & 0 \end{bmatrix},$$

$$\mathscr{R}'_{3\mathcal{J}\mathcal{K}}=\mathrm{diag}\left\{-\xi^{-1}I,-\xi I,-\Psi'_{\mathcal{J}\mathcal{K}}\right\},$$

$$\mathscr{O}_{1\mathcal{J}\mathcal{K}}=\left(\mathscr{R}_{(i,k)(\mathcal{J},\mathcal{K})}-\omega\right)X_{\mathcal{J}\mathcal{K}}+\beta^{-1}\vartheta Q_{\mathcal{J}\mathcal{K}},$$

$$\Xi_{5\mathcal{J}}=W_{2\mathcal{J}}^{p\mathrm{T}}W_{2\mathcal{J}}^{p}-\varphi I,$$

$$\Theta_{\mathcal{J}\mathcal{K}}=\left[\sqrt{r_{(\mathcal{J},\mathcal{K})}\nu_{(\mathcal{J},\mathcal{K})}^{(1)}}\,I,\ldots,\sqrt{r_{(\mathcal{J},\mathcal{K})}\nu_{(\mathcal{J},\mathcal{K})}^{\left(h_{(\mathcal{J},\mathcal{K})}\right)}}\,I\right],$$

$$\Psi'_{\mathcal{J}\mathcal{K}}=\mathrm{diag}\left\{X^{-1}_{\mathscr{R}^{(1)}_{(\mathcal{J},\mathcal{K})}},X^{-1}_{\mathscr{R}^{(2)}_{(\mathcal{J},\mathcal{K})}},\ldots,X^{-1}_{\mathscr{R}^{\left(h_{(\mathcal{J},\mathcal{K})}\right)}_{(\mathcal{J},\mathcal{K})}}\right\}. \tag{36}$$

Proof. We substitute $\overline{A}_{\mathcal{J}\mathcal{K}}^{p}$ and $\overline{C}_{\mathcal{J}\mathcal{K}}^{p}$ into inequality (34) and yields

$$\begin{bmatrix} \Xi'_{1\mathcal{J}\mathcal{K}} & \Xi_{4\mathcal{J}\mathcal{K}} & F_{\mathcal{J}}^{p\mathrm{T}}P_{\mathcal{J}\mathcal{K}} & \Theta_{\mathcal{J}\mathcal{K}} \\ * & \Xi_{5\mathcal{J}} & 0 & 0 \\ * & * & -\beta^{-1}I & 0 \\ * & * & * & -\Psi_{\mathcal{J}\mathcal{K}} \end{bmatrix}<0, \tag{37}$$

where

$$\begin{aligned} \Xi'_{1\mathcal{J}\mathcal{K}}&=\Xi_{1\mathcal{J}\mathcal{K}}+\Xi_{2\mathcal{J}\mathcal{K}}+\Xi_{3\mathcal{J}\mathcal{K}},\\ \Xi_{1\mathcal{J}\mathcal{K}}&=\mathbf{Her}\left(P_{\mathcal{J}\mathcal{K}}\left(A_{\mathcal{J}}^{p}+B_{\mathcal{J}}^{p}K_{\mathcal{K}}^{p}\right)\right),\\ \Xi_{2\mathcal{J}\mathcal{K}}&=e^{\omega T}\left(C_{\mathcal{J}}^{p}+D_{\mathcal{J}}^{p}K_{\mathcal{K}}^{p}\right)^{T}\left(C_{\mathcal{J}}^{p}+D_{\mathcal{J}}^{p}K_{\mathcal{K}}^{p}\right),\\ \Xi_{3\mathcal{J}\mathcal{K}}&=\left(\mathscr{R}_{(\mathcal{J},\mathcal{K})(\mathcal{J},\mathcal{K})}-\omega\right)P_{\mathcal{J}\mathcal{K}}+\beta^{-1}\vartheta I,\\ \Xi_{4\mathcal{J}\mathcal{K}}&=P_{\mathcal{J}\mathcal{K}}W_{1\mathcal{J}}^{p}+\left(C_{\mathcal{J}}^{p}+D_{\mathcal{J}}^{p}K_{\mathcal{K}}^{p}\right)^{\mathrm{T}}W_{2\mathcal{J}}^{p},\\ \Xi_{5\mathcal{J}}&=W_{2\mathcal{J}}^{p\mathrm{T}}W_{2\mathcal{J}}^{p}-\varphi I. \end{aligned} \tag{38}$$

We use $\mathrm{diag}\left\{P_{\mathcal{J}\mathcal{K}}^{-1},\ I,\ I\ I\right\}$ to pre- and postmultiply inequality (37), and let $X_{\mathcal{J}\mathcal{K}}=P_{\mathcal{J}\mathcal{K}}^{-1}$, $Y_{\mathcal{J}\mathcal{K}}^{p}=K_{\mathcal{K}}^{p}X_{\mathcal{J}\mathcal{K}}$, and $Q_{\mathcal{J}\mathcal{K}}=X_{\mathcal{J}\mathcal{K}}X_{\mathcal{J}\mathcal{K}}$, and we use the Schur complement lemma. It can be seen that the following inequality satisfies with positive scalar $\xi>0$:

$$\begin{bmatrix} \mathscr{R}'_{1\mathcal{J}\mathcal{K}} & \mathscr{R}'_{2\mathcal{J}\mathcal{K}} \\ * & \mathscr{R}'_{3\mathcal{J}\mathcal{K}} \end{bmatrix}<0, \tag{39}$$

where

$$\mathscr{R}'_{1\mathcal{J}\mathcal{K}}=\begin{bmatrix} \Xi'_{1\mathcal{J}\mathcal{K}} & W_{1\mathcal{J}}^{p}X_{\mathcal{J}\mathcal{K}} & X_{\mathcal{J}\mathcal{K}}F_{\mathcal{J}}^{pT} \\ * & \Xi_{5i} & 0 \\ * & * & -\beta^{-1}I \end{bmatrix},$$

$$\mathscr{R}'_{2\mathcal{J}\mathcal{K}}=\begin{bmatrix} \Xi'_{2\mathcal{J}\mathcal{K}} & \Xi'_{3\mathcal{J}\mathcal{K}} & X_{\mathcal{J}\mathcal{K}}\Theta_{\mathcal{J}\mathcal{K}} \\ 0 & X_{\mathcal{J}\mathcal{K}}W_{2\mathcal{J}}^{p\mathrm{T}} & 0 \\ 0 & 0 & 0 \end{bmatrix},$$

$$\begin{aligned} \mathscr{R}'_{3\mathcal{J}\mathcal{K}}&=\mathrm{diag}\left\{-\xi^{-1},-\xi,-\Psi_{\mathcal{J}\mathcal{K}}\right\},\\ \Psi'_{\mathcal{J}\mathcal{K}}&=\mathrm{diag}\left\{X^{-1}_{\mathscr{R}^{(1)}_{(\mathcal{J},\mathcal{K})}},X^{-1}_{\mathscr{R}^{(2)}_{(\mathcal{J},\mathcal{K})}},\ldots,X^{-1}_{\mathscr{R}^{\left(h_{(\mathcal{J},\mathcal{K})}\right)}_{(\mathcal{J},\mathcal{K})}}\right\},\\ \Xi'_{1\mathcal{J}\mathcal{K}}&=\mathbf{Her}\left(A_{\mathcal{J}}^{p}X_{\mathcal{J}\mathcal{K}}+B_{\mathcal{J}}^{p}Y_{\mathcal{J}\mathcal{K}}^{p}\right)+\left(r_{(\mathcal{J},\mathcal{K})(\mathcal{J},\mathcal{K})}-\omega\right)X_{\mathcal{J}\mathcal{K}}\\ &\quad+\beta^{-1}\vartheta Q_{\mathcal{J}\mathcal{K}},\\ \Xi'_{2\mathcal{J}\mathcal{K}}&=\left(C_{\mathcal{J}}^{p}X_{\mathcal{J}\mathcal{K}}+D_{\mathcal{J}}^{p}Y_{\mathcal{J}\mathcal{K}}^{p}\right)^{\mathrm{T}},\\ \Xi'_{3\mathcal{J}\mathcal{K}}&=e^{\omega T}\left(C_{\mathcal{J}}^{p}X_{\mathcal{J}\mathcal{K}}+D_{\mathcal{J}}^{p}Y_{\mathcal{J}\mathcal{K}}^{p}\right)^{\mathrm{T}}. \end{aligned} \tag{40}$$

Considering the asynchronous of (39), we rewrite inequality (39) as follows:

$$\mathscr{B}_{1,\mathcal{J}\mathcal{K}} + \mathscr{B}_{2,\mathcal{J}\mathcal{K}} < 0, \tag{41}$$

where

$$\mathscr{B}_{1,\mathcal{J}\mathcal{K}} = \begin{bmatrix} \mathscr{B}_{1,\mathcal{J}\mathcal{K}}' & \mathscr{B}_{2,\mathcal{J}\mathcal{K}}' \\ * & \mathscr{R}_{3,\mathcal{J}\mathcal{K}}' \end{bmatrix},$$

$$\mathscr{B}_{1ik}' = \begin{bmatrix} \mathscr{O}_{1,\mathcal{J}\mathcal{K}} & W_{1,\mathcal{J}}^{p} X_{\mathcal{J}\mathcal{K}} & X_{\mathcal{J}\mathcal{K}} F_{\mathcal{J}}^{p\mathrm{T}} \\ * & \Xi_{5,\mathcal{J}} & 0 \\ * & * & -\beta^{-1} I \end{bmatrix},$$

$$\mathscr{B}_{2,\mathcal{J}\mathcal{K}}' = \begin{bmatrix} 0 & 0 & X_{\mathcal{J}\mathcal{K}} \Theta_{\mathcal{J}\mathcal{K}} \\ 0 & X_{\mathcal{J}\mathcal{K}} W_{2,\mathcal{J}}^{p\mathrm{T}} & 0 \\ 0 & 0 & 0 \end{bmatrix},$$

$$\mathscr{B}_{2,\mathcal{J}\mathcal{K}} = \mathbf{Her}\left(\begin{bmatrix} A_{\mathcal{J}}^{p} X_{\mathcal{J}\mathcal{K}} + B_{\mathcal{J}}^{p} Y_{\mathcal{J}\mathcal{K}}^{p} \\ 0 \\ 0 \\ \left(C_{\mathcal{J}}^{p} X_{\mathcal{J}\mathcal{K}} + D_{\mathcal{J}}^{p} Y_{\mathcal{J}\mathcal{K}}^{p}\right)^{T} \\ e^{\omega T}\left(C_{\mathcal{J}}^{p} X_{\mathcal{J}\mathcal{K}} + D_{\mathcal{J}}^{p} Y_{\mathcal{J}\mathcal{K}}^{p}\right)^{T} \\ 0 \end{bmatrix} \begin{bmatrix} I \\ 0 \\ 0 \\ 0 \\ 0 \\ 0 \end{bmatrix}^{T} \right),$$

$$\mathscr{O}_{1,\mathcal{J}\mathcal{K}} = \left(r_{(\mathcal{J},\mathcal{K})(\mathcal{J},\mathcal{K})} - \omega\right) X_{\mathcal{J}\mathcal{K}} + \beta^{-1} \vartheta Q_{\mathcal{J}\mathcal{K}}. \tag{42}$$

For $\mathscr{B}_{2,\mathcal{J}\mathcal{K}}$, we define $X_{\mathcal{J}\mathcal{K}} = \mu_{\mathcal{J}} L_{\mathcal{J}} S_{\mathcal{K}}$, where $L_{\mathcal{J}}$ is a nonsingular unit matrix for $\forall i \in \mathscr{M}$. We can obtain

$$\begin{cases} A_{\mathcal{J}}^{p} X_{\mathcal{J}\mathcal{K}} + B_{\mathcal{J}}^{p} Y_{\mathcal{J}\mathcal{K}}^{p} = \mu_{\mathcal{J}}\left(A_{\mathcal{J}}^{p} + B_{\mathcal{J}}^{p} K_{\mathcal{K}}^{p}\right) L_{\mathcal{J}} S_{\mathcal{K}}, \\ C_{\mathcal{J}}^{p} X_{\mathcal{J}\mathcal{K}} + D_{\mathcal{J}}^{p} Y_{\mathcal{J}\mathcal{K}}^{p} = \mu_{\mathcal{J}}\left(C_{\mathcal{J}}^{p} + D_{\mathcal{J}}^{p} K_{\mathcal{K}}^{p}\right) L_{\mathcal{J}} S_{\mathcal{K}}. \end{cases} \tag{43}$$

Since $L_{\mathcal{J}}$ is a nonsingular unit matrix, we can get inequality (41) by inequality (33) with $Z_{\mathcal{J}\mathcal{K}}^{p} = K_{\mathcal{K}}^{p} L_{\mathcal{J}} S_{\mathcal{K}}$. Moreover, we know that $\mathbf{Her}(L_{\mathcal{J}} S_{\mathcal{K}}) > 0$, i.e., $\mathbf{Her}(S_{\mathcal{K}}) > 0$ from inequality (33). Thus, $Z_{\mathcal{K}}^{p}$ is also a nonsingular matrix, which means that $K_{\mathcal{K}}^{p} = Z_{\mathcal{K}}^{p} S_{\mathcal{K}}^{-1}$ can be defined and solved.

Defining $\overline{X}_{\mathcal{J}\mathcal{K}} = R_{\mathcal{J}\mathcal{K}}^{-(1/2)} X_{\mathcal{J}\mathcal{K}} R_{\mathcal{J}\mathcal{K}}^{-(1/2)}$, $\overline{\lambda}_{\overline{X}_{\mathcal{J}\mathcal{K}}} = \max_{(\mathcal{J},\mathcal{K})\in r} \lambda_{\max}(\overline{X}_{\mathcal{J}\mathcal{K}})$, and $\underline{\lambda}_{\overline{X}_{\mathcal{J}\mathcal{K}}} = \min_{(\mathcal{J},\mathcal{K})\in r} \lambda_{\min}(\overline{X}_{\mathcal{J}\mathcal{K}})$, letting $\underline{\lambda}_1 \le \underline{\lambda}_{\overline{X}_{\mathcal{J}\mathcal{K}}}$ and $\overline{\lambda}_1 \ge \overline{\lambda}_{\overline{X}_{\mathcal{J}\mathcal{K}}}$, and considering $\overline{\lambda}_{\overline{X}_{\mathcal{J}\mathcal{K}}} = 1/\underline{\lambda}_{P_{\mathcal{J}\mathcal{K}}'}$ and $\underline{\lambda}_{\overline{X}_{\mathcal{J}\mathcal{K}}} = 1/\overline{\lambda}_{P_{\mathcal{J}\mathcal{K}}'}$, inequality (12) can be rewritten as

$$\frac{\mathscr{J}_1}{\underline{\lambda}_1} + \varphi\varpi < \frac{\mathscr{J}_2 e^{-\omega T}}{\overline{\lambda}_1}. \tag{44}$$

By considering the eigenvalue conversion method and using the Schur complement lemma, inequalities (34) and (35) can be obtained. This completes the proof.

However, we also cannot get the state feedback controller gain matrix $K_{h_2(t)}^{p(t)}$ by Matlab LMI tools in Theorem 3 due to the dependence of the parameters. Next, the methods of approximate basis function and gridding technique will be used to deparameterize the parameter-dependent matrices in Theorem 3. The specific deparameterization process is as follows:

$$\mathscr{A}^{p} = \mathscr{A}_0^{p} + \sum_{\mathcal{J}=1}^{m} \mathscr{A}_{\mathcal{J}} p_{\mathcal{J}} < 0, \quad \forall p \in \mathfrak{Z}, \tag{45}$$

$$\mathfrak{Z} = \left\{ p(t) \in \mathbb{R}^{p} : \underline{p}_{1,\mathcal{J}} \leqslant p_{\mathcal{J}}(t) \leqslant \overline{p}_{1,\mathcal{J}}, \quad \forall \mathcal{J} \in 1, 2, \ldots, m] \right\}, \tag{46}$$

where $p(t)$ is the time-varying parameter. From inequalities (45) and (46), we know that $\mathfrak{Z}$ denotes an LMI and $\mathscr{A}^{p}$ has infinite number of LMIs. Then, we select the following basis function $\left\{F_{\mathcal{J}}^{(p(t))}\right\}_{\mathcal{J}=1}^{n_f}$ to solve inequality (45):

$$\mathscr{A}_{\mathcal{J}}^{p(t)} = \sum_{\mathcal{J}=1}^{n_f} F_{\mathcal{J}}^{(p(t))} \mathscr{A}_{\mathcal{J}\mathcal{J}}. \tag{47}$$

Furthermore, the infinite LMIs of the $\mathscr{A}^{p}$ can be transformed into the finite ones if we divide the space of parameter changes into finite-dimensional grids, which means the following relation satisfied for each set of parameters on the grid for $\forall p(t) \in \mathfrak{Z}$:

$$\mathscr{A}^{p} = \sum_{\mathcal{J}=1}^{n_f} F_{\mathcal{J}}^{(p(t))} \mathscr{A}_0 + \sum_{\mathcal{J}=1}^{n_f} \sum_{i=1}^{m} F_{\mathcal{J}}^{(p(t))} \mathscr{A}_{\mathcal{J}\mathcal{J}} < 0. \tag{48}$$

□

Remark 3. In Theorem 3, the difficulty of calculation will be increased because of the asynchronous characteristic between the controller modes and the system modes. In order to solve such difficulty, the controller modes $h_2(t)$ is converted $h_1(t)$. Moreover, some sufficient conditions are obtained to make the closed-loop HMJSs with linear parameter varying be SFTB-H_∞ by introduced auxiliary variables.

Remark 4. In addition, we have introduced the stochastic Lyapunov–Krasovskii functional methods in Theorem 3, which will induce somewhat conservatism of the main results. In future work, we can reduce the impact of conservativeness through replacing the quasi-one-sided Lipschitz condition or one-sided Lipschitz condition with local Lipschitz condition in Assumption 2.

4. Numerical Example

In this section, we consider a class of PV-HMJSs with two subsystems.

Subsystem 1:

$$
\begin{aligned}
A_1^{p(t)} &= \begin{bmatrix} -16.5 & 6 \\ 7 & -12.1 \end{bmatrix} + \begin{bmatrix} 0.05 & 0 \\ 0 & 0.05 \end{bmatrix} \sin(t) \\
&\quad + \begin{bmatrix} 0.02 & 0 \\ 0 & 0.02 \end{bmatrix} \cos(t), \\
B_1^{p(t)} &= \begin{bmatrix} 1 \\ 1 \end{bmatrix} + \begin{bmatrix} 0.2\sin(t) \\ 0.1\cos(t) \end{bmatrix}, \\
W_{11}^{p(t)} &= \begin{bmatrix} 0.5\sin(t) + 0.2\cos(t) \end{bmatrix}, \\
F_1^{p(t)} &= \begin{bmatrix} 0.4\sin(t) + 0.1\cos(t) \end{bmatrix}, \\
W_{21}^{p(t)} &= \begin{bmatrix} 0.3 & 0.1 \\ 0.2 & 0.2 \end{bmatrix} + \begin{bmatrix} 0.01 & 0 \\ 0 & 0.01 \end{bmatrix} \sin(t) \\
&\quad + \begin{bmatrix} 0.02 & 0 \\ 0 & 0.02 \end{bmatrix} \cos(t), \\
C_1^{p(t)} &= \begin{bmatrix} -3.3 & -0.2 \\ 0.1 & -2.8 \end{bmatrix} + \begin{bmatrix} -0.1 & 0 \\ 0 & -0.2 \end{bmatrix} \sin(t) \\
&\quad + \begin{bmatrix} -0.3 & 0 \\ 0 & -0.2 \end{bmatrix} \cos(t), \\
D_1^{p(t)} &= \begin{bmatrix} 0.3 \\ 0.2 \end{bmatrix} + \begin{bmatrix} 0.1\sin(t) \\ 0.02\cos(t) \end{bmatrix}.
\end{aligned} \tag{49}
$$

Subsystem 2:

$$
\begin{aligned}
A_2^{p(t)} &= \begin{bmatrix} -12.3 & 8 \\ 4 & -11.2 \end{bmatrix} + \begin{bmatrix} 0.02 & 0 \\ 0 & 0.01 \end{bmatrix} \sin(t) \\
&\quad + \begin{bmatrix} 0.01 & 0 \\ 0 & 0.01 \end{bmatrix} \cos(t), \\
B_2^{p(t)} &= \begin{bmatrix} 2 \\ 2 \end{bmatrix} + \begin{bmatrix} 0.4\sin(t) \\ 0.3\cos(t) \end{bmatrix}, \\
W_{12}^{p(t)} &= \begin{bmatrix} 0.4\sin(t) + 0.2\cos(t) \end{bmatrix}, \\
F_2^{p(t)} &= \begin{bmatrix} 0.3\sin(t) + 0.1\cos(t) \end{bmatrix}, \\
W_{22}^{p(t)} &= \begin{bmatrix} 0.1 & 0.2 \\ 0.2 & 0.1 \end{bmatrix} + \begin{bmatrix} 0.01 & 0 \\ 0 & 0.01 \end{bmatrix} \sin(t) \\
&\quad + \begin{bmatrix} 0.02 & 0 \\ 0 & 0.02 \end{bmatrix} \cos(t), \\
C_2^{p(t)} &= \begin{bmatrix} -2.8 & -0.1 \\ 0.2 & -3.1 \end{bmatrix} + \begin{bmatrix} -0.2 & 0 \\ 0 & -0.2 \end{bmatrix} \sin(t) \\
&\quad + \begin{bmatrix} -0.3 & 0 \\ 0 & -0.1 \end{bmatrix} \cos(t), \\
D_2^{p(t)} &= \begin{bmatrix} 0.3 \\ 0.2 \end{bmatrix} + \begin{bmatrix} 0.2\sin(t) \\ 0.01\cos(t) \end{bmatrix},
\end{aligned} \tag{50}
$$

where $\sin(t)$ and $\cos(t)$ are time-varying parameters and bounded with $[-1 \ 1]$. We assume the weighted matrix $R = I$, the initial consideration $\mathcal{J}_1 = 0.8$, the external disturbance $\omega(t) = \begin{bmatrix} 0.1\sin^2(2t) \\ 0.2\sin^2(t) \end{bmatrix}$, and the unknown state-dependent nonlinear function $f(x(t), t) = \begin{bmatrix} 0.3x_1(t) \\ 0.1x_2(t) \end{bmatrix}$ in finite-time interval $T = 5$. The other values of the constants are given as $\varpi = 0.3$, $\overline{\lambda}_1 = 5.089$, $\underline{\lambda}_1 = 0.5$, $\mu_1 = 1.2$, $\mu_2 = 1.5$, $\omega = 0.3$, $\beta = 0.3$, $\vartheta = 1$, and $\xi = 0.2$.

We assume the $h_2(t)$-dependent controller gain $K_{\mathscr{K}}^p$ with two control schemes for two different jump modes, i.e., $\mathscr{M} \in \{1, 2\}$ and $\mathscr{M} \in \{1, 2\}$. The Π-dependent conditional probability matrices are $\aleph^1 = \begin{bmatrix} -0.6 & 0.6 \\ 0.4 & -0.4 \end{bmatrix}$ and $\aleph^2 = \begin{bmatrix} 0.3 & -0.3 \\ -0.1 & 0.1 \end{bmatrix}$. The parameters of α_{jl}^k are $\alpha_1 = \alpha_{jl}^1 = \begin{bmatrix} 0.3 & 0.7 \\ 0.4 & 0.6 \end{bmatrix}$ and $\alpha_2 = \alpha_{jl}^2 = \begin{bmatrix} 0.2 & 0.8 \\ 0.5 & 0.5 \end{bmatrix}$.

Solving LMIs (33)–(35), we can get the following finite-time state feedback gain matrices:

$$
\begin{aligned}
K_1^p &= \begin{bmatrix} 2.9251 & -1.1431 \end{bmatrix} + \begin{bmatrix} -1.1633\sin(t) & 0.3333\cos(t) \end{bmatrix}, \\
K_2^p &= \begin{bmatrix} 3.0817 & -0.7694 \end{bmatrix} + \begin{bmatrix} -0.5792\sin(t) & -0.171\cos(t) \end{bmatrix}.
\end{aligned} \tag{51}
$$

Meanwhile, the other relevant solutions are given as $\mathcal{J}_2 = 5.0894$ and $\varphi = 9.8$. Then, the simulation results are shown in Figures 1–3.

The jump modes of $h_1(t)$ and $h_2(t)$ are shown in Figure 1. The state trajectory $x(t)$ and $y(t)$ of the closed-loop PV-HMJSs (8) are shown in Figures 2 and 3. From Figures 2 and 3, we can seen the SFTB-H_∞ condition is satisfied with $\mathbf{E}\{x(t)^T R_{\mathcal{J}\mathscr{K}} x(t)\} < \mathcal{J}_2$ in which $\mathcal{J}_2 = 5.0894$ and $\varphi = 9.8$.

Remark 5. Similar to some results of reinforcement learning methods [41–44], this paper also considered the problem of stabilization of stochastic Markov jump systems. Moreover, we also use the hidden Markov model to denote the asynchronous characteristic between system modes and controller modes. Different from some existing results on the finite-time control problem [35, 36], the problem of SFTB-H_∞ asynchronous control is studied for continuous-time HMJSs via parameter varying in this paper. Compared with the existing results of asynchronous control for discrete-time HMJSs [37–40], this paper firstly considers the asynchronous stabilization problem for the continuous-time HMJSs with parameter varying models.

For the future work, we can learn from the reinforcement learning methods to study the problem of finite-time asynchronous online control for the continuous-time PV-HMJSs.

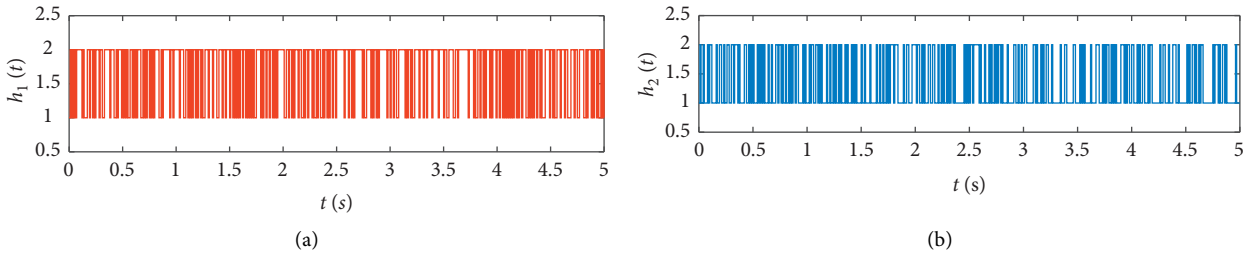

FIGURE 1: The jump mode $H(t)$ of the PV-HMJSs. (a) The jump mode of the hidden state $h_1(t)$. (b) The jump mode of the observation state $h_2(t)$.

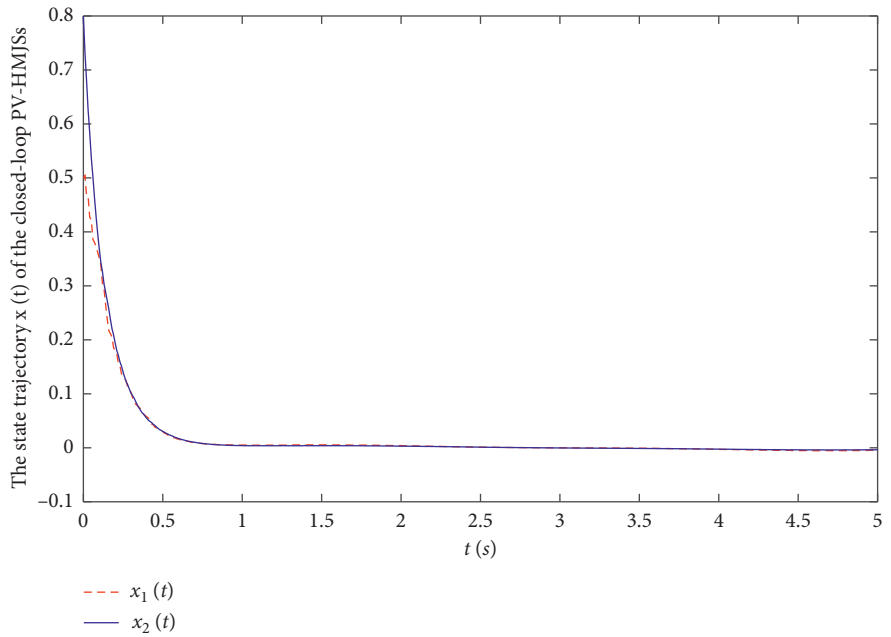

FIGURE 2: The $x(t)$ of the closed-loop PV-HMJSs.

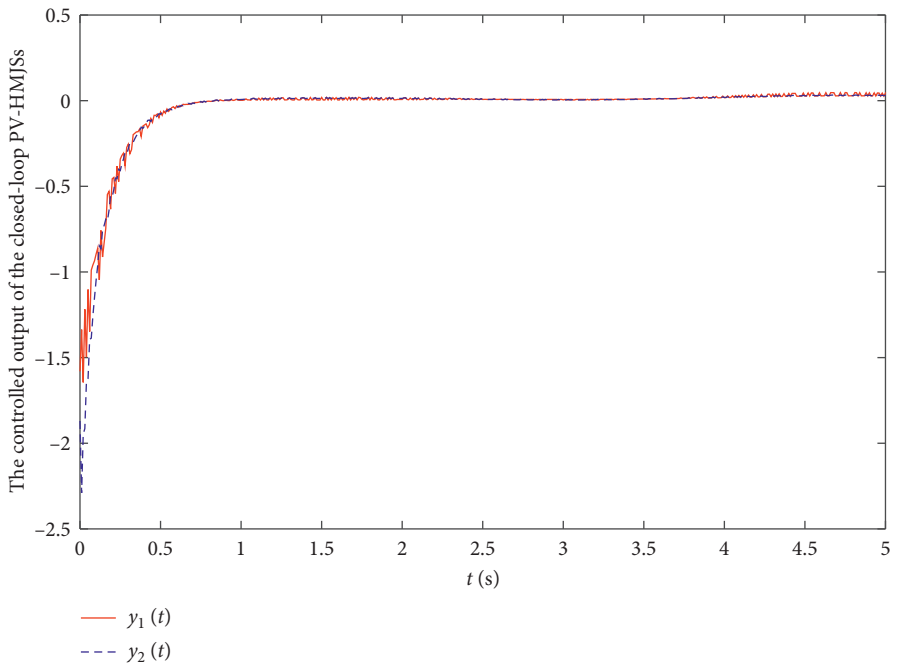

FIGURE 3: The $y(t)$ of the closed-loop PV-HMJSs.

5. Conclusion

This paper studied the SFTB-H_∞ asynchronous control problem for continuous-time PV-HMJSs. Some sufficient conditions are given to solve the SFTB-H_∞ asynchronous control gain by considering the methods of SLKF and LMIs. The designed SFTB-H_∞ asynchronous controller makes the closed-loop PV-HMJSs satisfy the SFTB-H_∞ condition. Finally, we use a numerical example to show the validity of the main results of this paper. For the future research work, the asynchronous control problem for fuzzy PV-HMJSs apply approximation method will be considered.

Data Availability

The data findings of this study are available from the corresponding author upon request.

Conflicts of Interest

The authors declare that they have no conflicts of interest.

References

[1] Y. A. Zabala and O. L. V. Costa, "Static output constrained control for discrete-time hidden Markov jump linear systems," *IEEE Access*, vol. 8, pp. 62969–62979, 2020.

[2] A. M. de Oliveira, O. L. V. Costa, and J. Daafouz, "Design of stabilizing dynamic output feedback controllers for hidden Markov jump linear systems," *IEEE Control Systems Letters*, vol. 2, no. 2, pp. 278–283, 2018.

[3] P. Cheng, J. Wang, S. He, X. Luan, and F. Liu, "Observer-based asynchronous fault detection for conic-type nonlinear jumping systems and its application to separately excited DC motor," *IEEE Transactions on Circuits and Systems I: Regular Papers*, vol. 67, no. 3, pp. 951–962, 2020.

[4] F. Li, S. Xu, and B. Zhang, "Resilient asynchronous H_∞ control for discrete-time Markov jump singularly perturbed systems based on hidden Markov model," *IEEE Transactions on Systems, Man, and Cybernetics: Systems*, vol. 50, no. 8, pp. 2420–2430, 2019.

[5] S. Dong, Z.-G. Wu, P. Shi, H. Su, and T. Huang, "Quantized control of Markov jump nonlinear systems based on fuzzy hidden Markov model," *IEEE Transactions on Cybernetics*, vol. 49, no. 7, pp. 2420–2430, 2019.

[6] C. Ren, S. He, X. Luan, F. Liu, and H. R. Karimi, "Finite-time L_2-gain asynchronous control for continuous-time positive hidden Markov jump systems via T-S fuzzy model approach," *IEEE Transactions on Cybernetics*, pp. 9–1, 2020.

[7] F. Stadtmann and O. L. V. Costa, "H_2-control of continuous-time hidden Markov jump linear systems," *IEEE Transactions on Automatic Control*, vol. 62, no. 8, pp. 4031–4037, 2017.

[8] S. Dong, Z.-G. Wu, Y.-J. Pan, H. Su, and Y. Liu, "Hidden-Markov-model-based asynchronous filter design of nonlinear Markov jump systems in continuous-time domain," *IEEE Transactions on Cybernetics*, vol. 49, no. 6, pp. 2294–2304, 2019.

[9] F. Stadtmann and O. L. V. Costa, "Exponential hidden Markov models for H_∞ control of jumping systems," *IEEE Control Systems Letters*, vol. 2, no. 4, pp. 845–850, 2018.

[10] J. Cheng, C. K. Ahn, H. R. Karimi, J. Cao, and W. Qi, "An event-based asynchronous approach to Markov jump systems with hidden mode detections and missing measurements," *IEEE Transactions on Systems, Man, and Cybernetics: Systems*, vol. 49, no. 9, pp. 1749–1758, 2019.

[11] H. Zheng, D. Yang, X. Xie, and Z. Zhang, "An adaptive algorithm for active vibration control of parameter-varying systems with a new online secondary path estimation method," *IEEE Signal Processing Letters*, vol. 27, pp. 705–709, 2020.

[12] M. S. de Oliveira and R. L. Pereira, "LMI-based filter design conditions for discrete-time LPV systems with bounded parameter variation," *IEEE Transactions on Automatic Control*, 2019.

[13] M. M. Seron and J. A. De Doná, "Robust fault estimation and compensation for LPV systems under actuator and sensor faults," *Automatica*, vol. 52, pp. 294–301, 2015.

[14] D. Rotondo, F. Nejjari, V. Puig, and J. Blesa, "Model reference FTC for LPV systems using virtual actuators and set-membership fault estimation," *International Journal of Robust and Nonlinear Control*, vol. 25, no. 5, pp. 735–760, 2015.

[15] W. M. H. Heemels, J. Daafouz, and G. Millerioux, "Observer-based control of discrete-time LPV systems with uncertain parameters," *IEEE Transactions on Automatic Control*, vol. 55, no. 9, pp. 2130–2135, 2010.

[16] M. Fleps-Dezasse, F. Svaricek, and J. Brembeck, "Design and experimental assessment of an active fault-tolerant LPV vertical dynamics controller," *IEEE Transactions on Control Systems Technology*, vol. 27, no. 3, pp. 1267–1274, 2019.

[17] J. Theis, P. Seiler, and H. Werner, "LPV model order reduction by parameter-varying oblique projection," *IEEE Transactions on Control Systems Technology*, vol. 26, no. 3, pp. 773–784, 2018.

[18] P. B. Cox, S. Weiland, and R. Tóth, "Affine parameter-dependent Lyapunov functions for LPV systems with affine dependence," *IEEE Transactions on Automatic Control*, vol. 63, no. 11, pp. 3865–3872, 2018.

[19] W. Qi, G. Zong, and H. R. Karimi, "H_∞control for positive delay systems with semi-Markov process and application to a communication network model," *IEEE Transactions on Industrial Electronics*, vol. 66, no. 3, pp. 2081–2091, 2019.

[20] J. Zhao, F. Gao, L. Kuang, Q. Wu, and W. Jia, "Channel tracking with flight control system for UAV mmWave MIMO communications," *IEEE Communications Letters*, vol. 22, no. 6, pp. 1224–1227, 2018.

[21] B. Chen, Y. Yang, B. Lee, and T. Leer, "Fuzzy adaptive predictive flow control of ATM network traffic," *IEEE Transactions on Fuzzy Systems*, vol. 11, no. 4, pp. 568–581, 2003.

[22] J. Xia, J. Zhang, W. Sun, B. Zhang, and Z. Wang, "Finite-time adaptive fuzzy control for nonlinear systems with full state constraints," *IEEE Transactions on Systems, Man, and Cybernetics: Systems*, vol. 49, no. 7, pp. 1541–1548, 2019.

[23] H. Wang, P. X. Liu, X. Zhao, and X. Liu, "Adaptive fuzzy finite-time control of nonlinear systems with actuator faults," *IEEE Transactions on Cybernetics*, vol. 50, no. 5, pp. 1786–1797, 2020.

[24] N. Wang, H. R. Karimi, H. Li, and S. Su, "Accurate trajectory tracking of disturbed surface vehicles: a finite-time control approach," *IEEE/ASME Transactions on Mechatronics*, vol. 24, no. 3, pp. 1064–1074, 2019.

[25] H. Ren, G. Zong, and T. Li, "Event-triggered finite-time control for networked switched linear systems with asynchronous switching," *IEEE Transactions on Systems, Man, and Cybernetics: Systems*, vol. 48, no. 11, pp. 1874–1884, 2018.

[26] P. Du, H. Liang, S. Zhao, and C. K. Ahn, "Neural-based decentralized adaptive finite-time control for nonlinear large-scale systems with time-varying output constraints," *IEEE*

Transactions on Systems, Man, and Cybernetics: Systems, pp. 1–12, 2019.

[27] F. Wang and X. Zhang, "Adaptive finite time control of nonlinear systems under time-varying actuator failures," *IEEE Transactions on Systems, Man, and Cybernetics: Systems*, vol. 49, no. 9, pp. 1845–1852, 2019.

[28] B. Xu, "Composite learning finite-time control with application to quadrotors," *IEEE Transactions on Systems, Man, and Cybernetics: Systems*, vol. 48, no. 10, pp. 1806–1815, 2018.

[29] H. Du, G. Wen, Y. Cheng, and J. Lu, "Design and implementation of bounded finite-time control algorithm for speed regulation of permanent magnet synchronous motor," *IEEE Transactions on Industrial Electronics*, 2020.

[30] S. Li, C. K. Ahn, and Z. Xiang, "Command filter based adaptive fuzzy finite-time control for switched nonlinear systems using state-dependent switching method," *IEEE Transactions on Fuzzy Systems*, 2019.

[31] S. Zheng and W. Li, "Fuzzy finite time control for switched systems via adding a barrier power integrator," *IEEE Transactions on Cybernetics*, vol. 49, no. 7, pp. 2693–2706, 2019.

[32] C. Ren and S. He, "Finite-time stabilization for positive Markovian jumping neural networks," *Applied Mathematics and Computation*, vol. 365, Article ID 124631, 2020.

[33] C. Ren, R. Nie, and S. He, "Finite-time positiveness and distributed control of Lipschitz nonlinear multi-agent systems," *Journal of the Franklin Institute*, vol. 356, no. 15, pp. 8080–8092, 2019.

[34] C. Ren and S. He, "Sliding mode control for a class of nonlinear positive Markov jumping systems with uncertainties in a finite-time interval," *International Journal of Control, Automation and Systems*, vol. 17, no. 7, pp. 1634–1641, 2019.

[35] P. Cheng, S. He, J. Cheng, X. Luan, and F. Liu, "Asynchronous output feedback control for a class of conic-type nonlinear hidden Markov jump systems within a finite-time interval," *IEEE Transactions on Systems, Man, and Cybernetics*, 2020.

[36] P. Cheng and S. He, "Observer-based finite-time asynchronous control for a class of hidden Markov jumping systems with conic-type non-linearities," *IET Control Theory and Applications*, vol. 14, no. 2, pp. 244–252, 2020.

[37] J. Song, Y. Niu, and Y. Zou, "Asynchronous sliding mode control of Markovian jump systems with time-varying delays and partly accessible mode detection probabilities," *Automatica*, vol. 93, pp. 33–41, 2018.

[38] J. Song, Y. Niu, and Y. Zou, "Asynchronous output feedback control of time-varying Markovian jump systems within a finite-time interval," *Journal of the Franklin Institute*, vol. 354, no. 15, pp. 6747–6765, 2017.

[39] M. Fang, L. Wang, and Z. Wu, "Asynchronous stabilization of boolean control networks with stochastic switched signals," *IEEE Transactions on Systems, Man, and Cybernetics: Systems*, pp. 1–8, 2019.

[40] S. Dong, M. Fang, P. Shi, Z. Wu, and D. Zhang, "Dissipativity-based control for fuzzy systems with asynchronous modes and intermittent measurements," *IEEE Transactions on Cybernetics*, vol. 50, no. 6, pp. 2389–2399, 2018.

[41] S. He, H. Fang, M. Zhang, F. Liu, and Z. Ding, "Adaptive optimal control for a class of nonlinear systems: the online policy iteration approach," *IEEE Transactions on Neural Networks and Learning Systems*, vol. 31, no. 2, pp. 549–558, 2020.

[42] S. He, H. Fang, M. Zhang, F. Liu, X. Luan, and Z. Ding, "Online policy iterative-based H_∞ optimization algorithm for a class of nonlinear systems," *Information Sciences*, vol. 495, pp. 1–13, 2019.

[43] S. He, H. Fang, M. Zhang, F. Liu, X. Luan, and Z. Ding, "Reinforcement learning and adaptive optimization of a class of Markov jump systems with completely unknown dynamic information," *Neural Computing and Applications*, vol. 32, pp. 14311–14320, 2020.

[44] C. Wang, H. Fang, and S. He, "Adaptive optimal controller design for a class of LDI-based neural network systems with input time-delays," *Neurocomputing*, vol. 385, pp. 292–299, 2020.

Hindawi
Complexity
Volume 2020, Article ID 8840784, 12 pages
https://doi.org/10.1155/2020/8840784

Research Article

Fuzzy Model-Based Asynchronous Control for Markov Switching Systems with Stochastic Fading Channels

Fayuan Wu,[1] Jinhui Tang,[1] Zhuang Liu,[1] Qi Xiao,[2] Xiaodong Zheng,[3] and Shuangsi Xue[3]

[1]*Electric Power Research Institute of State Grid Jiangxi Electric Power Co.Ltd., Nanchang 330096, China*
[2]*State Grid Jiangxi Electric Power Co.Ltd., Nanchan 330096, China*
[3]*School of Electrical Engineering, Xi'an Jiaotong University, Xi'an 710049, China*

Correspondence should be addressed to Shuangsi Xue; xssxjtu@stu.xjtu.edu.cn

Received 6 August 2020; Revised 24 August 2020; Accepted 8 September 2020; Published 18 September 2020

Academic Editor: Shuping He

This work investigates the asynchronous control for fuzzy Markov switching systems (MSSs) with randomly occurring fading channel. By resorting to a T-S fuzzy model, the nonlinear MSSs can be handled. Meanwhile, in the unreliable network, the Rice fading model is proposed to capture the randomly occurring channel fading, which covers packet dropouts and network-induced delays as special cases. In light of the hidden Markov model, the asynchronous phenomenon of controller is taken into consideration, and asynchronous fuzzy controller is obtained. In the end, a numerical example and a single-link robotic arm model are applied to demonstrate the validity of the derived results.

1. Introduction

In physical applications, such as power station monitoring systems, fire-fighting operating systems, and electric networks, the signals are transmitted through a shared wireless/wired communication channel. The stability of the systems is weakened by uncontrollable accidents on some occasions and external complex environment, and it is of importance to make the systems have certain robustness. However, because of the limited resources, the communication quality and computing load are affected, and the unexpected phenomenon occurs, such as networked-induced delay, quantization, and fading channel (FC). Normally, when signals are transmitted by wireless communication link, the phenomena of reflection/diffraction can be encountered, which results in multichannel-based fading. Recently, many scholars have devoted their attention to hybrid systems with FC [1–3]. It is remarkable that, compared with packet dropouts, FC is more general, which contains the finite coefficients. Lately, FC is widely applied in time-dependent probabilistic process, and many valuable results are reported in robust control [4], sliding mode control [5], and H_∞ filtering [6, 7].

As a special type of switching systems, Markov switching systems (MSSs) consist of finite subsystems, and different subsystems are activated by a random Markov process [8–10]. Note that MSSs have been successfully applied in practical systems with probabilistic parameter changes, for instance, component failures. Added by its powerful application, many fruitful results have been gained in the issues of admissibility and stabilization, robust control, and filtering [11–14]. As one can be seen from [11–14] that, the control designed scheme has major concerns on synchronous situation. Owing to the networked mechanism and time delay, it is unreasonable to consider the synchronous scenario. By resorting to the hidden Markov model (HMM) [15–17], the asynchronous controller/filter can be solved in an application perspective.

On the contrary, it can be observed that aforementioned literatures are constrained to linear systems, which limited the practical application [18–23]. In general, MSSs tend to nonlinearities for external nonlinear environments and

other factors, and it is urgent to take nonlinear MSSs into consideration [24–27]. Following this trend, many efforts have been devoted to nonlinear systems. Among them, Takagi–Sugeno (T-S) fuzzy model has been proved to be an efficient tool in tacking with nonlinear systems, in which by resorting to fuzzy inference strategy, the nonlinear systems are separated into finite local linear parts [28–30]. Recently, many meaningful results of T-S fuzzy MSSs (FMSSs) have been expressed in [20–22]. However, the FC issue has not been extended to FMSSs, not to mention asynchronous scenario.

Inspired by the above observation, we focus on the asynchronous control for FMSSs with randomly occurring FC. The major contributions are summarized as follows: (1) the FC model with disturbance is absorbed, which covers packet dropouts and network-induced delays as special cases; (2) added by parallel distributed compensation strategy and HMM scheme, the asynchronous control law is developed, which relaxes the limitation in existing results; and (3) by means of Lyapunov functional and stochastic analysis, sufficient criteria are gained and SLRAM is applied to illustrate the effectiveness of the proposed asynchronous control law.

The rest of this study is organized as below. The system descriptions are given in Section 2, and main results including stochastic stability of closed-loop system and controller gains are provided in Section 3. Computational experiments are expressed in Section 4. In the end, conclusions are shown in Section 5.

Notations: the notations utilized in this work are same as that in [10]. Furthermore, $\mathrm{sym}(L) = L + L^{\top}$ and $\mathrm{diag}\{\cdot\}$ means the block-diagonal matrix.

2. Problem Formulations

Consider the T-S FMSS (1) as follows:

Plant rule i: IF ϕ_{1k} is $M_{i1}, \ldots, \phi_{fk}$ is M_{if}, THEN

$$\begin{aligned} \delta(k+1) &= A(i,r_k)\delta(k) + B(i,r_k)u(k) + C(i,r_k)\omega(k), \\ z(k) &= D(i,r_k)\delta(k) + F(i,r_k)\omega(k), \end{aligned} \tag{1}$$

where $x(k) \in \mathbb{R}^{n_x}$ is the state vector, $u(k) \in \mathbb{R}^{n_u}$ is the control input, $z(k) \in \mathbb{R}^{n_z}$ is the output vector, and $\omega(k) \in \mathbb{R}^{n_\omega}$ is the external disturbance. Stochastic variable (SV) r_k is a discrete Markov chain (DMC) and $r_k \in \mathscr{R} = \{1, 2, \ldots, R\}$. For any $r_k \in \mathscr{R}$, $A_{r_k}, B_{r_k}, C_{r_k}, D_{r_k}$, and F_{r_k} indicate the predetermined matrices. M_{ij} are the fuzzy sets, and $\phi_{lk} \in \{\phi_{1k}, \phi_{2k}, \ldots, \phi_{fk}\}$ means the premise variable. Here, $i \in \{1, 2, \ldots, \kappa\}$ and κ implies the IF-THEN rules number.

In (1), for any $\mu, \nu \in \mathscr{R}$, the transition probability matrix (TPM) of original state is inferred by $\Gamma = [\vartheta_{\mu\nu}]$:

$$\Pr\{r_{k+1} = \nu \mid r_k = \mu\} = \vartheta_{\mu\nu}, \tag{2}$$

where $\mu, \nu \in \mathscr{R}$, $\vartheta_{\mu\nu} \in [0, 1]$, and $\forall \mu \in \mathscr{R}$, $\sum_{\nu\in\mathscr{R}} \vartheta_{\mu\nu} = 1$. For $r_k = \mu$, one has $\mathscr{R}(i, r_k) = \mathscr{R}_{i\mu}$, where $\mathscr{R}(i, r_k) = \{A(i, r_k), B(i, r_k), C(i, r_k), D(i, r_k), F(i, r_k)\}$.

By means of the T-S fuzzy model, FMSS (1) can be deduced as follows:

$$\begin{aligned} \delta(k+1) &= \sum_{i=1}^{\kappa} (\hbar_i(\eta_k))\big(A_{i\mu}\delta(k) + B_{i\mu}u(k) + C_{i\mu}\omega(k)\big), \\ z(k) &= \sum_{i=1}^{\kappa} (\hbar_i(\eta_k))\big(D_{i\mu}\delta(k) + F_{i\mu}\omega(k)\big), \end{aligned} \tag{3}$$

where $M_{ij}(\eta_{jk})$ symbolizes the grade of membership of η_{jk} in M_{ij}, $\mathfrak{F}_i(\eta_k) = \prod_{j=1}^{\kappa}(M_{ij}(\eta_{jk}))$, and $\hbar_i(\eta_k) = \mathfrak{F}_i(\eta_k)/\sum_{i=1}^{\kappa}(\mathfrak{F}_i(\eta_k))$; here, $\hbar_i(\eta_k) \geq 0$, and $\sum_{i=1}^{\kappa} \hbar_i(\eta_k) = 1$. For simplification, denoting

$$\begin{aligned} A_{\hbar\mu} &= \sum_{i=1}^{\kappa} \hbar_i(\eta_k)A_{i\mu}, \\ B_{\hbar\mu} &= \sum_{i=1}^{\kappa} \hbar_i(\eta_k)B_{i\mu}, \\ C_{\hbar\mu} &= \sum_{i=1}^{\kappa} \hbar_i(\eta_k)C_{i\mu}, \\ D_{\hbar\mu} &= \sum_{i=1}^{\kappa} \hbar_i(\eta_k)D_{i\mu}, \\ F_{\hbar\mu} &= \sum_{i=1}^{\kappa} \hbar_i(\eta_k)F_{i\mu}, \end{aligned} \tag{4}$$

apparently, the FMSS (3) can be rewritten as

$$\begin{aligned} \delta(k+1) &= A_{\hbar\mu}\delta(k) + B_{\hbar\mu}u(k) + C_{\hbar\mu}\omega(k), \\ z(k) &= D_{\hbar\mu}\delta(k) + F_{\hbar\mu}\omega(k). \end{aligned} \tag{5}$$

It is remarkable that the signals $\delta(k)$ are sending out via unreliable network; some unpredictable factors occur, such as channel fading (CF) and packet dropout. To model the randomly occurring CF, Lth-order CF model is proposed:

$$\overline{\delta}(k) = \sum_{l=0}^{L} (\alpha_l(k))\delta(k-l) + H\zeta(k), \tag{6}$$

where $\overline{\delta}(k)$ is the signal arrived at controller and $\alpha_l(k)$ $(l = 0, 1, \ldots, L)$ are mutually independent SVs with $\varepsilon\{\alpha_l(k)\} = \alpha_l$ subject to variances $\varepsilon\{(\alpha_l(k) - \alpha_l)^2\} = \overline{\alpha}_l^2$. $\zeta(k)$ represents the external disturbance and H is the known matrix.

Remark 1. In the unreliable network, aiming to depict the unexpected networked phenomenon including scattering and other factors, fading channel is proposed, which is characterized by the Rice fading model. The stochastic variables $\alpha_l(k)$ $(l = 1, 2, \ldots, L)$ can describe the variety of fading channel, which are applied and make the signal transmission more general.

In this work, by considering the unreliable of network medium, one establishes the following asynchronous control law (ACL):

Controller rule i: IF φ_{nk} is $\mathrm{Min}, n \in (l = 1, 2, \ldots, f)$, THEN

$$u(k) = K_{i\tau_k}\overline{\delta}(k), \tag{7}$$

where $K_{i\tau_k}$ indicates the unsolved controller gains. The SV τ_k is another DMC. DMC $\tau_k \in \mathscr{T} = \{1, 2, \ldots, T\}$ represents HMM and obeys the conditional probability matrix CPM $\Lambda = [\varphi_{\mu t}]$:

$$\Pr\{\tau_k = t \mid r_k = \mu\} = \varphi_{\mu t}, \tag{8}$$

where $\varphi_{\mu t} \in [0, 1]$ and $\sum_{t\in\mathscr{T}}\varphi_{\mu t} = 1$. Accordingly, the ACL (7) is inferred as

$$u(k) = K_{\hbar t}\overline{\delta}(k), \tag{9}$$

where $K_{\hbar t} = \sum_{i=1}^{\kappa}(\hbar_i(\eta_k))K_{it}$.

Remark 2. Note that asynchronous phenomenon comes from the network-induced delay, quantization, and other factors, which results in unreasonable of traditional synchronous control law [17, 31]. To tackle with such shortage, HMM is employed in designing controller, which is elaborated by $(r_k, \tau_k, \Gamma, \Lambda)$.

Substituting (6) and (9) into (5), the closed-loop FMSS can be acquired:

$$\begin{aligned}\delta(k+1) &= \left(A_{\hbar\mu} + \alpha_0 B_{\hbar\mu}K_{\hbar t}\right)\delta(k) + C_{\hbar\mu}\omega(k)\\ &\quad + \sum_{l=1}^{L}\alpha_l B_{\hbar\mu}K_{\hbar t}\delta(k-l) + B_{\hbar\mu}K_{\hbar t}H\zeta(k)\\ &\quad + \widetilde{\alpha}_0(k)B_{\hbar\mu}K_{\hbar t}\delta(k) + \sum_{l=1}^{L}\widetilde{\alpha}_l(k)B_{\hbar\mu}K_{\hbar t}\delta(k-l),\\ z(k) &= D_{\hbar\mu}\delta(k) + F_{\hbar\mu}\omega(k),\end{aligned} \tag{10}$$

where $\widetilde{\alpha}_l(k) = \alpha_l - \alpha_l(k)$.

Definition 1 (see [12]). Under the initial conditions $\delta(0), r_0$, the FMSS (10) is called stochastically stable (SS), such that

$$\mathrm{E}\left\{\sum_{k=0}^{\infty}\|\delta(k)\|^2 \mid \delta(0), r_0\right\} < \infty. \tag{11}$$

Definition 2 (see [12]). The FMSS (10) is SS with $\mathscr{H}_\infty$ performance γ such that

$$\sum_{k=0}^{\infty}\|z(k)\|^2 < \gamma^2\sum_{k=0}^{\infty}\varpi^{\top}(k)\varpi(k). \tag{12}$$

3. Main Results

Theorem 1. *If there exists a scalar $\gamma > 0$, matrices $P_\mu > 0\,(\mu \in \mathscr{R})$, $U_{\mu t} > 0\,(\mu \in \mathscr{R}, t \in \mathscr{T})$, and $Q_l > 0\,(l = 1, 2, \ldots, L)$, the FMSS (10) is SS with $\mathscr{H}_\infty$ performance γ, for any $\mu, \nu \in \mathscr{R}$, $t \in \mathscr{T}$, such that*

$$\sum_{t\in\mathscr{T}}\varphi_{\mu t}U_{\mu t} < P_\mu, \tag{13}$$

$$\Omega_{ii\mu t} < 0, \tag{14}$$

$$\Omega_{ij\mu t} + \Omega_{ji\mu t} < 0, \tag{15}$$

where

$$\begin{aligned}\Omega_{ij\mu t} &= \begin{bmatrix}\Omega^1_{ij\mu t} & \Omega^2_{ij\mu t}\\ & \Omega^3_{\mu}\end{bmatrix},\\ \mathscr{P}_\mu &= \sum_{\nu\in\mathscr{R}}\vartheta_{\mu\nu}P_\nu,\\ \Omega^1_{ij\mu t} &= \mathrm{diag}\left\{\Omega^{11}_{ij\mu t}, \Omega^{12}_{ij\mu t}, \Omega^{13}_{ij\mu t}, \Omega^{14}_{ij\mu t}\right\},\\ \Omega^2_{ij\mu t} &= \left[\Omega^{21}_{ij\mu t}\ \Omega^{22}_{ij\mu t}\ \Omega^{23}_{ij\mu t}\ \Omega^{24}_{ij\mu t}\right],\\ \Omega^3_{\mu} &= \mathrm{diag}\left\{-\mathscr{P}_\mu, -\mathscr{P}_\mu, -I_L\otimes\mathscr{P}_\mu, -I\right\},\\ \Omega^{11}_{ij\mu t} &= -U_{\mu t} + \sum_{q=1}^{L}Q_q,\\ \Omega^{13}_{ij\mu t} &= -\gamma^2 I,\\ \Omega^{12}_{ij\mu t} &= \mathrm{diag}-Q_1, -Q_2, \ldots, -Q_L,\\ \Omega^{14}_{ij\mu t} &= -\gamma^2 I,\\ \Omega^{21}_{ij\mu t} &= \begin{bmatrix}\left(A_{i\mu} + \alpha_0 B_{i\mu}K_{jt}\right)^{\top}\mathscr{P}_\mu\\ \left(B_{j\mu}K_{jt}\mathscr{Z}\right)^{\top}\mathscr{P}_\mu\\ C^{\top}_{i\mu}\mathscr{P}_\mu\\ \left(B_{i\mu}K_{jt}H\right)^{\top}\mathscr{P}_\mu\end{bmatrix},\\ \Omega^{22}_{ij\mu t} &= \begin{bmatrix}\overline{\alpha}_0\left(B_{i\mu}K_{jt}\right)^{\top}\mathscr{P}_\mu\\ 0\\ 0\\ 0\end{bmatrix},\\ \mathscr{Z} &= [\alpha_1 I\alpha_2 I\cdots\alpha_L I],\\ \Omega^{23}_{ij\mu t} &= \begin{bmatrix}0\\ \left(\overline{\Theta}\otimes B_{i\mu}K_{jt}\right)^{\top}\mathscr{P}_\mu\\ 0\\ 0\end{bmatrix},\\ \Omega^{24}_{ij\mu t} &= \left[D_{i\mu}\,0\,F_{i\mu}\,0\right]^{\top},\\ \overline{\Theta} &= \mathrm{diag}\{\overline{\alpha}_1, \overline{\alpha}_2, \ldots, \overline{\alpha}_L\}.\end{aligned} \tag{16}$$

Proof. It follows from (14) and (15) that

$$\begin{aligned}\Omega_{\hbar\mu t} &= \sum_{i=1}^{\kappa}\sum_{j=1}^{\kappa}\hbar_i(\eta_k)\hbar_j(\eta_k)\Omega_{ij\mu t}\\ &= \sum_{i=1}^{\kappa}\hbar_i^2(\eta_k)\Omega_{ii\mu t} + \sum_{i=1}^{\kappa-1}\sum_{j=i+1}^{\kappa}\hbar_i(\eta_k)\hbar_j(\eta_k)\left(\Omega_{ij\mu t}+\Omega_{ji\mu t}\right) < 0,\end{aligned} \tag{17}$$

where

$$\begin{aligned}
\Omega_{\hbar\mu t} &= \begin{bmatrix}\Omega_{\hbar\mu t}^1 & \Omega_{\hbar\mu t}^2\\ & \Omega_{\mu}^3\end{bmatrix},\\
\Omega_{\hbar\mu t}^1 &= \operatorname{diag}\left\{\Omega_{\hbar\mu t}^{11}, \Omega_{\hbar\mu t}^{12}, \Omega_{\hbar\mu t}^{13}, \Omega_{\hbar\mu t}^{14}\right\},\\
\Omega_{\hbar\mu t}^2 &= \begin{bmatrix}\Omega_{\hbar\mu t}^{21} & \Omega_{\hbar\mu t}^{22} & \Omega_{\hbar\mu t}^{23} & \Omega_{\hbar\mu t}^{24}\end{bmatrix},\\
\Omega_{\hbar\mu}^3 &= \operatorname{diag}\left\{-p_\mu, -p_\mu, -I_L\otimes p_\mu, -I\right\},\\
\Omega_{\hbar\mu t}^{11} &= -P_\mu + \sum_{q=1}^{L} Q_q,\\
\Omega_{\hbar\mu t}^{13} &= -\gamma^2 I,\\
\Omega_{\hbar\mu t}^{12} &= \operatorname{diag}\{-Q_1, -Q_2, \ldots, -Q_L\},\\
\Omega_{\hbar\mu t}^{21} &= \begin{bmatrix}\left(A_{\hbar\mu}+\alpha_0 B_{\hbar\mu}K_{\hbar t}\right)^T p_\mu\\ \left(B_{\hbar\mu}K_{\hbar t}Z\right)^T p_\mu\\ C_{\hbar\mu}^T p_\mu\\ \left(B_{\hbar\mu}K_{\hbar t}H\right)^T p_\mu\end{bmatrix},\\
\Omega_{\hbar\mu t}^{22} &= \begin{bmatrix}\overline{\alpha}_0\left(B_{\hbar\mu}K_{\hbar t}\right)^T p_\mu\\ 0\\ 0\\ 0\end{bmatrix},\\
\Omega_{\hbar\mu t}^{14} &= -\gamma^2 I,\\
\Omega_{\hbar\mu t}^{23} &= \begin{bmatrix}0\\ \left(\overline{\Theta}\otimes B_{\hbar\mu}K_{\hbar t}\right)^T p_\mu\\ 0\\ 0\end{bmatrix},\\
\Omega_{\hbar\mu t}^{24} &= \begin{bmatrix}D_{\hbar\mu} & 0 & F_{\hbar\mu} & 0\end{bmatrix}^T.
\end{aligned} \tag{18}$$

Construct the Lyapunov functional for FMSS (10):

$$V(k,\delta(k)) = V_1(k,\delta(k)) + V_2(k,\delta(k)), \tag{19}$$

where

$$\begin{aligned}V_1(k,\delta(k)) &= \delta^\top(k)P_\mu\delta(k),\\ V_2(k,\delta(k)) &= \sum_{q=1}^{L}\sum_{p=k-q}^{k-1}\delta^\top(p)Q_p\delta(p).\end{aligned} \tag{20}$$

Calculating the difference of $V(k,\delta(k))$ and taking expectation, one has

$$\mathrm{E}\{\Delta V(k)\} = \mathrm{E}\left\{V\left(k+1,\delta_{k+1}\right)\mid\delta(k),r_k\right\} - V(k,\delta(k)). \tag{21}$$

Along system (10), it yields that

$$\begin{aligned}\varepsilon\{\Delta V_1(k)\} &= \varepsilon\left\{\delta^T(k+1)p_\mu\delta(k+1) - \delta^T(k)p_\mu\delta(k)\right\}\\ &= \varepsilon\left\{\left[\left(A_{\hbar\mu}+\alpha_0 B_{\hbar\mu}K_{\hbar t}\right)\delta(k) + C_{\hbar\mu}\omega(k) + \sum_{l=1}^{L}\alpha_l B_{\hbar\mu}K_{\hbar t}\delta(k-l) + B_{\hbar\mu}K_{\hbar t}H\varsigma(k)\right]^T\right.\\ &\quad\cdot p_u\left[\left(A_{\hbar\mu}+\alpha_0 B_{\hbar\mu}K_{\hbar t}\right)\delta(k) + C_{\hbar\mu}\omega(k) + \sum_{l=1}^{L}\alpha_l B_{\hbar\mu}K_{\hbar t}\delta(k-1) + B_{\hbar\mu}K_{\hbar t}H\varsigma(k)\right]\\ &\quad+\widetilde{\alpha}_0^2(k)\delta^T(k)K_{\hbar t}^T B_{\hbar\mu}^T p_\mu B_{\hbar\mu}K_{\hbar t}\delta(k) + \left(\sum_{l=1}^{L}\widetilde{\alpha}_l(k)B_{\hbar\mu}K_{\hbar t}\delta(k-l)\right)^T\\ &\quad\left.\cdot p_\mu\times\left(\sum_{l=1}^{L}\widetilde{\alpha}_l(k)B_{\hbar\mu}K_{\hbar t}\delta(k-l)\right)\right\} - \delta^T(k)P_\mu\delta(k).\end{aligned} \tag{22}$$

Added by the variances in fading channels $\overline{\alpha}_l\,(l=0,1,\ldots,L)$, (22) can be reformulated as

$$\varepsilon\{\Delta V_1(k)\} \le \varepsilon\left\{\begin{array}{l}\left[\left(A_{\hbar\mu}+\alpha_0 B_{\hbar\mu}K_{\hbar t}\right)\delta(k) + C_{\hbar\mu}\omega(k) + B_{\hbar\mu}K_{\hbar t}\mathscr{Z}\delta_L(k) + B_{\hbar\mu}K_{\hbar t}H\zeta(k)\right]^\top\\ \times\mathscr{P}_\mu\left[\left(A_{\hbar\mu}+\alpha_0 B_{\hbar\mu}K_{\hbar t}\right)\delta(k) + C_{\hbar\mu}\omega(k) + B_{\hbar\mu}K_{\hbar t}\mathscr{Z}\delta_L(k) + B_{\hbar\mu}K_{\hbar t}H\zeta(k)\right]\\ +\overline{\alpha}_0^2\delta^\top(k)K_{\hbar t}^\top B_{\hbar\mu}^\top\mathscr{P}_\mu B_{\hbar\mu}K_{\hbar t}\delta(k) + \delta_L^\top(k)\left[\overline{\Theta}^2\otimes K_{\hbar t}^\top B_{\hbar\mu}^\top\mathscr{P}_\mu B_{\hbar\mu}K_{\hbar t}\right]\delta_L(k)\end{array}\right\} - \delta^\top(k)P_\mu\delta(k), \tag{23}$$

where

$$\delta_L(k) = \left[\delta^\top(k-1)\delta^\top(k-2)\cdots\delta^\top(k-L)\right]^\top. \tag{24}$$

On the contrary, for term $V_2(k,\delta(k))$, one has

$$\begin{aligned}\varepsilon\{\Delta V_2(k)\} &= \varepsilon\left\{\sum_{q=1}^{L}\sum_{p=k-q+1}^{k}\delta^\top(p)Q_p\delta(p) - \sum_{q=1}^{L}\sum_{p=k-q}^{k-1}\delta^\top(p)Q_p\delta(p)\right\}\\ &= \delta^\top(k)\sum_{q=1}^{L}Q_q\delta(k) - \sum_{q=1}^{L}\delta^\top(k-q)Q_q\delta(k-q).\end{aligned} \tag{25}$$

For simplification, denoting $\varpi(k) = [\omega^\top(k)\zeta^\top(k)]^\top$. Firstly, we will prove the SS of system (10) with $\varpi(k)=0$. Combining with (23) and (25), one obtains

$$\begin{aligned}\varepsilon\{\Delta V(k)\} \le \varepsilon&\left\{\begin{array}{c}\left[\left(A_{\hbar\mu}+\alpha_0 B_{\hbar\mu}K_{\hbar t}\right)\delta(k) + B_{\hbar\mu}K_{\hbar t}\mathscr{Z}\delta_L(k)\right]^\top\times\mathscr{P}_\mu\left[\left(A_{\hbar\mu}+\alpha_0 B_{\hbar\mu}K_{\hbar t}\right)\delta(k) + B_{\hbar\mu}K_{\hbar t}\mathscr{Z}\delta_L(k)\right]\\ +\overline{\alpha}_0^2\delta^\top(k)K_{\hbar t}^\top B_{\hbar\mu}^\top\mathscr{P}_\mu B_{\hbar\mu}K_{\hbar t}\delta(k) + \delta_L^\top(k)\left[\overline{\Theta}^2\otimes K_{\hbar t}^\top B_{\hbar\mu}^\top\mathscr{P}_\mu B_{\hbar\mu}K_{\hbar t}\right]\delta_L(k)\end{array}\right\}\\ &- \delta^\top(k)P_\mu\delta(k) + \delta^\top(k)\sum_{q=1}^{L}Q_q\delta(k) - \sum_{q=1}^{L}\delta^\top(k-q)Q_q\delta(k-q).\end{aligned} \tag{26}$$

Applying Schur complement to (26), it is clear that

$$\varepsilon\{\Delta V(k)\} \le \varepsilon\left\{\widetilde{\psi}^{\top}(k)\widetilde{\Omega}_{\hbar\mu}\widetilde{\psi}(k)\right\}, \tag{27}$$

where

$$\begin{aligned}
\widetilde{\psi}(k) &= \left[\delta^{\top}(k)\,\delta_L^{\top}(k)\right]^{\top},\\
\widetilde{\Omega}_{\hbar\mu t} &= \begin{bmatrix} \widetilde{\Omega}^1_{\hbar\mu t} & \widetilde{\Omega}^2_{\hbar\mu t} \\ & \widetilde{\Omega}^3_{\mu} \end{bmatrix},\\
\widetilde{\Omega}^1_{\hbar\mu t} &= \operatorname{diag}\left\{\Omega^{11}_{\hbar\mu t}, \Omega^{12}_{\hbar\mu t}\right\},\\
\widetilde{\Omega}^2_{\hbar\mu t} &= \left[\Omega^{21}_{\hbar\mu t}\ \Omega^{22}_{\hbar\mu t}\ \Omega^{23}_{\hbar\mu t}\right],\\
\widetilde{\Omega}^3_{\mu} &= \operatorname{diag}\left\{-\mathscr{P}_{\mu}, -\mathscr{P}_{\mu}, -\mathscr{P}_{\mu}\right\}.
\end{aligned} \tag{28}$$

In light of (27), it achieves that

$$\varepsilon\{\Delta V(k)\} \le \rho\varepsilon\{\delta^{\top}(k)\delta(k)\}, \tag{29}$$

where $\rho = \lambda_{\max}\{\widetilde{\Omega}_{\hbar\mu t}\}$, $(\forall i = 1, 2, \ldots, \kappa, \mu \in \mathscr{R}, t \in \mathscr{T})$. By (17), it is clear that $\rho < 0$, which indicates

$$\varepsilon\{\delta^{\top}(k)\delta(k)\} \le \frac{1}{\rho}\varepsilon\{\Delta V(k)\}. \tag{30}$$

For $N \longrightarrow \infty$, it yields

$$\varepsilon\left\{\sum_{k=0}^{\infty}\delta^{\top}(k)\delta(k)\right\} \le -\frac{1}{\rho}V(0,\delta(0)) < \infty. \tag{31}$$

By Definition 1, it is obviously that FMSS (10) is SS with $\varpi(k) = 0$.

Next, the FMSS (10) is SS with the $\mathscr{H}_{\infty}$ performance index will be verified. For $\varpi(k) \neq 0$ under zero-initial condition, denoting $\mathscr{J}(k) = \sum_{k=0}^{\infty}\varepsilon\{\|z(k)\|^2\} - \gamma^2\varepsilon\{\|\varpi(k)\|^2\}$, one has

$$\begin{aligned}
\mathscr{J}(k) &\le \sum_{k=0}^{\infty}\varepsilon\left\{z^T(k)z(k) - \gamma^2\varpi^T(k)\varpi(k) + \Delta V(k)\right\}\\
&\le \sum_{k=0}^{\infty}\varepsilon\Big\{\Big[\left(A_{\hbar\mu} + \alpha_0 B_{\hbar\mu}K_{\hbar t}\right)\delta(k) + C_{\hbar\mu}\omega(k) + B_{\hbar\mu}K_{\hbar t}Z\delta_L(k) + B_{\hbar\mu}K_{\hbar t}H\zeta(k)\Big]^T\\
&\quad\times P_{\mu}\Big[\left(A_{\hbar\mu} + \alpha_0 B_{\hbar\mu}K_{\hbar t}\right)\delta(k) + C_{\hbar\mu}\omega(k) + B_{\hbar\mu}K_{\hbar t}Z\delta_L(k) + B_{\hbar\mu}K_{\hbar t}H\zeta(k)\Big]\\
&\quad+ \overline{\alpha}_0^2\delta^T(k)K_{\hbar t}^T B_{\hbar t}^T P_{\mu}B_{\hbar\mu}K_{\hbar t}\delta(k) + \delta_L^T(k)\left[\overline{\Theta}^2 \otimes K_{\hbar\mu}^T B_{\hbar\mu}^T P_{\mu}B_{\hbar\mu}K_{\hbar t}\right]\delta_L(k)\\
&\quad- \delta^T(k)P_{\mu}\delta(k) + \delta^T(k)\sum_{q=1}^{L}Q_q\delta(k) - \sum_{q=1}^{L}\delta^T(k-q)Q_q\delta(k-q)\\
&\quad+\left[D_{\hbar\mu}\delta(k) + F_{\hbar\mu}\omega(k)\right]^T\left[D_{\hbar\mu}\delta(k) + F_{\hbar\mu}\omega(k)\right] - \gamma^2\varpi^T(k)\varpi(k)\Big\}.
\end{aligned} \tag{32}$$

Deploy Schur complement to (32), which results in

$$\mathscr{J}(k) \le \sum_{k=0}^{\infty}\left\{\psi^{\top}(k)\Omega_{\hbar\mu}\psi(k)\right\}, \tag{33}$$

where $\psi(k) = [\delta^{\top}(k)\delta_L^{\top}(k)\omega^{\top}(k)\zeta^{\top}(k)]^{\top}$.

In light of (17) and (33), it can be concluded that

$$\lim_{N\longrightarrow\infty}\varepsilon\left\{\sum_{k=0}^{N}z^{\top}(k)z(k)\right\} < \gamma^2\sum_{k=0}^{N}\omega^{\top}(k)\omega(k), \tag{34}$$

which indicates $\varepsilon\{\sum_{k=0}^{\infty}z^{\top}(k)z(k)\} < \gamma^2\sum_{k=0}^{\infty}\omega^{\top}(k)\omega(k)$. By Definition 2, the FMSS (10) is SS with $\mathscr{H}_{\infty}$ performance γ.

Theorem 2. *If there exists a scalar $\gamma > 0$, matrices $P_{\mu} > 0\,(\mu \in \mathscr{R})$, $U_{\mu t} > 0\,(\mu \in \mathscr{R}, t \in \mathscr{T})$, $Q_l > 0\,(l = 1, 2, \ldots, L)$, and matrices $W_t\,(t \in \mathscr{T})$, $Y_t\,(t \in \mathscr{T})$, $\overline{K}_{jt}\,(j = 1, 2, \ldots, \kappa, t \in \mathscr{T})$, the FMSS (10) is SS with $\mathscr{H}_{\infty}$ performance γ, for any $\mu, \nu \in \mathscr{R}$, $t \in \mathscr{T}$, such that*

$$W_t B_{i\mu} = B_{i\mu}Y_t, \tag{35}$$

$$\Upsilon_{ii\mu t} < 0, \tag{36}$$

$$\Upsilon_{ij\mu t} + \Upsilon_{ji\mu t} < 0, \tag{37}$$

where

$$
\begin{aligned}
\Upsilon_{ij\mu t} &= \begin{bmatrix} \Omega^1_{ij\mu t} & \Upsilon^2_{ij\mu t} \\ & \Upsilon^3_{\mu t} \end{bmatrix},\\
\Upsilon^2_{ij\mu t} &= \begin{bmatrix} \Upsilon^{21}_{ij\mu t} & \Upsilon^{22}_{ij\mu t} & \Upsilon^{23}_{ij\mu t} & \Upsilon^{24}_{ij\mu t} \end{bmatrix},\\
\Upsilon^{21}_{ij\mu t} &= \begin{bmatrix} A^T_{i\mu} W^T_t + \alpha_0 \overline{K}^T_{jt} B^T_{i\mu} \\ z^T \overline{K}^T_{jt} B^T_{i\mu} \\ C^T_{i\mu} W^T_t \\ H^T \overline{K}^T_{jt} B^T_{i\mu} \end{bmatrix},\\
\Upsilon^{22}_{ij\mu t} &= \begin{bmatrix} \overline{\alpha}_0 \overline{K}^T_{jt} B^T_{i\mu} \\ 0 \\ 0 \\ 0 \end{bmatrix},\\
\Upsilon^{23}_{ij\mu t} &\begin{bmatrix} 0 \\ \Theta \otimes \left(\overline{K}^T_{jt} B^T_{i\mu} \right) \\ 0 \\ 0 \end{bmatrix},\\
\Upsilon^3_{\mu t} &= \operatorname{diag}\left\{ \mathscr{P}_\mu - \operatorname{sym}\{W_t\}, \mathscr{P}_\mu - \operatorname{sym}\{W_t\}, \right.\\
&\quad \left. I_L \otimes \left(\mathscr{P}_\mu - sym\{W_t\} \right), -I \right\}.
\end{aligned} \tag{38}
$$

The controller parameters can be obtained by

$$
K_{jt} = Y_t^{-1} \overline{K}_{jt}, \quad (j = 1, 2, \ldots, \kappa, t \in \mathscr{T}). \tag{39}
$$

Proof. Define

$$
\mathscr{M}_{\mu t} = \operatorname{diag}\left\{ I, I, \ldots, I, \mathscr{P}^{-1}_\mu W^\top_t, \mathscr{P}^{-1}_\mu W^\top_t, I_L \otimes \mathscr{P}^{-1}_\mu W^\top_t, I \right\}. \tag{40}
$$

Applying a congruence transformation to (14), it yields that

$$
\overline{\Upsilon}_{ii\mu t} = \mathscr{M}^\top_{\mu t} \Omega_{ii\mu t} \mathscr{M}_{\mu t} < 0, \tag{41}
$$

where

$$
\begin{aligned}
\overline{\Upsilon}_{ii\mu t} &= \begin{bmatrix} \Omega^1_{ii\mu t} & \overline{\Upsilon}^2_{ii\mu t} \\ & \overline{\Upsilon}^3_{\mu t} \end{bmatrix},\\
\overline{\Upsilon}^2_{ii\mu t} &= \begin{bmatrix} \overline{\Upsilon}^{21}_{ii\mu t} & \overline{\Upsilon}^{22}_{ii\mu t} & \overline{\Upsilon}^{23}_{ii\mu t} & \Omega^{24}_{ii\mu t} \end{bmatrix},\\
\overline{\Upsilon}^{21}_{ii\mu t} &= \begin{bmatrix} A^\top_{i\mu} W^\top_t + \alpha_0 \overline{K}^\top_{it} B^\top_{i\mu} \\ \mathscr{Z}^\top K^\top_{it} B^\top_{i\mu} W^\top_t \\ C^\top_{i\mu} W^\top_t \\ H^\top K^\top_{it} B^\top_{i\mu} W^\top_t \end{bmatrix},\\
\overline{\Upsilon}^{22}_{ii\mu t} &= \begin{bmatrix} \overline{\alpha}_0 K^\top_{it} B^\top_{i\mu} W^\top_t \\ 0 \\ 0 \\ 0 \end{bmatrix},\\
\overline{\Upsilon}^{23}_{ii\mu t} &= \begin{bmatrix} 0 \\ \overline{\Theta} \otimes \left(K^\top_{it} B^\top_{i\mu} W^\top_t \right) \\ 0 \\ 0 \end{bmatrix},\\
\overline{\Upsilon}^3_{\mu t} &= \operatorname{diag}\left\{ -W_t \mathscr{P}^{-1}_\mu W^\top_t, -W_t \mathscr{P}^{-1}_\mu W^\top_t, \right.\\
&\quad \left. - I_L \otimes \left(W_t \mathscr{P}^{-1}_\mu W^\top_t \right), -I \right\}.
\end{aligned} \tag{42}
$$

From $(\mathscr{P}_\mu - W_t)\mathscr{P}^{-1}_\mu (\mathscr{P}_\mu - W^\top_t) > 0$, it follows that

$$
-W_t \mathscr{P}^{-1}_\mu W^\top_t < \mathscr{P}_\mu - \operatorname{sym}\{W_t\}. \tag{43}
$$

By resorting to (35), (39), and (43), (35) can be guaranteed if (14) holds. By the same way, (37) and (39) can be guaranteed if (15) and (17) hold.

4. Computational Experiments

4.1. Numerical Example. Consider the FMSS (1) with 3 modes, its parameters are chosen as follows:

$$
\begin{aligned}
A_{11} &= \begin{bmatrix} -0.7933 & -0.0250 \\ -0.4065 & 0.4676 \end{bmatrix}, \\
B_{11} &= \begin{bmatrix} -1.3569 \\ 1.6143 \end{bmatrix}, \\
C_{11} &= \begin{bmatrix} -0.2241 \\ -0.1587 \end{bmatrix}, \\
D_{11} &= \begin{bmatrix} 1.2622 & -0.3065 \end{bmatrix}, \\
A_{12} &= \begin{bmatrix} 0.5916 & -1.5784 \\ -0.6035 & 0.1609 \end{bmatrix}, \\
B_{12} &= \begin{bmatrix} -0.3191 \\ 0.9530 \end{bmatrix}, \\
C_{12} &= \begin{bmatrix} -1.4349 \\ 0.9430 \end{bmatrix}, \\
D_{12} &= \begin{bmatrix} -0.4898 & 0.6855 \end{bmatrix}, \\
A_{13} &= \begin{bmatrix} 0.6255 & 0.0520 \\ 0.2561 & -0.7916 \end{bmatrix}, \\
B_{13} &= \begin{bmatrix} 0.7225 \\ 0.2704 \end{bmatrix}, \\
C_{13} &= \begin{bmatrix} 1.4089 \\ -0.4147 \end{bmatrix}, \\
D_{13} &= \begin{bmatrix} 1.0335 & 2.2099 \end{bmatrix}, \\
A_{21} &= \begin{bmatrix} -0.3922 & -0.0717 \\ -0.4506 & -0.0868 \end{bmatrix}, \\
B_{21} &= \begin{bmatrix} -0.6664 \\ 0.5477 \end{bmatrix}, \\
C_{21} &= \begin{bmatrix} -0.0816 \\ 0.3037 \end{bmatrix}, \\
D_{21} &= \begin{bmatrix} -0.3504 & 2.6857 \end{bmatrix}, \\
A_{22} &= \begin{bmatrix} 0.8048 & 0.5603 \\ 0.6455 & -0.6569 \end{bmatrix}, \\
B_{22} &= \begin{bmatrix} 0.5714 \\ -1.1684 \end{bmatrix}, \\
C_{22} &= \begin{bmatrix} 1.9891 \\ 0.8228 \end{bmatrix}, \\
D_{22} &= \begin{bmatrix} -2.0949 & 0.4153 \end{bmatrix}, \\
A_{23} &= \begin{bmatrix} -0.3107 & 0.0627 \\ 0.4732 & 0.7070 \end{bmatrix}, \\
B_{23} &= \begin{bmatrix} 0.0078 \\ -0.8450 \end{bmatrix}, \\
C_{23} &= \begin{bmatrix} 0.0112 \\ 1.0132 \end{bmatrix}, \\
D_{23} &= \begin{bmatrix} -0.0921 & -0.5206 \end{bmatrix}, \\
F_{i\mu} &= 0.01, \quad (i = 1, 2, \mu = 1, 2, 3), \\
H &= \begin{bmatrix} 0.05 & 0.05 \end{bmatrix}^T.
\end{aligned} \tag{44}
$$

The TPM Γ and CPM Λ are inferred as

$$
\begin{aligned}
\Gamma &= \begin{bmatrix} 0.4 & 0.5 & 0.1 \\ 0.05 & 0.05 & 0.9 \\ 0.2 & 0.4 & 0.4 \end{bmatrix}, \\
\Lambda &= \begin{bmatrix} 0.8 & 0.2 \\ 0.5 & 0.5 \\ 0.7 & 0.3 \end{bmatrix}.
\end{aligned} \tag{45}
$$

One assumes that the Lth-order of CF model (6) with $L = 1$ and $\alpha_0 = 0.78$, $\alpha_1 = 0.36$, $\overline{\alpha}_0 = 0.3$, and $\overline{\alpha}_1 = 0.3$. $\omega(k) = (1.6 \sin^2(k))/1 + k^2$, $\zeta(k) = 0.8 \exp(-k^2)$. By solving the inequalities of Theorem 2, a set of controller gains are acquired:

$$
\begin{bmatrix} K_{11} & K_{12} \\ K_{21} & K_{22} \end{bmatrix} = \begin{bmatrix} -0.1301 & -0.1029 & -0.1329 & -0.1061 \\ 0.1855 & 0.1442 & 0.1709 & 0.1330 \end{bmatrix}. \tag{46}
$$

By applying the aforementioned controller gains, Figures 1 and 2 demonstrate the state mode and controller mode, respectively. The state trajectories with CF are shown in Figure 3, and the control input is depicted in Figure 4. Defining $\gamma_d(k) = \sqrt{\sum_{s=0}^{k} \|z(s)\|^2 / \sum_{s=0}^{k} \|\varpi(s)\|^2}$, Figure 5 plots the evolution of $\gamma_d(k)$.

4.2. Practical Example. Robot arms are essential parts in firefighting operating systems. In this case, we consider a single-link robotic arm model (SLRAM) stemmed from [12], which is inferred by

$$
\ddot{\phi}(t) = -\frac{g\mathscr{L}\mathscr{M}_k}{\mathscr{J}_k} \sin(\phi(t)) - \frac{\mathscr{R}}{\mathscr{J}_k} \dot{\phi}(t) + \frac{1}{\mathscr{J}_k} u(t) + \omega(t), \tag{47}
$$

where the meaning of g, $\phi(t)$, $\mathscr{L}$, $\mathscr{J}_k$, and $\mathscr{R}$ are explained in [12] and $g = 9.81\,\mathrm{m/s^2}$, $\mathscr{L} = 0.5\,\mathrm{m}$, $\mathscr{R} = 1\,\mathrm{kg \cdot m^2/s}$, $\mathscr{M}_1 = 1\,\mathrm{kg}$, $\mathscr{M}_2 = 5\,\mathrm{kg}$, $\mathscr{J}_1 = 1\,\mathrm{kg \cdot m^2}$, and $\mathscr{J}_2 = 5\,\mathrm{kg \cdot m^2}$.

According to [12], for sampling period $\mathscr{T} = 0.01\,\mathrm{s}$, the SLRAM is reestablished as the T-S FMSSs.

Plant rule 1: IF $\delta_1(k)$ is about 0 rad, THEN

$$
\begin{aligned}
\delta(k+1) &= A_{1,\mu}\delta(k) + B_{1,\mu}u(k) + C_{1,\mu}\omega(k), \\
z(k) &= D_{1,\mu}\delta(k) + F_{1,\mu}\omega(k).
\end{aligned} \tag{48}
$$

Plant rule 2: IF $\delta_2(k)$ is about $\pm\pi$ rad, THEN

$$
\begin{aligned}
\delta(k+1) &= A_{2,\mu}\delta(k) + B_{2,\mu}u(k) + C_{2,\mu}\omega(k), \\
z(k) &= D_{2,\mu}\delta(k) + F_{2,\mu}\omega(k),
\end{aligned} \tag{49}
$$

where

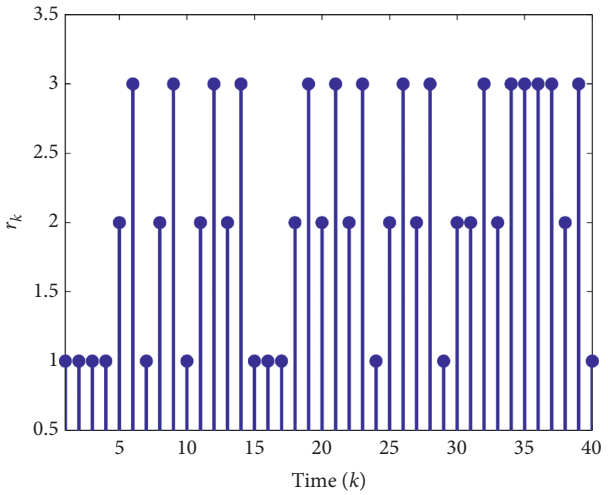

Figure 1: State mode.

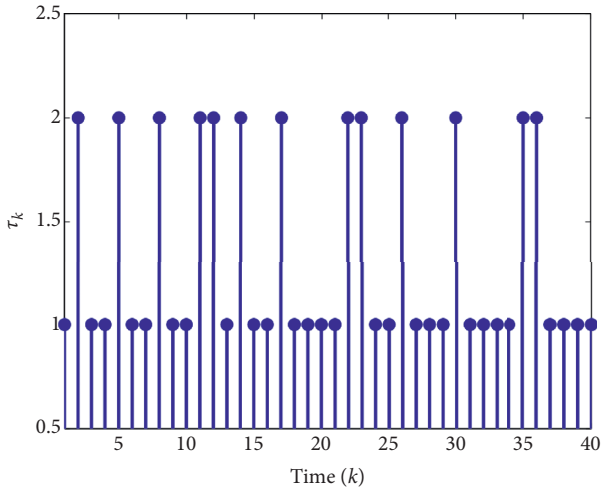

Figure 2: Controller mode.

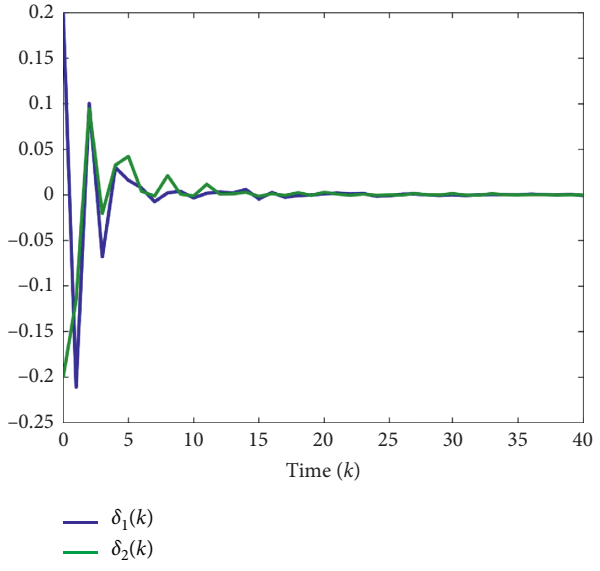

Figure 3: The state trajectories with CF.

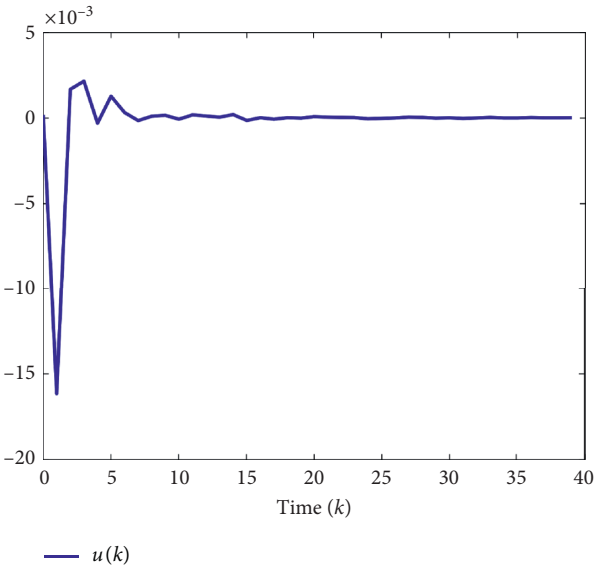

Figure 4: Control input.

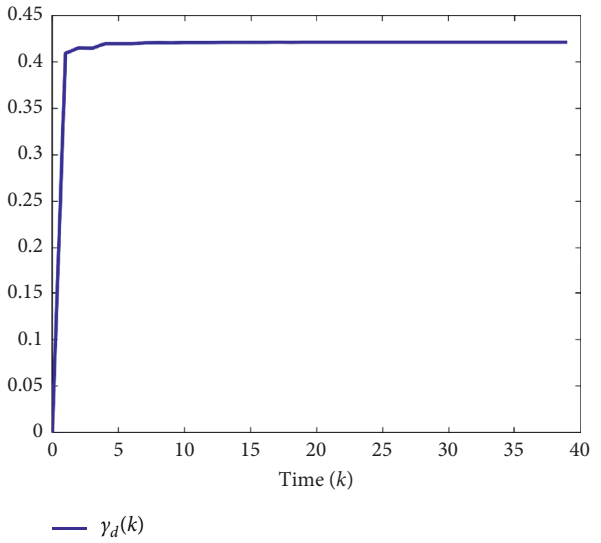

Figure 5: Evolution of $\gamma^{d(k)}$.

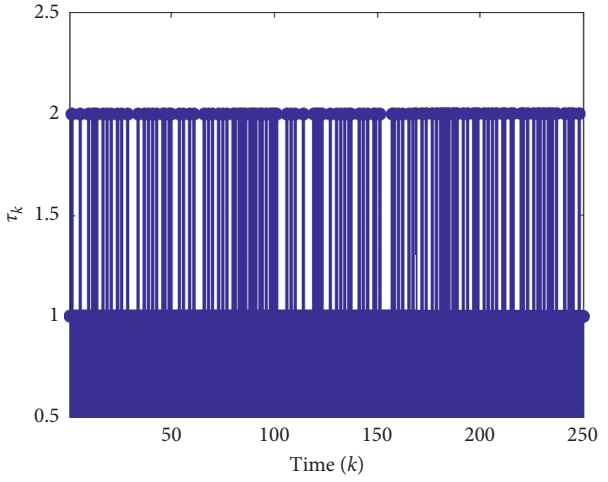

Figure 6: State mode.

$$A_{1\mu} = \begin{bmatrix} 1 & \mathscr{T} \\ \dfrac{\mathscr{T} g \mathscr{L} \mathscr{M}_\mu}{\mathscr{J}_\mu} & 1 - \dfrac{\mathscr{T} \mathscr{R}}{\mathscr{J}_\mu} \end{bmatrix},$$

$$B_{1\mu} = \begin{bmatrix} 0 \\ \dfrac{\mathscr{T}}{\mathscr{J}_\mu} \end{bmatrix},$$

$$C_{1\mu} = \begin{bmatrix} 0 \\ \mathscr{T} \end{bmatrix}, D_{1\mu} = [1\,0], F_{1\mu} = 1,$$

$$A_{2\mu} = \begin{bmatrix} 1 & \mathscr{T} \\ \varepsilon \dfrac{\mathscr{T} g \mathscr{L} \mathscr{M}_\mu}{\mathscr{J}_\mu} & 1 - \dfrac{\mathscr{T} \mathscr{R}}{\mathscr{J}_\mu} \end{bmatrix}, \tag{50}$$

$$B_{2\mu} = \begin{bmatrix} 0 \\ \dfrac{\mathscr{T}}{\mathscr{J}_\mu} \end{bmatrix},$$

$$C_{2\mu} = \begin{bmatrix} 0 \\ \mathscr{T} \end{bmatrix},$$

$$D_{2\mu} = [1\,0],$$

$$F_{2\mu} = 1,$$

$$H = [1\,1]^\top.$$

The TPM Γ and CPM Λ are expressed as follows:

$$\Gamma = \begin{bmatrix} 0.4 & 0.6 \\ 0.75 & 0.25 \end{bmatrix},$$
$$\Lambda = \begin{bmatrix} 0.7 & 0.3 \\ 0.45 & 0.55 \end{bmatrix}. \tag{51}$$

Assuming that $L = 1$ and $\alpha_0 = 0.81$, $\alpha_1 = 0.2236$, $\overline{\alpha}_0 = 0.13$, and $\overline{\alpha}_1 = 0.2236$. Meanwhile, $\omega(k)$ and $\zeta(k)$ are chosen as Example 4.1. Solving the inequalities of Theorem 2, the controller gains are achieved:

$$\begin{bmatrix} K_{11} & K_{12} \\ K_{21} & K_{22} \end{bmatrix} = \begin{bmatrix} 2.4702 & -10.3037 & 2.5196 & -9.9710 \\ -0.4982 & -8.7620 & -0.4263 & -7.9807 \end{bmatrix}. \tag{52}$$

For initial condition $\delta(0) = [0.2\ -0.3]^\top$, by resorting to the obtained filter gains, Figures 6 and 7 demonstrate the state mode and controller mode, respectively. The state trajectories with CF are shown in Figure 8, and control input is depicted in Figure 9. In the end, Figure 10 plots the evolution of $\gamma_d(k)$. It can be observed from Figures 8–10 that the proposed controller is effective.

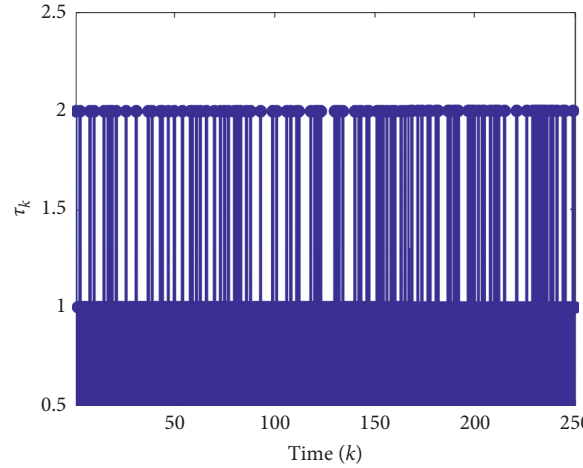

Figure 7: Controller mode.

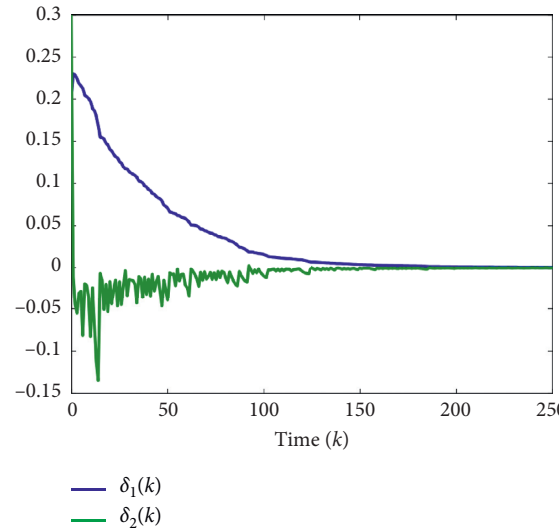

Figure 8: The state trajectories with CF.

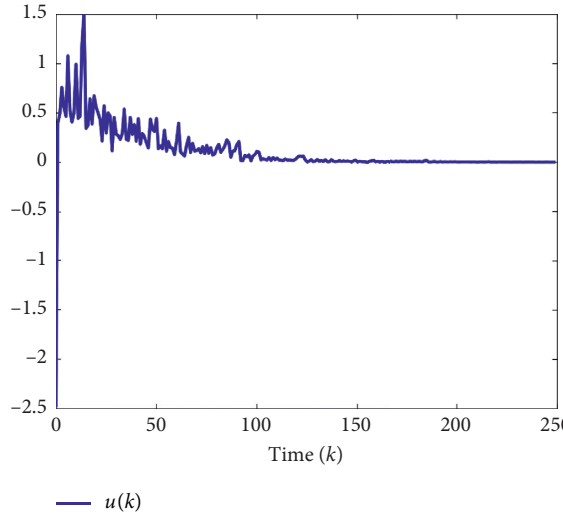

Figure 9: Control input.

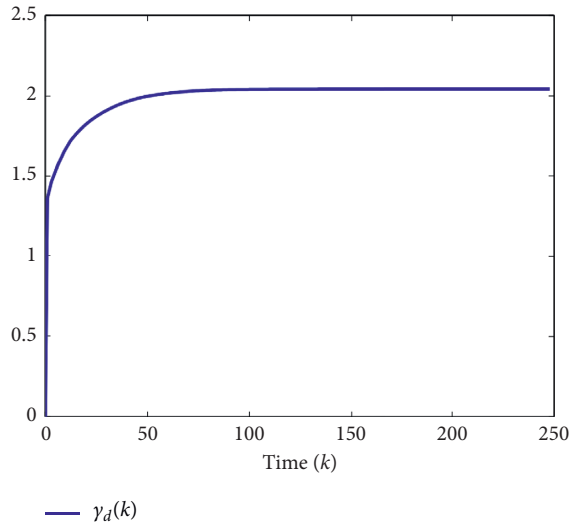

Figure 10: Evolution of $\gamma^{d(k)}$.

5. Conclusions

In this work, the asynchronous control for FMSSs with randomly occurring FC is designed. By resorting to the T-S fuzzy model, the nonlinear MSSs can be handled. Furthermore, the Rice fading model is proposed to capture the randomly occurring channel fading, which covers packet dropouts and network-induced delays as special cases. In light of HMM, the asynchronous phenomenon of controller is taken into consideration, and asynchronous fuzzy controller is obtained. In the end, two examples are applied to demonstrate the validity of the derived results. It can be observed that, compared with the existing approach, the obtained methodology is more general, and less conservatism results are expressed. In the networked scenario, sliding mode control for FMSSs with FC is significant in future works [32].

Data Availability

The data used to support the findings of this study are included within the article.

Conflicts of Interest

The authors declare that they have no conflicts of interest.

Acknowledgments

This work was supported by the Science and Technology Project of State Grid Jiangxi Electric Power Co. Ltd. (521820200036).

References

[1] R. Rajagopalan and P. Varshney, "Connectivity analysis of wireless sensor networks with regular topologies in the presence of channel fading," *IEEE Transactions on Wireless Communications*, vol. 8, no. 7, pp. 3475–3483, 2009.

[2] L. Su and G. Chesi, "Robust stability analysis and synthesis for uncertain discrete-time networked control systems over fading channels," *IEEE Transactions on Automatic Control*, vol. 62, no. 4, pp. 1966–1971, 2017.

[3] N. Elia, "Remote stabilization over fading channels," *Systems & Control Letters*, vol. 54, no. 3, pp. 237–249, 2005.

[4] J. Song, Y. Niu, and S. Wang, "Robust finite-time dissipative control subject to randomly occurring uncertainties and stochastic fading measurements," *Journal of the Franklin Institute*, vol. 354, no. 9, pp. 3706–3723, 2017.

[5] J. Li and Y. Niu, "Sliding mode control subject to rice channel fading," *IET Control Theory & Applications*, vol. 13, no. 16, pp. 2529–2537, 2019.

[6] S. Zhang, Z. Wang, D. Ding, H. Dong, F. E. Alsaadi, and T. Hayat, "Nonfragile H_∞ fuzzy filtering with randomly occurring gain variations and channel fadings," *IEEE Transactions on Fuzzy Systems*, vol. 24, no. 3, pp. 505–518, 2016.

[7] H. Dong, Z. Wang, S. X. Ding, and H. Gao, "Event-based H_∞ filter design for a class of nonlinear time-varying systems with fading channels and multiplicative noises," *IEEE Transactions on Signal Processing*, vol. 63, no. 13, pp. 3387–3395, 2015.

[8] P. Cheng, J. Wang, S. He, X. Luan, and F. Liu, "Observer-based asynchronous fault detection for conic-type nonlinear jumping systems and its application to separately excited DC motor," *IEEE Transactions on Circuits and Systems I: Regular Papers*, vol. 67, no. 3, pp. 951–962, 2020.

[9] J. Cheng, J. H. Park, J. Cao, and W. Qi, "Asynchronous partially mode-dependent filtering of network-based MSRSNSs with quantized measurement," *IEEE Transactions on Cybernetics*, vol. 50, no. 8, pp. 3731–3739, 2020.

[10] J. Cheng, J. H. Park, X. Zhao, H. R. Karimi, and J. Cao, "Quantized nonstationary filtering of network-based Markov switching RSNSs: a multiple hierarchical structure strategy," *IEEE Transactions on Automatic Control*, p. 1. 2019, In press.

[11] J. Cheng, J. H. Park, J. Cao, and W. Qi, "A hidden mode observation approach to finite-time SOFC of Markovian switching systems with quantization," *Nonlinear Dynamics*, vol. 100, pp. 509–521, 2020.

[12] J. Cheng, Y. Shan, J. Cao, and J. H. Park, "Nonstationary control for T-S fuzzy Markovian switching systems with variable quantization density," *IEEE Transactions on Fuzzy Systems*, p. 1. 2020, In press.

[13] H. Shen, F. Li, S. Y. Xu, and V. Sreeram, "Slow state variables feedback stabilization for semi-Markov jump systems with singular perturbations," *IEEE Transactions on Automatic Control*, vol. 63, no. 8, pp. 2709–2714, 2018.

[14] M. Ali and R. Saravanakumar, "Improved H_∞ performance analysis of uncertain Markovian jump systems with overlapping time-varying delays," *Complexity*, vol. 21, no. S1, pp. 460–477, 2016.

[15] Y. Shen, Z. G. Wu, P. Shi, Z. Shu, and H. R. Karimi, "H_∞ Control of Markov jump time-delay systems under asynchronous controller and quantizer," *Automatica*, vol. 99, pp. 352–360, 2019.

[16] Z. G. Wu, P. Shi, Z. Shu, H. Su, and R. Lu, "Passivity-based asynchronous control for Markov jump systems," *IEEE Transactions on Automatic Control*, vol. 62, no. 4, pp. 2020–2025, 2017.

[17] P. Cheng, S. He, J. Cheng, X. Luan, and F. Liu, "Asynchronous output feedback control for a class of conic-type nonlinear hidden Markov jump systems within a finite-time interval," *IEEE Transactions on Systems, Man, and Cybernetics: Systems*, pp. 1–8, 2020.

[18] L. Ma, X. Huo, X. Zhao, and G. Zong, "Observer-based adaptive neural tracking control for output-constrained switched MIMO nonstrict-feedback nonlinear systems with unknown dead zone," *Nonlinear Dynamics*, vol. 99, pp. 1019–1036, 2020.

[19] L. Ma, X. Huo, X. Zhao, and G. Zong, "Adaptive fuzzy tracking control for a class of uncertain switched nonlinear systems with multiple constraints: a small-gain approach," *International Journal of Fuzzy Systems*, vol. 21, pp. 2609–2624, 2019.

[20] G. M. Zhuang, S. F. Su, J. Xia, and W. Sun, "HMM-based asynchronous H_∞ filtering for fuzzy singular Markovian switching systems with retarded time-varying delays," *IEEE Transactions on Cybernetics*, 2020.

[21] T. Wu, J. Cao, L. Xiong, and H. Zhang, "New stabilization results for semi-Markov chaotic systems with fuzzy sampled-data control," *Complexity*, vol. 2019, Article ID 7875305, 2019.

[22] Y. Wang, H. R. Karimi, H. K. Lam, and H. Yan, "Fuzzy output tracking control and filtering for nonlinear discrete-time descriptor systems under unreliable communication links," *IEEE Transactions on Cybernetics*, vol. 50, no. 6, pp. 2369–2379, 2020.

[23] Y. Chang, Y. Wang, F. E. Alsaadi, and G. Zong, "Adaptive fuzzy output-feedback tracking control for switched stochastic pure-feedback nonlinear systems," *International Journal of Adaptive Control and Signal Processing*, vol. 33, no. 10, pp. 1567–1582, 2019.

[24] H. Ni, Z. Xu, J. Cheng, and D. Zhang, "Robust stochastic sampled-data-based output consensus of heterogeneous multi-agent systems subject to random DoS attack: a Markovian jumping system approach," *International Journal of Control, Automation and Systems*, vol. 17, no. 7, pp. 1687–1698, 2019.

[25] B. Wang, J. Cheng, and X. Zhou, "A multiple hierarchical structure strategy to quantized control of Markovian switching systems," *Applied Mathematics and Computation*, vol. 373, p. 125037, 2020.

[26] J. Cheng, D. Zhang, W. Qi, J. Cao, and K. Shi, "Finite-time stabilization of T-S fuzzy semi-Markov switching systems: a coupling memory sampled-data control approach," *Journal of The Franklin Institute*, 2019, In Press.

[27] J. Cheng, B. Wang, J. H. Park, and W. Kang, "Sampled-data reliable control for T-S fuzzy semi-Markovian jump system and its application to single-link robot arm mode," *IET Control Theory and Applications*, vol. 11, no. 12, pp. 1904–1912, 2017.

[28] R. Zhang, X. Liu, D. Zeng, S. Zhong, and K. Shi, "A novel approach to stability and stabilization of fuzzy sampled-data Markovian chaotic systems," *Fuzzy Sets and Systems*, vol. 344, pp. 108–128, 2018.

[29] K. Shi, J. Wang, S. Zhong, Y. Tang, and J. Cheng, "Non-fragile memory filtering of T-S fuzzy delayed neural networks based on switched fuzzy sampled-data control," *Fuzzy Sets and Systems*, vol. 394, pp. 40–64, 2020.

[30] K. Shi, J. Wang, Y. Tang, and S. Zhong, "Reliable asynchronous sampled-data filtering of TCS fuzzy uncertain delayed neural networks with stochastic switched topologies," *Fuzzy Sets and Systems*, vol. 381, pp. 1–25, 2020.

[31] P. Cheng and S. He, "Observer-based finite-time asynchronous control for a class of hidden Markov jumping systems with conic-type non-linearities," *IET Control Theory and Applications*, vol. 14, no. 2, pp. 244–252, 2020.

[32] W. Qi, G. Zong, and H. R. Karimi, "Observer-based adaptive SMC for nonlinear uncertain singular semi-Markov jump systems with applications to DC motor," *IEEE Transactions on Circuits and Systems I: Regular Papers*, vol. 65, no. 9, pp. 2951–2960, 2018.

Hindawi
Complexity
Volume 2020, Article ID 1063251, 7 pages
https://doi.org/10.1155/2020/1063251

WILEY | Hindawi

Research Article

Optimality Conditions and Scalarization of Approximate Quasi Weak Efficient Solutions for Vector Equilibrium Problem

Yameng Zhang, Guolin Yu, and Wenyan Han

Institute of Applied Mathematics, North Minzu University, Yinchuan 750021, China

Correspondence should be addressed to Guolin Yu; guolin_yu@126.com

Received 13 May 2020; Revised 6 July 2020; Accepted 30 August 2020; Published 15 September 2020

Academic Editor: Shuping He

This paper is devoted to the investigation of optimality conditions for approximate quasi weak efficient solutions for a class of vector equilibrium problem (VEP). First, a necessary optimality condition for approximate quasi weak efficient solutions to VEP is established by utilizing the separation theorem with respect to the quasirelative interior of convex sets and the properties of the Clarke subdifferential. Second, the concept of approximate pseudoconvex function is introduced and its existence is verified by a concrete example. Under the assumption of introduced convexity, a sufficient optimality condition for VEP in sense of approximate quasi weak efficiency is also presented. Finally, by using Tammer's function and the directed distance function, the scalarization theorems of the approximate quasi weak efficient solutions of the VEP are proposed.

1. Introduction

Vector equilibrium, which is closely related to complementarity problems, variational inequalities, and fixed point theory, is one of the momentous contents in the field of applied mathematics. The characteristics and optimality conditions of various solutions are the key study of vector equilibrium problems. For instance, the optimality conditions for efficient solutions to vector equilibrium problem were presented in [1]; the literatures [2, 3] derived the optimality conditions of weakly efficient solutions; some optimality conclusions related to several properly efficient solutions were established in [4–7]. In practical applications, the majority of solutions obtained by numerical algorithms are approximate solutions. Undoubtedly, it is of great theoretical and practical significance to study the approximate solutions of vector equilibrium problem. In recent years, the concept of approximate weak efficient solutions for vector equilibrium problem was introduced and its properties were discussed in [8, 9]. Das and Nahak [10] presented the concept of approximate quasi weak efficient solutions to vector equilibrium problem and examined its optimality conditions by generalized derivatives. One of the main purposes of this paper is to establish the necessary optimality condition for approximate quasi weak efficient solutions to vector equilibrium problem via the quasirelative interior-type separation theorem of convex sets. It is worth mentioning that our method is different from that of Das and Nahak [10].

Convexity and its generalization play a critical role in optimization and vector equilibrium theory, especially in establishing the sufficient optimality conditions. For instance, Gong [11, 12] derived the sufficient optimality condition to approximate efficient solutions for vector equilibrium problem under the cone convexity; under the assumptions of arcwise connected functions, the sufficient optimality conditions with regard to properly efficient solutions to vector equilibrium problem are presented in the literature [13]; based on the assumption of generalized cone subconvexlikeness, the literature [14] proposed the properties of globally efficient solutions to vector equilibrium problem. In this paper, we will introduce notion of approximate quasi-pseudoconvex function in terms of *Clarke* subdifferential, and under its assumption, we establish the sufficient optimality condition of approximate quasi weak efficient solutions to vector equilibrium problem, which is another aim of this paper.

Scalarization is to transform a vector problem into a numerical (scalar) problem which is equivalent to primal vector problem under mild conditions. There is no doubt that scalarization is one of the core topics in the study of vector equilibrium problem. In present paper, we will utilize Tammer's nonlinear scalar function and the directed distance function to deal with the scalarization theorems for the approximate quasi weak efficient solutions to vector equilibrium problem.

In the view of the above discussion, the paper will examine the optimality conditions and scalarization theorems in sense of approximate quasi weak efficient solutions to vector equilibrium problem. The article is arranged as follows: in section 2, some symbols, concepts, and lemmas will be presented, which will be used in the subsequent sections; Section 3 is devoted to establish the optimality conditions for approximate quasi weak efficient solutions to the discussed vector equilibrium problem; in section 4, the scalarization theorems will be proven.

2. Preliminaries

Throughout the paper, we set

$$\mathbb{R}_+^n = \{(x_1, x_2, \ldots, x_n): x_i \geq 0, \quad i = 1, 2, \ldots, n\}. \tag{1}$$

Let X and Y be real Banach spaces with topological dual spaces X^* and Y^*, respectively, and $\mathbb{B}(\overline{x}, r)$ stands for the open ball of radius $r > 0$ around $\overline{x} \in X$. For all $x \in X$ and $x^* \in X^*$, the value of linear functional x^* at x be denoted by $\langle x^*, x\rangle$. Let Q be a pointed closed convex cone in Y, then the dual cone of Q be defined as (see [15])

$$Q^* = \{y^* \in Y^*: \langle y^*, y\rangle \geq 0, \quad \forall y \in Q\}. \tag{2}$$

Without other specifications, we always suppose that Q is a pointed closed convex cone in Y. We will use the following properties of Q.

Lemma 1 (see [16]). *If $y^* \in Q^*/\{0\}$ and $y \in \text{int}Q$, then $\langle y^*, y\rangle > 0$, where* int *represents the interior of a set.*

Let K be a nonempty subset of X, and the Clarke contingent cone (see [1]) to set K at point $\overline{x} \in K$ is defined as

$$T(\overline{x}; K) = \{y \in X: \exists t_n \longrightarrow 0, y_n \longrightarrow y, \quad \text{s.t}\, \overline{x} + t_n y_n \in K\}. \tag{3}$$

The Clarke normal cone (see [1]) associated with $T(\overline{x}; K)$ is denoted by

$$N(\overline{x}; K) = \{\xi \in X^*: \langle \xi, y\rangle \leq 0, \quad \forall y \in T(\overline{x}; K)\}. \tag{4}$$

Especially when K be a convex set, the Clarke contingent cone to set K at $\overline{x}$ is given by (see [15])

$$T(\overline{x}; K) = \text{cl}\{y \in X: y = \beta(x - \overline{x}), \quad x \in K, \beta > 0\}. \tag{5}$$

The Clarke normal cone to set K at $\overline{x}$ is

$$N(\overline{x}; K) = \{\xi \in X^*: \langle \xi, x - \overline{x}\rangle \leq 0, \quad \forall x \in K\}, \tag{6}$$

where cl stands for the closure of a set.

Let $F: X \longrightarrow Y$ be a mapping. F is said to be locally Lipschitz at $\overline{x} \in X$, if there exist constant $L > 0$ and $r > 0$ such that

$$\|F(x_1) - F(x_2)\| \leq L\|x_1 - x_2\|, \quad \forall x_1, x_2 \in \mathbb{B}(\overline{x}, r). \tag{7}$$

If for any $x \in X$, F is locally Lipschitz at x, then F is called locally Lipschitz mapping. In particular, for a real-valued locally Lipschitz function $f: X \longrightarrow \mathbb{R}$ ($\mathbb{R}$ denotes real number), the Clarke generalized directional derivative of f at $\overline{x} \in X$ in the direction $d \in X$ is given by (see [15])

$$\begin{aligned} f^\circ(\overline{x}; d) &= \lim_{y \longrightarrow \overline{x}} \sup_{\lambda \longrightarrow 0^+} \frac{f(y + \lambda d) - f(y)}{\lambda}, \\ \partial f(\overline{x}) &= \{\xi \in X^*: f^\circ(\overline{x}; d) \geq \langle \xi, d\rangle, \quad \forall d \in X\}, \end{aligned} \tag{8}$$

which is defined as the Clarke subdifferential of f at $\overline{x}$.

We present below some significant properties of locally Lipschitz function that we shall use in the sequel.

Lemma 2 (see [15,17]). *Let function $f: K \subset X \longrightarrow \mathbb{R}$ is locally Lipschitz at $\overline{x} \in K$, if $\overline{x}$ is the minimum value point of f on K, then*

$$0 \in \partial f(\overline{x}) + N(\overline{x}; K). \tag{9}$$

Lemma 3 (see [15]). *Let $f_i: X \longrightarrow \mathbb{R}$, $i = 1, \ldots, m$, be locally Lipschitz at $\overline{x} \in X$, then function $\varphi(\cdot) := \max\{f_i(\cdot): i = 1, \ldots, m\}$ is also locally Lipschitz at $\overline{x}$, and*

$$\begin{aligned} \partial\varphi(\overline{x}) &\subset \bigcup \left\{ \sum_{i=1}^m \lambda_i \partial f_i(\overline{x}): \lambda_i \geq 0, \quad i = 1, 2, \ldots m, \ \sum_{i=1}^m \lambda_i = 1, \quad \lambda_i(f_i(\overline{x}) - \varphi(\overline{x})) = 0 \right\}, \\ \partial(f_1 + \cdots + f_m)(\overline{x}) &\subset \partial f_1(\overline{x}) + \cdots + \partial f_m(\overline{x}). \end{aligned} \tag{10}$$

Let $K \subset X$ be a nonempty subset, and $F: K \times K \longrightarrow Y$ be a mapping. Consider the following vector equilibrium problem (VEP):

$$\text{(VEP) find}\, \overline{x} \in K, \text{such that}\, F(\overline{x}, x) \notin -Q\backslash\{0\}, \quad \forall x \in K. \tag{11}$$

Given $\overline{x} \in K$, $F_{\overline{x}}: K \longrightarrow Y$ be vector-valued mapping of one variable, which is defined by

$$F_{\overline{x}}(x) \coloneqq F(\overline{x}, x), \quad \forall x \in K. \tag{12}$$

Throughout this paper, it is always assumed that $F_{\overline{x}}(\overline{x}) = 0$ and

$$F_{\overline{x}}(K) = F(\overline{x}, K) = \bigcup_{x \in K} F(\overline{x}, x). \tag{13}$$

Definition 1 (see [10]). Let $K \subset X$ be a nonempty subset, $\varepsilon \geq 0$, $e \in \text{int}Q$. $\overline{x} \in K$ is called an εe-quasi weak efficient solution to VEP, if

$$F(\overline{x}, x) + \varepsilon \|x - \overline{x}\| e \notin -\text{int}Q, \quad \forall x \in K. \tag{14}$$

The notion of εe-quasi weak efficient solution is illustrated by the following example.

Example 1. Let $X = Y = \mathbb{R}$, $K = \mathbb{R}_+$, $Q = \mathbb{R}_+^2$, and $\overline{x} \in K$. Consider the following questions:

$$F(\overline{x}, x) = (-|x - \overline{x}|, |x - \overline{x} - |x - \overline{x}|), \quad \forall x \in K. \tag{15}$$

Taking $\varepsilon = 1$ and $e = (1, 1)$, then

$$\begin{aligned} F(\overline{x}, x) + \varepsilon \|x - \overline{x}\| e &= (-|x - \overline{x}|, |x - \overline{x} - |x - \overline{x}|) \\ &\quad + (|x - \overline{x}|, |x - \overline{x}|) \\ &= (0,\ x - \overline{x}). \end{aligned} \tag{16}$$

Taking $\overline{x} = 0$, for all $x \in K$, we obtain

$$F(\overline{x}, x) + \varepsilon \|x - \overline{x}\| e = (0,\ x) \notin -\text{int}Q. \tag{17}$$

Hence, 0 is an εe-quasi weak efficient solution of VEP.

It is well known that, for a nonempty convex set, its interior may be empty, but its quasirelative interior is always nonempty (see [18]). In this paper, we will prove the optimality condition of VEP by the separation theorem with respect to the quasirelative interior of convex sets (see [19]).

Definition 2 (see [18]). Let $K \subset X$ is a convex subset; the quasirelative interior of K denoted by $\text{qri}K$ is defined as

$$\text{qri}K = \{x \in K: \ \text{clcone}(K - x) \text{ is a linear subset of } X\}, \tag{18}$$

where cl and cone stand for closure and cone hull.

Lemma 4 (see [19]). *Let M and N be nonempty convex subsets of Y, $\text{qri}M \neq \emptyset$ and $\text{qri}N \neq \emptyset$, and clcone $(\text{qri}M - \text{qri}N)$ is not a linear subset of Y, then there exists $\lambda \in Y^* \backslash \{0\}$ such that*

$$\langle \lambda, m \rangle \leq \langle \lambda, n \rangle, \quad \forall m \in M, \forall n \in N. \tag{19}$$

3. Optimality Conditions

In this section, first, we propose a necessary optimality condition for εe-quasi weak efficient solutions to VEP by using separation theorem in terms of quasirelative interiors of a convex set. Second, the concept of approximate quasi-pseudoconvex function is introduced and a sufficient optimality conditions is established under the introduced generalized convexity. Throughout this section, let $K \subset X$ be a nonempty convex set.

Theorem 1. *In VEP, let $\overline{x} \in K$, $\varepsilon \geq 0$, and $e \in \text{int}Q$. Assume that $\overline{x}$ be an εe-quasi weak efficient solution of VEP and $F_{\overline{x}}: X \longrightarrow Y$ is locally Lipschitz mapping at $\overline{x}$. In addition, $\text{qri}F_{\overline{x}}(K) \neq \emptyset$ and clcone $[\text{qri}(\text{co}F_{\overline{x}}(K)) + \text{qri}Q]$ is not a linear subspace of Y. Then, there exist $\lambda \in Q^* \backslash \{0\}$ such that*

$$0 \in \partial(\lambda \circ F_{\overline{x}}(\overline{x})) + N(\overline{x}; K) + \langle \lambda, e \rangle \varepsilon \mathbb{B}, \tag{20}$$

where $\text{co}(\cdot)$ stands for the convex hull, $\mathbb{B} := \mathbb{B}(0, 1)$, and $\lambda^\circ F_{\overline{x}}(\cdot) := \langle \lambda, F_{\overline{x}}(\cdot) \rangle$.

Proof 1. Since

$$\text{qri}Q = -\text{qri}(-Q), \tag{21}$$

and clcone $[\text{qri}(\text{co}F_{\overline{x}}(K)) + \text{qri}Q]$ is not a linear subspace of Y, then clcone $[\text{qri}(\text{co}F_{\overline{x}}(K)) - \text{qri}(-Q)]$ is not a linear subspace of Y. Moreover,

$$\text{qri}F_{\overline{x}}(K) \neq \emptyset. \tag{22}$$

Thus,

$$\text{qri}\left[\text{co}F_{\overline{x}}(K)\right] \neq \emptyset. \tag{23}$$

Noticing that $\text{qri}Q \neq \emptyset$, it follows from Lemma 4 that there exists $\lambda \in Y^* \backslash \{0\}$ such that

$$\langle \lambda, q \rangle \leq \langle \lambda, x \rangle, \quad \forall q \in -Q, \forall x \in \text{co}F_{\overline{x}}(K), \tag{24}$$

which means

$$\langle \lambda, q \rangle \leq \langle \lambda, F_{\overline{x}}(x) \rangle, \quad \forall q \in -Q, \forall x \in K. \tag{25}$$

Taking $x = \overline{x}$ in the above formula, we obtain

$$\langle \lambda, q \rangle \leq 0, \quad \forall q \in -Q. \tag{26}$$

Hence, $\lambda \in Q^* \backslash \{0\}$. Since

$$F(\overline{x}, x) + \varepsilon \|x - \overline{x}\| e \notin -\text{int}Q, \quad \forall x \in K, \tag{27}$$

and $F(\overline{x}, \overline{x}) = 0$, it leads to

$$F(\overline{x}, x) - F(\overline{x}, \overline{x}) + \varepsilon \|x - \overline{x}\| e \notin -\text{int}Q, \quad \forall x \in K. \tag{28}$$

It follows from $\lambda \in Q^* \backslash \{0\}$ and equation (28) that

$$\langle \lambda, F(\overline{x}, x) - F(\overline{x}, \overline{x}) + \varepsilon \|x - \overline{x}\| e \rangle \geq 0, \quad \forall x \in K, \tag{29}$$

that is

$$\langle \lambda, F_{\overline{x}}(x) \rangle - \langle \lambda, F_{\overline{x}}(\overline{x}) \rangle + \langle \lambda, e \rangle \varepsilon \|x - \overline{x}\| \geq 0, \quad \forall x \in K. \tag{30}$$

On the other hand, let $f := \lambda \circ F_{\overline{x}}$. Since $F_{\overline{x}}$ is locally Lipschitz at $\overline{x}$, it is obvious that f is a locally Lipschitz function at $\overline{x}$. We set

$$\varphi(x) = f(x) - f(\overline{x}) + \langle \lambda, e \rangle \varepsilon \|x - \overline{x}\|, \quad \forall x \in K. \tag{31}$$

It follows from equation (29) that

$$\varphi(x) \geq 0 = \varphi(\overline{x}), \quad \forall x \in K, \tag{32}$$

which shows that $\overline{x}$ is the minimum point of $\varphi(x)$ on K. Taking account of Lemma 2, we arrive at

$$0 \in \partial\varphi(\overline{x}) + N(\overline{x}; K). \tag{33}$$

Since f is a locally Lipschitz function at $\overline{x}$, by Lemma 3, we have

$$\begin{aligned} \partial\varphi(\overline{x}) &\subset \partial(f + \langle\lambda, e\rangle\varepsilon\|\cdot - \overline{x}\|)(\overline{x}), \\ &\subset \partial\left(\lambda \circ F_{\overline{x}}(\overline{x})\right) + \langle\lambda, e\rangle\varepsilon\mathbb{B}. \end{aligned} \tag{34}$$

Together with equation (33), we obtain

$$0 \in \partial\left(\lambda \circ F_{\overline{x}}(\overline{x})\right) + N(\overline{x}; K) + \langle\lambda, e\rangle\varepsilon\mathbb{B}. \tag{35}$$

Next, we introduce the concept of approximate quasi-pseudoconvex function, and under the assumption of this generalized convexity, a sufficient optimality condition for εe-quasi weak efficient solutions to VEP is derived.

Definition 3. Let $\varepsilon \geq 0$ and the function $f: X \longrightarrow \mathbb{R}$ be locally Lipschitz at $\overline{x} \in X$. f is said to be ε-quasi-pseudo-convex at $\overline{x}$, if there exists $\xi \in \partial f(\overline{x})$ such that for each $x \in X$ satisfying

$$\langle\xi, x - \overline{x}\rangle + \varepsilon\|x - \overline{x}\| \geq 0 \Longrightarrow f(x) - f(\overline{x}) + \varepsilon\|x - \overline{x}\| \geq 0. \tag{36}$$

Example 2. Let $X = \mathbb{R}$, then $f: \mathbb{R} \longrightarrow \mathbb{R}$ is defined by

$$f(x) = \begin{cases} \dfrac{2}{3}x^2 + x, & \text{if } x < 0, \\ \ln(x+1), & \text{if } x \geq 0. \end{cases} \tag{37}$$

Taking $\varepsilon = 1$ and $\overline{x} = 0$, by a simple computation, we derive $\partial f(\overline{x}) = \{1\}$. For any $x \in \mathbb{R}$, $1 = \xi \in \partial f(0)$, if

$$\langle\xi, x - \overline{x}\rangle + \varepsilon\|x - \overline{x}\| = 1 \cdot x + 1 \cdot |x| \geq 0, \tag{38}$$

then

$$f(x) - f(\overline{x}) + \varepsilon\|x - \overline{x}\| = f(x) + 1 \cdot |x| = \begin{cases} \dfrac{2}{3}x^2 \geq 0, & x < 0, \\ \ln(x+1) + x \geq 0, & x \geq 0. \end{cases} \tag{39}$$

Thus, f is a 1-quasi-pseudoconvex at 0.

Theorem 2. *In VEP, let $\varepsilon \geq 0$, $e \in \text{int}Q$, $\overline{x} \in K$, and $F_{\overline{x}}: K \longrightarrow Y$ be locally Lipschitz at $\overline{x}$. Suppose that there exists $\lambda \in Q^* \backslash \{0\}$ such that*

$$0 \in \partial\left(\lambda \circ F_{\overline{x}}(\overline{x})\right) + N(\overline{x}; K) + \langle\lambda, e\rangle\varepsilon\mathbb{B}. \tag{40}$$

If $\lambda \circ F_{\overline{x}}: K \longrightarrow \mathbb{R}$ is $\langle\lambda, e\rangle\varepsilon$-quasi-pseudoconvex at $\overline{x}$, then $\overline{x}$ is εe-quasi weak efficient solutions of VEP.

Proof 2. It follows from (40) that there exist $\xi \in \partial(\lambda \circ F_{\overline{x}}(\overline{x}))$, $\sigma \in N(\overline{x}; K)$, and $b \in \mathbb{B}$ such that

$$\xi + \sigma + \langle\lambda, e\rangle\varepsilon b = 0, \tag{41}$$

which implies for each $x \in K$,

$$\langle\xi + \sigma + \langle\lambda, e\rangle\varepsilon b,\ x - \overline{x}\rangle = 0, \tag{42}$$

which is equivalent to

$$\langle\xi, x - \overline{x}\rangle + \langle\sigma, x - \overline{x}\rangle + \langle\lambda, e\rangle\varepsilon\langle b, x - \overline{x}\rangle = 0, \quad \forall x \in K. \tag{43}$$

Since K is a convex set, according to the definition of contingent cone to set K at $\overline{x}$,

$$T(\overline{x}; K) = \text{cl}\{y \in X:\ y = \beta(x - \overline{x}), \quad x \in K, \beta > 0\}. \tag{44}$$

Therefore,

$$\langle\sigma, x - \overline{x}\rangle \leq 0, \quad \forall x \in K. \tag{45}$$

Combining (43) and (44), it is not difficult to find

$$\langle\xi, x - \overline{x}\rangle + \langle\lambda, e\rangle\varepsilon\langle b, x - \overline{x}\rangle \geq 0, \quad \forall x \in K. \tag{46}$$

Because $b \in \mathbb{B}$, we obtain $\|b\| = 1$. Hence,

$$\langle b, x - \overline{x}\rangle \leq \|x - \overline{x}\|, \quad \forall x \in K. \tag{47}$$

Together with equation (46), it leads to

$$\langle\xi, x - \overline{x}\rangle + \langle\lambda, e\rangle\varepsilon\|x - \overline{x}\| \geq 0, \quad \forall x \in K. \tag{48}$$

Since $\lambda \circ F_{\overline{x}}$ is $\langle\lambda, e\rangle\varepsilon$-quasi-pseudoconvex at $\overline{x}$, by Definition 3, we obtain

$$\lambda \circ F_{\overline{x}}(x) - \lambda \circ F_{\overline{x}}(\overline{x}) + \langle\lambda, e\rangle\varepsilon\|x - \overline{x}\| \geq 0, \quad \forall x \in K. \tag{49}$$

In view of $F_{\overline{x}}(\overline{x}) = 0$, we arrive at

$$\lambda \circ F_{\overline{x}}(x) + \langle\lambda, e\rangle\varepsilon\|x - \overline{x}\| \geq 0, \quad \forall x \in K. \tag{50}$$

Suppose that $\overline{x}$ is not εe-quasi weak efficient solutions of VEP, then there exists $\widehat{x} \in K$ such that

$$F(\overline{x}, \widehat{x}) + \varepsilon\|\widehat{x} - \overline{x}\|e \in -\text{int}Q. \tag{51}$$

Since $\lambda \in Q^* \backslash \{0\}$, it yields from Lemma 1 that

$$\langle\lambda, F(\overline{x}, \widehat{x}) + \varepsilon\|\widehat{x} - \overline{x}\|e\rangle < 0, \tag{52}$$

which means

$$\langle\lambda, F(\overline{x}, \widehat{x})\rangle + \langle\lambda, \varepsilon\|\widehat{x} - \overline{x}\|e\rangle < 0. \tag{53}$$

That is,

$$\lambda \circ F_{\overline{x}}(\widehat{x}) + \langle\lambda, e\rangle\varepsilon\|\widehat{x} - \overline{x}\| < 0, \tag{54}$$

which contradicts (50). Hence, $\overline{x}$ is εe-quasi weak efficient solutions of VEP.

4. Scalarization

In this section, the scalarization theorems for approximate quasi weak efficient solutions to VEP are established by using Tammer's function and the directed distance function, respectively.

4.1. Scalarization via Tammer's Function

Lemma 5 (see [20]). *Let $Q \subset Y$ is a pointed closed convex cone and $e \in \text{int}Q \neq \varnothing$ is a fixed element, then Tammer's function Ψ_e^Q: $Y \longrightarrow \mathbb{R}$ ($\mathbb{R}$ represents the set of real number) is defined by*

$$\Psi_e^Q(y) = \inf\{t \in R: y \in te - Q\}, \quad y \in Y. \tag{55}$$

Then, Ψ_e^Q is continuous sublinear functional and

$$\left\{y \in Y: \Psi_e^Q(y) < 0\right\} = -\text{int}Q. \tag{56}$$

Definition 4. Let K be a nonempty subset of X, $\varepsilon \geq 0$, and $f: X \longrightarrow \mathbb{R}$ is a real-valued function. Define optimization problem (P) as follows:

$$(P)\inf f(x), \quad \text{s.t. } x \in K. \tag{57}$$

$\overline{x}$ is called a ε-quasi-optimality solution of (P) if

$$f(x) - f(\overline{x}) + \varepsilon\|x - \overline{x}\| \geq 0, \quad \forall x \in K. \tag{58}$$

Let $\overline{x} \in K$ and $e \in \text{int}Q$. Based on VEP and Tammer's function Ψ_e^Q, consider the following scalarization problem $(P_{\Psi_e^Q})$:

$$\left(P_{\Psi_e^Q}\right)\inf\Psi_e^Q\left(F_{\overline{x}}(x)\right), \quad \text{s.t. } x \in K. \tag{59}$$

Theorem 3. *Let $\varepsilon \geq 0$ and $e \in \text{int}Q$. If $\overline{x} \in K$ is εe-quasi weak efficient solutions of VEP, then $\overline{x}$ is ε-quasi-optimality solutions of scalarization problem $(P_{\Psi_e^Q})$.*

Proof 3. Since $\overline{x} \in K$ is εe-quasi weak efficient solutions of VEP, then

$$F(\overline{x}, x) + \varepsilon\|x - \overline{x}\|e \notin -\text{int}Q, \quad \forall x \in K. \tag{60}$$

Considering Tammer's nonlinear scalarization function Ψ_e^Q,

$$\Psi_e^Q(y) = \inf\{t \in \mathbb{R}: y \in te - Q\}, \quad y \in Y. \tag{61}$$

According to Lemma 5 and combining (60) and (61) yield that

$$\Psi_e^Q(F(\overline{x}, x) + \varepsilon\|x - \overline{x}\|e) \geq 0, \quad \forall x \in K. \tag{62}$$

Since Ψ_e^Q is continuous sublinear functional, it holds that

$$\Psi_e^Q(F(\overline{x}, x)) + \varepsilon\|x - \overline{x}\| \geq 0, \quad \forall x \in K. \tag{63}$$

Since $F(\overline{x}, \overline{x}) = 0$, then

$$\Psi_e^Q(F(\overline{x}, x)) - \Psi_e^Q(F(\overline{x}, \overline{x})) + \varepsilon\|x - \overline{x}\| \geq 0, \quad \forall x \in K. \tag{64}$$

Therefore, $\overline{x}$ is ε-quasi-optimality solutions of scalarization problem $(P_{\Psi_e^Q})$.

Theorem 4. *Let $\varepsilon \geq 0$, $e \in \text{int}Q$, and $\overline{x} \in K$. Suppose function $\varphi: Y \longrightarrow \mathbb{R}$ satisfying the following:*

(i) φ is monotone with respect to the pointed closed convex cone Q, that is, if $y_1 - y_2 \in Q$, then $\varphi(y_1) \geq \varphi(y_2)$

(ii) $\varphi(0) = 0$, and φ is positively homogeneous functional that means $\varphi(ay) = a\varphi(y)$, $a > 0$

(iii) $\varphi(-\varepsilon e) < -\varepsilon$

Let scalarization problem (P_φ) be defined by

$$\left(P_\varphi\right)\inf\varphi\left(F_{\overline{x}}(x)\right), \quad \text{s.t. } x \in K. \tag{65}$$

If $\overline{x}$ is ε-quasi-optimality solutions of scalarization problem (P_φ), then $\overline{x}$ is εe-quasi weak efficient solutions of VEP.

Proof 4. If $\overline{x}$ is not εe-quasi weak efficient solutions of VEP, there would exist $\widehat{x} \in K$ such that

$$F(\overline{x}, \widehat{x}) + \varepsilon\|\widehat{x} - \overline{x}\|e \in -\text{int}Q, \tag{66}$$

which is equivalent to

$$-\varepsilon\|\widehat{x} - \overline{x}\|e - F(\overline{x}, \widehat{x}) \in \text{int}Q. \tag{67}$$

Then, we have

$$-\varepsilon\|\widehat{x} - \overline{x}\|e - F(\overline{x}, \widehat{x}) \in Q. \tag{68}$$

Since φ is monotone with respect to Q,

$$\varphi(F(\overline{x}, \widehat{x})) \leq \varphi(-\varepsilon\|\widehat{x} - \overline{x}\|e). \tag{69}$$

Noticing that $\overline{x}$ is ε-quasi-optimality solutions of problem (P_φ), we obtain

$$\varphi(F(\overline{x}, \widehat{x})) - \varphi(F(\overline{x}, \overline{x})) + \varepsilon\|\widehat{x} - \overline{x}\| \geq 0. \tag{70}$$

Because $F(\overline{x}, \overline{x}) = 0$ and $\varphi(0) = 0$, it holds that

$$\varphi(F(\overline{x}, \widehat{x})) + \varepsilon\|\widehat{x} - \overline{x}\| \geq 0. \tag{71}$$

Combining (69) and (71), we obtain

$$\varphi(-\varepsilon\|\widehat{x} - \overline{x}\|e) \geq -\varepsilon\|\widehat{x} - \overline{x}\|. \tag{72}$$

Since φ is positively homogeneous functional,

$$\varphi(-\varepsilon e) \geq -\varepsilon, \tag{73}$$

which contradicts to condition (iii).

4.2. Scalarization via the Directed Distance Function. Let us introduce the concept of directed distance function.

Definition 5 (see [21]). Let $A \subseteq Y$ is a nonempty subset, then the directed distance function $\Delta_A: Y \longrightarrow \mathbb{R}$ be defined as

$$\Delta_A(y) = d_A(y) - d_{Y\setminus A}(y), \quad y \in Y, \tag{74}$$

where

$$d_A(y) = \inf_{x \in A}\|y - x\|. \tag{75}$$

Lemma 6 (see [21]). *Let $A \subseteq Y$ is a nonempty subset, then the following properties hold:*

(i) Δ_A is real-valued Lipschitz function of rank 1.

(ii) If A is closed, then $A = \{y: \Delta_A(y) \leq 0\}$; if A is a cone, then $\triangle_A$ is positively homogeneous; if A is pointed closed convex cone, then Δ_A is sublinear.

(iii) If A is closed convex cone, then Δ_A is nonincreasing with respect to A, that is, if $y_1, y_2 \in Y$, then

$$y_1 - y_2 \in A \Longrightarrow \Delta_A(y_1) \leq \Delta_A(y_2); y_1 - y_2 \in \text{int}A \Longrightarrow \Delta_A(y_1) < \Delta_A(y_2). \tag{76}$$

Let $e \in \text{int}Q$ and $\overline{x} \in K$. Based on VEP and the directed distance function Δ_{-Q}, consider the following scalarization problem $(P_{\Delta_{-Q}})$:

$$\left(P_{\Delta_{-Q}}\right) \inf \Delta_{-Q}(F_{\overline{x}}(x)), \quad \text{s.t. } x \in K. \tag{77}$$

Theorem 5. *Let $\varepsilon > 0$, $e \in \text{int}Q$ with $\|e\| = 1$, and $\overline{x} \in K$. If $\overline{x}$ is εe-quasi weak efficient solutions to VEP, then for any $x \in K$, $\overline{x}$ is an ε-quasi-optimality solution of scalarization problem $(P_{\Delta_{-Q}})$.*

Proof 5. By the given conditions, we have

$$F(\overline{x}, x) + \varepsilon \|x - \overline{x}\| e \notin -\text{int}Q, \quad \forall x \in K. \tag{78}$$

Since Q is a pointed closed convex cone, by Lemma 6, it yields that

$$\Delta_{-Q}(F(\overline{x}, x)) + \varepsilon \|x - \overline{x}\|_{-Q}(e) \geq \Delta_{-Q}(F(\overline{x}, x) + \|x - \overline{x}\| e) \geq 0, \quad \forall x \in K. \tag{79}$$

Noticing that $\Delta_{-Q}(e) = \|e\| = 1$, $F(\overline{x}, \overline{x}) = 0$, and $\Delta_{-Q}(0) = 0$, we arrive at

$$\Delta_{-Q}(F(\overline{x}, x)) - \Delta_{-Q}(F(\overline{x}, x)) + \varepsilon \|x - \overline{x}\| \geq 0, \quad \forall x \in K. \tag{80}$$

Hence, $\overline{x}$ is an ε-quasi-optimality solution of scalarization problem $(P_{\Delta_{-Q}})$.

5. Conclusions

Making use of the quasirelative interior-type separation theorem of convex set, we have examined the optimality condition of the approximate quasi weak efficient solutions of VEP. In addition, the scalarization theorems of approximate quasi weak efficient solutions to VEP are also established via using Tammer's function and directed distance function, respectively, and scalarization theorems realize the purpose that solving the approximate quasi weak efficient solutions of vector equilibrium problem is equivalent to solving the approximate quasi-optimality solution of a specific scalar optimization problem.

Abbreviations

VEP: Vector equilibrium problem.

Data Availability

No data were used to support the findings of this study.

Conflicts of Interest

The authors declare that they have no conflicts of interest.

Authors' Contributions

All authors contributed equally to the manuscript and read and approved the final version of the manuscript.

Acknowledgments

This research was supported by the Natural Science Foundation of China under Grant no. 11861002, Natural Science Foundation of Ningxia under Grant no. NZ17112, The Key Project of North Minzu University under Grant no. ZDZX201804, and Nonlinear Analysis and Financial Optimization Research Center of North Minzu University.

References

[1] D. Luu and D. Hang, "Efficient solutions and optimality conditions for vector equilibrium problems," *Mathematical Methods of Operations Research*, vol. 79, no. 2, pp. 163–177, 2014.

[2] Y. Feng and Q. Qiu, "Optimality conditions for vector equilibrium problems with constraint in Banach spaces," *Optimization Letters*, vol. 8, no. 6, pp. 1931–1944, 2014.

[3] Z. F. Wei and X. H. Gong, "Kuhn-Tucker optimality conditions for vector equilibrium problems," *Journal of Inequalities and Applications*, vol. 2010, no. 1, 15 pages, Article ID 842715, 2010.

[4] X. H. Gong, W. T. Fu, and W. Liu, "Super efficiency for avector equilibrium in locally convex topological vector-spaces," in *Vector Variational Inequalities and Vector Equilibria: Mathematical Theories,* F. Giannessi, Ed., pp. 233–252, Kluwer, Alphen Aan Den Rijn, Netherlands, 2000.

[5] X.-H. Gong, "Optimality conditions for Henig and globally proper efficient solutions with ordering cone has empty

interior," *Journal of Mathematical Analysis and Applications*, vol. 307, no. 1, pp. 12–31, 2005.

[6] X.-H. Gong, "Scalarization and optimality conditions for vector equilibrium problems," *Nonlinear Analysis: Theory, Methods & Applications*, vol. 73, no. 11, pp. 3598–3612, 2010.

[7] X. J. Long, Y. Q. Huang, and Z. Y. Peng, "Optimality conditions for the Henig efficient solution of vector equilibrium problems with constraints," *Optimization Letters*, vol. 5, no. 4, pp. 717–728, 2011.

[8] Q. Qiu and X. Yang, "Some properties of approximate solutions for vector optimization problem with set-valued functions," *Journal of Global Optimization*, vol. 47, no. 1, pp. 1–12, 2010.

[9] Q. Qiu, X. M. Yang, and X. Yang, "Scalarization of approximate solution for vector equilibrium problems," *Journal of Industrial & Management Optimization*, vol. 9, no. 1, pp. 143–151, 2013.

[10] K. Das and C. Nahak, "Optimality conditions for approximate quasi efficiency in set-valued equilibrium problems," *SeMA Journal*, vol. 73, no. 2, pp. 183–199, 2016.

[11] X.-H. Gong, H.-B. Dong, and S.-Y. Wang, "Optimality conditions for proper efficient solutions of vector set-valued optimization," *Journal of Mathematical Analysis and Applications*, vol. 284, no. 1, pp. 332–350, 2003.

[12] X.-H. Gong, "Optimality conditions for vector equilibrium problems," *Journal of Mathematical Analysis and Applications*, vol. 342, no. 2, pp. 1455–1466, 2008.

[13] P. Q. Khanh and L. T. Tung, "First and second-order optimality conditions using approximations for vector equilibrium problems with constraints," *Journal of Global Optimization*, vol. 55, no. 4, pp. 901–920, 2013.

[14] Q. S. Qiu, "Optimality conditions of globally efficient solution for vector equilibrium problems with generalized convexity," *Journal of Inequalities and Applications*, vol. 2009, no. 1, 13 pages, Article ID 898213, 2009.

[15] F. H. Clarke, *Optimization and Nonsmooth Analysis*, John Wiley and Sons, New York, NY, USA, 1983.

[16] J. Jahn, *Mathematical Vector Optimization in Partially Ordered Linear Spaces*, Verlag Peter Lang, Frankfurt, Germany, 1986.

[17] X. J. Long, Y. B. Xiao, and N. J. Huang, "Optimality conditions of approximate solutions for nonsmooth semi-infinite programming problems," *Journal of the Operations Research Society of China*, vol. 6, no. 2, pp. 1–11, 2017.

[18] J. M. Borwein and A. S. Lewis, "Partially finite convex programming, part I: quasi relative interiors and duality theory," *Mathematical Programming*, vol. 57, no. 1–3, pp. 15–48, 1992.

[19] F. Cammaroto and B. D. Bella, "Separation theorem based on the quasirelative interior and application to duality theory," *Journal of Optimization Theory and Applications*, vol. 125, no. 1, pp. 223–229, 2005.

[20] C. Gerth and P. Weidner, "Nonconvex separation theorems and some applications in vector optimization," *Journal of Optimization Theory and Applications*, vol. 67, no. 2, pp. 297–320, 1990.

[21] A. Zaffaroni, "Degrees of efficiency and degrees of minimality," *SIAM Journal on Control and Optimization*, vol. 42, no. 3, pp. 1071–1086, 2003.

Hindawi
Complexity
Volume 2020, Article ID 8941652, 13 pages
https://doi.org/10.1155/2020/8941652

Research Article

A Penalized h-Likelihood Variable Selection Algorithm for Generalized Linear Regression Models with Random Effects

Yanxi Xie, Yuewen Li, Zhijie Xia, Ruixia Yan, and Dongqing Luan

School of Management, Shanghai University of Engineering Science, Shanghai 201620, China

Correspondence should be addressed to Yuewen Li; sues0305@126.com

Received 31 July 2020; Revised 28 August 2020; Accepted 6 September 2020; Published 15 September 2020

Academic Editor: Shuping He

Reinforcement learning is one of the paradigms and methodologies of machine learning developed in the computational intelligence community. Reinforcement learning algorithms present a major challenge in complex dynamics recently. In the perspective of variable selection, we often come across situations where too many variables are included in the full model at the initial stage of modeling. Due to a high-dimensional and intractable integral of longitudinal data, likelihood inference is computationally challenging. It can be computationally difficult such as very slow convergence or even nonconvergence, for the computationally intensive methods. Recently, hierarchical likelihood (h-likelihood) plays an important role in inferences for models having unobservable or unobserved random variables. This paper focuses linear models with random effects in the mean structure and proposes a penalized h-likelihood algorithm which incorporates variable selection procedures in the setting of mean modeling via h-likelihood. The penalized h-likelihood method avoids the messy integration for the random effects and is computationally efficient. Furthermore, it demonstrates good performance in relevant-variable selection. Throughout theoretical analysis and simulations, it is confirmed that the penalized h-likelihood algorithm produces good fixed effect estimation results and can identify zero regression coefficients in modeling the mean structure.

1. Introduction

Reinforcement learning is specified as trial and error (variation and selection and search) plus learning (association and memory) in Sutton and Barto [1]. Traditional variable selection procedures, such as LASSO in Tibshirani [2] and OMP in Cai and Wang [3], only consider the fixed effect estimates in the linear models in the past literature. However, in real life, a lot of existing data have both the fixed effects and random effects involved. For example, in the clinic trials, several observations are taken for a period of time for one particular patient. After collecting the data needed for all the patients, it is natural to consider random effects for each individual patient in the model setting since a common error term for all the observations is not sufficient to capture the individual randomness. Moreover, random effects, which are not directly observable, are of interest in themselves if inference is focused on each individual's response. Therefore, to solve the problem of the random effects and to get good estimates, Lee and Nelder [4] proposed hierarchical generalized linear models (HGLMs). HGLMs are based on the idea of h-likelihood, a generalization of the classical likelihood to accommodate the random components coming through the model. It is preferable because it avoids the integration part for the marginal likelihood and uses the conditional distribution instead.

Inspired by the idea of reinforcement learning and hierarchical models, this paper proposes a method by adding a penalty term to the h-likelihood. This method considers not only the fixed effects but also the random effects in the linear model, and it produces good estimation results with the ability to identify zero regression coefficients in joint models of mean-covariance structures for high-dimensional multilevel data.

The rest of this paper is organized as follows: Section 2 provides the literature review on current variable selection methods based on partial linear models and h-likelihood. Section 3 explains a penalty-based h-likelihood variable

selection algorithm and demonstrates via simulation that our proposed algorithm exhibits desired sample properties and can be useful in practical applications. Finally, Section 4 concludes the paper, and some future research directions are given.

2. Literature Review

2.1. Reinforcement Learning in the Perspective of Nonlinear Systems. Reinforcement learning, one of the most active research areas in artificial intelligence, is introduced and defined as a computational approach to learning whereby an agent tries to maximize the total amount of reward it receives when interacting with a complex, uncertain environment in Sutton and Barto [1]. In addition, in the paper of Sutton and Barto [5], reinforcement learning is specified to be trial and error (variation and selection and search) plus learning (association and memory). Furthermore, Barto and Mahadevan [6] propose hierarchical control architectures and associated learning algorithms. Approaches to temporal abstraction and hierarchical organization, which mainly rely on the theory of semi-Markov decision processes, are reviewed and discussed in Barto and Mahadevan's paper [6]. Recent works, such as Dietterich [7], have focused on the hierarchical methods that incorporate subroutines and state abstractions, instead of solving "flat" problem spaces.

Nonlinear control design has gained a lot of attention in the research area for a long time. In the industrial field, the controlled system usually has great nonlinearity. Various adaptive optimal control models have been applied to the identification of nonlinear systems in the past literature. In fact, the two important fundamental principles of controller design are optimality and veracity. He et al. [8] study a novel policy iterative scheme for the design of online H_∞ optimal laws for a class of nonlinear systems and establishes the convergence of the novel policy iterative scheme to the optimal control law. He et al. [9] investigate an online adaptive optimal control problem of a class of continuous-time Markov jump linear systems (MJLSs) by using a parallel reinforcement learning (RL) algorithm with completely unknown dynamics. A novel parallel RL algorithm is proposed, and the convergence of the proposed algorithm is shown. Wang et al. [10] study a new online adaptive optimal controller design scheme for a class of nonlinear systems with input time delays. An online policy iteration algorithm is proposed, and the effectiveness of the proposed method is verified. He et al. [11] propose the online adaptive optimal controller design for a class of nonlinear systems through a novel policy iteration (PI) algorithm. Cheng et al. [12] investigate the observer-based asynchronous fault detection problem for a class of nonlinear Markov jumping systems and introduces a hidden Markov model to ensure that the observer modes run synchronously with the system modes. Cheng et al. [13] propose the finite-time asynchronous output feedback control scheme for a class of Markov jump systems subject to external disturbances and nonlinearities.

2.2. Partial Linear Models. Linear models have been widely used and employed in the literature. One extension of linear models, which was introduced by Nelder and Wedderburn [14], is generalized linear models (GLMs). GLMs allow the class of distributions to be expanded from the normal distribution to that of one-parameter exponential families. In addition, GLMs generalize linear regression in the following two manners: first of all, GLMs allow the linear model to be related to the response variable via a link function, or equivalently a monotonic transform of the mean, rather than the mean itself. Second, GLMs allow the magnitude of the variance of each measurement to be a function of its predicted value.

On the contrary, Laird and Ware [15] propose linear mixed effect models (LMEs), which are widely used in the analysis of longitudinal and repeated measurement data. Linear mixed effect models have gained popular attention since they take into consideration within-cluster and between-cluster variations simultaneously. Vonesh and Chinchilli [16] have investigated and applied statistical estimation as well as inference for this class of LME models. However, it seems that model selection problem in LME models is ignored. This disregarded problem was noticed and pointed out by Vaida and Blanchard [17], stating that when the focus is on clusters instead of population, the traditional selection criteria such as AIC and BIC are not appropriate. In the paper of Vaida and Blanchard [17], the conditional AIC is proposed, for mixed effects models with detailed discussion on how to define degrees of freedom in the presence of random effects. Furthermore, Pu and Niu [18] study the asymptotic behavior of the proposed generalized information criterion method for selecting fixed effects. In addition, Rajaram and Castellani [19] use ordinary differential equations and the linear advection partial differential equations (PDEs) and introduce a case-based density approach to modeling big data longitudinally.

Recently, Fan and Li [20] develop a class of variable selection procedures for both fixed effects and random effects in linear mixed effect models by incorporating the penalized profile likelihood method. By this regularization method, both fixed effects and random effects can be selected and estimated. There are two outstanding aspects regarding Fan and Li's [20] method. First of all, the proposed procedures can estimate the fixed effects and random effects in a separate way. Or in other words, the fixed effects can be estimated without the random effects being estimated, and vice versa. In addition, the method works in the high-dimensional setting by allowing dimension of random effect to grow exponentially with sample size.

Combined with the idea of generalized linear models (GLMs) and linear mixed effect (LME) models, one extension, generalized linear mixed models (GLMMs), is developed. In the traditional GLMs, it is assumed that the observations are uncorrelated. To solve the constrained assumption, GLMMs allow for correlation between observations, which often happens in the longitudinal data and clustered designs. The advantages of GLMMs are presented as follows: first of all, GLMMs allow random effects to be included in the linear predictor. As a result, the correlations

between observations can be explained through an explicit probability model. Second, when the focus is on estimating the fixed effects on a particular individual, GLMMs provide good subject-specific parameter estimates. However, since GLMMs are also called multilevel models, it is generally more computationally intensive when fitting the model.

So far, all those GLMs and GLMMs are well-established parametric regression models. A serious disadvantage of parametric modeling is that a parametric model may be too restrictive in some applications. To overcome this restrictive assumption difficulty in the parametric regression, nonparametric regression has gained popular attention in the literature. There are many nonparametric and smoothing methods, such as kernel smoothing, local polynomial fitting, and penalized splines. In this section, two often-used smoothing methods in estimating a nonparametric model are described in the following paragraphs since they are used later in simulations and applications.

The first type is called local linear kernel smoothing. The main idea of local linear kernel smoothing is to locally approximate the function f linearly. Local linear kernel smoothing uses Taylor expansion as a fundamental tool. In particular, Taylor expansion states that any smooth function can be locally approximated by a polynomial of some degree.

Suppose we have a simple nonparametric model

$$y_i = f(t_i) + \varepsilon_i, \tag{1}$$

for $i = 1, \ldots, n$. Let t_0 be an arbitrary fixed point where the function f is estimated. Assume $f(t)$ has a first-order continuous derivative at t_0. Then, by Taylor expansion, $f(t)$ can be locally approximated by

$$f(t) \approx f(t_0) + (t - t_0) f^{(1)}(t_0), \tag{2}$$

in a neighborhood of t_0 that allows the above expansion where $f^{(1)}(t_0)$ denotes the first derivative of $f(t)$ at t_0.

Let $\alpha_0 = f(t_0)$ and $\alpha_1 = f^{(1)}(t_0)$. The local linear smoother is obtained by fitting a data set locally with a linear function, to minimize the following weighted least squares criterion:

$$\sum_{i=1}^{n} [y_i - \alpha_0 - \alpha_1 (t - t_0)]^2 K_h (t_i - t_0), \tag{3}$$

where $K_h(.) = K(./h)/h$, which is obtained by rescaling a kernel function $K(.)$ with a positive constant bandwidth h. The primary objective of the bandwidth h is to specify the size of the local neighborhood $[t_0 - h, t_0 + h]$, where the local fitting is conducted. Moreover, the kernel function $K(.)$ determines how observations within the neighborhood contribute to the fit at t_0. A detailed introduction of the kernel function will be provided in the later paragraphs.

The local linear smoother $\widehat{f_h(t_0)} = \widehat{\alpha_0}$ can be simply expressed as

$$\widehat{f_h(t_0)} = \frac{\sum_{i=1}^{n} [s_2(t_0) - s_1(t_0)(t - t_0)] K_h(t_i - t_0) y_i}{s_2(t_0) s_0(t_0) - s_1^2(t_0)}, \tag{4}$$

where

$$\begin{aligned} s_0(t_0) &= \sum_{i=1}^{n} K_h(t_i - t_0), \\ s_1(t_0) &= \sum_{i=1}^{n} K_h(t_i - t_0)(t_i - t_0), \\ s_2(t_0) &= \sum_{i=1}^{n} K_h(t_i - t_0)(t_i - t_0)^2. \end{aligned} \tag{5}$$

A local linear smoother is often good enough for most problems if the kernel function $K(.)$ and the bandwidth h are adequately determined. Moreover, it enjoys many good properties that the other linear smoothers may lack. Fan [21], Fan and Gijbels [22], and Hastie and Loader [23] separately discussed those good properties in detail.

The kernel function $K(.)$ used in the local linear smoother is a symmetric probability density function. The kernel $K(.)$ specifies how the observations contribute to the local linear kernel fit at t_0, whereas the bandwidth h specifies the size of the local neighborhood $[t_0 - h, t_0 + h]$. Several widely used kernel functions include the following:

(i) Uniform $K(u) = (1/2)\mathbf{I}_{\{|u| \le 1\}}$

(ii) Epanechnikov $K(u) = (3/4)(1 - u^2)\mathbf{I}_{\{|u| \le 1\}}$

(iii) Biweight $K(u) = (15/16)(1 - u^2)^2 \mathbf{I}_{\{|u| \le 1\}}$

(iv) Gaussian $K(u) = (1/\sqrt{2\phi})e^{-(1/2)u^2}$

Suppose, for instance, the uniform kernel is used. All the t_i's within the neighborhood $[t_0 - h, t_0 + h]$ contribute equally; or equivalently, the weights are the same, in the local linear kernel fit at t_0; on the contrary, all the t_i's outside the neighborhood $[t_0 - h, t_0 + h]$ contribute nothing. Suppose, for another example, the Gaussian kernel is used. The contribution of the t_i's is determined by the distance of t_i from t_0. In other words, smaller distance $(t - t_0)$ results in larger contribution since the Gaussian kernel is a bell-shaped curve, which peaks at the origin.

The second type of smoothing is called regression spline smoothing. In local linear kernel smoothing introduced above, local neighborhoods were defined by a bandwidth h and a fixed point t_0. On the contrary, in regression spline smoothing that will be introduced shortly, local neighborhoods are defined by a group of locations, known as knots, for example,

$$\tau_0, \tau_1, \ldots, \tau_K, \tau_{K+1}, \tag{6}$$

in an interval $[a, b]$, where $a = \tau_0 < \tau_1 < \cdots < \tau_k < \tau_{k+1} = b$. Moreover, τ_i, $i = 1, 2, \ldots, k$ are referred as interior knots or simple knots. Then, local neighborhoods are divided by these knots, i.e.,

$$[\tau_i, \tau_{i+1}), \quad i = 0, 1, \ldots, k, \tag{7}$$

and within any two neighboring knots, a Taylor's expansion up to some degree is applicable.

A regression spline can be constructed in terms of truncated power basis. As mentioned earlier, there are K knots $\tau_1, \ldots, \tau_K$, and the k-th degree truncated power basis can be expressed as

$$1, t, \ldots, t^k, (t-\tau_1)_+^k, \ldots, (t-\tau_K)_+^k, \quad (8)$$

where a_+^k denotes power k of the positive part of a with $a_+ = \max(0, a)$. In most of the literature, it is called "constant, linear, quadratic, and cubic" truncated power basis when $k = 0$, 1, 2, and 3 correspondingly. For the purpose of this chapter, cubic truncated power basis is used in subsequent sections of simulations and applications.

We still consider the abovementioned simple nonparametric model:

$$y_i = f(t_i) + \varepsilon_i, \quad (9)$$

for $i = 1, \ldots, n$. It is with conventional purpose to denote the truncated basis as

$$\Phi_p(t) = \left[1, t, \ldots, t^k, (t-\tau_1)_+^k, \ldots, (t-\tau_K)_+^k\right]^T, \quad (10)$$

where $p = K + k + 1$ is the number of the basis functions involved. Then, the regression fit of the function $f(t)$ in the nonparametric model can be expressed as

$$\widehat{f}_p(t) = \Phi_p(t)^T \left(X^T X\right)^{-1} X^T y, \quad (11)$$

where $y = (y_1, \ldots, y_n)^T$ and $X = (\Phi_p(t_1), \ldots, \Phi_p(t_n))^T$.

To sum up, parametric models are very useful for longitudinal data analysis since they provide a clear and easy description of the relationship between the response variable and its covariates. However, in most of data analysis, the parametric model does not fit the data well, resulting in biased estimates. To overcome the restricted assumptions on parametric forms, various nonparametric models such as nonparametric mixed effects models have been proposed for longitudinal data. Refer, for example, the study by Fan and Zhang [24] and Wu and Rice [25] among others. There is always a trade-off model assumption and model complexity. Parametric models are less robust against model assumptions, but they are efficient when the models are corrected assigned. On the contrary, nonparametric models are more robust against model assumptions, but they are less efficient and more complex. A trade-off between efficiency and complexity by the information measure is fully investigated and discussed in Caves and Schack [26]. Zhang et al. [27] propose an improved K-means clustering algorithm, which is called the covering K-means algorithm (C-K-means). There are two advantages for the C-K-means algorithm. First of all, it acquires efficient and accurate clustering results under both sequential and parallel conditions. Furthermore, it self-adaptively provides a reasonable number of clusters based on the data features.

Semiparametric models come across in the need to compromise and remain good features of both parametric and nonparametric models. In semiparametric models, parametric component and nonparametric component are the two essential components. More specifically, the parametric component is often used to model important factors that affect the responses parametrically, whereas the nonparametric component is often used for less important and nuisance factors. Various semiparametric models for longitudinal data include semiparametric population mean models proposed in Martinussen and Scheike [28] and Xu [29], among others, and semiparametric mixed effects models in the study by Zeger and Diggle [30], Groll and Tutz [31], and Heckman et al. [32]. For the purpose of this paper, we restrict our attention to partially linear regression models.

2.3. h-Likelihood. In longitudinal studies, there are two types of models, marginal models, and conditional models. By definition, marginal models are usually referred as population-average models by ignoring the cluster random effects. In contrast, conditional models have random effect or are subject-specific models. The main difference between marginal and conditional models is whether the regression coefficients describe an individual's response or the marginal response to changing covariates. Or in other words, changing covariates does not attempt to control for unobserved subjects' random effects. Diggle et al. [33] suggested the random effect model for inferences about individual responses and the marginal model for inferences about margins.

The idea of h-likelihood was introduced by Lee and Nelder [4]. h-likelihood is an extension of Fisher likelihood to models of GLMs with additional random effects in the linear predictor. The concept of h-likelihood is for inferences of unobserved random variables. In fact, h-likelihood is a special kind of extended likelihood, where the random effect parameter is specified to satisfy certain conditions as we shall talk more in details later. In the meantime, with the idea of h-likelihood, hierarchical generalized linear models (HGLMs) were introduced as well in Lee and Nelder's [4] paper. This class of hierarchical GLMs allows various distributions of the random component. In addition, these distributions are conjugate to the distributions of the response y. Four conjugate HGLMs were introduced in [4], namely, normal-normal, Poisson-gamma, binomial-beta, and gamma-inverse gamma (Table 1). If we let y be the response and u be the unobserved random component, v is the scale on which the random effect u happens linearly in the linear predictor. In other words, u and v are linked via some strictly monotonic function.

Consider the hierarchical model where $y|v$ and v follow some arbitrary distributions listed in Table 1. The definition of h-likelihood, denoted by l_h, is presented in the following way:

$$l_h = l(\beta, \phi; y \mid v) + l(\alpha; v), \quad (12)$$

where $l(\alpha; v)$ is the log likelihood function of v given parameter α and $l(\beta, \phi; y \mid v)$ is that of $y|v$ given parameter β and ϕ. One point to note is that the h-likelihood is not a traditionally defined likelihood since v are not directly observable. In the traditional standard maximum likelihood estimation for models with random effects, the method is based on the marginal likelihood as the objective function. In this marginal likelihood approach, random effects v are integrated out and what remain in the maximized function are the fixed effects β and dispersion parameter ϕ. There are

Table 1: Conjugate HGLMs.

$y\|u$	u	Link
Normal	Normal	Identity
Poisson	Gamma	Log
Binomial	Beta	Logit
Gamma	Inverse gamma	Log

two disadvantages of the marginal likelihood approach. First of all, the intractable integration of v is with obvious difficulty. In addition, random effects are nonestimable after integration. In contrast, the h-likelihood approach avoids such intractable integration. In fact, as clearly stated by Lee and Nelder [4], "we can treat the h-likelihood as if it were an orthodox likelihood for the fixed effects β and random effects v, where the v are regarded as fixed parameters for realized but unobservable values of the random effects." Furthermore, the h-likelihood allows us to have a fixed effect estimator that is asymptotically efficient as the marginal maximum likelihood estimator. Last but not least, the maximized h-likelihood estimates are derived by solving the two equations simultaneously:

$$\begin{aligned} \frac{\partial l_h}{\partial \beta} &= 0; \\ \frac{\partial l_h}{\partial v} &= 0. \end{aligned} \tag{13}$$

People always expect an outstanding property of likelihood inference to be invariant with respect to transformations. As for maximum h-likelihood estimates, estimates for random effects are invariant with respect to the transformation of the random components of u.

Furthermore, Lee and Nelder [4] mentioned adjusted profile h-likelihood, which is defined in the following way:

$$l(\beta) \approx \left[l_h - \frac{1}{2} \log \det \left\{ \frac{D(l_h)}{2\pi} \right\} \right]_{v=\widehat{v}}, \tag{14}$$

where $D(l_h) = -\partial^2 l_h / \partial v \, \partial v^T$. It eliminates the nuisance effects v from the h-likelihood. Moreover, the $D(l_h)$ part is often referred as the adjusted term for such elimination. In fact, this adjusted profile h-likelihood, which is used for the estimation of dispersion components, acts as an approximation of the marginal likelihood, without integrating v out.

There are a few outstanding contributions in Lee and Nelder's [4] publication. First of all, it widens the choice of random effect distributions in mixed generalized linear models. In addition, it brings about the h-likelihood as a device for estimation and prediction in hierarchical generalized linear models. Compared to the traditional marginal likelihood, the h-likelihood avoids the messy integration for the random effects and hence is convenient to use. Furthermore, maximized h-likelihood estimates are obtained by iteratively solving equation (14). To conclude, the h-likelihood is used for inference about the fixed and random effects given dispersion parameter ϕ.

On the contrary, Lee and Nelder [34] demonstrated the use of an adjusted profile h-likelihood for inference about the dispersion components given fixed and random effects. In this paper, the focus is on the joint modeling of the mean and dispersion structure. Iterative weighted least squares (IWLS) algorithm is used for estimations of both the fixed and random effects by the extended likelihood and dispersion parameters by the adjusted profile likelihood. Later, in [35], the algorithm was adjusted by replacing the extended likelihood to the first-order adjusted profile likelihood, as to estimate fixed effects in the mean structure.

Lee and Nelder [36] proposed a class of double hierarchical generalized linear models in which random effects can be specified for both the mean and dispersion. Compared with HGLMs, double hierarchical generalized linear models allow heavy-tailed distributions to be present in the model. Random effects are introduced in the dispersion model to solve heteroscedasticity between clusters. Then, h-likelihood is applied for statistical references and efficient algorithm, as the synthesis of the inferential tool. In addition, Lee and Noh [37] proposed a class of double hierarchical generalized linear models in which random effects can be specified for both the mean and dispersion, allowing models with heavy-tailed distributions and providing robust estimation against outliers. Greenlaw and Kantabutra [38] address the parallel complexity of hierarchical clustering. Instead of the traditional sequential algorithms, the described top-down algorithm in Greenlaw and Kantabutra [38] is parallelized and the computational cost of the top-down algorithm is with $O(\log n)$ time.

In conclusion, for both hierarchical generalized linear models (HGLMs) and double hierarchical generalized linear models (DHGLMs), h-likelihood plays an important role in inferences for models having unobservable or unobserved random variables. Furthermore, numerical studies have been investigated and shown that h-likelihood gives statistically efficient estimates for HGLMs as well as DHGLMs. In addition, Noh and Lee [39] have shown that the h-likelihood procedure outperforms existing methods, including MCMC-type methods, in terms of bias. Last but not least, compared to the traditional marginal likelihood, the h-likelihood avoids the messy integration for the random effects and hence is convenient to use. Therefore, the h-likelihood method is worth attention.

3. Variable Selection via Penalized h-Likelihood

3.1. Model Setup. Suppose that we have k independent groups and each group contains m subjects. Let y_{ij} be the j^{th} subject of group i, where $i = 1, \ldots, k$ and $j = 1, \ldots, m$. Based on the idea of modeling the mean structure in the HGLM framework, we consider a partial linear model for modeling the conditional mean:

$$g\left(\mu_{ij}\right) = f\left(t_{ij}\right) + x_{ij}^T \beta + v_i, \tag{15}$$

where $f(.)$ is an unknown smooth function in t, t_{ij} is an univariate explanatory variable in $[0, 1]$ for simplicity, $g(.)$ is the canonical link function for the conditional distribution

of y_{ij}, and x_{ij} is a $p \times 1$ covariate vector with β as the associated coefficients. In matrix representation,

$$y = f(t) + X\beta + Zv + \varepsilon. \tag{16}$$

We assume that conditional random variables u_i and y_{ij} are from an exponential family with mean and variance:

$$\begin{aligned} E\left(y_{ij} \mid u_i\right) &= \mu_{ij}, \\ V\left(y_{ij} \mid u_i\right) &= \phi V\left(\mu_{ij}\right). \end{aligned} \tag{17}$$

We also assume that $(X^T, t)^T$ and ε are independent. The random effects presented in the mean model v_i are linked to u_i via the relationship $v_i = v(u_i)$, where $u_i \sim \mathbf{N}(0, \sigma_u^2)$. This allows for the definition of h-likelihood given in Lee and Nelder [4]. In this paper, the identity link $v_i = u_i$ is used, and hence, this canonical scale corresponds to the case that the conditional distribution of the response y is normal, i.e., $y_{ij} \sim \mathbf{N}(\mu_{ij}, \phi)$.

For simplicity, random effects are considered in the form of a random intercept throughout this paper. If a random intercept is not sufficient to represent the variation exhibited in the data, then the model can be easily extended to a more general form by considering a more complex random effects structure.

3.2. Estimation Procedure via Penalized h-Likelihood

$$\begin{aligned} \text{h} - \text{likelihood} &= \prod_{i=1}^{k} f(v_i) \prod_{j=1}^{m} f\left(y_{ij} \mid v_i\right) \\ &= \prod_{i=1}^{k} \frac{1}{\sqrt{2\pi}\sigma_u} \exp\left\{-\frac{(v_i - 0)^2}{2}\right\} \prod_{j=1}^{m} \frac{1}{\sqrt{2\pi}} \exp\left\{-\frac{\left(y_{ij} - x_{ij}^T\beta - v_i - f\left(t_{ij}\right)\right)^2}{2}\right\} \\ &= \frac{1}{\left(\sqrt{2\pi}\,\sigma_u\right)^k} \frac{1}{\left(\sqrt{2\pi}\right)^{km}} \prod_{i=1}^{k} \exp\left\{-\frac{v_i^2}{2\sigma_u^2}\right\} \prod_{j=1}^{m} \exp\left\{-\frac{\left(y_{ij} - x_{ij}^T\beta - v_i - f\left(t_{ij}\right)\right)^2}{2}\right\} \\ &= \frac{1}{\left(\sqrt{2\pi}\,\sigma_u\right)^k} \frac{1}{\left(\sqrt{2\pi}\right)^{km}} \exp\left\{-\frac{\sigma_u^2 \sum_{i=1}^{k} \sum_{j=1}^{m} \left(y_{ij} - x_{ij}^T\beta - v_i - f\left(t_{ij}\right)\right)^2 + \sum_{i=1}^{k} v_i^2}{2\sigma_u^2}\right\}. \end{aligned} \tag{18}$$

Thus, the log of h-likelihood is

$$\begin{aligned} l_h(\beta, v) &= -k \log\left\{\sqrt{2\pi}\,\sigma_u \left(\sqrt{2\pi}\right)^m\right\} \\ &\quad - \frac{\sum_{i=1}^{k} \sum_{j=1}^{m} \left(y_{ij} - x_{ij}^T\beta - v_i - f\left(t_{ij}\right)\right)^2}{2} - \frac{\sum_{i=1}^{k} v_i^2}{2\sigma_u^2} \\ &= -k \log\left\{\sqrt{2\pi}\,\sigma_u \left(\sqrt{2\pi}\right)^m\right\} \\ &\quad - \frac{1}{2}\left\|y - X\beta - Zv - f(t)\right\|_2^2 - \frac{1}{2\sigma_u^2}\|v\|_2^2. \end{aligned} \tag{19}$$

For the purpose of this paper, the first and second derivatives of $l_h(\beta, v)$ with respect to β and v are derived and listed below:

$$\begin{aligned} \nabla l_h(\beta, v) &= \frac{\partial l_h(\beta, v)}{\partial \beta} = X^T(y - X\beta - Zv - f(t)); \\ \overset{2}{\nabla} l_h(\beta, v) &= \frac{\partial^2 l_h(\beta, v)}{\partial \beta\, \partial \beta^T} = -X^T X; \\ \frac{\partial l_h(\beta, v)}{\partial v} &= Z^T(y - X\beta - Zv - f(t)) - \frac{1}{\sigma_u^2} v; \\ \frac{\partial^2 l_h(\beta, v)}{\partial v\, \partial v^T} &= -Z^T Z - \frac{1}{\sigma_u^2} I. \end{aligned} \tag{20}$$

The maximum likelihood estimate for the random effects $\hat{v}$ is obtained by setting $\partial l_h(\beta, v)/\partial v$ to zero. Then, an approximated likelihood for the fixed effects can be obtained by plugging the estimate $\hat{v}$ in $l_h(\beta, v)$. In addition, the marginal likelihood is approximated by the adjusted profile likelihood:

$$l(\beta) \approx \left[l_h(\beta, v) - \frac{1}{2}\log\det\left\{\frac{D(l_h(\beta, v))}{2\pi}\right\}\right]_{v=\widehat{v}}, \quad (21)$$

where $D(l_h(\beta, v)) = -\partial^2 l_h(\beta, v)/\partial v\,\partial v^T$.

Now the problem of how to estimate the smooth function $f(t)$ rises. In this paper, we use two nonparametric approaches to estimate $f(t)$: local linear regression technique and spline technique.

In the framework of penalized variable selection, we apply a penalty on the approximated marginal likelihood so that

$$l_p(\beta) = l(\beta) - n\sum_{j=1}^{p} P_\lambda\left(\left|\beta_j\right|\right), \quad (22)$$

where $P_\lambda(.)$ is the penalty function with tuning parameter λ. Our aim is to maximize $l_p(\beta)$ and get the maximum likelihood estimates for the fixed effects β. We will give a brief theoretical support on how to derive the estimation in the following paragraphs.

First of all, the L_1 penalty functions are singular at the origin, and they do not have continuous second-order derivatives. However, they can be locally approximated by a quadratic function as follows. Assume that we are given an initial value β_0 that is close to the maximizer of $l_h(\beta)$. If β_{j0} is very close to 0, then set $\widehat{\beta}_j = 0$. Otherwise, they can be locally approximated by a quadratic function as

$$\begin{aligned}\left[P\lambda\left(\left|\beta_j\right|\right)\right]' &= P'_\lambda\left(\left|\beta_j\right|\right)\operatorname{sgn}\left(\beta_j\right)\\ &\approx \frac{P'_\lambda\left(\left|\beta_{j0}\right|\right)}{\left|\beta_{j0}\right|}\beta_j\\ &\approx \frac{P'_\lambda\left(\left|\beta_{j0}\right|\right)}{\left|\beta_{j0}\right|}\frac{\beta_j + \beta_{j0}}{2},\end{aligned} \quad (23)$$

when $\beta_j \neq 0$. In other words,

$$P_\lambda\left(\left|\beta_j\right|\right) \approx P_\lambda\left(\left|\beta_{j0}\right|\right) + \frac{1}{2}\frac{P'_\lambda\left(\left|\beta_{j0}\right|\right)}{\left|\beta_{j0}\right|}\left(\beta_j^2 - \beta_{j0}^2\right), \quad (24)$$

for $\beta_j \approx \beta_{j0}$. A drawback of this approximation is that once a coefficient is shrunk to zero, it will stay at zero.

Furthermore, note the first two derivatives of the log h-likelihood function $l_h(\beta, v)$ are continuous. Around a given point β_0, the log h-likelihood function can be approximated by

$$\begin{aligned}l_h(\beta) \approx\ & l_h(\beta_0) + \left[\frac{\partial l_h(\beta_0)}{\partial\beta}\right]^T(\beta - \beta_0)\\ &+ \frac{1}{2}(\beta - \beta_0)^T\left[\frac{\partial^2 l_h(\beta_0)}{\partial\beta\,\partial\beta^T}\right](\beta - \beta_0).\end{aligned} \quad (25)$$

Similarly, $l_p(\beta)$ can be locally approximated by the quadratic function

$$\begin{aligned}l_p(\beta) =\ & l(\beta_0) + \nabla l(\beta_0)^T(\beta - \beta_0)\\ &+ \frac{1}{2}(\beta - \beta_0)^T\overset{2}{\nabla} l(\beta_0)(\beta - \beta_0)\\ &- \frac{1}{2}n\beta^T\sum_\lambda(\beta_0)\beta + C,\end{aligned} \quad (26)$$

where C is a constant term, $\nabla l(\beta_0) = \partial l(\beta_0)/\partial\beta$, $\nabla^2 l(\beta_0) = \partial^2 l(\beta_0)/\partial\beta\,\partial\beta^T$, and $\sum_\lambda(\beta_0) = \operatorname{diag}\{P'_\lambda(|\beta_{10}|)/|\beta_{10}|, \ldots, P'_\lambda(|\beta_{p0}|)/|\beta_{p0}|\}$. The quadratic maximization problem yields the solution iteratively by

$$\beta_1 = \beta_0 + \left\{\overset{2}{\nabla} l(\beta_0) - n\sum_\lambda(\beta_0)\right\}^{-1}\left\{n\sum_\lambda(\beta_0)\beta_0 - \nabla l(\beta_0)\right\}. \quad (27)$$

When the algorithm converges, the estimator satisfies the penalized likelihood equation condition

$$\frac{\partial l\left(\widehat{\beta}_0\right)}{\partial\beta_j} - nP'_\lambda\left(\left|\widehat{\beta_{j0}}\right|\right)\operatorname{sgn}\left(\widehat{\beta_{j0}}\right) = 0, \quad (28)$$

for nonzero elements of $\widehat{\beta}_0$.

As stated in Fan and Li [20], in the maximum likelihood estimation (MLE) setting, with good initial value of β_0, the one-step procedure can be as efficient as the fully iterative procedure, when the Newton–Raphson algorithm is used. Thus, if we have a good initial value for β, the very next iteration can be regarded as a one-step procedure, and the resulting estimator can be as efficient as the fully iterative method.

3.3. Variable Selection via the Adaptive Lasso Penalty. There are many penalized likelihood variable selection criteria available in the literature review on penalized approaches, such as lasso penalty and SCAD. In this paper, we focus on the adaptive lasso penalty, which was introduced by Zou [40]. The form of the penalty function for adaptive lasso is given by

$$P_\lambda\left(\left|\beta_j\right|\right) = \lambda w_j\left(\left|\beta_j\right|\right), \quad (29)$$

where w is a known weights vector and λ is the tuning parameter satisfying $\lambda > 0$. It has been shown if the weights are data-dependent and cleverly chosen, the weighted lasso can achieve the oracle properties, or in other words, it performs well as if the true underlying model was known in advance. This is the main reason for our choice of penalty function. In addition, the adaptive lasso is less complicated than the smoothly clipped absolute deviation (SCAD) penalty introduced by Fan and Li [20] and hence is easier to implement.

For the choice of the data-dependent weights vector w, we use the hierarchical generalized linear model to estimate $\widehat{\beta}_{\text{hglm}}$. To specify,

$$w = \frac{1}{\left|\widehat{\beta}_{\text{hglm}}\right|^{0.5}}. \quad (30)$$

As the sample size grows, the weights for zero-coefficient estimators get to infinity, whereas the weights for nonzero-coefficients converge to a finite constant.

A significant part of our proposed method is the process of variable selection by choosing an appropriate penalty function. As a result, the choice of the tuning parameter λ in the penalty function becomes important. The most popular methods for choosing such tuning parameters are K-fold cross-validation and generalized cross-validation procedures in the literature. In fact, the consistency of selection of various shrinkage methods relies on an appropriate choice of the tuning parameters, and the method of generalized cross-validation (GCV) method has been widely used in the past literature. Therefore, we adopt the traditional method and generalized cross-validation method, for the choice of the tuning parameter. In particular, suppose we have the fitted $\widehat{Y} = HY$ for a linear method under squared error, then the standard formula for the generalized cross-validation is

$$\mathrm{GCV}_\lambda = \frac{1}{n}\sum_{i=1}^{n}\left(\frac{y_i - \widehat{f}_\lambda(x_i)}{(1 - \mathrm{tr}(H))/n}\right)^2. \tag{31}$$

Then, we obtain the tuning parameter λ with the minimized GCV.

3.4. Computational Algorithm. We propose the following h-likelihood algorithm (Algorithm 1) for developing the method discussed in this paper.

The computational cost of the proposed penalized h-likelihood algorithm is of order $O(np^2)$, where n is the sample size and p is the number of associated coefficients in equation (16). The efficient path algorithm makes the proposed penalized h-likelihood algorithm an attractive method for real applications. In particular, if we have a good initial value for β, the very next iteration can be regarded as a one-step procedure, and the resulting estimator can be as efficient as the fully iterative method.

3.5. Simulation Studies. To assess the finite sample performance of our proposed method, we conduct several simulation studies. All simulations are conducted using *R* codes. Our models have the form

$$y_{ij} = f\left(t_{ij}\right) + x_{ij}^T\beta + v_i + \varepsilon_{ij}, \tag{32}$$

with $v_i \sim \mathbf{N}(0, \sigma_u^2)$ and $\varepsilon_{ij} \sim \mathbf{N}(0, \phi)$. It has been assumed throughout this chapter $\sigma_u^2 = 0.2$ and $\phi = 1$. In addition, the distribution of the response y_{ij} conditional on the random components v_i is also assumed to be $\mathbf{N}(\mu_{ij}, \phi)$, where $\mu_{ij} = f(t_{ij}) + x_{ij}^T\beta + v_i$. To form the covariates $x_{ij} = (x_{ij1}, \ldots, x_{ij10})^T$ for the model, we draw random samples from a multivariate normal distribution $\mathbf{N}(0, \Sigma)$, where the covariance matrix Σ is assumed to have an AR (1) structure with $\sigma^2 = 1$ and $\rho = 0.5$. The choice of the correlation parameter ρ is fixed here since the choice of the correlation has little impact on the resulting penalized estimates for β by trying several values for $\rho \in [0.1, 0.9]$. Furthermore, t_{ij} are simulated from a uniform [0, 1] distribution. We do the simulation studies through several examples. For each of the cases, we run a simulation study over 100 simulated datasets.

Furthermore, for the nonparametric part of the model, we use three different functions for simulation purposes: $f(t) = \exp(0.1t)$, $f(t) = \sin(0.1\pi t)$, and $f(t) = t^2$. Both $f(t) = \exp(0.1t)$ and $f(t) = t^2$ represent a nonlinear and increasing function, whereas $f(t) = \sin(0.1\pi t)$ represents a nonlinear and nonmonotonic function.

In order to examine the finite sample performance of our proposed method, we run simulations based on the following six examples.

Example 1. We generate a balanced dataset such that there are 10 subjects within each 100 groups. In other words, we have 100 clusters and 10 subjects within each cluster, denoted by $i = 1, \ldots, 100$ and $j = 1, \ldots, 10$. The size of the true model is $d_0 = 5$ with the true values of the parameters is set to be $\beta = (7.7, 4.6, 3.8, 2.9, 5.3, 0, 0, 0, 0, 0)^T$. In addition to the linear component, the nonparametric component is $f(t) = t^2$.

Example 2. Similar to Example 1 but with reduced number of within cluster subjects. We generate a balanced dataset, such that there are 5 subjects within each 100 groups. In other words, we have 100 clusters and 5 subjects within each cluster, denoted by $i = 1, \ldots, 100$ and $j = 1, \ldots, 5$. The size of the true model is $d_0 = 5$ with the true values of the parameters set to be $\beta = (7.7, 4.6, 3.8, 2.9, 5.3, 0, 0, 0, 0, 0)^T$. In addition to the linear component, the nonparametric component is $f(t) = t^2$.

Example 3. We generate a balanced dataset such that there are 10 subjects within each 100 groups. In other words, we have 100 clusters and 10 subjects within each cluster, denoted by $i = 1, \ldots, 100$ and $j = 1, \ldots, 10$. The size of the true model is $d_0 = 3$ with the true values of the parameters set to be $\beta = (2, 1, 3, 0, 0, 0, 0, 0, 0, 0)^T$. In addition to the linear component, the nonparametric component is $f(t) = \exp(0.1t)$.

Example 4. Similar to Example 3 but with reduced number of within cluster subjects. We generate a balanced dataset, such that there are 5 subjects within each 100 groups. In other words, we have 100 clusters and 5 subjects within each cluster, denoted by $i = 1, \ldots, 100$ and $j = 1, \ldots, 5$. The size of the true model is $d_0 = 3$ with the true values of the parameters set to be $\beta = (2, 1, 3, 0, 0, 0, 0, 0, 0, 0)^T$. In addition to the linear component, the nonparametric component is $f(t) = \exp(0.1t)$.

Example 5. We generate a balanced dataset, such that there are 10 subjects within each 100 groups. In other words, we have 100 clusters and 10 subjects within each cluster, denoted by $i = 1, \ldots, 100$ and $j = 1, \ldots, 10$. The size of the true model is $d_0 = 3$ with the true values of the parameters set to be $\beta = (2, 1, 3, 0, 0, 0, 0, 0, 0, 0)^T$. In addition to the linear component, the nonparametric component is $f(t) = \sin(0.1\pi t)$.

[(Step 1)] (initialization).

(i) Assume a partial linear model excluding variable selection. Express $f(t_{ij})$ in a parametric way. For example, a cubic regression spline can be expressed by using the truncated power basis:
$f(t_{ij}) = \sum_{k=0}^{s} \alpha_k t_{ij}^k + \sum_{l=1}^{r} \alpha_{l+3} (t_{ij} - \tau_l)_+^3$,
where the 5 knots $\tau_1, \ldots, \tau_5$ are percentiles of t, $\alpha_0, \ldots, \alpha_8$ are the associated coefficients, and $s = 3, r = 5$, are the numbers corresponding to the cubic regression spline representation.

(ii) Initialize the fixed effects $\widehat{\beta}^{(0)} = \widehat{\beta}_{\text{hglm}}$, where $\widehat{\beta}_{\text{hglm}}$ is the h-likelihood estimates by treating $f(t_{ij})$ in a parametrical way. Then, we have
$w_j = 1/|\widehat{\beta}_j^{(0)}|^{0.5}$.

(iii) Denote the estimates by $\widehat{f}(t_{ij})$:
$\widehat{f}(t_{ij}) = \sum_{k=0}^{s} \widehat{\alpha}_k t_{ij}^k + \sum_{l=1}^{r} \widehat{\alpha}_{l+3} (t_{ij} - \tau_l)_+^3$,
where $\widehat{\alpha} = \widehat{\alpha}_{\text{hglm}}$ are the h-likelihood estimates.

(iv) Determine initial value for random effects using
$\widehat{v}_i^{(0)} = (\sigma_u^2 / m\sigma_u^2 + \phi) \sum_{j=1}^{m} [y_{ij} - x_{ij}^T \widehat{\beta}^{(0)} - \widehat{f}(t_{ij})]$,
with $\sigma_u^2 = 0.2$ and $\phi = 1$.

[(Step 2)] (loop).

(i) Use $\widehat{\beta}^{(k)}$ and $\widehat{v}_i^{(k)}$ to get
$\widehat{v}_i = (\sigma_u^2 / m\sigma_u^2 + \phi) \sum_{j=1}^{m} [y_{ij} - x_{ij}^T \widehat{\beta}^{(k)} - \widehat{f}(t_{ij})]$.

(ii) For the $(k+1)^{\text{th}}$ iteration, set the estimator $\widehat{\beta}^{(k)}$ from the k^{th} iteration and update β by
$$\widehat{\beta}^{(k+1)} = \beta^{(k)} + \left\{ \overset{2}{\nabla} l(\beta^{(k)}) - n \sum_{\lambda} (\beta^{(k)}) \right\}^{-1} \left\{ n \sum_{\lambda} (\beta^{(k)}) \beta^{(k)} - \nabla l(\beta^{(k)}) \right\}.$$

(iii) For $s = 1, \ldots, p$, set $\widehat{\beta}^{(k+1)} = 0$ if $\widehat{\beta}^{(k+1)} < c \sum_{s=1}^{p} |\widehat{\beta}^{(k+1)}|$, for a small cutoff value c.

(iv) Compute $|(\widehat{\beta}^{(k+1)} - \widehat{\beta}^{(k)}) / \widehat{\beta}^{(k)}|$ and compare to a small predetermined value c'. If $|(\widehat{\beta}^{(k+1)} - \widehat{\beta}^{(k)}) / \widehat{\beta}^{(k)}|$ is smaller than c', stop the loop.

Algorithm 1

Example 6. Similar to Example 5 but with reduced number of within cluster subjects. We generate a balanced dataset, such that there are 5 subjects within each 100 groups. In other words, we have 100 clusters and 5 subjects within each cluster, denoted by $i = 1, \ldots, 100$ and $j = 1, \ldots, 5$. The size of the true model is $d_0 = 3$ with the true values of the parameters set to be $\beta = (2, 1, 3, 0, 0, 0, 0, 0, 0, 0)^T$. In addition to the linear component, the nonparametric component is $f(t) = \sin(0.1\pi t)$.

We simulate each random effect v_i from a normal distribution with 0 mean and $\sigma_u^2 = 0.2$. Moreover, we simulate t_{ij} from uniform distribution of $[0, 1]$. Then, we obtain the smoothing function $f(t)$ by plugging in the values of t_{ij}. Once we have the random effects and the nonparametric part of $f(t)$, we can simulate the response y_{ij} by computing its mean and variance through the model. In this case, $y_{ij} \sim \mathbf{N}(\mu_{ij}, \phi)$, where $\mu_{ij} = f(t_{ij}) + x_{ij}^T \beta + v_i$ and $\phi = 1$.

By default, we estimate the unknown smooth function $f(t)$ by two methods: local linear kernel smoothing method and cubic spine smoothing method. We denote the estimates with respective to those two methods by PHKernel and PHSpline. In addition, we also calculated the cubic spline smoothing method without the penalty term, i.e., $\lambda = 0$, and denote the estimates algorithm by HSpline. However, due to the computational complexity of the local linear kernel smoothing method, we only consider the comparison between local linear kernel smoothing method and cubic spine smoothing method for Examples 1 and 2. For the rest of the four examples, we only run the simulations in terms of HSpline and PHSpline.

Before we report the simulation performances of our proposed penalty-based procedure, several terms, which will be listed in the summary tables, are introduced. First of all, let percentage of correctly fitted and percentage of overfitted be the proportions of selected models that are correctly fitted and overfitted, respectively. In the case of overfitting, the columns "1," "2," and ">2" represent the proportions of selected models including one, two, and more than two irrelevant predictors, correspondingly.

Furthermore, to characterize the capability of a method in producing sparse solutions, we define

$$\text{percentage of correct zeros (\%)} = \frac{1}{d - d_0} \left\{ \frac{1}{100} \sum_{k=1}^{100} \sum_{j=1}^{d} I\left(\widehat{\beta}_{j(k)} = 0\right) \times I\left(\beta_j = 0\right) \right\}. \tag{33}$$

To characterize the method's underfitting effect, we further define

$$\text{percentage of incorrect zeros (\%)} = \frac{1}{d_0} \left\{ \frac{1}{100} \sum_{k=1}^{100} \sum_{j=1}^{d} I\left(\widehat{\beta}_{j(k)} = 0\right) \times I\left(\beta_j \neq 0\right) \right\}. \tag{34}$$

Table 2 presents a detailed summary of variable selection accuracy for all the six examples provided above. Several key

Table 2: Simulation summary of PHSpline for six examples.

Example	d_0	Underfitted (%)	Correctly fitted (%)	Overfitted (%)			Correct zeros (%)	Incorrect zeros (%)
				1	2	3		
1	5	0	100	0	0	0	100	0
2	5	0	94	2	2	0	98.8	0
3	3	0	74	14	8	4	93.3	0
4	3	0	69	16	10	5	84.4	0
5	3	0	71	20	2	7	93.1	0
6	3	0	64	21	6	9	88.3	0

findings can be observed from Table 2. First of all, all the six examples do not have the underfitting problem, which means all the relevant predictors can be discovered by the PHSpline method. Equivalently, results of zeros for percent of incorrect zeros column double confirm the above statement.

Furthermore, our proposed PHSpline method is in good performance in terms of variable selection consistency for Example 1, with 100% correctly fit. Similarly, simulation results of our proposed PHSpline method for Example 2 provides a 94% correct fit, a 2% of overfit with 1 irrelevant predictor included, and a 2% of overfit with 2 irrelevant predictors included. The overall performance of variable selection consistency for Example 2 is good with a 98.8% of correct zeros.

Thirdly, when we have a more sparse representation for the fixed effects β with smaller magnitudes, our proposed PHSpline tends to provide a little bit conservative result compared to Examples 1 and 2, in terms of variable selection accuracy. In particular, simulation results of our proposed PHSpline method for Example 3 provide a 74% of correct fit, a 14% of overfit with 1 irrelevant predictor included, a 8% of overfit with 2 irrelevant predictors included, and a 4% of overfit with more than 2 irrelevant predictors included. In fact, the overall performance of variable selection consistency for Example 3 is good with a 93.3% of correct zeros. On the contrary, when the number of within-cluster subjects decreases from 10 to 5 in Example 4, percent of correct zeros decreases to 84.4%, meaning that more irrelevant predictors are included in the model.

Last but not least, similar trends can be observed for Examples 5 and 6 compared to Examples 3 and 4. Example 5 returns a 71% of correct fit, a 20% of overfit with 1 irrelevant predictor included, a 2% of overfit with 2 irrelevant predictors included, and a 7% of overfit with more than 2 irrelevant predictors included. On the contrary, Example 6 returns a 64% of correct fit, a 21% of overfit with 1 irrelevant predictor included, a 6% of overfit with 2 irrelevant predictors included, and a 9% of overfit with more than 2 irrelevant predictors included. As a result, the 71% of correct fit for Example 5 outperforms the 64% of correctly fit for Example 6, in terms of the variable selection consistency. Hence, generally speaking, our proposed PHSpline method works better when the number of within cluster subjects increases.

Besides the variable selection accuracy summarized in Table 2, prediction accuracy for the fixed effects β for various examples is also with our interest. In the following paragraphs, results of prediction accuracy for the fixed effects β are discussed and interpreted, with Tables 3–8 presented.

Table 3: Simulation result of Example 1.

Coefficients	Truth	HSpline (s.e.)	PHKernel (s.e.)	PHSpline (s.e.)
β_1	7.7	7.741 (0.043)	7.724 (0.139)	7.704 (0.048)
β_2	4.6	4.529 (0.059)	4.562 (0.179)	4.588 (0.062)
β_3	3.8	3.930 (0.060)	3.830 (0.200)	3.806 (0.078)
β_4	2.9	2.800 (0.079)	2.878 (0.177)	2.883 (0.086)
β_5	5.3	5.363 (0.081)	5.311 (0.144)	5.298 (0.090)
β_6	0	−0.031 (0.048)	0 (—)	0 (—)
β_7	0	−0.001 (0.076)	0 (—)	0 (—)
β_8	0	−0.040 (0.109)	0 (—)	0 (—)
β_9	0	−0.004 (0.040)	0 (—)	0 (—)
β_{10}	0	−0.001 (0.063)	0 (—)	0 (—)

Table 4: Simulation result of Example 2.

Coefficients	Truth	HSpline (s.e.)	PHKernel (s.e.)	PHSpline (s.e.)
β_1	7.7	7.703 (0.050))	7.701 (0.051)	7.685 (0.067)
β_2	4.6	4.604 (0.064)	4.593 (0.065)	4.608 (0.108)
β_3	3.8	3.792 (0.075)	3.872 (0.078)	3.778 (0.115)
β_4	2.9	2.909 (0.078)	2.850 (0.091)	2.891 (0.125)
β_5	5.3	5.295 (0.079))	5.308 (0.087)	5.282 (0.133)
β_6	0	0.003 (0.072)	0.005 (0.083)	0.006 (0.058)
β_7	0	−0.003 (0.061)	0 (—)	0 (—)
β_8	0	0.001 (0.058)	0 (—)	0 (—)
β_9	0	−0.002 (0.059)	0 (—)	0 (—)
β_{10}	0	0.0004 (0.042)	0 (—)	0 (—)

Table 3 summarizes simulation result over 100 replications for Example 1. As we can see, both PHkernel and PHSpline can recover the relevant predictors accurately. In addition, the estimates of the fixed effects for both PHkernel and PHSpline are comparably making very little difference with the true values of β. However, in terms of speed of the algorithm, the PHSpline method is way fast than the PHKernel method, and hence, the PHSpline method is fast

Table 5: Simulation result of Example 3.

Coefficients	Truth	HSpline (s.e.)	PHSpline (s.e.)
β_1	2	2.001 (0.045)	1.995 (0.043)
β_2	1	1.002 (0.064)	0.995 (0.061)
β_3	3	2.994 (0.075)	2.992 (0.074)
β_4	0	0.006 (0.078)	0.005 (0.043)
β_5	0	0.004 (0.079)	0.004 (0.053)
β_6	0	0.003 (0.072)	−0.004 (0.060)
β_7	0	−0.003 (0.061)	0 (—)
β_8	0	0.001 (0.058)	0 (—)
β_9	0	−0.002 (0.059)	0.001 (0.023)
β_{10}	0	0.0004 (0.042)	0 (—)

Table 6: Simulation result of Example 4.

Coefficients	Truth	HSpline (s.e.)	PHSpline (s.e.)
β_1	2	1.930 (0.120)	1.977 (0.074)
β_2	1	0.951 (0.102)	0.997 (0.100)
β_3	3	2.943 (0.089)	2.979 (0.115)
β_4	0	0.041 (0.081)	0.012 (0.106)
β_5	0	−0.005 (0.072)	−0.009 (0.104)
β_6	0	0.011 (0.096)	0.008 (0.093)
β_7	0	0.022 (0.103)	0 (—)
β_8	0	−0.009 (0.085)	0.011 (0.088)
β_9	0	0.008 (0.084)	0 (—)
β_{10}	0	0.003 (0.077)	0 (—)

Table 7: Simulation result of Example 5.

Coefficients	Truth	HSpline (s.e.)	PHSpline (s.e.)
β_1	2	2.012 (0.064)	1.999 (0.046)
β_2	1	0.988 (0.055)	1.002 (0.062)
β_3	3	2.986 (0.070)	3.000 (0.067)
β_4	0	0.003 (0.048)	0 (—)
β_5	0	0.005 (0.050)	0 (—)
β_6	0	0.010 (0.062)	0.001 (0.040)
β_7	0	−0.007 (0.079)	−0.003 (0.058)
β_8	0	0.002 (0.070)	0 (—)
β_9	0	0.006 (0.061)	0 (—)
β_{10}	0	0.009 (0.069)	−0.001 (0.014)

to implement. On the contrary, the HSpline method returns the h-likelihood estimates of the fixed effects, without the penalty term. As we can observe from Table 3, the HSpline method gives nonzero estimates for all the β, resulting in bad variable selection performance compared with PHSpline, which involves a penalty term. Furthermore, PHSpline estimates tend to have relatively smaller standard deviations than those computed in HSpline estimates. Therefore, the PHSpline method outperforms the other two methods by either variable selection accuracy or efficiency of the implementation speed.

Simulation result over 100 replications for Example 2 is summarized in Table 4. Example 2 has a smaller number of within-cluster subjects than that in Example 1. In fact, similar to the results obtained in Example 1, both PHKernel and PHSpline methods return relatively good estimates of the fixed effects β in terms of variable selection accuracy and prediction accuracy. In particular, both PHKernel and

Table 8: Simulation result of Example 6.

Coefficients	Truth	HSpline (s.e.)	PHSpline (s.e.)
β_1	2	1.990 (0.063)	1.982 (0.071)
β_2	1	0.992 (0.070)	0.984 (0.096)
β_3	3	2.973 (0.089)	2.972 (0.106)
β_4	0	0.022 (0.061)	0.017 (0.085)
β_5	0	0.019 (0.072)	−0.023 (0.090)
β_6	0	0.004 (0.089)	0.019 (0.079)
β_7	0	−0.041 (0.080)	0.002 (0.078)
β_8	0	0.031 (0.067)	0.001 (0.061)
β_9	0	−0.014 (0.071)	0.001 (0.073)
β_{10}	0	0.009 (0.087)	−0.001 (0.015)

PHSpline methods select one irrelevant covariate wrongly. In addition, the estimates of the fixed effects for both PHKernel and PHSpline methods are comparably making very little difference with the true values of β. On the contrary, as we can observe from Table 4, the HSpline method gives nonzero estimates for all the β, resulting in bad variable selection performance compared with PHSpline. Furthermore, PHSpline estimates tend to have relatively smaller standard deviations than those computed in HSpline estimates. In fact, it is not surprising to see that both PHkernel and PHSpline methods include X_6 as a relevant predictor in the model. Or in an equivalent way, both PHKernel and PHSpline methods return nonzero β_6. The reason is that we have a AR (1) model, which means there is a correlation of $\rho = 0.5$ between X_5 and X_6.

`As we compare simulation results of Examples 1 and 2, our proposed PHSpline method tends to perform better when the number of within-cluster subjects increases. In addition, a similar conclusion can be drawn for the PHKernel method. Furthermore, both PHKernel and PHSpline methods work well when the nonparametric component is $f(t) = t^2$.

Tables 5 and 6 present simulation results over 100 replications for Examples 3 and 4. In these two examples, we have a more sparse representation in terms of the fixed effects β than those in Examples 1 and 2. On top of that, the magnitudes of the fixed effects β are set to be smaller than those in Examples 1 and 2. For both of the results, the PHSpline method outperforms the HSpline method in terms of variable selection performance in two ways. First of all, the PHSpline method identifies some of the irrelevant predictors accurately, whereas the HSpline method gives nonzero estimates for all the β. Though PHSpline cannot guarantee 100% selection accuracy, it does improve the poor variable selection performance of HSpline by adding a penalty term. Furthermore, PHSpline estimates tend to have relatively smaller standard deviations than those computed in HSpline estimates. Therefore, the PHSpline method performs better than the HSpline method, even for the sparse fixed effects β situation.

Similarly, simulation results over 100 replications for Examples 5 and 6 are presented in Tables 7 and 8. Again, we have a more sparse representation in terms of the fixed effects β than those in Examples 1 and 2, with smaller magnitudes of the fixed effects β. The PHSpline method works pretty well in terms of variable selection for Example 5

even though it does not guarantee a 100% selection accuracy. On the contrary, the PHSpline method returns nonzero estimates for all the β, resulting in poor variable selection performance for Example 6, where the number of within cluster subjects reduces to 5.

Overall, the simulation results show that our proposed penalized h-likelihood approach performs good in terms of variable selection accuracy because of its ability to recover the true zeros, especially when the number of within-cluster subjects is not too small. Generally, our proposed PHSpline method works better when the number of within cluster subjects increases. In addition, even when the true model is sparse, our penalized estimator still does no worse than the h-likelihood estimator in terms of estimation accuracy.

4. Conclusion

To conclude, we have introduced a new penalized h-likelihood approach to identify nonzero relevant fixed effects in the partial linear model setting in this paper. This penalized h-likelihood incorporates variable selection procedures in the setting of mean modeling via h-likelihood. A few advantages of this newly proposed method are listed below. First of all, compared to the traditional marginal likelihood, the h-likelihood avoids the messy integration for the random effects and hence is convenient to use. In addition, h-likelihood plays an important role in inferences for models having unobserved random variables. Last but not least, it has been demonstrated by simulation studies that the proposed penalty-based method is able to identify zero regression coefficients in modeling the mean structure and produces good fixed effects estimation results.

As for future research, it would be interesting to apply the proposed penalized h-likelihood approach to be extended for more complicated circumstances for the partial linear models. In other words, the model in this paper assumes only a simple one-component structure for the random effects, such that only a random intercept is considered. For possible future research, we may consider a partial linear model for modeling the conditional mean with more than one random effect, i.e., the extended multi-component random effects model. Other future work, including variance components estimates of the random effects and study of penalized h-likelihood estimator's theoretical and asymptotical property such as convergence rate, would be investigated and discussed.

Data Availability

This is a theoretical study, and we do not have experimental data.

Disclosure

This work was part of the originally written Ph.D. thesis by the first author in 2013 [41].

Conflicts of Interest

The authors declare that they have no conflicts of interest.

Acknowledgments

This work was funded by the Ministry of Education of Humanities and Social Science Project (Grant no. 17YJCZH199). The authors gratefully acknowledge the Ministry of Education of Humanities and Social Science for the technical and financial support.

References

[1] R. S. Sutton and A. G. Barto, "Reinforcement learning: an introduction," *IEEE Transactions on Neural Networks*, vol. 9, no. 5, p. 1054, 1998.

[2] R. Tibshirani, "Regression shrinkage and selection via the Lasso," *Journal of the Royal Statistical Society: Series B (Methodological)*, vol. 58, no. 1, pp. 267–288, 1996.

[3] T. T. Cai and L. Wang, "Orthogonal matching pursuit for sparse signal recovery with noise," *IEEE Transactions on Information Theory*, vol. 57, no. 7, pp. 4680–4688, 2011.

[4] Y. Lee and J. A. Nelder, "Hierarchical generalized linear models," *Journal of the Royal Statistical Society: Series B (Methodological)*, vol. 58, no. 4, pp. 619–678, 1996.

[5] R. Sutton and G. Barto, "Reinforcement learning," *A Bradford Book*, vol. 15, no. 7, pp. 665–685, 1998.

[6] A. Barto and S. Mahadevan, "Recent advances in hierarchical reinforcement learning," *Discrete Event Dynamic Systems*, vol. 13, no. 1-2, pp. 341–379, 2003.

[7] T. Dietterich, "An overview of MAXQ hierarchical reinforcement learning," in *Proceedings of the International Symposium on Abstraction*, Horseshoe Bay, TX, USA, July 2000.

[8] S. He, H. Fang, M. Zhang, F. Liu, X. Luan, and Z. Ding, "Online policy iterative-based H_∞ optimization algorithm for a class of nonlinear systems," *Information Sciences*, vol. 495, pp. 1–13, 2019.

[9] S. He, M. Zhang, H. Fang, F. Liu, X. Luan, and Z. Ding, "Reinforcement learning and adaptive optimization of a class of Markov jump systems with completely unknown dynamic information," *Neural Computing and Applications*, 2019.

[10] C. Wang, H. Fang, and S. He, "Adaptive optimal controller design for A class of LDI-based neural network systems with input time-delays," *Neurocomputing*, vol. 385, pp. 292–299, 2019.

[11] S. He, H. Fang, M. Zhang, F. Liu, and Z. Ding, "Adaptive optimal control for a class of nonlinear systems: the online policy iteration approach," *IEEE Transactions on Neural Networks and Learning Systems*, vol. 31, no. 2, pp. 549–558, 2020.

[12] P. Cheng, J. Wang, S. He, X. Luan, and F. Liu, "Observer-based asynchronous fault detection for conic-type nonlinear jumping systems and its application to separately excited DC motor," *IEEE Transactions on Circuits and Systems I: Regular Papers*, vol. 67, no. 3, 2020.

[13] P. Cheng, S. He, J. Cheng, X. Luan, and F. Liu, "Asynchronous output feedback control for a class of conic-type nonlinear hidden Markov jump systems within a finite-time interval," *IEEE Transactions on Systems, Man, and Cybernetics: Systems*, vol. 99, pp. 1–8, 2020.

[14] J. A. Nelder and R. W. M. Wedderburn, "Generalized linear models," *Journal of the Royal Statistical Society. Series A (General)*, vol. 135, no. 3, pp. 370–384, 1972.
[15] N. M. Laird and J. H. Ware, "Random-effects models for longitudinal data," *Biometrics*, vol. 38, no. 4, pp. 963–974, 1982.
[16] F. Vonesh, C. Edward, and M. Vernon, "Linear and nonlinear models for the analysis of repeated measurements," *Journal of Biopharmaceutical Statistics*, vol. 18, no. 4, pp. 595–610, 1996.
[17] F. Vaida and S. Blanchard, "Conditional Akaike information for mixed-effects models," *Biometrika*, vol. 92, no. 2, pp. 351–370, 2005.
[18] W. Pu and X. Niu, "Selecting mixed-effects models based on a generalized information criterion," *Journal of Multivariate Analysis*, vol. 97, no. 3, pp. 733–758, 2008.
[19] R. Rajaram and B. Castellani, "The utility of nonequilibrium statistical mechanics, specifically transport theory, for modeling cohort data," *Complexity*, vol. 20, no. 4, pp. 45–57, 2015.
[20] J. Fan and R. Li, "Variable selection via nonconcave penalized likelihood and its oracle properties," *Journal of the American Statistical Association*, vol. 96, no. 456, pp. 1348–1360, 2001.
[21] J. Fan and I. Gijbels, "Variable bandwidth and local linear regression smoothers," *The Annals of Statistics*, vol. 20, no. 4, pp. 2008–2036, 1992.
[22] J. Fan, "Design-adaptive nonparametric regression," *Journal of the American Statistical Association*, vol. 87, no. 420, pp. 998–1004, 1992.
[23] T. Hastie and C. Loader, "Local regression: automatic kernel carpentry (with discussion)," *Statistical Science*, vol. 8, pp. 120–143, 1993.
[24] J. Fan and J.-T. Zhang, "Two-step estimation of functional linear models with applications to longitudinal data," *Journal of the Royal Statistical Society: Series B (Statistical Methodology)*, vol. 62, no. 2, pp. 303–322, 2000.
[25] Wu and Rice, "Nonparametric mixed effects models for unequally sampled noisy curves," *Biometrics*, vol. 57, no. 1, pp. 253–259, 2001.
[26] C. Caves and R. Schack, "Unpredictability, information, and chaos," *Complexity*, vol. 3, no. 1, pp. 46–57, 2015.
[27] Y. Zhang, Y. Zhou, X. Guo et al., "Self-adaptive K-means based on a covering algorithm," *Complexity*, vol. 2018, Article ID 7698274, 16 pages, 2018.
[28] T. Martinussen and T. Scheike, "Sampling corrected analysis of dynamic additive regression models for longitudinal data," *University of Copenhagen*, vol. 28, no. 2, pp. 303–323, 2001.
[29] R. Xu, "Measuring explained variation in linear mixed effects models," *Statistics in Medicine*, vol. 22, no. 22, pp. 3527–4354, 2003.
[30] S. L. Zeger and P. J. Diggle, "Semiparametric models for longitudinal data with application to CD4 cell numbers in HIV seroconverters," *Biometrics*, vol. 50, no. 3, pp. 689–699, 1994.
[31] A. Groll and G. Tutz, "Variable selection for generalized linear mixed models by L 1-penalized estimation," *Statistics and Computing*, vol. 24, no. 2, pp. 137–154, 2014.
[32] N. Heckman, R. Lockhart, and J. D. Nielsen, "Penalized regression, mixed effects models and appropriate modelling," *Electronic Journal of Statistics*, vol. 7, pp. 1517–1552, 2013.
[33] P. Diggle, K. Liang, and S. Zeger, *Analysis of Longitudinal Data*, Clarendon Press, Oxford, UK, 1994.
[34] Y. Lee and J. A. Nelder, "Modelling and analysing correlated non-normal data," *Statistical Modelling*, vol. 1, no. 1, pp. 3–16, 2001.
[35] M. Noh and Y. Lee, "Hierarchical-likelihood approach for nonlinear mixed-effects models," *Computational Statistics & Data Analysis*, vol. 52, no. 7, pp. 3517–3527, 2008.
[36] Y. Lee and J. Nelder, "Double hierarchical generalized linear models (with discussion)," *Journal of the Royal Statistical Society*, vol. 55, no. 4, pp. 139–185, 2010.
[37] M. Noh and Y. Lee, "Double hierarchical generalized linear models," *Journal of the Royal Statistical Society*, vol. 55, no. 2, pp. 139–185, 2017.
[38] R. Greenlaw and S. Kantabutra, "On the parallel complexity of hierarchical clustering and CC-complete problems," *Complexity*, vol. 14, no. 2, pp. 18–28, 2010.
[39] M. Noh and Y. Lee, "REML estimation for binary data in GLMMs," *Journal of Multivariate Analysis*, vol. 98, no. 5, pp. 896–915, 2007.
[40] H. Zou, "The adaptive Lasso and its oracle properties," *Journal of the American Statistical Association*, vol. 101, no. 476, pp. 1418–1429, 2006.
[41] Y. Xie, "Variable selection procedures in linear regression models," Ph.D. dissertation, Stats Department, NUS, Singapore, 2013.

Hindawi
Complexity
Volume 2020, Article ID 8849483, 9 pages
https://doi.org/10.1155/2020/8849483

Research Article

Analytical Multiloop Control for Multivariable Systems with Time Delays

Zhiguo Wang and Peng Wei

Key Laboratory of Advanced Process Control for Light Industry (Ministry of Education), Institute of Automation, Jiangnan University, Wuxi 214122, China

Correspondence should be addressed to Zhiguo Wang; zhiguowang@jiangnan.edu.cn

Received 6 August 2020; Revised 2 September 2020; Accepted 8 September 2020; Published 14 September 2020

Academic Editor: Shuping He

In this paper, a new design method with performance improvements of multiloop controllers for multivariable systems is proposed. Precise expression is developed to show the relationship between the dynamic- and steady-state characteristics of the multiloop control system and its parameters. First, an equivalent transfer function (ETF) is introduced to decompose the multivariable system, based on which the multiloop controller parameters are calculated. According to the ETF matrix property, an analytical expression for the PI controller for multivariable systems is derived in terms of substituting the ETF matrix for the inverse open-loop transfer function. In the proposed controller design method, no approximation of the inverse of the process model is needed, implying that this method can be applied to some multivariable systems with high dimensions. The simulation results obtained from several examples demonstrate the effectiveness of the proposed method.

1. Introduction

In the actual industrial process, especially in multivariable systems such as petroleum, chemical, and biological, the interconnections introduced by the process configuration and control architecture are very common [1]. Due to the existence of these interconnection characteristics, a disturbance or a small change of process variable in one or more loops would be propagated to other loops, and in turn, feedback to the source loop to some extent, thereby critically affecting the controller performance and stability of the overall system. At the same time, this interconnection phenomenon makes the design process of multivariable controllers very complicated.

Compared to the single loop system, the multiloop control system's design issues become very complicated as a result of these interconnections, which make it an open topic for many years. There are many reports on this field in the existing literature. From the perspective of controller structure design, these methods can classify into three categories, namely, decoupling plus single loop controller structure, centralized control structure, and multiloop control structure. The classic multiloop PID controller has been widely used in processes with moderate interaction due to some advantages, such as simple control structure, less adjustable parameters, and easy to understand features. For example, a multiloop controller design method is given by Huang et al. [2]. In this method, the multivariable target systems are decomposed into several single but equivalent loops for design. By doing this, prior information of controller dynamics in other loops is no longer needed in each loop, resulting in an interesting method designing controller directly and independently. Shen et al. [3] designed selected loop controllers independently based on equivalent transfer functions. Vu and Lee [4] propose an independent design method for multivariable processes, and firstly the multiloop system is decomposed into a set of single loops using effective open-loop transfer function (EOTF); then, the individual controller of every single loop is designed based on the corresponding EOTF model. Estévez-Sánchez et al. [5] proposed a design method of a multiloop PI controller with the linear quadratic regulator (LQR) methodology.

For the same target, meanwhile, the multiple time delays commonly occur in multivariable processes of high complexity. Particular examples can be found, such as pilot plant distillation columns and high purity distillation columns. The essence of the reason for time delay is the complex interactions between the numerous different pairs of input and output variables. Therefore, approximating the actual model by a reduced-order form by using some model reduction techniques is necessary, for example, the first-order plus dead time (FOPDT) and second-order plus dead time (SOPDT). On the contrary, for systems with time delays, the internal model control (IMC) method is a very practical approach for the design of IMC-PID controllers. Several results have been discussed and reported with some interesting results, extending the IMC-PID of the single-input and single-output (SISO) case to the multivariable case [6]. To overcome the above problems or drawbacks, an intuitive solution is designed multivariable controllers that are fully crosscoupled. To implement this kind of controllers, however, it is not an easy job since all the computation of control input is coupled, and the designers are required to compute the inverse of the transfer function matrix. For the system of high dimensions, the inverse of the transfer function can be quite complex and hard to be determined. Furthermore, based on the approach of direct synthesis, Vu and Lee [7] proposed a method of analytical solution for the design of the PI controller in a multiloop system. As the complication to obtain the inversion of the transfer function, the method has the limitation of only suitable for low-dimensional multivariable systems.

Motivated by the above, a novel decoupling method is proposed for multivariable control systems in this paper. By taking the essential effects of the interactions into account, we use the concept of the equivalent transfer function (ETF) to decompose the multivariable system under consideration into multiple univariate loops equivalently. After that, the properties of the ETF matrix and the target closed-loop diagonal transfer function that was specified to the nonminimum phase zeros and inherent time delays are used to derivate the controller parameters. The relationship between proposed controller parameters and the open-loop transfer function is obtained without the prior acknowledge of the specific ETF model. We have established some equations directly to deduce the parameters of the multiloop PI controller. Finally, the proposed approach is applied to different industrial objects to verify its effectiveness.

2. Preliminaries

In the existing literatures, the idea that decomposes a system of the multiloop controller into several signal loops equivalently is the main approach to design controller for the multiloop system. By doing this, the next step is to design the controller for the transfer function obtained with open-loop feature. To give more details, for ETF loop i, its open-loop function is achieved as the transfer function of u_i with y_i, where only the loop i is open and all the other loops are closed. We show this idea by Figure 1, where the function of u_i to other outputs is indicated by the y_i, while the effect of y_i by all the other control loops with closed feature is indicated by $\overline{y}_i$. The $\mathbf{u}^i$ and $\mathbf{y}^i$ represent r, u, and y with the corresponding ith elements, r_i, u_i, y_i, and $c_i(s)$, removed, respectively. Once the ETF is obtained, model reduction was used to approximate the ETF to FOPDT or SOPDT model. Therefore, some classic and well-understood PID parameter tuning methods for common univariate system can be used in the design of each individual PID controller obtained here.

The IMC-PID controller tuning method introduced by Lee et al. [8] is used to calculate the parameter of controller. The reduced ETF, $\widehat{g}_{ii}$, is decomposed to $\widehat{g}_{ii} = \widehat{g}_{m,ii}\widehat{g}_{p,ii}$, where $\widehat{g}_{m,ii}$ and $\widehat{g}_{p,ii}$ are the minimum phase portion and nonminimum phase portion, respectively. Through simple derivation, we can get the desired closed-loop response under the action of the ideal feedback controller, which is given by

$$g_{ci} = \frac{q_i}{(1 - \widehat{g}_{ii})} = \frac{\widehat{g}_{m,ii}^{-1}(s)}{(\lambda_i s + 1) - \widehat{g}_{p,ii}(s)}, \tag{1}$$

where q_i is the IMC controller and is designed by

$$q_i = \widehat{g}_{ii}^{-1} f_i. \tag{2}$$

The IMC filter, $f(s)$, can be rewritten in the form of $f_i(s) = 1/(\lambda_i s + 1)^{m_i}$, where the adjustable filtering parameter λ_i balances the trade-off between performance and robustness. Besides, to ensure the controller is practical and suitable, the order parameter m_i is selected as a positive integer.

To use the above controller as the standard PID form, we need to approximate the feedback controller g_{ci} by the PI controller forms of equivalent property. To this end, expanding g_{ci} by the Maclaurin series in s yields the following equation:

$$g_{ci} \equiv \frac{f_i(s)}{s} = \frac{1}{s}\left[f_i(0) + f_i'(0)s + \frac{f_i''(0)}{2!}s^2 + \cdots \right]. \tag{3}$$

The controller stated by equation (3) can be interpreted as the traditional PID controller by using the first two terms given by

$$g_{ci}(s) = k_{ci}\left(1 + \frac{1}{\tau_{Ii}s}\right), \tag{4}$$

where

$$k_{ci} = f_i'(0), \tag{5}$$

$$\tau_{Ii} = \frac{f_i'(0)}{f_i(0)}. \tag{6}$$

Through the above descriptions, the concept of the ETF is introduced to solve the controllers design problem. In the following section, we will utilize the property of the ETF matrix to find the important relationship between the parameters of the controller and that of the considered model.

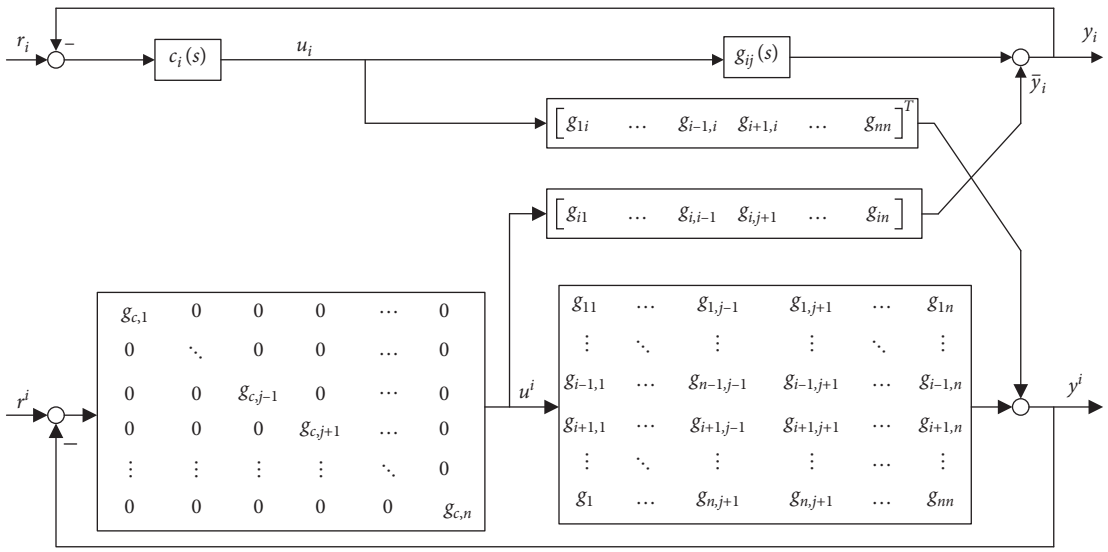

FIGURE 1: Block diagram for the concept of the ETF.

3. Design of Multiloop Controller

3.1. Controller Parameter Design. For a multivariable system with closed-loop controllers, we can write the forward transfer function to be of the form [9]

$$G(s)G_c(s) \approx G(s)G^{-1}(s) = \frac{I}{s}. \tag{7}$$

In the above formula, $G(s)$ is the process transfer function matrix and $G_c(s)$ represents diagonal controller matrix of multivariable system. The detailed structure of these two matrices is as follows:

$$G(s) = \begin{bmatrix} g_{11}(s) & \cdots & g_{1n}(s) \\ \vdots & \ddots & \vdots \\ g_{n2}(s) & \cdots & g_{nn}(s) \end{bmatrix},$$
$$G_c(s) = \begin{bmatrix} g_{c,11}(s) & \cdots & 0 \\ \vdots & \ddots & \vdots \\ 0 & \cdots & g_{c,nn}(s) \end{bmatrix}. \tag{8}$$

Due to the right half plane zeros and time delays in multivariable systems, which make an ideal controller that is equal to the inverse of open-loop transfer function matrix unrealizable, the closed-loop transfer function matrix of the IMC system [10] is given to

$$G(s)G_c(s) = H(s) = \mathrm{diag}\{h_i\}, \quad i = 1, 2, \ldots, n, \tag{9}$$

where

$$h_i = e^{-(\tau(G)-\tau_i)s} \prod_{z \in Z^+_{|G|}} \left(\frac{z-s}{z+s}\right)^{\eta_z(|G|)-\eta_i(z)}, \tag{10}$$

$(\tau(G) - \tau_i)$ is the largest time delay of ith row element of $G(s)$ and $\eta_z(|G|) - \eta_i(z)$ is on its, h_i, the nonminimum phase zeros. In order to ensure system stability and realization, we should restrict on the following conditions:

$$\begin{aligned} \tau(h_i) &\geq \tau(|G|) - \tau_i, \\ \eta_z(h_i) &\geq \eta_z(|G|) - \eta_z(z). \end{aligned} \tag{11}$$

According to the properties of the ETF, we have

$$G^{-1}(s) = \begin{bmatrix} g_{11}(s) & \cdots & g_{1n}(s) \\ \vdots & \ddots & \vdots \\ g_{n1}(s) & \cdots & g_{nn}(s) \end{bmatrix}^{-1} = \begin{bmatrix} \frac{1}{\widehat{g}_{m,11}} & \cdots & \frac{1}{\widehat{g}_{m,1n}} \\ \vdots & \ddots & \vdots \\ \frac{1}{\widehat{g}_{m,n1}} & \cdots & \frac{1}{\widehat{g}_{m,nn}} \end{bmatrix}^T. \tag{12}$$

Comparing equations (1) and (9) and from literatures [11, 12], we can obtain

$$\begin{bmatrix} g_{11}(s) & \cdots & g_{1n}(s) \\ \vdots & \ddots & \vdots \\ g_{n1}(s) & \cdots & g_{nn}(s) \end{bmatrix} \begin{bmatrix} \frac{1}{\widehat{g}_{m,11}} & \cdots & \frac{1}{\widehat{g}_{m,1n}} \\ \vdots & \ddots & \vdots \\ \frac{1}{\widehat{g}_{m,n1}} & \cdots & \frac{1}{\widehat{g}_{m,nn}} \end{bmatrix} = \begin{bmatrix} h_1(s) & \cdots & 0 \\ \vdots & \ddots & \vdots \\ 0 & \cdots & h_n(s) \end{bmatrix}. \tag{13}$$

Then,

$$\begin{bmatrix} \frac{1}{\widehat{g}_{m,11}} & \cdots & \frac{1}{\widehat{g}_{m,1n}} \\ \vdots & \ddots & \vdots \\ \frac{1}{\widehat{g}_{m,n1}} & \cdots & \frac{1}{\widehat{g}_{m,nn}} \end{bmatrix} = \begin{bmatrix} g_{11}(s) & \cdots & g_{1n}(s) \\ \vdots & \ddots & \vdots \\ g_{n1}(s) & \cdots & g_{nn}(s) \end{bmatrix}^{-1} \begin{bmatrix} h_1(s) & \cdots & 0 \\ \vdots & \ddots & \vdots \\ 0 & \cdots & h_n(s) \end{bmatrix}. \tag{14}$$

In literatures [4, 7], for a weak coupling between each loop, a multiloop controller will give satisfied performance. By means of equation (14), we summarize it as follows:

$$\frac{1}{\widehat{g}_{m,ii}} = \left\{G^{-1}(s)H\right\}_{ii},$$
$$\widehat{g}_{p,ii} = h_i. \tag{15}$$

From equation (1), we can obtain

$$g_{ci} = \frac{\left\{G^{-1}(s)H\right\}_{ii}}{(\lambda_i s + 1) - h_i} = \frac{\left\{G^{-1}(s)\right\}_{ii} h_i}{(\lambda_i s + 1) - h_i}. \tag{16}$$

Similar to equations (5) and (6), the PI controller parameters are calculated as

$$k_{I,ii} = \frac{\mathrm{adj}K_{ii}}{|K|} \left.\frac{sh_{ii}}{1 - h_{ii}}\right|_{s=0}, \tag{17}$$

$$k_{C,ii} = \left(\frac{\mathrm{adj}\, G_{ii}}{|G|} \frac{sh_i}{1 - h_i}\right)'\Bigg|_{s=0} = \frac{\mathrm{adj}\, K_{ii}}{|K|}\left(\frac{sh_i}{1 - h_i}\right)'\Bigg|_{s=0} - \frac{1}{|K|^2}\left(\sum_{p=1}^{n}\left(\sum_{q=1}^{n}\left(\mathrm{adj}\, K_{iq}\right)g'_{qp}\right)\mathrm{adj}K_{pi}\right)\left.\frac{sh_i}{1 - h_i}\right|_{s=0}, \tag{18}$$

where g_{qp}' represents the first derivative of $g_{qp}$and

$$|K| = \begin{vmatrix} k_{11} & \cdots & k_{1n} \\ \vdots & \ddots & \vdots \\ k_{n1} & \cdots & k_{nn} \end{vmatrix}. \tag{19}$$

For the convenience of presentation, we simplified $\mathrm{adj}\, K_{ji}$, $\mathrm{adj}\, K_{jp}$, and $\mathrm{adj}\, K_{pi}$ into the same formula using subscripts v and w, which are defined as

$$\mathrm{adj}\, K_{vw} = (-1)^{v+w}\begin{vmatrix} k_{11} & \cdots & k_{1,v-1} & k_{v+1} & \cdots & k_{1,n} \\ \vdots & \ddots & \vdots & \vdots & \ddots & \vdots \\ k_{w-1,1} & \cdots & k_{w-1,v-1} & k_{w-1,v+1} & \cdots & k_{w-1,n} \\ k_{w+1,1} & \cdots & k_{w+1,v-1} & k_{w+1,v+1} & \cdots & k_{w+1,n} \\ \vdots & \ddots & \vdots & \vdots & \ddots & \vdots \\ k_{n,1} & \cdots & k_{n,v-1} & k_{n,v+1} & \cdots & k_{n,n} \end{vmatrix}, \tag{20}$$

where k_{vw} is the steady gain.

Based on the analysis conventional methods to calculate the PI parameters, which decomposed multivariable systems to a set of multiloop control systems, then utilized single-input and single-output design technique, we establish some equations to deduce and solve the parameters of PI directly and omit the intermediate step, i.e., how to calculate ETF parameters. This section derivates a direct relationship between the parameters of the multiloop controller and that of the open-loop transfer function matrix.

3.2. Performance of the Control System. To demonstrate the robust stability and also show its distinctive features, a popular and commonly used method of analysing robust stability is used in the presence of other controller design approaches. We use the output multiplication uncertainties to measure the robustness of the target system instead of input uncertainties, due to its advantage of less restrictive [4]. For the following system specified with an output uncertainty by

$$\Delta G_0(s) = G(s)\left[I + \Delta_0(s)\right], \tag{21}$$

where $\Delta_0(s)$ denotes the uncertainties occurring at multiplicative outputs, if the following relationship is found, we can conclude that the closed-loop system is stable:

$$\gamma < \frac{1}{\overline{\sigma}}\left[\left(I + G(jw)G_c(jw)\right)^{-1}G(jw)G_c(jw)\right], \tag{22}$$

where γ is used to indicate the robust stability and $\overline{\sigma}$ represents maximum singular value. The larger the value of γ is, the better the robust stability is.

The error integration criterion is a performance index, which is computed by the integral of the deviation between the actual output and the expected output. The integral absolute error (IAE) index and integrated time absolute error (ITAE) index are widely used because of their good practicability and selectivity. The IAE is introduced as follows：

$$\mathrm{IAE} = \int_0^\infty |e(t)|\mathrm{d}t, \tag{23}$$

where

$$e(t) = r(t) - y(t). \tag{24}$$

To analyse the underlying performance, the IAE is first employed to evaluate the control performance of the target closed-loop systems. After that, the ITAE criterion comes in to give a new indicator showing closed-loop performance from the initial point to time infinity:

$$\mathrm{ITAE} = \int_0^\infty t|e(t)|\mathrm{d}t. \tag{25}$$

The system is optimal, which means the IAE and the ITAE get smaller than the relative methods.

4. Examples and Results

In order to illustrate the control performance and robustness of the controller achieved by the proposed method, three typical industrial examples are used for testing. To be specific, the purpose of Example 1 and Example 2 is to show that the proposed method provides better performance than other existing methods for nominal systems. The main target of Example 3 is to demonstrate the performance of the proposed method to the systems of high dimensions.

4.1. Example 1. Consider the VL process [11], in which transfer function is given as

$$\begin{bmatrix} \dfrac{-2.2e^{(-s)}}{7s+1} & \dfrac{1.3e^{(-0.3s)}}{7s+1} \\ \dfrac{-2.8e^{(-1.8s)}}{9.5s+1} & \dfrac{4.3e^{(-0.35s)}}{9.2s+1} \end{bmatrix}. \tag{26}$$

We compare the multiloop tuning results obtained by the proposed method with those presented by Lee et al. [12] and Chen and Seborg [13]. For a fair comparison, we adjust the λ_i used in the proposed method to be the same value of γ or larger than that of others. The control parameters used in the process are shown in Table 1.

Figure 2 shows the closed-loop response performance of the method developed in this paper and the algorithms introduced by [12, 13], where the sequential step changes are set at $t = 0$ and $t = 150$ to the first loop and second loop. From Figure 2, it is clear to see that the PI controller designed by the method proposed in this paper has a faster response than the other two methods and has well-balanced responses.

To further investigate the robustness of the proposed method, a perturbation uncertainty of +50% in process gain is inserted to the simulation study. As shown in Table 2, the IAE_s and ITAE_s values are smaller than those obtained by traditional methods. This verifies that the proposed method provides with better robust performance, where IAE_s and ITAE_s are the sum values of IAE and ITAE for each loop.

4.2. Example 2. Consider a 3×3 multivariable system:

$$\begin{bmatrix} \frac{0.66e^{(-2.6s)}}{6.7s+1} & \frac{-0.61e^{(-3.5s)}}{8.64s+1} & \frac{-0.0049e^{(-s)}}{9.06s+1} \\ \frac{1.11e^{(-6.5s)}}{3.25s+1} & \frac{-2.36e^{(-3s)}}{5s+1} & \frac{-0.012e^{(-1.2s)}}{7.09s+1} \\ \frac{-33.68e^{(-9.2s)}}{8.15s+1} & \frac{46.2e^{(-9.4s)}}{10.9s+1} & \frac{0.87e^{(-s)}(11.61s+1)}{(3.89s+1)(18.8s+1)} \end{bmatrix}. \tag{27}$$

According to equations (17) and (18), the controller parameters are calculated in Table 3. Multiloop tuning results presented by literatures [14, 15] are employed to compare with the proposed methods.

Figure 3 gives the closed-loop responses of the proposed method and the compared methods, where the sequential step changes are made at $t = 0$, $t = 300$, and $t = 600$ to the first, second, and third loop. From Figure 3, we can see that the fluctuation degree of the output signal corresponding to the proposed method is obviously smaller than that of other methods, and the steady state can be reached quickly.

Similar to the previous method, we also insert a perturbation uncertainty of +50% in process gain to test the robust performance. The performance indices results are shown in Table 4; the IAE_s and ITAE_s values show that the proposed method in this paper has better robust performance.

4.3. Example 3. To further illustrate the effectiveness of the proposed method in high-dimensional systems, a system of four dimensions is introduced to verify the control performance and robustness. The corresponding transfer function of A2 system [16] is stated as

$$\begin{bmatrix} \frac{4.09e^{(-1.3s)}}{(33s+1)(8.3s+1)} & \frac{-6.36e^{(-0.2s)}}{(31.6s+1)(20s+1)} & \frac{-0.25e^{(-0.4s)}}{21s+1} & \frac{-0.49e^{(-5s)}}{(22s+1)^2} \\ \frac{-4.17e^{(-4s)}}{45s+1} & \frac{6.93e^{(-1.01s)}}{44.6s+1} & \frac{-0.05e^{(-5s)}}{(34.5s+1)^2} & \frac{1.53e^{(-2.8s)}}{48s+1} \\ \frac{-1.73e^{(-17s)}}{(13s+1)^2} & \frac{5.11e^{(-11s)}}{(13.3s+1)^2} & \frac{4.61e^{(-1.02s)}}{18.5s+1} & \frac{-5.48e^{(-0.5s)}}{15s+1} \\ \frac{-11.18e^{(-2.6s)}}{(43s+1)(6.5s+1)} & \frac{14.04e^{(-0.02s)}}{(45s+1)(10s+1)} & \frac{-0.1e^{(-0.05s)}}{(31.6s+1)(5s+1)} & \frac{4.49e^{(-0.6s)}}{(48s+1)(6.3s+1)} \end{bmatrix}. \tag{28}$$

Using equations (27) and (28), the controller parameters are obtained in Table 5. Since Shen et al. [3] and He et al. [16] designed the controller by utilizing the simple IMC method [17] and gain phase margin, the parameter λ_i is not adjusted in this simulation.

The curves in Figure 4 show the closed-loop time response of the proposed method proposed in this paper as well as the other two methods reported in literature [3, 16]. It can be seen that, except for the lager overshoot of signal y_1, other signals have good dynamic- and steady-state

Table 1: Controller parameters.

Methods	Loop	$k_{C,ij}$	$k_{I,ij}$	λ_i	γ
Proposed	1	−1.7730	−0.2710	1.72	0.59
	2	2.9550	0.3436	0.75	
Lee	1	−1.3100	0.5800	—	0.53
	2	3.9700	1.6400	—	
Chen	1	1.2100	0.2600	—	0.50
	2	3.7400	3.4000	—	

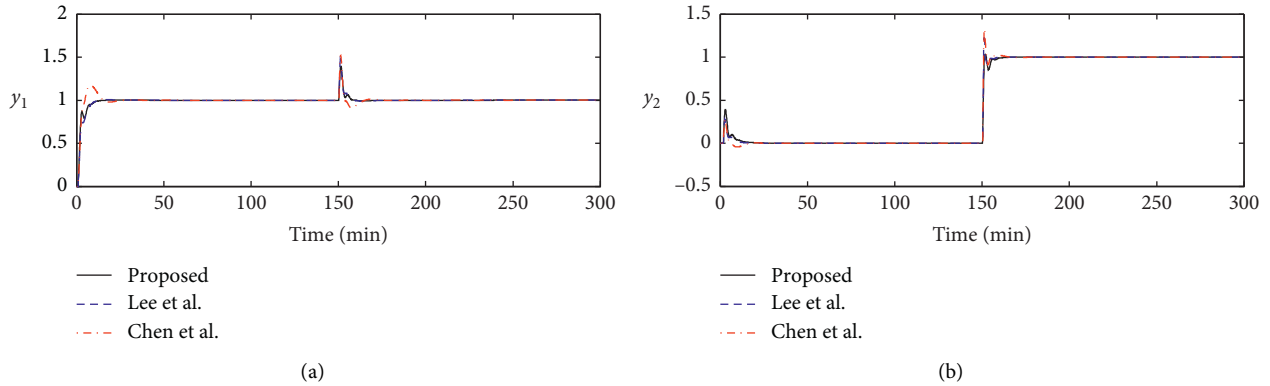

(a) (b)

Figure 2: Closed-loop step responses for Example 1.

Table 2: Performance indices.

Methods	IAE_s		$ITAE_s$	
	Nominal	+50%	Nominal	+50%
Proposed	6.391	6.007	22.675	19.24
Lee	7.102	6.899	32.369	23.99
Chen	7.370	7.506	27.066	25.23

Table 3: Controller parameters.

Methods	Loop	$k_{C,ij}$	$k_{I,ij}$	λ_i	γ
Proposed	1	0.9939	0.2976	8.00	0.07
	2	−0.1309	−0.0471	12.0	
	3	7.5314	0.7602	1.00	
SAT [14]	1	2.7100	0.3640	—	0.01
	2	−0.3660	−0.0350	—	
	3	4.5600	1.4760	—	
Lee [15]	1	0.5930	0.1730	—	0.06
	2	−0.1240	−0.0430	—	
	3	3.2200	0.4210	—	

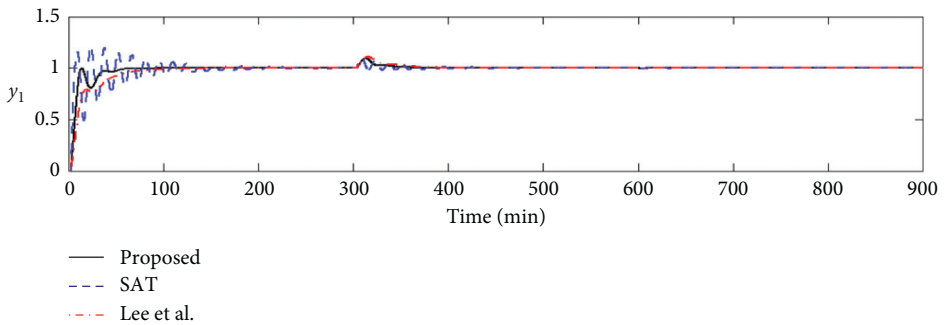

(a)

Figure 3: Continued.

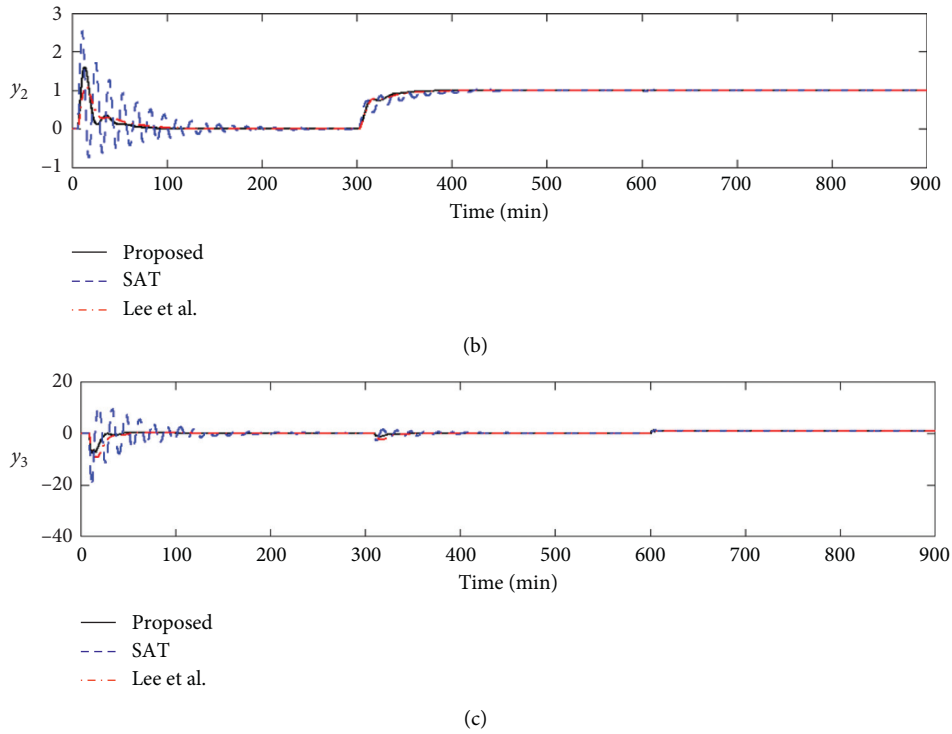

Figure 3: Closed-loop step responses for Example 2.

Table 4: Performance indices.

Method	IAE_s		$ITAE_s$	
	Nominal	+50%	Nominal	+50%
Proposed	180.9597	160.7001	4431.40	3713.8710
SAT	696.4530	2233.640	40341.5	46454.8606
Lee	274.4191	223.4985	7456.57	5722.0498

Table 5: Controller parameters.

Methods	Loop	$k_{C,ij}$	$k_{I,ij}$	$k_{D,ij}$	λ_i	γ
Proposed	1	2.4881	0.0915	—	7.0	0.15
	2	3.2068	0.2241	—	2.0	
	3	4.3252	0.1664	—	1.0	
	4	5.7641	0.0340	—	5.0	
He	1	3.8840	0.0940	25.75	—	0.02
	2	2.5490	0.0570	—	—	
	3	1.3110	0.0710	—	—	
	4	4.2330	0.0780	23.57	—	
Shen	1	3.0503	0.0739	20.23	—	0.03
	2	2.5020	0.0561	—	—	
	3	1.5450	0.0835	—	—	
	4	1.7530	0.0634	19.18	—	

performance. This shows that the proposed PI controller yields fast, satisfying and well-balance response, though the model dimension is high.

Table 6 shows the robustness performance of the proposed methods when the process gain is increased by perturbation uncertainty of +50%. From Table 6, we can see that the IAE_s and $ITAE_s$ values obtained by the new method is smaller than the other methods, which further verify that the proposed method provides with good robust performance for high dimension.

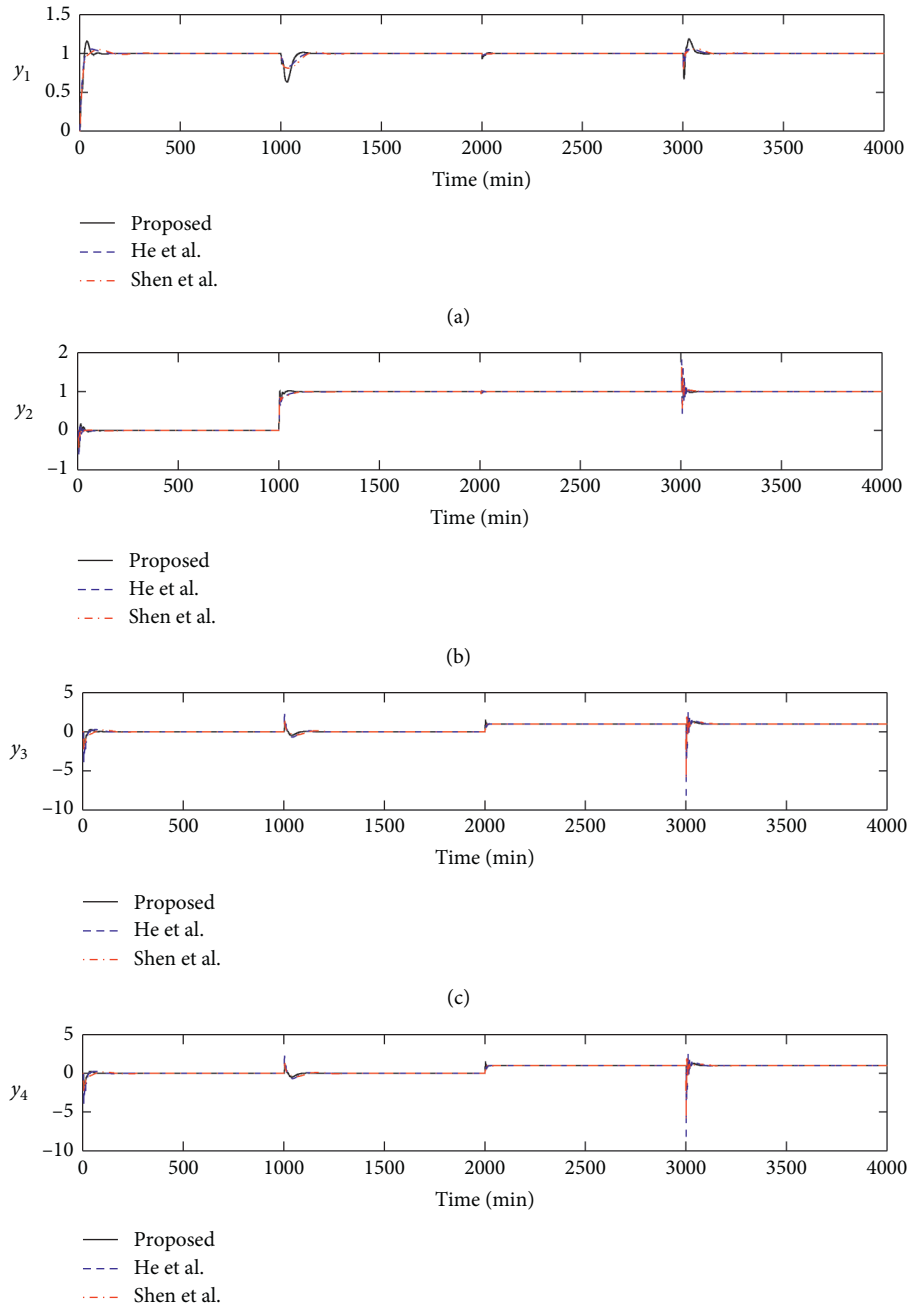

Figure 4: Closed-loop step responses for Example 3.

Table 6: Performance indices.

Methods	IAE_s		$ITAE_s$	
	Nominal	+50%	Nominal	+50%
Proposed	234.4048	219.1850	16824.34	14245.40
He	278.6150	447.8400	10393.18	20731.42
Shen	316.1688	323.3098	25146.40	22231.41

5. Conclusions

In this paper, an effective controller design method for multivariable systems has been developed. Based on the properties of the ETF and the IMC design principle, the decentralized PI controller is established directly by the proposed method. This method analytically derivates the relationships between controller parameters and the open-loop process transfer function. Three different simulation examples have proved the effectiveness of this method and it also can be applied to high-dimensional system. Further work will focus on designing the decentralized controller for nonsquare multivariable systems.

Data Availability

The data used to support the findings of this study are included within the article.

Conflicts of Interest

The authors declare that there are no conflicts of interest regarding the publication of this paper.

Acknowledgments

This work was supported by the Natural Science Foundation of China, under Grant no. 61773183.

References

[1] S. Gigi and A. K. Tangirala, "Quantification of interaction in multiloop control systems using directed spectral decomposition," *Automatica*, vol. 49, no. 5, pp. 1174–1183, 2013.

[2] H.-P. Huang, J.-C. Jeng, C.-H. Chiang, and W. Pan, "A direct method for multi-loop PI/PID controller design," *Journal of Process Control*, vol. 13, no. 8, pp. 769–786, 2003.

[3] Y. Shen, W.-J. Cai, and S. Li, "Multivariable process control: decentralized, decoupling, or sparse?" *Industrial & Engineering Chemistry Research*, vol. 49, no. 2, pp. 761–771, 2010.

[4] T. N. L. Vu and M. Lee, "Independent design of multi-loop PI/PID controllers for interacting multivariable processes," *Journal of Process Control*, vol. 20, no. 8, pp. 922–933, 2010.

[5] K. H. Estévez-Sánchez, A. Sampieri-Croda, M. A. García-Alvarado, and I. I. Ruiz-López, "Design of multiloop PI controllers based on quadratic optimal approach," *ISA Transactions*, vol. 70, pp. 338–347, 2017.

[6] S. Cha, D. Chun, and J. Lee, "Two-step IMC–PID method for multiloop control system design," *Industrial & Engineering Chemistry Research*, vol. 41, no. 12, pp. 3037–3041, 2002.

[7] T. N. L. Vu and M. Lee, "Multi-loop PI controller design based on the direct synthesis for interacting multi-time delay processes," *ISA Transactions*, vol. 49, no. 1, pp. 79–86, 2010.

[8] Y. Lee, S. Park, M. Lee, and C. Brosilow, "PID controller tuning for desired closed-loop responses for SI/SO systems," *AIChE Journal*, vol. 44, no. 1, pp. 106–115, 1998.

[9] Q. Wang, W. J. Cai, and M. J. He, "Equivalent transfer function method for PI/PID controller design of Multivariable processes," *Journal of Process Control*, vol. 17, no. 18, pp. 665–673, 2007.

[10] Q.-G. Wang, Y. Zhang, and M.-S. Chiu, "Non-interacting control design for multivariable industrial processes," *Journal of Process Control*, vol. 13, no. 3, pp. 253–265, 2003.

[11] T. Liu, W. Zhang, and F. Gao, "Analytical decoupling control strategy using a unity feedback control structure for MIMO processes with time delays," *Journal of Process Control*, vol. 17, no. 2, pp. 173–186, 2007.

[12] J. Lee, D. Hyun Kim, and T. F. Edgar, "Static decouplers for control of multivariable processes," *AICHE Journal*, vol. 51, no. 10, pp. 2712–2720, 2005.

[13] D. Chen and D. E. Seborg, "Design of decentralized PI control systems based on Nyquist stability analysis," *Journal of Process Control*, vol. 13, no. 1, pp. 27–89, 2003.

[14] A. P. Loh, C. C. Hang, C. K. Quek, and V. U. Vasnani, "Autotuning of multivariable PI controllers using relay feedback," *Industrial & Engineering Chemistry Research*, vol. 32, no. 6, pp. 1102–1107, 1993.

[15] M. Lee, K. Lee, C. Kim, and J. Lee, "Analytical design of multiloop PID controllers for desired closed-loop responses," *AICHE Journal*, vol. 50, no. 7, pp. 1631–1635, 2004.

[16] M.-J. He, W.-J. Cai, and B.-F. Wu, "Design of decentralized IMC-PID controller based on dRI analysis," *AICHE Journal*, vol. 52, no. 11, pp. 3852–3863, 2006.

[17] S. Skogestad, "Simple analytic rules for model reduction and PID controller tuning," *Journal of Process Control*, vol. 13, no. 4, pp. 291–309, 2003.

Hindawi
Complexity
Volume 2020, Article ID 6843730, 14 pages
https://doi.org/10.1155/2020/6843730

Research Article

Convergence Analysis of Iterative Learning Control for Two Classes of 2-D Linear Discrete Fornasini–Marchesini Model

Kai Wan

School of Electronic Information and Electrical Engineering, Huizhou University, Huizhou 516007, China

Correspondence should be addressed to Kai Wan; wankai606815@163.com

Received 2 July 2020; Revised 23 August 2020; Accepted 1 September 2020; Published 14 September 2020

Academic Editor: Guangchen Zhang

This paper first investigates convergent property of two iterative learning control (ILC) laws for two kinds of two-dimensional linear discrete systems described by the first Fornasini–Marchesini model (2-D LDFFM with a direct transmission from inputs to outputs and 2-D LDFFM with input delay). Different from existing ILC results for 2-D LDFFM, this paper provides convergence analysis in a three-dimensional (3-D) framework. By using row scanning approach (RSA) or column scanning approach (CSA), it is theoretically proved no matter which method is adopted, perfect tracking on the desired reference surface is accomplished. In addition, linear matrix inequality (LMI) technique is utilized to computer the learning gain of the ILC controller. The effectiveness and feasibility of the designed ILC law are illustrated through numerical simulation on a practical thermal process.

1. Introduction

In practical industrial applications for two-dimensional (2-D) dynamical systems, for example, in form-closure grasps, the immobilized manipulation of 2-D serial chains could be regarded as a repetitive control problem [1]. Also, mold processing and material manufacturing usually require repeated operations of the controlled processing units to obtain a high-precision reference surface [2]. With regard to this kind of repetitive tracking problem, the traditional control methods in infinite coordinate domain, such as H_∞ control [3], stochastic stability analysis [4], and sliding mode control [5], are difficult to be used because the precise model information is known in advance. Clearly, for the repetitively tracking cases mentioned above, the traditional tracking control approaches for 2-D dynamical systems in infinite coordinate domain are difficult to be applicable. Clearly, for the repetitively tracking cases mentioned above, the traditional tracking control approaches for 2-D dynamical systems in infinite coordinate domain are difficult to be applicable.

To the best of our knowledge, iterative learning control (ILC), as a data-driven and unsupervised control approach, does not require accurate knowledge of the controlled system, which makes ILC be widely prevalent in practical applications. A large number of ILC research results reported in the past few decades have fundamentally designed for one-dimensional (1-D) dynamical systems [6–14], only very few results involved in 2-D dynamical systems [15–22], which concentrate on mainly 2-D linear discrete first Fornasini–Marchesini model (2-D LDFFM). An optimal ILC algorithm was proposed in [16], such that the ILC tracking error converges to zero monotonically. Unfortunately, the system parameters of 2-D LDFFM are known. In [15], five ILC algorithms were proposed, the effectiveness and feasibility of which is verified through only numerical example. Afterwards, by using the column scanning approach (CSA), the iterative process of 2-D LDFFM is transformed into a iterative process of 1D systems; rigorously, theoretical proof on convergence and robustness of a two-gain ILC law is provided in [17]. Also, using the CSA as [18], to track a class of nonrepetitive reference surface described by a high-order internal model operator (HOIM), two HOIM-based ILC laws were, respectively, investigated in [23] for 2-D LDFFM by using 2-D HOIM-based linear inequality theory, but the ultimate ILC tracking error can only converge to a bounded range. To this end, adaptive ILC approach was proposed in [21, 22] to identify all unknown system parameters of 2-D

LDFFM, and the ILC result of perfect tracking on iteration-varying reference surface can be obtained. Unfortunately, the gain matrix in 2-D LDFFM is required to be positive definite, such that the proposed adaptive ILC algorithm, in practical applications, is greatly restricted. Notably, the aforementioned ILC results have concerned mainly on 2-D LDFFM without input delay.

Time delay, recognized as one of the main sources for poor performance or even instability of control systems, is frequently encountered in the signal transmission process of engineering and biological systems [24]. Over the past few years, with respect to 2-D systems with time delay on horizontal direction and vertical direction, some initial results have been reported on the states estimation [25], H_∞ control and filtering [26, 27], and nonfragile robust optimal guaranteed cost control [28]. For instance, the authors in [23] have investigated the robust state estimation problem for 2-D linear discrete systems with state delay, and a robust H_∞ filter for 2-D discrete systems with time delays has been designed in [23]. A delay-dependent H_∞ controller for 2-D discrete state delay systems was designed in [27]. Nonfragile robust optimal guaranteed cost control subject to both state delay and input delay is discussed in [28]. However, no works have considered the ILC tracking problem for 2-D linear discrete systems with input delay, which motivates our current study.

This paper first investigates the convergence property of two ILC laws for 2-D LDFFM with a direct transmission from inputs to outputs and 2-D LDFFM with input delay to track the desired reference surface, respectively. The 2-D LDFFM is very typical, and many practical 2-D engineering systems can be represented as the form of 2-D LDFFM [29, 30]. Under a 3-D framework, a 3-D dynamical process is converted into a 2-D dynamical process by using CSA or row scanning approach (RSA), and it is theoretically proved no matter which method is used; perfect tracking on the desired reference surface is fulfilled. Additionally, this paper theoretically provides a linear matrix inequality (LMI) technique to computer the learning gain matrix of the ILC law. The main contributions of this paper are summarized as follows:

(1) All of the existing ILC results for 2-D dynamical systems have not considered input delay. To the best of our knowledge, it is the first time to investigate ILC algorithms for 2-D LDFFM with a direct transmission from inputs to outputs and for 2-D LDFFM with input delay.

(2) Compared with the adaptive ILC algorithm for 2-D LDFFM in [21, 22], two ILC algorithms proposed in this paper have no restriction on the numbers of system inputs and outputs.

(3) Different from the existing ILC work for 2-D LDFFM [17, 18], a 3-D framework learning mechanism is presented in this paper and can reveal the dynamical behavior of the 2-D LDFFM in the horizontal dynamical direction, vertical dynamical direction, and iteration direction.

(4) It is theoretically proved that RSA or CSA can guarantee perfect tracking on the desired reference surface.

(5) Compared with the literature [20], this paper has addressed the ILC issue on nonidentical boundary states. In addition, this paper successfully avoids strong Assumption 2.2 on desired reference surface and Assumption 2.3 on the system matrix, and LMI technique is utilized to computer the learning gain of the ILC controller.

The rest of this paper is arranged as follows: Section 2 presents problem formulation and some preliminaries. Sections 3 and 4 provide convergence analysis of a symmetrical P-type ILC law and extend to 2-D LDFFM with input delay, respectively. Two simulation examples are introduced in Section 5. Finally, a conclusion on this article is drawn in Section 6. Notations: $A>0$ ($A<0$) denotes positive-definite (negative-definite) matrix. $\{i\}_{m_1}^{m_2}$ represents $i \in \{m_1, m_1+1, m_1+2, \ldots, m_2\}$ with positive integer m_2, and $\{i\}_0^\infty$ represents $i \in \{0, 1, 2, \ldots\}$. I_m denotes identity matrix with dimension $m \times m$. $\rho(\cdot)$ represents spectral radius of matrix.

2. Problem Formulation and Some Preliminaries

Consider the following 2-D LDFFM with a direct transmission from inputs to outputs [23], executing designated tracking tasks repetitively over dynamical region $\{n_1\}_0^{N_1}$ and $\{n_2\}_0^{N_2}$:

$$\begin{cases} x_k(n_1+1, n_2+1) = A_1 x_k(n_1+1, n_2) + A_2 x_k(n_1, n_2) \\ \quad + A_3 x_k(n_1, n_2+1) + B u_k(n_1, n_2), \\ y_k(n_1, n_2) = C x_k(n_1, n_2) + D u_k(n_1, n_2), \end{cases} \tag{1}$$

where $u_k(n_1, n_2) \in R^m$, $x_k(n_1, n_2) \in R^p$, and $y_k(n_1, n_2) \in R^l$ represent, respectively, control input, system state, and control output; A_1, A_2, A_3, B, C, and D are real matrices with appropriate dimensions. $\{k\}_0^\infty$ denotes the k-th repetitive number (or iteration number) of 2-D LDFFM (1); n_1 and n_2 are, respectively, discrete indexes along the horizontal dynamical direction and vertical dynamical direction. The independent indexes n_1 and n_2 in practical 2-D LDFFM, i.e., chemical reactors, heater exchangers, and pipe furnaces, usually represent space locations and time instants, respectively [31]. As $D = 0$, 2-D LDFFM (1) has been investigated in [17, 18].

For $\{n_1\}_0^{N_1}$ and $\{n_2\}_0^{N_2}$, let the desired trajectory surface and the corresponding tracking error at kth iteration, respectively, be denoted as $y_r(n_1, n_2)$ and $e_k(n_1, n_2)$, and the control objective of ILC for 2-D LDFFM is to update the control input $u_k(n_1, n_2)$ iteratively, such that the system output $y_k(n_1, n_2)$ converges to desired reference surface $y_r(n_1, n_2)$ asymptotically, i.e.,

$$\lim_{k \longrightarrow +\infty} y_k(n_1, n_2) = y_r(n_1, n_2), \quad \{n_1\}_1^{N_1}, \{n_2\}_1^{N_2}. \tag{2}$$

For the convenience of discussing the ILC problem for 2-D LDFFM, the property on a block matrix, assumptions, and Lemma is provided as follows.

Property 1. (see [32]). Give the following block matrix H with a nonsingular matrix $H_1 \in R^{m\times m}$:

$$H = \begin{bmatrix} H_1 & 0 & 0 & \cdots & 0 \\ -H_2 & H_1 & 0 & \cdots & \vdots \\ 0 & -H_2 & H_1 & \ddots & 0 \\ \vdots & \ddots & \ddots & \ddots & 0 \\ 0 & \cdots & 0 & -H_2 & H_1 \end{bmatrix} \in R^{mN\times mN}, \tag{3}$$

and the inverse matrix of which is given as

$$H^{-1} = \begin{bmatrix} \overline{H}_1 & 0 & 0 & \cdots & 0 \\ \overline{H}_2 & \overline{H}_1 & 0 & \cdots & \vdots \\ \overline{H}_3 & \overline{H}_2 & \overline{H}_1 & \ddots & 0 \\ \vdots & \ddots & \ddots & \ddots & 0 \\ \overline{H}_N & \cdots & \overline{H}_3 & \overline{H}_2 & \overline{H}_1 \end{bmatrix} \in R^{mN\times mN}, \tag{4}$$

with

$$\begin{cases} \overline{H}_1 = H_1^{-1}, \\ \overline{H}_2 = H_1^{-1}H_2H_1^{-1}, \\ \overline{H}_3 = \left(H_1^{-1}H_2\right)^2 H_1^{-1}, \\ \quad \vdots \\ \overline{H}_N = \left(H_1^{-1}H_2\right)^{N-1} H_1^{-1}. \end{cases} \tag{5}$$

In particular, as $H_1 = I_m$, H^{-1} becomes

$$H^{-1} = \begin{bmatrix} I_m & 0 & 0 & \cdots & 0 \\ H_2 & I_m & 0 & \cdots & \vdots \\ H_2^2 & H_2 & I_m & \ddots & 0 \\ \vdots & \ddots & \ddots & \ddots & 0 \\ H_2^{N-1} & \cdots & H_2^2 & H_2 & I_m \end{bmatrix}. \tag{6}$$

Property 2 (see [32]). For H^{-1} in Property 1, according to matrix theory, there is $\rho(H^{-1}) = \rho(\overline{H}_1)$, which is irrelevant to $\overline{H}_2$, $\overline{H}_3$, ..., and $\overline{H}_N$.

Remark 1. Properties 1 and 2 are often used in the ILC convergence analysis for 2-D linear discrete dynamical systems to track reference surface described by a high-order internal model or varying uniformly between $(k+1)$-th iteration and k-th iteration [18]. Certainly, Properties 1 and 2 are also suitable to track repetitive reference surface considered in this paper.

Assumption 1. The matrix D is full-row rank.

Assumption 2. The boundary states $x_k(0,n_2)$ and $x_k(n_1,0)$ of 2-D LDFFM (1) are assumed to satisfy $x_k(0,n_2) = x_0(0,n_2)$, $\{n_2\}_1^{N_2}$ and $x_k(n_1,0) = x_0(n_1,0)$, $\{n_1\}_0^{N_1}$, where $x_0(0,n_2)$ and $x_0(n_1,0)$ are iteration-invariant functions with respective to n_2 and n_1.

Lemma 1. *Consider the following 3-D linear discrete system for $\{n_1\}_0^{N_1}$, $\{n_2\}_0^{N_2}$, and $\{k\}_0^{\infty}$:*

$$\theta_{k+1}(n_1,n_2) = \alpha_1\theta_k(n_1,n_2) + \alpha_2\delta_k(n_1,n_2), \tag{7}$$

where $\theta_k(n_1,n_2) \in R^{L_1}$ and $\delta_k(n_1,n_2) \in R^{L_2}$, respectively, are state and control input; α_1 and α_2 denote real matrices. Suppose the boundary state $\theta_0(n_1,n_2) = f(n_1,n_2)$, where $f(n_1,n_2)$ is a bounded vector function. When $\lim_{k\longrightarrow+\infty}\delta_k(n_1,n_2) = 0$, if $\rho(\alpha_1) < 1$ is satisfied, then the 3-D system is asymptotically stable along the dynamical direction k, i.e.,

$$\lim_{k\longrightarrow+\infty}\theta_k(n_1,n_2) = 0, \quad \{n_1\}_0^{N_1}, \{n_2\}_0^{N_2}. \tag{8}$$

In particular, when $\delta_k(n_1,n_2) = 0$, for $\{n_1\}_0^{N_1}$ and $\{n_2\}_0^{N_2}$, $\lim_{k\longrightarrow+\infty}\theta_k(n_1,n_2) = 0$ can still be obtained for $\{n_1\}_0^{N_1}$ and $\{n_2\}_0^{N_2}$. The proof process of Lemma 1 is shown in Appendix.

3. Convergence Analysis of a Symmetrical P-Type ILC Law

The following symmetrical P-type ILC law is applied to 2-D LDFFM (1) for $\{n_1\}_0^{N_1}$ and $\{n_2\}_0^{N_2}$:

$$u_{k+1}(n_1,n_2) = u_k(n_1,n_2) + \Gamma e_k(n_1,n_2), \tag{9}$$

where $e_k(n_1,n_2) = y_r(n_1,n_2) - y_k(n_1,n_2)$. The learning gain $\Gamma \in R^{m\times l}$ is to be designed.

Remark 2. It is worth noting that 2-D LDFFM (1) is a zero relative degree system; the proposed ILC law (9) is extended on the existing ILC work for 1D linear discrete dynamical systems with zero relative degree [33]. Additionally, 2-D LDFFM (1) and the ILC law (9) are symmetrical on the discrete indexes $\{n_1\}_0^{N_1}$ and $\{n_2\}_0^{N_2}$; therefore, row scanning approach (RSA) or column scanning approach (CSA) can guarantee the same ILC tracking result, which is demonstrated in Theorem 1 and Appendix.

Theorem 1. *Consider the 2-D LDFFM with a direct transmission from inputs to outputs (1) under Assumptions 1 and 2 and use the symmetrical P-type ILC law (9). If the learning gain Γ satisfies*

$$\rho(I_l - D\Gamma) < 1, \tag{10}$$

then the tracking error $e_k(n_1,n_2)$ converges to zero, i.e.,

$$\lim_{k\longrightarrow+\infty} e_k(n_1,n_2) = 0, \quad \{n_1\}_0^{N_1}, \{n_2\}_0^{N_2}. \tag{11}$$

Proof 1. For $\{n_1\}_0^{N_1-1}$ and $\{n_2\}_0^{N_2-1}$, let

$$\begin{aligned} \delta x_k(n_1,n_2) &= x_{k+1}(n_1,n_2) - x_k(n_1,n_2), \\ \delta u_k(n_1,n_2) &= u_{k+1}(n_1,n_2) - u_k(n_1,n_2). \end{aligned} \tag{12}$$

Using (1), for $\{n_1\}_0^{N_1-1}$ and $\{n_2\}_0^{N_2-1}$, there is

$$\begin{aligned}\delta x_k(n_1+1,n_2+1) &= x_{k+1}(n_1+1,n_2+1)\\ &\quad - x_k(n_1+1,n_2+1)\\ &= A_1\delta x_k(n_1+1,n_2) + A_2\delta x_k(n_1,n_2)\\ &\quad + A_3\delta x_k(n_1,n_2+1) + B\delta u_k(n_1,n_2).\end{aligned} \tag{13}$$

Applying the ILC law (9) into (13), it generates

$$\begin{aligned}\delta x_k(n_1+1,n_2+1) &= A_1\delta x_k(n_1+1,n_2) + A_2\delta x_k(n_1,n_2)\\ &\quad + A_3\delta x_k(n_1,n_2+1) + B\Gamma e_k(n_1,n_2).\end{aligned} \tag{14}$$

On the contrary, according to $e_k(n_1,n_2) = y_r(n_1,n_2) - y_k(n_1,n_2)$ and (1), we have

$$\begin{aligned}e_{k+1}(n_1,n_2) - e_k(n_1,n_2) &= y_r(n_1,n_2) - y_{k+1}(n_1,n_2)\\ &\quad - y_r(n_1,n_2) + y_k(n_1,n_2)\\ &= -C[x_{k+1}(n_1,n_2) - x_k(n_1,n_2)]\\ &\quad - D[u_{k+1}(n_1,n_2) - u_k(n_1,n_2)],\end{aligned} \tag{15}$$

where $\{n_1\}_0^{N_1}$ and $\{n_2\}_0^{N_2}$. Substituting the ILC law (9) into (15), it yields

$$\begin{aligned}e_{k+1}(n_1,n_2) - e_k(n_1,n_2) &= -C[x_{k+1}(n_1,n_2) - x_k(n_1,n_2)]\\ &\quad - D\Gamma e_k(n_1,n_2).\end{aligned} \tag{16}$$

Rearranging (16), there is

$$e_{k+1}(n_1,n_2) = -C\delta x_k(n_1,n_2) + (I_l - D\Gamma)e_k(n_1,n_2). \tag{17}$$

Let

$$\delta X_k(n_2) = \left[\, \delta x_k^T(1,n_2) \;\; \delta x_k^T(2,n_2) \;\; \cdots \;\; \delta x_k^T(N_1,n_2) \,\right]^T, \tag{18}$$

$$E_k(n_2) = \left[\, e_k^T(0,n_2) \;\; e_k^T(1,n_2) \;\; \cdots \;\; e_k^T(N_1,n_2) \,\right]^T, \tag{19}$$

where $\{n_2\}_0^{N_2}$. According to (18) and (19), using the CSA on horizontal dynamical direction n_1, (14) can be rewritten as

$$\begin{aligned}\Phi_1\delta X_k(n_2+1) &= \Phi_2\delta X_k(n_2) + \Phi_3 E_k(n_2) + \widehat{A}_2\delta x_k(0,n_2)\\ &\quad + \widehat{A}_3\delta x_k(0,n_2+1),\end{aligned} \tag{20}$$

where

$$\Phi_1 = \begin{bmatrix} I_p & 0 & 0 & \cdots & 0\\ -A_3 & I_p & 0 & \cdots & 0\\ 0 & -A_3 & I_p & \ddots & \vdots\\ \vdots & \ddots & \ddots & \ddots & 0\\ 0 & \cdots & 0 & -A_3 & I_p \end{bmatrix} \in R^{pN_1\times pN_1},$$

$$\Phi_2 = \begin{bmatrix} A_1 & 0 & 0 & \cdots & 0\\ A_2 & A_1 & 0 & \cdots & 0\\ 0 & A_2 & A_1 & \ddots & \vdots\\ \vdots & \ddots & \ddots & \ddots & 0\\ 0 & \cdots & 0 & A_2 & A_1 \end{bmatrix} \in R^{pN_1\times pN_1},$$

$$\Phi_3 = \begin{bmatrix} B\Gamma & 0 & 0 & \cdots & 0\\ 0 & B\Gamma & \ddots & \ddots & \vdots\\ 0 & 0 & B\Gamma & 0 & 0\\ \vdots & \ddots & \ddots & \ddots & 0\\ 0 & \cdots & 0 & 0 & B\Gamma \end{bmatrix} \in R^{pN_1\times l(N_1+1)}, \tag{21}$$

$$\widehat{A}_2 = \begin{bmatrix} A_2\\ 0\\ 0\\ \vdots\\ 0 \end{bmatrix} \in R^{pN_1\times p},$$

$$\widehat{A}_3 = \begin{bmatrix} A_3\\ 0\\ 0\\ \vdots\\ 0 \end{bmatrix} \in R^{pN_1\times p}.$$

Then, since Φ_1 is a nonsingular matrix, premultiplying Φ_1^{-1} on both sides of (20), we get

$$\begin{aligned}\delta X_k(n_2+1) &= \overline{\Phi}_1\delta X_k(n_2) + \overline{\Phi}_2 E_k(n_2) + \Phi_1^{-1}\widehat{A}_2\delta x_k(0,n_2)\\ &\quad + \Phi_1^{-1}\widehat{A}_3\delta x_k(0,n_2+1),\end{aligned} \tag{22}$$

where $\overline{\Phi}_1 = \Phi_1^{-1}\Phi_2$ and $\overline{\Phi}_2 = \Phi_1^{-1}\Phi_3$. Similarly, (17) can also rewritten as

$$E_{k+1}(n_2) = \varphi_1\delta X_k(n_2) + \varphi_2 E_k(n_2) - C\delta x_k(0,n_2), \tag{23}$$

where

$$\varphi_1 = \begin{bmatrix} 0 & 0 & 0 & \cdots & 0 \\ -C & 0 & 0 & \cdots & 0 \\ 0 & -C & 0 & \ddots & \vdots \\ \vdots & \ddots & \ddots & \ddots & 0 \\ 0 & \cdots & 0 & -C & 0 \end{bmatrix} \in R^{l(N_1+1)\times pN_1},$$

$$\varphi_2 = \begin{bmatrix} I_l - D\Gamma & 0 & \cdots & 0 \\ 0 & I_l - D\Gamma & \ddots & \vdots \\ \vdots & \ddots & \ddots & 0 \\ 0 & \cdots & 0 & I_l - D\Gamma \end{bmatrix} \in R^{l(N_1+1)\times l(N_1+1)},$$

$$\widehat{C} = \begin{bmatrix} C \\ 0 \\ \vdots \\ 0 \end{bmatrix} \in R^{l(N_1+1)\times p}. \tag{24}$$

From Assumption 2, we obtain $\delta x_k(0, n_2) = x_{k+1}(0, n_2) - x_k(0, n_2) = 0$ for $\{n_2\}_0^{N_2}$. Thus, (22) and (23) can be reformulated as

$$\begin{cases} \delta X_k(n_2+1) = \overline{\Phi}_1 \delta X_k(n_2) + \overline{\Phi}_2 E_k(n_2), \\ E_{k+1}(n_2) = \varphi_1 \delta X_k(n_2) + \varphi_2 E_k(n_2), \end{cases} \tag{25}$$

where $\{n_2\}_0^{N_2-1}$. In (25), based on Assumption 2, we deduce

$$\delta X_k(0) = \left[\delta x_k^T(1,0) \;\; \delta x_k^T(2,0) \;\; \cdots \;\; \delta x_k^T(N_1,0) \right]^T = 0, \tag{26}$$

and $E_0(n_2)$ is bounded for $\{n_2\}_0^{N_2-1}$. Using Lemma 4 in [18], if $\rho(\varphi_2) < 1$ (equivalently, $\rho(I_l - D\Gamma) < 1$, see Property 2), there is

$$\begin{cases} \lim_{k\longrightarrow+\infty} \delta X_k(n_2) = 0, \; \{n_2\}_1^{N_2}, \\ \lim_{k\longrightarrow+\infty} E_k(n_2) = 0, \; \{n_2\}_0^{N_2-1}. \end{cases} \tag{27}$$

Additionally, taking $n_2 = N_2$ in (17), we have

$$e_{k+1}(n_1, N_2) = -C\delta x_k(n_1, N_2) + (I_l - D\Gamma) e_k(n_1, N_2), \tag{28}$$

where $\{n_1\}_0^{N_1}$. From (27) and $\delta x_k(0, N_2) = 0$, we obtain $\lim_{k\longrightarrow+\infty} \delta x_k(n_1, N_2) = 0$, $\{n_1\}_0^{N_1}$. Using Lemma 1, if $\rho(I_l - D\Gamma) < 1$ is satisfied, there is

$$\lim_{k\longrightarrow+\infty} e_k(n_1, N_2) = 0, \quad \{n_1\}_0^{N_1}. \tag{29}$$

From (27) and (29) and the definition on $E_k(n_2)$ in (19), it yields

$$\lim_{k\longrightarrow+\infty} e_k(n_1, n_2) = 0, \quad \{n_1\}_0^{N_1}, \{n_2\}_0^{N_2}. \tag{30}$$

Theorem 1 is completed.

Remark 3. The convergence condition $\rho(I_l - D\Gamma) < 1$ in Theorem 1 only depends on the matrix D and is irrelevant to A_1, A_2, A_3, C, and B, which is in accordance with the ILC convergence condition of the following 1D linear discrete iterative system to track repetitive reference trajectory [33]:

$$\begin{cases} x_k(t+1) = Ax_k(t) + Bu_k(t), \\ y_k(t) = Cx_k(t) + Du_k(t), \end{cases} \tag{31}$$

under a P-type ILC law $u_{k+1}(t) = u_k(t) + \Gamma e_k(t)$ and initial iterative state $x_k(t) = x_0(t)$.

Remark 4. Taking advantage of the estimated information on D, the learning gain matrix Γ of $\rho(I_l - D\Gamma) < 1$ can be determined by using LMI technique. For the following 1D linear discrete dynamical system described by $I_l - D\Gamma$,

$$x(k+1) = (I_l - D\Gamma)x(k), \quad \{k\}_0^{\infty}. \tag{32}$$

Asymptotically stable condition $\rho(I_l - D\Gamma) < 1$ is satisfied if and only if there exists a $Q \succ 0$ such that

$$(I_l - D\Gamma)^T Q (I_l - D\Gamma) - Q \prec 0. \tag{33}$$

Using Schur complement theorem [34], it yields

$$\begin{bmatrix} -Q^{-1} & I_l - D\Gamma \\ I_l - \Gamma^T D^T & -Q \end{bmatrix} \prec 0. \tag{34}$$

Pre- and postmultiplying by $\mathrm{diag}\{I_l, Q^{-1}\}$ on both sides of (34), we have

$$\begin{bmatrix} -Q^{-1} & Q^{-1} - D\Gamma Q^{-1} \\ Q^{-1} - Q^{-1}\Gamma^T D^T & -Q^{-1} \end{bmatrix} \prec 0. \tag{35}$$

Therefore, $\rho(I_l - D\Gamma) < 1$ is equivalent to solving the following LMI: there exists positive-definite matrix $Q \in R^{l\times l}$ and matrix $X \in R^{m\times l}$ such that

$$\begin{bmatrix} -Q^{-1} & Q^{-1} - DX \\ Q^{-1} - X^T D^T & -Q^{-1} \end{bmatrix} \prec 0, \tag{36}$$

with $X = \Gamma Q^{-1}$. Therefore, the selection problem of the learning gain matrix Γ is transformed into the feasibility problem on solving LMI (36).

Remark 5. Theorem 1 employs the CSA on dynamical direction n_1 to obtain ILC result under Assumption 2. As the RSA on dynamical direction n_2 is applied to 2-D LDFFM (1) and the ILC law (9), we can still acquire the same ILC result with Theorem 1 due to the symmetrical characteristics on n_1 and n_2 in 2-D LDFFM (1) and the ILC law (9), and see Appendix.

4. Extension to 2-D LDFFM with Input Delay

In this section, under Assumption 2, we investigate the ILC issues for 2-D LDFFM with input delay [23], which is described in the following for $\{n_1\}_0^{N_1-1}$ and $\{n_2\}_0^{N_2-1}$:

$$\begin{cases} x_k(n_1+1, n_2+1) = A_1 x_k(n_1+1, n_2) + A_2 x_k(n_1, n_2) \\ \quad + A_3 x_k(n_1, n_2+1) + Bu_k(n_1 - \tau_1, n_2 - \tau_2), \\ y_k(n_1, n_2) = Cx_k(n_1, n_2), \end{cases} \tag{37}$$

where τ_1 and τ_2 are two positive integers. $x_k(n_1,n_2)$, $u_k(n_1,n_2)$, and $y_k(n_1,n_2)$ have been described in (1).

Remark 6. It is worthwhile noting that ILC tracking issues for 2-D LDFFM with $\tau_1 = 0$ and $\tau_2 = 0$ in (37) have been investigated in [17, 18]. It is the first time that ILC issues for 2-D LDFFM with input delay are investigated in this paper.

Assumption 3. The matrix CB is full-row rank.

Next, we discuss the convergence property of the ILC law for 2-D LDFFM with input delay (37) under Assumptions 2 and 3, and there is the following Theorem 2.

Theorem 2. *Consider the 2-D LDFFM with input delay (37) under Assumptions 2 and 3 and use the following ILC law for* $\{n_1\}_{-\tau_1}^{N_1-\tau_1-1}$ *and* $\{n_2\}_{-\tau_2}^{N_2-\tau_2-1}$:

$$u_{k+1}(n_1,n_2) = u_k(n_1,n_2) + \Gamma e_k(n_1+\tau_1+1, n_2+\tau_2+1). \tag{38}$$

If the learning gain Γ *satisfies*

$$\rho(I_l - CB\Gamma) < 1, \tag{39}$$

then the tracking error $e_k(n_1,n_2)$ *converges to zero, i.e.,*

$$\lim_{k\longrightarrow+\infty} e_k(n_1,n_2) = 0, \quad \{n_1\}_1^{N_1}, \{n_2\}_1^{N_2}. \tag{40}$$

Proof 2. For $\{n_1\}_0^{N_1}$ and $\{n_2\}_0^{N_2}$, let

$$\delta\widehat{x}_k(n_1,n_2+1) = x_{k+1}(n_1,n_2) - x_k(n_1,n_2). \tag{41}$$

From (37), there is

$$\begin{aligned}\delta\widehat{x}_k(n_1+1,n_2+1) &= x_{k+1}(n_1+1,n_2) - x_k(n_1+1,n_2)\\ &= A_1\delta\widehat{x}_k(n_1+1,n_2) + A_2\delta\widehat{x}_k(n_1,n_2)\\ &\quad + B[u_{k+1}(n_1-\tau_1,n_2-\tau_2-1)\\ &\quad - u_k(n_1-\tau_1,n_2-\tau_2-1)],\end{aligned} \tag{42}$$

where $\{n_1\}_0^{N_1-1}$ and $\{n_2\}_1^{N_2}$. Inserting the ILC law (38) into (42), it generates

$$\begin{aligned}\delta\widehat{x}_k(n_1+1,n_2+1) &= A_1\delta\widehat{x}_k(n_1+1,n_2) + A_2\delta\widehat{x}_k(n_1,n_2)\\ &\quad + A_3\delta\widehat{x}_k(n_1,n_2+1) + B\Gamma e_k(n_1+1,n_2).\end{aligned} \tag{43}$$

On the contrary, according to $e_k(n_1,n_2) = y_r(n_1,n_2) - y_k(n_1,n_2)$ and using (37), we have

$$\begin{aligned}&e_{k+1}(n_1+1,n_2) - e_k(n_1+1,n_2)\\ &\quad = y_r(n_1+1,n_2) - y_{k+1}(n_1+1,n_2) - y_r(n_1+1,n_2)\\ &\qquad + y_k(n_1+1,n_2)\\ &\quad = -C[x_{k+1}(n_1+1,n_2) - x_k(n_1+1,n_2)]\\ &\quad = -C\delta\widehat{x}_k(n_1+1,n_2+1),\end{aligned} \tag{44}$$

where $\{n_1\}_0^{N_1-1}$ and $\{n_2\}_0^{N_2}$. Let

$$\delta\widehat{X}_k(n_2) = \left[\begin{array}{cccc}\delta\widehat{x}_k^T(1,n_2) & \delta\widehat{x}_k^T(2,n_2) & \cdots & \delta\widehat{x}_k^T(N_1,n_2)\end{array}\right]^T, \tag{45}$$

$$E_k(n_2) = \left[\begin{array}{cccc}e_k^T(1,n_2) & e_k^T(2,n_2) & \cdots & e_k^T(N_1,n_2)\end{array}\right]^T, \tag{46}$$

where $\{n_2\}_1^{N_2}$. From (45) and (46), (43) can be rewritten as

$$\begin{aligned}\phi_1\delta\widehat{X}_k(n_2+1) &= \phi_2\delta\widehat{X}_k(n_2) + \phi_3E_k(n_2) + \widehat{A}_2\delta\widehat{x}_k(0,n_2)\\ &\quad + \widehat{A}_3\delta\widehat{x}_k(0,n_2+1),\end{aligned} \tag{47}$$

where

$$\begin{aligned}\phi_1 &= \begin{bmatrix} I_p & 0 & 0 & \cdots & 0\\ -A_3 & I_p & 0 & \cdots & 0\\ 0 & -A_3 & I_p & \ddots & \vdots\\ \vdots & \ddots & \ddots & \ddots & 0\\ 0 & \cdots & 0 & -A_3 & I_p\end{bmatrix} \in R^{pN_1\times pN_1},\\ \phi_2 &= \begin{bmatrix} A_1 & 0 & 0 & \cdots & 0\\ 0 & A_1 & 0 & \cdots & 0\\ 0 & 0 & A_1 & \ddots & \vdots\\ \vdots & \ddots & \ddots & \ddots & 0\\ 0 & \cdots & 0 & 0 & A_1\end{bmatrix} \in R^{pN_1\times pN_1},\\ \phi_3 &= \begin{bmatrix} B\Gamma & 0 & 0 & \cdots & 0\\ 0 & B\Gamma & 0 & \cdots & 0\\ 0 & 0 & B\Gamma & \ddots & \vdots\\ \vdots & \ddots & \ddots & \ddots & 0\\ 0 & \cdots & 0 & 0 & B\Gamma\end{bmatrix} \in R^{pN_1\times lN_1},\end{aligned} \tag{48}$$

and $\widehat{A}_2$ and $\widehat{A}_3$ have been described in (20). Similarly, (44) can also be reformulated as

$$E_{k+1}(n_2) = \psi_1\delta\widehat{X}_k(n_2+1) + \psi_2E_k(n_2), \tag{49}$$

where

$$\begin{aligned}\psi_1 &= \begin{bmatrix} -C & 0 & 0 & \cdots & 0\\ 0 & -C & 0 & \ddots & \vdots\\ 0 & 0 & -C & \ddots & 0\\ \vdots & \ddots & \ddots & \ddots & 0\\ 0 & \cdots & 0 & 0 & -C\end{bmatrix} \in R^{lN_1\times pN_1},\\ \psi_2 &= \begin{bmatrix} I_l & 0 & 0 & \cdots & 0\\ 0 & I_l & 0 & \cdots & 0\\ 0 & 0 & I_l & \ddots & \vdots\\ \vdots & \ddots & \ddots & \ddots & 0\\ 0 & \cdots & 0 & 0 & I_l\end{bmatrix} \in R^{lN_1\times lN_1}.\end{aligned} \tag{50}$$

Then, since ϕ_1 is a nonsingular matrix, premultiplying ϕ_1^{-1} on both sides of (47), we get

$$\delta\widehat{X}_k(n_2+1) = \overline{\phi}_1\delta\widehat{X}_k(n_2) + \overline{\phi}_2 E_k(n_2) + \phi_1^{-1}\widehat{A}_2\delta\widehat{x}_k(0,n_2) + \phi_1^{-1}\widehat{A}_3\delta\widehat{x}_k(0,n_2+1), \tag{51}$$

where $\overline{\phi}_1 = \phi_1^{-1}\phi_2$ and $\overline{\phi}_2 = \phi_1^{-1}\phi_3$. Substituting (51) into (49), it yields

$$E_{k+1}(n_2) = \psi_1\overline{\phi}_1\delta\widehat{X}_k(n_2) + \left(\psi_1\overline{\phi}_2 + \psi_2\right)E_k(n_2) + \psi_1\phi_1^{-1}\widehat{A}_2\delta\widehat{x}_k(0,n_2) + \psi_1\phi_1^{-1}\widehat{A}_3\delta\widehat{x}_k(0,n_2+1), \tag{52}$$

where $\{n_2\}_1^{N_2}$. From Assumption 2, we obtain $\delta\widehat{x}_k(0,n_2+1) = x_{k+1}(0,n_2) - x_k(0,n_2) = 0$ for $\{n_2\}_0^{N_2}$. Thus, for $\{n_2\}_1^{N_2}$, (51) and (52) can be represented as

$$\begin{cases} \delta\widehat{X}_k(n_2+1) = \overline{\phi}_1\delta\widehat{X}_k(n_2) + \overline{\phi}_2 E_k(n_2), \\ E_{k+1}(n_2) = \psi_1\overline{\phi}_1\delta\widehat{X}_k(n_2) + \left(\psi_1\overline{\phi}_2 + \psi_2\right)E_k(n_2). \end{cases} \tag{53}$$

In (53), based on Assumption 2, we obtain $\delta\widehat{x}_k(n_1,1) = x_{k+1}(n_1,0) - x_k(n_1,0) = 0$. Furthermore,

$$\delta\widehat{X}_k(1) = \left[\ \delta\widehat{x}_k^T(1,1)\ \ \delta\widehat{x}_k^T(2,1)\ \cdots\ \delta\widehat{x}_k^T(N_1,1)\ \right]^T = 0, \tag{54}$$

and $E_0(n_2)$ is bounded for $\{n_2\}_1^{N_2}$ due to the boundedness property of $e_0(n_1,n_2)$. Using Lemma 4 in [18], if $\rho(\psi_1\overline{\phi}_2 + \psi_2) < 1$ holds (equivalently, $\rho(I_l - C\mathrm{B}\Gamma) < 1$, see Remark 7), there is

$$\lim_{k\longrightarrow+\infty} E_k(n_2) = 0, \quad \{n_2\}_1^{N_2}. \tag{55}$$

From (46), we obtain

$$\lim_{k\longrightarrow+\infty} e_k(n_1,n_2) = 0, \quad \{n_1\}_1^{N_2}, \{n_2\}_1^{N_2}, \tag{56}$$

Theorem 2 is completed.

Remark 7. The convergence condition $\rho(\psi_1\overline{\phi}_2 + \psi_2) < 1$ in (53) depends on a complicated matrix $\psi_1\overline{\phi}_2 + \psi_2$; thus, there is a need to simplify it. From the definition of $\psi_1\overline{\phi}_2 + \psi_2$ and using Property 1, the simplifying process is shown as follows:

$$\begin{aligned} \psi_1\overline{\phi}_2 + \psi_2 &= \begin{bmatrix} -C & 0 & \cdots & 0 \\ 0 & -C & \ddots & \vdots \\ \vdots & \ddots & \ddots & 0 \\ 0 & \cdots & 0 & -C \end{bmatrix} \begin{bmatrix} I_p & 0 & 0 & \cdots & 0 \\ -A_3 & I_p & 0 & \cdots & 0 \\ 0 & -A_3 & I_p & \ddots & \vdots \\ \vdots & \ddots & \ddots & \ddots & 0 \\ 0 & \cdots & 0 & -A_3 & I_p \end{bmatrix}^{-1} \begin{bmatrix} B\Gamma & 0 & \cdots & 0 \\ 0 & B\Gamma & \ddots & \vdots \\ \vdots & \ddots & \ddots & 0 \\ 0 & \cdots & 0 & B\Gamma \end{bmatrix} + \begin{bmatrix} I_l & 0 & \cdots & 0 \\ 0 & I_l & \ddots & \vdots \\ \vdots & \ddots & \ddots & 0 \\ 0 & \cdots & 0 & I_l \end{bmatrix} \\ &= \begin{bmatrix} I_l - C\mathrm{B}\Gamma & 0 & 0 & \cdots & 0 \\ -C\mathrm{A}_3B\Gamma & I_l - C\mathrm{B}\Gamma & 0 & \cdots & 0 \\ -C\mathrm{A}_3^2B\Gamma & -C\mathrm{A}_3B\Gamma & I_l - C\mathrm{B}\Gamma & \ddots & \vdots \\ \vdots & \ddots & \ddots & \ddots & 0 \\ -C\mathrm{A}_3^{N_1-1}B\Gamma & \cdots & -C\mathrm{A}_3^2B\Gamma & -C\mathrm{A}_3B\Gamma & I_l - C\mathrm{B}\Gamma \end{bmatrix}. \end{aligned} \tag{57}$$

From (57) and Property 2, we can know $\rho(\psi_1\overline{\phi}_2 + \psi_2) = \rho(I_l - C\mathrm{B}\Gamma)$. Consequently, $\rho(\psi_1\overline{\phi}_2 + \psi_2) < 1$ can be replaced by a more convenient condition $\rho(I_l - C\mathrm{B}\Gamma) < 1$ without using any knowledge on the system matrix A_3 and the interval length N_1 in the 2-D LDFFM with input delay (37).

Remark 8. In Remark 7, using the estimated information on C and B, the learning gain matrix Γ of $\rho(I_l - C\mathrm{B}\Gamma) < 1$ can be decided by using the LMI technique. Therefore, a similar Remark 4 can be obtained.

Remark 9. When the RSA on dynamical direction n_2 is applied to 2-D LDFFM with input delay (37) and the ILC law (38), the same ILC result with Theorem 2 can be obtained, the proof process of which is shown in Appendix 7.3.

Remark 10. It is noted that 2-D LDFFM (1) and (37) contain 2-D Attasi model as a special case, i.e., $A_2 = -A_1A_3 = -A_3A_1$. And the 2-D Roesser model under some specified coefficient matrix requirements can also be converted into 2-D LDFFM [29]. Consequently, depending on the ILC results obtained from 2-D LDFFM (1) and (37), it is easy to extend 2-D Roesser model and 2-D Attasi model with input delay.

5. Illustrative Examples

To show the effectiveness and feasibility of the proposed ILC algorithms (9) and (38) for the 2-D LDFFM with a direct transmission from inputs to outputs (1) and 2-D LDFFM with input delay (37), two simulation examples are introduced in this section.

Example 1. Consider the following 2-D LDFFM with a direct transmission from inputs to outputs over dynamical region $\{n_1\}_0^{20}$ and $\{n_2\}_0^{20}$:

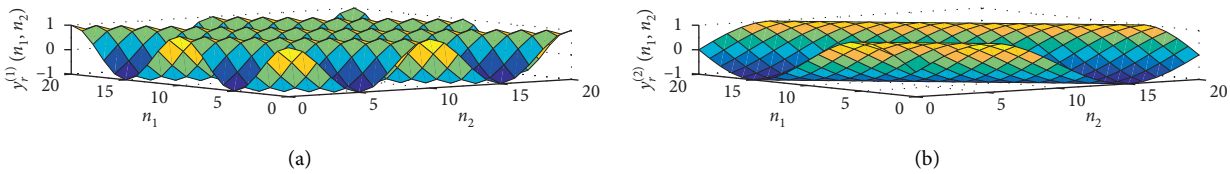

Figure 1: Reference surfaces $y_r^{(1)}(n_1,n_2)$ and $y_r^{(2)}(n_1,n_2)$ for $\{n_1\}_0^{20}$ and $\{n_2\}_0^{20}$.

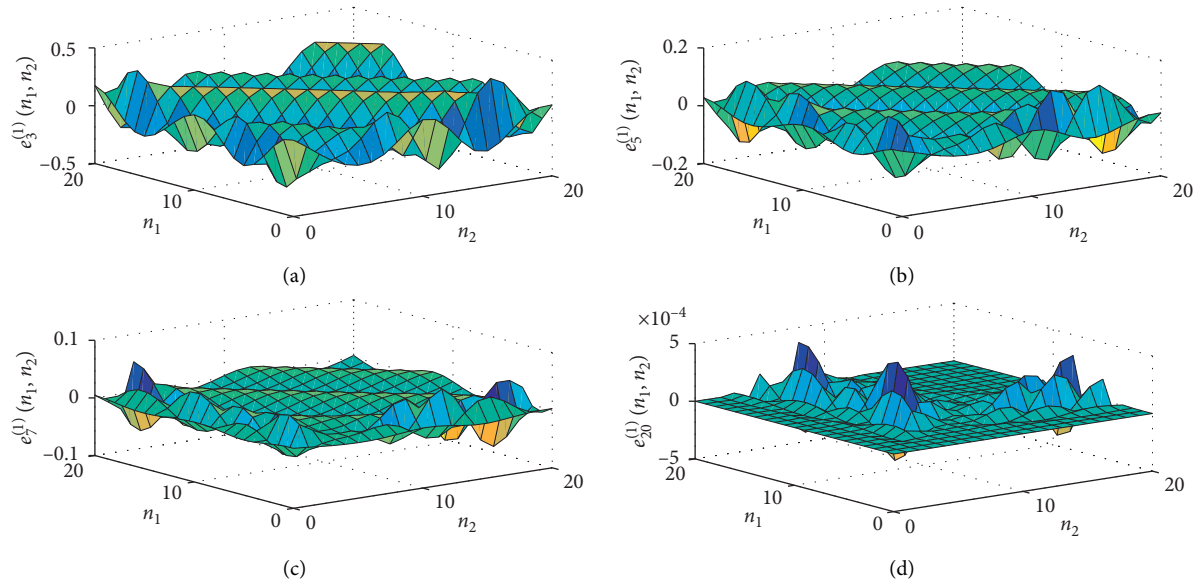

Figure 2: Tracking error surface $e_k^{(1)}(n_1,n_2)$ at $k = 3,5,7,20$ by using the ILC law (9).

$$\begin{bmatrix} x_k^{(1)}(n_1+1,n_2+1) \\ x_k^{(2)}(n_1+1,n_2+1) \end{bmatrix} = \begin{bmatrix} 0.01 & 0.01 \\ 0.01 & 0.03 \end{bmatrix} \begin{bmatrix} x_k^{(1)}(n_1+1,n_2) \\ x_k^{(2)}(n_1+1,n_2) \end{bmatrix} + \begin{bmatrix} 0.01 & 0.02 \\ 0.01 & 0.04 \end{bmatrix} \begin{bmatrix} x_k^{(1)}(n_1,n_2) \\ x_k^{(2)}(n_1,n_2) \end{bmatrix} + \begin{bmatrix} 0.01 & 0.02 \\ 0.01 & 0.3 \end{bmatrix} \begin{bmatrix} x_k^{(1)}(n_1,n_2+1) \\ x_k^{(2)}(n_1,n_2+1) \end{bmatrix} + \begin{bmatrix} 1 & 0.2 \\ 0.3 & 0.5 \end{bmatrix} \begin{bmatrix} u_k^{(1)}(n_1,n_2) \\ u_k^{(2)}(n_1,n_2) \end{bmatrix}, \tag{58a}$$

$$\begin{bmatrix} y_k^{(1)}(n_1,n_2) \\ y_k^{(2)}(n_1,n_2) \end{bmatrix} = \begin{bmatrix} 1 & 0.2 \\ -0.2 & 1 \end{bmatrix} \begin{bmatrix} x_k^{(1)}(n_1,n_2) \\ x_k^{(1)}(n_1,n_2) \end{bmatrix} + \begin{bmatrix} 2 & 0 \\ 0 & 2 \end{bmatrix} \begin{bmatrix} u_k^{(1)}(n_1,n_2) \\ u_k^{(2)}(n_1,n_2) \end{bmatrix}, \tag{58b}$$

which is required to repetitively track a desired reference surface $y_r(n_1,n_2) = [\cos(2\pi(n_1+n_2))/10 \ \ \sin(\pi(n_1+n_2))/10]^T$ for $\{n_1\}_0^{20}$ and $\{n_2\}_0^{20}$ shown in Figure 1. Under Assumption 2, the boundary states of 2-D LDFFM (58) are given as $x_k(0,n_2) = [0.1 \ \ \sin(n_2)]^T$, $\{n_2\}_1^{20}$, and $x_k(n_1,0) = [-0.1\sin(n_1) \ \ 0]^T$, $\{n_1\}_0^{20}$. Using the proposed ILC law (9) with the initial control input $u_0(n_1,n_2) = [0 \ \ 0]^T$ for $\{n_1\}_0^{20}$ and $\{n_2\}_0^{20}$, the gain matrix Γ is selected as $\Gamma = \text{diag}\{0.3 \ \ 0.3\}$, which satisfies the convergence condition $\rho(I_l - D\Gamma) = 0.6 < 1$ in Theorem 1. In order to evaluate the accuracy of ILC tracking, the following maximum absolute tracking error index

$$\text{MATE}_k^{(h)} = \max_{\{n_1\}_0^{20}} \max_{\{n_2\}_0^{20}} \left| y_r^{(h)}(n_1,n_2) - y_k^{(h)}(n_1,n_2) \right|, \quad \{h\}_1^2, \tag{59}$$

is used. As a result, the ILC tracking error surfaces $e_k^{(1)}(n_1,n_2)$ at $k = 3,5,7,25$, and $e_k^{(2)}(n_1,n_2)$ at $k = 4,6,8,24$ are depicted in Figures 2 and 3, respectively. Also, Figure 4 presents the profiles of the ILC tracking error indexes $\text{MATE}_k^{(1)}$ and $\text{MATE}_k^{(2)}$ in iteration domain k by utilizing the ILC law (9). Obviously, it is observed from Figures 2–4 that the convergent effect of the ILC law (9) against the iteration-invariant boundary states is illustrated.

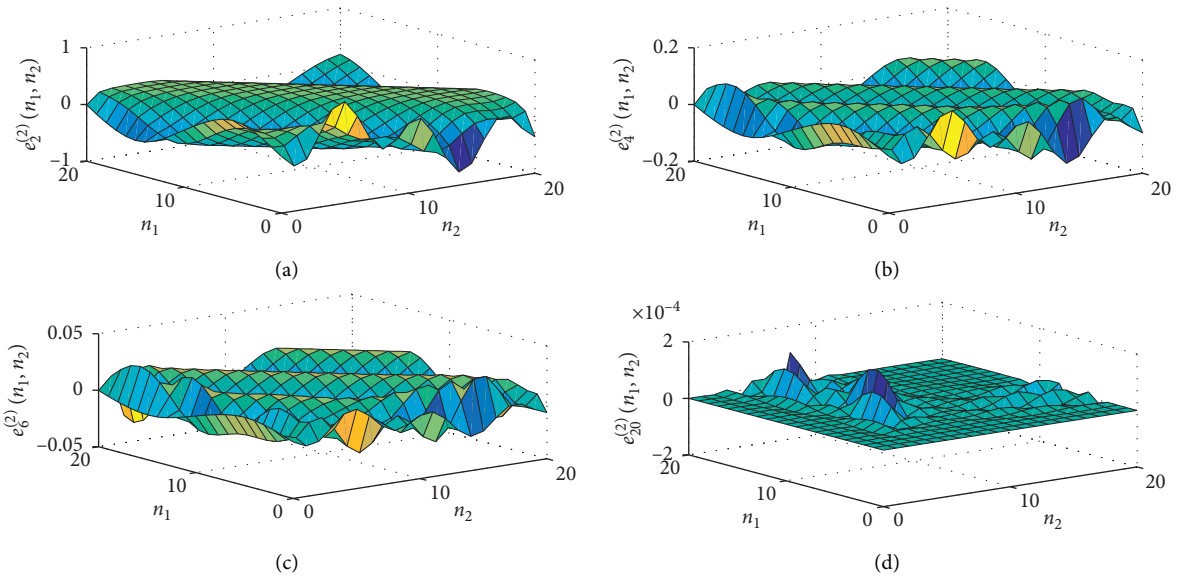

Figure 3: Tracking error surface $e_k^{(2)}(n_1,n_2)$ at $k = 2, 4, 6, 20$ by using the ILC law (9).

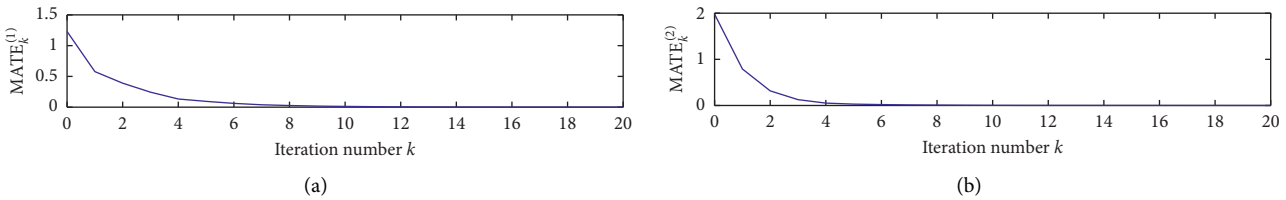

Figure 4: Tracking error indexes $\mathrm{MATE}_k^{(1)}$ and $\mathrm{MATE}_k^{(2)}$ with iteration number k by using the ILC law (9).

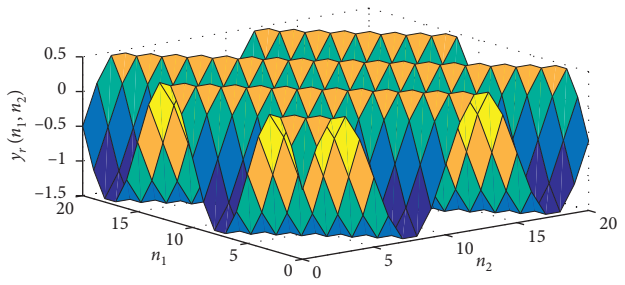

Figure 5: Reference surface $y_r(n_1,n_2)$ for $\{n_1\}_0^{20}$ and $\{n_2\}_0^{20}$.

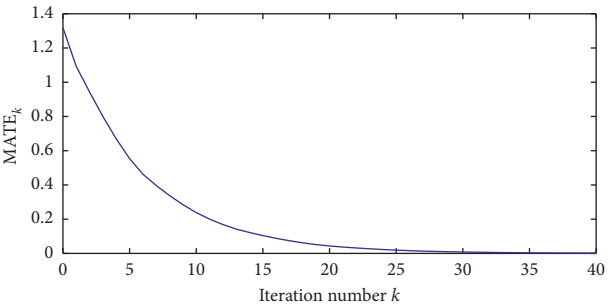

Figure 6: Tracking error index MATE_k with iteration number k by using the ILC law (38).

Example 2. Some practical thermal processes can be represented by the following partial differential equation (PDE) [31]:

$$\frac{\partial^2 s_k(w,t)}{\partial w\,\partial t} = a_1\frac{\partial s_k(w,t)}{\partial t} + a_2\frac{\partial s_k(w,t)}{\partial w} + a_0 s_k(w,t) + b f_k(w-d_w, t-d_t), \tag{60}$$

where d_w and d_t, respectively, denote space delay and time delay; a_0, a_1, a_2, and b are real coefficients. The repetitive index k implies that the ILC issue is investigated in the example. Through the discretization approximation on (60), system parameters and delay factors of 2-D LDFFM with input delay (37) are given as follows:

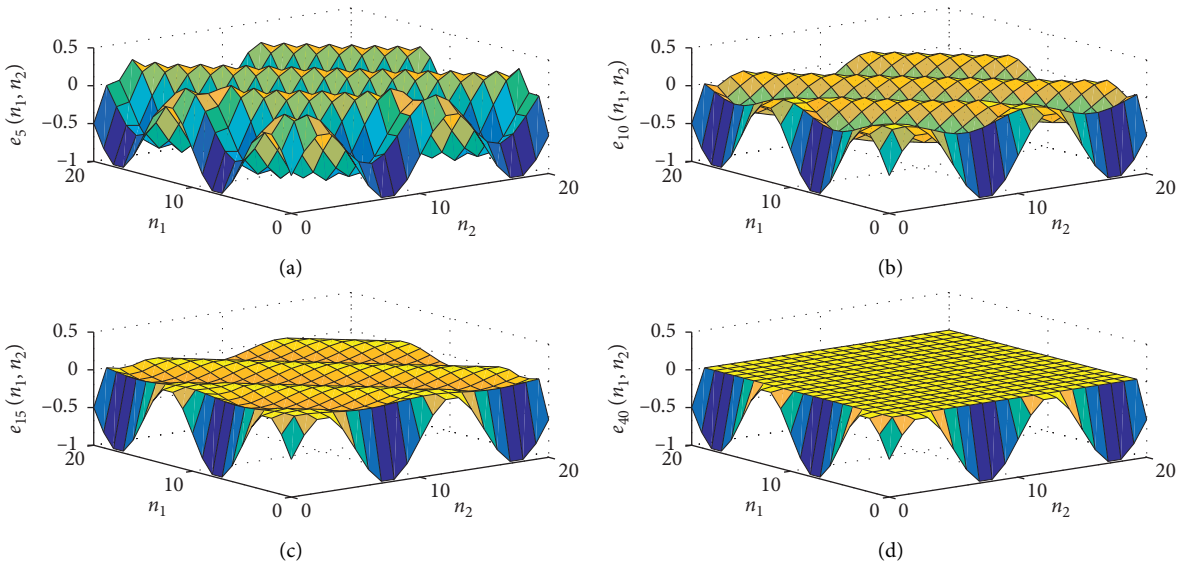

Figure 7: Tracking error surface $e_k(n_1, n_2)$ at $k = 5, 10, 15, 40$ by using the ILC law (38).

$$
\begin{aligned}
A_1 &= 1 + a_2\Delta t,\\
A_2 &= a_0\Delta w\Delta t - a_1\Delta w - a_2\Delta t - 1,\\
A_3 &= 1 + a_1\Delta w,\\
B &= b\Delta w\Delta t,\\
\tau_1 &= \operatorname{int}\left(\frac{d_w}{\Delta w}\right),\\
\tau_2 &= \operatorname{int}\left(\frac{d_t}{\Delta t}\right),
\end{aligned}
\tag{61}
$$

where is shown in Figure 5. And the boundary states satisfy $x_k(0, n_2) = 0.5\sin(2\pi n_2/10)$, $\{n_2\}_1^{20}$, and $x_k(n_1, 0) = 0.5\sin(2\pi n_1/10)$, $\{n_1\}_0^{20}$. Under the ILC law (38) with initial control input $u_0(n_1, n_2) = 0$ for $\{n_1\}_{-1}^{18}$ and $\{n_2\}_{-2}^{17}$, let the learning gain Γ be selected as $\Gamma = 0.9$ and compute $\rho(I_l - CB\Gamma) = 0.7885 < 1$, which satisfies the convergent condition in Theorem 2. The maximum absolute tracking error index MATE_k is adopted to evaluate the ILC tracking performance, which is given as follows:

$$
\mathrm{MATE}_k = \max_{\{n_1\}_1^{20}} \max_{\{n_2\}_1^{20}} \left| y_r(n_1, n_2) - y_k(n_1, n_2) \right|. \tag{62}
$$

And Figure 6 displays the profile of MATE_k with iteration number k by using the ILC law (38). The tracking error surface $e_k(n_1, n_2)$ at $k = 5, 10, 15, 40$ is shown in Figure 7. Apparently, perfect tracking on repetitive reference surface can be observed from Figures 6 and 7.

6. Conclusions

To date, ILC tracking issues for 2-D LDFFM with a direct transmission from inputs to outputs and with input delay are first concerned in this paper. Different from existing ILC results for 2-D LDFFM, a 3-D analysis approach is first applied to the convergent property of the proposed ILC law, which supplies a new tool for follow-up ILC development for 2-D systems. Additionally, the LMI technique is used to compute the learning gain. In our future work, reinforcement learning (RL) [35–38] will be incorporated into the ILC designs for 2-D dynamical systems such that more ILC results are made.

Appendix

Proof of Lemma 1. The solution to $\theta_{k+1}(n_1, n_2) = \alpha_1\theta_k(n_1, n_2) + \alpha_2\delta_k(n_1, n_2)$ is given as follows:

$$
\theta_k(n_1, n_2) = \alpha_1^{k-1}\theta_0(n_1, n_2) + \sum_{i=0}^{k-1} \alpha_1^{k-i-1}\alpha_2\delta_i(n_1, n_2). \tag{A.1}
$$

Then, taking the limit on both sides of (A.1), there is

$$
\begin{aligned}
\lim_{k\longrightarrow+\infty} \theta_k(n_1, n_2) = &\lim_{k\longrightarrow+\infty} \alpha_1^{k-1}\theta_0(n_1, n_2)\\
&+ \lim_{k\longrightarrow+\infty} \sum_{i=0}^{k-1} \alpha_1^{k-i-1}\alpha_2\delta_i(n_1, n_2).
\end{aligned}
\tag{A.2}
$$

Under $\lim_{k\longrightarrow+\infty} \theta_k(n_1, n_2) = 0$ in Lemma 1, if $\rho(\alpha_1) < 1$ holds, we obtain

$$
\lim_{k\longrightarrow+\infty} \theta_k(n_1, n_2) = 0. \tag{A.3}
$$

Lemma 1 is completed.

Proof of Theorem 1 by using the RSA. Let

$$\delta\overline{X}_k(n_1) = \left[\, \delta x_k^T(n_1,1) \;\; \delta x_k^T(n_1,2) \;\; \cdots \;\; \delta x_k^T(n_1,N_2) \,\right]^T, \tag{A.4}$$

$$\overline{E}_k(n_1) = \left[\, e_k^T(n_1,0) \;\; e_k^T(n_1,1) \;\; \cdots \;\; e_k^T(n_1,N_2) \,\right]^T. \tag{A.5}$$

From (A.4) and (A.5), using the RSA on vertical direction n_2, for $\{n_1\}_0^{N_1-1}$, (14) can be rewritten as

$$\begin{aligned}\widehat{\Phi}_1\delta\overline{X}_k(n_1+1) = {} & \widehat{\Phi}_2\delta\overline{X}_k(n_1) + \widehat{\Phi}_3\overline{E}_k(n_1) + \widehat{A}_2\delta x_k(n_1,0) \\ & + \widehat{A}_1\delta x_k(n_1+1,0),\end{aligned} \tag{A.6}$$

where

$$\widehat{\Phi}_1 = \begin{bmatrix} I_p & 0 & 0 & \cdots & 0 \\ -A_1 & I_p & 0 & \cdots & 0 \\ 0 & -A_1 & I_p & \ddots & \vdots \\ \vdots & \ddots & \ddots & \ddots & 0 \\ 0 & \cdots & 0 & -A_1 & I_p \end{bmatrix} \in R^{pN_2\times pN_2},$$

$$\widehat{\Phi}_2 = \begin{bmatrix} A_3 & 0 & 0 & \cdots & 0 \\ A_2 & A_3 & 0 & \cdots & 0 \\ 0 & A_2 & A_3 & \ddots & \vdots \\ \vdots & \ddots & \ddots & \ddots & 0 \\ 0 & \cdots & 0 & A_2 & A_3 \end{bmatrix} \in R^{pN_2\times pN_2},$$

$$\widehat{\Phi}_3 = \begin{bmatrix} B\Gamma & 0 & 0 & \cdots & 0 \\ 0 & B\Gamma & \ddots & \ddots & \vdots \\ 0 & 0 & B\Gamma & 0 & 0 \\ \vdots & \ddots & \ddots & \ddots & 0 \\ 0 & \cdots & 0 & 0 & B\Gamma \end{bmatrix} \in R^{pN_2\times p(N_2+1)}, \tag{A.7}$$

$$\widehat{A}_1 = \begin{bmatrix} A_1 \\ 0 \\ \vdots \\ 0 \end{bmatrix} \in R^{pN_2\times p},$$

$$\widehat{A}_2 = \begin{bmatrix} A_2 \\ 0 \\ \vdots \\ 0 \end{bmatrix} \in R^{pN_2\times p}.$$

Since $\widehat{\Phi}_1$ is a nonsingular matrix, premultiplying $\widehat{\Phi}_1^{-1}$ on both sides of (A.6), we get

$$\begin{aligned}\delta\overline{X}_k(n_1+1) = {} & \widehat{\Phi}_1^{-1}\widehat{\Phi}_2\delta\overline{X}_k(n_1) + \widehat{\Phi}_1^{-1}\widehat{\Phi}_3\overline{E}_k(n_1) \\ & + \widehat{\Phi}_1^{-1}\widehat{A}_2\delta x_k(n_1,0) + \Phi_1^{-1}\widehat{A}_1\delta x_k(n_1+1,0).\end{aligned} \tag{A.8}$$

Similarly, (17) can also be reformulated as

$$\overline{E}_{k+1}(n_1) = \varphi_1\delta\overline{X}_k(n_1) + \varphi_2\overline{E}_k(n_1) - \widehat{C}\delta x_k(n_1,0), \tag{A.9}$$

where

$$\varphi_1 = \begin{bmatrix} 0 & 0 & 0 & \cdots & 0 \\ -C & 0 & 0 & \cdots & 0 \\ 0 & -C & 0 & \ddots & 0 \\ \vdots & \ddots & \ddots & \ddots & \vdots \\ 0 & \cdots & 0 & -C & 0 \end{bmatrix} \in R^{l(N_2+1)\times pN_2},$$

$$\varphi_2 = \begin{bmatrix} I_l - D\Gamma & 0 & \cdots & 0 \\ 0 & I_l - D\Gamma & \ddots & \vdots \\ \vdots & \ddots & \ddots & 0 \\ 0 & \cdots & 0 & I_l - D\Gamma \end{bmatrix} \in R^{l(N_2+1)\times l(N_2+1)},$$

$$\widehat{C} = \begin{bmatrix} C \\ 0 \\ \vdots \\ 0 \end{bmatrix} \in R^{l(N_2+1)\times p}. \tag{A.10}$$

From Assumption 2, we obtain $\delta_k(n_1,0) = x_{k+1}(n_1,0) - x_k(n_1,0) = 0$ for $\{n_1\}_0^{N_1}$. Thus, (A.8) and (A.9) can be expressed as

$$\begin{cases} \delta\overline{X}_k(n_1+1) = \widehat{\Phi}_1^{-1}\widehat{\Phi}_2\delta\overline{X}_k(n_1) + \widehat{\Phi}_1^{-1}\widehat{\Phi}_3\overline{E}_k(n_1), \\ \overline{E}_{k+1}(n_1) = \varphi_1\delta\overline{X}_k(n_1) + \varphi_2\overline{E}_k(n_1), \end{cases} \tag{A.11}$$

where $\{n_1\}_0^{N_1-1}$. In (A.11), according to Assumption 2, we deduce

$$\delta\overline{X}_k(0) = \left[\, \delta x_k^T(0,1) \;\; \delta x_k^T(0,2) \;\; \cdots \;\; \delta x_k^T(0,N_2) \,\right]^T = 0, \tag{A.12}$$

and $E_0(n_1)$ is bounded for $\{n_1\}_0^{N_1-1}$. Using Lemma 4 in [18] and Property 2, if $\rho(I_l - D\Gamma) < 1$, there is

$$\begin{cases} \lim\limits_{k\longrightarrow+\infty} \delta\overline{X}_k(n_1) = 0, \; \{n_1\}_1^{N_1}, \\ \lim\limits_{k\longrightarrow+\infty} \overline{E}_k(n_1) = 0, \; \{n_1\}_0^{N_1-1}. \end{cases} \tag{A.13}$$

In addition, taking $n_1 = N_1$ in (17), we have

$$e_{k+1}(N_1,n_2) = -C\delta x_k(N_1,n_2) + (I_l - D\Gamma)e_k(N_1,n_2). \tag{A.14}$$

From (A.13) and $\delta x_k(N_1,0) = 0$, using Lemma 1, if $\rho(I_l - D\Gamma) < 1$, it yields

$$\lim_{k\longrightarrow+\infty} e_k(N_1,n_2) = 0, \quad \{n_2\}_0^{N_2}. \tag{A.15}$$

From (A.13) and (A.15) and the definition of $\overline{E}_k(n_1)$ in (A.5), we obtain

$$\lim_{k\longrightarrow+\infty} e_k(n_1,n_2) = 0, \quad \{n_1\}_0^{N_1}, \{n_2\}_0^{N_2}. \tag{A.16}$$

Theorem 1 is completed.

Proof of Theorem 2 by using the RSA. For $\{n_1\}_0^{N_1}$ and $\{n_2\}_0^{N_2}$, define

$$\delta\widetilde{x}_k(n_1+1,n_2)=x_{k+1}(n_1,n_2)-x_k(n_1,n_2). \tag{A.17}$$

From (A.17), there is

$$\begin{aligned}\delta\widetilde{x}_k(n_1+1,n_2+1)&=x_{k+1}(n_1,n_2+1)-x_k(n_1,n_2+1)\\&=A_1\delta\widetilde{x}_k(n_1+1,n_2)+A_2\delta\widetilde{x}_k(n_1,n_2)\\&\quad+A_3\delta\widetilde{x}_k(n_1,n_2+1)\\&\quad+B[u_{k+1}(n_1-\tau_1-1,n_2-\tau_2)\\&\quad-u_k(n_1-\tau_1-1,n_2-\tau_2)],\end{aligned} \tag{A.18}$$

where $\{n_1\}_1^{N_1}$ and $\{n_2\}_0^{N_2-1}$. Inserting the ILC law (38) into (A.18), it generates

$$\begin{aligned}\delta\widetilde{x}_k(n_1+1,n_2+1)&=A_1\delta\widetilde{x}_k(n_1+1,n_2)+A_2\delta\widetilde{x}_k(n_1,n_2)\\&\quad+A_3\delta\widetilde{x}_k(n_1,n_2+1)\\&\quad+B\Gamma e_k(n_1,n_2+1).\end{aligned} \tag{A.19}$$

On the contrary, according to $e_k(n_1,n_2)=y_r(n_1,n_2)-y_k(n_1,n_2)$ and using (A.17), we have

$$\begin{aligned}&e_{k+1}(n_1,n_2+1)-e_k(n_1,n_2+1)\\&\quad=y_r(n_1,n_2+1)-y_{k+1}(n_1,n_2+1)-y_r(n_1,n_2+1)\\&\qquad+y_k(n_1,n_2+1)\\&\quad=-C[x_{k+1}(n_1,n_2+1)-x_k(n_1,n_2+1)]\\&\quad=-C\delta\widetilde{x}_k(n_1+1,n_2+1),\end{aligned} \tag{A.20}$$

where $\{n_1\}_0^{N_1}$ and $\{n_2\}_0^{N_2-1}$. Let

$$\delta\widetilde{X}_k(n_1)=\left[\,\delta x_k^T(n_1,1)\;\;\delta x_k^T(n_1,2)\;\;\cdots\;\;\delta x_k^T(n_1,N_2)\,\right]^T, \tag{A.21}$$

$$\widetilde{E}_k(n_1)=\left[\,e_k^T(n_1,1)\;\;e_k^T(n_1,2)\;\;\cdots\;\;e_k^T(n_1,N_2)\,\right]^T, \tag{A.22}$$

where $\{n_1\}_1^{N_1}$. From (A.21) and (A.22), using the RSA on vertical dynamical direction n_2, (A.19) can be rewritten as

$$\begin{aligned}\widetilde{\Phi}_1\delta\widetilde{X}_k(n_1+1)&=\widetilde{\Phi}_2\delta\widetilde{X}_k(n_1)+\widetilde{\Phi}_3\widetilde{E}_k(n_1)+\widetilde{A}_2\delta\widetilde{x}_k(n_1,0)\\&\quad+\widetilde{A}_1\delta\widetilde{x}_k(n_1+1,0),\quad \{n_1\}_0^{N_1-1},\end{aligned} \tag{A.23}$$

where

$$\begin{aligned}\widetilde{\Phi}_1&=\begin{bmatrix}I_p&0&0&\cdots&0\\-A_1&I_p&0&\ddots&\vdots\\0&-A_1&I_p&\ddots&0\\\vdots&\ddots&\ddots&\ddots&0\\0&\cdots&0&-A_1&I_p\end{bmatrix}\in R^{pN_2\times pN_2},\\\widetilde{\Phi}_2&=\begin{bmatrix}A_3&0&0&\cdots&0\\A_2&A_3&0&\ddots&\vdots\\0&A_2&A_3&\ddots&0\\\vdots&\ddots&\ddots&\ddots&0\\0&\cdots&0&A_2&A_3\end{bmatrix}\in R^{pN_2\times pN_2},\\\widetilde{\Phi}_3&=\begin{bmatrix}B\Gamma&0&0&\cdots&0\\0&B\Gamma&0&\ddots&\vdots\\0&0&B\Gamma&\ddots&0\\\vdots&\ddots&\ddots&\ddots&0\\0&\cdots&0&0&B\Gamma\end{bmatrix}\in R^{pN_2\times lN_2},\\\widetilde{A}_1&=\begin{bmatrix}A_1\\0\\\vdots\\0\end{bmatrix}\in R^{pN_2\times p},\\\widetilde{A}_2&=\begin{bmatrix}A_2\\0\\\vdots\\0\end{bmatrix}\in R^{pN_2\times p}.\end{aligned} \tag{A.24}$$

Premultiplying $\widetilde{\Phi}_1^{-1}$ on both sides of (A.23), we get

$$\begin{aligned}\delta\widetilde{X}_k(n_1+1)&=\widetilde{\Phi}_1^{-1}\widetilde{\Phi}_2\delta\widetilde{X}_k(n_1)+\widetilde{\Phi}_1^{-1}\widetilde{\Phi}_3\widetilde{E}_k(n_1)\\&\quad+\widetilde{\Phi}_1^{-1}\widetilde{A}_2\delta\widetilde{x}_k(n_1,0)+\widetilde{\Phi}_1^{-1}\widetilde{A}_1\delta\widetilde{x}_k(n_1+1,0).\end{aligned} \tag{A.25}$$

Similarly, (A.20) can also be reformulated as

$$\widetilde{E}_{k+1}(n_1)=\widetilde{\varphi}_1\delta\widetilde{X}_k(n_1+1)+\widetilde{\varphi}_2\widetilde{E}_k(n_1), \tag{A.26}$$

where

$$\widetilde{\varphi}_1 = \begin{bmatrix} -C & 0 & \cdots & 0 \\ 0 & -C & \ddots & \vdots \\ \vdots & \ddots & \ddots & 0 \\ 0 & \cdots & 0 & -C \end{bmatrix} \in R^{lN_2 \times pN_2},$$
$$\widetilde{\varphi}_2 = \begin{bmatrix} I_l & 0 & \cdots & 0 \\ 0 & I_l & \ddots & \vdots \\ \vdots & \ddots & \ddots & 0 \\ 0 & \cdots & 0 & I_l \end{bmatrix} \in R^{lN_2 \times lN_2}. \tag{A.27}$$

Substituting (A.25) into (A.26), consider $\delta\widetilde{x}_k(n_1+1,0) = x_{k+1}(n_1,0) - x_k(n_1,0) = 0$ for $\{n_1\}_0^{N_1}$. Thus, (A.25) and (A.26) can be reformulated as

$$\begin{cases} \delta\widetilde{X}_k(n_1+1) = \widetilde{\Phi}_1^{-1}\widetilde{\Phi}_2\delta\widetilde{X}_k(n_1) + \widetilde{\Phi}_1^{-1}\widetilde{\Phi}_3\widetilde{E}_k(n_1), \\ \widetilde{E}_{k+1}(n_1) = \widetilde{\varphi}_1\widetilde{\Phi}_1^{-1}\widetilde{\Phi}_2\delta\widetilde{X}_k(n_1) + \left(\widetilde{\varphi}_1\widetilde{\Phi}_1^{-1}\widetilde{\Phi}_3 + \widetilde{\varphi}_2\right)\widetilde{E}_k(n_1), \end{cases} \tag{A.28}$$

where $\{n_1\}_1^{N_2}$. Based on Assumption 2, the initial condition in (A.28) is given as

$$\delta\widetilde{X}_k(1) = \left[\, \delta\widetilde{x}_k^T(1,1) \;\; \delta\widetilde{x}_k^T(1,2) \;\; \cdots \;\; \delta\widetilde{x}_k^T(1,N_2) \,\right]^T = 0, \tag{A.29}$$

and $\widetilde{E}_0(n_1)$ is bounded for $\{n_1\}_1^{N_1}$. Using Lemma 4 in [18], if $\rho(\widetilde{\varphi}_1\widetilde{\Phi}_1\widetilde{\Phi}_3 + \widetilde{\varphi}_2) < 1$ (equivalently, $\rho(I_l - \mathrm{CB}\Gamma) < 1$, see Property 2), there is

$$\lim_{k\longrightarrow+\infty} \widetilde{E}_k(n_1) = 0, \quad \{n_1\}_1^{N_1}. \tag{A.30}$$

From (A.22), it yields

$$\lim_{k\longrightarrow+\infty} e_k(n_1,n_2) = 0, \quad \{n_1\}_1^{N_1}, \{n_2\}_1^{N_2}. \tag{A.31}$$

Theorem 2 is completed.

Data Availability

All the data have been included in the paper; therefore, there are no other data available.

Conflicts of Interest

The authors declare that there are no conflicts of interest.

Acknowledgments

This work was supported in part by the National Natural Science Foundation of China (Grant nos. 61903096, 61573385, and 61703444), Science and Technology Program of Guangzhou (Grant no. 201904010475), Professorial and Doctoral Scientific Research Foundation of Huizhou University (Grant no. 2020JB017), and Huizhou Science and Technology Plan Project (Grant no. 2020SD0406034).

References

[1] E. Rimon and A. Stappen, "Immobilizing 2-D serial chains in form-closure grasps," *IEEE Transactions on Robotics*, vol. 28, no. 1, pp. 32–43, 2012.

[2] Z. Wei, M. J. Wang, Y. J. Cai, and L. Wang, "Milling force prediction for ball-end milling of 3D curved surfaces," *Journal of Mechanical Engineering*, vol. 49, no. 01, pp. 178–184, 2013.

[3] Y. Q. Luo, Z. D. Wang, G. L. Liang, and F. E. Alsaadi, "H_∞ control for 2-D fuzzy systems with interval time-varying delays and missing measurements," *IEEE Transactions on Cybernetics*, vol. 47, no. 2, pp. 365–377, 2017.

[4] C. K. Ahn, L. Wu, and P. Shi, "Stochastic stability analysis for 2-D Roesser systems with multiplicative noise," *Automatica*, vol. 69, pp. 356–363, 2016.

[5] L. Wu and H. Gao, "Sliding mode control of two-dimensional systems in Roesser model," *IET Control Theory & Applications*, vol. 2, no. 4, pp. 352–364, 2008.

[6] D. A. Bristow, M. Tharayil, and A. G. Alleyne, "A survey of iterative learning control," *IEEE Control Systems Magazine*, vol. 26, no. 3, pp. 96–114, 2006.

[7] J.-X. Xu, "A survey on iterative learning control for nonlinear systems," *International Journal of Control*, vol. 84, no. 7, pp. 1275–1294, 2011.

[8] D. Shen and X. Li, "A survey on iterative learning control with randomly varying trial lengths: model, synthesis, and convergence analysis," *Annual Reviews in Control*, vol. 48, pp. 89–102, 2019.

[9] M. Yu and S. Chai, "A survey on high-order internal model based iterative learning control," *IEEE Access*, vol. 7, pp. 127024–127031, 2019.

[10] D. Meng, "Convergence conditions for solving robust iterative learning control problems under nonrepetitive model uncertainties," *IEEE Transactions on Neural Networks and Learning Systems*, vol. 30, no. 6, pp. 1908–1919, 2019.

[11] X. Bu and Z. Hou, "Adaptive iterative learning control for linear systems with binary-valued observations," *IEEE Transactions on Neural Networks and Learning Systems*, vol. 29, no. 1, pp. 232–237, 2018.

[12] X. Bu, Q. Yu, Z. Hou, and W. Qian, "Model free adaptive iterative learning consensus tracking control for a class of nonlinear multiagent systems," *IEEE Transactions on Systems, Man, and Cybernetics: Systems*, vol. 49, no. 4, pp. 677–686, 2019.

[13] X. H. Bu, P. P. Zhu, Z. S. Hou, and J. Q. Liang, "Finite-time consensus for linear multiagent systems using data-driven terminal ILC," *IEEE Transactions on Circuits and Systems II: Express Briefs*, 2019.

[14] R. H. Chi, Y. Hui, B. Huang, and Z. S. Hou, "Adjacent-agent dynamic linearization-based iterative learning formation control," *IEEE Transactions on Cybernetics*, 2019.

[15] H. Afkhami, A. Argha, M. Roopaei, and M. A. Nouri, "Optimal iterative learning control method for 2-D systems using 1-D model (WAM) of 2-D systems," *World Applied Sciences Journal*, vol. 13, pp. 2410–2419, 2011.

[16] M. Roopaei, A. Argha, and P. Karimaghaee, "On the control of 2-D systems by intelligent schemes," *World Applied Sciences Journal*, vol. 6, pp. 385–392, 2009.

[17] K. Wan and X.-D. Li, "Iterative learning control for two-dimensional linear discrete systems with Fornasini-Marchesini model," *International Journal of Control, Automation and Systems*, vol. 15, no. 4, pp. 1710–1719, 2017.

[18] K. Wan and X. D. Li, "High-order internal model based iterative learning control for 2-D linear FMMI systems with

iteration-varying trajectory tracking," *IEEE Transactions on Systems, Man, Cybernetics: Systems*, 2019.

[19] K. Wan and X. D. Li, "Robust iterative learning control of 2-D linear discrete FMMII systems subject to iteration-dependent uncertainties," *IEEE Transactions on Systems, Man, Cybernetics: Systems*, 2019.

[20] K. Wan, D. Xu, and Y.-s. Wei, "Iterative learning control for 2-D linear discrete Fornasini-Marchesini model with input saturation," *International Journal of Systems Science*, vol. 51, no. 8, pp. 1482–1494, 2020.

[21] K. Wan and Y. S. Wei, "Adaptive ILC of tracking non-repetitive trajectory for two dimensional nonlinear discrete time-varying Fornasini-Marchesini systems with iteration-varying boundary states," *International Journal of Control, Automation and Systems*, in press, 2020.

[22] Q.-Y. Xu, X.-D. Li, and M.-M. Lv, "Adaptive ILC for tracking non-repetitive reference trajectory of 2-D FMM under random boundary condition," *International Journal of Control, Automation and Systems*, vol. 14, no. 2, pp. 478–485, 2016.

[23] L. G. Wu and Z. D. Wang, *Filtering and Control for Classes of Two-Dimensional Systems*, Springer, New York, NY, USA, 2014.

[24] S. I. Niculescu, *Delay Effects on Stability: A Robust Control Approach*, Springer, London, UK, 2001.

[25] J. Liang, Z. Wang, and X. Liu, "Robust state estimation for two-dimensional stochastic time-delay systems with missing measurements and sensor saturation," *Multidimensional Systems and Signal Processing*, vol. 25, no. 1, pp. 157–177, 2014.

[26] L. Wu, Z. Wang, H. Gao, and C. Wang, "Filtering for uncertain 2-D discrete systems with state delays," *Signal Processing*, vol. 87, no. 9, pp. 2213–2230, 2007.

[27] J. Xu and L. Yu, "Delay-dependent H∞ control for 2-D discrete state delay systems in the second FM model," *Multidimensional Systems and Signal Processing*, vol. 20, no. 4, pp. 333–349, 2009.

[28] A. Tandon and A. Dhawan, "An LMI approach to non-fragile robust optimal guaranteed cost control of uncertain 2-D discrete systems with both state and input delays," *Transactions of the Institute of Measurement and Control*, vol. 40, no. 3, pp. 785–804, 2018.

[29] T. Kaczorek, *Two-dimensional Linear Systems*, Springer-Verlag, Heidelberg, Germany, 1985.

[30] R. Thamvichai and T. Bose, "Stability of 2-D periodically shift variant filters," *IEEE Transactions on Circuits and Systems II: Analog and Digital Signal Processing*, vol. 49, no. 1, pp. 61–64, 2002.

[31] W. Marszalek, "Two-dimensional state-space discrete models for hyperbolic partial differential equations," *Applied Mathematical Modelling*, vol. 8, no. 1, pp. 11–14, 1984.

[32] R. A. Horn and C. R. Johnson, *Matrix Analysis*, Cambridge University Press, Cambridge, UK, 1985.

[33] X.-D. Li and J. K. L. Ho, "Further results on iterative learning control with convergence conditions for linear time-variant discrete systems," *International Journal of Systems Science*, vol. 42, no. 6, pp. 989–996, 2011.

[34] S. Boyd, L. E. Ghaoui, E. Feron, and V. Balakrishnan, *Linear Matrix Inequalities in System and Control Theory*, SIAM, Philadelphia, PA, USA, 1984.

[35] S. He, H. Fang, M. Zhang, F. Liu, and Z. Ding, "Adaptive optimal control for a class of nonlinear systems: the online policy iteration approach," *IEEE Transactions on Neural Networks and Learning Systems*, vol. 31, no. 2, pp. 549–558, 2020.

[36] S. He, H. Fang, and M. G. Zhang, "Online policy iterative-based H∞ optimization algorithm for a class of nonlinear systems," *Information Sciences*, vol. 495, pp. 1–13, 2019.

[37] S. He, M. Zhang, H. Fang, F. Liu, X. Luan, and Z. Ding, "Reinforcement learning and adaptive optimization of a class of Markov jump systems with completely unknown dynamic information," *Neural Computing and Applications*, 2019.

[38] C. Wang, H. Fang, and S. He, "Adaptive optimal controller design for a class of LDI-based neural network systems with input time-delays," *Neurocomputing*, vol. 385, pp. 292–299, 2020.

Hindawi
Complexity
Volume 2020, Article ID 5093620, 6 pages
https://doi.org/10.1155/2020/5093620

Research Article

Research on Sentiment Classification Algorithms on Online Review

Ruixia Yan, Zhijie Xia, Yanxi Xie, Xiaoli Wang, and Zukang Song

School of Management, Shanghai University of Engineering Science, Shanghai 201620, China

Correspondence should be addressed to Ruixia Yan; yanruixia8@163.com

Received 5 August 2020; Revised 30 August 2020; Accepted 31 August 2020; Published 8 September 2020

Academic Editor: Shuping He

The product online review text contains a large number of opinions and emotions. In order to identify the public's emotional and tendentious information, we present reinforcement learning models in which sentiment classification algorithms of product online review corpus are discussed in this paper. In order to explore the classification effect of different sentiment classification algorithms, we conducted a research on Naive Bayesian algorithm, support vector machine algorithm, and neural network algorithm and carried out some comparison using a concrete example. The evaluation indexes and the three algorithms are compared in different lengths of sentence and word vector dimensions. The results present that neural network algorithm is effective in the sentiment classification of product online review corpus.

1. Introduction

In the field of natural language processing, emotion analysis has always been a hot research field. With the development of the Internet, a large number of business reviews have emerged on various platforms, most of which are mixed with users' personal opinions on commodities. Therefore, the discriminative research on the emotional polarity of these review texts can help enterprises better understand the customer satisfaction of their products or services [1]. Based on the emotional polarity of comments, we could mine the advantages and disadvantages of products. Then, we could obtain suggestions for product promotion and improvement. The traditional method of discriminating emotional polarity of text is based on machine learning since the 1990s. Traditional machine learning methods are mainly divided into two steps. The first step is to construct the word vector feature manually to obtain the required text information. The second step requires the construction of a classifier to classify the emotional polarity of the text. Classical reinforcement learning methods can be basically used in text classification, such as support vector machine, random forest, Naive Bayesian, neural network, and other algorithms.

1.1. Construct Word Vector Features Manually. In this step, the traditional method of generating word vectors is Bag-of-word (BOW) [2], which converts each word into a one-hot vector based on the pre-established dictionary. One disadvantage of this method is that the text vector obtained has the characteristics of high dimension and lack of semantics. Therefore, methods such as TF-IDF and SVD model are used to reduce the dimension of word vector appearance. Karie and Venter calculate semantic similarity of the returned results by means of external engines and input words into searching engines, expanding the semantic information of word vectors [3]. In order to enable vectors to represent context information, models such as LDA and word embedding have also been presented [4]. The word embedding model is an important research result that introduces deep learning algorithm into the field of natural language.

1.2. Research on Text Classification Model Based on Naive Bayesian. Naive Bayesian model is one of the earliest classification algorithms used for text classification task. Its principle is very simple. Based on Bayes' theorem, it assumes that the word vectors of each word are independent from each other. Then, the prior probability of each word in the

corpus is calculated in the training set of the sample. The probability that the test set of the sample is summarized in each category is predicted [5]. Although Bayesian algorithm is simple, it depends on the prior probability of samples much more. Therefore, when the distribution of each sample category in the training set is different, the features of a small number of samples will be replaced by those of a large number of samples.

1.3. Research on Text Classification Based on Support Vector Machine Model. Support vector machine (SVM, for short) model, first proposed by Vapnik in 1995, is based on a combination of the VC dimension theory and risk structure minimization theory. The sample information needed by support vector machine is very limited, so it performs well in solving the problem of small sample and nonlinear text classification. Support vector machine can solve dual problems and use linear method to solve nonlinear problems. Support vector machine can solve the problem of linear inseparability of samples in low-dimensional space by introducing a kernel function. Support vector machine learning algorithm is proposed, and it combines the features of words, parts of speech, and named entities for the text classification task with named entity elements which could achieve good results in the text classification task [6].

1.4. Research on Text Classification Model Based on Deep Learning. In recent years, deep learning has been widely applied in the field of constructing classifiers to classify the emotional polarity of texts. Deep learning model can automatically extract features from the data [7, 8]. For example, Bengio et al. build a neural probabilistic model based on the idea of deep learning and use various deep neural networks to learn on a large-scale English corpus [9]. Deep learning can solve multiple tasks of natural language processing such as named entity recognition and syntactic analysis. In the industrial field, the controlled system usually has great nonlinearity [10–15]. Neural network models have been applied to the identification of nonlinear systems. Convolutional Netural Network (CNN, for short) and Recurrent Neural Network (RNN, for short) have been proved to be effective models for effective classification tasks in the nonlinear system. In terms of the emotional classification of the text, some models of cyclic neural network and convolutional neural network are used to classify the emotions of the short text, and excellent results were obtained [16–20]. However, due to the gradient explosion problem of RNN model, LSTM and GRU models based on the RNN model are more commonly used models [21–25]. Miyamoto et al. applied the LSTM model to text prediction [26]. Duyu et al. applied the LSTM model to emotion classification and the LSTM model achieved good results [27]. The LSTM model has good long-distance feature extraction ability and can extract the relationship between two sequences that are far apart. For classification, important information is not uniformly distributed in the text in the LSTM model. In order to solve this problem, researchers have put forward the attention mechanism [28]. Different weights of each element in the text were presented in the mechanism in the LSTM model, and weights of each element in the text were iteratively updated through training in the LSTM model.

2. Reinforcement Learning of Text Sentiment Classification Algorithm

Reinforcement learning, one of the most active research areas in artificial intelligence, is a computational approach to learning whereby an agent tries to maximize the total amount of reward it receives when interacting with a complex, uncertain environment. Naive Bayesian algorithm, support vector machine, and neural network model are models of reinforcement learning for text sentiment classification.

2.1. Naive Bayesian Algorithm. Naive Bayesian is a machine learning algorithm based on probability theory. Its core theory is Bayes' Theorem. Suppose that, after word segmentation, a certain sentence corpus X is composed of words: $x_1, x_2, \ldots x_n$. X is presented as an n-dimensional vector by cut-off or adding 0. There are m categories in total, noted as $y_1, y_2, \ldots y_m$. The category with the highest probability is obtained through the Bayesian classifier. The highest probability is computed using

$$P(Y \mid x_1 x_2 x_3 \ldots x_n) = \frac{P(x_1 x_2 x_3 \ldots x_n \mid Y) P(Y)}{P(x_1 x_2 x_3 \ldots x_n)}. \quad (1)$$

For each sentence of the fixed corpus X, $P(x_1 x_2 x_3 \ldots x_n)$ is a certain value. So, formula (1) can be transformed into solving the maximum value of

$$P(Y \mid x_1 x_2 x_3 \ldots x_n) = \max P(x_1 x_2 x_3 \ldots x_n \mid Y) P(Y). \quad (2)$$

Naive Bayesian classifier is based on an assumption that each dimension of the word vector is independent of each other. It means that each feature of the data is independent when it applied to statistics. So, formula (2) can be converted into a solution maximum value of

$$P(Y \mid x_1 x_2 x_3 \ldots x_n) = \max P(x_1 \mid Y) P(x_2 \mid Y) P(x_3 \mid Y) \ldots P(x_n \mid Y) P(Y), \quad (3)$$

where $P(x_i \mid Y)$ is the prior probability, which represents the frequency of occurrence of word x_i in a certain category as

$$P(x_i \mid Y) = \frac{\text{count}(x_i \mid Y)}{\text{count}(Y)}, \quad (4)$$

where $\text{count}(x_i \mid Y)$ indicates the number of times the current word appears in the current category and $\text{count}(Y)$ indicates the total number of words in the current category.

2.2. Support Vector Machine. Support vector machine model is used to classify the data. T is the set of sample data points. s_i is the i sentence corpus. l_i is the corresponding label. Text sentiment classification defined the problem which is the optimization problem solved from

$$\begin{aligned} &\min_{\omega,b} \quad p \\ &\text{s.t.} \quad -p \le (\omega \bullet s_i) + b - l_i \le p, \quad i = 1, \ldots, n. \end{aligned} \tag{5}$$

Because the data are linearly inseparable in the process of training, the kernel function and penalty factors of support vector machine are introduced to solve from

$$\min_{\alpha^{(*)} \in R^{2l}} \left(\frac{1}{2} \sum_{i,j=1}^{l} (\alpha_l^* - \alpha_l)(\alpha_j^* - \alpha_j) K(x_i, x_j) + \varepsilon \sum_{i=1}^{l} (\alpha_i^* - \alpha_i) - \sum_{i=1}^{l} l_i (\alpha_i^* - \alpha_i) \right), \tag{6}$$

$\overline{\alpha}^* = (\overline{\alpha_1}, \overline{\alpha_1}^*, \ldots, \overline{\alpha_l}, \overline{\alpha_l}^*)^T$ is the optimal solution. Formula (7) is the decision function:

$$l = \sum_{i=1}^{l} (\alpha_i^* - \alpha_i) K(s_i, s) + \overline{b}. \tag{7}$$

2.3. Neural Network Model. We use the Gated Recurrent Unit (GRU, for short) model as the basic model of the text sentiment classification model in this paper. The GRU model can learn long-term dependence information. GRU usually acts as a recurrent unit that leverages a reset gate and an update gate to control how much information flow from the history state and the current input, respectively. In the GRU model, the current unit state is obtained by calculating and summing the previous unit state. The GRU model can obtain historical information and current information, which is very helpful for extracting the above information in language processing.

The hidden layer of the GRU model could do most of the work. The GRU has two gates, a reset gate and an update gate. The GRU model can learn the long-term dependence of the text. The reset gate is calculated from

$$r_t = \sigma(W_r \cdot [h_{t-1}, x_t]), \tag{8}$$

h_{t-1} is the state of the previous time step. x_t is the input of the current time step. W_r is the weight. The update gate is calculated from

$$Z_t = \sigma(W_z \cdot [h_{t-1}, x_t]). \tag{9}$$

GRU unit status is update from

$$\tilde{h}_t = \tan f\left(W_{\tilde{h}_t} \cdot [r_t * h_{t-1}, x_t]\right) \text{and} \, h_t = (1 - z_t) * h_{t-1} + z_t * \tilde{h}_t. \tag{10}$$

The unit output layer is calculated from

$$y_t = g(W_y \cdot h_t). \tag{11}$$

The input layer is noted as $\{x_1, x_2, x_3, \ldots x_{n-1}, x_n\}$. The output of the hidden layer is noted as $\{s_1, s_2, s_3, \ldots s_{m-1}, s_m\}$.

The calculation method for each layer of the GRU model is as follows:

$$t_i = W_{\text{hx}} x_i + W_{\text{hh}} h_{i-1} + b_h, \tag{12}$$

$$h_i = e(t_i), \tag{13}$$

$$s_i = W_{yh} h_i + b_y, \tag{14}$$

$$y_i = g(s_i). \tag{15}$$

Here, $\tan f(x) = e^x - e^{-x}/e^x + e^{-x}$ and $g(x) = \text{softmax}(x_i) = e^{x_i}/\sum_{k=1}^{K} e^{x_k}$.

In order to evaluate the generalization ability of the model on the test set accurately, we use the ten-fold training method to test the model performance. The basic steps of the ten-fold training method are as follows:

Step 1: first, we divide the test set data into ten parts.

Step 2: then, we put nine pieces of data into the classification for training. The remaining piece of data is used as the test set. We calculate the accuracy and recall rate of the test set on the classifier after training.

Step 3: we repeat Step 2. Here, we select one of the nine training sets that have been trained as the test set. Then, we convert the original test set to the training set for model training until ten sets of data are selected in turn.

Step 4: we calculate the average value of the evaluation parameters, which is the final result.

3. Training and Evaluation Parameters of Reinforcement Learning

We select accuracy and F value as evaluation parameters in this paper. First, we introduce the confusion matrix in information retrieval, which is shown in Table 1. Among them, TP is a pair of feature views that are correctly classified as positive emotions. FP is misclassified as negative emotions. About feature opinion pairs, FN is a feature opinion pair that

Table 1: Confusion matrix.

		Positive emotion	
		True (the number of texts belonging to this type of sentiment)	False (the number of texts that do not fall into this category)
Negative or invalid emotion	Positive (the number of real positive cases in the data)	TP True positive	FP False positive
	Negative (the number of real negative cases in the data)	FN False negative	TN True negative

is misclassified as positive emotion. TN is a feature opinion pair that is classified as negative emotion correctly.

The calculation formulas for accuracy and F value are as follows:

$$\text{Accuracy} = \frac{\text{TP} + \text{TN}}{\text{TP} + \text{TN} + \text{FP} + \text{FN}}, \tag{16}$$

$$F = \frac{2\text{TP}}{2\text{TP} + \text{FP} + \text{FN}}. \tag{17}$$

In the training process of the model, we use the grid search technique to find the optimal parameters of Naive Bayesian classifier support and the support vector machine classifier in this paper. The training parameters of each classifier are shown in Tables 2 and 3.

4. Model Test of Reinforcement Learning

In order to evaluate the results of the classification model in different word vector dimensions and different sentence lengths, we train models in different dimensions of word vectors and different sentence lengths. The training set contains 7000 online comments of a certain brand of tablet computers (the data is product online review corpus in 2017-2018 which is crawled by us from an online mall. It can be downloaded from https://pan.baidu.com/s/16AYTrzjWZDKXJ0iPqlZUvw (Extraction code: wr01)). The training set and the test set are divided according to the ratio of 7 : 3. From the statistical information of the corpus, it can be seen that the number of words in most of the sentence is below 50 words. If the number of words in the sentence is too low, it would lose the meaning of training. Therefore, we select sentences in which the number of words is in an interval of [15, 50] and the word vector dimension to an interval of [100, 250].

The training result is shown in Tables 4–6. Table 4 is the classification results in different sentence lengths and different dimensions by the Bayesian classifier.

Table 5 is the classification results in different sentence lengths and different dimensions by support vector machine classifier.

Table 6 is the classification results in different sentence lengths and different dimensions by the GRU classifier.

From Tables 4–6, we find that the RNN model algorithm has a better classification effect and the RNN model algorithm effect is significantly better than the other two algorithms. From Table 4, we find the accuracy is stable at about 64% from the Naive Bayesian model. However, the F value continues to rise with the increase of sentence length and the highest value is still

Table 2: Support vector machine training parameters.

Parameters	Parameter values
C: penalty coefficient	1
Kernel: the sum function type used in the algorithm	RBF
Probability: whether to use probability AVB Estimation	True
tol: residual convergence condition	0.001

Table 3: Recurrent neural network training parameters.

Parameters	Parameter values
Input layer	128
Decision function	Relu
Output layer	1

Table 4: Bayesian classifier classification results.

Sentence length	Word vector dimension	Accuracy (%)	F value
15	100	61.43	0.580
15	150	60.90	0.570
15	200	60.86	0.572
15	250	61.27	0.577
20	100	61.87	0.613
20	150	61.97	0.616
20	200	62.66	0.625
20	250	61.99	0.613
25	100	60.74	0.629
25	150	61.43	0.631
25	200	61.83	0.633
25	250	61.71	0.631
30	100	61.24	0.649
30	150	61.81	0.649
30	200	61.57	0.645
30	250	62.60	0.652
35	100	61.21	0.652
35	150	62.99	0.664
35	200	61.47	0.650
35	250	61.84	0.655
40	100	62.53	0.677
40	150	61.44	0.660
40	200	63.03	0.675
40	250	61.86	0.668
45	100	60.24	0.641
45	150	62.14	0.674
45	200	61.44	0.668
45	250	61.49	0.662

Table 5: Support vector machine classifier classification results.

Sentence length	Word vector dimension	Accuracy (%)	F value
15	100	75.54	0.738
15	150	75.00	0.732
15	200	74.47	0.729
15	250	73.11	0.720
20	100	76.59	0.753
20	150	76.63	0.754
20	200	76.27	0.750
20	250	76.33	0.751
25	100	77.74	0.769
25	150	77.51	0.766
25	200	77.03	0.761
25	250	77.03	0.761
30	100	77.99	0.772
30	150	77.67	0.769
30	200	77.67	0.768
30	250	77.64	0.767
35	100	78.11	0.773
35	150	78.79	0.779
35	200	78.10	0.773
35	250	78.94	0.782
40	100	78.13	0.773
40	150	78.47	0.779
40	200	79.19	0.785
40	250	78.73	0.781
45	100	76.87	0.750
45	150	78.06	0.770
45	200	78.41	0.777
45	250	79.19	0.785

Table 6: GRU classification results.

Sentence length	Word vector dimension	Accuracy (%)	F value
15	100	85.02	0.863
15	150	87.44	0.864
15	200	83.77	0.862
15	250	87.78	0.866
20	100	89.31	0.881
20	150	87.92	0.887
20	200	89.03	0.889
20	250	87.97	0.886
25	100	85.64	0.866
25	150	90.71	0.888
25	200	89.47	0.885
25	250	92.60	0.903
30	100	88.26	0.894
30	150	87.72	0.871
30	200	88.13	0.901
30	250	90.60	0.894
35	100	90.70	0.905
35	150	87.47	0.904
35	200	90.16	0.901
35	250	87.23	0.899
40	100	87.60	0.897
40	150	91.33	0.919
40	200	93.34	0.922
40	250	73.62	0.809
45	100	89.07	0.912
45	150	91.16	0.900
45	200	92.01	0.912
45	250	89.25	0.908

only about 67% from the Naive Bayesian model. We believe that the Bayesian model is a prior probability model and is more dependent on the big data. In this paper, the sample set is small or medium and its prior probability distribution is not accurate. So, the result is not well as expected from the Naive Bayesian model. In contrast, the result from the support vector machine model is much better. With the continuous increase of sentence length and word vector dimensions, the accuracy and F value from the support vector machine model are maintained at about 78%. It can be seen that when the sentence length is increased to 40, the accuracy has also decreased slightly, and similar accuracy rates are maintained before and after this length from the support vector machine. It can be considered that the model has converged at this length from the support vector machine. The result from the neural network model is the best. The accuracy is around 90% from the neural network model. Due to the powerful feature extraction capabilities, the neural network model is better than the other two models. It can be seen from Table 6 that the GRU model has the best classification effect on a sentence of which the number of words is 40 words and 200 dimensions of word vector.

5. Conclusions

At present, more general scenarios for reinforcement learning and adaptive optimization present a major challenge in complex dynamic systems. The judgment of text sentiment tendency is a hot direction in the field of natural language. We study the sentiment classification algorithm of online reviews. Due to the remarkable effect of machine learning, we select three kinds of machine learning methods: Naive Bayesian, support vector machine, and neural network for comparative research. In order to evaluate the performance of the algorithm on different sentence lengths and word vector dimensions, we train these three models in different dimensions. Finally, using an experiment on an online, we find that the neural network algorithm is effective in classification.

Data Availability

Data used to support the findings of this study are available from the corresponding author upon request or can be downloaded from https://pan.baidu.com/s/16AYTrzjWZDKXJ0iPqlZUvw, Extraction code: wr01.

Conflicts of Interest

The authors declare that there are no conflicts of interest regarding the publication of this paper.

Acknowledgments

This work was funded by the National Philosophy and Social Science General Foundation of China (no. 19BGL234) and Ministry of Education of Humanities and Social Science Foundation of China (no. 17YJCZH199). The authors gratefully acknowledge the National Office for Philosophy and Social Sciences of China and Ministry of Education of China for financial support.

References

[1] Z. Wang, X. Zhang, X. Yang, S. Wang, and W. Xia, "PortraitAI: a deep learning-based approach for generating user portrait for online dating website," in *Proceedings of the International Conference on Education, Economics and Information Management (ICEEIM 2019)*, p. 2020, December 2019, Wuhan, China.

[2] M. Andrew, D. Raymond, P. Pham, D. Huang, A. Ng, and C. Potts, "Learning word vectors for sentiment analysis," in *Proceedings of the Meeting of the Association for Computational Linguistics: Human Language Technologies*, pp. 142–150, Florence, Italy, June 2011.

[3] K. Nickson and H. . s. Venter, "Measuring semantic similarity between digital forensics terminologies using web search engines," in *Proceedings of the Information Security for South Africa IEEE*, pp. 1–9, Johannesburg, South Africa, July 2012.

[4] J. Fei, L. Yiqun, L. Huanbo, and S. Ma, "Microblog sentiment analysis with emoticon space model," *Journal of Computer Science and Technology*, vol. 30, no. 5, pp. 1120–1129, 2014.

[5] K. Yoon, "Convolutional neural networks for sentence classification," *Eprint Arxiv*, vol. 61, no. 6, pp. 2–12, 2014.

[6] S. Tong and K. Daphne, "Support vector machine active learning with applications to text classification," *The Journal of Machine Learning Research*, vol. 2, no. 1, pp. 999–1006, 2002.

[7] J. Dai and J. Chen, "Feature selection via normative fuzzy information weight with application into tumor classification," *Applied Soft Computing*, vol. 92, pp. 106299–106314, 2020.

[8] J. Dai, H. Hu, W.-Z. Wu, Y. Qian, and D. Huang, "Maximal-discernibility-pair-based approach to attribute reduction in fuzzy rough sets," *IEEE Transactions on Fuzzy Systems*, vol. 26, no. 4, pp. 2174–2187, 2018.

[9] Y. Bengio, H. Schwenk, S. Jean-Sébastien, F. Morin, and J.-L. Gauvain, "Neural probabilistic language models," *Innovations in Machine Learning*, vol. 194, pp. 137–186, 2006.

[10] P. Cheng, J. Wang, S. He, X. Luan, and F. Liu, "Observer-based asynchronous fault detection for conic-type nonlinear jumping systems and its application to separately excited DC motor," *IEEE Transactions on Circuits and Systems I: Regular Papers*, vol. 67, pp. 1–12, 2019.

[11] P. Cheng and S. He, "Observer-based finite-time asynchronous control for a class of hidden Markov jumping systems with conic-type nonlinearities," *IET Control Theory & Applications*, vol. 14, 2019.

[12] P. Cheng, S. He, J. Cheng, X. Luan, and F. Liu, "Asynchronous output feedback control for a class of conic-type nonlinear hidden markov jump systems within a finite-time interval," *IEEE Transactions on Systems, Man, and Cybernetics: Systems*, vol. 99, pp. 1–8, 2020.

[13] J. Liu, T. Yin, Y. Dong, H. Reza Karimi, and J. Cao, "Event-based secure leader-following consensus control for multi-agent systems with multiple cyber-attacks," *IEEE Transactions on Cybernetics*, vol. 99, 2020.

[14] J. Liu, W. Suo, L. Zha, E. Tian, and X. Xie, "Security distributed state estimation for nonlinear networked systems against DoS attacks," *International Journal of Robust and Nonlinear Control*, vol. 30, no. 3, pp. 1156–1180, 2020.

[15] J. Liu, Y. Wang, J. Cao, Y. Dong, and X. Xie, "Secure adaptive-event-triggered filter design with input constraint and hybrid cyber-attack," *IEEE Transactions on Cybernetics*, 2020.

[16] Y. Shuhan, W. Xintao, and X. Yang, "Incorporating pre-training in long short-term memory networks for tweets classification," in *Proceedings of the IEEE International Conference on Data Mining IEEE*, pp. 12–19, Pisa, Italy, December 2017.

[17] J. P. A. Vieira and R. S. Moura, "An analysis of convolutional neural networks for sentence classification," in *Proceedings of the Computer Conference IEEE*, pp. 1–5, Cordoba, Argentina, December 2017.

[18] Y. Zhao, B. Qin, and T. Liu, "Encoding syntactic representations with a neural network for sentiment collocation extraction," *Science China (Information Sciences)*, vol. 60, no. 011, pp. 3–14, 2017.

[19] Y. Zhang and J. Meng, N. Wang and M. Pratama, Sentiment classification using comprehensive attention recurrent models," in *Proceedings of the International Joint Conference on Neural Networks IEEE*, pp. 45–54, Vancouver, BC, Canada, July 2016.

[20] Q.-H. Vo, N. Huy-Tien, B. Le, and M.-Le Nguyen, "Multi-channel LSTM-CNN model for Vietnamese sentiment analysis," in *Proceedings of the 2017 9th International Conference on Knowledge and Systems Engineering (KSE) IEEE*, pp. 12–19, Hue, Vietnam, October 2017.

[21] L.-x. Luo, "Network text sentiment analysis method combining LDA text representation and GRU-CNN," *Personal and Ubiquitous Computing*, vol. 23, no. 3-4, pp. 405–412, 2019.

[22] A. Graves and J. Schmidhuber, "Framewise phoneme classification with bidirectional LSTM and other neural network architectures," *Neural Networks*, vol. 18, no. 5-6, pp. 602–610, 2005.

[23] T. H. Shiou, M. Changsung, J. Paul, and N. F. Samatova, "A hybrid CNN-RNN alignment model for phrase-aware sentence classification," in *Proceedings of the 15th Conference of the European Chapter of the Association for Computational Linguistics*, Valencia, Spain, April 2017.

[24] H. Liu, B. Lang, M. Liu, and H. Yan, "CNN and RNN based payload classification methods for attack detection," *Knowledge-Based Systems*, vol. 163, pp. 332–341, 2019.

[25] R. Rajalakshmi, H. Tiwari, J. Patel, and R. Rameshkannan, "Bidirectional GRU-based attention model for kid-specific URL classification," *Deep Learning Techniques and Optimization Strategies in Big Data Analytics*, IGI Global, Hershey, PA, USA, 2020.

[26] M. Yasumasa and K. Cho, "Gated word-character recurrent language model," in *Proceedings of the 2016 Conference on Empirical Methods in Natural Language Processing*, pp. 1992–1997, Austin, TX, USA, November 2016.

[27] T. Duyu, Q. Bing, and L. Ting, "Document modeling with gated recurrent neural network for sentiment classification," in *Proceedings of the 2015 Conference on Empirical Methods in Natural Language Processing*, pp. 1422–1432, Lisbon, Portugal, September 2015.

[28] Y. Wang, M. Huang, xiaoyan Zhu, and Li Zhao, "Attention-based LSTM for aspect-level sentiment classification," in *Proceedings of the 2016 Conference on Empirical Methods in Natural Language Processing*, pp. 606–615, Austin, TX, USA, November 2016.

Hindawi
Complexity
Volume 2020, Article ID 3046769, 12 pages
https://doi.org/10.1155/2020/3046769

Research Article

A Deep Reinforcement Learning Approach to the Optimization of Data Center Task Scheduling

Haiying Che,[1] Zixing Bai,[1] Rong Zuo,[1] and Honglei Li[2]

[1]*Beijing Institute of Technology, Zhongguancun South Street No. 5, Beijing 100081, China*
[2]*Liaoning Normal University, Huanghelu 850, Dalian 116029, China*

Correspondence should be addressed to Honglei Li; lhl@lnnu.edu.cn

Received 25 May 2020; Revised 19 July 2020; Accepted 13 August 2020; Published 31 August 2020

Academic Editor: Shuping He

With more businesses are running online, the scale of data centers is increasing dramatically. The task-scheduling operation with traditional heuristic algorithms is facing the challenges of uncertainty and complexity of the data center environment. It is urgent to use new technology to optimize the task scheduling to ensure the efficient task execution. This study aimed at building a new scheduling model with deep reinforcement learning algorithm, which integrated the task scheduling with resource-utilization optimization. The proposed scheduling model was trained, tested, and compared with classical scheduling algorithms on real data center datasets in experiments to show the effectiveness and efficiency. The experiment report showed that the proposed algorithm worked better than the compared classical algorithms in the key performance metrics: average delay time of tasks, task distribution in different delay time levels, and task congestion degree.

1. Introduction

For the data centers with a huge number of servers, even a little bit improvement of the operation can save millions of dollars. Good task scheduling has been proved to be a practical way to bring benefits without extra hardware investment. Today's data center scheduling systems mostly use heuristic algorithms such as Fair Scheduling (Fair), First-Come-First-Service (FCFS) scheduling, and Shortest-Job-First (SJF) scheduling. These algorithms are easy to understand and implement but only take effects in some certain situations due to the limitation of the complicated production environment. The challenges of data center scheduling in the real world are as follows:

(1) The data center environment is complex and dynamically changing. To achieve efficient and effective scheduling, traditional heuristic algorithms mostly rely on precise environment modeling. In other words, if the environment cannot be accurately modeled, the reasonable and effective scheduling algorithm will not be successfully applied. Therefore, most data center scheduling algorithms still use basic and simple heuristic algorithms, such as Fair, FCFS, and SJF. Practically, it is too hard to model the environment precisely due to the uncertainty of the coming tasks and the dynamic environment. For example, the execution time of a task is affected by network bandwidth, the processing performance of different machines, the disk speed, and the location of the required resources to support the task execution.

(2) Data center scheduling is usually performed without sufficient information support. There are no patterns to predict the task arriving way. That is, the number and size of tasks coming next are unknown. So, the algorithm has to schedule the tasks at once without any prior experience and prepared information.

(3) Resource requirements change dynamically. For data center services or tasks, the demand for resources varies according to different time period, environmental conditions, and so on. The scheduling algorithm needs automatically optimize resource utilization based on the changing demand.

In order to solve the above problems, a lot of related studies are carried out. Most of them focus on specific scheduling scenarios or rely on the acquired details of the coming tasks in advance. In addition, most of the previous studies are single objective optimization-oriented.

In recent years, the deep reinforcement learning [1, 2] which achieves outstanding performance in complex control fields strongly shows its superiority of decision making in complex and unknown environments. Mao et al. tried to translate the problem of packing tasks with multiple resource demands into a learning problem. Their work shows that deep reinforcement learning performs comparably to state-of-the-art heuristics, adapts to different conditions, converges quickly, and learns strategies that are sensible in hindsight [3]. Inspired by these research results, we believe that deep reinforcement learning is suitable for task scheduling of data centers in complex production environments. This paper proposed a method based on deep reinforcement learning to improve task scheduling performance and resource utilization of data centers. With the neural network model trained through deep reinforcement learning, tasks scheduling and resource utilization improvement were achieved.

In this study, we used deep reinforcement learning and aimed at two objectives: minimizing the average task completion time and improving resource utilization efficiency without any prior knowledge of the coming tasks. The experiments and verification were performed using real production data from the Alibaba Cluster Trace Program sponsored by Alibaba Group [4]. The results showed that compared with the traditional heuristic algorithms, the proposed method achieved better performance.

This paper is organized as follows. In Section 2, related studies were discussed. Reinforcement learning-based scheduling as the prevailing technology used in task scheduling of the data center was introduced. In Section 3, the technical architecture and related definitions of the scheduling system proposed in this paper were illustrated. In Section 4, the reinforcement learning algorithm for scheduling optimization was introduced in detail. In Section 5, experiments were performed on Alibaba real production dataset to show the advantage of the proposed scheduling model. In the last section, the conclusion and future work were discussed.

2. Related Studies

For data center task scheduling, many studies have been launched in the past decade. Heuristic algorithms and reinforcement learning are popular in this domain.

2.1. Heuristic Algorithm-Based Studies. The traditional methods are mainly based on heuristic algorithms. Typically, Delimitrou and Kozyrakis proposed the ARQ algorithm, a multiclass admission control protocol that constrains application waiting time and limits application latency to achieve QoS [5]. They evaluated the algorithm with a wide range of workload scenarios, on both small- and large-scale systems and found that it enforces performance guarantees for 91 percent of applications, while the utilization is improved. Perry et al. proposed a Fastpass algorithm to improve data center transmission efficiency [6]. Fastpass incorporates two fast algorithms: the first determines the time at which each packet should be transmitted, while the second determines the path used for that packet. They deployed and evaluated Fastpass in a portion of Facebook's data center network, which shows that Fastpass achieves better efficiency in transmission. Tseng et al. argued that previous studies have typically focused on modifying the original TCP or increasing additional switch hardware costs, and rarely focused on the existing data center network (DCN) environments. So, they proposed a cross-layer flow schedule with a dynamic grouping (CLFS-DG) algorithm to reduce the effect of TCP incast in DCNs [7]. Yuan et al. solved the cost optimization problem under CDCs (cloud data centers) from two aspects. Firstly, a revenue-based workload admission control method is proposed to selectively accept requests. Then, a cost-aware workload scheduling method is proposed to allocate requests among multiple Internet service providers connected to the distributed CDCs. Finally, intelligent scheduling requests are realized, which can achieve lower cost and higher throughput for CDC providers [8]. Yuan et al. proposed the profit maximization algorithm (PMA) for the profit maximization challenge in the hybrid cloud scenario. The algorithm uses the hybrid heuristic optimization algorithm to simulate annealing particle swarm optimization (SAPSO) to improve the throughput and profit of private cloud [9]. Bi et al. proposed a new dynamic hybrid meta heuristic algorithm based on simulated annealing and particle swarm optimization (PSO) for minimizing energy cost and maximizing revenue of various applications running in virtualized cloud data centers [10]. Yuan et al. proposed a heuristic time scheduling algorithm (TTSA) to minimize the cost of private cloud data centers in hybrid cloud, which can effectively improve the throughput of private cloud data centers [11]. Yuan et al. proposed a biological target differential evolution algorithm (SBDE) based on simulated annealing, aiming at the challenges of maximizing profit and minimizing the probability of average task loss in distributed green data centers scenario. Compared with several existing scheduling algorithms, SBDE achieves greater benefits [12].

With the development of data centers, reasonable prediction is very important to improve the efficiency of task scheduling. Although prediction is not involved in the experiment, it is necessary to predict the execution time when the model is transferred to the actual scene. Zhang et al. (2018) proposed an integrated forecasting method equipped with noise filtering and data frequency representation, named Savitzky–Golay and wavelet-supported stochastic configuration networks (SGW-SCNs) [13]. Bi et al. also proposed an integrated forecasting method that combines Savitzky–Golay filtering and wavelet decomposition with stochastic configuration networks to get the

workload forecast in the next period [14]. Bi et al. proposed an integrated prediction method that combines the Savitzky–Golay filter and wavelet decomposition with stochastic configuration networks to predict workload at the next time slot [15].

Although the previous research results are quite abundant, Luo et al. argued that not only because the scheduling problem is theoretically NP-hard, but also because it is tough to perform practical flow scheduling in large-scale DCNs. It is quite challenging to minimize the task completion time in today's DCNs [16]. That means because of the scalability, complexity, and variability of data center production environment, heuristic algorithms cannot achieve the expected performance even with the deliberated design and exhausting tuning work in real production environment.

2.2. Reinforcement Learning-Based Studies. Reinforcement learning [1, 17], as the prevailing machine learning technology, dramatically becomes a new way to the task scheduling of data centers in recent years. Unlike supervised learning which requires amount of manpower and time to prepare the labeled data, reinforcement learning can work with unlabeled data. This so-called model-free mode allows users to start the modeling without the preparation of accurate server environmental data from the scratch. Therefore, at present, more researchers turn to try reinforcement learning to solve task scheduling in complex data center environments. For example, for the purpose of energy saving, Yuan et al. used the Q-learning algorithm to reduce the data center energy consumption. They tested the algorithm in the CloudSim, a cloud computing simulation framework issued by cloud computing, and distributed system laboratory of the University of Melbourne. The result shows that it can reduce about 40% of the energy consumption of the non-power-aware data center and reduce 1.7% energy consumption of the greedy scheduling algorithm in data center scheduling area [18]. Lin et al. used TD-error reinforcement learning to reduce the energy consumption of data centers, which does not rely on any given stationary assumptions of the job arrival and job service processes. The effectiveness of the proposed reinforcement learning-based data center power management framework was verified with real Google cluster data traces [19]. Li et al. also proposed an end-to-end cooling control algorithm (CCA) that is based on the deep deterministic policy gradient algorithm (DDPG) to optimize the control of cooling system in the data center. The result shows that CCA can achieve about 11% cooling cost saving on the simulation platform compared with a manually configured baseline control algorithm [20]. Shaw et al. proposed an advanced reinforcement learning consolidation agent (ARLCA) based on the Sarsa algorithm to reduce cloud energy consumption [21]. Their work proved that the ARLCA makes a significant improvement in energy saving while the number of service violations is reduced.

Scholars also apply reinforcement learning to solve the problems on other purposes of the data center task scheduling. Basu et al. applied reinforcement learning to build cost-models on standard online transaction processing datasets [22]. They modeled the execution of queries and updates as a Markov decision process whose states are database configurations, actions are configuration changes, and rewards are functions of the cost of configuration change and query and update evaluation. The approach was empirically and comparatively evaluated on a standard OLTP dataset. The result shows that the approach is competitive with state-of-the-art adaptive index tuning, which is dependent on a cost model. Peng et al. tried Gaussian process regression with reinforcement learning based on the Q-learning algorithm to solve the problem of state-action space incomplete exploration of reinforcement in cloud data centers [23]. The computational results demonstrated that the schema can balance the exploration and exploitation in the learning process and accelerate the convergence to a certain extent. Ruffy et al. presented a new emulator, Iroko, to support different network topologies, congestion control algorithms, and deployment scenarios. Iroko interfaces with the OpenAI Gym toolkit, which allows for fast and fair evaluation of different reinforcement learning and traditional congestion control algorithms under the same conditions [24]. By the way, some scholars try to combine neural network with heuristic algorithm and have achieved valuable research results. For example, He et al. proposed a new strategy iteration method for online H ∞ optimal control law design based on neural network for nonlinear systems. Numerical simulation is carried out to verify the feasibility and applicability of the algorithm [25]. In the next year, a PI algorithm based on neural network was proposed to solve the problem of online adaptive optimal control of nonlinear systems. Two examples were given to illustrate the effectiveness and applicability of the method [26].

The above studies show that reinforcement learning can help us to deal with the scheduling problems of data centers in many domains. However, most of them aim at single objective or are based on the ideal hypothesis that the information about the coming tasks and environment are accurate and adequate in advance, which limits the application of the related studies in real production environment.

Furthermore, for most of today's data centers, resources in fixed scale are usually allocated in advance for most business, which is apparently a low-efficiency mode. In fact, the amount of resources required by business may change with time. If we cannot customize the resource amount according to the changing requirement, when more resources are needed, it will cause serious task delay and affect the user experience badly. Or if fewer resources are needed, more unused resources will be wasted. In this article, we proposed reinforcement learning to optimize scheduling efficiency and to improve resource utilization simultaneously. This is a two-objective optimization work which addresses the primary demand of data center operations.

Table 1: Notations in the scheduling system model.

Notation	Memo	Type
T	The duration of period of task scheduling	Model parameter
$\widehat{T}$	The duration of period of resource optimization	Model parameter
$p(i)$	The priority function to estimate the priority of task i	Function
t	The start time of task scheduling which also represents the ID of period of task scheduling (the period is also called time slot)	Variable
$\widehat{t}$	The start time of resource optimization which also represents the ID of period of resource optimization	Variable
(s_1, a_1, r_1)	The state, action, and reward vector for task scheduling agent	Variable
(s_2, a_2, r_2)	The state, action, and reward vector for resource optimization agent	Variable
μ, η	Calibration parameters to adjust the influence of average task priority and active virtual machine proportion	Model parameter
$\widehat{\mu}$, $\widehat{\eta}$	Calibration parameters to tune the proportion of the active virtual machine and the proportion of idle virtual machines	Model parameter
$e\_t_{\widehat{t}}$,$e\_t'_{\widehat{t}}$	The sum of the execution time of tasks arriving in period $\widehat{t}$ and the sum of the execution time of tasks not executed in period $\widehat{t}$	Variable
$n\_t_{\widehat{t}}$,$n\_t'_{\widehat{t}}$	The number of tasks arriving in period $\widehat{t}$ and the number of tasks not executed in period $\widehat{t}$	Variable
M	The number of virtual machines in cloud server	Model parameter
K	The ratio of $\widehat{T}$ to T	Model parameter
α,β,H,γ	The hyperparameter of A2C algorithm	Hyperparameter

3. The Reinforcement Learning-Based Scheduling Model

In this session, all key parts of the scheduling model as well as the related definitions and equations were illustrated. The important notations are listed in Table 1 for better understanding.

3.1. The Model of Scheduling System. The reinforcement learning-based scheduling system consisted of two parts: environment and scheduling agents. As shown in Figure 1, the environment contained task queue, virtual machine cluster, and scheduler. The task queue was the pool to collect the unimplemented tasks in the data center. The virtual machine cluster was the container of virtual machine handlers. The scheduler was the dispatcher to execute the actions from scheduling agents. In this scheduling system, it was assumed that the number of virtual machines was fixed. The configuration and performance of all virtual machines were the same. Tasks in task queue can be scheduled to any idle virtual machine. The virtual machine cluster was defined as $\text{VMs} = \text{vm}_1, \text{vm}_2, \text{vm}_3, \ldots, \text{vm}_m$ where vm_i was the handler of virtual machine i.

The agent part included two scheduling agents: Agent1 and Agent2. Each agent was responsible for its optimization objective. Agent1 was for task scheduling, and Agent2 was for resource utilization.

In the scheduling model, time is an important factor in task scheduling and optimization of resource utilization. The time in the scheduling model was divided into two types, time t and time $\widehat{t}$ shown in Figure 2. t was the start time of task scheduling, and $\widehat{t}$ was the start time of optimization of resource utilization. Time t and $\widehat{t}$ were defined in the relative time period for ease of calculation. The initial value of t and $\widehat{t}$ was 0. In the scheduling model, each task scheduling last Tseconds and each optimization of resource utilization last $\widehat{T}$ seconds. $\widehat{T} = K * T\,(K > 0)$, where K was a parameter in the scheduling model configuration, which hinted the optimization of resource utilization spends more time than task scheduling. In this paper, we defined the interval between t and $t + 1$ as time slot t. So, T was the duration of time slot t. The same definitions were for time slot $\widehat{t}$.

At time t, Agent1 made the decision on whether to execute each task in the task queue. The scheduling action decision was stored in a_{1t}. After $\widehat{T}$ seconds, that is, at time $\widehat{t}$, the system started to optimize resource utilization. The virtual machine cluster would turn on or off a certain number of virtual machines according to the optimization decision action $a_{2\widehat{t}}$ output by Agent2. The procedure was illustrated in detail as follows.

Whenever time t came, the system would receive the tasks arriving from time $t$and store the tasks in the task queue. Then, the following actions were performed in sequence:

(i) The system selected tasks according to the priority calculated by $p(i)$, the task priority function defined in equation (1), and input the current state of the environment s_{1t} to Agent1

(ii) Agent1 output action a_{1t} and returned it to the environment

(iii) The environment executed a_{1t} and returned the reward r_{1t} to Agent1 when $a_{1t}$was finished

When all tasks in the queue were arranged to execute according to a_{1t}, the system entered the next task scheduling time slot $t + 1$.

When the system reached time $\widehat{t}$, the system would start the optimization of resource utilization. At time $\widehat{t}$, the corresponding actions were performed in the following steps:

(i) The system input the current environment status $s_{2\widehat{t}}$ to Agent2

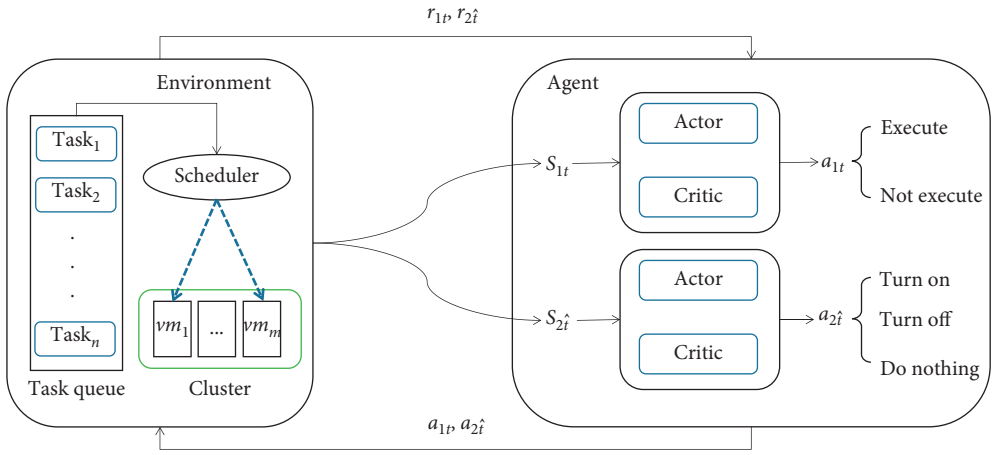

Figure 1: Scheduling system architecture.

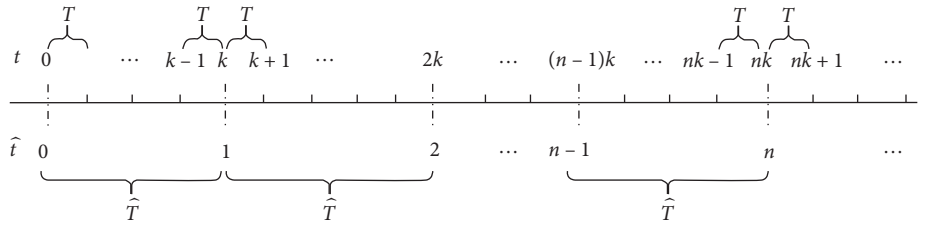

Figure 2: Model of scheduling time.

(ii) Agent2 output action decision $a_{2\hat{t}}$ and returned it to the environment

(iii) The environment executed action decision $a_{2\hat{t}}$ to shut down or start up a certain number of virtual machines and returned the reward r_{2t} to Agent2; then, the system entered the next time slot $\hat{t}+1$

3.2. Related Definitions

3.2.1. Task Priority. Tasks were the jobs running on virtual machine cluster. Tasks arriving in time slot t were added to the task queue waiting for virtual machine allocation. As mentioned above, the environment had little information about the exact number and size of tasks in advance, so the task priority could hardly be simply calculated by waiting time or task execution time. We proposed function $p(i)$ to estimate the priority of task i. In this function, e_i was the execution time of the task i and w_i was the waiting time of the task i. $p(i)$ is defined in the following equation:

$$p(i) = \frac{(e_i + w_i)}{e_i}. \tag{1}$$

After the priorities were calculated, all tasks were scheduled according to their priorities.

3.2.2. Action1. Action1 was the action space of all actions in task schedule. The element of Action1, a_{1i}, indicated whether a certain virtual machine was allocated to the task i. $a_{1i} \in [0, 1]$. The values of a_{1i} were determined in the following equation:

$$a_{1i} = \begin{cases} 1, & \text{if task } i \text{ gets a virtual machine,} \\ 0, & \text{if task } i \text{ does not get a irtual machine.} \end{cases} \tag{2}$$

3.2.3. State1. State1 was the status space of environment for task scheduling. s_{1t}, the instance of State1, was defined as the vector $(e_{1t}, p_t, m_{1t}, n_{1t})$, where e_{1t} was the execution time of the task that was allocated a virtual machine, p_t was the priority of the task that was allocated a virtual machine, m_{1t} was the average priority of all the tasks in the task queue (see equation (3)), n_{1t} was the proportion of the active virtual machines in virtual machine cluster (see equation (4)), and Nt was the number of tasks in time slot t:

$$m_{1t} = \frac{1}{Nt} \sum_{i=1}^{Nt} p(i), \tag{3}$$

$$n_{1t} = \frac{n_{\text{active\_vm}}}{M}. \tag{4}$$

3.2.4. Reward1. The reward value represented the feedback value after the action was performed. The reward value of time slot t is defined in the following equation:

$$r_{1t} = \mu * m_{1t} + \eta * n_{1t}, \tag{5}$$

where μ and η were calibration parameters, which were used to adjust the influence of average task priority m_{1t} and active virtual machine proportion n_{1t}. The values of μ and η were between -1 and 1.

3.2.5. Action2. Action2 represented the number of virtual machines turned on or off in time slot $\widehat{t}$. The instance of Action2 was defined as $a_{2\widehat{t}} \in [-M, M]$. When $a_{2\widehat{t}}$ was greater than 0, it meant there were $a_{2\widehat{t}}$ virtual machines turned on. When $a_{2\widehat{t}}$ was equal to 0, it meant that no change occurred. When $a_{2\widehat{t}}$ was less than 0, it meant that there were $a_{2\widehat{t}}$ virtual machines shut down.

3.2.6. State2. State2 was the state space for Agent2. $s_{2\widehat{t}}$, the instance of State2, was defined as $(e_{2\widehat{t}}, l_{\widehat{t}}, m_{2\widehat{t}}, n_{2\widehat{t}})$, where $e_{2\widehat{t}}$ was defined as the logarithm of the sum of e_$t_{\widehat{t}}$ and e_$t'_{\widehat{t}-1}$, where e_$t_{\widehat{t}}$ was the sum of the task execution time of the tasks arrived in time slot $\widehat{t}$, and e_$t'_{\widehat{t}-1}$ was the sum of the task execution time of the tasks not executed at previous time slot $\widehat{t}-1$. $l_{\widehat{t}}$ was the logarithm of the sum of $n\_t_{\widehat{t}}$ and $n\_t'_{\widehat{t}-1}$, where $n\_t_{\widehat{t}}$ was the number of tasks arrived in time slot $\widehat{t}$ and $n\_t'_{\widehat{t}-1}$ was the number of tasks not executed in the previous time slot $\widehat{t}-1$. $m_{2\widehat{t}}$ was the average value of m_{1t} in time slot $\widehat{t}$. $n_{2\widehat{t}}$ was the average proportion of idle virtual machines in time slot $\widehat{t}$. `

$$\begin{aligned} e_{2\widehat{t}} &= \log\left(e\_t_{\widehat{t}} + e\_t'_{\widehat{t}-1}\right), \quad \widehat{t} = 0, 1, 2, 3, \ldots, \\ l_{\widehat{t}} &= \log\left(n\_t_{\widehat{t}} + n\_t'_{\widehat{t}-1}\right), \quad \widehat{t} = 0, 1, 2, 3, \ldots, \\ m_{2\widehat{t}} &= \frac{1}{K} \sum_{i=K^*(\widehat{t}-1)}^{K*\widehat{t}} m_{1i}, \quad \widehat{t} = 0, 1, 2, 3, \ldots; K = \frac{\widehat{T}}{T}, \\ n_{2\widehat{t}} &= \frac{1}{K} \sum_{i=k*(\widehat{t}-1)}^{k*\widehat{t}} 1 - n_{1i}, \quad \widehat{t} = 0, 1, 2, 3, \ldots; K = \frac{\widehat{T}}{T}. \end{aligned} \tag{6}$$

3.2.7. Reward2. Reward2 was the value of reward function for Agent2. It was determined in equation (7), where $\widehat{\mu}$ and $\widehat{\eta}$ were calibration parameters. We adjusted the value of $\widehat{\mu}$ and $\widehat{\eta}$ according to the actual situation to tune the proportion of the active virtual machine and the proportion of idle virtual machines in time slot $\widehat{t}$:

$$r_{2\widehat{t}} = \widehat{\mu} n_{2\widehat{t}} - \widehat{\eta} m_{2\widehat{t}}. \tag{7}$$

4. Reinforcement Learning Algorithm for Scheduling Optimization

In this section, the actor-critic deep reinforcement learning algorithm [21, 27, 28] was applied to create the model for scheduling optimization of data centers. The actor-critic algorithm is a hybrid algorithm based on Q-learning and policy gradient which are two classic algorithms of reinforcement learning. The actor-critic algorithm shows outstanding performance in complicated machine learning missions.

A2C was selected in this study. The structure based on A2C is shown in Figure 3. In A2C, the actor network is used for action selection and the critic network is used to evaluate the action.

As mentioned in Section 3, Agent1 acted as the optimization model for task scheduling and Agent2 as the optimization model for resource utilization. (State1, Action1, Reward1) and (State2, Action2, Reward2) were used to describe the state space, action space, and reward function of Agent1 and Agent2, respectively. Hence, (s_{1t}, a_{1t}, r_{1t}) and $(s_{2\widehat{t}}, a_{2\widehat{t}}, r_{2\widehat{t}})$ separately represented one instance in the state spaces, action space, and the reward functions of Agent1 and Agent2 at time slot t and time slot $\widehat{t}$. The data entry (s_t, a_t, r_t, s_{t+1}) was recorded as a sample for the training with the A2C algorithm.

The parameter of the actor network is updated by advantage function $A(s_t, a_t)$ (see equation (8)). θ_a (see equation (9)) and θ_c (see equation (10)) are the parameters of the actor network and critic network, respectively:

$$A(s_t, a_t) = r_t + \gamma V^{\pi_\theta}(s_{t+1}; \theta_c) - V^{\pi_\theta}(s_{t+1}; \theta_c), \tag{8}$$

$$\theta_a \longleftarrow \theta_a + \alpha \sum_t \nabla \log \pi_{\theta_a}(s_t, a_t) A(s_t, a_t) + \beta \nabla_{\theta_a} H\left(\pi_\theta\left(\cdot \mid s_t\right)\right), \tag{9}$$

$$\theta_c \longleftarrow \theta_c - \alpha' \sum_t \nabla_{\theta_c} \left(A(s_t, a_t)\right)^2, \tag{10}$$

where α is the learning rate of the actor network; β is a hyperparameter, and H is the entropy of the policy.

In this study, the full-connection layers were used to build the network, in which Agent1 used the six-layer full-connection network, and Agent2 used the four-layer full-connection network. The size of the hidden layer in both agents was 1024. In the training phase, in order to solve the cold start problem of reinforcement learning and accelerate the convergence of the model, the First-Come-First-Service tactic was applied in the early stage for the allocation of virtual machines in the virtual machine cluster and experiences were collected from the results to achieve a better initial status. In the experiences, running_steps, agent1_batch_size, and agent2_batch_size were the control parameters of the training algorithm. The flowchart of the training algorithm is shown in Figure 4.

In this study, floating point operations per second (FLOPS) was used to evaluate the complexity of the proposed scheduling algorithm. According to the structure of the full-connection network and the input data shown in Figure 3, the complexity of the proposed algorithm was evaluated by

$$\text{Time} \sim O\left(L * I^2 * K * N\right), \tag{11}$$

where K was the ratio of duration of resource utilization $\widehat{T}$ to the duration of task scheduling T defined in the model of scheduling time in Section 3.1; N was the maximum number

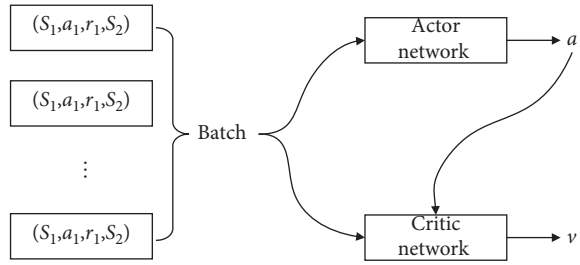

Figure 3: Advantage actor-critic structure.

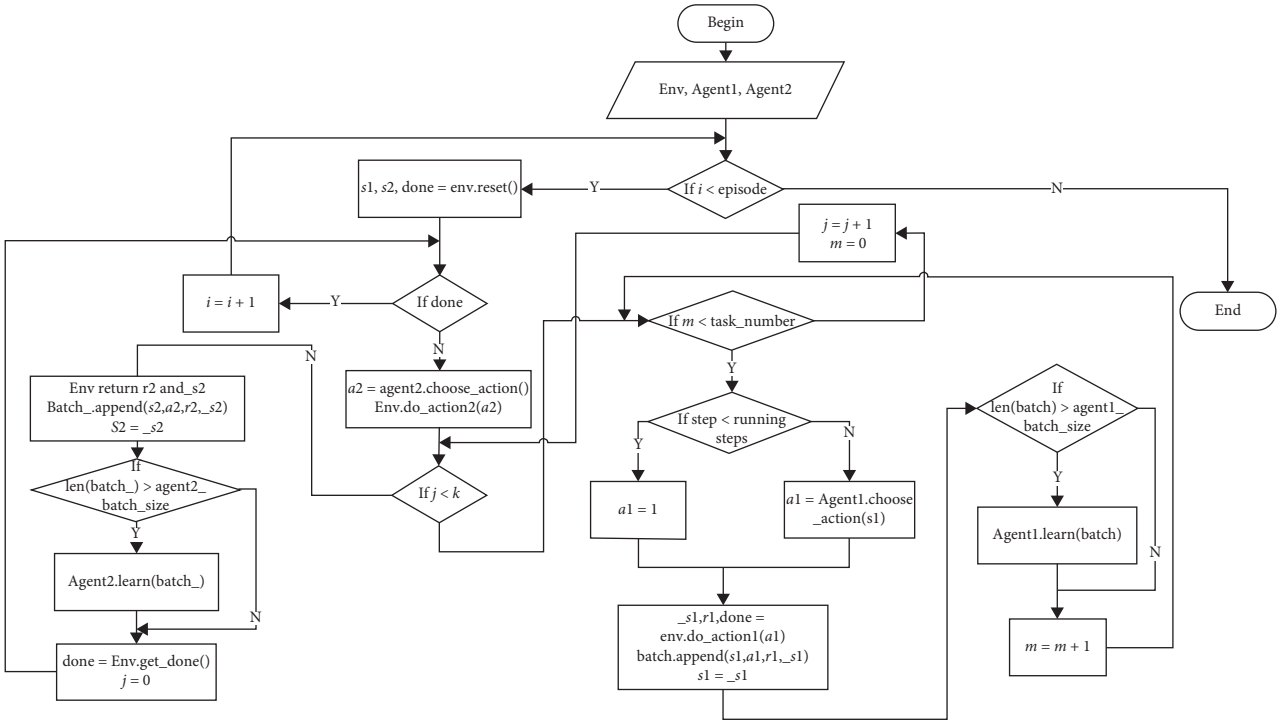

Figure 4: The flowchart of model training process.

of tasks in time slot t; I was the number of nodes in the hidden layer, and L was the number of hidden layers of the network of Agent1 and Agent2. It hinted that given the A2C-based model above, the performance of the proposed algorithm was highly influenced by K and N. In this study, the complexity of the proposed algorithm with the model trained above was about $O(6 * 2^{20} * K * N)$.

5. Experiment Study

5.1. Dataset. Most previous studies used self-generated datasets in their training work, which was not suitable to validate the applicability of the algorithm in the real production environment. In order to verify the effectiveness of the proposed algorithm in the real production environment, cluster-trace-v2017, the real production dataset published by the Alibaba Cluster Trace Program was used in the experiment study. The data are about the cluster trace from real production environment, which helps the researchers to get better understanding of the characteristics of modern Internet data centers (IDCs) and the workloads [4]. The trace dataset includes the collocation of online services and batch workloads about 1300 machines in a period of 12 hours. The trace dataset contains six kinds of collections: machine_meta.csv, machine_usage.csv, container_meta.csv, container_usage.csv, batch_instance.csv, and batch_task.csv. The task information used in the experiment was from batch_instance.csv collection. In this collection, task id, start time, end time, and other attributes are provided.

5.2. Experiment Settings. Here, it was assumed that one virtual machine could not perform multiple tasks at the same time. The virtual machine was equipped with i7-8700k CPU, gtx2080 graphics card, and 32G RAM. The parameters of scheduling system were set as shown in Table 2.

T_{and} $\widetilde{T}$ were set to the empirical value in scheduling. M was the number of virtual machines in different clouding configurations for comparison. α,α',γ, and γ' were set to the empirical value in the A2C algorithm. μ and η were used to control the average priority of tasks and the proportion of active virtual machines. The default value of them was −1. If

Table 2: System parameter setting of scheduling experiment.

Parameter	Value	Parameters	Value
T	3 sec.	M	300~500
$\widehat{T}$	300 sec.	α	1e–4
μ	−1.0	α'	1e–4
η	−0.9	γ	0.9
$\widehat{\mu}$	−1.0	γ'	0.9
$\widehat{\eta}$	1.0		

the goal was to reduce the priority, the ratio of μ/η was increased appropriately. If the goal was to control the cost and reduce the proportion of idle virtual machines, the ratio of μ/η was decreased. The setting of $\widehat{\mu}$ and $\widehat{\eta}$ was the same.

5.3. Model Training. With the trace data from the real production environment, we trained the model with the algorithm introduced in Section 4 and recorded the loss value at each training step. The reward values were represented by the average reward of each episode.

Figure 5 shows the trend of the loss and the reward in training process. Figure 5(a) shows loss trend graph, in which x-axis is the number of training steps and y-axis is the value of loss. It can be seen from the graph that with the increase of training steps, loss gradually decreases until convergence. Figure 5(b) is the reward trend graph, in which the y-axis is reward value and the x-axis is the episode. It shows that with the increase of episode, reward gradually increases and eventually converges at a higher value. It hinted that the performance of the model trained by the algorithm was satisfactory.

5.4. Comparison with Traditional Scheduling Methods. We compared the proposed A2C scheduling algorithm with classical First-Come-First-Service (FCFS), Shortest-Job-First (SJF), and Fair algorithms in the following two experiments.

5.4.1. Experiment1. The fixed number of virtual machines was set to 300, 350, 400, 450, and 500 in the cluster and ran the different algorithms on the dataset. For the proposed algorithm of this paper, only the task scheduling agent (Agent1) worked in experiment1. The result of experiment 1 shown in Figure 6 shows that the average task delay time and the average task priority of the proposed A2C algorithm are less than those of other algorithms with different size of clusters. The results implied that the proposed algorithm worked better in task scheduling than others with different fixed numbers of resources.

5.4.2. Experiment2. In this experiment, Agent 2 worked with Agent1 to schedule the task with dynamic resource allocation. The performance of the proposed algorithm was compared with other algorithms in three dimensions: average delay time of tasks, tasks distribution in different delay time levels, and task congestion degree.

The initial size of virtual machine cluster (M) was set the same for FCFS, SJF, and Fair algorithms, and a dynamic size (M') was set for the proposed algorithm. In order to ensure the fair resources supporting for all algorithms, the maximum value of M' was set up to $1.1 \times M$.

(1) Comparison of Average Delay Time of Tasks. The experiment results on different size of virtual machine clusters are shown in Table 3.

It shows that the proposed algorithm automatically expands the cluster size when the cluster scale is smaller than 400. When the size is set to 300, the cluster size increases by 4% with the task delay decreases by at least 22% compared with those of other algorithms. When the size is set to 350, the cluster size increases by 2.8% with the task delay decreases by at least 28% compared with others. When the cluster size is at a larger level over 400, the proposed algorithm can automatically reduce the cluster size significantly, while the task delay is also considerably smaller than that of Fair, FCFS, and SJF algorithms. In order to show the performance of the proposed algorithm clearly, we defined the relative delay time τ in equation (12). If $\tau = 1$, it means the performance of the compared algorithm is as good as the proposed algorithm. If $\tau > 1$, it means the performance of the compared algorithm is worse than the proposed algorithm; otherwise, it means the performance of the algorithm is better than the proposed algorithm:

$$\tau_m^i = \frac{t_m^i}{t_m'} * \frac{m}{m'}, \tag{12}$$

where $i \in$ (Fair, FCFS, SJF):

$$\begin{aligned} M &\in (300, 350, 400, 450, 500), \\ M' &\in (312, 360, 387, 438, 464), \end{aligned} \tag{13}$$

t_m^i was the average delay time of algorithm i with the cluster size m. t_m' was the average delay time of the proposed algorithm with the cluster size M'.

According to equation (12), the relative delay time was converted from the data in Table 2 and is shown in Table 4.

The results are all greater than 1, which indicates that the task scheduling performance of other compared algorithms with resource utilization is not as good as the proposed algorithm.

(2) *Comparison of Task Distribution in Different Delay Time Levels.* In this section, the tasks in different delay time intervals were considered. The unit of the delay time interval was T, the duration of task scheduling. Table 5 shows the statistical result.

The data in Table 5 are about the percentage of tasks whose delay time is less than the delay time interval. The statistical result clearly shows that the proposed algorithm has higher percentage than other algorithms in all delay time intervals. It means, compared with other algorithms, the less the delay time interval, the higher the percentage of undelayed tasks in this delay time interval. Especially, in the

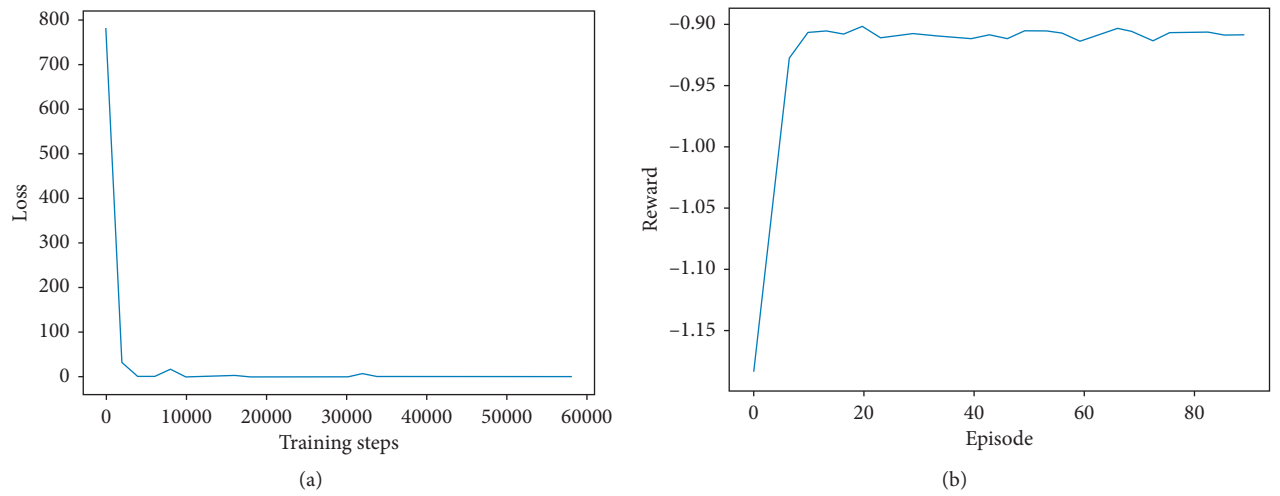

Figure 5: Trend of the loss and the trend of the reward. (a) Loss trend. (b) Reward trend.

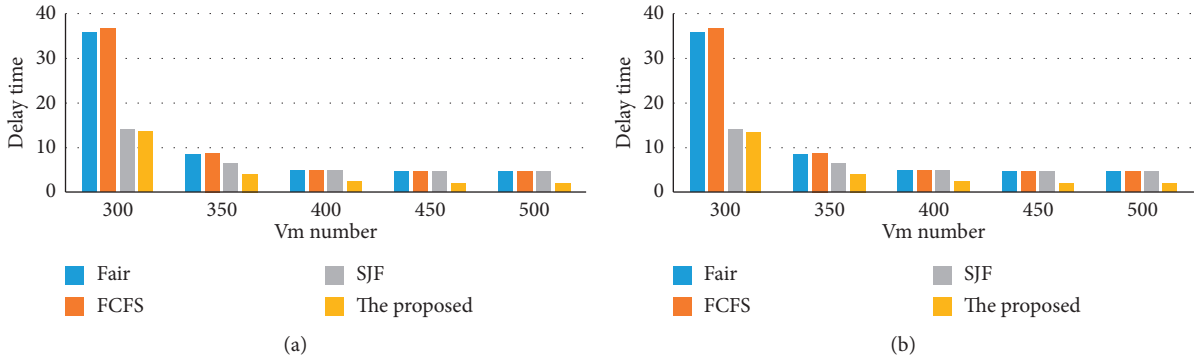

Figure 6: Results of experiment 1. (a) Comparison of average task delay. (b) Comparison of average task priority.

Table 3: Average delay time of different algorithms on different size of virtual machine clusters (in seconds).

Cluster size	Fair	FCFS	SJF	Proposed algorithm (dynamic cluster size)
300	35.9267	36.8301	14.1581	10.5032 (312)
350	8.5735	8.7036	6.3110	2.86432 (360)
400	4.9019	4.9312	4.8311	2.284914 (387)
450	4.6944	4.6953	4.6936	2.0014 (438)
500	4.6931	4.6931	4.6931	1.9975 (464)

Table 4: The relative delay time of the compared algorithms.

Cluster size	Fair	FCFS	SJF
300	3.371	3.371	1.296
350	2.954	2.954	2.142
400	2.231	2.231	2.185
450	2.410	2.410	2.409
500	2.531	2.531	2.532

1T level, the percentage of tasks out of all is almost twice as much as that of others.

(3) Comparison of Task Congestion Degree. Task congestion degree reflected the number of tasks waiting for execution in the task queue at the end of each time slot. It was measured by the percentage of time slots in which the number of congested tasks was less than a certain benchmark number. Therefore, with a certain benchmark number, the less the congestion degree was, the better the scheduling algorithm worked. The statistical result is illustrated in Table 6 and Figure 7.

It can be seen from the data in first row of Table 6 that the proposed algorithm makes all tasks executed in over 82% time slots and for other algorithms, all tasks are executed only in about 30% of all time slots. The change of task congestion degree of all algorithms with more benchmark numbers is visualized by the plot chart in Figure 7, which shows that the congestion degree with the proposed algorithm remains relatively stable and better than other algorithms with all benchmark numbers of congested tasks.

Table 5: The task distribution in different delay time intervals.

Task delay time interval (T)	SJF (%)	FCFS (%)	Fair (%)	The proposed algorithm (%)
1	36.675	13.045	25.688	51.781
2	66.734	46.833	51.021	81.115
3	77.775	65.546	63.935	84.691
4	83.226	71.036	70.797	87.173
5	86.451	73.118	74.603	88.783
10	92.610	76.438	80.914	92.954
15	94.807	78.642	83.803	94.905
20	95.948	80.761	86.011	96.017

Table 6: Task congestion degree.

Number of congested tasks	SJF (%)	FCFS (%)	Fair (%)	The proposed algorithm (%)
0	33.739	31.778	31.802	82.277
5	65.444	62.005	61.990	83.320
10	75.056	70.965	71.107	84.335
15	79.332	74.847	74.999	85.325
20	81.584	76.622	76.867	86.248
25	83.204	77.809	77.952	87.044
30	84.366	78.685	78.643	87.835
...	...	...	...	...

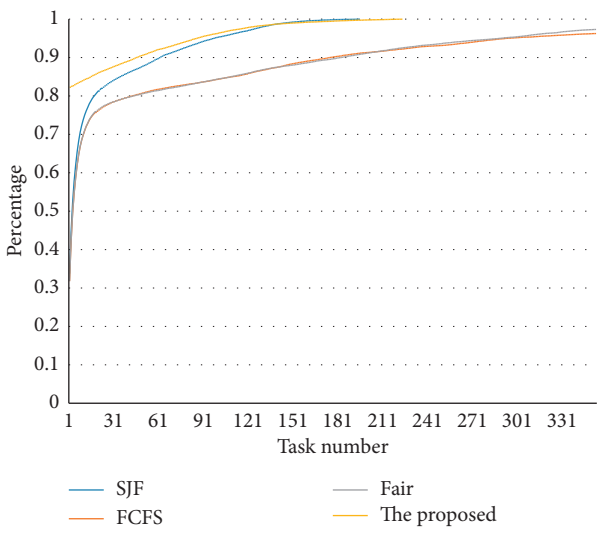

Figure 7: Task congestion degree chart.

6. Conclusions and Further Study

With the expansion of online business in data center, task scheduling and resource utilization optimization become more and more pivotal. Large data center operation is facing the proliferation of uncertain factors, which leads to the geometric increase of environmental complexity. The traditional heuristic algorithms are difficult to cope with today's complex and constantly changing data center environment. However, most of the previous studies focused on one aspect of data center optimization and most of them did not verify their algorithms on the real data center dataset.

Based on the previous studies, this paper designed a reasonable deep reinforcement learning model, optimized the task scheduling and resource utilization. Experiments were also performed with the real production dataset to validate the performance of the proposed algorithm. Average delay time of tasks, task distribution in different delay time levels, and task congestion degree as performance indicators were used to measure the scheduling performance of all algorithms applied in the experiments. The experiment results showed that the proposed algorithm worked significantly better than the compared algorithms in all indexes listed in experiments, ensured the efficient task scheduling and dynamically optimized the resource utilization of clusters.

It should be noted that reinforcement learning is a kind of time-consuming work. In this study, it took 12 hours to train the model with the sample data from the real production environment containing 1300 virtual machines. We also used other production data (cluster-trace-v2018) from the Alibaba Cluster Trace Program to train the scheduling model. The dataset is about 4000 virtual machines in an 8-day period, which is much bigger than the former dataset. As the dataset's scale increased, the training time became considerably longer and underfit occurred if the number of layers of the machine learning model was not increased. As shown in equation (11), the performance of the proposed algorithm is determined by the complexity of the full-connection network, time slot ratio, and the number of tasks in a time slot. Considering the trade-off of the training time cost and the performance, it is strongly recommended to prepare the sample dataset to a reasonable scale with sampling technology to reduce the complexity of the scheduling model.

In addition, we did not consider other task attributes and constraints of data center environment. Fox example, in this study, it was assumed that the number of virtual machines was not dynamically changed, and the ability of all virtual

machines were the same. It was also assumed that one virtual machine cannot perform multiple tasks at the same time. Therefore, we do not imply that the proposed model is available for all kinds of clusters. Notwithstanding its limitation, in the future study, the proposed model should be improved to optimize the task scheduling in the heterogeneous environments of the data center clusters through taking more constraints and attributes of real production environment into account.

Data Availability

The dataset used to support the study is available at the Alibaba Cluster Trace Program (https://github.com/alibaba/clusterdata).

Conflicts of Interest

The authors declare that there are no conflicts of interest regarding the publication of this paper.

Acknowledgments

The research for this article was sponsored under the project "Intelligent Management Technology and Platform of Data-Driven Cloud Data Center", National Key R&D Program of China, no. 2018YFB1003700.

References

[1] K. Arulkumaran, M. P. Deisenroth, M. Brundage, and A. A. Bharath, "Deep reinforcement learning: a brief survey," *IEEE Signal Processing Magazine*, vol. 34, no. 6, pp. 26–38, 2017.

[2] Z. Wang, Z. Schaul, M. Hessel, H. Hasselt, M. Lanctot, and N. Freitas, "Dueling network architectures for deep reinforcement learning," in *Proceedings of the 33rd International Conference on Machine Learning*, pp. 1995–2003, New York, NY, USA, June 2016.

[3] H. Mao, M. Alizadeh, I. Menache, and S. Kandula, "Resource management with deep reinforcement learning," in *Proceedings of the 15th ACM Workshop on Hot Topics in Networks*, pp. 50–56, Atlanta, GA, USA, November 2016.

[4] Alibaba Group, "Alibaba cluster trace program," 2019, https://github.com/alibaba/clusterdata.

[5] C. Delimitrou and C. Kozyrakis, "QoS-Aware scheduling in heterogeneous datacenters with paragon," *ACM Transactions on Computer Systems*, vol. 31, no. 4, pp. 1–34, 2013.

[6] J. Perry, A. Ousterhout, H. Balakrishnan, and D. Shah, "Fastpass: a centralized zero-queue datacenter network," *ACM SIGCOMM Computer Communication Review*, vol. 44, no. 4, pp. 307–318, 2014.

[7] H. W. Tseng, W. C. Chang, I. H. Peng, and P. S. Chen, "A cross-layer flow schedule with dynamical grouping for avoiding TCP Incast problem in data center networks," in *Proceedings of the International Conference on Research in Adaptive and Convergent Systems*, pp. 91–96, Odense, Denmark, October 2016.

[8] H. Yuan, J. Bi, W. Tan, and B. H. Li, "CAWSAC: cost-aware workload scheduling and admission control for distributed cloud data centers," *IEEE Transactions on Automation Science and Engineering*, vol. 13, no. 2, pp. 976–985, 2016.

[9] H. Yuan, J. Bi, W. Tan, and B. H. Li, "Temporal task scheduling with constrained service delay for profit maximization in hybrid clouds," *IEEE Transactions on Automation Science and Engineering*, vol. 14, no. 1, pp. 337–348, 2017.

[10] J. Bi, H. Yuan, W. Tan et al., "Application-aware dynamic fine-grained resource provisioning in a virtualized cloud data center," *IEEE Transactions on Automation Science and Engineering*, vol. 14, no. 2, pp. 1172–1183, 2017.

[11] H. Yuan, J. Bi, W. Tan, M. Zhou, B. H. Li, and J. Li, "TTSA: an effective scheduling approach for delay bounded tasks in hybrid clouds," *IEEE Transactions on Cybernetics*, vol. 47, no. 11, pp. 3658–3668, 2017.

[12] H. Yuan, H. Liu, J. Bi, and M. Zhou, "Revenue and energy cost-optimized biobjective task scheduling for green cloud data centers," *IEEE Transactions on Automation Science and Engineering*, vol. 17, pp. 1–14, 2020.

[13] L. Zhang, J. Bi, and H. Yuan, "Workload forecasting with hybrid stochastic configuration networks in clouds," in *Proceedings of the 2018 5th IEEE International Conference on Cloud Computing and Intelligence Systems (CCIS)*, pp. 112–116, Nanjing, China, November 2018.

[14] J. Bi, H. Yuan, L. Zhang, and J. Zhang, "SGW-SCN: an integrated machine learning approach for workload forecasting in geo-distributed cloud data centers," *Information Sciences*, vol. 481, pp. 57–68, 2019.

[15] J. Bi, H. Yuan, and M. Zhou, "Temporal prediction of multiapplication consolidated workloads in distributed clouds," *IEEE Transactions on Automation Science and Engineering*, vol. 16, no. 4, pp. 1763–1773, 2019.

[16] S. Luo, H. Yu, Y. Zhao, S. Wang, S. Yu, and L. Li, "Towards practical and near-optimal coflow scheduling for data center networks," *IEEE Transactions on Parallel and Distributed Systems*, vol. 27, no. 11, pp. 3366–3380, 2016.

[17] R. S. Sutton and A. G. Barto, *Reinforcement Learning: An Introduction*, MIT Press, Cambridge, MA, USA, 1998.

[18] J. Yuan, X. Jiang, L. Zhong, and H. Yu, "Energy aware resource scheduling algorithm for data center using reinforcement learning," in *Proceedings of 2012 Fifth International Conference on Intelligent Computation Technology and Automation*, pp. 435–438, Hunan, China, January 2012.

[19] X. Lin, Y. Wang, and M. Pedram, "A reinforcement learning-based power management framework for green computing data centers," in *Proceedings of 2016 IEEE International Conference on Cloud Engineering (IC2E)*, pp. 135–138, Berlin, Germany, April 2016.

[20] Y. Li, Y. Wen, D. Tao, and K. Guan, "Transforming cooling optimization for green data center via deep reinforcement learning," *IEEE Transactions on Cybernetics*, vol. 50, no. 5, pp. 2002–2013, 2020.

[21] R. Shaw, E. Howley, and E. Barrett, "An advanced reinforcement learning approach for energy-aware virtual machine consolidation in cloud data centers," in *Proceedings of 2017 12th International Conference for Internet Technology and Secured Transactions (ICITST)*, pp. 61–66, Cambridge, UK, December 2017.

[22] D. Basu, Q. Lin, W. Chen et al., "Regularized cost-model oblivious database tuning with reinforcement learning," *Lecture Notes in Computer Science*, vol. 9940, pp. 96–132, 2016.

[23] Z. Peng, D. Cui, J. Xiong, B. Xu, Y. Ma, and W. Lin, "Cloud job access control scheme based on Gaussian process regression and reinforcement learning," in *Proceedings of 2016 IEEE 4th*

International Conference on Future Internet of Things and Cloud (FiCloud), pp. 276–284, Vienna, Austria, August 2016.

[24] F. Ruffy, M. Przystupa, I. Beschastnikh, and " Iroko, "A framework to prototype reinforcement learning for data center traffic control," 2018, http://arxiv.org/abs/1812.09975.

[25] S. He, H. Fang, M. Zhang, F. Liu, X. Luan, and Z. Ding, "Online policy iterative-based H∞ optimization algorithm for a class of nonlinear systems," *Information Sciences*, vol. 495, pp. 1–13, 2019.

[26] S. He, H. Fang, M. Zhang, F. Liu, and Z. Ding, "Adaptive optimal control for a class of nonlinear systems: the online policy iteration approach," *IEEE Transactions on Neural Networks and Learning Systems*, vol. 31, no. 2, pp. 549–558, 2020.

[27] R. S. Sutton, D. McAllester, S. Singh, and Y. Mansour, "Policy gradient methods for reinforcement learning with function approximation," *Advances in Neural Information Processing Systems*, vol. 12, pp. 1057–1063, MIT Press, Cambridge, MA, USA, 2000.

[28] Y. Wu, E. Mansimov, S. Liao, A. Radford, and J. Schulman, "OpenAI baselines: ACKTR & A2C," 2017, https://openai.com/blog/baselines-acktr-a2c.

Hindawi
Complexity
Volume 2020, Article ID 5070354, 12 pages
https://doi.org/10.1155/2020/5070354

Research Article

Inverse Jacobian Adaptive Tracking Control of Robot Manipulators with Kinematic, Dynamic, and Actuator Uncertainties

Bing Zhou,[1,2] Liang Yang,[1,2] Chengdong Wang,[2] Yong Chen,[2] and Kairui Chen[3]

[1]*School of Computer Engineering, University of Electronic Science and Technology of China, Zhongshan Institute, Zhongshan, Guangdong 528402, China*
[2]*School of Automation Engineering, University of Electronic Science and Technology of China, Chengdu, Sichuan 611731, China*
[3]*School of Mechanical and Electrical Engineering, Guangzhou University, Guangzhou, Guangdong 510006, China*

Correspondence should be addressed to Liang Yang; alex_yangliang@foxmail.com

Received 24 April 2020; Revised 30 June 2020; Accepted 25 July 2020; Published 24 August 2020

Academic Editor: Shuping He

In this paper, we mainly solve the adaptive control problem of robot manipulators with uncertain kinematics, dynamics, and actuators parameters, which has been a long-standing, yet unsolved problem in the robotics field, because of the technical difficulties in handling highly coupled effect between control torque and the mentioned uncertainties. To overcome the difficulties, we propose a new Lyapunov-based adaptive control methodology, which effectively fuses the inverse Jacobian technique and the actuator adaptation law, with which the chattering in tracking errors caused by actuator parameter perturbation is well suppressed. It is demonstrated that the asymptotic convergence of all closed-loop signals is guaranteed. Moreover, the effectiveness of our control scheme is illustrated through simulation studies.

1. Introduction

Control of robot manipulators has attracted a great deal of attentions in the past few decades, due to its wide application in industrial manufacturing [1], military [2], medical [3], and other fields [4]. Some promising results studying robot manipulators have been reported in [5–14]. In [5], an adaptive strategy was developed for visual tracking problem of robot manipulators based on the image-based look-and-move structure, without using image velocity measurements. In [6], by using nonlinear model to depict friction and load change, a switched adaptive controller was designed to achieve asymptotic tracking control for robot manipulators with friction and changing loads. Moreover, in [15], an adaptive sliding mode control scheme based on delay estimation was proposed to deal with uncertainties and external disturbances, and an excellent tracking performance with small chattering effect was guaranteed.

It is worth noting that the aforementioned control schemes are all based on joint space (using dynamics), which may be inconvenient in practical application compared with task-space control schemes (using dynamics and kinematics). To cope with this restriction, some interesting results have been reported in [16–18]. In [16], a task-space controller was developed to guarantee asymptotic tracking of end-effector position and orientation by utilizing a model-based observer. In [18], a new task-space controller based on regional feedback was proposed for various control problems in task-space such as singularity problem and limited sensing zone. However, in these aforementioned approaches, the kinematic parameters are assumed to be accurately known. As pointed out earlier in [19, 20], such assumption is hard to be satisfied in practice. For robot manipulator, neglecting the effects of uncertain kinematics and dynamics will lead to the degradation of control performance, especially in high precision control scenario.

To address this challenging problem, much results have been achieved in [21–29]. These methods for designing controllers in task-space are all based on the Jacobian matrix. In [22], Galicki proposed a class of absolutely continuous Jacobian transpose robust controllers to solve the problems of uncertain dynamics and external disturbances. In [23], Cheah et al. designed an adaptive Jacobian control method to handle the control problem of robot manipulators with both kinematic and dynamic uncertainties. In [22, 23, 26] and [27], the design of the feedback controllers was based on the transposed Jacobian matrix, and all showed excellent stability characteristics. However, when the manipulator moves in a wide range, using the transposed Jacobian feedback method does not make the manipulator tracking maintain good performance. In [30], Craig proposed another control scheme based on inverse Jacobian matrix, and in fact, the stability of the control system based on inverse Jacobian feedback was reformulated and solved in [21], which theoretically explained that the mechanism of the inverse Jacobian control system can be stabilized. The results in [29, 31] demonstrate the effectiveness of using inverse Jacobian feedback control methods to resolve kinematic uncertainties.

It is well known that uncertainty is an important and complex research topic in engineering, and much progress has been made in complex system (e.g., [32, 33]). However, how to deal with the uncertainties in robot system is still an open question. The first challenge stems from the coupling of uncertain kinematics, dynamics, and actuator. It is worth mentioning that, for linear time-invariant systems, we can design closed-loop poles properly to ensure the stability. However, it is not applicable for a nonlinear system (see, e.g., [34–37]), especially under the case of kinematic and dynamic parameters being unknown. Furthermore, there is no in-depth discussion on the decoupling of kinematics, dynamics, and actuator uncertainties. The second challenge arises from the perturbation in actuator parameters. As pointed out in [23], the actuator parameters may also change due to overheating of motor, which may degrade the control performance. In this case, even the dynamic and kinematic parameters can be calibrated, and the overall tracking error of the system cannot be guaranteed to achieve good convergence effect. It has been illustrated through simulation and experiment examples that the chattering phenomenon exists due to the perturbation in actuator parameters.

Inspired by the above observation, this paper investigates the adaptive tracking control problem of robot manipulators, in which both kinematics and dynamics are uncertain. Actually, one of the most challenging difficulties in controller design is to search an effective adaptive approach to cope with the uncertainty of actuator model, whose parameters may change after long time running. To deal with this challenge, by designing new adaptation laws, an efficient inverse Jacobian adaptive control scheme is constructed. Our approaches in this paper can be summarized as follows:

(1) Unlike previous available results in the literature on tracking control of robot manipulators, e.g., [28, 29, 38], we take the perturbation of actuator parameters into account in our design, with particular interest in the compensation of unknown actuator uncertainty whose model may not be accurate due to the imprecise measurement. In our scheme, a new adaptive method is developed to cancel the overlarge actuator compensation error and the unknown disturbances, and the development of such a compensation mechanism can well handle the unknown-in-time perturbation of actuator parameters. Hence, our proposed adaptive controller is feasible in dealing with the highly coupled effect of uncertain dynamics, kinematics, and actuator model.

(2) Traditionally, the tracking control algorithms of robot manipulators are based on the transpose Jacobian matrix (see [23, 27, 28] for example), which may not be convenient because what we can only design is the joint velocity in this mode (see, e.g., [29]). By using the inverse Jacobian, a new joint reference velocity is defined to replace the joint velocity command for the control loop, and in addition, combined with new control law, the separation of the kinematics and dynamics is achieved. Moreover, with the fusion of inverse Jacobian and actuator adaptation law, the chattering phenomenon of tracking errors caused by actuator parameter perturbation is successfully suppressed.

The remainder of this paper is organized as follows. In Section 2, the model of robot manipulators and the control problem are illustrated. Section 3 is devoted to designing an adaptive controller and analyzing the stability of the system. In Section 4, the effectiveness of the proposed adaptive control method is illustrated by simulation experiments. Finally, the conclusions are given in Section 5.

2. Mathematical Model of Robot Manipulators and Problem Statement

2.1. Dynamics and Kinematics Model of Robot Manipulators. If each actuator of the robot is a direct current (DC) motor, the robot manipulators system can be modeled as [30]

$$\mathbb{M}(\theta)\ddot{\theta} + \mathbb{C}(\theta, \dot{\theta})\dot{\theta} + \mathbb{G}(\theta) = K_T u, \tag{1}$$

where $\mathbb{M}(\theta) \in R^{n\times n}$ represents the inertia matrix, $\mathbb{C}(\theta, \dot{\theta}) \in R^{n\times n}$ denotes the Coriolis and Centrifugal matrix, and $\mathbb{G}(\theta) \in R^n$ is the vector of gravitational force. $\theta \in R^n$ is the joint-space position, and $\dot{\theta} \in R^n$ and $\ddot{\theta} \in R^n$ denote the joint-space velocity and acceleration, respectively. $u \in R^n$ is current input to DC motor, and $K_T \in R^{n\times n}$ is a positive definite constant diagonal matrix that converts actuator inputs u into control torque. In real applications, the value of K_T is usually unknown and varies due to external disturbance. In other words, actuator parameter perturbation phenomenon always exists.

Let $x \in R^n$ denote the position of the end-effector in task-space, and the mapping function between x and θ can be given as [30, 39]

$$x = f(\theta), \tag{2}$$

where $f(\theta) \in R^n \longrightarrow R^n$ is a nonlinear differentiable transformation describing the forward kinematics of the manipulator.

By differentiating (2), we have

$$\dot{x} = J(\theta)\dot{\theta}, \tag{3}$$

where $J(\theta) = (\partial f/\partial\theta) \in R^{n\times n}$ is the differentiable manipulator Jacobian matrix. In most cases, $J(\theta)$ is unknown (because kinematic parameters always vary while performing different tasks, e.g., [23]). Therefore, the position/velocity in task-space can not be directly obtained from the kinematics formula given above. Instead, the information on position/velocity in task space can be measured by utilizing cameras.

To facilitate the design and stability analysis, four properties related to robot dynamics (1) and kinematics (3) are listed below [23, 39, 40].

Property 1. The inertia matrix $\mathbb{M}(\theta)$ in the dynamic model (1) is symmetric and uniformly positive definite for all θ.

Property 2. The matrices $\mathbb{C}(\theta, \dot{\theta})$ and $\dot{\mathbb{M}}(\theta)$ satisfy $X^T(\dot{\mathbb{M}}(\theta) - 2\mathbb{C}(\theta, \dot{\theta}))X = 0$, $\forall X \in R^n$, and $(\dot{\mathbb{M}}(\theta) - 2\mathbb{C}(\theta, \dot{\theta}))$ is a skew-symmetric matrix.

Property 3. The left-hand side of dynamic (1) is linear in a set of physical parameters $\phi_d = (\phi_{d1}, \phi_{d2}, \ldots, \phi_{dl})^T$, and thus

$$\mathbb{M}(\theta)\dot{\xi} + \mathbb{C}(\theta, \dot{\theta})\xi + \mathbb{G}(\theta) = Y_d(\theta, \dot{\theta}, \xi, \dot{\xi})\phi_d, \tag{4}$$

where $\xi \in R^n$ is a differentiable vector, $\dot{\xi}$ is the time derivative of ξ, and $Y_d(\theta, \dot{\theta}, \xi, \dot{\xi}) \in R^{n\times l}$ is the dynamic regressor matrix.

Property 4. The right-hand side of kinematic (3) is linear in a set of kinematic parameters $\phi_k = (\phi_{k1}, \phi_{k2}, \ldots, \phi_{km})^T$, which leads to

$$J(\theta)\zeta = Y_k(\theta, \zeta)\phi_k, \tag{5}$$

where $\zeta \in R^n$ is a vector and $Y_k(\theta, \zeta) \in R^{n\times m}$ is the kinematic regressor matrix.

2.2. Problem Statement. In real applications, when a robot manipulator grabs tools, the kinematic and dynamic parameters of robot will inevitably change. Meanwhile, the actuator model may be uncertain due to overheating of motor or changes in ambient. Moreover, the kinematics, dynamics, and uncertain actuator model are highly coupled, which makes the design of the controller more difficult. In the following content, our goal is to design an adaptive controller with separation characteristics to solve the tracking error or unstable response caused by uncertain parameters.

Also, what needs to be explained is the measurable state parameters in practical application, joint-space position θ, joint-space velocity $\dot{\theta}$ and task-space position x, but $J(\theta)$ cannot be accurately obtained by measurement, which means that $\dot{x}$ cannot be got directly through (3). In this paper, the control purpose is to make $\lim_{t\longrightarrow\infty}(x_d(t) - x(t)) = 0$, where x_d denotes the desired trajectory.

3. Adaptive Tracking Control

We first discuss the controller design of robot manipulators with known model, then design adaptive laws and control law for the robot with uncertain kinematics, dynamics, and actuator model to realize trajectory tracking control. In addition, we assume that x_d, $\dot{x}_d$, and $\ddot{x}_d$ are all bounded.

3.1. Control Design of Robot Manipulators with Known Model. Following [23], we define the position tracking error as

$$\Delta x = x - x_d, \tag{6}$$

and task-space reference velocity as

$$\dot{x}_r = \dot{x}_d - \alpha\Delta x, \tag{7}$$

where x_r is task-space reference position and α is a constant satisfying $\alpha > 0$.

As kinematic parameters ϕ_k and $J(\theta)$ are known clearly, the joint-space reference velocity can be defined as

$$\dot{\theta}_r = J^{-1}(\theta)\dot{x}_r, \tag{8}$$

where θ_r is the joint-space reference position and $J^{-1}(\theta)$ is the inverse of $J(\theta)$. In addition, a sliding vector is designed as

$$s = \dot{\theta} - \dot{\theta}_r. \tag{9}$$

By differentiating (9) with respect to time, we further get

$$\dot{s} = \ddot{\theta} - \ddot{\theta}_r. \tag{10}$$

Similarly, when the actuator parameters are known, the dynamics model of DC motor can be described as $K_T u = \tau$, where $\tau \in R^n$ is the joint control torque. Therefore, the task-space tracking control law can be given as

$$\tau = -K_o s + \mathbb{M}(\theta)\ddot{\theta}_r + \mathbb{C}(\theta, \dot{\theta})\dot{\theta}_r + \mathbb{G}(\theta), \tag{11}$$

where $K_o \in R^{n\times n}$ is a positive definite symmetric matrix.

By substituting (9)–(11) into (1), we have

$$\mathbb{M}(\theta)\dot{s} + \mathbb{C}(\theta, \dot{\theta})s = -K_o s. \tag{12}$$

Then, the Lyapunov function is chosen as

$$V_o = \frac{1}{2}s^T\mathbb{M}(\theta)s. \tag{13}$$

By differentiating (13) with respect to time and using (12) and Property 1, we can obtain

$$\begin{aligned}\dot{V}_o &= \frac{1}{2}s^T\dot{\mathbb{M}}(\theta)s + s^T\mathbb{M}(\theta)\dot{s}\\ &= s^T\left\{\frac{1}{2}\dot{\mathbb{M}}(\theta) - \mathbb{C}(\theta, \dot{\theta})\right\}s - s^T K_o s\\ &= -s^T K_o s \le 0.\end{aligned} \tag{14}$$

It implies that $s \longrightarrow 0$ as $t \longrightarrow \infty$. Multiplying $J(\theta)$ to (9), and using (3) and (6), we can further obtain $\Delta\dot{x} + \alpha\Delta x = J(\theta)s \longrightarrow 0$ as $t \longrightarrow \infty$. Therefore, we have $\Delta x \longrightarrow 0$ and $\Delta\dot{x} \longrightarrow 0$ as $t \longrightarrow \infty$, since $\alpha > 0$.

3.2. Control Design of Robot Manipulators with Unknown Model. In practice, we cannot get $\dot{x}$ or $\dot{\theta}$ directly through (3) and (8) since kinematic parameters are uncertain. In this part, we design the controller by using task-space reference velocity, joint-space reference velocity, and estimated Jacobian matrix.

From Property 4, equation (2) can be further reformulated as

$$\dot{x}_r = \widehat{J}(\theta)\dot{\theta}_r = Y_k\left(\theta, \dot{\theta}_r\right)\widehat{\phi}_k, \tag{15}$$

where $\widehat{\phi}_k$ is the estimation of ϕ_k, and $\widehat{J}(\theta)$ is the estimation of $J(\theta)$, which is computed via $\widehat{\phi}_k$. Furthermore, we can redefine the joint-space reference velocity as [29].

$$\dot{\theta}_r = \widehat{J}^{-1}(\theta)\dot{x}_r, \tag{16}$$

$$\ddot{\theta}_r = \widehat{J}^{-1}(\theta)\left[\ddot{x}_r - \dot{\widehat{J}}(\theta)\dot{\theta}_r\right]. \tag{17}$$

Substituting (6), (15), and (16) into (9), we have

$$\begin{aligned} s &= J^{-1}(\theta)\left[\dot{x} - J(\theta)\dot{\theta}_r\right] \\ &= J^{-1}(\theta)\left[\Delta\dot{x} + \alpha\Delta x + Y_k\left(\theta, \dot{\theta}_r\right)\Delta\phi_k\right]. \end{aligned} \tag{18}$$

From [41, 42], left-multiplying (18) by $J(\theta)$, we can further get

$$\Delta\dot{x} = J(\theta)s - \alpha\Delta x - Y_k\left(\theta, \dot{\theta}_r\right)\Delta\phi_k, \tag{19}$$

where $\Delta\phi_k = \widehat{\phi}_k - \phi_k$ is the estimation error of kinematic parameter.

Substituting (9) and (10) into (1), the equations of dynamics can be expressed as

$$\mathbb{M}(\theta)\dot{s} + \mathbb{C}(\theta)s + \left\{\mathbb{M}(\theta)\ddot{\theta}_r + \mathbb{C}(\theta, \dot{\theta})\dot{\theta}_r + \mathbb{G}(\theta)\right\} = K_T u. \tag{20}$$

From Property 3, replace the vector ξ in (4) with θ_r; hence, (20) can be rewritten as

$$\mathbb{M}(\theta)\dot{s} + \mathbb{C}(\theta, \dot{\theta})s + Y_d\left(\theta, \dot{\theta}, \dot{\theta}_r, \ddot{\theta}_r\right)\phi_d = K_T u. \tag{21}$$

Now, we define the control law as

$$u = -K^{-1}K_r s + K^{-1}Y_d\left(\theta, \dot{\theta}, \dot{\theta}_r, \ddot{\theta}_r\right)\widehat{\phi}_d + K^{-1}Y_a(\delta_o)\widehat{\phi}_a, \tag{22}$$

where $K \in R^{n\times n}$ is a positive definite constant approximate matrix of K_T, $K_r \in R^{n\times n}$ is a positive definite symmetric matrix, and $\widehat{\phi}_d$ is the estimated vector of ϕ_d. Furthermore, $Y_a(\delta_o)\widehat{\phi}_a$ is an adaptive term that is designed to deal with the uncertainty in actuator model, where $Y_a(\delta_o) = \mathrm{diag}\{\delta_{o1}, \delta_{o2}, \ldots, \delta_{on}\}$, and δ_{oi} is the ith element of the vector δ_o, which is defined as

$$\delta_o = K_r s - Y_d\left(\theta, \dot{\theta}, \dot{\theta}_r, \ddot{\theta}_r\right)\widehat{\phi}_d. \tag{23}$$

The adaptation laws are designed as follows:

$$\dot{\widehat{\phi}}_k = \Gamma_k Y_k^T\left(\theta, \dot{\theta}_r\right)(\varphi\Delta\dot{x} + \Delta x), \tag{24}$$

$$\dot{\widehat{\phi}}_d = -\Gamma_d Y_d^T\left(\theta, \dot{\theta}, \dot{\theta}_r, \ddot{\theta}_r\right)s, \tag{25}$$

$$\dot{\widehat{\phi}}_a = -\Gamma_a Y_a^T(\delta_o)s, \tag{26}$$

where $\Gamma_d \in R^{l\times l}$ and $\Gamma_k \in R^{m\times m}$ are positive definite symmetric matrices, $\Gamma_a \in R^{n\times n}$ is a positive definite diagonal matrix, and φ is a design constant that satisfies $\varphi \geq 0$ and $\alpha\varphi \leq 1$.

Remark 1. An assumption is firstly made that the robot manipulators will not reach the singular configuration, and its kinematic can be parameterized linearly as (15). Thus, the estimated Jacobian matrix $\widehat{J}(\theta)$ and its inverse $\widehat{J}^{-1}(\theta)$ remain nonsingular while being updated by θ and $\widehat{\phi}_k$.

Remark 2. In the control law (22), the first term is a feedback law contains task-space position and velocity errors and kinematic parameters estimation error, which can be further rewritten as $-K^{-1}K_r J^{-1}(\theta)[\Delta\dot{x} + \alpha\Delta x + Y_k(\theta, \dot{\theta}_r)\Delta\phi_k]$. Hence, (22) can be interpreted as a controller using inverse Jacobian matrix feedback, rather than a transposed approximate Jacobian matrix feedback controller as [23]. The last two terms are estimated dynamic and actuator model compensation terms. The control law (22) expands the adaptive scheme of task space and kinematic parameter estimation error in [29] based on inverse Jacobian feedback and further increases the actuator parameter estimation error feedback, which provides it with the ability to handle the uncertainty of the actuator model.

By substituting (22) into (21), we get

$$\begin{aligned} \mathbb{M}(\theta)\dot{s} + \mathbb{C}(\theta, \dot{\theta})s = &-K_r s + Y_d\left(\theta, \dot{\theta}, \dot{\theta}_r, \ddot{\theta}_r\right)\Delta\phi_d \\ &+ K_T K^{-1}Y_a(\delta_o)\widehat{\phi}_a - \left(K_T K^{-1} - I\right)\delta_o, \end{aligned} \tag{27}$$

where $\Delta\phi_d = \widehat{\phi}_d - \phi_d$.

Following [23], since K_T and K are all defined as diagonal matrices, we have

$$\begin{aligned} \left(K_T K^{-1} - I\right)\delta_o &= \mathrm{diag}\{\delta_{o1}, \delta_{o2}, \ldots, \delta_{on}\}\overline{\phi}_a \\ &= Y_a(\delta_o)\overline{\phi}_a, \end{aligned} \tag{28}$$

where $\overline{\phi}_a = [(k_{t1}/k_1) - 1, (k_{t2}/k_2) - 1, \ldots, (k_{tn}/k_n) - 1]$, and k_{ti} and k_i denote the ith diagonal elements of the K_T and K, respectively. Therefore, the last two terms of (27) can be expressed as

$$K_T K^{-1}Y_a(\delta_o)\widehat{\phi}_a - \left(K_T K^{-1} - I\right)\delta_o = Y_a(\delta_o)\left(K_T K^{-1}\widehat{\phi}_a - \overline{\phi}_a\right). \tag{29}$$

By substituting (29) into (27), we have

$$\mathbb{M}(\theta)\dot{s} + \mathbb{C}(\theta,\dot{\theta})s = -K_r s + Y_d\left(\theta,\dot{\theta},\dot{\theta}_r,\ddot{\theta}_r\right)\Delta\phi_d + Y_a(\delta_o)\Delta\overline{\phi}_a, \tag{30}$$

where $\Delta\overline{\phi}_a = K_T K^{-1}\widehat{\phi}_a - \overline{\phi}_a$. Thus, the closed-loop system can be described as

$$\begin{cases} \Delta\dot{x} = J(\theta)s - \alpha\Delta x - Y_k\left(\theta,\dot{\theta}_r\right)\Delta\phi_k, \\ \mathbb{M}(\theta)\dot{s} + \mathbb{C}(\theta,\dot{\theta})s = -K_r s + Y_d\left(\theta,\dot{\theta},\dot{\theta}_r,\ddot{\theta}_r\right)\Delta\phi_d + Y_a(\delta_o)\Delta\overline{\phi}_a. \end{cases} \tag{31}$$

3.3. Stability Analysis. Through the above efforts, the relationships among the stability of closed-loop system and design parameters have been successfully established, as shown in the following theorem.

Theorem 1. *Consider the closed-loop system consisting of robot manipulator (1) with uncertain kinematics, dynamics, and actuator model. Under control of the adaptive controller (22), (24)–(26), the position and velocity tracking errors of the task-space converge to zero.*

Proof:. Consider the following Lyapunov-like function in terms of dynamics:

$$V_1 = \frac{1}{2}s^T\mathbb{M}(\theta)s + \frac{1}{2}\Delta\phi_d^T\Gamma_d^{-1}\Delta\phi_d + \frac{1}{2}\Delta\overline{\phi}_a^T\Gamma_a^{-1}KK_T^{-1}\Delta\overline{\phi}_a. \tag{32}$$

Differentiating V_1 with respect to time and using $\Delta\dot{\phi}_d = \widehat{\phi}_d$, $\Delta\overline{\phi}_a = K_T K^{-1}\widehat{\phi}_a$, we have

$$\dot{V}_1 = s^T\mathbb{M}(\theta)\dot{s} + \frac{1}{2}s^T\dot{\mathbb{M}}(\theta)s + \Delta\phi_d^T\Gamma_d^{-1}\dot{\widehat{\phi}}_d + \Delta\overline{\phi}_a^T\Gamma_a^{-1}\dot{\widehat{\phi}}_a. \tag{33}$$

By substituting $\mathbb{M}(\theta)\dot{s}$ from (31), dynamic adaptation law $\widehat{\phi}_d$ from (25), and actuator adaptation law $\widehat{\phi}_a$ from (26) into (33), we have

$$\dot{V}_1 = -s^T K_r s \le 0. \tag{34}$$

From Property 1 and (34), we can obtain that V_1 is bounded. This implies that s, $\Delta\phi_d$, and $\Delta\overline{\phi}_a$ are bounded vectors and, hence, implies that $\widehat{\phi}_d$ and $\widehat{\phi}_a$ are bounded.

Since all the joints of the manipulator are rotatable, it can be concluded that $J(\theta)$ is bounded, and hence we have $J(\theta)s \in \mathscr{L}_2$. Thus, according to $\mathscr{L}_2$ norm properties [[43], p. 17], there exists a positive constant ψ such that $\int_0^t \{J(\theta)s\}^T J(\theta)s\mathrm{d}\sigma \le \psi$. Therefore, following the result in [[44], p. 118] and [29], the quasi-Lyapunov function candidate can be considered as

$$V_2 = \frac{1-\alpha\varphi}{2}\Delta x^T\Delta x + \frac{1}{2}\Delta\phi_k^T\Gamma_k^{-1}\Delta\phi_k + \frac{1}{2\alpha}\left[\psi - \int_0^t \{J(\theta)s\}^T J(\theta)s\mathrm{d}\sigma\right]. \tag{35}$$

By differentiating V_2 with respect to time, we have

$$\begin{aligned} \dot{V}_2 &= (1-\alpha\varphi)\Delta x^T\Delta\dot{x} + \Delta\phi_k^T\Gamma_k^{-1}\dot{\widehat{\phi}}_k - \frac{1}{2\alpha}s^T J^T(\theta)J(\theta)s \\ &= (1-\alpha\varphi)\Delta x^T\left(-\alpha\Delta x - Y_k\left(\theta,\dot{\theta}_r\right)\Delta\phi_k + J(\theta)s\right) \\ &\quad + \Delta\phi_k^T\Gamma_k^{-1}\dot{\widehat{\phi}}_k - \frac{1}{2\alpha}s^T J^T(\theta)J(\theta)s \\ &= -\alpha(1-\alpha\varphi)\Delta x^T\Delta x - (1-\alpha\varphi)\Delta\phi_k^T Y_k^T\left(\theta,\dot{\theta}_r\right)\Delta x \\ &\quad - \frac{1-\alpha\varphi}{2\alpha}s^T J^T(\theta)J(\theta)s - \frac{\varphi}{2}s^T J^T(\theta)J(\theta)s + \Delta\phi_k^T\Gamma_k^{-1}\dot{\widehat{\phi}}_k \\ &\quad + (1-\alpha\varphi)\Delta x^T J(\theta)s. \end{aligned} \tag{36}$$

Using $J(\theta)s = \Delta\dot{x} + \alpha\Delta x + Y_k(\theta,\dot{\theta}_r)\Delta\phi_k$ from (19) and using kinematic adaptation law $\dot{\widehat{\phi}}_k$, we can write (36) as

$$\begin{aligned} \dot{V}_2 &= -\alpha(1-\alpha\varphi)\Delta x^T\Delta x + \Delta\phi_k^T Y_k^T\left(\theta,\dot{\theta}_r\right)[\varphi\Delta\dot{x} + \alpha\varphi\Delta x] \\ &\quad + (1-\alpha\varphi)\Delta x^T J(\theta)s - \frac{1-\alpha\varphi}{2\alpha}s^T J^T(\theta)J(\theta)s \\ &\quad - \frac{\varphi}{2}s^T J^T(\theta)J(\theta)s \\ &= -\alpha(1-\alpha\varphi)\Delta x^T\Delta x - \frac{\varphi}{2}(\Delta\dot{x} + \alpha\Delta x)^T(\Delta\dot{x} + \alpha\Delta x) \\ &\quad + (1-\alpha\varphi)\Delta x^T J(\theta)s - \frac{1-\alpha\varphi}{2\alpha}s^T J^T(\theta)J(\theta)s \\ &\quad - \frac{\varphi}{2}\Delta\phi_k^T Y_k^T\left(\theta,\dot{\theta}_r\right)Y_k\left(\theta,\dot{\theta}_r\right)\Delta\phi_k. \end{aligned} \tag{37}$$

From Young's inequality, we can derive the inequality $\Delta x^T J(\theta)s \le (\alpha/2)\Delta x^T\Delta x + [1/(2\alpha)]s^T J^T(\theta)J(\theta)s$. Therefore, (37), can be simplified as

$$\dot{V}_2 \le -\frac{\varphi}{2}(\Delta\dot{x} + \alpha\Delta x)^T(\Delta\dot{x} + \alpha\Delta x) - \frac{\alpha(1-\alpha\varphi)}{2}\Delta x^T\Delta x \le 0. \tag{38}$$

Referring to the input-output properties of the exponentially stable and strictly proper closed-loop systems given in [[43], p. 59], the result of (38) implies that for $\alpha\varphi \le 1$, V_2 is a nonincreasing function, and thus $\Delta\phi_k$ and Δx are bounded.

Next, let us discuss the boundedness of other variables. From (7), we can obtain that $\dot{x}_r$ is bounded if $\dot{x}_d$ and Δx are bounded. Thus, $\dot{\theta}_r$ in (8) is bounded if $\widehat{J}(\theta)$ is of full rank. Since s and $\dot{\theta}_r$ are bounded, $\dot{\theta}$ from (9) is also bounded, and $\dot{x}$ from (3) is bounded. Thus, Δx is uniformly continuous and $\ddot{x}_r = \ddot{x}_d - \alpha\Delta\dot{x}$ is bounded. This implies that $\widehat{\phi}_k$, $\widehat{J}(\theta)$ and $\ddot{\theta}_r$ are bounded. Hence, from the closed-loop robot manipulators system (31), we can obtain that $\dot{s}$ is bounded. The boundedness of $\dot{s}$ implies that $\ddot{\theta}$ is bounded from (10), and $\ddot{x} = J(\theta)\ddot{\theta} + \dot{J}(\theta)\dot{\theta}$ is also bounded. Thus, $\Delta\ddot{x}$ is bounded, and $\Delta\dot{x}$ is uniformly continuous.

For simplicity, define $W(t) = Y_k(\theta,\dot{\theta}_r)\Delta\phi_k$, and we can obtain that $W(t)$ and $\dot{W}(t)$ are bounded since $\dot{\theta},\dot{\theta}_r,\ddot{\theta}_r$, $\Delta\phi_k$

and $\Delta\dot{\phi}_k$ are bounded. Differentiating (37) with respect to time, we further get

$$\ddot{V}_2 = -\frac{1}{\alpha}\Delta\dot{x}^T\left(\alpha^2\varphi\Delta\dot{x} + \Delta\ddot{x}\right) - \alpha\Delta x^T(\Delta\dot{x} + \varphi\Delta\ddot{x}) - \frac{1-\alpha\varphi}{\alpha}\Delta\dot{x}^T\dot{W}(t) - \frac{1-\alpha\varphi}{\alpha}W^T(t)\Delta\ddot{x} - \frac{1}{\alpha}W^T(t)\dot{W}(t), \tag{39}$$

which implies that $\ddot{V}_2$ is bounded since $\dot{\theta}$, $\dot{\theta}_r$, $\ddot{\theta}_r$, $\Delta\phi_k$, $\Delta\dot{\phi}_k$, Δx, $\Delta\dot{x}$ and $\Delta\ddot{x}$ are all bounded, and thus $\dot{V}_2$ is uniformly continuous. Finally, using the conclusions obtained above and Barbalat's lemma, we obtain that $\Delta x \longrightarrow 0$ and $\Delta\dot{x} \longrightarrow 0$ as $t \longrightarrow \infty$.

In order to select design parameters more efficiently, we summarize some guidelines as follows:

(1) In the controller (22), the designed matrix K is required to be positive definite and diagonal, and the designed matrix K_r is required to be positive definite and symmetric.

(2) The designed parameters φ and α are positive constants, which are also required to satisfy the relations $\alpha > 0, \varphi \geq 0$ and $\alpha\varphi \leq 1$.

(3) The designed matrices Γ_k and Γ_d in (24) and (25) are required to be positive definite symmetric. The designed matrix Γ_a is required to be positive definite diagonal. Since the diagonal matrix is symmetric, for convenience, Γ_k and Γ_d can be set as positive definite diagonal matrices.

(4) Supposing that the parameter φ and the matrices Γ_a and Γ_d are set to be smaller, but α, K_r and the matrix Γ_k are chosen larger, then the tracking error could be made smaller and transient performance could be improved. □

4. Simulation and Analysis

4.1. Parameter Design. A planar manipulator with 2 degrees-of-freedom (DOFs) is considered, in which the lengths of the first and second links are roughly set to 0.31 m and 0.35 m, respectively. The mass of the first link together with actuator is approximately equal to 1 kg. The second link, with actuator and the payload attached, can be regarded as an augmented link with a mass of approximately 3 kg. Let the equivalent-length of the object held by the robot be 0.10 meters and the grab angle be 45°. The desired tracking trajectory is given as $x_d = [0.33 + 0.1\sin(0.54 + 3t), 0.41 + 0.1\cos(0.54 + 3t)]^T$.

According to [23], we have

$$\dot{x}_r = \widehat{J}(\theta)\dot{\theta}_r = Y_k\left(\theta, \dot{\theta}_r\right)\widehat{\phi}_k = \begin{bmatrix} -s_1\dot{\theta}_{r1} & -s_{12}\left(\dot{\theta}_{r1} + \dot{\theta}_{r2}\right) & -c_{12}\left(\dot{\theta}_{r1} + \dot{\theta}_{r2}\right) \\ c_1\dot{\theta}_{r1} & c_{12}\left(\dot{\theta}_{r1} + \dot{\theta}_{r2}\right) & -s_{12}\left(\dot{\theta}_{r1} + \dot{\theta}_{r2}\right) \end{bmatrix} \times \begin{bmatrix} \widehat{l}_1 \\ \widehat{l}_2 + \widehat{l}_o c_o \\ \widehat{l}_o s_o \end{bmatrix}, \tag{40}$$

where $s_1 = \sin\theta_1$, $c_1 = \cos\theta_1$, $s_{12} = \sin(\theta_1 + \theta_2)$, $c_{12} = \cos(\theta_1 + \theta_2)$, $c_o = \cos\widehat{\theta}_o$, and $s_o = \sin\widehat{\theta}_o$. $\widehat{l}_1$ and $\widehat{l}_2$ are the estimated link lengths, and $\widehat{l}_o$ and $\widehat{\theta}_o$ are the estimated equivalent-length and grasping angle of the object, respectively.

4.2. Result and Analysis. At first, the robot is required to follow a typical kind of the reference trajectory in task space. In what follows, simulation studies are carried out to validate our control scheme.

4.2.1. Trajectory Tracking without Actuator Parameters Perturbation. In this case, the link lengths were estimated as $\widehat{l}_1 = 0.31$ m and $\widehat{l}_2 = 0.32$ m. The actuator model can be equivalently set as a fixed matrix as $K_T = \mathrm{diag}\{1.2, 1\}$. In the controller, the actuator model is estimated as $K = \mathrm{diag}\{0.8, 0.9\}$. Following the guidelines summarized in Section 4, the controller parameters α, φ, Γ_a, Γ_d, Γ_k and K_r are chosen as $\alpha = 3.2$, $\varphi = 0.11$, $\Gamma_a = 0.001I_2$, $\Gamma_d = 0.001I_4$, $\Gamma_k = 2.8I_3$ and $K_r = 3.5I_2$, respectively. The initial values of the estimated parameters are selected as $\widehat{\phi}_d(0) = [0, 0, 0, 0]^T$, $\widehat{\phi}_k(0) = [0.26, 0.08, 0.07]^T$ and $\widehat{\phi}_a(0) = [-19, -16]^T$; in fact, their actual values are $\phi_d = [0.6278, 0.2875, 0.1162, 0.2013]^T$, $\phi_k = [0.30, 0.31, 0.087]^T$ and $\phi_a = [-19.02, -16.01]^T$.

Simulation results are presented in Figure 1. Figure 1(a) shows the position tracking performances in a horizontal plane. The tracking errors of end-effector in the task-space (Δx_1 and Δx_2) are presented in Figure 1(b). As seen from Figures 1(a) and 1(b), our proposed control scheme guarantees the convergence of the tracking error. The joint control torques of the tracking process are shown in Figure 1(c). As seen from the figures, the tracking controls are satisfactory in terms of the proposed method. It is noted that the added unknown actuator models do not degrade the tracking performances in the case of tracking control without actuator parameters perturbation.

To validate the proposed method, the comparison with other controllers is conducted on robot manipulators. The following control laws from [23, 29] are employed to complete the tracking objective:

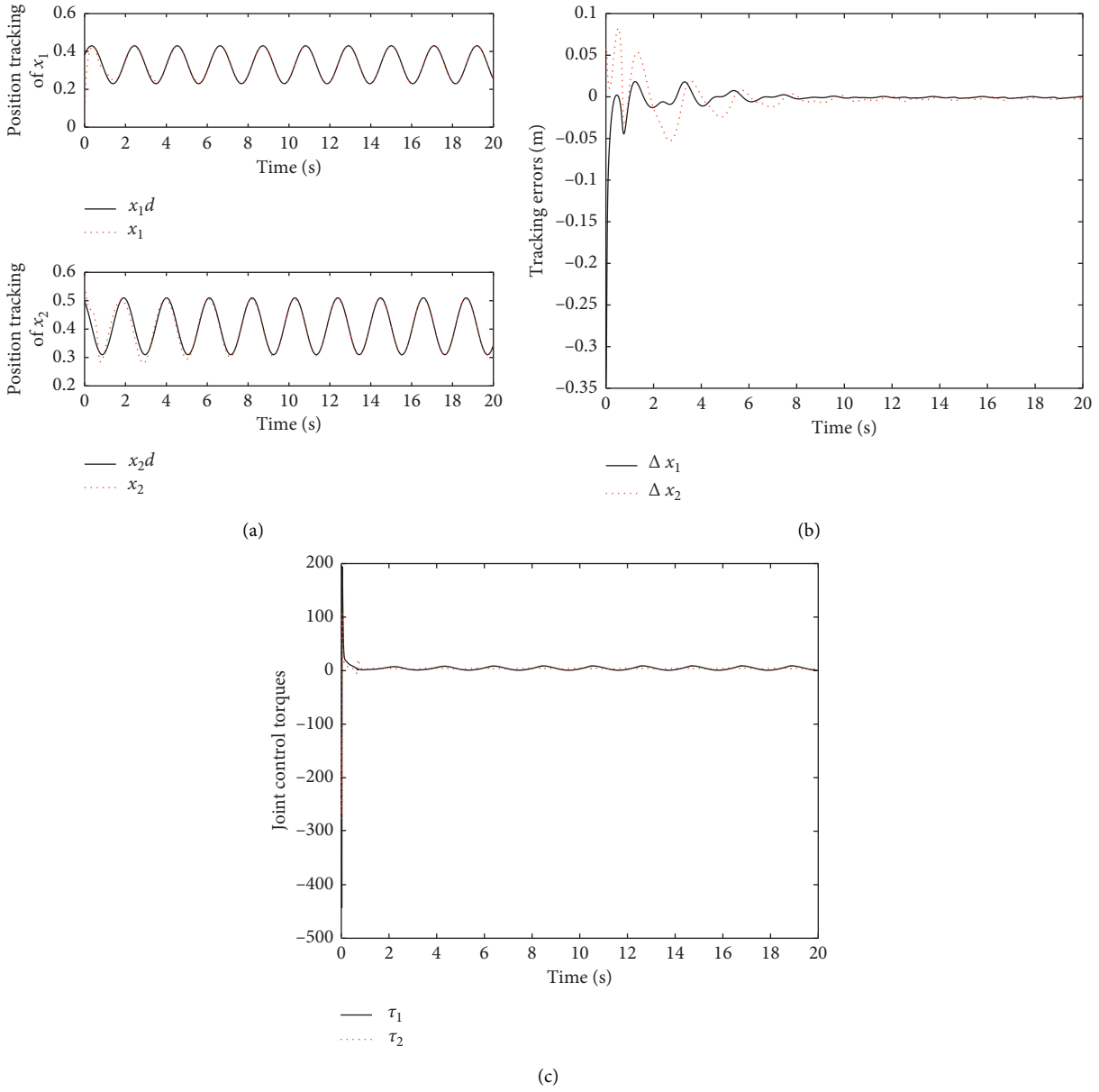

FIGURE 1: End-effector position tracking performance without actuator parameters perturbation. (a) Tracking performance. (b) Tracking errors. (c) Control torques.

$$u' = -K^{-1}\hat{J}^T\left(\theta, \hat{\phi}_k\right)\left(K_v \Delta\dot{x} + K_p \Delta x\right) + K^{-1} Y_d\left(\theta, \dot{\theta}, \dot{\theta}_r, \ddot{\theta}_r\right)\hat{\phi}_d + K^{-1} Y_a\left(\delta_o\right)\hat{\phi}_a, \tag{41}$$

$$u'' = -K^{-1} K_r s + K^{-1} Y_d\left(\theta, \dot{\theta}, \dot{\theta}_r, \ddot{\theta}_r\right)\hat{\phi}_d, \tag{42}$$

where K_v and K_p are symmetric positive definite gain matrices. Specifically, the controller (41) is based on transpose Jacobian feedback (method in [23]), and the controller (42) does not contain the adaptive term for uncertain actuator model (method in [29]).

The comparative results are presented in Figure 2. As seen from Figures 2(a) and 2(b), the controllers (41) and (42) are not exactly tracking the desired trajectory. Moreover, with these two controllers, the tracking errors fail to converge to zero in a short time under the same control conditions. It can be further obtained by the qualitative analysis that the proposed controller (22) has a more stable tracking performance. Therefore, it can be concluded that the adaptive term $Y_a(\delta_o)\hat{\phi}_a$ designed in the controller (22) can effectively handle the uncertainty of the actuator model. In addition, the inverse-Jacobian-based controller (22) has better tracking performance than the transposed-Jacobian-based controller.

4.2.2. Trajectory Control with Actuator Parameters Perturbation. In this case, actuator parameters may change according to the operating environment temperature. The

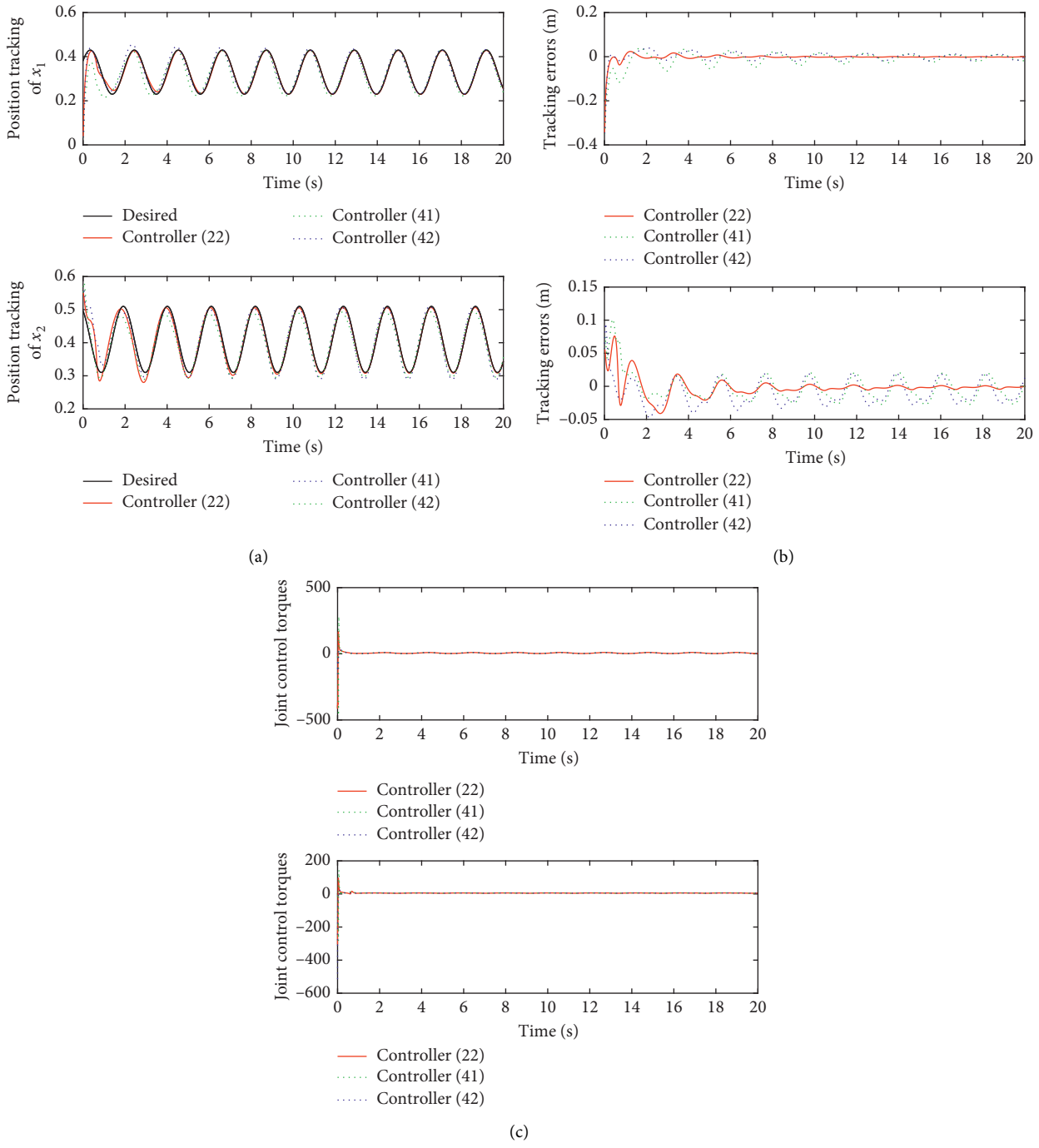

FIGURE 2: Comparisons of end-effector position tracking performance. (a) Comparisons of tracking performance. (b) Comparisons of tracking errors. (c) Comparisons of control torques.

control objective in this case is to design appropriate control torque to force the actual trajectory to converge to the desired one in the presence of actuator parameters perturbation. To simulate this dynamic procedure, the diagonal transmission matrix K is set to the next state values: $K_T = \text{diag}\{1.2, 1\}$ in $[0, 5]s$, $K_T = \text{diag}\{2, 1.2\}$ in $[5, 13]s$ and $K_T = \text{diag}\{4, 3\}$ in $[13, 20]s$, and the designed parameter K is provided as $K = \text{diag}\{0.8, 0.9\}$. The controller parameters α and Γ_k are chosen as $\alpha = 3.5$ and $\Gamma_k = 2.5I_3$, and the other parameters are the same as those of the first simulation.

The performance results in the dynamic trajectory tracking are presented in Figure 3. From the results shown in Figures 3(a) and 3(b), it is apparent that the proposed controller can guarantee that the tracking errors asymptotically converge to zero. Furthermore, the simulation results in Figures 3(a)–3(c) reveal that, with our control

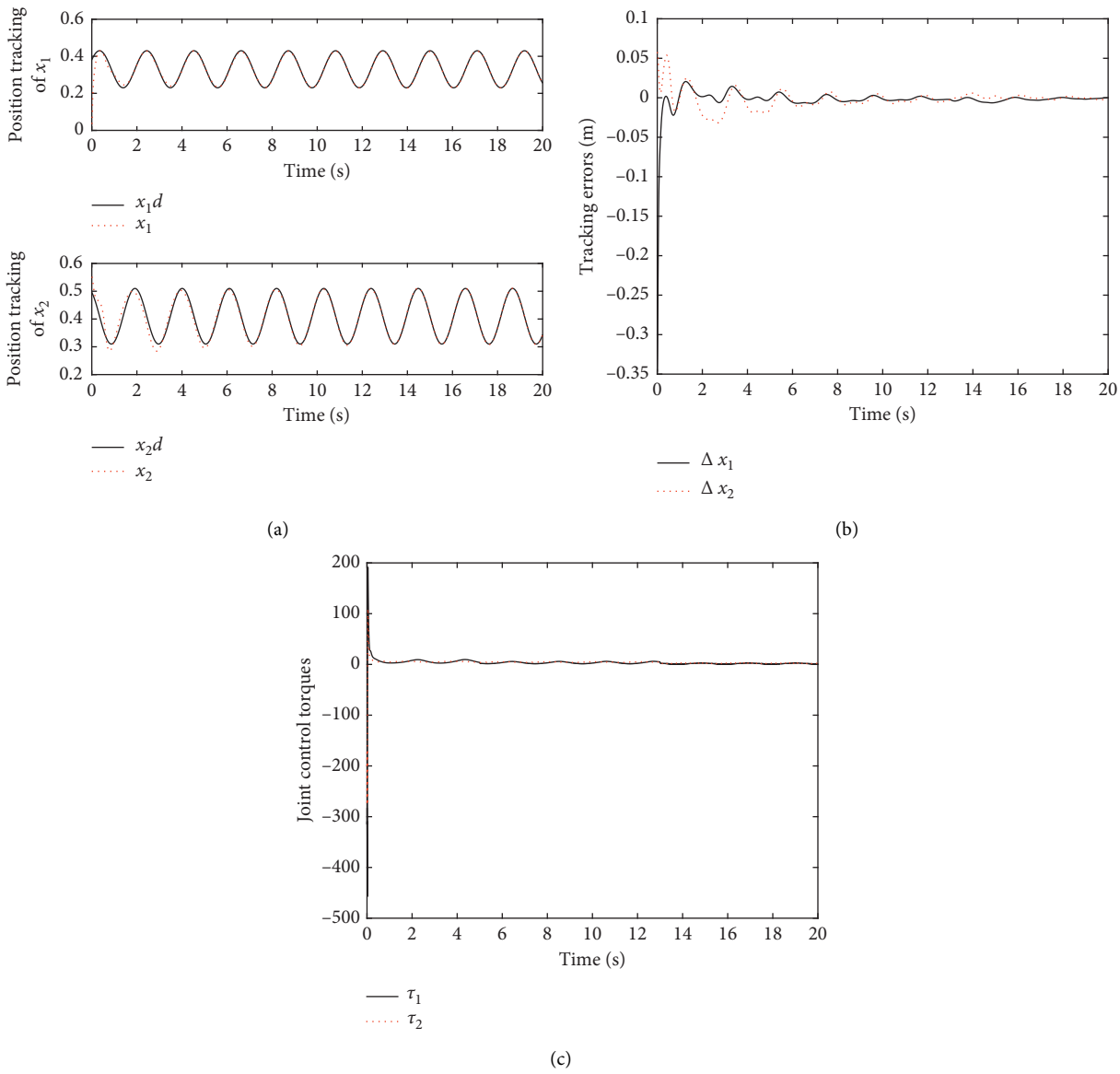

FIGURE 3: End-effector position tracking performance with actuator parameters perturbation. (a) Tracking performance. (b) Tracking errors. (c) Control torques.

scheme, the effect on stability caused by actuator parameters perturbation is successfully suppressed.

Similar to case 1, the comparisons of our controller (22) with controllers (41) and (42) have been carried out, and the results are presented in Figure 4. From Figures 4(a)–4(c), it is apparent that, with our method, a better tracking performance is guaranteed in the case that the actuator parameters perturbation exists.

Moreover, in order to evaluate the quality of different control approaches, the tracking results of x are also shown in Table 1 in terms of the relative Root Mean Squared Error (RMSE), which is defined:

$$\text{RMSE} = \sqrt{\frac{\sum_{i=1}^{N} \left(x(i) - x_d(i)\right)^2}{N}}, \tag{43}$$

where $x(i)$ represents the ith real trajectory of end-effector and $x_d(i)$ represents the ith desired trajectory of end-effector, respectively, and N is the number of samples.

As seen from Table 1, in case 1 and case 2, similar RMSE values (only with a difference of 0.0001) are achieved, which indicates that the proposed controller can well solve the perturbation problem of actuator parameters. In particular, with proposed case 2, the RMSE values of x_1 are reduced nearly 54.7% and 33.1% in comparison with controller (41) and controller (42), respectively. Analogously, the RMSE values of x_2 are reduced nearly 50.7% and 50.4%, respectively. Therefore, it further reveals that our approach is more appropriate for the tracking tasks under the perturbation of actuator parameters.

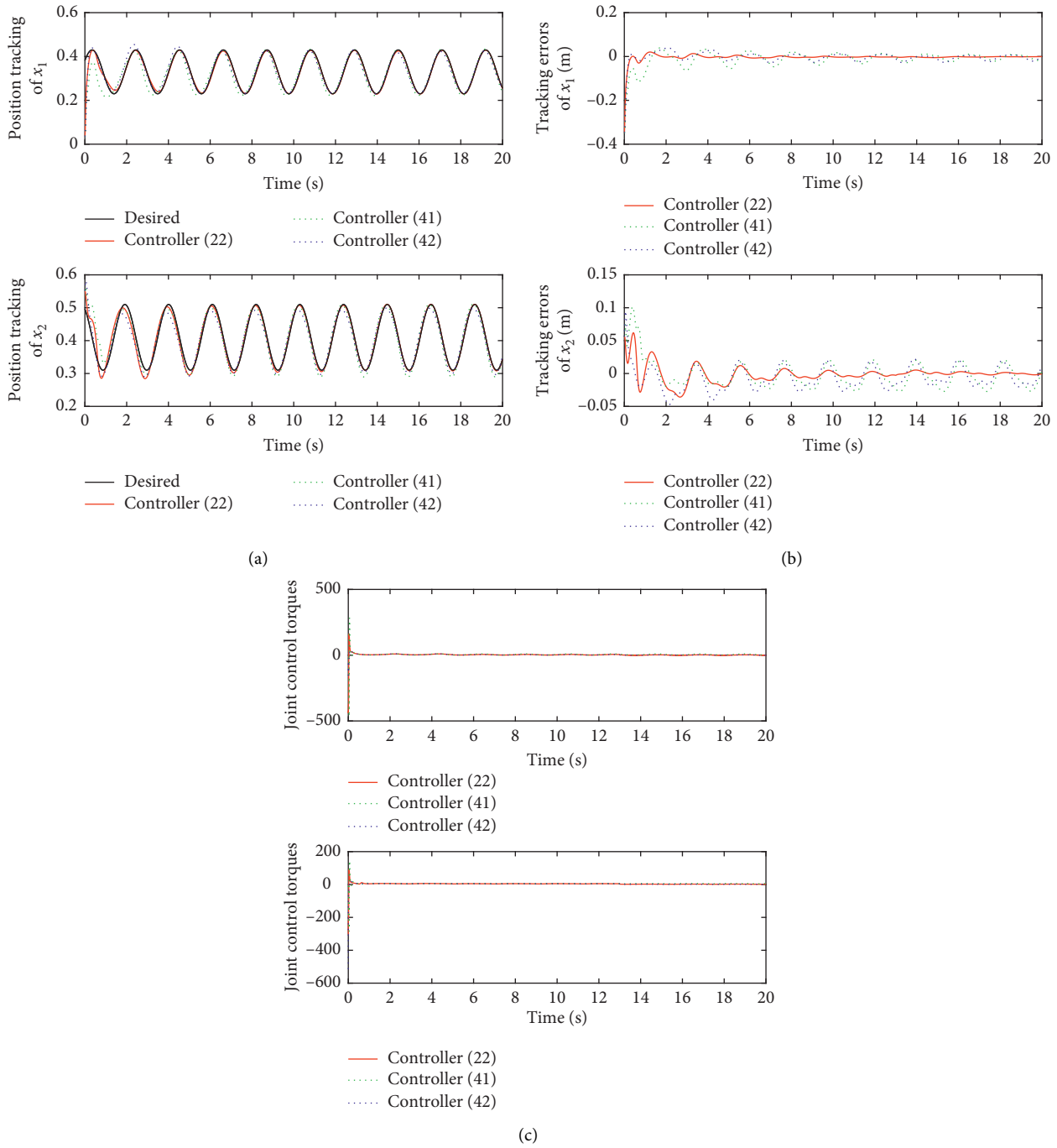

Figure 4: Comparisons of end-effector position tracking performance. (a) Comparisons of tracking performance. (b) Comparisons of tracking errors. (c) Comparisons of control torques.

Table 1: RMSE values of proposed methods and other methods.

RMSE	Proposed case 1	Proposed case 2	Controller (41)	Controller (42)
RMSE of x_1	0.0345	0.0346	0.0765	0.0517
RMSE of x_2	0.0126	0.0127	0.0258	0.0256

5. Conclusion

In this paper, we cope with the adaptive control problem of robot manipulators by utilizing inverse-Jacobian-based technique. To remove the effect on tracking performance caused by the perturbation in actuator parameters, this paper proposes a new inverse Jacobian tracking control approach, which differs from those traditionally presented in that an actuator parameter transform matrix is additionally incorporated in the controller and corresponding adaptation laws are designed to deal with actuator uncertainty. Moreover, the asymptotic convergence of tracking error is proved by the strict Lyapunov stability analysis. Finally, the simulation and comparison results are illustrated to validate our control scheme.

However, how to achieve finite time convergence and the optimal control performance is still a challenging problem in trajectory tracking control. Some interesting results have been reported in [45–48]. Specifically, the solution proposed in [47] gave a novel clue to address this challenge, and the finite-time stabilization technique may be the topic of our future research.

Data Availability

Some or all data, models, or codes generated or used during the study are available from the corresponding author upon request.

Conflicts of Interest

The authors declare that they have no conflicts of interest.

Acknowledgments

This work was supported by the National Natural Science Foundation of China under Grant nos. 61941301, 61573108, U1613223, and U1501251, in part by the Postdoctoral Science Foundation of China under Grant no. 2018M633353, in part by the Special Program for Key Field of Guangdong Colleges under Grant no. 2019KZDZX1037, in part by the Natural Science Foundation of Guangdong Province under Grant nos. 2016A030313715 and 2016A030313018, in part by the Fundamental Research Funds for the Central Universities under Grant no. ZYGX2016J140, in part by the Scientific and Technical Supporting Programs of Sichuan Province under Grant nos. 2016GZ0395, 2017GZ0391, and 2017GZ0392, and in part by the Science and Technology Foundation of Guangdong Province under Grant no. 2019B090910001.

References

[1] D. Yan, "Research and application status of industrial robot control system," in *Proceedings of the 2018 3rd International Conference on Mechanical, Control and Computer Engineering (ICMCCE)*, pp. 16–20, Huhhot, China, September 2018.

[2] X. Xiaozhu, P. Xueqin, and K. Deqi, "Terminal sliding mode control for a military robot system with nonlinear disturbance observer," in *Proceedings of the 2012 7th IEEE Conference on Industrial Electronics and Applications (ICIEA)*, pp. 2139–2143, Singapore, July 2012.

[3] S. Zou, B. Pan, Y. Fu, and S. Guo, "Extended high-gain observer based adaptive control of flexible-joint surgical robot," in *Proceedings of the 2016 IEEE International Conference on Robotics and Biomimetics (ROBIO)*, pp. 2128–2133, Qingdao, China, December 2016.

[4] E.-J. Jung, J. H. Kim, and M. Jin, "Kinematic analysis of hydraulic manipulators for a disaster response robot," in *Proceedings of the 2017 14th International Conference on Ubiquitous Robots and Ambient Intelligence (URAI)*, pp. 208-209, Jeju, South Korea, June 2017.

[5] F. Lizarralde, A. C. Leite, L. Hsu, and R. R. Costa, "Adaptive visual serving scheme free of image velocity measurement for uncertain robot manipulators," *Automatica*, vol. 49, no. 5, pp. 1304–1309, 2013.

[6] X. Wang and Z. Jun, "Switched adaptive tracking control of robot manipulators with friction and changing loads," *International Journal of Systems Science*, vol. 46, no. 6, 2015.

[7] J. Li, W. Zhang, and Q. Zhu, "Weighted multiple-model neural network adaptive control for robotic manipulators with jumping parameters," *Complexity*, vol. 2020, no. 3, pp. 1–12, 2020.

[8] S. Ahmed, H. Wang, and Y. Tian, "Adaptive high-order terminal sliding mode control based on time delay estimation for the robotic manipulators with backlash hysteresis," *IEEE Transactions on Systems, Man, and Cybernetics: Systems*, pp. 1–10, 2019.

[9] S. Ahmed, H. Wang, M. S. Aslam, I. Ghous, and I. Qaisar, "Robust adaptive control of robotic manipulator with input time-varying delay," *International Journal of Control, Automation and Systems*, vol. 17, no. 9, pp. 2193–2202, 2019.

[10] H. Wang, W. Ren, C. C. Cheah, Y. Xie, and S. Lyu, "Dynamic modularity approach to adaptive control of robotic systems with closed architecture," *IEEE Transactions on Automatic Control*, vol. 65, no. 6, pp. 2760–2767, 2020.

[11] J. Baek, W. Kwon, B. Kim, and S. Han, "A widely adaptive time-delayed control and its application to robot manipulators," *IEEE Transactions on Industrial Electronics*, vol. 66, no. 7, pp. 5332–5342, 2019.

[12] X. Chen, H. Zhao, S. Zhen, and H. Sun, "Adaptive robust control for a lower limbs rehabilitation robot running under passive training mode," *IEEE/CAA Journal of Automatica Sinica*, vol. 6, no. 2, pp. 493–502, 2019.

[13] M. Van, M. Mavrovouniotis, and S. S. Ge, "An adaptive backstepping nonsingular fast terminal sliding mode control for robust fault tolerant control of robot manipulators," *IEEE Transactions on Systems, Man, and Cybernetics: Systems*, vol. 49, no. 7, pp. 1448–1458, 2019.

[14] D. Nojavanzadeh and M. Badamchizadeh, "Adaptive fractional-order non-singular fast terminal sliding mode control for robot manipulators," *IET Control Theory & Applications*, vol. 10, no. 13, pp. 1565–1572, 2016.

[15] J. Baek, M. Jin, and S. Han, "A new adaptive sliding-mode control scheme for application to robot manipulators," *IEEE Transactions on Industrial Electronics*, vol. 63, no. 6, pp. 3628–3637, 2016.

[16] B. Xian, M. S. deQueiroz, D. Dawson, and I. Walker, "Task-space tracking control of robot manipulators via quaternion feedback," *IEEE Transactions on Robotics and Automation*, vol. 20, no. 1, pp. 160–167, 2004.

[17] X. Liang, H. Wang, Y.-H. Liu, W. Chen, G. Hu, and J. Zhao, "Adaptive task-space cooperative tracking control of networked robotic manipulators without task-space velocity

measurements," *IEEE Transactions on Cybernetics*, vol. 46, no. 10, pp. 2386–2398, 2016.

[18] X. Li and C. C. Cheah, "Global task-space adaptive control of robot," *Automatica*, vol. 49, no. 1, pp. 58–69, 2013.

[19] C. C. Cheah, M. Hirano, S. Kawamura, and S. Arimoto, "Approximate jacobian control for robots with uncertain kinematics and dynamics," *IEEE Transactions on Robotics and Automation*, vol. 19, no. 4, pp. 692–702, 2003.

[20] W. E. Dixon, "Adaptive regulation of amplitude limited robot manipulators with uncertain kinematics and dynamics," *IEEE Transactions on Automatic Control*, vol. 52, no. 3, pp. 488–493, 2007.

[21] C. C. Cheah and H. C. Liaw, "Inverse jacobian regulator with gravity compensation: stability and experiment," *IEEE Transactions on Robotics*, vol. 21, no. 4, pp. 741–747, 2005.

[22] M. Galicki, "Finite-time trajectory tracking control in a task space of robotic manipulators," *Automatica*, vol. 67, pp. 165–170, 2016.

[23] C. C. Cheah, C. Liu, and J. J. E. Slotine, "Adaptive jacobian tracking control of robots with uncertainties in kinematic, dynamic and actuator models," *IEEE Transactions on Automatic Control*, vol. 51, no. 6, pp. 1024–1029, 2006.

[24] D. Braganza, W. E. Dixon, D. M. Dawson, and B. Xian, "Tracking control for robot manipulators with kinematic and dynamic uncertainty," *International Journal of Robotics and Automation*, vol. 23, no. 2, pp. 117–126, 2008.

[25] H. Wang, "Task-space bilateral control of teleoperators with time-varying delay," in *Proceedings of the 2019 IEEE 58th Conference on Decision and Control (CDC)*, pp. 1698–1703, Nice, France, December 2019.

[26] J. Peng, Z. Yang, and T. Ma, "Position/force tracking impedance control for robotic systems with uncertainties based on adaptive jacobian and neural network," *Complexity*, vol. 2019, Article ID 1406534, 16 pages, 2019.

[27] H. Wang, "Adaptive visual tracking for robotic systems without image-space velocity measurement," *Automatica*, vol. 55, pp. 294–301, 2015.

[28] B. Xiao, S. Yin, and O. Kaynak, "Tracking control of robotic manipulators with uncertain kinematics and dynamics," *IEEE Transactions on Industrial Electronics*, vol. 63, no. 10, pp. 6439–6449, 2016.

[29] H. Wang, "Adaptive control of robot manipulators with uncertain kinematics and dynamics," *IEEE Transactions on Automatic Control*, vol. 62, no. 2, pp. 948–954, 2017.

[30] J. J. Craig, *Introduction to Robotics: Mechanics and Control*, Prentice-Hall, Upper Saddle River, NJ, USA, 2005.

[31] B. Xiao and S. Yin, "Exponential tracking control of robotic manipulators with uncertain dynamics and kinematics," *IEEE Transactions on Industrial Informatics*, vol. 15, no. 2, pp. 689–698, 2019.

[32] J. Xiong, X.-H. Chang, and X. Yi, "Design of robust nonfragile fault detection filter for uncertain dynamic systems with quantization," *Applied Mathematics and Computation*, vol. 338, pp. 774–788, 2018.

[33] X.-H. Chang, Y. Liu, and M. Shen, "Resilient control design for lateral motion regulation of intelligent vehicle," *IEEE/ASME Transactions on Mechatronics*, vol. 24, no. 6, pp. 2488–2497, 2019.

[34] J. Yang, J. Na, G. Gao, and C. Zhang, "Adaptive neural tracking control of robotic manipulators with guaranteed nn weight convergence," *Complexity*, vol. 2018, Article ID 7131562, 11 pages, 2018.

[35] H. Pan, X. Jing, W. Sun, and H. Gao, "A bioinspired dynamics-based adaptive tracking control for nonlinear suspension systems," *IEEE Transactions on Control Systems Technology*, vol. 26, no. 3, pp. 903–914, 2018.

[36] V. Narayanan, S. Jagannathan, and K. Ramkumar, "Event-sampled output feedback control of robot manipulators using neural networks," *IEEE Transactions on Neural Networks and Learning Systems*, vol. 30, no. 6, pp. 1651–1658, 2019.

[37] Q. Zhou, S. Zhao, H. Li, R. Lu, and C. Wu, "Adaptive neural network tracking control for robotic manipulators with dead zone," *IEEE Transactions on Neural Networks and Learning Systems*, vol. 30, no. 12, pp. 3611–3620, 2019.

[38] H. Wang, "Task-space synchronization of networked robotic systems with uncertain kinematics and dynamics," *IEEE Transactions on Automatic Control*, vol. 58, no. 12, pp. 3169–3174, 2013.

[39] M. W. Spong, S. Hutchinson, and M. Vidyasagar, *Robot Modeling and Control*, Wiley, Hoboken, NJ, USA, 2006.

[40] J.-J. E. Slotine and W. Li, *Applied Nonlinear Control*, Prentice-Hall, Englewood Cliffs, NJ, USA, 1991.

[41] B. Ma and W. Huo, "Adaptive control of space robot system with an attitude controlled base," in *Proceedings of the 1995 IEEE International Conference on Robotics and Automation*, vol. 2, pp. 1265–1270, Nagoya, Japan, May 1995.

[42] L. Cheng, Z.-G. Hou, and M. Tan, "Adaptive neural network tracking control for manipulators with uncertain kinematics, dynamics and actuator model," *Automatica*, vol. 45, no. 10, pp. 2312–2318, 2009.

[43] C. A. Desoer and M. Vidyasagar, "Feedback systems: input-output properties," *Siam*, vol. 55, 1975.

[44] R. Lozano, B. Brogliato, O. Egeland, and B. Maschke, *Dissipative Systems Analysis and Control: Theory and Applications*, Springer-Verlag, London, UK, 2000.

[45] S. He, H. Fang, M. Zhang, F. Liu, and Z. Ding, "Adaptive optimal control for a class of nonlinear systems: the online policy iteration approach," *IEEE Transactions on Neural Networks and Learning Systems*, vol. 31, no. 2, pp. 549–558, 2020.

[46] S. He, H. Fang, M. Zhang, F. Liu, X. Luan, and Z. Ding, "Online policy iterative-based H∞ optimization algorithm for a class of nonlinear systems," *Information Sciences*, vol. 495, pp. 1–13, 2019.

[47] C. Ren, R. Nie, and S. He, "Finite-time positiveness and distributed control of lipschitz nonlinear multi-agent systems," *Journal of the Franklin Institute*, vol. 356, no. 15, pp. 8080–8092, 2019.

[48] C. Ren and S. He, "Finite-time stabilization for positive markovian jumping neural networks," *Applied Mathematics and Computation*, vol. 36, Article ID 124631, 2020.

Hindawi
Complexity
Volume 2020, Article ID 3156787, 11 pages
https://doi.org/10.1155/2020/3156787

Research Article

Adaptive Backstepping Sliding Mode Control of Trajectory Tracking for Robotic Manipulators

Zhu Dachang,[1] Du Baolin,[1] Zhu Puchen,[2] and Wenqiang Wu[1]

[1]*School of Mechanical and Electrical Engineering, Guangzhou University, Guangzhou 510006, China*
[2]*School of Automation, Guangdong University of Technology, Guangzhou 510006, China*

Correspondence should be addressed to Wenqiang Wu; gz_wwq@gzhu.edu.cn

Received 31 May 2020; Revised 28 June 2020; Accepted 17 July 2020; Published 14 August 2020

Academic Editor: Shuping He

To achieve precise trajectory tracking of robotic manipulators in complex environment, the precise dynamic model, parameters identification, nonlinear characteristics, and disturbances are the factors that should be solved. Although parameters identification and adaptive estimate method were proposed for robotic control in many literature studies, the essential factors, such as coupling and friction, are rarely mentioned as it is difficult to build the precise dynamic model of the robotic manipulator. An adaptive backstepping sliding mode control is proposed to solve the precise trajectory tracking under external disturbances with complex environment, and the dynamic response characteristics of a two-link robotic manipulator are described in this paper. First, the Lagrange kinetic method is used to derive the precise dynamic model which includes the nonlinear factor with friction and coupling. Moreover, the dynamic model of two-link robotic manipulator is built. Second, the estimate function for the nonlinear part is selected, and backstepping algorithm is used for analyzing the stabilities of the sliding mode controller by using Lyapunov theory. Furthermore, the convergence of the proposed controller is verified subject to the external disturbance. At last, numerical simulation results are reported to demonstrate the effectiveness of the proposed method.

1. Introduction

Nowadays, with the development of modern industrial technology, robotic manipulators are widely used in automobile manufacturing, aerospace, electronic assembly, precision medical operation, and other fields. To obtain steady state accuracy and fast dynamical response, it is necessary for high precision of the trajectory tracking ability of robotic manipulator. Unfortunately, it is difficult to be satisfied on account of the nonlinear characteristics in complex environment like clearance of joints, friction, external disturbance, strong couple, and so on. The first stage of trajectory tracking is to establish the precise mathematical model of the robotic manipulator. However, the nonlinear part of the dynamic model of the robotic manipulator is ignored in many literatures [1–5] or parameter identification by many approaches [6–8]; even the torque in the joint space and the moment of inertia were ignored in [9]. By calculating kinetic energy, potential energy, and generalized force, the Lagrange equation was utilized to build the dynamic equation for robotic manipulator [10, 11]. As the recurrence relationship is not established between multiple links, it cannot be applied easily to the whole dynamic modeling for robotic manipulators. To overcome inaccuracy of the dynamical model of robotic manipulator, friction, clearance, and external disturbance were considered, and intelligent control strategies have been developed by many researchers for the uncertain manipulator [12–14], for example. In this paper, the dynamic equation with recurrence method by using Lagrange energy method is provided as an accurate mathematical model for precision trajectory tracking.

Furthermore, the design of intelligence controllers for nonlinear systems affected by disturbances is a topic that has been studied by several authors, and many different approaches have been proposed for this problem [15–17]. Backstepping is a systematic and recursive design method for nonlinear control applied to the feedback linearization system, which can guarantee global regulation and tracking

performance [18, 19]. It is a regression design method which combines the selection of Lyapunov function with the design of controller, and the virtual control is designed with the requirements step by step, and then, control law of complex uncertain system is finally designed. The basic design idea is to decompose the complex nonlinear system into subsystems of no more than systematic order and then design the Lyapunov function of each subsystem separately. On the basis of ensuring that the subsystem has guaranteed convergence, the control law of the subsystem is obtained. In the design of the next subsystem, the control law of the preceding subsystem is taken as the tracking target of this subsystem, and finally the control law of the last subsystem is obtained. By analogy, the control law of the entire closed-loop system can be obtained, and the convergence of the closed-loop system is guaranteed by Lyapunov stability analysis method. Backstepping with intelligent algorithm can increase the quality of the transition process, reduce or even eliminate the uncertainty of the matching constraints, and provide a structured and systematic design method for the Lyapunov function design for complex nonlinear systems [20–23]. Sliding mode control (SMC) is another robust control method, which produces a switching control law (equivalent control law) to force the system to converge to the sliding surface within a boundary layer near the sliding surface under the convergence of the Lyapunov stability theory [24, 25]. Trajectory tracking control of a 6-DOF pneumatically actuated Gough-Stewart parallel robot was investigated by Lafmejani [26], and position control of the pneumatic actuator was performed based on backstepping sliding mode controller according to the dynamic model of system. A methodology of dynamic analysis and control for a hybrid humanoid robot arm was presented in [27], and an adaptive backstepping sliding mode controller was developed for the parameters uncertainties and disturbances of the hybrid humanoid robot arm.

For the multi-input-multi-output (MIMO) nonlinear system with uncertainties and disturbances, sliding mode PI control with backstepping approach [28], presence of bounded uncertainties from unmodeled dynamic, parameters variations, disturbances, and visual fusion technology [29, 30], and asynchronous control with fuzzy approach [31] were proposed. To make the dynamic model of the robotic manipulator more accurate, an impedance-control strategy with dynamic compensation for interactive control of robot manipulators was presented in [32]. The kinematics and dynamics of multiple cooperative welding robot manipulators were studied on the basis of the Denavit–Hartenberg and Lagrange method, and adaptive neural control and dynamic movement primitives were considered in [33]. An adaptive backstepping sliding mode control of robotic manipulators is proposed in this paper to achieve the precision trajectory tracking with external disturbances. The main contributions of the current paper are summarized as follows:

(1) By using Lagrange energy function, the precise dynamic model of the robotic manipulator is built, and the nonlinear characteristics and uncertainties are analyzed. Furthermore, dynamic model of a two-link robotic manipulator is derived.

(2) According to the precision dynamic model of the two-link robotic manipulator, an estimate function of the nonlinear and coupling parts is proposed. Backstepping algorithm is used to construct the equivalent control law of sliding mode control through three steps, and the stability of the proposed controller is convergent by using Lyapunov theory.

This paper is organized in the following manner: Section 2 presents the precise dynamic modeling method and the precise dynamic model of the robotic manipulator. According to the previous method, the precise dynamic model of a two-link robotic manipulator is derived. Section 3 describes the sliding mode control with backstepping algorithm. Through the estimate function of nonlinear and coupling parts, the controller is proposed for the trajectory tracking under external disturbances, and its stability is discussed. Numerical simulation results are reported to demonstrate the effectiveness of the proposed method in Section 4. Finally, conclusions are provided in Section 5.

2. Description of Robotic Manipulator and Dynamic Modeling

To make the dynamic model recursive, the Newton–Euler method is used to establish all force balance between the links of the robotic manipulator, and the dynamic equation can be derived. Forward recursion is used for speed and acceleration transfer between all of the links and backward recursion is used for force transfer from the end-effector to each link of the robotic manipulator.

2.1. Description of Link Parameters of Robotic Manipulator. The dynamic parameters which describe the dynamic model are important for the control algorithms, effective simulation results, and accurate trajectory tracking algorithms. Dynamic equation of the robotic manipulator with n-DOF has been characterized in many literature studies [1–11] as follows:

$$D(q)\ddot{q} + C(q,\dot{q})\dot{q} + G(q) + F(q,\dot{q}) + \tau_d = \tau, \quad (1)$$

where $q, \dot{q}, \ddot{q} \in R^n$ are the link position, velocity, and acceleration vectors, respectively, $D(q) \in R^{n\times n}$ is the symmetric positive definite inertia matrix, $C(q,\dot{q}) \in R^{n\times n}$ is the Coriolis or centrifugal forces, $G(q) \in R^{n\times 1}$ consolidates the gravitational force, $F(q,\dot{q}) \in R^{n\times 1}$ incorporates the friction terms, and τ_d represents external disturbance.

However, quadratic velocity terms and dynamic coupling terms are not taken into account. So, the problem of model accuracy cannot be solved essentially only through parameter identification and compensation methods. The kinematic description of the i^{th} link is shown in Figure 1.

An infinitesimal element e_i is selected which lies on the i^{th} link, and the position of the center of mass c_i is represented by vector p_i, the position vector of e_i is presented by vector p_i^*, and the position vector from the center of mass to

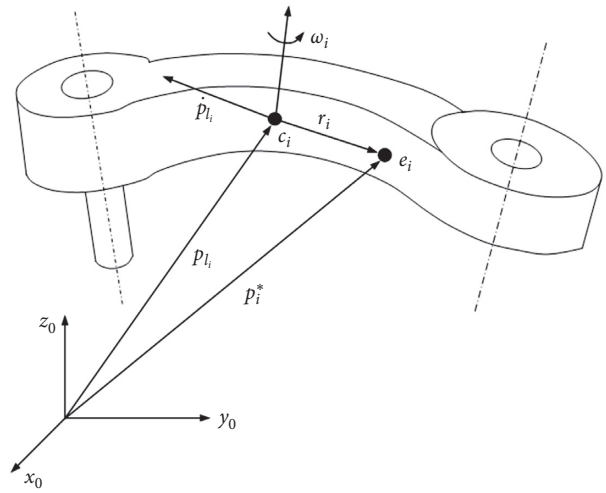

Figure 1: Kinematic description of the i^{th} link.

the infinitesimal element is r_i. When integrating in the whole area of the i^{th} link, the infinitesimal element can represent the motion performance of the whole link.

The kinetic energy component E_{kl_i} of the i^{th} link can be given by

$$E_{kl_i} = \frac{1}{2}\int_{V_{l_i}} (\dot{p}_i^*)^T \dot{p}_i^* \rho \mathrm{d}V, \tag{2}$$

where $\dot{p}_i^*$ is the linear velocity vector of the infinitesimal element, ρ is material density, and dV is the volume of the infinitesimal element.

The position vector relationship between c_i and e_i is satisfied with

$$r_i = \begin{bmatrix} r_{ix} & r_{iy} & r_{iz} \end{bmatrix}^T = p_i^* - p_{l_i}, \tag{3}$$

where p_{l_i} is calculated by centroid theorem as

$$p_{l_i} = \frac{1}{m_{l_i}}\int_{V_{l_i}} p_i^* \rho \mathrm{d}V, \tag{4}$$

where m_{l_i} is the mass of the i^{th} link.

Differentiating equation (3) with respect to time, one can get

$$\dot{p}_i^* = \dot{p}_{l_i} + \omega_i \times r_i = \dot{p}_{l_i} + S(\omega_i) r_i, \tag{5}$$

where $\dot{p}_{l_i}$ is the linear velocity vector of the center of mass, ω_i is angular velocity of the infinitesimal element around the center of mass, and $S(\omega_i)$ is the antisymmetric matrix of three-dimensional vector $\omega_i = \begin{bmatrix} \omega_{ix} & \omega_{iy} & \omega_{iz} \end{bmatrix}^T$ and defined as follows:

$$S(\omega_i) = \begin{bmatrix} 0 & -\omega_{iz} & \omega_{iy} \\ \omega_{iz} & 0 & -\omega_{ix} \\ -\omega_{iy} & \omega_{ix} & 0 \end{bmatrix}. \tag{6}$$

Substituting equation (5) into equation (2), one can obtain

$$E_{kl_i} = \frac{1}{2}\int_{V_{l_i}} \left(\dot{p}_{l_i} + S(\omega_i) r_i\right)^T \left(\dot{p}_{l_i} + S(\omega_i) r_i\right) \rho \mathrm{d}V. \tag{7}$$

Equation (7) shows that the kinetic energy of each link consists of three parts, described as follows:

(1) Translational kinetic energy is expressed as

$$\frac{1}{2}\int_{V_{l_i}} \dot{p}_{l_i}^T \dot{p}_{l_i} \rho \mathrm{d}V = \frac{1}{2} m_{l_i} \dot{p}_{l_i}^T \dot{p}_{l_i}. \tag{8}$$

(2) Implicated motion kinetic energy is expressed as

$$2\left(\frac{1}{2}\int_{V_{l_i}} \dot{p}_{l_i} S(\omega_i) r_i \rho \mathrm{d}V\right) = 2\left(\frac{1}{2}\dot{p}_{l_i}^T S(\omega_i)\right)\int_{V_{l_i}} \left(p_i^* - p_{l_i}\right)\rho \mathrm{d}V = 0. \tag{9}$$

(3) Rotation kinetic energy, combining with equation (6), is expressed as

$$\begin{aligned} \frac{1}{2}\int_{V_{l_i}} r_i^T S^T(\omega_i) S(\omega_i) r_i \rho \mathrm{d}V &= \frac{1}{2}\omega_i^T \left(\int_{V_{l_i}} S^T(r_i) S(r_i) \rho \mathrm{d}V\right)\omega_i \\ &= \frac{1}{2}\omega_i^T I_{l_i} \omega_i, \end{aligned} \tag{10}$$

where $S(\omega_i) r_i = -S(r_i)\omega_i$; I_{l_i} is defined as

$$I_{l_i} = \begin{bmatrix} \int \left(r_{iy}^2 + r_{iz}^2\right)\rho \mathrm{d}V & -\int r_{ix} r_{iy} \rho \mathrm{d}V & -\int r_{ix} r_{iz} \rho \mathrm{d}V \\ -\int r_{ix} r_{iy} \rho \mathrm{d}V & \int \left(r_{ix}^2 + r_{iz}^2\right)\rho \mathrm{d}V & -\int r_{iz} r_{iy} \rho \mathrm{d}V \\ -\int r_{ix} r_{iz} \rho \mathrm{d}V & -\int r_{iz} r_{iy} \rho \mathrm{d}V & \int \left(r_{iy}^2 + r_{ix}^2\right)\rho \mathrm{d}V \end{bmatrix}, \tag{11}$$

(1) where I_{l_i} is symmetric matrix and denotes inertia tensor related to the center of mass of the i^{th} link in base coordinate system.

Combining equation (8) with equation (10), the kinetic energy of the i^{th} link can be given by

$$E_{kl_i} = \frac{1}{2} m_{l_i} \dot{q}^T \left(J_p^{(l_i)} \right)^T J_p^{(l_i)} \dot{q} + \frac{1}{2} \dot{q}^T \left(J_o^{(l_i)} \right)^T I_{l_i} J_o^{(l_i)} \dot{q}, \quad (12)$$

where $q = \begin{pmatrix} q_1 & q_2 & \cdots & q_i \end{pmatrix}^T$ is joint variable vector.

The kinetic energy component of the motor of $i^{\#}$ joint can be calculated in a similar way. Under the assumption of rigid transmission, there is

$$k_{ti} \dot{q}_i = \dot{\theta}_{m_i}, \quad (13)$$

where k_{ti} is the transmission ratio of gear speed reducer and θ_{m_i} is the rotor angular position.

With the law of angular velocity synthesis, the total angular velocity is derived as follows:

$$\omega_{m_i} = \omega_{i-1} + k_{ti} \dot{q}_i z_{m_i}, \quad (14)$$

where ω_{i-1} is the angular velocity of the $(i-1)^{\#}$ link and z_{m_i} is the unit vector of rotor axis.

The linear and angular velocities of the rotor center of mass can be expressed as

$$\begin{aligned} \dot{p}_{m_i} &= J_p^{(m_i)} \dot{q}, \\ \omega_{m_i} &= J_o^{(m_i)} \dot{q}, \end{aligned} \quad (15)$$

where $J_p^{(m_i)} = \begin{bmatrix} J_{p_1}^{(m_i)} & \cdots & J_{p_{i-1}}^{(m_i)} & 0 & \cdots & 0 \end{bmatrix}$, $J_o^{(m_i)} = \begin{bmatrix} J_{o_1}^{(m_i)} & \cdots & J_{o_i}^{(m_i)} & 0 & \cdots & 0 \end{bmatrix}$, and the elements of matrix are given by

$$\begin{aligned} J_{p_i}^{(m_i)} &= z_{i-1} \times \left(p_{m_i} - p_{i-1} \right), \\ J_{o_j}^{(m_i)} &= \begin{cases} J_{o_j}^{(l_i)}, & j = 1, 2, \ldots, i-1, \\ k_{ti} z_{m_i}, & j = i. \end{cases} \end{aligned} \quad (16)$$

If the rotor turns around its center, then, $J_{p_i}^{(m_i)} = 0$.

So, the kinetic energy component E_{km_i} of the i^{th} rotor can be given by

$$E_{km_i} = \frac{1}{2} m_{m_i} \dot{q}^T \left(J_p^{(m_i)} \right)^T J_p^{(m_i)} \dot{q} + \frac{1}{2} \dot{q}^T \left(J_o^{(m_i)} \right)^T I_{m_i} J_o^{(m_i)} \dot{q}, \quad (17)$$

where m_{m_i} is the mass of the rotor and I_{m_i} is the inertia matrix of rotor.

Summing different components of a single link in (12) and a single motor in (17), the total kinetic energy of the robotic manipulator can be calculated and yields

$$E_k = E_{kl_i} + E_{km_i} = \frac{1}{2} \sum_{i=1}^{n} \sum_{j=1}^{n} b_{ij}(q) \dot{q}_i \dot{q}_j = \frac{1}{2} \dot{q}^T B(q) \dot{q}, \quad (18)$$

where $B(q)$ is the inertia matrix, satisfied with

$$B(q) = \sum_{i=1}^{n} \left(m_{l_i} \left(J_p^{(l_i)} \right)^T J_p^{(l_i)} + \left(J_o^{(l_i)} \right)^T I_{l_i} J_o^{(l_i)} + m_{m_i} \left(J_p^{(m_i)} \right)^T J_p^{(m_i)} + \left(J_o^{(m_i)} \right)^T I_{m_i} J_o^{(m_i)} \right). \quad (19)$$

The potential energy of the i^{th} link can be calculated as follows:

$$U_{l_i} = -\int_{V_{l_i}} g_0^T p_i^* \rho \mathrm{d}V = -m_{l_i} g_0^T p_{l_i}, \quad (20)$$

where g_0 is acceleration vector of gravity in the base coordinate system.

So, the total potential energy U of the robotic manipulator can be expressed as

$$U = \sum_{i=1}^{n} \left(U_{l_i} + U_{m_i} \right) = -\sum_{i=1}^{n} \left(m_{l_i} g_0^T p_{l_i} + m_{m_i} g_0^T p_{m_i} \right), \quad (21)$$

where p_{m_i} is the position vector of rotor center of mass.

According to (18) and (21), the Lagrange function is constructed as follows:

$$L(q, \dot{q}) = E_k(q, \dot{q}) - U(q). \quad (22)$$

The dynamic equation is derived by using Lagrange function, yielding

$$\tau_i = \frac{\mathrm{d}}{\mathrm{d}t} \left(\frac{\partial L}{\partial \dot{q}_i} \right) - \frac{\partial U}{\partial q_i}, \quad (23)$$

where

$$\begin{aligned} \frac{\mathrm{d}}{\mathrm{d}t} \left(\frac{\partial L}{\partial \dot{q}_i} \right) &= \frac{\mathrm{d}}{\mathrm{d}t} \left(\frac{\partial E_k}{\partial \dot{q}_i} \right) = \sum_{j=1}^{n} b_{ij}(q) \ddot{q}_j + \sum_{j=1}^{n} \sum_{k=1}^{n} \frac{\partial b_{ij}(q)}{\partial q_k} \dot{q}_k \dot{q}_j, \\ \frac{\partial E_k}{\partial q_i} &= \frac{1}{2} \sum_{j=1}^{n} \sum_{k=1}^{n} \frac{\partial b_{ij}(q)}{\partial q_i} \dot{q}_k \dot{q}_j, \\ \frac{\partial U}{\partial q_i} &= -\sum_{j=1}^{n} \left(m_{l_j} g_0^T J_{p_i}^{(l_i)}(q) + m_{m_j} g_0^T J_{p_i}^{(m_i)}(q) \right) = g_i(q). \end{aligned} \quad (24)$$

The dynamic equation of robotic manipulator with n-DOF can be derived as

$$\sum_{j=1}^{n} b_{ij}(q) \ddot{q}_j + \sum_{j=1}^{n} \sum_{k=1}^{n} h_{ijk}(q) \dot{q}_k \dot{q}_j + g_i(q) = \tau_i, \quad i = 1, 2, \ldots, n, \quad (25)$$

where $h_{ijk} = (\partial \dot{b}_{ij}/\partial q_k) - ((1/2)(\partial b_{ij}/\partial q_i))$.

Comparing (25) with (1), the elements c_{ij} of $C(q, \dot{q})$ should be satisfied with

$$\sum_{j=1}^{n} c_{ij} q_j = \sum_{j=1}^{n} \sum_{k=1}^{n} h_{ijk} \dot{q}_k \dot{q}_j. \tag{26}$$

Considering the viscous friction and Coulomb friction, equation (25) can also be rewritten as follows:

$$B(q)\ddot{q} + C(q, \dot{q})\dot{q} + F_v \dot{q} + F_s \mathrm{sgn}(\dot{q}) + g(q) = \tau - J^T(q) h_e, \tag{27}$$

where h_e is contact force of end-effector, $J(q)$ is velocity Jacobi matrix, $F_v\dot{q}$ is the torque of viscous friction, and $F_s \mathrm{sgn}(\dot{q})$ is the torque of Coulomb friction.

2.2. Parameters and Dynamic Model of Two-Link Robotic Manipulator. The dynamic mathematical model for a rigid planar robotic manipulator having two links and a contact surface with the external force acting on the surface is shown in Figure 2. According to the coordinate system $\{o - xy\}$, it consists of two links having link lengths l_1 and l_2 with their centers of mass m_1 and m_2 lying at the middle of links, respectively. The length of the center of mass is p_1 and p_2, respectively.

The Lagrange method is used to build the precise dynamic model of a two-link robotic manipulator with their nominal values as listed in Table 1.

The total kinetic energy of the two-link robotic manipulator is

$$E_k = E_{k1} + E_{k2} = \frac{1}{2} m_1 p_1^2 \dot{\theta}_1^2 + \frac{1}{2} m_2 l_1^2 \dot{\theta}_1^2 + \frac{1}{2} m_2 p_2^2 \left(\dot{\theta}_1 + \dot{\theta}_2\right)^2 + m_2 l_1 p_2 \left(\dot{\theta}_1^2 + \dot{\theta}_1 \dot{\theta}_2\right) \cos\theta_2, \tag{28}$$

where θ_1 and θ_2 are joint variables of the two-link robotic manipulator.

The total potential energy of the two-link robotic manipulator is

$$E_p = E_{p1} + E_{p2} = m_1 g p_1 \cos\theta_1 + m_2 g (l_1 \cos\theta_1 + p_2 \cos(\theta_1 + \theta_2)). \tag{29}$$

By using (23), the dynamic equation of two-link robotic manipulator can be derived as

$$\tau_1 = \frac{\mathrm{d}}{\mathrm{d}t} \frac{\partial L}{\partial \dot{\theta}_1} - \frac{\partial L}{\partial \theta_1} = D_{11} \ddot{\theta}_1 + D_{12} \ddot{\theta}_2 + D_{112} \dot{\theta}_1 \dot{\theta}_2 + D_{122} \dot{\theta}_2^2 + D_1, \tag{30}$$

where $s_1 = \sin\theta_1$, $c_1 = \cos\theta_1 s_{12} = \sin(\theta_1 + \theta_2)$, and

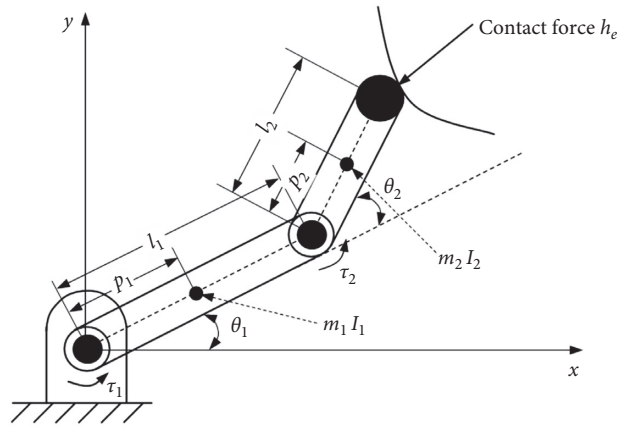

Figure 2: Two-link robotic manipulator plant with contact force at tip.

Table 1: Variables description of the two-link robotic manipulator.

Description	Nominal value
Center of mass link 1: m_1 (kg)	0.1
Length of link 1: l_1 (m)	0.8
Length of center of mass link 1: p_1 (m)	0.4
Centroid inertia of link 1: I_1 (kgm^2)	0.064
Center of mass link 2: m_2 (kg)	0.1
Length of link 2: l_2 (m)	0.4
Length of center of mass link 2: p_2 (m)	0.2
Centroid inertia of link 2: I_2 (kgm^2)	0.016

$$\begin{cases} D_{11} = m_1 p_1^2 + m_2 p_2^2 + m_2 l_1^2 + 2 m_2 l_1 p_2 c_2, \\ D_{12} = m_2 p_2^2 + m_2 l_1 p_2 c_2, \\ D_{112} = -2 m_2 l_1 p_2 s_2, \\ D_{122} = -m_2 l_1 p_2 s_2, \\ D_1 = (m_1 p_1 + m_2 l_1) g s_1 + m_2 p_2 g s_{12}. \end{cases} \tag{31}$$

Meanwhile, the torque of joint $2\tau_2$ can be also derived as

$$\tau_2 = \frac{\mathrm{d}}{\mathrm{d}t} \frac{\partial L}{\partial \dot{\theta}_2} - \frac{\partial L}{\partial \theta_2} = D_{21} \ddot{\theta}_1 + D_{22} \ddot{\theta}_2 + D_{212} \dot{\theta}_1 \dot{\theta}_2 + D_{211} \dot{\theta}_2^2 + D_2, \tag{32}$$

where

$$\begin{cases} D_{21} = m_1 p_2^2 + m_2 l_1 p_2 c_2, \\ D_{22} = m_2 p_2^2, \\ D_{212} = 0, \\ D_{211} = m_2 l_1 p_2 s_2, \\ D_2 = m_2 p_2 g s_{12}. \end{cases} \tag{33}$$

Combining (30) with (32), the robotic plant can be rewritten with following mathematical model:

$$\begin{bmatrix} D_{11} & D_{12} \\ D_{21} & D_{22} \end{bmatrix} \begin{bmatrix} \ddot{\theta}_1 \\ \ddot{\theta}_2 \end{bmatrix} + \begin{bmatrix} D_{112} \\ D_{212} \end{bmatrix} \begin{bmatrix} \dot{\theta}_1 \dot{\theta}_2 \\ \dot{\theta}_2 \dot{\theta}_1 \end{bmatrix} + \begin{bmatrix} D_{211} \\ D_{122} \end{bmatrix} \begin{bmatrix} \dot{\theta}_2^2 \\ \dot{\theta}_1^2 \end{bmatrix} + \begin{bmatrix} D_1 \\ D_2 \end{bmatrix} = \begin{bmatrix} \tau_1 \\ \tau_2 \end{bmatrix}. \tag{34}$$

Equation (14) completely represents the relationship between actuated torque and displacement, velocity, and acceleration in the joint space. The issues with D_{11} and D_{22} represent the moment of inertia caused by the acceleration of joint 1 and joint 2, respectively. The issues with D_{12} and D_{21} represent the moment of inertia of the acceleration coupling between two joints. The issues with D_{122} and D_{211} represent the coupling moment term of the centripetal force caused by the velocity between two joints. The issues with D_{112} and D_{212} represent the coupling moment term of the Coriolis force between two joints. D_1 and D_2 represent the gravity moment term. Considering the effect of centroid inertia, (35) can be modified as

$$\begin{aligned} D'_{11} &= I_1 + I_2 + D_{11}, \\ D'_{12} &= I_2 + D_{12}, \\ D'_{21} &= I_2 + D_{21}, \\ D'_{22} &= I_2 + D_{22}. \end{aligned} \tag{35}$$

Furthermore, to consider the effect of the contact force acting on the end-effector, the right side of (34) can be replaced by

$$\tau' = \tau - J^T(q)h_e, \tag{36}$$

where h_e is the force and moment vector applied by the end-effector in the working environment and $J^T(q)$ is the velocity Jacobian matrix, yielding

$$J(q) = \begin{bmatrix} -l_1 s_1 - l_2 s_{12} & -l_2 s_{12} \\ l_1 c_1 + l_2 c_{12} & l_2 c_{12} \end{bmatrix}. \tag{37}$$

3. Adaptive Backstepping Sliding Mode Control Algorithm

In this section, an adaptive backstepping sliding mode controller is presented which achieves precision trajectory tracking property by guaranteeing the robustness and stability of the closed-loop system of robotic manipulator. The uncertainties included in the system are required for compensating the external disturbances and nonlinear dynamics in terms described as (27). The adaptive backstepping sliding mode control is constructed at the final step.

The inverse dynamic equation can be expressed as

$$\begin{aligned} \ddot{q} &= -B^{-1}(q)\left[C(q,\dot{q})\dot{q} + F_v\dot{q} + F_s\mathrm{sgn}(\dot{q}) + g(q)\right] \\ &\quad + B^{-1}(q)\left(\tau - J^T(q)h_e\right). \end{aligned} \tag{38}$$

Property 1. $B(q)$ is the $n \times n$ symmetric inertial matrix and bounded:

$$c_1\|A\|^2 \le A^T B(q) A \le c_2\|A\|^2, \quad \forall A \in R^{n\times 1}, \tag{39}$$

where c_1 and c_2 are positive constants.

Property 2. $\dot{B}(q) - 2C(q,\dot{q})$ is skew symmetric matrix and satisfies

$$A^T\left(\dot{B}(q) - 2C(q,\dot{q})\right)A = 0. \tag{40}$$

Property 3. $C(q,\dot{q})$, $g(q)$, and $F_v\dot{q} + F_s\mathrm{sgn}(\dot{q})$ are bounded as follows:

$$\begin{aligned} \|C(q,\dot{q})\dot{q}\| &\le c_k\|\dot{q}\|^2, \\ \|g(q)\| &\le g_k, \\ \left\|F_v\dot{q} + F_s\mathrm{sgn}(\dot{q})\right\| &\le f_k\|\dot{q}\|, \end{aligned} \tag{41}$$

where c_k, g_k, and f_k are positive constants.

Property 4. $J^T(q)h_e \in R^n$ is unknown disturbance and bounded as

$$\left\|J^T(q)h_e\right\| \le \tau_k, \quad \tau_k > 0. \tag{42}$$

Defining vectors $x_1 = q$, $x_2 = \dot{q}$, $x = \begin{bmatrix} x_1 & x_2 \end{bmatrix}^T$, the desired track is defined as $x_d = \begin{bmatrix} x_{1d} & x_{2d} \end{bmatrix}^T$, so the state equation of the robotic manipulator can be given by

$$\begin{aligned} \dot{x}_1 &= x_2, \\ \dot{x}_2 &= B^{-1}(q)\left(\tau - C(q,\dot{q})\dot{q} - g(q) - \varphi(q,\dot{q})\right), \end{aligned} \tag{43}$$

where $\varphi(q,\dot{q})$ is defined as the disturbance nonlinear function.

Assuming that q_d is the desired trajectory of the robotic manipulator in joint space, select e_1 as the trajectory tracking error; it is defined as

$$e_1 = q - q_d = x_1 - x_{1d}. \tag{44}$$

Differentiating (44) with respect to time, one can get

$$\dot{e}_1 = \dot{q} - \dot{q}_d = \dot{x}_1 - \dot{x}_{1d} = x_2 - \dot{x}_{1d}. \tag{45}$$

By using backstepping algorithm, let e_2 be a virtual input; then, the feedback control law can be expressed as

$$e_2 = \dot{e}_1 + k_1 e_1, \tag{46}$$

where $k_1 \in R^{n\times n}$ is a positive definite diagonal coefficient matrix according to the DOF of robotic manipulator.

Theorem 1. *Consider a robotic manipulator with n-DOF with the dynamic in (28), by designing the following sliding mode controller as*

$$\tau_{eq} = -h\left[\lambda\left(e_2 - k_1 e_1\right) + B^{-1}(q)\left(\tau - C(q,\dot{q})\dot{q} - g(q) - \varphi(q,\dot{q})\right) - \ddot{q}_d + k_1\dot{e}_1\right] = -hs, \tag{47}$$

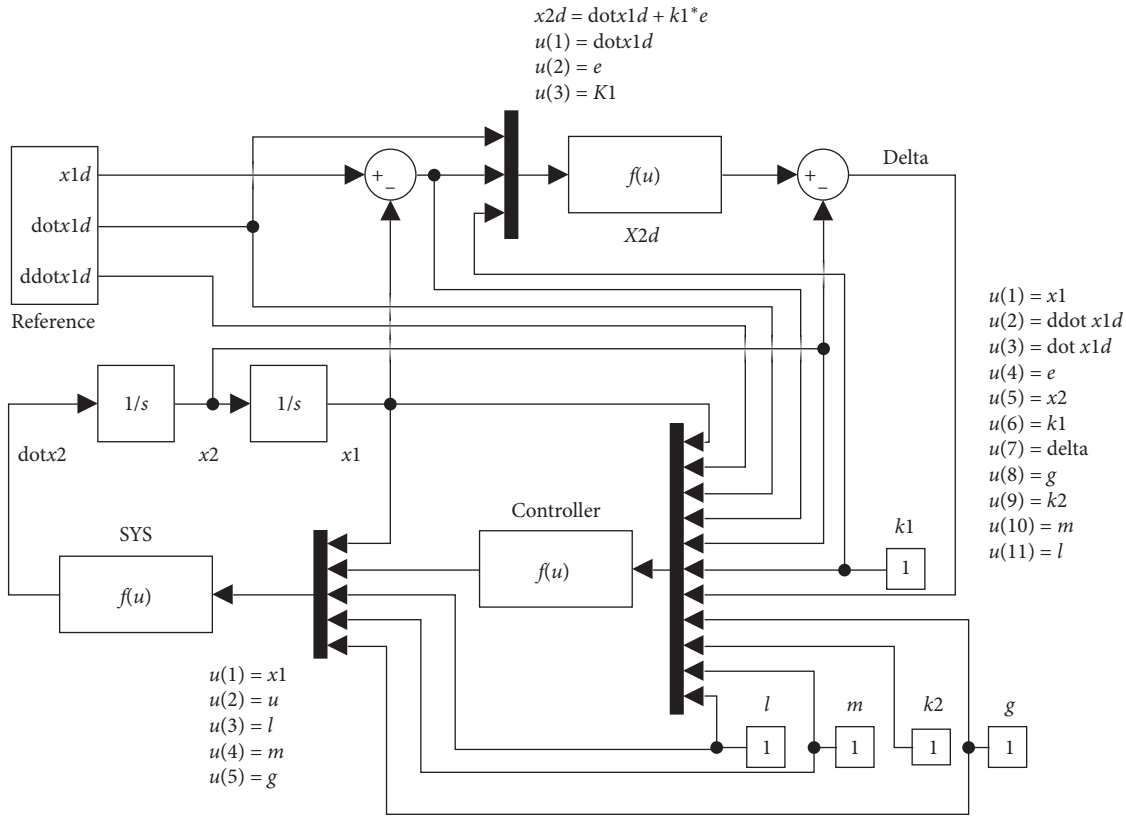

Figure 3: Schematic for backstepping algorithm by using Matlab@ software.

where $h \in R^{n\times n}$ is a positive definite diagonal coefficient matrix.

Select the Lyapunov function of the first step as

$$V_1 = \frac{1}{2}e_1^T e_1. \tag{48}$$

Differentiating (48) with respect to time, one can get

$$\dot{V}_1 = e_1^T \dot{e}_1 = e_1^T (e_2 - k_1 e_1) = e_1^T e_2 - e_1^T k_1 e_1. \tag{49}$$

If $e_2 = 0$, then $\dot{V}_1 = -e_1^T k_1 e_1 \le 0$. So, the sliding surface function is defined as $s = \lambda e_1 + e_2$, and the Lyapunov function of the second step is selected as

$$V_2 = V_1 + \frac{1}{2}s^T s, \tag{50}$$

where $\lambda \in R^{n\times n}$ is a positive definite diagonal coefficient matrix according to the DOF of robotic manipulator.

Differentiating (50) with respect to time, one can get

$$\begin{aligned}\dot{V}_2 &= e_1^T e_2 - e_1^T k_1 e_1 + s^T [\lambda \dot{e}_1 + \dot{e}_2] \\ &= e_1^T e_2 - e_1^T k_1 e_1 + s^T [\lambda (e_2 - k_1 e_1) + \ddot{e}_1 + k_1 \dot{e}_1] \\ &= e_1^T e_2 - e_1^T k_1 e_1 + s^T \left[\lambda (e_2 - k_1 e_1) + B^{-1}(q)(\tau - C(q,\dot{q})\dot{q} \right. \\ &\quad \left. - g(q) - \varphi(q,\dot{q})) - \ddot{q}_d + k_1 \dot{e}_1\right].\end{aligned} \tag{51}$$

An adaptive algorithm can be assigned for nonlinear function $\varphi(q,\dot{q})$, yielding

$$\begin{aligned} e_{\varphi(q,\dot{q})} &= \varphi(q,\dot{q}) - \hat{\varphi}(q,\dot{q}), \\ \dot{e}_{\varphi(q,\dot{q})} &= -\dot{\hat{\varphi}}\ (q,\dot{q}), \end{aligned} \tag{52}$$

where $e_{\varphi(q,\dot{q})}$ is the estimation error and $\hat{\varphi}(q,\dot{q})$ is the estimated value of the nonlinear function $\varphi(q,\dot{q})$.

The Lyapunov function of the third step is selected as

$$V_3 = V_2 + \frac{1}{2}k_2 e_{\varphi(q,\dot{q})}^T e_{\varphi(q,\dot{q})}. \tag{53}$$

Differentiating (53) with respect to time, one can get

$$\dot{V}_3 = \dot{V}_2 - k_2 e_{\varphi(q,\dot{q})}^T \left(\dot{\hat{\varphi}}\ (q,\dot{q}) + \frac{1}{k_2}\left(\left(M^{-1}(q)\right)^T s\right)\right). \tag{54}$$

So, the adaptive control law is derived as $\dot{\hat{\varphi}}\ (q,\dot{q}) = -1/k_2\,((M^{-1}(q))^T s)$.

Considering the boundary of $\varphi(q,\dot{q})$ and Property 3, (54) can be rewritten as follows:

$$\begin{aligned}\dot{V}_3 &\le e_1^T e_2 - e_1^T k_1 e_1 - (\lambda e_1 + e_2)^T h (\lambda e_1 + e_2) \\ &= -\begin{bmatrix} e_1 & e_2 \end{bmatrix}^T M \begin{bmatrix} e_1 & e_2 \end{bmatrix},\end{aligned} \tag{55}$$

where

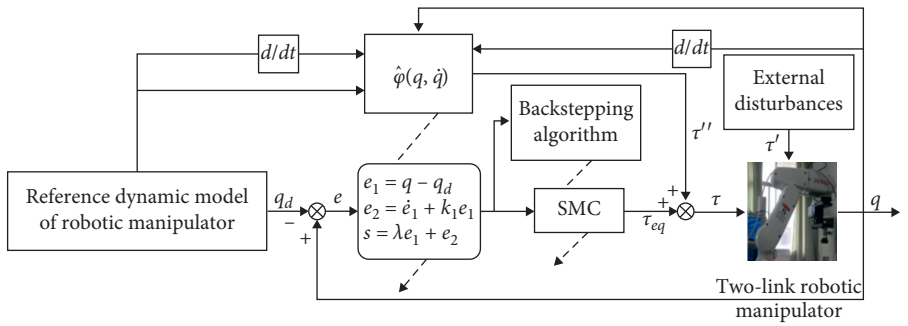

FIGURE 4: Schematic of the proposed control strategy.

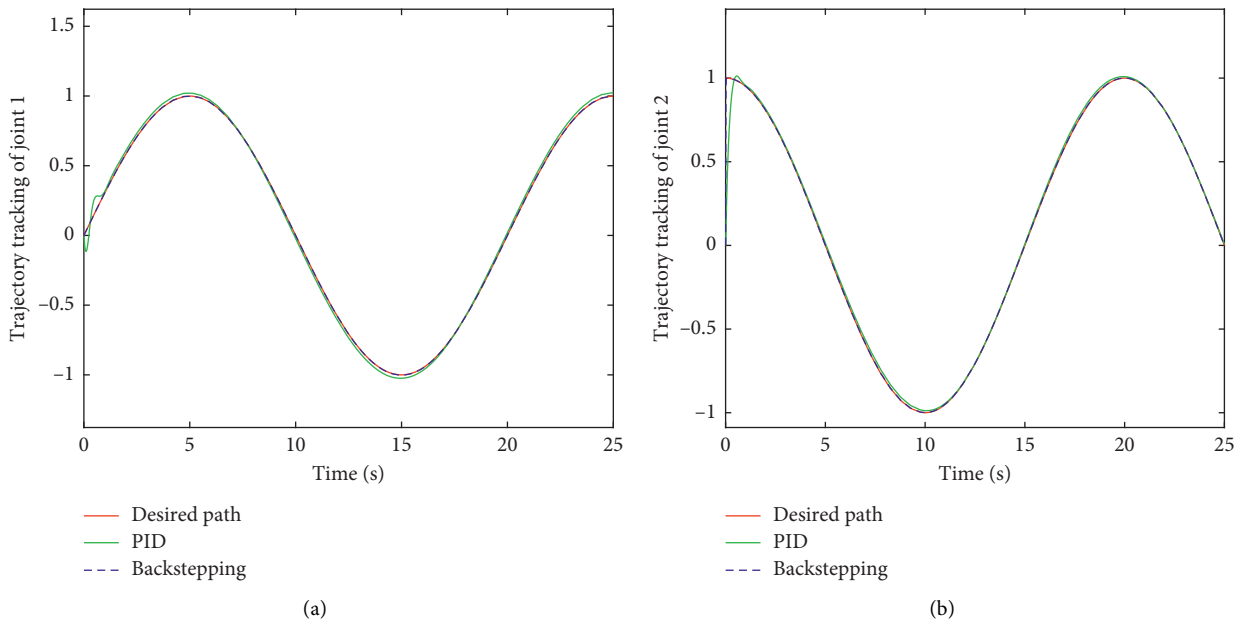

FIGURE 5: Trajectory tracking of two-link robotic manipulator. (a) $1^{\#}$link with q_1. (b) $2^{\#}$link with q_2.

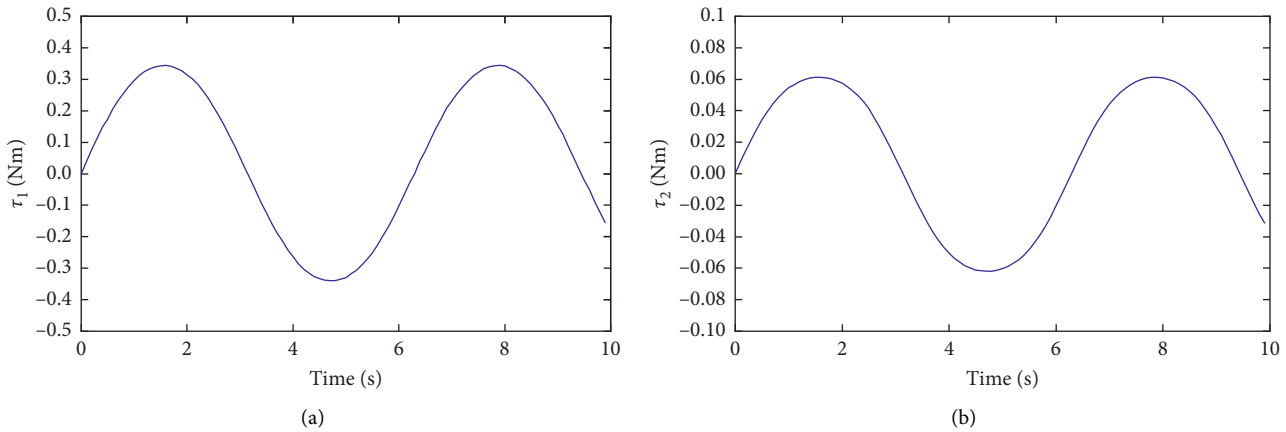

FIGURE 6: Actuated torque in the joint space as control signal. (a) τ_1. (b) τ_2.

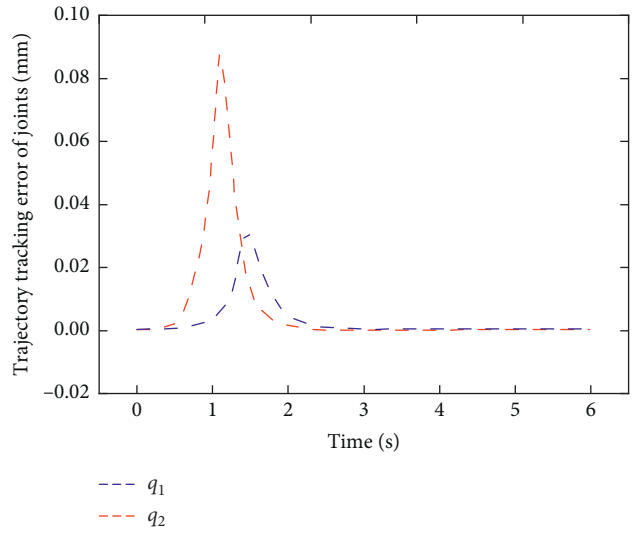

Figure 7: Trajectory tracking errors of the two-link robotic manipulator in joint space.

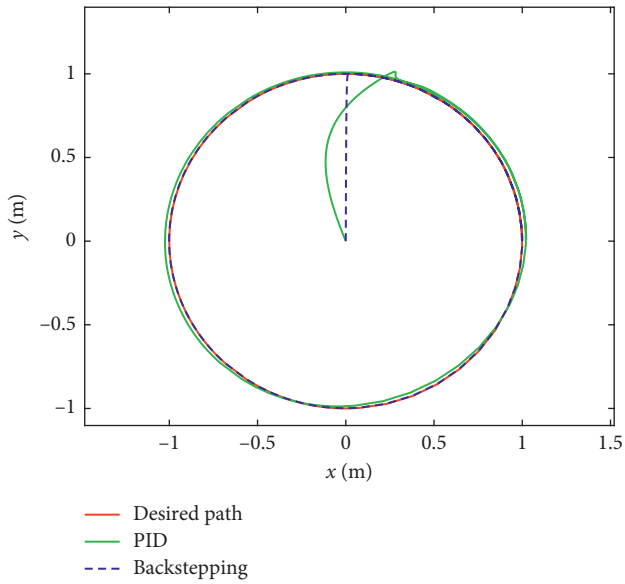

Figure 8: Trajectory tracking performance in the operating space of the end-effector.

$$M = \begin{bmatrix} k_1 + \lambda^T h\lambda & h\lambda - \frac{1}{2}I \\ h\lambda - \frac{1}{2}I & h \end{bmatrix}. \quad (56)$$

By giving the proper values of k_1, h, and λ, the matrix M can be positive, and $\dot{V}_3 \leq 0$, and the stability of the robotic manipulator is guaranteed.

4. Simulation and Discussion

In this section, a two-link robotic manipulator is utilized to verify the effectiveness of the proposed control strategy. The structural parameters are described in Table 1, and the dynamic equation is given by (35). The desired trajectory tracking of two joints is $\theta_{1d} = \theta_{2d} = 0.5\sin(t)$.

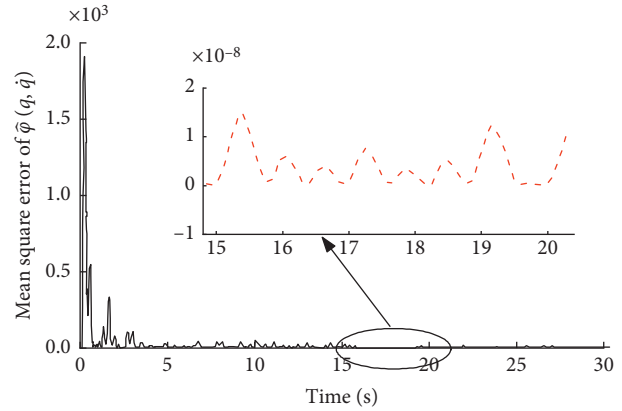

Figure 9: Mean square error of the estimation function $\hat{\varphi}(q, \dot{q})$.

The parameter values used in the adaptive backstepping sliding mode control system are $\lambda = \text{diag}[5, 5]$, $k_1 = \text{diag}[50, 50]$, $h = \text{diag}[3, 3]$, and the external disturbance is added by a pulse signal $\phi = 0.5\delta(t)$ in 6 s, which is used to verify the robustness and stability of the two-link robotic manipulator system. The schematic for backstepping algorithm by using Matlab® software is shown in Figure 3, and the schematic for the proposed control strategy is shown in Figure 4.

Figure 5 shows the trajectory tracking performance of the proposed control with the actuated torque in joint space τ_1 and τ_2, shown in Figure 6, respectively.

The trajectory tracking errors of the two joints are shown in Figure 7, respectively. The maximum tracking error of the $1^{\#}$ joint is equal to 0.0296 mm and in 1.6 s is 5.92%. The maximum tracking error of the $2^{\#}$ joint is equal to 0.0896 mm and in 1.2 s is 17.92% and in 2.2 s tends to convergence. However, the convergence time of $1^{\#}$ joint is in 2.8 s, which is affected by the coupling of $2^{\#}$ joint.

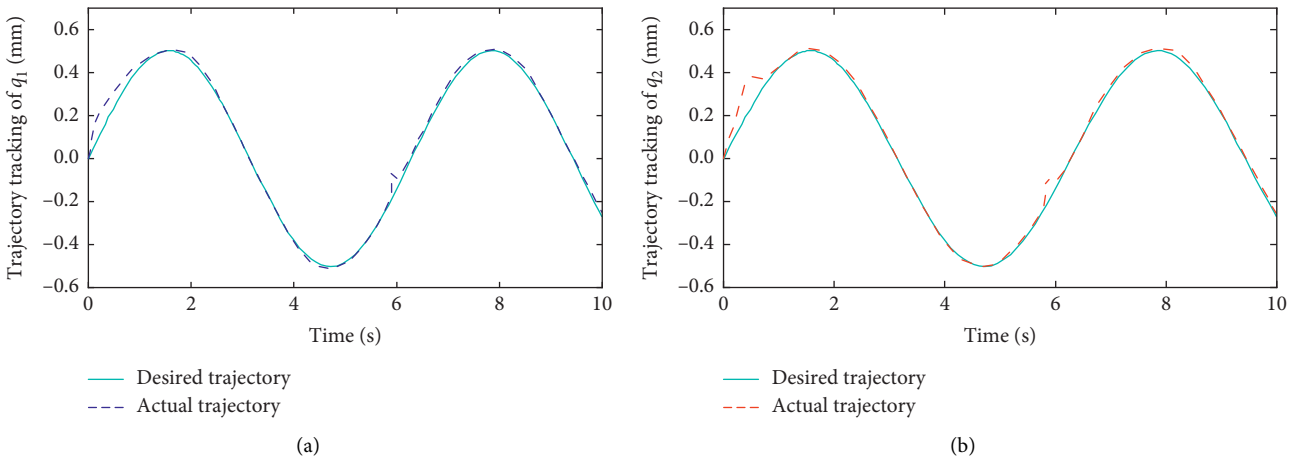

Figure 10: Trajectory tracking of the two-link robotic manipulator under external disturbances.

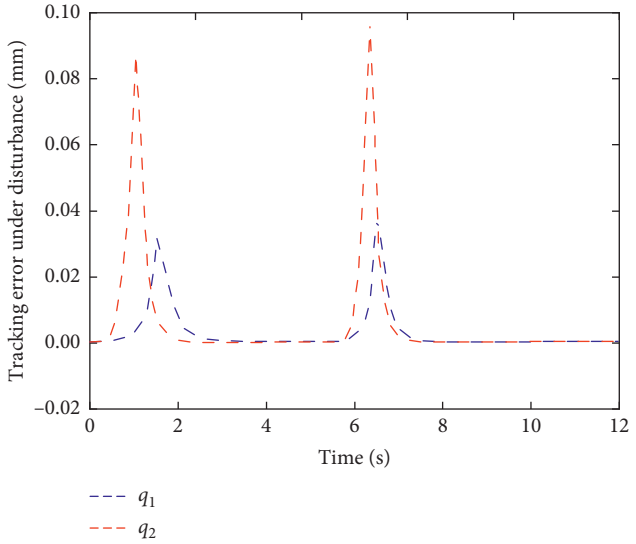

Figure 11: Tracking errors of the two-link robotic manipulator under external disturbances.

The trajectory tracking performance in end-effector space (operating space) is shown in Figure 8. Furthermore, the mean square error of the estimation function $\widehat{\varphi}(q, \dot{q})$ is derived, shown in Figure 9. Figure 9 shows that the maximum estimation error is 1.8×10^{-3}, and the minimum error is 1.68×10^{-8}, meaning that the proposed controller has a good effect in nonlinear estimation and tracking abilities.

To verify the robustness of the proposed control system, an external disturbance is added to the system in 6 s. The trajectory tracking of the two-link robotic manipulator under external disturbances is shown in Figure 10. Furthermore, the trajectory tracking errors in joint space are shown in Figure 11. It shows that the maximum tracking error of the $1^{\#}$ joint is equal to 0.0316 mm, and the maximum tracking error of the $2^{\#}$ joint is equal to 0.076 mm. According to the given external disturbance, the percentages of the tracking errors are 6.32% and 15.2%, respectively.

5. Conclusions

In this article, an adaptive backstepping sliding mode control subject to external disturbance is proposed. The dynamic model of the robotic manipulator is built by considering the coupling and nonlinear characteristics, and the estimate function of these nonlinear factors is proposed and used for the equivalent control law of sliding mode control. The control system is designed by the backstepping algorithm, and the stability and robustness of the two-link robotic manipulator are analyzed. Simulation results show that the proposed control system has good tracking performance and strong robustness for the external disturbance.

Data Availability

The data used to support the findings of this study are available from the corresponding author upon request.

Conflicts of Interest

The authors declare that they have no conflicts of interest.

Acknowledgments

The authors are grateful for the financial support from the National Natural Science Foundation of China (Grant no. 51165009) and Innovation School Project of Education Department of Guangdong Province, China (Grant nos. 2017KZDXM060 and 2018KCXTD023).

References

[1] B. Lavinia, P. Glovanni, C. N. Joseph, L. O. Keith, and V. Pietro, "Adaptive dynamic control for magnetically actuated medical robots," *IEEE Robotics and Automation Letters*, vol. 4, no. 4, pp. 3633–3640, 2019.

[2] H. Wang and Y. Xie, "Adaptive inverse dynamics control of robots with uncertain kinematics and dynamics," *Automatica*, vol. 45, no. 9, pp. 2114–2119, 2009.

[3] H. Shi, Y. Liang, and Z. Liu, "An approach to the dynamic modeling and sliding mode control of the constrained robot," *Advances in Mechanical Engineering*, vol. 9, no. 2, pp. 1–10, 2017.

[4] R. Yang, C. Yang, M. Chen, and A. S. Annamalai, "Discrete-time optimal adaptive RBFNN control for robot manipulators with uncertain dynamics," *Neurocomputing*, vol. 234, pp. 107–115, 2017.

[5] S. Mohammad, N. Pedro, and B. Richard, "Robot dynamics: a recursive algorithm for efficient calculation of Christoffel symbols," *Mechanism and Machine Theory*, vol. 142, p. 103589, 2019.

[6] J. Wu, J. Wang, and Z. You, "An overview of dynamic parameter identification of robots," *Robotics and Computer-Integrated Manufacturing*, vol. 26, pp. 414–419, 2010.

[7] M. Wang, Y. Zhang, and H. Ye, "Dynamic learning from adaptive neural control of uncertain robots with guaranteed full-state tracking precision," *Complexity*, vol. 2017, Article ID 5860649, 14 pages, 2017.

[8] M. Gautier, A. Janot, and P. O. Vandanjon, "A new closed-loop output error method for parameter identification of robot dynamics," *IEEE Transactions on Control Systems Technology*, vol. 21, no. 3, pp. 428–444, 2013.

[9] X. Yang, X. Zhang, S. Xu, Y. Ding, K. Zhu, and P. X. Liu, "An approach to the dynamics and control of uncertain robot manipulators," *Algorithm*, vol. 12, no. 66, 2019.

[10] X. Li, X. Wang, and J. Wang, "A kind of Lagrange dynamic simplified modeling method for multi-DOF robot1," *Journal of Intelligent & Fuzzy Systems*, vol. 31, no. 4, pp. 2393–2401, 2016.

[11] H. B. Mojtaba, M. Vahid, R. G. Reza, A. N. Seyyed, and E. Arash, "Dynamic analysis, simulation, and control of a 6-DOF IRB-120 robot manipulator using sliding mode control and boundary layer method," *Journal of Central South University*, vol. 25, pp. 2219–2214, 2018.

[12] J. Y. Cheong, S. I. H. Han, and J. M. Lee, "Adaptive fuzzy dynamic surface sliding mode position control for a robot manipulator with friction and deadzone," *Mathematical Problems in Engineering*, vol. 2013, Article ID 161325, 15 pages, 2013.

[13] S. He, J. Song, and F. Liu, "Robust finite-time bounded controller design of time-delay conic nonlinear systems using sliding mode control strategy," *IEEE Transactions on Systems, Man, and Cybernetics: Systems*, vol. 48, no. 11, pp. 1863–1873, 2018.

[14] X. Cheng, X. Tu, Y. Zhou, and R. Zhou, "Active disturbance rejection control of multi-joint industrial robots based on dynamic feedforward," *Electronics*, vol. 8, no. 5, p. 591, 2019.

[15] R.-J. Wai and R. Muthusamy, "Design of fuzzy-neural-network-inherited backstepping control for robot manipulator including actuator dynamics," *IEEE Transactions on Fuzzy Systems*, vol. 22, no. 4, pp. 709–722, 2014.

[16] S. He, W. Lyu, and F. Liu, "Robust H_∞ sliding mode controller design of a class of time-delayed discrete conic-type nonlinear systems," *IEEE Transactions on Systems, Man, and Cybernetics: Systems*, 2019.

[17] S.-H. Yen, P.-C. Tang, Y.-C. Lin, and C.-Y. Lin, "A sensorless and low-gain brushless DC motor controller using a simplified dynamic force compensator for robot arm application," *Sensors*, vol. 19, no. 14, p. 3171, 2019.

[18] B. Deng, J. Wang, and X. Fei, "Synchronizing two coupled chaotic neurons in external electrical stimulation using backstepping control," *Chaos Solitons & Fractals*, vol. 29, no. 1, pp. 182–189, 2006.

[19] J. Zhou, C. Wen, and Y. Zhang, "Adaptive backstepping control of a class of uncertain nonlinear systems with unknown backlash-like hysteresis," *IEEE Transactions on Automatic Control*, vol. 49, no. 10, pp. 1751–1757, 2004.

[20] S. He, H. Fang, M. Zhang, F. Liu, and Z. Ding, "Adaptive optimal control for a class of nonlinear systems: the online policy iteration approach," *IEEE Transactions on Neural Networks and Learning Systems*, vol. 31, no. 2, pp. 549–558, 2020.

[21] S. He, H. Fang, M. Zhang, F. Liu, X. Luan, and Z. Ding, "Online policy iterative-based Hco optimization algorithm for a class of nonlinear systems," *Information Sciences*, vol. 495, pp. 1–13, 2019.

[22] R. Nie, S. He, F. Liu, and X. Luan, "Sliding mode controller design for conic-type nonlinear semi-markovian jumping systems of time-delayed Chua's circuit," *IEEE Transactions on Systems, Man, and Cybernetics: Systems*, 2019.

[23] H. Chaudhary, V. Panwar, R. Prasad, and N. Sukavanam, "Adaptive neuro fuzzy based hybrid force/position control for an industrial robot manipulator," *Journal of Intelligent Manufacturing*, vol. 27, no. 6, pp. 1299–1308, 2016.

[24] C. Yang, Y. Jiang, W. He, J. Na, Z. Li, and B. Xu, "Adaptive parameter estimation and control design for robot manipulators with finite-time convergence," *IEEE Transactions on Industrial Electronics*, vol. 65, no. 10, pp. 8112–8123, 2018.

[25] T. Y. Vu, Y. N. Wang, and V. C. Pham, "Robust adaptive sliding mode neural networks control for industrial robot manipulators," *International Journal of Control, Automation and Systems*, vol. 17, no. 3, pp. 783–792, 2019.

[26] A. S. Lafmejani, M. T. Masouleh, and A. Kalhor, "Trajectory tracking control of a pneumatically actuated 6-DOF Gough-Stewart parallel robot using backstepping-sliding mode control and geometry-based quasi forward kinematic method," *Robotics and Computer Integrated Manufacturing*, vol. 54, pp. 96–114, 2018.

[27] L. Qin, F. Liu, and L. Liang, "The application of adaptive backstepping sliding mode for hybrid humanoid robot arm trajectory tracking control," *Advances in Mechanical Engineering*, vol. 6, Article ID 307985, 2014.

[28] I. O. Aksu and R. Coban, "Sliding mode PI control with backstepping approach for MIMO nonlinear cross-coupled tank systems," *International Journal of Robust and Nonlinear Control*, vol. 29, no. 6, pp. 1854–1871, 2019.

[29] X. Xu, W. Wu, and W. Zhang, "Sliding mode control for a nonlinear aeroelastic system through backstepping," *Journal of Aerospace Engineering*, vol. 31, no. 1, Article ID 04017080, 2018.

[30] C. Yang, H. Wu, Z. Li, W. He, N. Wang, and C.-Y. Su, "Mind control of a robotic arm with visual fusion technology," *IEEE Transactions on Industrial Informatics*, vol. 14, no. 9, pp. 3822–3830, 2018.

[31] C. Ren, S. He, X. Luan, F. Liu, and H. R. Karimi, "Finite-time L_2-gain asynchronous control for continuous-time positive hidden markov jump systems via T-S fuzzy model approach," *IEEE Transactions on Cybernetics*, 2020.

[32] I. Bonilla, F. Reyes, M. Mendoza, and E. J. González-Galván, "A dynamic-compensation approach to impedance control of robot manipulators," *Journal of Intelligent & Robotic Systems*, vol. 63, no. 1, pp. 51–73, 2011.

[33] C. Yang, C. Chen, W. He, R. Cui, and Z. Li, "Robot learning system based on adaptive neural control and dynamic movement primitives," *IEEE Transactions on Neural Networks and Learning Systems*, vol. 30, no. 3, pp. 777–787, 2019.

Hindawi
Complexity
Volume 2020, Article ID 8257168, 24 pages
https://doi.org/10.1155/2020/8257168

WILEY | Hindawi

Research Article

Reinforcement Learning-Based Routing Protocol to Minimize Channel Switching and Interference for Cognitive Radio Networks

Tauqeer Safdar Malik[1] **and Mohd Hilmi Hasan**[2]

[1]*Department of Computer Science, Air University Multan Campus, Multan 60000, Pakistan*
[2]*Centre for Research in Data Science, Department of Computer and Information Sciences, Universiti Teknologi Petronas, Seri Iskandar 32610, Perak, Malaysia*

Correspondence should be addressed to Tauqeer Safdar Malik; tauqeer.safdar@aumc.edu.pk

Received 15 May 2020; Revised 5 July 2020; Accepted 25 July 2020; Published 13 August 2020

Academic Editor: Shuping He

In the existing network-layered architectural stack of Cognitive Radio Ad Hoc Network (CRAHN), channel selection is performed at the Medium Access Control (MAC) layer. However, routing is done on the network layer. Due to this limitation, the Secondary/Unlicensed Users (SUs) need to access the channel information from the MAC layer whenever the channel switching event occurred during the data transmission. This issue delayed the channel selection process during the immediate routing decision for the channel switching event to continue the transmission. In this paper, a protocol is proposed to implement the channel selection decisions at the network layer during the routing process. The decision is based on past and expected future routing decisions of Primary Users (PUs). A learning agent operating in the cross-layer mode of the network-layered architectural stack is implemented in the spectrum mobility manager to pass the channel information to the network layer. This information is originated at the MAC layer. The channel selection is performed on the basis of reinforcement learning algorithms such as No-External Regret Learning, *Q*-Learning, and Learning Automata. This leads to minimizing the channel switching events and user interferences in the Reinforcement Learning- (RL-) based routing protocol. Simulations are conducted using Cognitive Radio Cognitive Network simulator based on Network Simulator (NS-2). The simulation results showed that the proposed routing protocol performed better than all the other comparative routing protocols in terms of number of channel switching events, average data rate, packet collision, packet loss, and end-to-end delay. The proposed routing protocol implies the improved Quality of Service (QoS) of the delay sensitive and real-time networks such as Cellular and Tele Vision (TV) networks.

1. Introduction

Cognitive Radio (CR) was first coined by Mitola et al. in 2002 [1]. CR technology is yet different from conventional wireless radios since it can opportunistically detect the available channels of wireless spectrum [2]. It is the foundation for CR Network establishment. This is made possible through its network layer capability that controls communication and the spectrum awareness between layers. In this case, the layers are Medium Access Control (MAC) and Network layers. Overall, CR is about providing localized control of radios within one node/user, while CR network functions according to end-to-end controls of network performance. The end-to-end controls are governed at run-time by the requirements of operators, users and applications, and the available resources. The difference in control from local to end-to-end enables easier operation for CR network across all network protocol stack layers [3]. In CR networks, Primary Users (PUs) are supposed to be the legitimate licensed users while the Secondary Users (SUs) are unlicensed users. We can classify the CR networks on the basis of their architectures such as infrastructure-based and infrastructureless networks. The former networks are developed through a centralized Service Access Point (SAP) while the latter networks are established without the centralized architecture; such networks are also called as CR Ad Hoc Networks (CRAHNs) [4]. In infrastructure-based CR networks, SAP manages the network operations just like a

base station in the cellular networks. On the other hand, SUs in CRAHNs can communicate with each other in a peer to peer fashion [5]. The ultimate goal of the CRAHN is to choose and assign channels to SUs that are currently not being utilized by the incumbent PUs [6].

In CR networks, PUs and SUs have unique rights in terms of channel utilization. PUs are the incumbent users having priority rights to occupy the licensed channels. On the other hand, SUs are less privileged users such that they can only access the licensed channel whenever the PUs are inactive. Therefore, each SU needs to select its transmission parameters based on channel utilization rights. The transmission parameters, for instance, channel availability, transmission rate, and transmission time, are dependent on the time-varying availability of the channel and user type. An SU can utilize a licensed channel in the absence of PUs whenever the PU returns and SU needs to revoke its transmission on that channel. However, it can switch to any other available channel to resume its transmissions. The frequent arrival of PU can lead SU to observe incremental channel-switching events which can seriously degrades the Quality of Service (QoS) during the end-to-end routing process at the network layer. To maintain the QoS during routing, it is very important to manage the time-varying availability of transmission parameters, such as channel availability, type of modulation, channel transmission rate, and transmission time, during the whole communication process of SUs. Therefore, the CRAHN must act as a highly intelligent network so that it can intelligently change its transmission parameters and maintain QoS during SUs' transmissions.

The CRAHN should also have the abilities of self-management and self-awareness so that the routing parameters can change on the basis of the current network requirements in a decentralized way. The routing parameters can be selected by each SU through the spectrum mobility and time-varying availability of a channel, known as Dynamic Spectrum Access (DSA) [7]. Federal Communications Commission (FCC) allowed DSA implementation in 2003 [8]. For DSA in CRAHNs, routing parameters like delay, link length, capacity, throughput, channel availability, and/or user interference, are directly related to the QoS required by the application [9]. User interferences are stated in DSA as the unexpected arrival of the PU on its licensed channel and contention between SUs on channel selection. SU must switch a channel to any other available channel to continue its transmission during the routing process to avoid harmful interference. As more and more unexpected arrivals of PUs occur, more and more channel switching events happen, thus degrading the QoS during end-to-end routing. According to user characteristics, user interferences can be categorized into interflow and intraflow interferences. The inter-flow interference occurs between PU and SU when the unexpected arrival of PU happens. However, the intra-flow interference can occur between SUs themselves due to channel contentions on the MAC layer. So, the property of DSA in terms of spectrum mobility and time-varying availability user interferences management is not only for efficient routing process but also for the better utilization of channels.

The QoS that is observed by the users is supposed to be the overall performance of any network. In this regards, various quantitative parameters like average data rate, packet loss, and end-to-end delay (EED) are used to measure the QoS observed by the different users. The overall throughput of any network is dependent on the end-to-end data delivery without any packet loss or delay to maintain the QoS. It is very challenging and demanding for SUs to make decisions of end-to-end routing by selecting the appropriate channel for its transmission in the CRAHNs so that QoS can be maintained during the transmission with less channel-switching events. A routing protocol for the CRAHNs must have the ability to select the appropriate channel where less channel-switching events occur due to user interferences.

In this paper, we propose a new channel selection routing protocol for CRAHNs, which is implemented in the network layer with multiple disjoint PUs operating on the same frequency channels. The proposed routing protocol is able to minimize the number of channel switching events by minimizing user interferences through Reinforcement Learning (RL) techniques such as No External Regret learning, Q-learning and Learning Automata. The proposed protocol adds the channel information through the header of Route Request (RREQ) and Route Reply (RREP) as the List of Available Channels (LAC), Channel Assigned (CA), Channel Access Duration (CAD), and Path Identifier (PI). We have analyzed the performance of the proposed protocol in Network Simulator (NS-2) and compared with various routing protocols. Simulation results reveal that our proposed routing protocol outperforms existing routing algorithms in terms of packet loss, number of channel switching events, and end-to-end delay.

The key contributions of this paper are listed as the following:

(i) We propose a routing protocol for CRAHNs to minimize channel switching events during network transmissions.

(ii) We have implemented RL techniques to retrieve channel information in the route discovery messages so that SUs can make judicious decisions while making judgements regarding channel-switching at the network layer.

(iii) We analyze the performance of the proposed routing protocol in terms of packet loss, number of channel switching events, and end-to-end delay and compare the results with existing routing protocols.

The rest of this paper is organized as follows. We summarize the overview of the related works in Section 2 and after then the proposed routing protocol is discussed in detail with its working and implementation. The simulation environment is explained in Section 5 followed by the Results section, and finally we conclude the paper in Section 7.

2. Related Work

Routing issues are considered in the CRAHN implementation to assist in making the route decision and become part of future planning to provide better route on the previous decision's basis. The two major decision planning frameworks applied to CRAHN are Markov Jumping

Systems (MJSs) and game theory. Game theory is also differentiated from optimization theory in their ability to model multiagent decision making scenarios whereby the decisions of each agent affect each other. Meanwhile, MJSs have been applied extensively in communication network which includes a routing framework for single agent in single and multiple states decision and planning [10]. MJSs approach is nonlinear for an "optimal" control problem in which the aim is to select actions that maximize some measure of long-term reward [11]. For MJSs, there exist many results on Kalman filtering, H∞ filtering, passive filtering, and dissipative filtering [11]. However, it should be noted that most of the developed filters are mode-dependent. This may limit their applications in some complex network environments. One solution is to design asynchronous control filters for a class of Hidden Markov Jumping Systems (HMJSs) [10]. HMJSs have been extensively used in CRAHN for a wide range of problems. They can be used for spectrum prediction, PU detection, signal classification, etc. A potential drawback when using HMJSs is that a training sequence is needed, with the training process being potentially computationally complex in case of routing in CRAHN. Therefore, if the probabilities of MJSs are unknown, then the problem becomes a RL task.

In RL, an agent aims to determine a sequence of actions or policy which maps the state of an unknown stochastic environment to an optimal action plan. We note here that MJSs, on the other hand, address this planning problem for known stochastic environments [12]. Since RL agents work in a stochastic environment, they have to balance two potentially conflicting considerations: on one hand, it needs to explore the feasible actions and their consequences (to ensure that it does not get stuck in a rut), while on the other hand, it needs to exploit the knowledge, attained through past experience, of favorable actions which received the most positive reinforcement. A cross-layer routing approach is proposed to improve the QoS parameters for multimedia applications in CR Networks. However, in this solution, the routing is performed in a centralized way, and hence, it is not applicable for the distributed environment such as CRAHN [5]. Several learning solutions for CRAHN have been proposed to address the load balancing and characterization of channel stability of routing problem [13, 14]. To this end, researchers have proposed many metrics for improving the link quality of the CRAHN such as extensions of the Expected-Transmission-Count (ETX) metric [15]. In [16], spectrum allocation strategy is used to improve the QoS for Cognitive network, which is not suitable for varying the link reliability Spectrum-aware routing, by introducing a new routing metric to locate the available channel through PUs' activities. In [17], a new routing metric is developed for the link positions by adding extra functionalities of Cat swarm approach to improve energy efficiency. However, the implementation of this approach is not sufficient to support link quality in DSA paradigm due to the limitations of channel movement. In CRAHN, routing protocols have twofold objectives, which are finding a path from source to destination and avoiding channels used for the PUs' transmissions. This routing solution improves QoS requirements in the domain of event-driven applications yet not applicable for environment learning applications [18]. We can find a thorough overview of routing metrics based on QoS, and factors influencing the performance of routing protocols are proposed in [19]. Furthermore, the RL-based routing protocols are investigated in [20], which have shown the need for new routing metrics to handle user interferences in the DSA environment of CRAHN. RL can be employed without training data as its objective is to capitalize on the long-term online performance [21]. In the CRAHN, the two most crucial tasks of routing protocols are offering reconfigurability due to channel switching and managing the end-to-end route in the time-varying availability of the channel due to user interferences [22]. Hence, Q-learning can be used as a model-free-based RL approach while implementing CRAHN routing tasks on the basis of reward and penalty [23]. On the other hand, Temporal Difference (TD) learning approach of model-free RL is used to implement any action on the basis of guess and guess again which is updated based on another guess. Q-learning is rather a better choice to be utilized for the purpose of CRAHN routing to decide on the selection of future actions from those with reward or penalty based on explorations of the dynamic environment.

The geographic forwarding routing protocol based on spectrum awareness jointly undertakes path and channel selections so that the regions of PUs' activities can be avoided during route formation [24]. However, avoidance mostly does not fulfill CRAHN's exploitation requirement. Hence, a modified version based on spectrum awareness is used to minimize the overall hop count [25]. However, many complexities are exposed during the process of the data transmission such as topological changes, faulty nodes, and link degradation which cannot be handled using the avoidance technique [26]. A stability-oriented routing protocol is presented to find a stable route, which comprises link quality and user interference when PUs become agile [27]. The other strategy presented is based on a probabilistic approach with exact ways by which to locate an efficient path in the networks that are random in nature [28]. The least priced path routing based on DSA for the CRAHN is presented to minimize the EED for the opportunistic transmission of data [24]. This least priced path affects each hop that lies within the routing path and the transmission becomes slower for the overall network.

Two metrics, i.e., Frequency Diversity (or Link Stability) and Channel Stability (or Path Stability), are used to count the lowest and balance spectrum utilization areas of PUs' activities for path stability in [29]. These metrics are based on the busyness ratio of PUs. When the busyness ratio of PUs increases, channel switching delay increases. In [30], another algorithm uses three metrics to handle user interference between PUs and SUs. However, it creates multiple paths which results in larger routing tables in every SUs. In [31], a routing protocol for CRAHN is presented as a new routing protocol especially for the multipath basis by adding a new metric for channel and path selection at the same time. This protocol ensures the path stability in terms of high connectivity but not offers the best QoS path. Similarly, recently

a routing solution is offered to reduce the channel switching events during the transmission using the mobility pattern of PU [32]. This protocol offers the routing predictions based on the user mobility and previous routing pattern matching, which results in higher channel selection time due to the lower mobility and routing pattern prediction. The limitation of lower routing prediction is managed by proper reinforcement learning mechanism implemented on network layer [33]. However, the problem of channel switching events is still an open challenge due to the limitation of user interference [34]. The routing protocol which manages the channel switching events so that the use interference is managed is still in its infancy. In best route selection, best channel availability is not considered which creates the problem of multiple channel-switching events. Hence, multiple routing paths create frequent channel switching events due to user interference and overall network performance is degraded than the CRAHN's QoS requirements. User interferences are managed during end-to-end routing decisions using the PU activity On-Off model in RL-based routing protocols. However, the effect of user interferences on channel switching has not been addressed in spectrum mobility approaches [33]. The effects of user interferences were not differentiated into interflow and intraflow interferences during routing decisions to minimize packet collisions. The channel switching due to user interferences in routing must be addressed to manage spectrum mobility on the network layer. These issues need to be handled to minimize EED and packet loss. By doing so, the overall throughput of the network could be improved in RL-based routing protocols.

3. Methodology of the Proposed Minimization of Channel Switching and User Interferences (MCSUI) Routing Protocol

Our proposed protocol extends the functionality of the existing network-layered stack to accommodate the channel selection decisions in the network layer for minimizing the channel switching and user interference overhead during the end-to-end routing process. There are three modules appended at the network layer named Network Tomography, Minimization of Channel Switching and User Interferences (MCSUI) routing, and QoS and Error Control as shown in Figure 1. The MCSUI routing module is the core of the proposed routing protocol, in which routing tables are created based on the channel selection information passed from the MAC layer through spectrum sensing. The routing tables are updated through the learning agent at the network layer for the channel selection decision. The functionality of the learning agent is correlated within the spectrum mobility manager to manage channel switching and user interferences for resource allocation and event monitoring in a cross-layer fashion.

The learning agent estimates the quality of the routing path based on the available channel list (which is received from the MAC layer through the spectrum mobility manager) in a cross-layer approach. For the routing tables, various parameters such as the number of channels switching events, channel transmission rate, next-hop, and all available routes from source to destination for each link are included. The choice of multiple paths and channels is saved in the routing table and if a PU suddenly returns to its channel, the SU needs to switch to any other available channel. This sudden arrival of PU is defined as user interference by SU and due to the increment of user interference, the channel switching events occur, and hence, the routing table increases.

The implementation of Artificial Intelligence- (AI-) based RL techniques is the core of the proposed routing protocol to handle and properly manage the user interferences. The user interferences are observed and saved in the learning block so that the appropriate channel is selected for future routing decisions. The decision block coordinates with the learning block for making a decision on channel selection as shown in Figure 2. Further, it correlates with the QoS and Error Control to select the best available channel among the List of Available Channel (LAC) according to its traffic type. The decision of the best available channel depends on the history of channel selection by PU. The channel parameters are also selected with routing parameters in order to improve the QoS in terms of average data rate, packet loss, and End to End Delay (EED). All modules work collaboratively using the learning agent through the spectrum mobility manager in a cross-layer approach. The modifications in the functions of the learning and decision blocks are discussed in the following subsections.

3.1. Learning Block. The learning block learns through exploration and exploitation learning to select the best available channel based on the saved history information of user interferences. The exploration and exploitation of channel selection are tracked using AI-based RL techniques. Three RL techniques including No-External Regret learning, *Q*-learning and Learning Automata are used for the selection of best available channels for routing. The exploitation learning is based on No-External Regret learning to utilize the previous (past) best channel selected for a successful routing decision. On the other hand, *Q*-learning is used for the exploration of newly available channels for SUs' transmissions. The implementation of No-External Regret learning is beneficial for updating the saved channel information so that the routing table size can be minimized in case of bad channel selection. Finally, the Learning Automata technique is used to balance between the exploitation and exploration learning for channel selection by maximizing or minimizing the rewards of any channel. Hence, a channel is saved and it remains in the available channel list based on the reward value.

The available channel information such as channel transmission rate and channel ID is passed from the MAC layer to the network layer through the message exchange process between SUs by modifying the existing RREQ, RREP, and Redirecting messages. These messages are maintained for the reward (maximum reward) or penalty (minimum reward) of a channel from Learning Automata

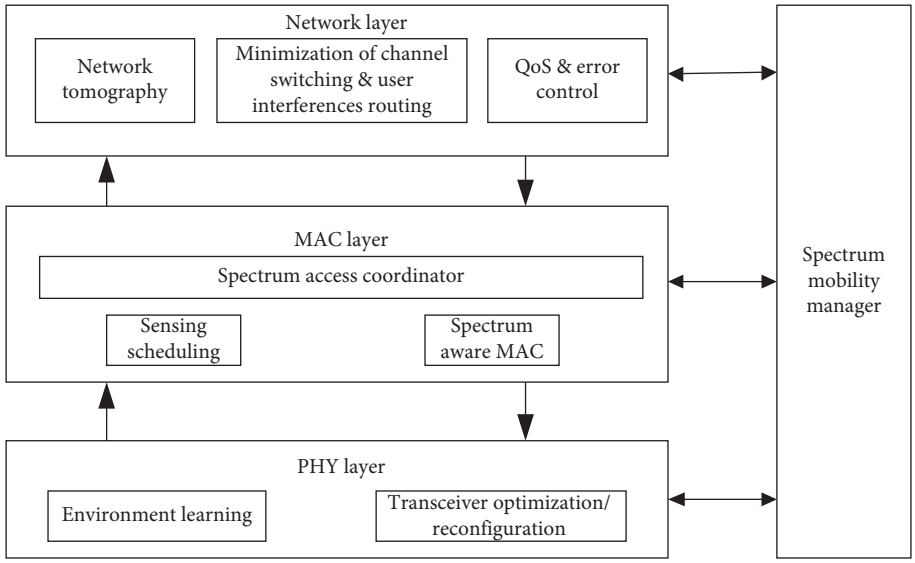

Figure 1: Communication model for the proposed routing protocol.

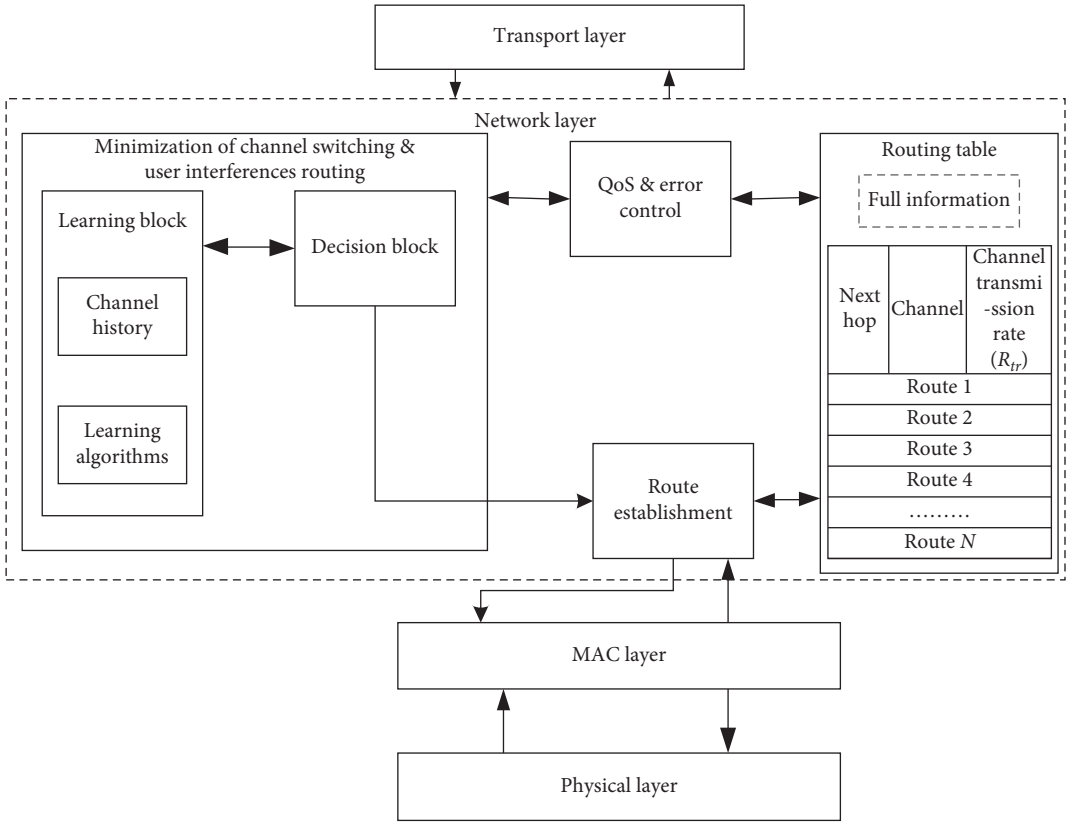

Figure 2: Implementation of MCSUI routing protocol at the network layer.

through the hello interval and active_route_timeout (ART) parameters. These two routing parameters, hello interval and ART, in the Ad-hoc On-demand Distance Vector (AODV) [35] routing protocol specify the value of the lifetime for node-to-node connectivity.

The channel is selected through the message exchange process using the learning mechanism during the end-to-end routing decision. Whenever the SU wants to send a new transmission, it has to send the RREQ message to the intermediate node SU and the neighborhood status is updated in the SU by using the database of the available channel list. It is maintained and updated in the learning block using the No-External Regret learning and Q-learning. The intermediate node then accesses the new channel list and sends the

Redirecting request message to the neighboring intermediate nodes. The Redirecting request message is used to update the LAC through all neighboring nodes (or SUs). In this way, all the SUs have the same available channel information and have no competition in channel selection, and hence, intraflow interference can be minimized, as shown in Figure 3. The destination is selected on the basis of Redirecting Reply messages of different neighboring nodes. In the case of inter-flow interference, the message exchange mechanism works in the same way except that the intermediate node is a PU. Once the Redirecting request is received, the neighboring nodes evaluate its validity in correspondence with the message and update of the ongoing traffic flow using the message exchange process. The neighboring nodes then send the Redirecting Reply message to the intermediate node. Finally, the Route Reply (RREP) message is passed to the source node. The best available channel is selected which is user interference-free on the basis of reward and punishment value of Learning Automata technique.

3.2. Decision Block. The channel is selected on the basis of various pieces of channel information with the help of decision block. For this purpose, the routing may avoid channels which have a high level of PU interference. The decision block co-ordinates with the learning block to select the best available channel according to the QoS and Error Control requirement. Furthermore, the decision block carries out the route establishment after a channel is selected and passes that channel to the routing tables. The selection of the best channel is not only dependent on channel availability but also on the QoS parameter for that channel. The learning block is providing the LAC on the basis of previous (past) and present channel selection decisions. At the channel selection time, the QoS and Error Control parameters such as traffic type, interference, channel bandwidth, transmission time, and Packet Error Rate (PER) are also essential for end-to-end routing. Therefore, QoS requirement of a SU is also incorporated within the learning block using the decision block. The detailed implementation of RL techniques in the proposed routing protocol is discussed in the next section.

4. RL-Based Proposed MCSUI Routing Protocol

Most RL algorithms can be classified into becoming either model-free or model-based. In the model-based approach, the agent builds a model of the environment through interaction with it is typically in the form of an MJS analogous to the approach taken in adaptive optimal control with input time-delays. With a model in hand, given a state and action, the resultant next state and next reward can be predicted. This allows for planning through which a future course of action can be contemplated by considering possible future situations before they are actually experienced. Based on the MJS model in the model-based approach, a planning problem is solved to find the optimal policy function with techniques from the related field of dynamic programming. The commonly used algorithms to solve MJSs include the celebrated dynamic programming algorithms of online value iteration and online policy iteration. In online value iterating learning techniques, the optimal policy is calculated on the basis of optimal value function. In online policy iterating learning techniques, on the other hand, the learning is directly performed in the policy space. We are using the Q-learning as an online value-iterating model-free technique and learning automata as online policy-iterating technique. In the online model-free approach, on the other hand, the agent aims to directly determine the optimal policy by mapping environmental states to actions without constructing an MJS model of the environment [12].

The proposed MCSUI routing is based on RL techniques using the existing AODV routing protocol mechanism. Therein, the route set-up is in accordance with an expanding ring search mechanism, whereby it uses RREQ and RREP messages of AODV routing. The maintenance of route utilizes Route Error (RERR) packets generated due to SUs' mobility and wireless propagation instability. However, SUs MCSUI routing is capable enough to obtain channel information of licensed channels without causing interference and delay to incumbent PUs. Moreover, SUs should be able to accomplish channel selection from the spectrum mobility provided by the CR environment without causing excessive overhead for route formation. Three RL techniques are used to modify the routing mechanism in the CRAHN, namely, No-External Regret learning, Q-learning, and Learning Automata. Various routes emerge through different channels, and each route is derived through the various channels using exploitation learning. The selected channel must be idle and user interference-free from PUs' activities to successfully make an end-to-end transmission through this route. Therefore, this routing strategy is beneficial in finding user interference-free channel for the whole transmission. The exploration in Q-learning allows SUs to explore various routes through different channels for a transmission to overcome user interference during transmission. The channel is selected either through exploitation or exploration. In Figure 4, a path selection is used as a routing path selection through one of the channel selection decisions either from exploitation or exploration.

One advantage of this strategy is the handling of routing loops through the route maintenance process for handling PUs' activities. The Route Error (RERR) message is used to inform all intermediate nodes of a route that the link has failed; hence, a new route is needed, while the route maintenance process derives an additional type of message to handle the PU activity as PU-Route Error (PU-RERR); that is, the PU-RERR message is utilized to tell neighbor nodes that some PU activities are detected on a specific channel and that a new channel is needed to accomplish the transmission. The routing process is implemented with the help of RREQ, RREP, and PU-RERR messages.

The RREQ message to update the routing table is shown in Figure 5, whereby the channel selection process is started when an intermediate node receives a RREQ message through the available Channel i; then it sends back a reverse route to source on the same channel. In case of the intermediate node, a valid route can provide the channel

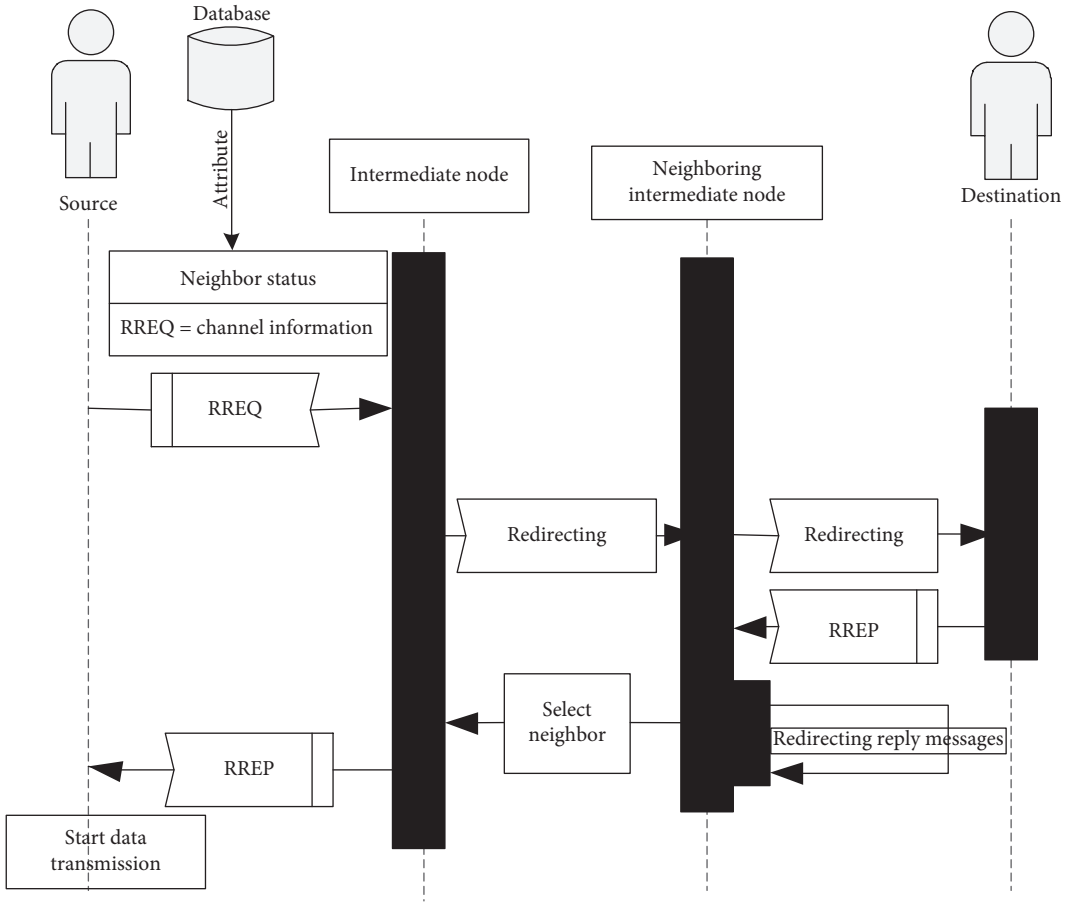

Figure 3: Message exchange process using learning block.

information for the desired destination. Finally, a unicast RREP will be sent to the source through the reverse route for the selected channel. On the other hand, if it cannot provide a valid route, it re-broadcasts the received RREQ message on the same channel to all other neighboring nodes. If any additional RREQ message is received for the same source and destination by the same intermediate node on the same (or different) channels, the received RREQ message is then compared against all available routes stored in the routing table. If the reverse route or the received RREQ message contains a better route, then it is selected for the transmission and stored in the routing table as a newer route or better reverse route. It is simply discarded otherwise. The different routes available through the various available channels are stored in the routing table and updated in a reactive manner. The various channels are selected on the basis of exploitation and exploration learning and available on the network layer for the routing purpose. If any channel is unavailable for a stored route, it is referred to as 'regret' and the route is discarded from the routing table using the exploitation learning technique of No-External Regret. To minimize regrets, exploration learning (Q-learning) is used to find options for new routes through the available channels for routing. At this stage, Learning Automata helps to select the best available channel among all available channel lists maintained in learning block for a specific route.

The process of RREP is shown in Figure 6. According to the process, when the first RREP message is received by an intermediate node from an available channel selected through the learning process, it sends a forward route to the destination on the same channel. It also forwards the RREP message with the reverse route available on the same channel stored in its routing table. If an extra RREP message is received for the same source and destination by any intermediate node, then it is compared against the stored reverse route on the same or different channels. If the forward route is better than the stored one, then it is processed and updated in the routing table; otherwise, it is discarded.

The unexpected arrival of the PU is handled by providing the available channel list on the network layer through route maintenance during routing as shown in Figure 7. When any PU activity is detected through the Poisson process, the mean value will be assigned using the Box-Muller transform method on the selected channel through exploitation or exploration. The SU abolishes all the routing entries available in the routing table from that channel using a PU-RERR message. The SU also informs all the neighbor nodes that the channel is currently unavailable. All other SUs that receive the PU-RERR message also abolish the routes from all channels which involve the channel of the source of the PU-RERR message. In this way, the proposed routing protocol minimizes the switching delay and manages channel

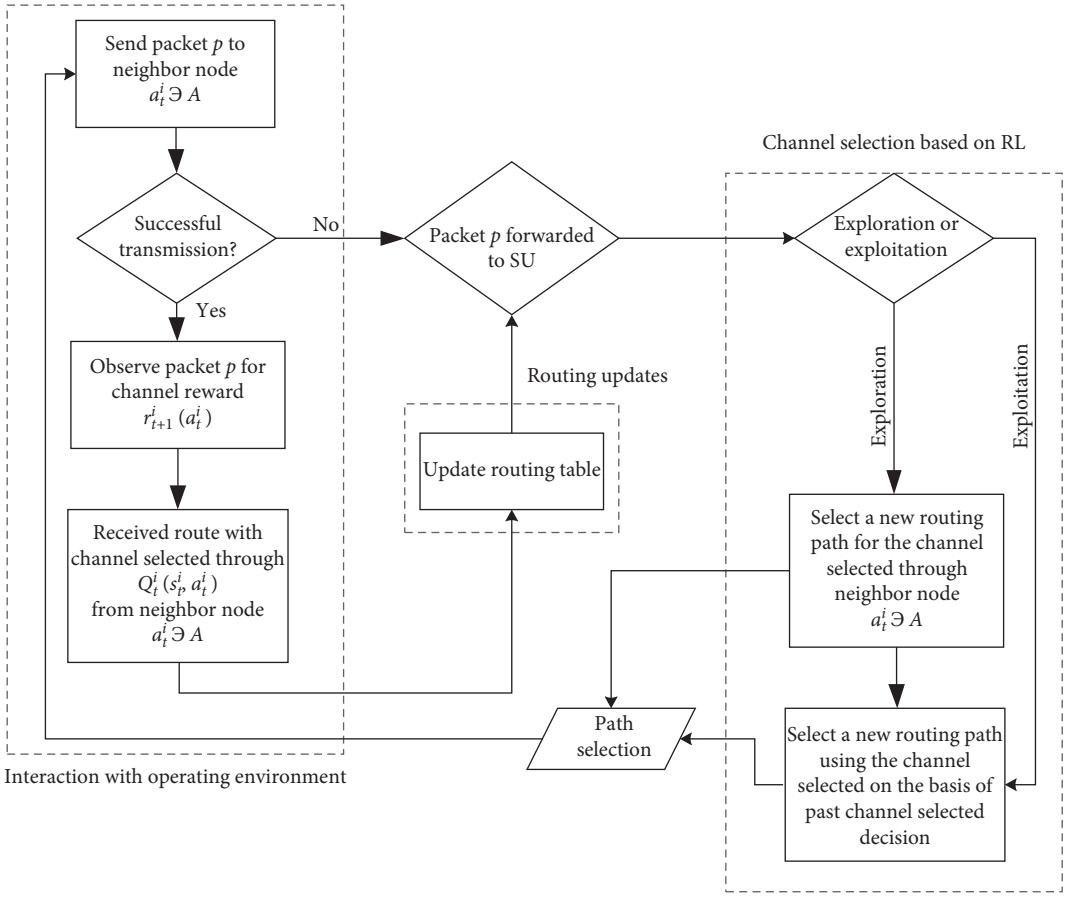

Figure 4: Path selection process in the proposed MCSUI protocol.

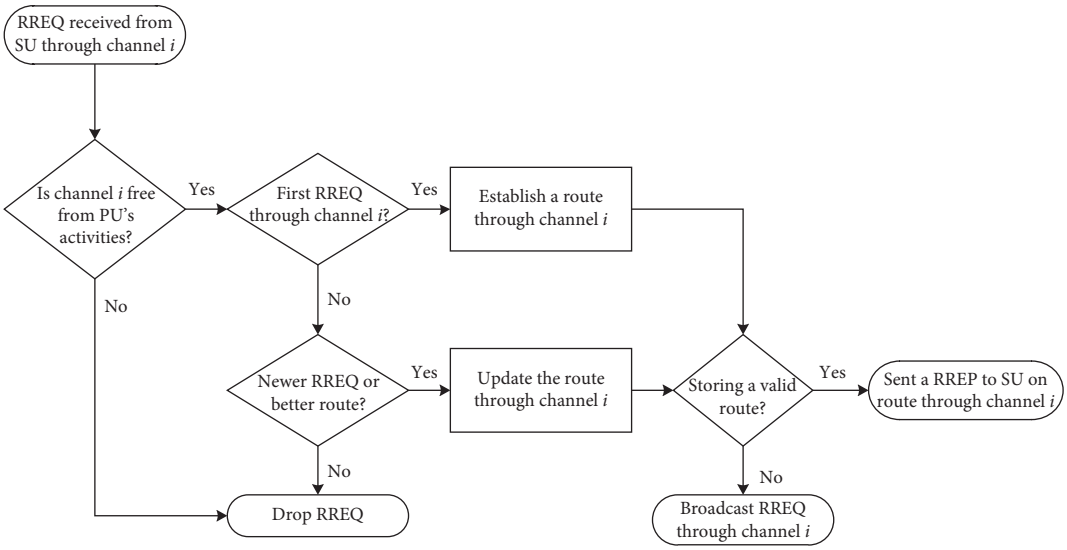

Figure 5: RREQ mechanism in proposed MCSUI protocol.

switching events due to user interferences, and therefore, EED is minimized with the improved average data rate. The PU-RERR messages also enable the MCSUI routing protocol to have the spectrum mobility and DSA functionality during routing on the network layer.

The RL-based routing is improved using the PU-RERR message because whenever the SU receives a PU-RERR message, the availability of extra routes is checked in the routing table from other channels for a specific destination. If so, the SU can continue the transmission through other

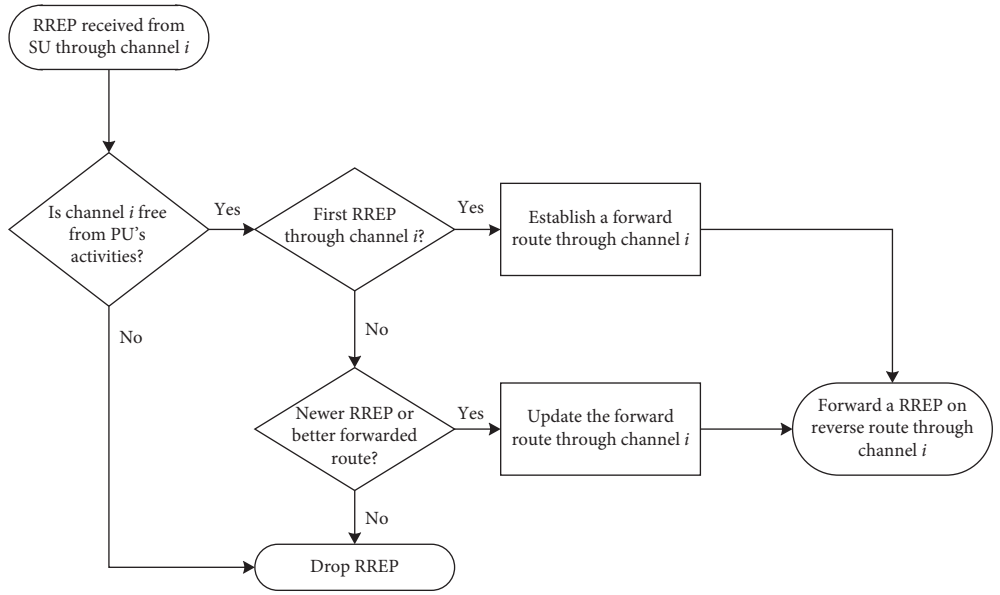

Figure 6: RREP mechanism in proposed MCSUI protocol.

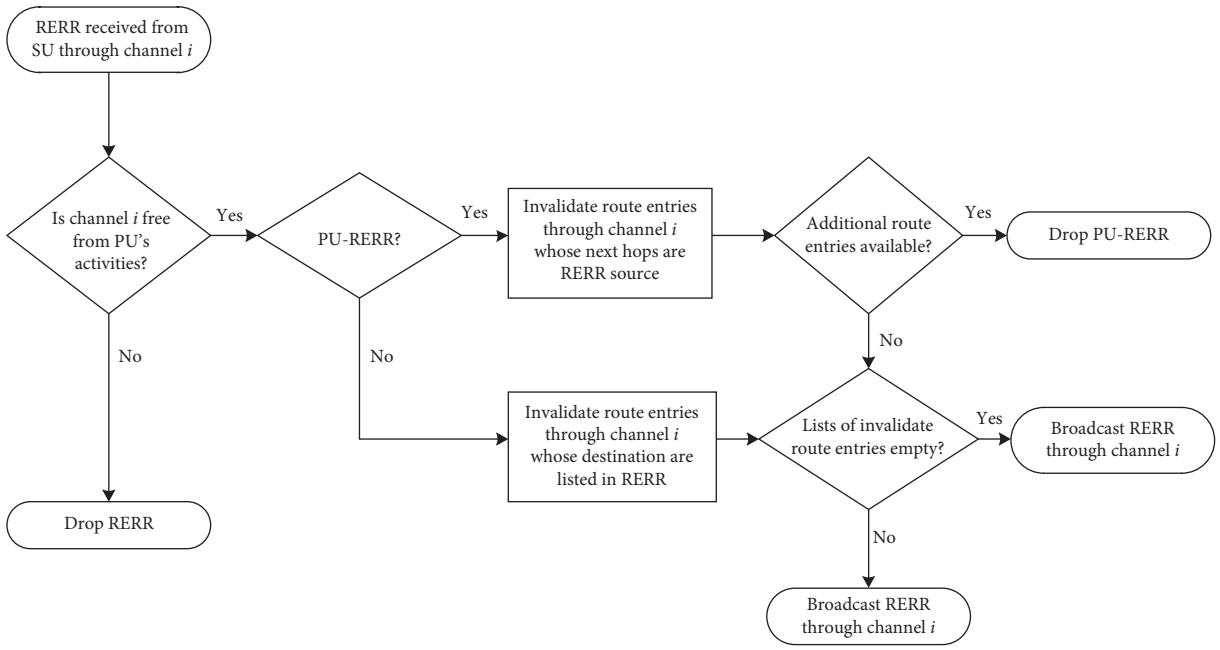

Figure 7: PU-RERR mechanism in proposed MCSUI protocol.

available routes from other channels. Else, a new route discovery process is initiated using the traditional RERR message. In order to minimize the EED, the MCSUI routing protocol updates different routes through different channels to minimize the channel switching delay. For this purpose, every SU first identifies the shortest routes using Dijkstra's algorithm from all available routes through various available channels. Secondly, it starts transmission on these shortest paths. The various available channels are selected in such a way that the spectrum mobility allows the MCSUI routing protocol to implement DSA in CRAHNs.

4.1. Channel Selection in MCSUI Protocol. We used the multiagent Q-learning based channel selection model of the network layer in our proposed MCSUI Protocol. The update rule for the Q-learning values for the first agent is as follows:

$$\text{absolute growth of } Q_{a_i} = Q_{a_i}(t+1) - Q_{a_i}(t) = \alpha\left(r_{a_i}(t+1) - Q_{a_i}(t)\right), \tag{1}$$

where Q_{a_i} represents the Q-value of agent α for action i at time $t+1$ and time t, respectively, and r_{a_i} accounts for the reward at time $t+1$ by subtracting the previous Q-value of the agent α. This difference indicates the absolute growth in

Q_{a_i} between time t and time $t+1$. The approximate growth of Q_{a_i} for the small amount of time (for the continuous time version of $\Delta t \in [0, 1]$) is given by

$$\text{appro growth of } Q_{a_i} = Q_{a_i}(t+\Delta t) - Q_{a_i}(t) \approx \Delta t \times \alpha\left(r_{a_i}(t+\Delta t) - Q_{a_i}(t)\right). \tag{2}$$

When $\Delta t = 0$ and $\Delta t = 0$, equation (2) becomes an identity equation. The linear approximation can be achieved by equation (2) for the continuous time version between 0 and 1 ($0 < \Delta t < 1$). Hence, the approximation equation for the continuous time version of equation (1) is achieved by dividing Δt and taking the limit for $\Delta \longrightarrow 0$ as in [36], given by

$$\lim_{\Delta t \longrightarrow 0} \frac{Q_{a_i}(t+\Delta t) - Q_{a_i}(t)}{\Delta t} \approx \alpha\left(r_{a_i}(t) - Q_{a_i}(t)\right), \qquad \frac{dQ_{a_i}(t)}{dt} \approx \alpha\left(r_{a_i}(t) - Q_{a_i}(t)\right), \tag{3}$$

which is achieved by applying integration as follows:

$$Q_{a_i}(t) = Ce^{-\alpha t} + r_{a_i}, \tag{4}$$

where C is the integration constant, e^{-x} is the monotonic function, and $\lim_{\Delta t \longrightarrow 0} e^{-x}$. Hence, the reward achieved by the Q-values through applying the limit to Equation 4 when $t \longrightarrow \infty$ is given by

$$\lim_{t \longrightarrow \infty} Q_{a_i}(t) = \lim_{t \longrightarrow \infty} \left(Ce^{-\alpha t} + r_{a_i}\right) = r_{a_i}. \tag{5}$$

For channel selection, the first agent learns through the learning process and the other user uses the previous learned states by utilizing the exploitation as a reward. The users are user interference-free since the same reward will be generated for the first agent to take a channel selection action, and the channel will be added to the List of Available Channel (LAC). For this case, equation (5) assures the monotonically increasing (or decreasing) of initial Q-values. The reward is monotonically increasing if $Q_{a_i}(0) < r_{a_i}$ and is otherwise monotonically decreasing if $Q_{a_i}(0) > r_{a_i}$. When a SU wants to transmit, it sees the availability time of each channel and if it meets the channel transmission rate and time, the channel is then added to the LAC. The user can use the exploration to find a new strategy for channel selection decisions. If a SU is using exploration, the game is then played repeatedly in such a way that the rewards can be replaced as

$$E\left[r_{a_i}\right] E\left[r_{y_j}\right] = \sum_j a_{i_j} r_j, \tag{6}$$

where $E[r_{a_i}]$ represents the expected reward for the first user and y_j is the strategy for the second user. It is very important that the Nash Equilibrium Point (NEP) is the specific point of the strategy of any user, in which the probability 1 is given to one of the channel selection actions. After this, equations (3) and (4) become

$$\frac{dQ_{a_i}(t)}{dt} \approx \alpha\left(E\left[r_{a_i}\right](t) - Q_{a_i}(t)\right), \tag{7}$$

which is achieved by applying integration as follows:

$$Q_{a_i}(t) = Ce^{-\alpha t} + E\left[r_{a_i}\right]. \tag{8}$$

Hence, if the user is not learning any more for new channel selection decisions in case of exploitation, then the Q-values are selected as an expected reward $E[r_{a_i}]$ in a monotonic function where they are either never decreasing or never increasing. On the other hand, the learning process is used to find new Q-values for channel selection in the case of exploration, which is a complex task, and the expected reward is possibly changed over time. Exploration learning can change the probability which consequently changes the expected reward. The expected reward modifies the associated direction field using equation (7) and so NEP is changed. If the expected reward changes every time, then a new channel selection direction is generated. Both the limit and direction of Q-values are changed by this modification as in equation (8). This mechanism is also responsible for unifying the deal between exploitation and exploration, so that the user can reinforce the evaluation of actions that already known to be good while also exploring new actions. For this purpose, Q-greedy exploration is used to select a random action with Q-probability and the best action which has the highest Q-value with the probability of $1 - Q$. The probability is updated by the Q-greedy mechanism whenever it finds a new action with the highest Q-value. The overall behavior of a user depends on the assembly of these crossing points which define the Q-values.

An important note is that equation (7) cannot be solved in the same way as equation (3) when changes occur in the expected rewards over time although the initial Q-values can be derived from the early direction paths. Another aspect is the updating speed of Q-values that depends on the learning rate. In the learning process, actions hold different probabilities depending on convergence to the NEP. This speed is selected as a constant learning rate for the stochastic random selection problem as $\alpha = 0.1$. The message exchange process is used to update the Q-tables for the learning block to exploit and explore the channel information using the learning mechanism. Learning Automata is used to identify an action as a reward (or punishment) on the basis of its opponent's utility function. So, the average channel reward information can be updated in Learning Automata. The Q-values can be evaluated on the basis of the action's success. The Q-value is marked as a reward when that value gives a successful transmission during which there is no user interference and no channel switching occurs. By contrast, the Q-value is marked as a punishment/penalty for an unsuccessful transmission due to channel switching caused.

The reward value of actions is calculated using the two values of Q, i.e., Q_{penalty} and Q_{reward}. $Q_{\text{penalt}}y$ resulted from the node taking one of the two actions: decreasing hello-interval and active_route_timeout. In case of decrements in hello_interval and active_route_timeout values, the channel will no longer be available for transmission and the routing choice will not be available through that channel. Connectivity information may be provided by a node through broadcasting the local hello messages. However, this must

only be used if the node is part of an active route. For every hello_interval, the node verifies whether a broadcast RREQ has been sent or not in the last hello_interval so that it can update the channel selection choices of its opponents. In the case whereby sending has not taken placed, it may broadcast a RREP with Time-To-Live (TTL), TTL = 1, which is called a hello message with the RREP message. This lifetime value is equal to hello_interval multiplied by allowed-hello-loss (an integer). Their default values are 1 second and 2 seconds. To manage the network status of instability, exploration is utilized to identify the new action for channel selection using the learning mechanism to reduce the chances of punishments/penalties. Q_{reward} presents the stability status of the network and the node performs actions such as increasing the value of hello_interval and active_route_timeout. The increments in hello_interval and active_route_timeout indicate the stability of the route for transmission and also the reward achieved has the highest Q-value. The Q-learning-based calculation of Q_{penalty} and Q_{reward} can be found in [25] as follows:

$$Q_{\text{penalty}} = (1 - a)Q(s, a)_{\text{penalty}} + aQ(s', a'), \tag{9}$$

$$Q_{\text{reward}} = (1 - \alpha)Q(s, a)_{\text{reward}} + \alpha Q(s', a')_{\text{reward}}, \tag{10}$$

which is embedded in each SU to make interference-free routing decisions for channel selection with the support of the learning mechanism. The learning process is accomplished in three stages named state, action, and reward. The state denotes the decision-making factor for channel selection while the reward shows the negative (penalty/punishment) or positive (reward) effect as a result of an action being taken in a state. A positive action is calculated as a reward and negative action as a penalty. A SU i is considered for the reward r selected from the actions $A_i = \{1, 2, \ldots, J\}$ through $S = \{1, 2, \ldots, N\}$ number of states to show the proposed routing process to reach destination n. The state $s_i \in S$ is the channel selection state of SU i at time t for achieving the reward r_{a_i} through the action $a_i \in A_i$.

Whenever SU i sends packet to the destination at time t, then SU updates the Q-value at time $t + 1$ as a reward for the destination node through the next hop node j in its routing table as follows:

$$Q^i_{t+1}\left(s^i_t, j\right) \longleftarrow (1 - \alpha)Q^i_t\left(s^i_t, j\right) + \alpha\left(r^i_{t+1}(j) + \max_{k \varepsilon A^j} Q^j_t\left(s^j_t, k\right)\right), \tag{11}$$

where $0 \le \alpha \le 1$ is the learning rate, node $k \in A^j$ is an upstream node (opponent node), and j is the next-hop node. The reward $r_i(j)$ shows the successful channel selection for SU i to transmit to the neighbor node j. The Q-value $Q^j_t(s^j_t, k)$ collectively represents the channel transmission rate through $k \in A^j$. This Q-value calculating model is used by SUs for routing decisions to a destination through learning about the available channels from multiple paths for its reward. The multiple paths are explored from the available channels which are affected by the different levels of the PU's utilization. Hence, higher utilization by a PU of a channel lowers the Q-value for that channel due to higher user interference which results in higher channel switching events and delay for the transmission. For the transmission by a SU i, the action is selected to adopt a policy $\pi^i_{t+1}(s^i_t)$ that selects a SU next-hop node holding the maximum Q-value as

$$\pi^i_{t+1}\left(s^i_t\right) = \arg\max_{a \varepsilon A^i}\left(Q^i_t\left(s^i_t, a^i_t\right)\right). \tag{12}$$

Algorithm 1 shows channel selection through the three learning processes based on RL, which is initialized with the Q-value as 0 at time t and selects a default channel to check the availability of various users. If a packet is received successfully through that channel, the action of transmission is awarded (incremented), and the channel remains same otherwise. This condition is checked for every channel available on the spectrum and average reward is calculated in case of unavailability of a free channel on the spectrum in both ways. Finally, at timestamp t, the Q-value of user i for the strategy is updated based on the average reward of the channel availability. This is due to the channel is selected for the transmission on the basis of action probability calculated through Q-greedy exploration from all the available channels on the spectrum. The reward action is calculated using the RL algorithms and updates the action strategies according to equation (11). These equations are derived through the RL algorithms, No-External Regret Learning, Q-Learning, and Learning Automata. The learning agent is capable of this channel selection mechanism, which is implemented in cross layer fashion of CRAHNs architecture.

4.2. Network Co-Ordination. Suppose that N SUs in a CRAHN opportunistically access M orthogonal licensed channels. Common Hopping will take effect, whereby time-slotting procedure upon the channels is carried out and SUs are synchronously communicating among each other. If no packet requires transmission, all SUs carry out transmission using channels according to the same number of channel sequence. For instance, the sequences of channels as 1, 2, . . ., M. In this regard, β denotes the time slot length (i.e., the time on each channel transmission). During a transmission attempt, Request-to-Send (RTS), and Clear-to-Send (CTS) packets are firstly exchanged by a pair of SUs during a time slot. When the CTS packet is received by SU transmitter, the channel switching is paused. Moreover, the particular SU transmitter will remain on the same channel for the transmissions of data. However, nontransmitting SUs continue channel switching otherwise. Once the data packet is successfully transmitted, the SU pair can rejoin the channel if required.

In spectrum mobility, different sets of SUs may utilize diverse channels for exchanging control information and constructing several links simultaneously. For instance, this type of channel switching is shown in Figure 8, in which SUs A, B and C, D are two transmitting pairs that intend to initiate new transmissions at the same time. Each SU generates a distinct pseudorandom channel sequence number for its transmission instead of using the same channel number for all the SUs. The channel sequence number for

SU A is 2-4-1-3 and for SU B is 3-2-1-4. The default sequence of channel for transmitting on the channels is followed by a SU when it is in idle condition. When a SU wants to perform data sending to a receiver, it will temporarily tune to the ongoing receiver channel and an RTS packet will be sent during a time slot. In the event that the receiver sends a reply containing CTS packet, channel switching will be stopped by the transmitter and receiver. Then data transmission will begin using the same channel. In the event that the data transmission completes, the default sequence of channel will be resumed by them. It is assumed that strict time synchronization among SUs for the purpose of channel transmission may be accomplished even if the exchange of control messages on a Common Control Channel (CCC) does not occur. It is considered that a synchronization scheme in each SU by including a time stamp for each of the packets it sends. After that, the specific SU receiver's clock information is obtained by the SU transmitter. This is performed using two actions–listen to the corresponding channel as well as estimation of clock drift rate to produce time synchronization. SU transmits the data packet and stops the transmission at the start and end of a time slot, respectively. Consequently, the multiple time slots will represent the SU data packet length, denoted by σ.

4.3. Network Implementation. The activity of every licensed channel is learned in the form of ON/OFF operation to maintain the LAC for the routing purpose. As shown in Figure 9, a PU ON period or data packet on a channel is represented with the gray rectangle while the OFF or idle period is denoted by the white space. The gray rectangle length designates the PU data packet length. Hence, a channel can only be utilized by a SU if there is no PU carrying out the transmission simultaneously. A SU starts channel learning for its availability as t_0 which represents the transmission time of a PU. Hence, at any time in the future t ($t > t_0$), the channel status is represented by $N_i(t)$ for the i-th channel. The $N_i(t)$ notation denotes a binary random variable, representing the idle and busy states with values 0 and 1, respectively. For the packet arrival process, each PU is following the Poisson distribution process with the MAR λ_i and an arbitrary probability density function (pdf) $f_{Li}(l)$ is followed by the data packet length. We assumed each SU of two radios. The first radio manages data and controls traffic, and it is known as the transmitting radio. Meanwhile, the second radio, named the scanning radio, is dedicated to scanning the whole spectrum in order to gain the information of channel occupancy. The scanning radio has two functions: (1) monitoring channel transmission time and storing channel information in memory so that channel availability in learning block can be retrieved in the future; and (2) confirming whether the channel that is just selected is idle or not for transmitting SU.

An SU can learn the channel availability before starting the transmission so that the channel switching delay could be minimized. Based on that learning, SU will make a decision from three possibilities: (1) staying in the current channel; (2) switching to a new channel; (3) ending the current transmission according to the history of a channel. Our proposed protocol determines whether a channel switching should follow or not based on the following two criteria: (1) the learning probability that the current channel and the potential channel that could be chosen to continue the ongoing transmission of data (which we called as candidate channel is either busy or idle; (2) the expected transmission of the channel idle duration. The traffic activity of PU user on channel i is shown in Figure 9. In the figure, X_i denotes time of interarrival, while T_i denotes time of arrival. Both times refer to i-th packet.

By following the assumption that the arrival of PU packets is based on Poisson distribution pattern, X_i is exponentially distributed with the MAR λ_i packets per second and the PU packet length follows the pdf $f_{Li}(l)$. According to Figure 9, for any future time t, the learning probability (L_P) that the i-th channel is busy or idle can be written as follows:

$$\begin{aligned} &L_P\left(N_i(t)=1\right) \text{ if } T_i^k < t \text{ and } T_i^k + L_i^k \geq t, \quad k \geq 1, \\ &L_P\left(N_i(t)=0\right) \text{ if } T_i^k + L_i^k < t \text{ and } T_i^{k+1} \geq t, \quad k \geq 1, \\ &\qquad\qquad T_i^{k+1} \geq t, \quad k = 0, \end{aligned} \tag{13}$$

where Lk denotes the length of the k-th PU transmission on channel i. Hence, the learning probability (L_P) that channel i is idle at any future time t can be obtained as

$$\begin{aligned} L_P\left(N_i(t)=0\right) &= \int_0^\infty \left[\sum_{k=1}^{\infty} L_P\left(T_i^k + L_i < \frac{t}{k}\right) L_P\left(T_i^{k+1} \geq \frac{t}{k}\right) L_P(k) + L_P\left(T_i^l \geq t\right) L_P(k=0)\right] f_{Li}(l)\mathrm{d}l \\ &= \int_0^\infty \left\{\sum_{k=1}^{\infty}\left[\frac{\lambda_i (t-L_i)^k}{k!} e^{-\lambda_i (t-L_i)}\right]\left(\frac{(\lambda_i t)^k}{k!} e^{-\lambda_i t}\right) \frac{(\lambda_i t)^k}{k!} e^{-\lambda_i t} + e^{-2\lambda_i t}\right\} f_{Li}(l)\mathrm{d}l. \end{aligned} \tag{14}$$

Let t_{off} denote the *OFF* period duration. The following equation defines the cumulative distribution function (CDF) of *OFF* period duration for real valued variable t, for the i-th channel:

$$\begin{aligned} L_P\left(t_{\text{off}} < x\right) &= \int_0^\infty \int_0^{l+x} \lambda_i e^{-\lambda_i t} f L_i(l)\mathrm{d}t\ \mathrm{d}l \\ &= \int_0^\infty \left(1 - e^{-\lambda_i (l+x)}\right) f L_i(l)\mathrm{d}l. \end{aligned} \tag{15}$$

(1) Initialize $Q(Sa_i) \longleftarrow 0$;
(2) Start with default channel selection;
(3) Transmit packet using multiple access scheme;
(4) **while** channel < C **do**
(5) **if** packet received is "yes" **then**
(6) Utility of channel is calculated from the arrived packet rate;
(7) **else**
(8) Get channel utility from the ACK packet;
(9) **end if**
(10) Calculate average utility reward using equation (11);
(11) Update Q (s^i) using equation (12);
(12) channel $\longleftarrow$ channel + 1;
(13) **end while**
(14) Assign channel using the probability reward of Q-greedy exploration;
(15) End of session;

Algorithm 1: Channel Selection of the proposed MCSUI routing protocol in SUs.

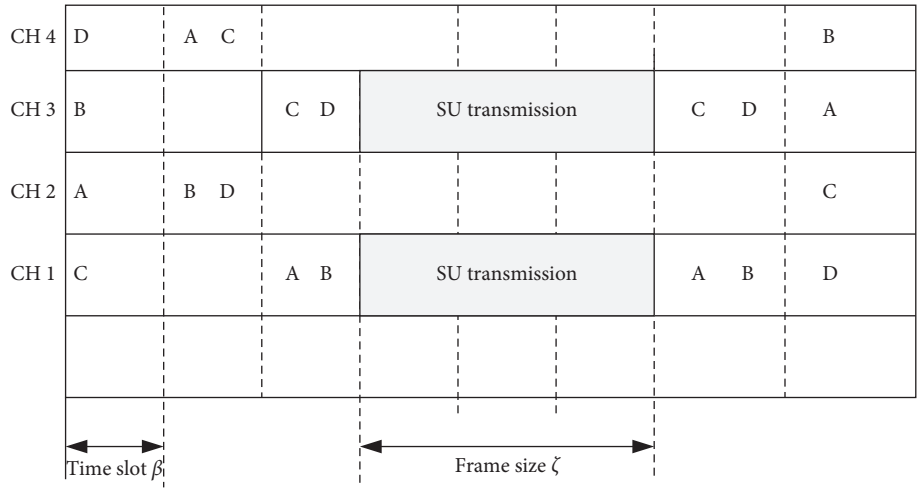

Figure 8: An example of the channel switching events by proposed protocol.

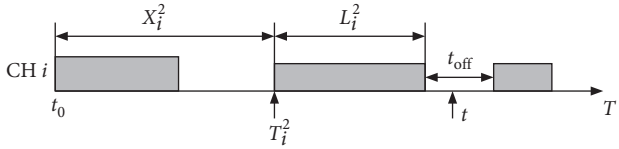

Figure 9: PU traffic activity on channel i.

The decision which requires a SU to make a switching to a new channel (based on the above learning probability) is as follows:

$$L_P\left(N_i(t) = 0\right) < \tau_L, \tag{16}$$

where τ_L accounts for the threshold value of a channel. If τ_L is less than learning probability, then the channel is assumed as being busy and so SU needs to carry out a channel switching event. This means that the channel is not being assumed as idle until the end of the current transmission. Additionally, the decision that a channel j at time t is available simply depends on the following:

$$\begin{aligned} L_P\left(N_j(t) = 0\right) &\geq \tau_H, \\ L_P\left(t_{j,\text{off}} > \eta\right) &\geq \Theta, \end{aligned} \tag{17}$$

where τ_H is the learning probability threshold for a channel H, which is considered as idle at the end of the current transmission, whereby η is the length of transmission plus a time slot (i.e., $\eta = \zeta + \beta$), and θ is the learning probability threshold for a channel to be considered as idle for the next transmission period. This would be helpful to note that the probability of learning that the idleness time of j−th channel is more than transmission time must be higher than or equal to θ in order to support at least one transmission.

For data transmission, SUs first perform the procedure that senses whether the existing operating channel is available or not. Toward this end, our proposed protocol MCSUI assumes that each SU has to wait on the chosen target channel until it becomes idle. An example is shown in Figure 10 to explain the minimization of channel switching delay when channel switching occurs during transmission. Therein, HLU is High-priority Licensed Users (i.e., PUs) while LUU is Low-priority

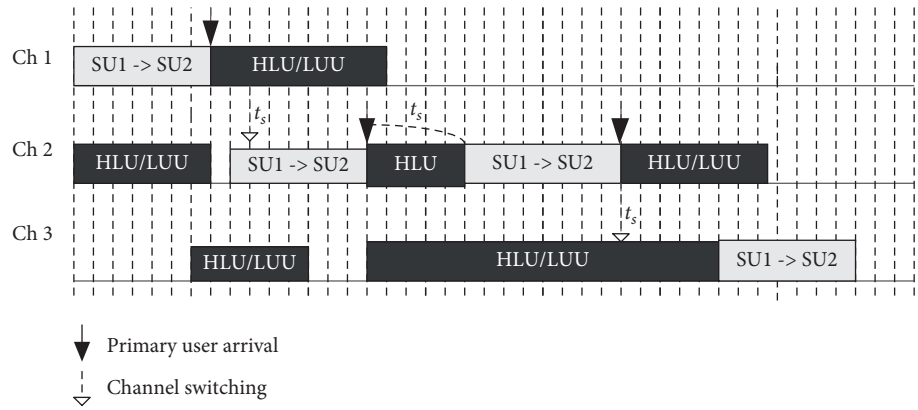

Figure 10: Example scenario of transmission process with channel switching.

Unlicensed Users (i.e., SUs). We see channel Ch1 becomes SU1's default channel. Initially, SU1 performs transmission to the matching receiver SU2. The channel switching process is described as the following. Channel Ch1 is changed to the idle channel Ch2 by SU1 during the first interruption. The channel switching time, t_s, represents the channel switching delay. Then, SU1 remains on the existing channel Ch2 during the second interruption. The channel can only be accessed by SU2 after the transmissions are completed by HLU of Ch2. With respect to this, channel switching delay refers to the busy duration produced from PUs of Ch2. SU then performs a change to Ch3 during the third interruption. This is due to the fact that Ch3 is busy, SU1 will only be served after all other users in the ongoing Ch3 queue finish being served. Therefore, switching delay refers to the total of t_s and the waiting time occurred in Ch3. Overall, SU1 transmission finally finishes on Ch3. The total service time refers to the period between the instance of transmission beginning and the instance of transmission completion. Moreover, channel switching delay refers to the duration from the instant of pausing transmission until the instant of resuming the unfinished transmission.

The proposed protocol consists of two parts. The first part describes how an SU pair initiates a new transmission regardless of the channel selection mechanism used during channel switching. If a data packet arrives at a SU, the SU predicts the availability of the next transmitting channel (or the channel of the receiver) at the starting of the subsequent time slot. By referring to the learning results, when the learning probability is satisfied by the channel as in equation (17) for the transmissions of data, an RTS packet will be sent by the transmitter to the receiver using the same channel at the starting of the subsequent time slot. Upon receiving the RTS packet, the intended SU receiver replies a CTS packet in the same time slot. Then, if the CTS packet is successfully received by the SU transmitter, the two SUs pause the channel switching and start the data transmission on the same channel to minimize the channel switching delay. This part is effectively minimized the overall End-to-End Delay (EED) by minimizing the switching delay so that the overall throughput is improved. The second part is based on the proactive channel switching events during the transmission of a SU to determine whether or not the SU transmitting pair has to perform channel switching to a new channel at the end of a transmission. The decision of channel switching event during the transmission is performed according to the Algorithm 2.

The proposed protocol is able to avoid interference between the SU transmitting pair and PUs using Algorithm 2. It is based on the observed channel transmission time information of an SU, which checks the channel switching policy, as in equation (16), for the current channel by learning the list of available channels (LAC) at the end of the transmission. If the policy is not satisfied at a moment, this means that the current channel is still available for the next transmission. This is shown in Algorithm 2 as next available channel (NAC). Then, the SU transmitting pair does not perform a channel switching and keeps staying on the same channel. However, if the policy is satisfied, the Channel-Switching Event (CSE) is set to 1 as shown in Algorithm 2 online 6; that is the current channel is considered to be busy during the next transmission time and the SUs need to perform a channel switching by the end of the transmission to avoid user interference to a PU who may use the current channel. After the CSE is set, the two SUs rejoin the channel in the next time slot after the previous transmission.

The channel selection during switching is proposed according to Algorithm 2, in which the SUs should update the available channel information to the rest of SUs, so that the SUs must have channel information of neighboring SUs before transmitting at the same channel. Hence, when the CSE is incremented, the ongoing transmission will be paused by those SUs that have to carry out channel switching. The channel will be resumed by them using the identical sequence number, in order to ensure that the same channel is used for the transmission. Nevertheless, each SU follows a default channel sequence which may not be the same as other's channel sequence numbers. To gain the ability to exchange information of channel availability among SUs on the same channel, SUs have to use the same channel sequence number only in the event that they are carrying out channel switching. Meanwhile, the criterion in equation (17) is checked by the SU transmitter for available channels in the spectrum. When there is no available channel, the ongoing

(1) Initialization: CSE $\longrightarrow$ 0; DSF $\longrightarrow$ 0; NAC $\longrightarrow$ 0; LAC $\longrightarrow \theta$;
(2) **for** $j \longleftarrow 0$ to $j \longleftarrow M$ **do**
(3) Learning L_{P} $(N_j(t) = 0)$, L_{P} $(t_{j,\mathrm{off}} > 0)$;
(4) **end for**
(5) **if** L_{P} $(N_i(t) = 0) < \tau_{\mathrm{L}}$ and DAT = 1 **then**
(6) CSE $\longleftarrow$ 1;
(7) **end if**
(8) **if** CSE 1 **then**
(9) **for** $k \longleftarrow 0$ to $k \leq M$ **do**
(10) **if** L_{P} $(N_j(t) = 0)$ $\tau_H \geq$ And $L_{\mathrm{P}}(t_{j,\mathrm{off}}) \geq \theta$ **then**
(11) NAC $\longleftarrow$ NAC + 1;
(12) LAC(NAC) $\longleftarrow k$;
(13) **end if**
(14) **end for**
(15) **end if**
(16) **if** CSE $\longleftarrow \theta$ **then**
(17) Stop transmission and goto Line 1;
(18) **else if** LAC = θ **then**
(19) Start scanning radio;
(20) Launch channel selection of Algorithm 1 for LAC;
(21) Send CSR packet;
(22) **end if**
(23) **if** CSA packet is received **then**
(24) Switch to selected channel and start scanning radio;
(25) **end if**
(26) **if** channel is busy **then**
(27) Stop transmission and goto Line 1;
(28) **else**
(29) DSF $\longleftarrow$ 1; CSE $\longleftarrow$ 0;
(30) **end if**
(31) **if** DSF $\longleftarrow$ 1 **then**
(32) DSF $\longleftarrow$ 0;
(33) Transmit a DATA packet;
(34) DAT $\longleftarrow$ 0 when transmission ends;
(35) **end if**

Note. CSE–Channel Switching Event, DSF–Data Sending for Current Channel, NAC–Next Available Channel, LAC–List of Available Channel and DAT–Data Sending for next channel.

Algorithm 2: Channel switching control in SUs during transmission.

transmission will stop immediately. Both SUs switch to the subsequent channel for another time slot, and the channel availability at the starting of the subsequent time slot will be checked by them using equation (17) criteria. However, if the LAC is not empty, Algorithm 2 will be triggered by the SU transmitter, and the sending of a Channel-Switching-Request (CSR) packet comprising information of the newly selected channel in the subsequent time slot will take place. When the CSR packet is received, a Channel-Switching-Acknowledgement (CSA) packet will be responded by the SU receiver. Then, if the SU transmitter successfully receives the CSA packet, the establishment of channel switching agreement between the two SU nodes will occur. Thus, both SU nodes switch to the selected channel and start the data transmission. The switching delay of a channel switching is defined as "the duration from the time an SU vacates the current channel to the time it resumes the transmission". It is possible that inaccurate prediction is produced and there exists another PU on the channel that the SUs switch to. Hence, at the beginning of the transmission, the SU transmitting pair restarts the scanning radio to confirm that the selected channel is idle. If the channel is sensed busy, the two SUs immediately resume the channel switching and launch Algorithm 2. The number of available channels for data transmission is maintained in a list named Next Available Channel (NAC). The DAT and DSF denote data transmission requesting data sending for Channel i (current channel) and j (next channel), respectively. The proposed MCSUI routing protocol is not only aimed at minimizing the switching delay but also the number of channel switching events using the learning mechanism incorporated in the learning block for future routing decisions.

5. Simulation Environment

This section presents details of the simulation environment regarding the implementation of the proposed routing protocol. The simulation environment includes

the network model and implementation set-up to present the channel selection for the RL-based routing protocol. The implementation set-up is carried out through the system model, simulation parameters, and assumptions for the implementation of the proposed MCSUI routing protocol. The performance of the proposed MCSUI routing protocol is compared with that of the existing Ad Hoc On-Demand Distance Vector (AODV) [35], Opportunistic Spectrum Access (OSA) [33], and the Coolest Path (CP) [34] routing protocols. MSCUI is compared with the AODV since it is the most frequently used reactive routing protocol for real-world solutions. The CP protocol is used as a benchmark because it is the first routing protocol that identifies the issue of user interference in CRAHN. In addition, the proposed MCSUI routing protocol is evaluated based on the learning mechanism used for routing decisions. For this purpose, the OSA is chosen as the routing protocol to compare the implementation of the learning algorithms.

5.1. Network Model. To simulate the proposed MCSUI routing protocol, a network model of the CRAHNs is implemented with mobile SUs which can dynamically access any available licensed channel. The PUs are implemented as fixed users to utilize their licensed channels. Whenever there are free channels, SUs can gain access for data packets transmissions. The network is modeled in a two-dimensional Cartesian scenario in which the availability of PUs' channels is unknown to SUs. The LAC is collected on the network layer using the learning agent through spectrum sensing of the MAC layer in each SU. The SU uses one of the available channels for its transmission. However, SU switches to any other available channel with the unexpected arrival of a PU. This issue is referred to as channel switching due to user interference at the network layer during the transmission of data. To reduce the effect of PU activity on routing by minimizing channel-switching events during transmission, we consider a network that consists of four SUs with two PUs as shown in Figure 11. The implementations of exploitation and exploration learning are shown in Figures 11(a) and 11(b), respectively. The proposed routing protocol is implemented with four SUs (denoted by SU_A, SU_B, SU_C, and SU_D) within the transmission ranges of four PUs (denoted by PU_1, PU_2, PU_3, and PU_4). SU_A can communicate with SU_D using the routes of $SU_A \longrightarrow SU_B$ on Channel 1 and $SU_B \longrightarrow SU_D$ using Channel 2. In this scenario, a SU can dynamically switch a channel during routing using exploitation and exploration learning of channel selection on the network layer. Another option for route and channel selection is available through the routes of $SU_A \longrightarrow SU_C$ on Channel 1 and $SU_C \longrightarrow SU_D$ using Channel 2 depending on the activity of PUs. In this scenario, both the interflow and intraflow interferences can be minimized by PU and/or SU, respectively. This scenario also enables properties of spectrum mobility and dynamic spectrum access during the routing process since the channel and route both can be selected at the network layer for the routing purpose to improve the RL-based routing. The proposed MCSUI routing protocol jointly learns by exploiting and exploring the route and channel during the routing for end-to-end transmission. This characteristic allows SUs to dynamically select any other available channel and route which are user interference-free to reduce the number of channel switching events. The channel selection is based on RL which not only makes it dynamic but also reduces the user interference. The implementation of these features is carried out through the RREQ, RREP, and PU-RERR messages of the routing protocol.

5.2. Simulation Setup. The implementation setup is carried out using the CR Cognitive Network (CRCN) simulator, which is an extension of the famous Network Simulator (NS-2). The CRCN simulator supports the three layers of the CRAHN architectural stack, namely, the network, MAC, and Physical (PHY) layers. The network layer maintains the neighboring node list and the available channel list for routing purposes. The channel availability information is received from spectrum sensing by the MAC layer. The PHY layer maintains the information, such as transmission power, Signal-to-Interference-Noise ratio (SINR), and the propagation model. All layers share this information with each other through the spectrum mobility manager which is already available in the cross-layer network architecture of CRAHNs. Currently, the CRCN simulator is not modeling the activity of PU to observe the effect of PU's activity on SU. For the proposed MCSUI routing protocol, the PU activity on the channel is modeled as a Poisson process based on an expected mean and a standard deviation with the mean value determined using the Box-Muller transform [36]. The PU's arrival rate is fixed and the mean for the discrete data is used in the implementation setup to calculate the user interferences for the best available channel. The CogMAC protocol is used for spectrum sensing at MAC layer to find the channel availability information, while the SINR is used on the PHY layer.

The mobility parameters such as pause time and speed are selected to describe the changed behavior of speed and direction for a node. The Random WayPoint (RWP) model correlates the changed behavior of speed and direction with the time between two events. The detailed parameters selection is given in Table 1. An adjustable input parameter of the model is not used; it depends otherwise on the speed of the nodes, size, and shape of the area of the network. A higher mobile node speed results in a higher frequency of direction changes of a node for a given area. Therefore, the area selected for the RWP mobility model is 500 meters square (m^2), and the analytical expression of its Probability Density Function (PDF) is used for the speed of the node [35]. The distance and time between two consecutive way points are analyzed for the transmissions of SUs in the RWP mobility model. These way points represent the starting and ending points of a user movement period and are uniformly distributed per transmission. The system model to implement these properties is described in the next subsection.

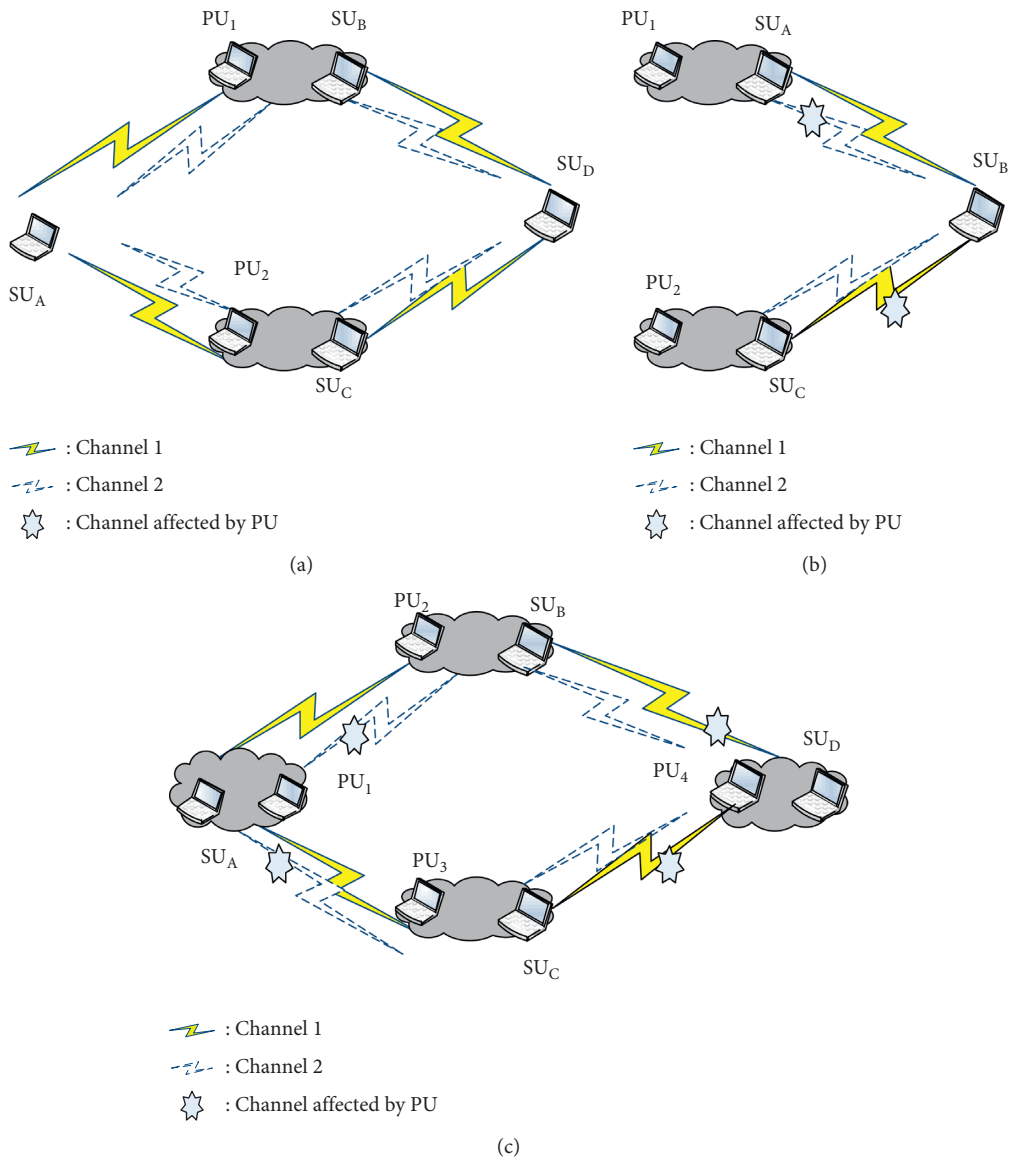

Figure 11: Network model of proposed routing protocol.

5.3. System Model. The simulation network is defined in a two-dimensional Cartesian scenario of 2000 m × 2000 m with 100 mobile SUs and 7 fixed PUs. Simulation results are averaged over 50 runs. Each simulation run lasts for 700 seconds. For spectrum mobility, 10 channels are used with a channel capacity of 2, 4, 6, 8, 10, 12, 14, 16, 18, and 20 each to support the wideband spectrum-sensing technique with interference-based detection. This is used to sense over a large spectral bandwidth and to select the channel according to the user's requirement. The models of traffic used for collecting simulation results consist of Constant Bit-Rate (CBR) video conferencing and File Transfer Protocol (FTP) application traffic profiles. In the simulation, each SU changes its location within the network based on the RWP mobility model. According to this model, a node randomly selects a destination, moves toward that destination at a speed not exceeding the maximum speed, and then get pauses. The interval of pause is known as pause-time. Pause-time ranges from 0 to 240 seconds of duration so as to observe the impact of high mobility on the protocol.

Since the mobile nodes are constantly moving during the simulation, a pause-time of 0 second signifies the worst-case scenario regarding high topological instability. The SU moves using the RWP mobility model in which nodes can move randomly and freely without restrictions. To be more specific, the destination, speed, and direction are all chosen randomly and independently of other nodes. Each user starts by pausing for a fixed number of seconds. The user then selects a random destination in the simulation area and a random speed between 0 m/s and the maximum mobility speed of 15 m/s with random speed selected uniformly. The node moves to the destination and again pauses for a fixed period before selecting another random speed and location. This behavior is repeated for the length of the simulation.

Table 1: Default simulation and structural parameters.

Parameter	Value
Simulation area	$2000 \times 2000\ m^2$
Number of SUs	100 users/nodes
Number of PUs	18 maximum
Model for PUs	Uniform model
No. of channels	10
Propagation model	Two-way
Round channel bandwidth	2, 4, 6, 8, 10, 12, 14, 16, 18, 20 MHz
Channel mean packet error rate (PER)	0.05 packet/ms
Standard deviation of PER (σPER)	0.025
Mobility model for SUs	Random waypoint
Mobility speed for SUs	0–15 m/s (uniform)
Pause time	0, 60, 120, 180, 240 seconds
Data type	Best effort
Packet payload	8184 bits
MAC header	272 bits
Mean arrival rate (MAR)	[0.0, 1.0]
Transmission delay by SU (d_{trSU})	1.0 ms
Processing delay by SU (d_{prSU})	1.0 ms
Packets generation at MAR (λ_{SU})	0.6 packets/ms
Learning rate (α)	0.1
Routing weight factor (ω)	1.2 ms
Transmission delay by PU (d_{trPU})	120 bits
Standard deviation of MAR (σMAR)	0.0, 0.4, 0.8
Mobile user traffic	5 sources
Fixed destinations	2 static and 3 mobile
Packet size	15 kb
Transmission rate	10 packets/sec
Application profile	Low-resolution video

The simulation reporting interval is 1 second, which shows that an average value is calculated for the results at each second of the simulation running time.

Each training episode for the simulation starts from the beginning of the simulation to 30 seconds. Each node initially conducts channel selection at random using the learning agent based on decreasing or increasing the Active-Route-Time out (ART) and hello-interval parameters.

The learning agent uses a 0.1 learning rate according to the randomly distributed radio environment of the CRAHN. During the simulations, the proposed MCSUI routing protocol selects the path using the ART parameter between 3 and 10 seconds and the hello-interval parameter between 1 and 10 seconds. The channel quality parameters are used to evaluate the performance of routing protocols for different packet error rate (PER) and levels of PU's activity. The results are evaluated on the standard deviation of PER (σPER) and Mean Arrival Rate (MAR) of PU. The MAR for the activity of the PU indicates the channel utilization, channel availability information, channel transmission rate, and channel transmission time. On the other hand, the standard deviation represents the channel access probability of PU. Similar representations are used for the PER as Mean PER and standard deviation of PER but with fixed values for all data channels for the sake of simplicity of the system. The activity of a PU is modeled as a Poisson process with a mean which is assigned using the Box-Muller transform [36] for an expected mean arrival rate of [0, 1] and standard deviation of [0.0, 0.4, 0.8] as given in Table 1 at the SU, and packets are generated by using the Poisson process with a MAR of 0.6 packets/ms in accordance with the Box-Muller transform. Further, PUs are distributed through Poison Process in a stochastic network environment between the mean arrival rate of [0, 1]. The mean distribution is checked for the standard error with 0.0 as a low, 0.4 as a medium, and 0.8 as a high arrival rate of PU using the standard deviation of the mean.

6. Results and Discussion

The proposed MCSUI routing protocol is aimed at minimizing channel-switching events, packet collisions, EED, and packet loss. EED is calculated in milliseconds by considering delays in transmission, queuing, processing, and back-off process along with the path from source to destination. The transmission delay of SU is shorter than that of the PU since PUs have higher priority rights than SUs. The queuing delay is assumed as a finite 1000 packets queue size in each SU with 1.0 ms being the fixed processing delay. The Q-values are initialized as zero to inspire exploration at the start of the simulation with a learning rate as 0.1. We have compared the network performance of the proposed routing protocol with the traditional AODV, recent routing protocol Opportunistic Spectrum Access (OSA) based on reinforcement learning, and Collest Path (CP) routing protocols. For a good comparison, the CP routing protocol was chosen in this simulation study since it emerges as the optimal approach for minimizing the SU's

interference to the PU. The route having the minimum accumulated amount of PU's activities will be selected by CP routing; that means, the least number of PUs is encountered by the particular route. So, MAR of PUs along the route may be the lowest. However, OSA routing is based on RL and implemented through a centralized approach that requires network-wide information on the MAR for each link and channel.

6.1. Normalization of Channel Switching Events. The performance of the proposed MCSUI routing protocol is analyzed for the number of channel switching events on the basis of three different standard deviation values of mean arrival rate of PU as shown in Figures 12–14. The results are compared with the AODV, CP, and OSA routing protocols of the CRAHN, and it shows that there is an increment in number of SUs as well as the number of channels with the simulation time passage. In general, users focus on two measurements regarding the spectrum selection. The first relates to the integrated power measurement across the assigned channel, normally being known as the occupied bandwidth (W), power-in-band (or channel power). In this measurement, power is integrated across the channel from the start to assigned channel frequency. In addition to measuring the power in the channel, there is also a need to ensure that transmissions are not leaking into channels assigned to other users, especially those on either side of the licensed channel. A common approach is by filling up the occupied channel with a test signal. This is to measure or compare the integrated power against frequency in the channels that are adjacent to the occupied channel. The PUs are fixed on a channel with activity time on frequency of $1/\lambda = 200$ seconds with the bandwidth of W. The performance of the MCSUI protocol is analyzed in terms of Channel Switching Events against the simulation time in a relatively large network of 100 SUs. As shown in Figure 12, it is observed that the MCSUI protocol initially has a higher number of channel switching events compared to other routing protocols. This occurs due to the Q-value being initialized with zero, and there is no channel available for channel selection at the start of the simulation. Nevertheless, the MCSUI routing protocol converges to a stable state using exploitation as well as exploration learnings as time passes. The learning rate is a decreasing function of time and so in learning algorithms, it works inversely proportional to the time. In the stable state, users have very few channel-switching events. This behavior can be justified because the SUs are distributed among multipath routes on different channels in the MCSUI routing protocol. Therefore, less channel and user contention occurred. This happens as the exploration learning initially started with action 0 for the 0.0 standard deviation of the mean arrival rate of PU, once it reaches to the Nash Equilibrium Point (NEP) through the exploration learning. The NEP works according to the strategies of its opponents and selects the best available channel using the learning mechanisms. As shown in Figure 13, when the standard deviation of MAR is 0.4, the NEP is not achieved due to the increment in interference of PUs. Hence, the number of channel switching events is increasing due to user activities. The network will utilize the whole learning process for channel selection, and this will require more time. As shown in Figure 14, the number of channel switching events is decreasing. This is happening due to the increment of the participating number of users as the standard deviation of MAR for PU is increased to 0.8 for the transmission. Hence, the MCSUI routing protocol performs better in the reduction of channel switching events compared to the other well-known routing protocols of the CRAHN. The proposed protocol is reducing the number of channel switching events up to 65%, 29%, and 41% than that of the AODV, CP, and OSA routing protocols, respectively.

6.2. Reduction of User Interferences in Terms of Packet Collisions. Each PU activity in a channel is modeled as a Poisson process to observe the effect of user interferences. We consider the Mean Arrival Rate (MAR) of PU and its' standard deviation (sd) of PU arrival using Box-Muller transform, which is based on an expected MAR between [0, 1]. The standard deviation for the activity of PU is $\in \{0.0, 0.4, 0.8\}$ that shows the low, medium, and high levels of availability of the Pus, respectively. User interferences are observed for these different values of the availability of PUs according to the stochastic environment property of the CRAHN. The effect of user interferences on network performance is calculated in terms of packet collisions for the MAR of the PUs. It is assumed that the channels have a low level of noise with a fixed Packet Error Rate (PER) as 0.05 and a mean PER (σPER) as 0.025. The packets are generated in SU to transmit with a fixed MAR (λ_{SU}) of 0.6 packets/ms. The effect of user interferences is observed for each of the three levels of PUs' availability in terms of packet collisions on a channel.

We observed that if the PU's standard deviation with MAR is low such as 0 (user/ms), most next-hop users or nodes can select the same channel pairs, having the same MAR. Hence, all the routing protocols achieve a similar probability of packet collisions by PU and SU across a CRAHN (see Figure 15). This happens due to the unavailability of PU on a channel. So, no activity is detected on any channel. In case of medium (0.4 (user/ms)) PU's standard deviation with MAR, the channel and user pairs have a difference in user interferences of the SU to the PU and the SU to the SU in the MCSUI routing protocol (Figure 16). This reduces the packet collisions with PUs up to 30% compared to the AODV routing. The CP routing reduces collisions with PUs up to 19% and 14% for OSA routing. Similarly, a high standard deviation level (0.8 (user/ms)) of MAR of the PU also shows similar trends to the number of packet collisions with increment in activities of PUs (Figure 17). This happens due to the increment in duration of channel availability and also the number of available channels. It is noted that the MCSUI routing protocol is more appropriate in minimizing user interferences than the other routing protocols, since it uses an additional type of control packet (PU-RERR) to improve the route efficiency.

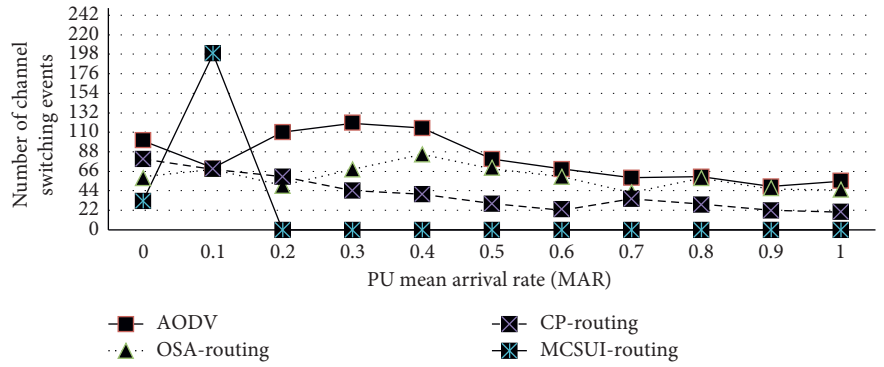

Figure 12: Channel switching events of SU at PU's sd of MAR as 0.0 (user/ms).

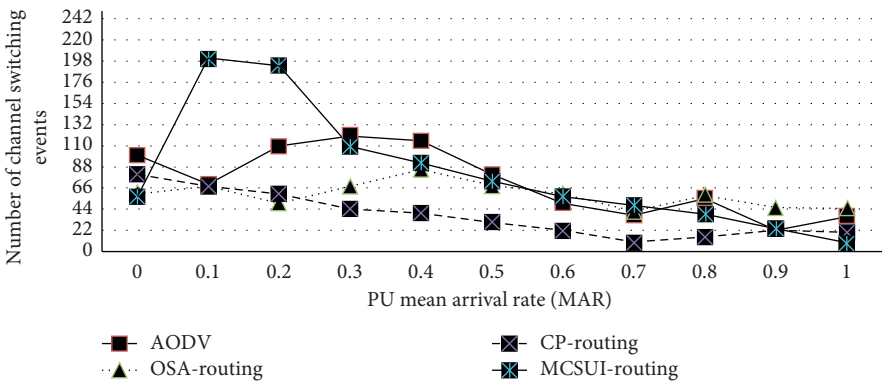

Figure 13: Channel switching events of SU at PU's sd of MAR as 0.4 (user/ms).

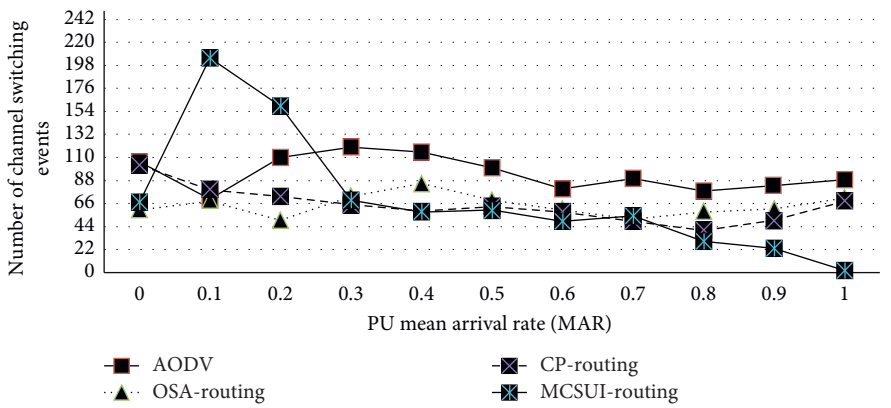

Figure 14: Channel switching events of SU at PU's sd of MAR as 0.8 (user/ms).

6.3. Minimizing in End-To-End Delay (EED). The number of channel switching events is reduced due to minimized user interferences, and this effect also helps in minimizing EED. It is observed that the EED of the SU increases with the increase in PU's activities (see Figure 18). The EED consists of switching, transmission, and queuing and back-off delays. When the standard deviation of MAR for the activity of PU is low, the EED is observed as high due to less routing choices available for SUs. The availability of channels and routing paths choices are increases with increment in the standard deviation of MAR of PUs. When the PU's availability level of MAR increases from 0.4 (user/ms) (Figure 19) to 0.8 (user/ms) (Figure 20), the EED decreases proportionally. The MCSUI routing protocol selects routes that reduces the number of channel switching events caused by PU-SU user interferences contributing to minimizing EED. The MCSUI routing achieves a minimized EED for the SU up to 89% in compared to that of the other routing protocols. This happens due to the increment in the standard deviation of MAR of PUs, which ultimately

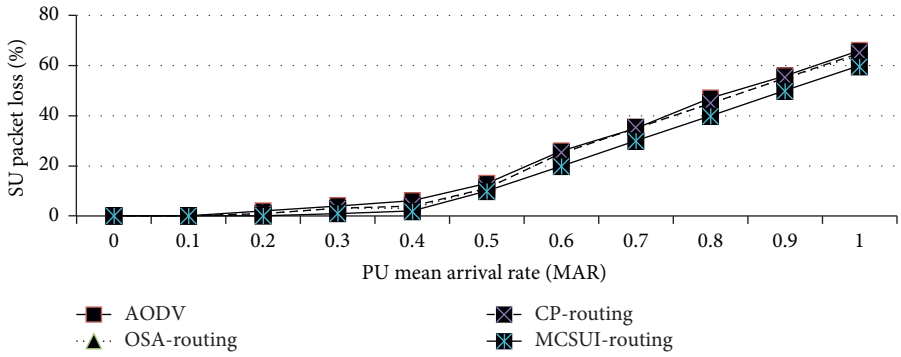

Figure 15: Packet loss of SU at PU's sd of MAR as 0.0 (user/ms).

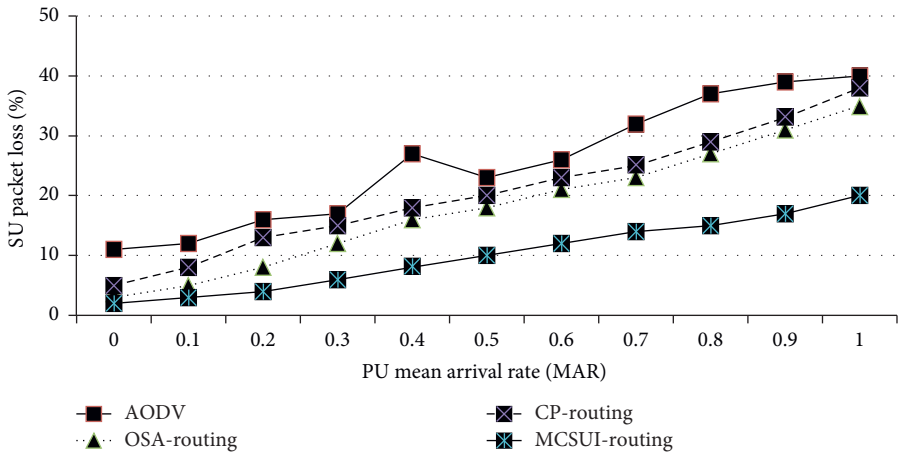

Figure 16: Packet loss of SU at PU's sd of MAR = 0.4 (user/ms).

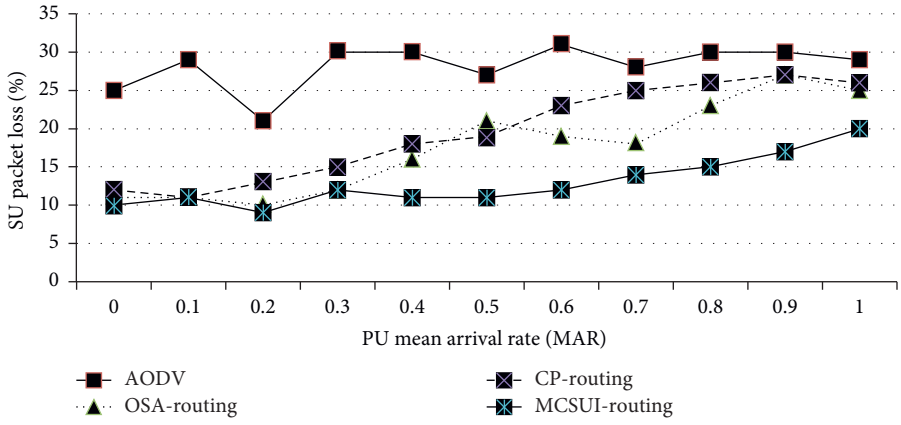

Figure 17: Packet loss of SU at PU's sd of MAR = 0.8 (user/ms).

creates routes with more available channel and route choices.

Moreover, we have the following two key observations. Firstly, the fluctuations in EED of the SU can be observed because the routes of AODV and CP routing protocols are static and unaware of the unpredictability of the PU, while the routes of the MCSUI routing protocol are aware of the channel availability during the routing decision. Secondly, the CP routing protocol and the AODV routing protocol lead to deterioration in the network's routing performance with increments in PUs' activities. Hence, when the MAR of the PU increases, the CP and AODV routing protocols select the longer routes resulting in maximizing of EED for the SU. In contrast, the MCSUI routing protocol minimizes

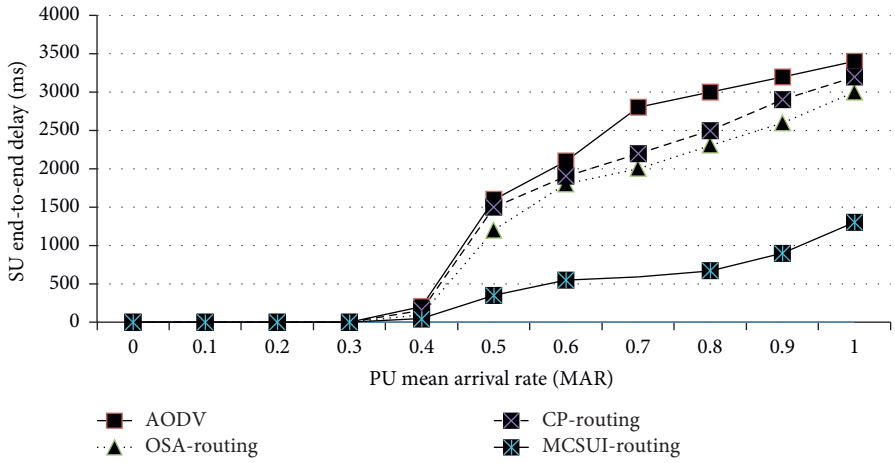

Figure 18: EED of SU for PU's sd of MAR as 0.0 (user/ms).

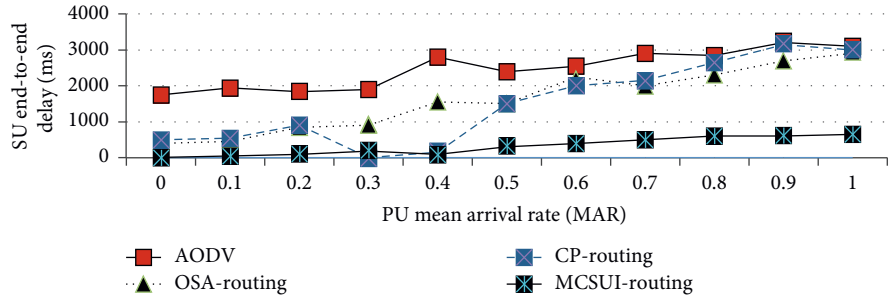

Figure 19: EED of SU for PU's sd of MAR as 0.4 (user/ms).

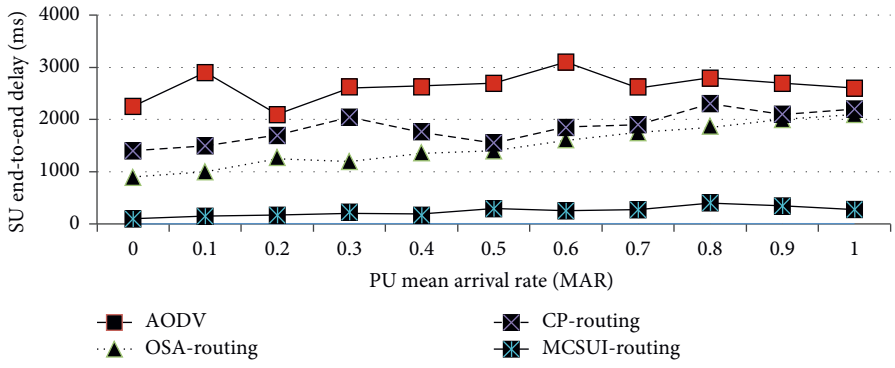

Figure 20: EED of SU for PU's sd of MAR as 0.8 (user/ms).

channel-switching events due to user interferences and, hence, selects the shortest routes using the available channel list on the network layer. Generally, the MCSUI routing minimizes the overall EED of SUs in the CRAHN as compared to the other routing protocols.

7. Conclusion

We have enabled the proposed routing protocol to minimize the number of channel switching events, packet collisions due to user interferences, and end-to-end delay during the transmission. Therein, various Reinforcement Learning- (RL-) based techniques called No-External Regret learning, Q-learning, and Learning Automata are used to Minimize Channel Switching and User Interferences. The overall Quality of Service (QoS) of CRAHN is improved through iterative network state observation of the traditional AODV routing protocol. The user interferences are categorized according to the user characteristics so that the upcoming routing decisions can be based on the channel selection history of PU or SUs over channel selection. Hence, the intraflow interference is minimized by

the implementation of No-External Regret Learning and interflow interference through the Q-Learning. The simulations are carried out with NS-2 environment. Several RL-based routing parameters are applied in the implementation to investigate the performance of the proposed routing protocol. We evaluate the performance of the proposed routing protocol against the various existing AODV, OSA, and CP protocols. We observe that our proposed routing protocol outperforms the existing protocols and achieves good results in terms of the number of channel switching events, packet loss due to user interferences, and end-to-end delay. In future, the efficiency of the proposed routing protocol can be improved using the recent machine learning techniques and the effect of mobile PUs. It is very important to observe the impact of data-aggregation mechanism in conjunction with RL-based routing on energy-efficiency and its effect on performance of proposed MCSUI routing protocol.

Data Availability

All data generated or analysed during this study are included in this published article.

Conflicts of Interest

The authors declare no conflicts of interest.

Acknowledgments

This work was supported by the Yayasan Universiti Teknologi Petronas, Malaysia, Grant no. 015LC0-029.

References

[1] J. Mitola and G. Q. Maguire, "Cognitive radio: making software radios more personal," *Journal of IEEE on Personal Communications*, vol. 6, no. 4, pp. 13–18, 2002.

[2] H. Afzal, M. Mufti, A. Raza, and A. Hassan, "Performance analysis of QoS in IoT based cognitive radio Ad Hoc network," *Concurrency and Computation: Practice and Experience*, vol. 32, Article ID e5853, 2020.

[3] T. D. Le and C. Seong-Gon, "Connectivity analysis of cognitive radio ad-hoc networks with multi-pair primary networks," *Sensors*, vol. 19, no. 3, p. 565, 2019.

[4] K. Sehgal and S. Markande, "Comparative study of routing protocols in cognitive radio networks," in *Proceedings of the IEEE International Conference on Pervasive Computing (ICPC)*, vol. 6, pp. 1–5, Pune, India, January 2015.

[5] A. Ali, S. Tariq, M. Iqbal et al., "Adaptive bitrate video transmission over cognitive radio networks using cross layer routing approach," *IEEE Transactions on Cognitive Communications and Networking*, 2020.

[6] G. Arsany, K. Mohammed, H. Karim et al., "Cooperation-based multi-hop routing protocol for cognitive radio network," *Journal of Network and Computer Applications*, vol. 110, no. 5, pp. 27–42, 2018.

[7] M. Cesana, F. Cuomo, and E. Ekici, "Routing in cognitive radio networks: Challenges and solutions," *Ad Hoc Networks*, vol. 9, no. 3, pp. 228–248, 2011.

[8] FCC (Federal Communications Commission), "Spectrum policy task force," Federal Communications Commission, Washington, DC, USA, 2020, https://transition.fcc.gov/sptf/files/SEWGFinalReport_1.pdfReport of the Spectrum Efficiency Working Group: Technical Report.

[9] R. Kumbhkar, T. Kuber, N. B. Mandayam, and I. Seskar, "Opportunistic spectrum allocation for max-min rate in NC-OFDMA," in *Proceedings of the IEEE International Symposium on Dynamic Spectrum Access Networks (DySPAN)*, pp. 385–391, Stockholm, Sweden, September 2015.

[10] P. Cheng and S. He, "Observer-based finite-time asynchronous control for a class of hidden Markov jumping systems with conic-type non-linearities," *IET Control Theory & Applications*, vol. 14, no. 2, pp. 244–252, 2020.

[11] P. Cheng, J. Wang, S. He, X. Luan, and F. Liu, "Observer-based asynchronous fault detection for conic-type nonlinear jumping systems and its application to separately excited DC motor," *IEEE Transactions on Circuits and Systems I: Regular Papers*, vol. 67, no. 3, pp. 951–962, 2020.

[12] P. Cheng, S. He, J. Cheng, X. Luan, and F. Liu, "Asynchronous output feedback control for a class of conic-type nonlinear hidden Markov jump systems within a finite-time interval," *IEEE Transactions on Systems, Man, and Cybernetics: Systems*, vol. 50, 2020.

[13] L. Duan, J. Huang, and B. Shou, "Duopoly competition in dynamic spectrum leasing and pricing," *IEEE Transactions on Mobile Computing*, vol. 11, no. 11, pp. 1706–1719, 2012.

[14] Z. Mahdi, A. K. M. M. Islam, B. Sabariah et al., "Medium access control protocols for cognitive radio ad hoc networks: a survey," *Sensors*, vol. 17, no. 9, p. 2136, 2017.

[15] S. S. Mahsa, E. S. Mohammad, and S. Masoud, "A reinforcement learning based routing in cognitive radio networks for primary users with multi-stage periodicity," *Journal of Wireless Personal Communications*, vol. 101, no. 1, pp. 465–490, 2018.

[16] R. Li and P. Zhu, "Spectrum allocation strategies based on QoS in cognitive vehicle networks," *IEEE Access*, vol. 8, pp. 99922–99933, 2020.

[17] L. Singh and N. Dutta, "A novel approach for better QoS in cognitive radio ad hoc networks using Cat optimization," *Data Management, Analytics and Innovation*, Springer, vol. 1042Berlin, Germany, 2020.

[18] G. Jakllari, S. Eidenbenz, N. Hengartner, S. V. Krishnamurthy, and M. Faloutsos, "Link positions matter: a noncommutative routing metric for wireless mesh networks," *IEEE Transactions on Mobile Computing*, vol. 11, no. 1, pp. 61–72, 2012.

[19] R. E. Tuggle, "Cognitive multipath routing for mission critical multi-hop wireless networks," in *Proceedings of the IEEE 42nd Southeastern Symposium on System Theory (SSST)*, Tyler, TX, USA, March 2010.

[20] M. Radi, B. Dezfouli, K. Abu Bakar, S. Abd Razak, and M. A. Nematbakhsh, "Interference-aware multipath routing protocol for QoS improvement in event-driven wireless sensor networks," *Tsinghua Science and Technology*, vol. 16, no. 5, pp. 475–490, 2011.

[21] A. S. Cacciapuoti, M. Caleffi, and L. Paura, "Reactive routing for mobile ad hoc networks," *Ad Hoc Networks*, vol. 10, no. 5, pp. 803–815, 2012.

[22] L. Indhumathi and R. Vadivel, "Adaptive delay tolerant routing protocol (ADTRP) for cognitive radio mobile ad hoc networks," *International Journal of Computer Applications*, vol. 128, no. 6, pp. 19–24, 2015.

[23] A. L. Nisar, A. B. Altaf, G. M. Mir, and R. A. Simnani, "Quality of service provisioning in cognitive radio network," *Orient*

Journal of Computer Science & Technology, vol. 10, no. 4, pp. 780–787, 2017.

[24] W. Y. Lee and I. F. Akyildiz, "Optimal spectrum sensing framework for cognitive radio networks," *Journal of IEEE Transactions on Wireless Communication*, vol. 7, no. 10, pp. 3845–3857, 2008.

[25] D. Niyato, E. Hossain, and P. Wang, "Optimal channel access management with QoS support for cognitive vehicular networks," *IEEE Transactions on Mobile Computing*, vol. 10, no. 4, pp. 573–591, 2011.

[26] X. Jin, R. Zhang, J. Sun, and Y. Zhang, "TIGHT: a geographic routing protocol for cognitive radio mobile ad hoc networks," *IEEE Transactions on Wireless Communications*, vol. 13, no. 8, pp. 4670–4681, 2014.

[27] F. Z. Benidris, B. Benmammar, and F. T. Bendimerad, "An efficient spectrum allocation mechanism for cognitive radio networks," *Journal of IEEE Transactions on Communications*, vol. 13, no. 7, pp. 534–547, 2014.

[28] L. Gul, X. Zhong, and S. Zhou, "Traffic assignment algorithm for multi-path routing in cognitive radio ad hoc networks," in *Proceeedings of the IEEE Wireless Communications and Networking Conference (WCNC)*, Shanghai, China, April 2013.

[29] J. Chen, H. Li, and J. Wu, "WHAT: A novel routing metric for multi-hop cognitive wireless networks," in *Proceeedings of the 19th IEEE Annual Wireless and Optical Communications Conference*, Shanghai, China, May 2010.

[30] J. Jia, J. Zhang, and Q. Zhang, "Cooperative relay for cognitive radio networks," in *Proceedings of the IEEE INFOCOM*, pp. 2304–2312, Turin, Italy, April 2009.

[31] R. Biswas and J. Wu, "Minimizing the number of channel switches of mobile users in cognitive radio ad-hoc networks," *Journal of Sensor and Actuator Networks*, vol. 9, no. 2, p. 23, 2020.

[32] S. AlQahtani and A. Alotaibi, "A route stability-based multipath QoS routing protocol in cognitive radio ad hoc networks," *Wireless Networks*, vol. 25, no. 5, pp. 2931–2951, 2019.

[33] Y. Yao, A. Popescu, and A. Popescu, "On prioritised opportunistic spectrum access in cognitive radio cellular networks," *Transactions on Emerging Telecommunications Technologies*, vol. 27, no. 2, pp. 294–310, 2016.

[34] X. Huang, D. Lu, P. Li, and Y. Fang, "Coolest path: spectrum mobility aware routing metrics in cognitive ad hoc networks," in *Proceeding of the 31st International Conference of IEEE on Distributed Computing Systems (ICDCS)*, Minneapolis, MN, USA, June 2011.

[35] C. Perkins and E. Belding-Royer, "Ad hoc on-demand distance vector (AODV) routing protocol," The Internet Society, Reston, VA, USA, 2003, http://www.ietf.org/rfc/rfc3561.txtRequest for Comments 3561 in Internet Engineering Task Force.

[36] G. E. Box and M. E. Muller, "Multi-agent learning using a variable learning rate," *Artificial Intelligence*, vol. 136, no. 2, pp. 215–250, 2002.

Hindawi
Complexity
Volume 2020, Article ID 2903635, 13 pages
https://doi.org/10.1155/2020/2903635

Research Article

Stochastic Stabilization of Malware Propagation in Wireless Sensor Network via Aperiodically Intermittent White Noise

Xiaojing Zhong,[1] **Baihao Peng**,[1] **Feiqi Deng**,[2] **and Guiyun Liu**[1]

[1]*School of Mechanical and Electrical Engineering, Guangzhou University, Guangzhou 510006, China*
[2]*School of Automation Science and Engineering, South China University of Technology, Guangzhou 510640, China*

Correspondence should be addressed to Guiyun Liu; liugy@gzhu.edu.cn

Received 22 May 2020; Accepted 10 July 2020; Published 13 August 2020

Academic Editor: Shuping He

In this paper, we propose a novel heterogeneous model to describe the propagation dynamics of malware (viruses, worms, Trojan horses, etc.) in wireless sensor networks. Our model takes into consideration different battery-level sensor nodes contrary to existing models. In order to control the spread of malware, we design an aperiodically intermittent controller driven by white noise, which has striking advantages of lower cost and more flexible control strategy. We give a distinct condition on stability in probability one using graph-theoretical Lyapunov function and stochastic analysis method. Our results show that the nonlinear malware propagation system can be stabilized by intermittent stochastic perturbation under the intermittent time related to stochastic perturbation intensity. Our theoretical results can be applied to understand the observed mechanisms of malware and design interventions to control the spread of malware. Numerical simulations illustrate our analytical results clearly.

1. Introduction

With the improvement of wireless sensor technology, wireless sensor networks (WSNs) are used in many new scenarios: intelligent transportation network, water quality monitoring, military target detection, etc. Due to wireless feature and special structure of wireless sensor network, it is vulnerable to malware attack which can eavesdrop and paralyze the network [1–3]. Consequently, mathematical modeling and control strategies of malware propagation are of vital importance in order to predict its effects and defend it. In recent years, many scientific literatures have appeared, specifically, global model and the related global behaviour of WSNs by the concept of epidemiology. In the epidemic system, all people separate into different compartments such as S (Susceptible), E (Exposed), I (Infectious), R (Recovered), and so on. Toutonji et al. [4] proposed a VEIS-V worm attack propagation model which considers security countermeasures during worm attack. Bimal and Keshri [5] established a SEIRSV model by introducing a maintenance mechanism to sleep nodes. Zhu and Zhao [6] considered a SIR model which has logistic growth. Wang et al. [7] proposed a SCI model to describe the propagation dynamics of mobile sensor worm.

However, the above global models cannot cover individual feature and capability. In this sense, individual-based model will be more accurate to model malware propagation since it values individual diversity and derives both malware relationship and individual feature from malware propagation. Under the framework of heterogeneous complex network theory, the connection topology of nodes can be defined by node degree and the related degree distribution. Several complex network models have been studied for the epidemic model [8–11], alcoholism model [12], information spreading model [13–17], etc. But for wireless sensor network, there are few achievements: del Rey et al. [18] established heterogeneous SIS and SIR models for malware propagation in WSNs; all nodes are separated into three

compartments based on the classic SIR epidemic model. Li et al. [19] considered a SIR network malware propagation model; Li's SIR model is different from del Rey's heterogeneous model which considers tree-based networks. Inspired by stifler state in the rumor spreading model, Hosseini and Azgomi [20] proposed a SEIRS model. They assumed that nodes could be vaccinated and immunized to the malware infection. All of the above models did not consider sensor's energy consumption, which affects seriously the information transmission quality. Nodes may not have enough energy to propagate malware by sending information to their neighbors. Proceeding from this angle, infected state should be separated into infected state with high capacity level and infected state with low capacity level. It is worth to mention that most of the results concentrate on dynamic analysis of the deterministic model (global or individual-based model) by the basic reproduction number R_0, which is calculated by the next generation matrix method. But there are rare results on malware control strategies if malware becomes endemic ($R_0 > 1$).

As is well known, stochastic noises can stabilize an unstable system [21–27]. Its application extends to many practical areas, such as sleep improvement, tone discrimination [28], and financial stability [21, 23]. From the consideration of reducing control cost and control time, discontinuous controllers have been designed to stabilize a given system such as feedback control [29–32], pinning control [33], impulsive control [34], adaptive control [35–40], and intermittent control [41–44]. As for intermittent control, control time is divided into periodic and aperiodic type. Periodically intermittent control has been studied by many authors especially in synchronization problems. Zhang et al. [41] designed a periodically intermittent linear controller driven by white noises to stabilize an unstable memristor-based system. As Liu and Chen [45, 46] have mentioned before, the requirement of periodicity is unusual in real world application, while aperiodically intermittent control strategy needs a complex management to study the dynamic behaviour of the controlled system. We highlight Liu and Chen [45, 46] who investigated aperiodically intermittent deterministic controller for complex coupled deterministic system, and sufficient conditions have been given to guarantee global synchronization.

Stochastic control has been proved to be sufficiently useful in many fields. But for the best of our knowledge, there is no work on aperiodically intermittent stochastic stabilization for malware propagation; the application on malware propagation needs to be explored. This motivates us to investigate this kind of scheme oriented to the security issue for WSNs. In this paper, we will design an aperiodically intermittent control strategy. In this strategy, we will focus on quantitative conditions for network to stabilize. The main contributions can be summarized as follows:

(i) Compared with the previous works on malware spreading models on WSNs, our SI^LI^HA model is a new model which considers both individual behaviours and sensor capacitance. It can be used to solar heterogeneous network system.

(ii) Compared with the previous works on spreading control, the control itself is random perturbation and the control time is aperiodically intermittent rather than continuous, and starting time and control length are arbitrary. We can control steady rate autonomously by adjusting the work width. In this angle, our control strategy is more flexible.

The paper is organized as follows. In Section 2, we establish a new malware propagation model on WSNs at first, which considers different battery-level sensor nodes. Then, we analyze the dynamic behaviour of the model. In Section 3, we design an aperiodically intermittent stochastic noise controller to control malware spreading. The control intensity expression reflects the relationship between system parameters and network topological structure. In Section 4, numerical simulations of the proposed model are given to show the power of aperiodically intermittent noise controller. Finally, we conclude the paper in Section 5.

2. Model Formulation

According to topological structures of WSNs, all nodes partition into n groups based on different nodal degrees. Each group i is further compartmentalized into four states:

(1) Susceptible (S_i): the nodes in this state are prone to being infected by the implantation of malware and will become an infected one if it connects to an infected node.

(2) Infectious with high energy level (I_i^H): the nodes in this state have already been infected by malware successfully and have stored up enough energy to continue propagating the malware.

(3) Infectious with low energy level (I_i^L): the nodes in this state have already been infected by malware successfully but do not have sufficient energy to propagate malware by sending information to their neighbors.

(4) Antimalware program activated (A_i): when nodes in state I^H and state I^L are detected to be infected, the nodes will activate antimalware program to clear up the infection. The node activated by the antimalicious program will no longer be invaded by the same malware.

Based on the sensor features and transition characters, the malware propagation process is described as follows: when a susceptible node connects to an infected node, the susceptible node with high energy level becomes an infected node with probability β_1 and the susceptible with low energy level node becomes an infected node with probability β_2. Both the contact rates β_1 and β_2 are positive constants. The malware itself will not cause additional cost to infected node. The infected node with low energy level can become infected

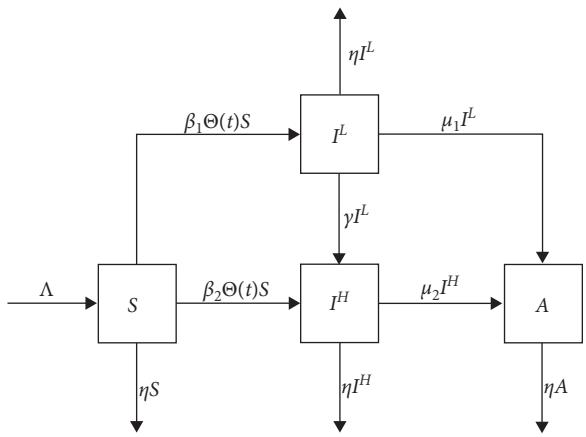

Figure 1: The flow diagram of the propagation model.

node with high level if it is recharged, and the charge rate is a positive constant γ. The influence of the malware on the natural mortality rate of infected nodes should be ignored and nodes in four states are assigned equal natural mortality rate η which satisfies $\eta \geq 0$. Figure 1 shows state transition diagram of the model.

Thus, our model can be formulated by the following ordinary differential equations:

$$\begin{cases} S_i(t)' = \Lambda - \beta_1 i\Theta(t)S_i(t) - \beta_2 i\Theta(t)S_i(t) - \eta S_i(t), \\ I_i^L(t)' = \beta_1 i\Theta(t)S_i(t) - \gamma I_i^L(t) - \mu_1 I_i^L(t) - \eta I_i^L(t), \\ I_i^H(t)' = \beta_2 i\Theta(t)S_i(t) + \gamma I_i^L(t) - \mu_2 I_i^H(t) - \eta I_i^H(t), \\ A_i(t)' = \mu_1 I_i^L(t) + \mu_2 I_i^H(t) - \eta A_i(t), \end{cases} \tag{1}$$

with initial values

$$\begin{aligned} S_i(0) &\geq 0, \\ I_i^L(0) &\geq 0, \\ I_i^H(0) &\geq 0, \\ A_i(0) &\geq 0, \\ S_i(0) + I_i^L(0) + I_i^H(0) + A_i(0) &= \frac{\Lambda}{\eta}, \end{aligned} \tag{2}$$

where $i = 1, \ldots, n$, represents the nodal degree. $\Theta(t)$ represents the probability that an edge connects to an infectious sensor node at time t. Its expression is

$$\Theta(t) = \frac{1}{\langle j \rangle} \sum_{j=1}^{n} jp(t) \frac{I_i^H(t)}{N_i(t)}, \tag{3}$$

where $\langle j \rangle = \sum_{j=1}^{n} jp(j)$ represents the average nodal degree. $p(j)$ represents the probability that a randomly chosen sensor node has degree j, $\sum_{j=1}^{n} p(j) = 1$. Obviously, for all i and $t \geq 0$,

$$N_i(t) = S_i(t) + I_i^L(t) + I_i^H(t) + A_i(t) = \frac{\Lambda}{\eta}. \tag{4}$$

Then, we can deduce system (1) into

$$\begin{cases} S_i(t)' = \Lambda - \beta_1 i\Theta(t)S_i(t) - \beta_2 i\Theta(t)S_i(t) - \eta S_i(t), \\ I_i^L(t)' = \beta_1 i\Theta(t)S_i(t) - \gamma I_i^L(t) - \mu_1 I_i^L(t) - \eta I_i^L(t), \\ I_i^H(t)' = \beta_2 i\Theta(t)S_i(t) + \gamma I_i^L(t) - \mu_2 I_i^H(t) - \eta I_i^H(t). \end{cases} \tag{5}$$

About the dynamic behaviour of the above deterministic model (5), we give the following corollary.

Corollary 1. *Define*

$$R_0 = \frac{[\beta_1\gamma + \beta_2(\gamma + \mu_1 + \eta)]\langle j^2 \rangle}{(\eta + \mu_2)(\gamma + \eta + \mu_1)\langle j \rangle}. \tag{6}$$

(1) If $R_0 < 1$, the malware-free equilibrium is globally asymptotically stable.

(2) If $R_0 > 1$, there is an endemic equilibrium, and it is persistent.

Remark 1. The threshold is obtained by $R_0 = ([\beta_1\gamma + \beta_2(\gamma + \mu_1 + \eta)\langle j^2 \rangle]/(\eta + \mu_2)(\gamma + \eta + \mu_1)\langle j \rangle)$, which depends on the fluctuations of the degree distribution and system parameters. Since malware will die out when $R_0 < 1$, malware prevention measures can be designed to decrease R_0, such as decreasing node connectivity to decrease the contact rates β_1, β_2 and increasing monitoring efforts on infective nodes to increase the detective rate μ_2.

3. Control Strategy

In this section, we mainly concentrate on the control strategy of malware propagation. In the context of aperiodically intermittent stochastic noise stabilization of the complex heterogeneous network system, we propose a design procedure for the noise control input to stabilize system (5). At first, we consider a stochastic noise driven by Brownian motions and a g-type structure of the controller. The controller's mathematical expression is $g(t, x(t))\dot{B}(t)$, where $B(t)$ is a $3n$-dimensional Brownian motion corresponding to system variables and $\dot{B}(t)$ is the related white noise. To be flexible and to save cost, we design the control time as aperiodically intermittent type, which admits uncertain rest times. We give a sketch of aperiodically intermittent control strategy in Figure 2, under the perturbation of g-type; the time span $[t_k, t_{k+1})$ contains the work time $[t_k, t_k + c_k)$ and the rest time $[t_k + c_k, t_{k+1})$, and c_k denotes the k-th noise width. Naturally, the noise widths satisfy $0 \leq c_k \leq t_{k+1} - t_k$. The stochastic control input system is

$$\mathrm{d}x(t) = f(t, x(t))\mathrm{d}t + g(t, x(t))\mathrm{d}B(t), \tag{7}$$

where

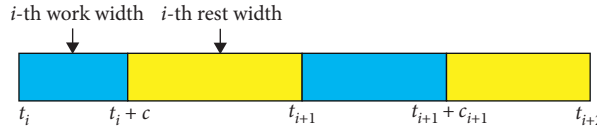

Figure 2: The sketch of aperiodically intermittent control strategy.

$$x(t) = \left(I_1^L(t), I_1^H(t), A_1(t), I_2^L(t), I_2^H(t), A_2(t), \ldots, I_n^L(t), I_n^H(t), A_n(t)\right)^T,$$

$$f(x) = \begin{bmatrix} \beta_1 i\Theta(t)S_i(t) - \gamma I_i^L(t) - \mu_1 I_i^L(t) - \eta I_i^L(t) \\ \beta_2 i\Theta(t)S_i(t) + \gamma I_i^L(t) - \mu_2 I_i^H(t) - \eta I_i^H(t) \\ \mu_1 I_i^L(t) + \mu_2 I_i^H(t) - \eta A_i(t) \end{bmatrix}_{i=1}^{n}, \tag{8}$$

$$g(t, x(t)) = \begin{cases} \sigma x(t), & t \in [t_k, t_k + c_k), \\ 0, & t \in [t_k + c_k, t_{k+1}), \end{cases}$$

with $i, k \in N$, g_1: $[t_0, \infty) \times R^n \longrightarrow R^{n\times m}$. For the aperiodically intermittent perturbation strategy, the start time and the noise width might be different, but the total perturbation time ratio should be fixed in the long term. Mathematically, there exists a positive scalar τ, such that the above time nodes satisfy the following assumption:

$$\lim_{n\longrightarrow\infty} \frac{\sum_{k=0}^{n} c_k}{t_{n+1} - t_0} = \tau. \tag{9}$$

We call τ as the control time ratio. Moreover, we assume $g(t, 0) \equiv 0$ for stochastic stability analysis, which guarantees the existence of a trivial solution $x(t, t_0, 0) \equiv 0$.

Theorem 1. *If the aperiodically perturbed intensity σ satisfies $\sigma^2 > ((2[\beta_1\gamma + \beta_2(\gamma + \mu_1 + \eta) \quad \langle j^2\rangle]/\tau(\gamma + \eta + \mu_1)\langle j\rangle) - (2(\eta + \mu_2)/\tau))$, then the infected nodes will die out with probability one.*

Proof. Define a matrix M:

$$M = \frac{[\beta_1\gamma + \beta_2(\gamma + \mu_1 + \eta)]}{(\gamma + \eta + \mu_1)\langle j\rangle} \begin{pmatrix} 1p(1) & 2p(2) & \cdots & np(n) \\ 2p(1) & 2^2p(2) & \cdots & 2np(n) \\ \vdots & \vdots & \ddots & \vdots \\ np(1) & 2np(2) & \cdots & n^2p(n) \end{pmatrix}. \tag{10}$$

We can calculate that $\rho(M) = ([\beta_1\gamma + \beta_2(\gamma + \mu_1 + \eta)\langle j^2\rangle]/(\gamma + \eta + \mu_1)\langle j\rangle)$. Let $\omega = (\omega_1, \omega_2, \ldots, \omega_n)$ be the eigenvector of M corresponding to $\rho(M)$; then, we have

$$(\omega_1, \omega_2, \ldots, \omega_n)\rho(M) = (\omega_1, \omega_2, \ldots, \omega_n)M, \tag{11}$$

where $\omega_i > 0$, $i = 1, 2, \ldots, n$. Define a Lyapunov function:

$$V\left(I_1^L, I_1^H, I_2^L, I_2^L, \ldots, I_n^L, I_n^H\right) = (\varpi\overline{x})^a, \tag{12}$$

where

$$\varpi = \left(\frac{\gamma\omega_1}{\gamma + \mu_1 + \eta}, \omega_1, \frac{\gamma\omega_2}{\gamma + \mu_1 + \eta}, \omega_2, \ldots, \frac{\gamma\omega_n}{\gamma + \mu_1 + \eta}, \omega_n\right),$$
$$\overline{x} = \left(I_1^L, I_1^H, I_2^L, I_2^H, \ldots, I_n^L, I_n^H\right)^T, \tag{13}$$

and $0 < a < 1/2$ is a constant. Using Itô formula, we obtain

$$\mathscr{L}V = a(\varpi\overline{x})^{a-1}\varpi\overline{f}(\overline{x}) + \frac{a(a-1)(\varpi\overline{x})^{a-2}}{2} Tr\left[\overline{g}^T(\overline{x})\varpi^T\varpi\overline{g}(\overline{x})\right],$$
$$V(\overline{x}) = V(t_0, \overline{x}_0) + \int_{t_0}^{t} \mathscr{L}V\overline{x}(s)ds + \int_{t_0}^{t} a(\varpi\overline{x})^{a-1}\varpi\overline{g}(\overline{x})\mathrm{d}B(s), \tag{14}$$

where

$$\overline{f}(\overline{x}) = \begin{pmatrix} \beta_1\Theta(t)S_1 - \gamma I_1^L - \mu_1 I_1^L(t) - \eta I_1^L(t) \\ \beta_2\Theta(t)S_1 + \gamma I_1^L(t) - \mu_2 I_1^H(t) - \eta I_1^H(t) \\ \vdots \\ n\beta_1\Theta(t)S_n - \gamma I_n^L - \mu_1 I_n^L(t) - \eta I_n^L(t) \\ (n\beta_2\Theta(t)S_n + \gamma I_n^L(t) - \mu_2 I_n^H(t) - \eta I_n^H(t))^T \end{pmatrix}, \tag{15}$$
$$\overline{g}(\overline{x}) = \begin{cases} \sigma\overline{x}, & t \in [t_k, t_k + c_k), \\ 0, & t \in [t_k + c_k, t_{k+1}). \end{cases}$$

Note that $\overline{f}(\overline{x})$ can be regarded as a linear growth function of S_i; as $S_i \le N_i = \Lambda/\eta$ for $t \ge t_0$, we can derive that

$$\begin{aligned} \int_{t_0}^{t} \mathscr{L}V(\overline{x}(s))\mathrm{d}s &= \int_{t_0}^{t} e^{c(s-t_0)} a(\varpi\overline{x})^{a-1}\varpi\overline{f}(\overline{x})\mathrm{d}t \\ &\quad + \int_{t_0}^{t} \frac{a(a-1)(\varpi\overline{x})^{a-2}}{2} Tr\left[\overline{g}^T(\overline{x})\varpi^T\varpi\overline{g}(\overline{x})\right]\mathrm{d}t \\ &\le \int_{t_0}^{t} a(\varpi\overline{x})^{a-1}(M - (\mu_2 + \eta)E)(I_1, I_2, \ldots, I_n)^T\mathrm{d}t \\ &\quad + \int_{t_0}^{t} \frac{a(a-1)(\varpi\overline{x})^{a-2}}{2} Tr\left[\overline{g}^T(\overline{x})\varpi^T\varpi\overline{g}(\overline{x})\right]\mathrm{d}t, \end{aligned} \tag{16}$$

where E represents an elementary matrix or an identity matrix. By condition (11), the above inequation becomes

$$\int_{t_0}^{t} \mathscr{L}V(\overline{x}(s))\mathrm{d}s \le \int_{t_0}^{t} a(\rho(M)-\mu_2-\eta)(\omega\overline{x})^a \mathrm{d}t + \int_{t_0}^{t} \frac{a(a-1)(\omega\overline{x})^{a-2}}{2} Tr\left[\overline{g}^T(\overline{x})\omega^T\omega\overline{g}(\overline{x})\right]\mathrm{d}t. \tag{17}$$

Then, we discuss the time t in different time intervals. Obviously, there exists one positive integer m such that $t \in [t_m, t_{m+1})$.

(1) If $t \in [t_m, t_m + c_m)$, then

$$\begin{aligned}\int_{t_0}^{t} \frac{a(a-1)(\omega\overline{x})^{a-2}}{2} Tr\left[\overline{g}^T(\overline{x})\omega^T\omega\overline{g}(\overline{x})\right]\mathrm{d}t &= \int_{t_0}^{t_0+c_0} \frac{a(a-1)(\omega\overline{x})^{a-2}}{2} Tr\left[\overline{g}_1^T(\overline{x})\omega^T\omega\overline{g}_1(\overline{x})\right]\mathrm{d}t + 0 \\ &+ \int_{t_1}^{t_1+c_1} \frac{a(a-1)(\omega\overline{x})^{a-2}}{2} Tr\left[\overline{g}_1^T(\overline{x})\omega^T\omega\overline{g}_1(\overline{x})\right]\mathrm{d}t + 0 + \cdots \\ &+ \int_{t_m}^{t} \frac{a(a-1)(\omega\overline{x})^{a-2}}{2} Tr\left[\overline{g}_1^T(\overline{x})\omega^T\omega\overline{g}_1(\overline{x})\right]\mathrm{d}t \\ &= \int_{t_0}^{t_0+c_0} \frac{a(a-1)\sigma^2(\omega\overline{x})^a}{2}\mathrm{d}t + 0 + \int_{t_1}^{t_1+c_1} \frac{a(a-1)\sigma^2(\omega\overline{x})^a}{2}\mathrm{d}t + 0 + \cdots \\ &+ \int_{t_m}^{t} \frac{a(a-1)\sigma^2(\omega\overline{x})^a}{2}\mathrm{d}t,\end{aligned} \tag{18}$$

which means

$$\begin{aligned}\int_{t_0}^{t} \mathscr{L}V(\overline{x}(s))\mathrm{d}s &= \int_{t_0}^{t_0+c_0} \left[\rho(M)-\eta-\mu_2+\frac{1}{2}(a-1)\sigma^2\right] a(\overline{\omega x})^a \mathrm{d}t \\ &+ \int_{t_0+c_0}^{t_1} (\rho(M)-\eta-\mu_2) a(\overline{\omega x})^a \mathrm{d}t + \int_{t_1}^{t_1+c_1} \left[\rho(M)-\eta-\mu_2+\frac{1}{2}(a-1)\sigma^2\right] a(\overline{\omega x})^a \mathrm{d}t \\ &+ \int_{t_1+c_1}^{t_2} (\rho(M)-\eta-\mu_2) a(\overline{\omega x})^a \mathrm{d}t + \cdots + \int_{t_m}^{t} \left[\rho(M)-\eta-\mu_2+\frac{1}{2}(a-1)\sigma^2\right] a(\overline{\omega x})^a \mathrm{d}t \\ &\le \sup_{t_0\le s\le t} a(\overline{\omega x})^a \left[(\rho(M)-\eta-\mu_2)(t-t_0)t + n\frac{1}{2}q(a-1)h\left(\sigma^2\sum_{i=0}^{m-1} c_i + t - t_m\right)\right].\end{aligned} \tag{19}$$

(2) If $t \in [t_m + c_m, t_{m+1})$, then

$$\begin{aligned}\int_{t_0}^{t} \frac{a(a-1)(\omega\overline{x})^{a-2}}{2} Tr\left[\overline{g}^T(\overline{x})\omega^T\omega\overline{g}(\overline{x})\right]\mathrm{d}t &= \int_{t_0}^{t_0+c_0} \frac{a(a-1)(\omega\overline{x})^{a-2}}{2} Tr\left[\overline{g}_1^T(\overline{x})\omega^T\omega\overline{g}_1(\overline{x})\right]\mathrm{d}t + 0 \\ &+ \int_{t_1}^{t_1+c_1} \frac{a(a-1)(\omega\overline{x})^{a-2}}{2} Tr\left[\overline{g}_1^T(\overline{x})\omega^T\omega\overline{g}_1(\overline{x})\right]\mathrm{d}t + 0 + \cdots \\ &+ \int_{t_m}^{t_m+c_m} \frac{a(a-1)(\omega\overline{x})^{a-2}}{2} Tr\left[\overline{g}_1^T(\overline{x})\omega^T\omega\overline{g}_1(\overline{x})\right]\mathrm{d}t + 0 \\ &= \int_{t_0}^{t_0+c_0} \frac{a(a-1)\sigma^2(\omega\overline{x})^a}{2}\mathrm{d}t + 0 + \int_{t_1}^{t_1+c_1} \frac{a(a-1)\sigma^2(\omega\overline{x})^a}{2}\mathrm{d}t + 0 + \cdots \\ &+ \int_{t_m}^{t_m+c_m} \frac{a(a-1)\sigma^2(\omega\overline{x})^a}{2}\mathrm{d}t + 0,\end{aligned} \tag{20}$$

which means

$$\begin{aligned}\int_{t_0}^{t} LV(\overline{x}(s))\mathrm{d}s &= \int_{t_0}^{t_0+c_0}\left[\rho(M)-\eta-\mu_2+\frac{1}{2}(a-1)\sigma^2\right]a(\overline{\omega x})^a\mathrm{d}t\\ &+\int_{t_0+c_0}^{t_1}(\rho(M)-\eta-\mu_2)a(\overline{\omega x})^a\mathrm{d}t+\int_{t_1}^{t_1+c_1}\left[\rho(M)-\eta-\mu_2+\frac{1}{2}(a-1)\sigma^2\right]a(\overline{\omega x})^a\mathrm{d}t\\ &+\int_{t_1+c_1}^{t_2}(\rho(M)-\eta-\mu_2)a(\overline{\omega x})^a\mathrm{d}t+\cdots+\int_{t_m}^{t_m+c_m}\left[\rho(M)-\eta-\mu_2+\frac{1}{2}(a-1)\sigma^2\right]a(\overline{\omega x})^a\mathrm{d}t\\ &+\int_{t_m+c_m}^{t}(\rho(M)-\eta-\mu_2)a(\overline{\omega x})^a\mathrm{d}t\\ &\le \sup_{t_0\le s\le t}a(\overline{\omega x})^a\left[(\rho(M)-\eta-\mu_2)(t-t_0)+\frac{1}{2}(a-1)\left(\sigma^2\sum_{i=0}^{m}c_i\right)\right].\end{aligned} \tag{21}$$

Comparing Case (1) and Case (2), we can conclude for $t_m \le t < t_{m+1}$ that

$$\begin{aligned}(\overline{\omega x})^a &\le (\overline{\omega x}_0))^a+\sup_{t_0\le s\le t}a(\overline{\omega x})^a\left[(\rho(M)-\eta-\mu_2)(t_{m+1}-t_0)+\frac{1}{2}(a-1)\left(\sigma^2\sum_{i=0}^{m}c_i\right)\right]\\ &+\int_{t_0}^{t}a(\omega\overline{x})^{a-1}\omega\overline{g}(\overline{x})\mathrm{d}B(s).\end{aligned} \tag{22}$$

Taking the expectation on both sides of the above inequation gives

$$\begin{aligned}E(\overline{\omega x})^a &\le (\overline{\omega x}_0))^a+E\sup_{t_0\le s\le t}a(\overline{\omega x})^a\left[(\rho(M)-\eta-\mu_2)(t_{m+1}-t_0)+\frac{1}{2}(a-1)\left(\sigma^2\sum_{i=0}^{m}c_i\right)\right]\\ &=(\overline{\omega x}_0))^a+aE\left(\sup_{t_0\le s\le t}(\overline{\omega x})^a\right)\left[(\rho(M)-\eta-\mu_2)(t_{m+1}-t_0)+\frac{1}{2}(a-1)\left(\sigma^2\sum_{i=0}^{m}c_i\right)\right]\\ &=(\overline{\omega x}_0))^a+a(t_{m+1}-t_0)\left[(\rho(M)-\eta-\mu_2)+\frac{1}{2}(a-1)\sigma^2\tau_m\right]E\left(\sup_{t_0\le s\le t}(\overline{\omega x})^a\right)\\ &=(\overline{\omega x}_0))^a+\zeta_{m,a}E\left(\sup_{t_0\le s\le t}(\overline{\omega x})^a\right),\end{aligned} \tag{23}$$

where $\zeta_{m,a}=a(t_{m+1}-t_0)[(\rho(M)-\eta-\mu_2)+(1/2)(a-1)\sigma^2\tau_m]$. Since $\lim_{m\longrightarrow\infty}\tau_m=\tau$, there exists a positive integer m_0 such that when $m>m_0$,

$$\begin{aligned}\left(1-\zeta_{m,a}\right)E(\overline{\omega x})^a &\le E(\overline{\omega x})^a-\zeta_{m,a}E\left(\sup_{t_0\le s\le t}(\overline{\omega x})^a\right)\\ &\le (\overline{\omega x}_0))^a,\end{aligned} \tag{24}$$

which implies

$$E(\|\overline{x}\|^a)\le\frac{E(\overline{\omega x})^a}{\xi^a}\le\frac{(\overline{\omega x}_0))^a}{\xi^a\left(1-\zeta_{m,a}\right)}, \tag{25}$$

where $\xi=\min\{(\gamma/(\gamma+t\eta n+q\mu_1))\omega_1 t, n(\gamma/(\gamma+\eta+\mu_1))q\ \omega_2 h,_{\ldots}\ x, 7(\gamma/(\gamma+\eta+\mu_1))C\omega_n\}$. By Chebyshev inequality, for any $\varepsilon>0$, we have

$$P\{\|\overline{x}\|\ge\varepsilon\}\le\frac{E(\|\overline{x}\|^a)}{\varepsilon^a}\le\frac{(\overline{\omega x}_0))^a}{(\varepsilon\xi)^a\left(1-\zeta_{m,a}\right)}. \tag{26}$$

If $(\rho(M)-\eta-\mu_2)+(1/2)(a-1)\sigma^2\tau_m<0$, from the definition of $\zeta_{m,a}$, we can obtain $\zeta_{m,a}\longrightarrow-\infty$ when $m\longrightarrow\infty$. Consequently, we have

$$\lim_{t\longrightarrow\infty} P\{\|\overline{x}\| \geq \varepsilon\} \leq \lim_{t\longrightarrow\infty} \frac{(\overline{\omega x}_0))^a}{(\varepsilon\xi)^a\left(1-\zeta_{m,a}\right)} = \lim_{t\longrightarrow\infty} \frac{(\overline{\omega x}_0))^a}{(\varepsilon\xi)^a\left(1-\zeta_{m,a}\right)} = 0. \tag{27}$$

Then, we deduce that

$$P\left\{\lim_{t\longrightarrow\infty} \|\overline{x}\| \geq \varepsilon\right\} = 0. \tag{28}$$

Since ε is arbitrary, we obtain

$$P\left\{\lim_{t\longrightarrow\infty} \|\overline{x}\| = 0\right\} = 1. \tag{29}$$

Then, sending $a \longrightarrow 0$, we obtain the minimum control intensity expression:

$$\underline{\sigma^2} = \frac{2\left[\beta_1\gamma + \beta_2(\gamma+\mu_1+\eta)\langle j^2\rangle\right]}{\tau(\gamma+\eta+\mu_1)\langle j\rangle} - \frac{2(\eta+\mu_2)}{\tau}. \tag{30}$$

Therefore, system (7) is almost surely stable if σ^2 is bigger than the minimum control intensity. The proof is complete.

In Theorem 1, we give the global stability of the malware-free equilibrium. It is worth to mention that we separate interaction terms in the stochastic model (7) by using the group-theoretic approaching method, and then the infected groups $I_i^L(t)$ and $I_i^H(t)$ can be considered separately. Calculating the Lyapunov exponents, we obtain the global stability of the malware-free equilibrium. □

Proof of Corollary 1. Set $\sigma = 0$; then, stochastic model (7) becomes deterministic model (5). The control intensity mathematical expression becomes

$$0 > \frac{2\left[\beta_1\gamma + \beta_2(\gamma+\mu_1+\eta)\right]\langle j^2\rangle}{\tau(\gamma+\eta+\mu_1)\langle j\rangle} - \frac{2(\eta+\mu_2)}{\tau}. \tag{31}$$

It implies

$$\frac{2T\tau\left[\beta_1\gamma + \beta_2(\gamma+\mu_1+\eta)\right]\langle j^2\rangle}{\delta(\gamma+\eta+\mu_1)\langle j\rangle} > \frac{2(\eta+\mu_2)}{\tau}, \tag{32}$$

which means $R_0 < 1$. Applying Theorem 1, the malware-free equilibrium is globally asymptotically stable.

To get the endemic equilibrium solution $S_i^*, I_i^{L*}, I_i^{H*}, A_i^*$, the right side of system (1) should equal to zero. The solution definitely satisfies the restrictive condition on the total quality of nodes:

$$S_i^* + I_I^{L*} + I_i^{H*} + A_i^* = \frac{\Lambda}{\eta}, \quad \text{for all } i. \tag{33}$$

Combining and solving all the above equations, we can obtain an equation containing $\Theta(t)$ and $S_i^*, I_i^{L*}, I_i^{H*}, A_i^*$. To guarantee a nontrivial solution of it, R_0 need to be bigger than one, and thus we obtain that there is an endemic equilibrium when $R_0 > 1$.

Then, we prove the malware will be persistent when $R_0 > 1$. If $R_0 > 1$, the derivative of function V becomes positive for $S_i(t)\,(i = 1, 2, \ldots, n)$ sufficiently close to Λ/η except when $I_i^L = I_i^H = 0\,(i = 1, 2, \ldots, n)$. Otherwise, system (1) reduces to $\mathrm{d}S_i = \Lambda - \eta S_i$, which implies $S_i \longrightarrow (\Lambda/\eta)$ as $t \longrightarrow \infty$. This establishes the malware-free equilibrium's unstable property. Since the necessary and sufficient condition for uniform persistence is equivalent to the malware-free equilibrium being unstable, system (1) is persistent. □

Remark 2. If $t_{k+1} - t_k = T$ and $c_k = \delta$ for all $k \in N$, system (7) becomes a periodic intermittent system. The minimum control intensity becomes

$$\sigma^2 > \frac{2T\left[\beta_1\gamma + \beta_2(\gamma+\mu_1+\eta)\right]\langle j^2\rangle}{\delta(\gamma+\eta+\mu_1)\langle j\rangle} - \frac{2T(\eta+\mu_2)}{\delta}. \tag{34}$$

This agrees with Theorem 1 in Zhang et al. [41]. Our results can be regarded as a generalization of Zhang et al. [41].

Remark 3. According to the expression of σ, the control intensity depends on the network topological structure and system parameters. Apparently, if the degree distribution of WSNs follows a power law (like a scale-free network) and the number of nodes is huge enough, then $(\langle j^2\rangle/\langle j\rangle) \longrightarrow \infty$, so the absence of control intensity, i.e., $\sigma \longrightarrow \infty$, is observed. Moreover, the disappearance of malware is related to perturbation time ratios τ. Thus, we can enhance or weaken noise intensity to decrease or increase the corresponding control time ratios. Control strategy would be designed based on our theoretical results.

4. Numerical Simulation

The aperiodically intermittent noise controller can stabilize system (1) under the intensity σ. From the expression, control intensity is directly proportional to the contact rates β_1, β_2 and inversely proportional to the control time ratio. Using Milstein's higher order method [47], the discretized equations for the system (7) are

$$\begin{aligned}
I_{i,k+1}^L &= I_{i,k}^L + \left(\beta_1 i\Theta(t)S_i - \gamma I_i^L(t) - \mu_1 I_i^L(t) - \eta I_i^L(t)\right)\Delta t + \sigma I_{i,k}^L\sqrt{\Delta t}\xi_i + \frac{1}{2}\sigma^2\left(I_{i,k}^L\right)^2\left(\xi_i^2 - 1\right)\Delta t,\\
I_{i,k+1}^H &= I_{i,k}^H + \left(\beta_2 i\Theta(t)S_i + \gamma I_i^L(t) - \mu_2 I_i^H(t) - \eta I_i^H(t)\right)\Delta t + \sigma I_{i,k}^H\sqrt{\Delta t}\xi_i + \frac{1}{2}\sigma^2\left(I_{i,k}^H\right)^2\left(\xi_i^2 - 1\right)\Delta t,\\
A_{i,k+1} &= A_{i,k} + \left(\mu_1 I_i^L(t) + \mu_2 I_i^H(t) - \eta A_i\right)\Delta t + A_{i,k}\sqrt{\Delta t}\xi_i + \frac{1}{2}\sigma^2 A_{i,k}^2\left(\xi_i^2 - 1\right)\Delta t,
\end{aligned} \tag{35}$$

Table 1: System parameters.

Λ	η	β_1	β_2	μ_1	μ_2	γ
1	0.01	0.009	0.01	0.0015	0.0016	0.01

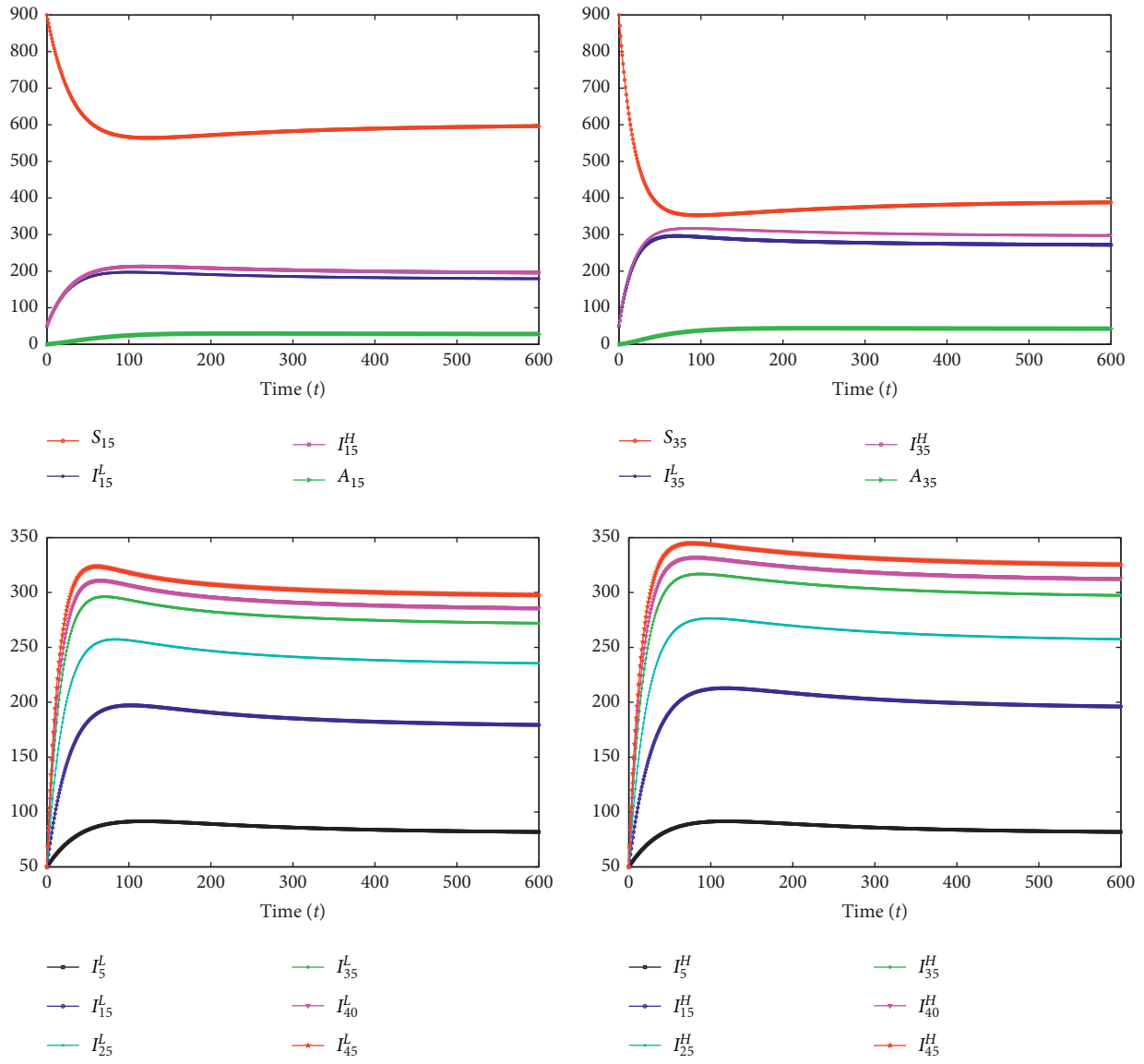

Figure 3: The time series and orbits of system (1) with $R_0 > 1$. The malware persists in the end.

where ξ_i are independent random variables $N(0, 1)$, $i = 1, 2, \ldots, n$. Generally, we assume WSN is a scale-free network with the power law distribution $P(j) = aj^3$, where a satisfies $\sum_{j=1}^{n} aj^3 = 1$. We set the initial values to $S_i(0) = 900, I_i^L(0) = 50, I_i^h = 50, A_i = 0, i = 1, 2, \ldots, n$ and $n = 50$.

Choosing parameter values in Table 1, the reproduction number is

$$R_0 = \frac{[\beta_1\gamma + \beta_2(\gamma + \mu_1 + \eta)]\langle j^2\rangle}{(\eta + \mu_2)(\gamma + \eta + \mu_1)\langle j\rangle} = 3.2678 > 1. \quad (36)$$

According to Corollary 1, the malware is persistent. The top two pictures in Figure 3 show that the solution of system (1) converges to the endemic equilibrium. The last two pictures in Figure 3 show clearly that the number of infected nodes I_k^H and I_k^L converge to a positive constant.

To stabilize the above deterministic model, we choose different control intensities σ by adjusting control time to compare the stabilization effects.

(i) Let control time ratio $\tau = 0.5$ and initial value (900, 50, 50, 0, ..., 900, 50, 50, 0). Generating the

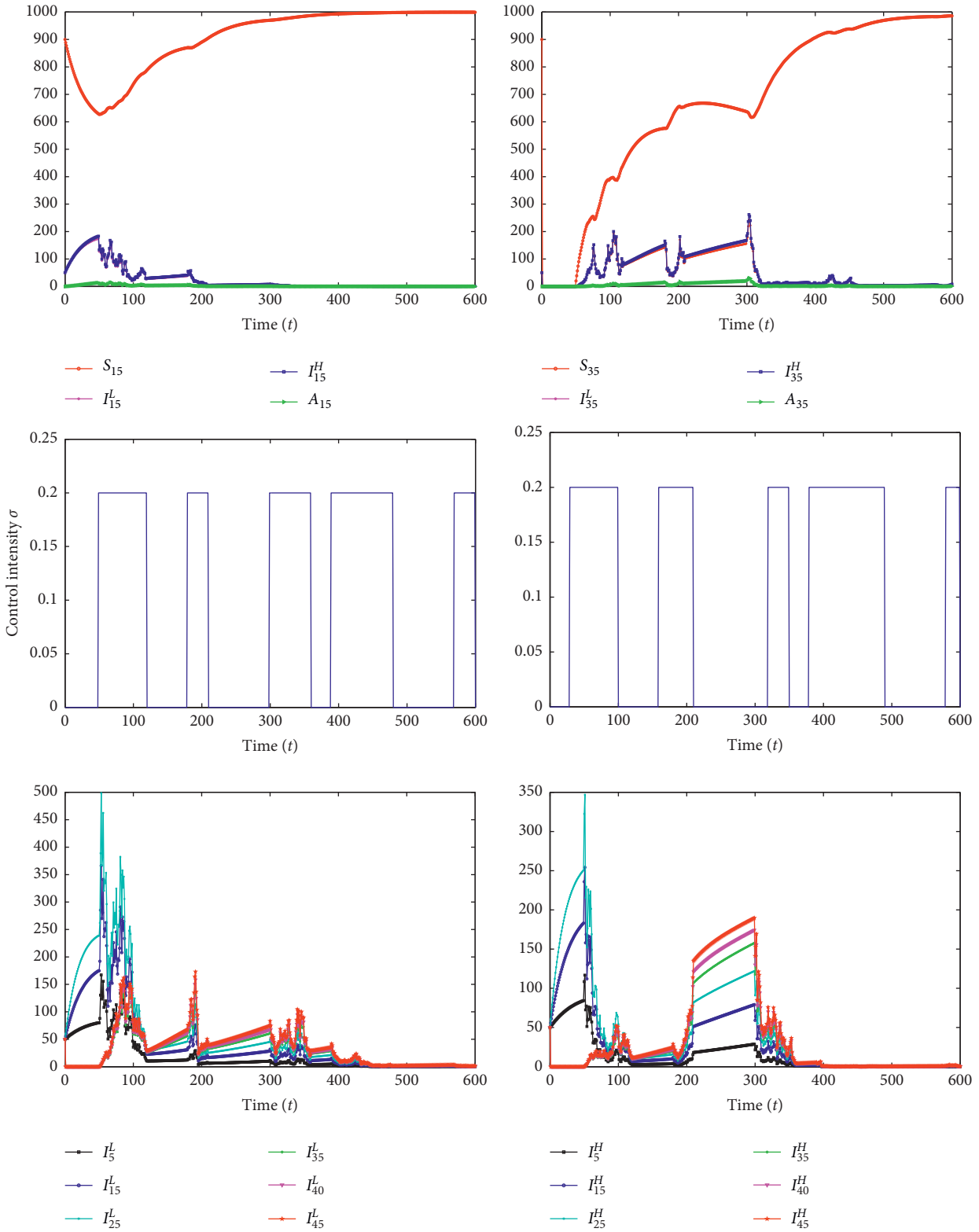

FIGURE 4: The time series and orbits of system (7) with $R_0 > 1$ and stochastic control. The top two pictures are the sample paths of $S_{15}(t), I_{15}^L(t), I_{15}^H(t), A_{15}(t)$ and $S_{35}(t), I_{35}^L(t), I_{35}^H(t), A_{35}(t)$. The middle pictures are two different time strategies with $\tau = 0.5$ and $\sigma = 0.2$. The last two pictures are sample paths of $I^L(t)$ and $I^H(t)$ with degree $k = 5, 15, 25, 35, 40, 45$. The malware will be extinct in the end.

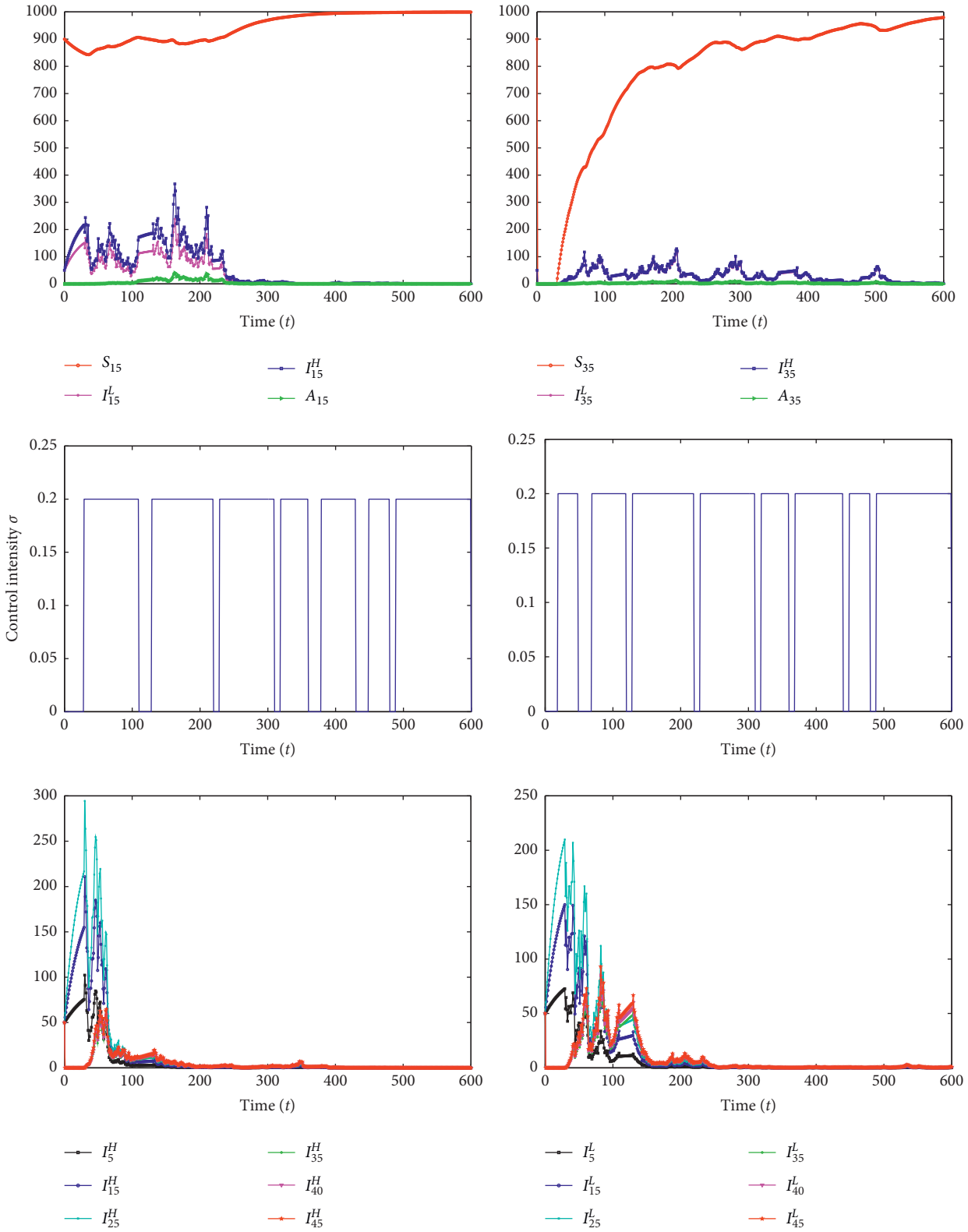

FIGURE 5: The time series and orbits of system (7) with $R_0 > 1$ and stochastic control. The top two pictures are the sample paths of $S_{15}(t), I_{15}^L(t), I_{15}^H(t), A_{15}(t)$ and $S_{35}(t), I_{35}^L(t), I_{35}^H(t), A_{35}(t)$. The middle pictures are two different time strategies with $\tau = 0.8$ and $\sigma = 0.2$. The last two pictures are sample paths of $I^L(t)$ and $I^H(t)$ with degree $k = 5, 15, 25, 35, 40, 45$. The malware will be extinct in the end.

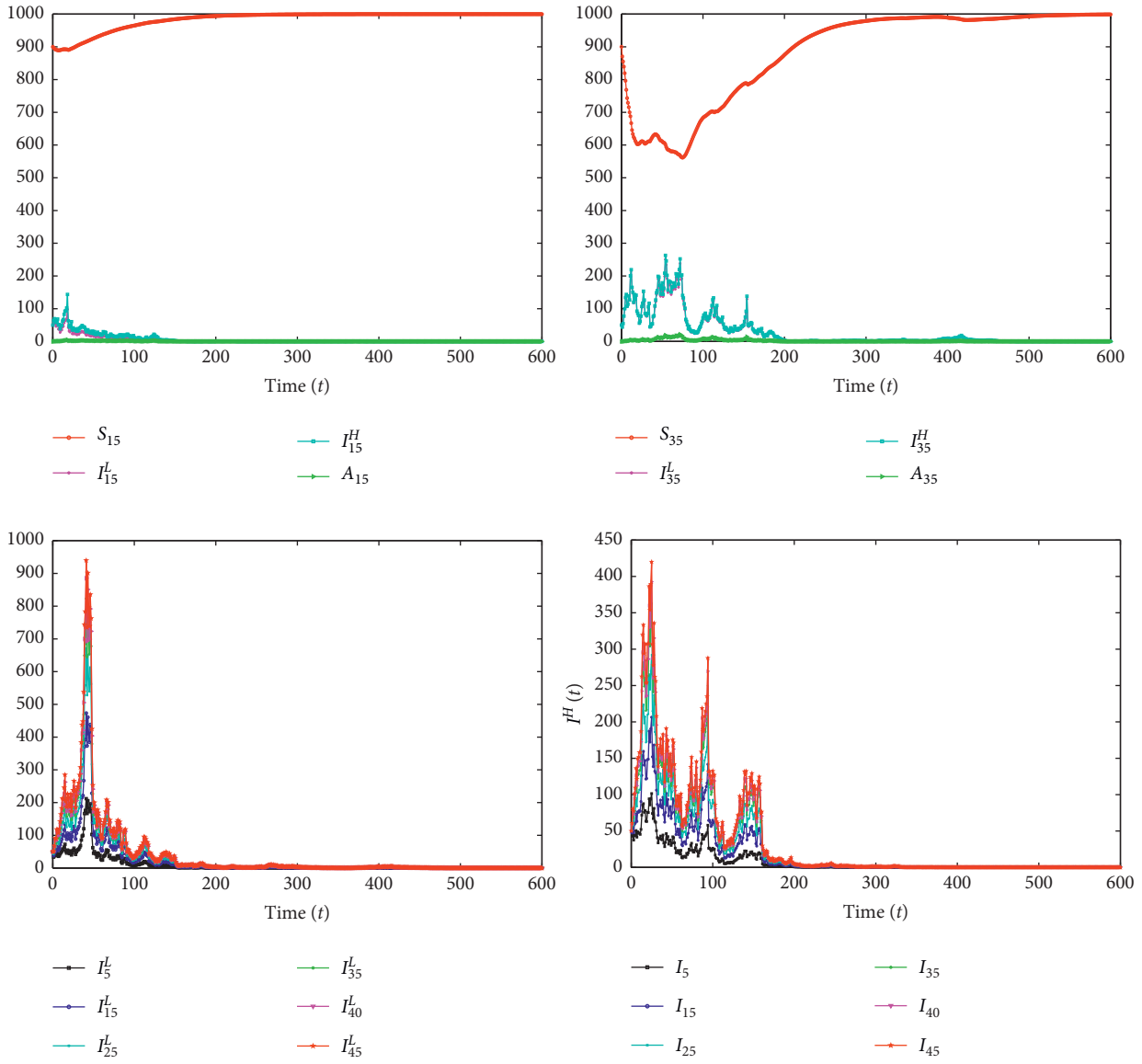

FIGURE 6: The time series and orbits of system (7) with $R_0 > 1$ and stochastic control. The top two pictures are the sample paths of $S_{15}(t), I_{15}^L(t), I_{15}^H(t), A_{15}(t)$ and $S_{35}(t), I_{35}^L(t), I_{35}^H(t), A_{35}(t)$. The last two pictures are sample paths of $I^L(t)$ and $I^H(t)$ with degree $k = 5, 15, 25, 35, 40, 45$. The malware will be extinct in the end.

aperiodically intermittent time intervals randomly, we give two examples in the middle two pictures of Figure 4. We can calculate that $\sigma^2 = 0.04 > 0.0254$; according to Theorem 1, I_k^H and I_k^L all tend to zero; Figure 4 shows clearly that the malware disappears.

(ii) Increase the control time ratio to $\tau = 0.8$; specific aperiodically intermittent time intervals are shown in the middle two pictures of Figure 5. We can obtain that $\sigma^2 = 0.04 > 0.0211$, the condition in Theorem 1 is satisfied, and I_k^H and I_k^L all tend to zero. The top two and the last two pictures of Figure 5 show clearly that all the infected nodes go to zero.

(iii) Adding control time to full time. Figure 6 shows the solution of system (7) converges to the malware-free equilibrium, I_k^H and I_k^L all tend to zero, and the malware nodes will disappear. Comparing Figures 4–6, we can conclude that the bigger the perturbation intensity is, the faster the steady speed is.

5. Conclusion

Based on network topology and malware propagation property, we established a heterogeneous wireless sensor network model which considers the influence of energy consumption to node communication. The basic reproduction number R_0 has been given which determines the extinction or persistence of malware: if $R_0 < 1$, the malware will die out; if $R_0 > 1$, the malware will be persistent. To control malware spreading, we design a kind of aperiodically

intermittent stochastic noise controller, starting time and control length of which are arbitrary. We can control steady rate autonomously by adjusting the work width. Using the straightening operator and Markov inequality, we calculate the specific stochastic noise intensity σ, which is inversely proportional to intermittent time. When stochastic noise controller's intensity is greater than σ, malware propagation will be controlled with probability 1. Otherwise, the malware program will destroy the wireless sensor networks. This stochastic stabilization method presents a new theoretical strategy for wireless sensor network security: stochastic noise controller. Numerical simulations are given to illustrate the stabilization effect of stochastic noise.

Data Availability

No data were used to support this study.

Conflicts of Interest

The authors declare that they have no conflicts of interest.

Acknowledgments

This study was supported by the Guangzhou Education Bureau science foundation project (1201630502) and Research Fund for Guangzhou University (YG2020010).

References

[1] E. Fadel, V. C. Gungor, L. Nassef et al., "A survey on wireless sensor networks for smart grid," *Computer Communications*, vol. 71, pp. 22–33, 2015.

[2] A. M. del Rey and A. Peinado, "Mathematical models for malware propagation in wireless sensor networks: an analysis," in *Computer and Network Security Essentials*, K. Daimi, Ed., Springer, Cham, Switzerland, pp. 299–313, 2018.

[3] V. Karyotis and M. H. R. Khouzani, *Malware Diffusion Models for Modern Complex Networks: Theory and Applications*, Morgan Kaufmann, Burlington, MA, USA, 2016.

[4] O. A. Toutonji, S.-M. Yoo, and M. Park, "Stability analysis of VEISV propagation modeling for network worm attack," *Applied Mathematical Modelling*, vol. 36, no. 6, pp. 2751–2761, 2012.

[5] K. M. Bimal and N. Keshri, "Mathematical model on the transmission of worms in wireless sensor network," *Applied Mathematical Modelling*, vol. 37, no. 6, pp. 4103–4111, 2013.

[6] L. Zhu and H. Zhao, "Dynamical analysis and optimal control for a malware propagation model in an information network," *Neurocomputing*, vol. 149, pp. 1370–1386, 2015.

[7] T. Wang, Q. Wu, S. Wen et al., "Propagation modeling and defending of a mobile sensor worm in wireless sensor and actuator networks," *Sensors*, vol. 17, no. 12, pp. 139–156, 2017.

[8] P. S. Romualdo and V. Alessandro, "Epidemic spreading in scale-free networks," *Physical Review Letters*, vol. 86, no. 14, pp. 3200–3203, 2001.

[9] S. Huang, F. Chen, and L. Chen, "Global dynamics of a network-based SIQRS epidemic model with demographics and vaccination," *Communications in Nonlinear Science and Numerical Simulation*, vol. 43, pp. 296–310, 2017.

[10] G. Zhu, X. Fu, and G. Chen, "Spreading dynamics and global stability of a generalized epidemic model on complex heterogeneous networks," *Applied Mathematical Modelling*, vol. 36, no. 12, pp. 5808–5817, 2012.

[11] G. Zhu, G. Chen, and X. Fu, "Effects of active links on epidemic transmission over social networks," *Physica A: Statistical Mechanics and Its Applications*, vol. 468, pp. 614–621, 2017.

[12] H. Xiang, Y.-P. Liu, and H.-F. Huo, "Stability of an SAIRS alcoholism model on scale-free networks," *Physica A: Statistical Mechanics and Its Applications*, vol. 473, pp. 276–292, 2017.

[13] T. Li, X. Liu, J. Wu, C. Wan, Z.-H. Guan, and Y. Wang, "An epidemic spreading model on adaptive scale-free networks with feedback mechanism," *Physica A: Statistical Mechanics and Its Applications*, vol. 450, pp. 649–656, 2016.

[14] X. Liu, T. Li, H. Xu, and W. Liu, "Spreading dynamics of an online social information model on scale-free networks," *Physica A: Statistical Mechanics and Its Applications*, vol. 514, pp. 497–510, 2019.

[15] W. Liu, T. Li, X. Liu, and H. Xu, "Spreading dynamics of a word-of-mouth model on scale-free networks," *IEEE Access*, vol. 6, pp. 65563–65572, 2018.

[16] Y. Lei, T. Li, Y. Wang, G. Ye, S. Sun, and Z. Xia, "Spreading dynamics of a CPFB group booking preferential information model on scale-free networks," *IEEE Access*, vol. 7, pp. 156287–156300, 2019.

[17] X. D. Liu, T. Li, X. Cheng, W. Liu, and H. Xu, "Spreading dynamics of a preferential information model with hesitation psychology on scale-free networks," *Advances in Difference Equations*, vol. 2019, pp. 1–13, 2019.

[18] A. M. del Rey, J. D. H. Guillén, and G. R. Sánchez, "Modeling malware propagation in wireless sensor networks with individual-based models," in *Advances in Artificial Intelligence*, vol. 9868, pp. 194–203, Springer, Cham, Switzerland, 2016.

[19] Q. Li, B. Zhang, L. Cui, Z. Fan, and V. V. Athanasios, "Epidemics on small worlds of tree-based wireless sensor networks," *Journal of Systems Science and Complexity*, vol. 27, no. 6, pp. 1095–1120, 2014.

[20] S. Hosseini and M. A. Azgomi, "A model for malware propagation in scale-free networks based on rumor spreading process," *Computer Networks*, vol. 108, pp. 97–107, 2016.

[21] R. Khasminskii, "Stochastic stability of differential equations," in *Sijthoff & Noordhoff*, Springer, Berlin, Germany, 1980.

[22] L. Arnold, H. Crauel, and V. Wihstutz, "Stabilization of linear systems by noise," *SIAM Journal on Control and Optimization*, vol. 21, no. 3, pp. 451–461, 1983.

[23] X. R. Mao, *Stochastic Differential Equations and Applications*, Woodhead Publishing, Cambridge, UK, 2nd edition, 2008.

[24] L. Huang, "Stochastic stabilization and destabilization of nonlinear differential equations," *Systems & Control Letters*, vol. 62, no. 2, pp. 163–169, 2013.

[25] T. Caraballo, A. Settati, M. E. Fatini, A. Lahrouz, and A. Imlahi, "Global stability and positive recurrence of a stochastic SIS model with lévy noise perturbation," *Physica A: Statistical Mechanics and Its Applications*, vol. 523, pp. 677–690, 2019.

[26] L. Liu and T. Caraballo, "Analysis of a stochastic 2D-navier-stokes model with infinite delay," *Journal of Dynamics and Differential Equations*, vol. 31, no. 4, pp. 2249–2274, 2019.

[27] T. Caraballo, R. Colucci, J. López-de-la-Cruz, and A. Rapaport, "A way to model stochastic perturbations in population dynamics models with bounded realizations," *Communications in Nonlinear Science and Numerical Simulation*, vol. 77, pp. 239–257, 2019.

[28] R. K. Christensen, H. Lindén, M. Nakamura, and T. R. Barkat, "White noise background improves tone discrimination by suppressing cortical tuning curves," *Cell Reports*, vol. 29, no. 7, pp. 2041–2053, 2019.

[29] W. Chen, S. Xu, and Y. Zou, "Stabilization of hybrid neutral stochastic differential delay equations by delay feedback control," *Systems & Control Letters*, vol. 88, pp. 1–13, 2016.

[30] Q. Zhu and Q. Zhang, "Pth moment exponential stabilisation of hybrid stochastic differential equations by feedback controls based on discrete-time state observations with a time delay," *IET Control Theory & Applications*, vol. 11, no. 12, pp. 1992–2003, 2017.

[31] G. Song, B.-C. Zheng, Q. Luo, and X. Mao, "Stabilisation of hybrid stochastic differential equations by feedback control based on discrete-time observations of state and mode," *IET Control Theory & Applications*, vol. 11, no. 3, pp. 301–307, 2017.

[32] R. Yong, W. S. Yin, and R. Sakthivel, "Stabilization of stochastic differential equations driven by G-Brownian motion with feedback control based on discrete-time state observation," *Automatica*, vol. 95, pp. 146–151, 2018.

[33] H. Ren, Y. Peng, F. Deng, and C. Zhang, "Impulsive pinning control algorithm of stochastic multi-agent systems with unbounded distributed delays," *Nonlinear Dynamics*, vol. 92, no. 4, pp. 1453–1467, 2018.

[34] P. Cheng, F. Deng, and F. Yao, "Almost sure exponential stability and stochastic stabilization of stochastic differential systems with impulsive effects," *Nonlinear Analysis: Hybrid Systems*, vol. 30, pp. 106–117, 2018.

[35] Y.-J. Liu, S. Lu, D. Li, and S. Tong, "Adaptive controller design-based ABLF for a class of nonlinear time-varying state constraint systems," *IEEE Transactions on Systems, Man, and Cybernetics: Systems*, vol. 47, no. 7, pp. 1546–1553, 2017.

[36] S. He, H. Fang, M. Zhang, F. Liu, and Z. Ding, "Adaptive optimal control for a class of nonlinear systems: the online policy iteration approach," *IEEE Transactions on Neural Networks and Learning Systems*, vol. 31, no. 2, pp. 549–558, 2020.

[37] S. He, H. Fang, M. Zhang, F. Liu, X. Luan, and Z. Ding, "Online policy iterative-based h optimization algorithm for a class of nonlinear systems," *Information Sciences*, vol. 495, no. 1, 2019.

[38] P. Cheng, J. Wang, S. He, X. Luan, and F. Liu, "Observer-based asynchronous fault detection for conic-type nonlinear jumping systems and its application to separately excited DC motor," *IEEE Transactions on Circuits and Systems I: Regular Papers*, vol. 67, no. 3, pp. 1–12, 2020.

[39] P. Cheng and S. He, "Observer-based finite-time asynchronous control for a class of hidden Markov jumping systems with conic-type nonlinearities," *IET Control Theory and Applications*, vol. 14, no. 2, pp. 244–252, 2020.

[40] P. Cheng, S. He, J. Cheng, X. Luan, and F. Liu, "Asynchronous output feedback control for a class of conic-type nonlinear hidden markov jump systems within a finite-time interval," *IEEE Transactions on Systems, Man, and Cybernetics: Systems*, pp. 1–8. In press, 2020.

[41] B. Zhang, F. Deng, S. Peng, and S. Xie, "Stabilization and destabilization of nonlinear systems via intermittent stochastic noise with application to memristor-based system," *Journal of the Franklin Institute*, vol. 355, no. 9, pp. 3829–3852, 2018.

[42] S. Yang, C. Li, and T. Huang, "Exponential stabilization and synchronization for fuzzy model of memristive neural networks by periodically intermittent control," *Neural Networks*, vol. 75, pp. 162–172, 2016.

[43] G. Zhang and Y. Shen, "Exponential stabilization of memristor-based chaotic neural networks with time-varying delays via intermittent control," *IEEE Transactions on Neural Networks and Learning Systems*, vol. 26, no. 7, pp. 1431–1441, 2015.

[44] L. Liu, M. Perc, and J. Cao, "Aperiodically intermittent stochastic stabilization via discrete time or delay feedback control," *Science China Information Sciences*, vol. 62, no. 7, pp. 1–13, 2019.

[45] X. Liu and T. Chen, "Synchronization of nonlinear coupled networks via aperiodically intermittent pinning control," *IEEE Transactions on Neural Networks and Learning Systems*, vol. 26, no. 10, pp. 113–126, 2015.

[46] X. Liu and T. Chen, "Synchronization of complex networks via aperiodically intermittent pinning control," *IEEE Transactions on Automatic Control*, vol. 60, no. 2, pp. 3316–3321, 2015.

[47] D. J. Higham, "An algorithmic introduction to numerical simulation of stochastic differential equations," *SIAM Review*, vol. 43, no. 3, pp. 525–546, 2001.

[48] P. van den Driessche and J. Watmough, "Reproduction numbers and sub-threshold endemic equilibria for compartmental models of disease transmission," *Mathematical Biosciences*, vol. 180, no. 1-2, pp. 29–48, 2002.

[49] M. Y. Li and Z. Shuai, "Global-stability problem for coupled systems of differential equations on networks," *Journal of Differential Equations*, vol. 248, no. 1, pp. 1–20, 2010.

Hindawi
Complexity
Volume 2020, Article ID 9849636, 8 pages
https://doi.org/10.1155/2020/9849636

Research Article

Optimality Conditions for a Nonsmooth Uncertain Multiobjective Programming Problem

Wenyan Han, Guolin Yu, and Tiantian Gong

Institute of Applied Mathematics, North Minzu University, Yinchuan 750021, China

Correspondence should be addressed to Guolin Yu; guolin_yu@126.com

Received 13 April 2020; Accepted 1 July 2020; Published 25 July 2020

Academic Editor: Sigurdur F. Hafstein

This note is devoted to the investigation of optimality conditions for robust approximate quasi weak efficient solutions to a *nonsmooth uncertain multiobjective programming* problem (NUMP). Firstly, under the extended nonsmooth Mangasarian–Fromovitz constrained qualification assumption, the optimality necessary conditions of robust approximate quasi weak efficient solutions are given by using an alternative theorem. Secondly, a class of generalized convex functions is introduced to the problem (NUMP), which is called the pseudoquasi-type-I function, and its existence is illustrated by a concrete example. Finally, under the pseudopseudo-type-I generalized convexity hypothesis, the optimality sufficient conditions for robust approximate quasi weak efficient solutions to the problem (NUMP) are established.

1. Introduction

It is well known that multiobjective programming problems are widely used in the fields of portfolio, resource allocation, and information transfer. In practical problems, most of the objectives or constraints to the optimization model are nonsmooth and are affected by various factors with uncertain information. Therefore, it is a very valuable work to study the nonsmooth uncertain optimization problems. Robust optimization is one of the effective methods to deal with uncertain optimization problems. The robust method is committed to ensuring the worst-case solution which is immunized against the data uncertainty to optimization problems, and for its more details, the reader is referred to [1]. In this paper, the optimality conditions to the *nonsmooth uncertain multiobjective programming* problem (NUMP) are described by using the robust optimization method.

Convexity and its generalization play an important role in mathematical programming, especially in establishing optimality sufficient conditions of optimization problems. Chuong and Kim [2] presented the generalized convex-affine function based on the Mordukhovich subdifferential for a class of nonsmooth multiobjective fractional programming problems. For objective and constraint functions (f, g) of a class of nonsmooth robust multiobjective programming problems, the concept that (f, g) is a generalized convexity of degree n is introduced in literature [3]. Inspired by the generalized convexity in the above literatures, this paper introduces a kind of generalized convexities based on the Clarke subdifferential, which is called the (f, g)-pseudo-quasi-type-I function, and under its assumption, it proves the optimality conditions of the problem (NUMP).

As we all know, the (weak) efficient solution of multiobjective optimization problems usually does not exist in the noncompact case, but the approximate solution exists under very mild conditions. In addition, most of the solutions obtained by the numerical algorithm are approximate solutions in the real world. Therefore, there exist the important theoretical value and practical significance to study the approximate solution of the optimization problem. Recently, Lee and Jiao [4] dealt with the optimality conditions of the robust approximate solution for an uncertain convex optimization problem involving a kind of constraint qualifications, which is called closed convex cone constrained qualification; Sun [5] established the optimality conditions of the robust optimal solution under the constrained qualification with respect to the subdifferential of the convex function; Sun and Li [6] discussed the optimality conditions

of the robust approximate weak efficient solution under the hypothesis of closed convex cone constrained qualification. It is worth mentioning that the approximate weak efficient solution is a special case of the approximate quasi weak efficient solution. The purpose of this paper is to study optimality conditions of the robust approximate quasi weak efficient solution for the problem (NUMP). The convexities and constrained qualification are different from those of mentioned literatures, and we adopt the newly introduced (f, g)-pseudopseudo-type-I convexity and extended nonsmooth Mangasarian–Fromovitz constrained qualification (see [7]).

The content of this paper is arranged as follows: In Section 2, some basic concepts and lemmas which will be used in subsequent sections are proposed. The concept of the (f, g)-pseudoquasi-type-I generalized convexity with respect to the Clarke subdifferential is introduced, and an example is given to illustrate its existence. The main results are present in Section 3, in which the optimality conditions of the robust approximate quasi weak efficient solution to the problem (NUMP) are proven.

2. Preliminaries

This paper considers the following *nonsmooth multiobjective programming* problem (NMP):

$$(\text{NMP})\begin{cases}\min & f(x) = \left(f_1(x), f_2(x), \ldots, f_l(x)\right),\\ \text{s.t.} & x \in C,\ g_j(x) \le 0, \quad j = 1, \ldots, m,\end{cases} \tag{1}$$

where C is a nonempty subset of n dimension Euclid space $\mathbb{R}^n$ and $f_i, g_j\colon \mathbb{R}^n \longrightarrow \mathbb{R}$, $i = 1, \ldots, l$, $j = 1, \ldots, m$, are the Lipschitz functions. The feasible set of the problem (NMP) is denoted as

$$\mathscr{F}_0 := \left\{x \in C\colon\ g_j(x) \le 0,\ j = 1, \ldots, m\right\}. \tag{2}$$

When the constraint set of problem (NMP) contains uncertain data, the corresponding *nonsmooth uncertain multiobjective programming* problem (NUMP) is expressed as

$$(\text{NUMP})\begin{cases}\min & f(x) = \left(f_1(x),\ f_2(x), \ldots,\ f_l(x)\right),\\ \text{s.t.} & x \in C,\ g_j\left(x, v_j\right) \le 0, \quad j = 1, \ldots, m,\end{cases} \tag{3}$$

where $v_j \in \mathscr{V}_j \subset \mathbb{R}^q$ is the uncertain parameter, $\mathscr{V}_j$ is the compact convex set, and $g_j\colon \mathbb{R}^n \times \mathbb{R}^q \longrightarrow \mathbb{R}$, $j = 1, \ldots, m$, are the Lipschitz functions with respect to the first variable. We denote $v = (v_1, \ldots, v_m) \in \mathscr{V} = (\mathscr{V}_1, \ldots, \mathscr{V}_m)$. The feasible set of problem (NUMP) is defined by

$$\mathscr{F}_v := \left\{x \in C\colon\ g_j\left(x, v_j\right) \le 0,\ j = 1, \ldots, m\right\}. \tag{4}$$

The optimality conditions of problem (NUMP) will be studied by the robust optimization method in this note. For this purpose, we consider the following robust counterpart (see [8]) of the problem (NUMP):

$$(\text{NRMP})\begin{cases}\min & f(x) = \left(f(x),\ f_2(x), \ldots,\ f(x)\right),\\ \text{s.t.} & x \in C,\ g_j\left(x, v_j\right) \le 0,\ \forall v_j \in \mathscr{V}_j, \quad j = 1, \ldots, m.\end{cases} \tag{5}$$

The robust counterpart problem is called as the *nonsmooth robust multiobjective programming* problem (NRMP), and the robust feasible set of problem (NRMP) is given by

$$\mathscr{F} := \bigcap_{v \in \mathscr{V}} \mathscr{F}_v. \tag{6}$$

Let

$$\psi_j(x) := \max\left\{g_j\left(x, v_j\right)\colon\ v_j \in \mathscr{V}_j\right\}, \quad j = 1, \ldots, m,\ \forall x \in \mathbb{R}^n. \tag{7}$$

For a given $\overline{x} \in \mathbb{R}^n$, we divide $J = \{1, \ldots, m\}$ into two index sets, $J = J_1(\overline{x}) \cup J_2(\overline{x})$, where

$$\begin{aligned} J_1(\overline{x}) &= \left\{j \in J\colon\ \psi_j(\overline{x}) = 0\right\},\\ J_2(\overline{x}) &= \frac{J}{J_1(\overline{x})}. \end{aligned} \tag{8}$$

For any $j \in J_1(\overline{x})$, let

$$\mathscr{V}_j(\overline{x}) := \left\{v_j \in \mathscr{V}_j\colon\ g_j\left(\overline{x}, v_j\right) = \psi_j(\overline{x})\right\}. \tag{9}$$

Let $\mathbb{B}$ be a closed unit ball in $\mathbb{R}^n$. For any $x, y \in \mathbb{R}^n$, use $\langle x, y\rangle$ to represent the inner product between x and y. Set

$$\begin{aligned} \mathbb{R}^n_+ &= \left\{x \in \mathbb{R}^n\colon\ x_i \ge 0, \quad (i = 1, \ldots, n)\right\},\\ \mathbb{R}^n_{++} &= \left\{x \in \mathbb{R}^n\colon\ x_i > 0, \quad J_1(\overline{x})\right\}. \end{aligned} \tag{10}$$

It is said that $\varphi\colon \mathbb{R}^n \longrightarrow \mathbb{R}$ is a convex function, if for any $x, y \in \mathbb{R}^n$, $\lambda \in [0, 1]$,

$$\varphi(\lambda x + (1 - \lambda)y) \le \lambda\varphi(x) + (1 - \lambda)\varphi(y). \tag{11}$$

If $-\varphi$ is a convex function, then is said to be a concave function. For any $x \in \mathbb{R}^n$, if

$$\limsup_{y \longrightarrow x} \varphi(y) \le \varphi(x), \tag{12}$$

then φ is termed to be a upper semicontinuous function. Let $X \subset \mathbb{R}^n$ be a nonempty open subset. It is said that $\varphi\colon X \longrightarrow \mathbb{R}$ is a Lipschitz function, if there exists $L > 0$, such that

$$\left\|\varphi(x_1) - \varphi(x_2)\right\| \le L\left\|x_1 - x_2\right\|, \quad \forall x_1, x_2 \in X. \tag{13}$$

Let $d \in \mathbb{R}^n$, and the directional derivative (see [9]) of φ at $\overline{x} \in X$ in the direction d is given by

$$\varphi'(\overline{x}; d) = \lim_{t \longrightarrow 0^+} \frac{\varphi(\overline{x} + t\,d) - \varphi(\overline{x})}{t}, \tag{14}$$

and the Clarke generalized directional derivative (see [9]) of φ at $\overline{x}$ in the direction d is defined by

$$\varphi^{\circ}(\overline{\mathrm{x}}; \mathrm{d}) = \limsup_{\mathrm{y} \longrightarrow \overline{\mathrm{x}}\,\mathrm{t} \longrightarrow 0^+} \frac{\varphi'(\mathrm{y} + \mathrm{t}\,\mathrm{d}) - \varphi(\mathrm{y})}{\mathrm{t}}, \tag{15}$$

If

$$\varphi^{\circ}(\overline{x};d) = \varphi\prime(\overline{x};d), \quad \forall d \in \mathbb{R}^{n}, \tag{16}$$

then φ is called to be regular at $\overline{x}$. The Clarke subdifferential (see [9]) of φ at $\overline{x}$ is denoted as

$$\partial\varphi(\overline{x}) := \{\xi \in \mathbb{R}^{n}: \ \varphi^{\circ}(\overline{x};d) \geq \langle \xi, d\rangle, \ \forall d \in \mathbb{R}^{n}\}. \tag{17}$$

Lemma 1 (see [7]). *Let φ: $X \subset \mathbb{R}^n \longrightarrow \mathbb{R}$ be a Lipschitz function, then the following conclusions hold:*

(i) $\partial\varphi(x)$ is a nonempty compact convex set in X, and for any $\xi \in \partial\varphi(x)$, one has $\|\xi\| \leq L$ (L is Lipschitz constant of φ).

(ii) $d \mapsto \varphi^{\circ}(x;d)$ is convex, and

$$|\varphi^{\circ}(x;d)| \leq L\|d\|. \tag{18}$$

(iii) For any $d \in \mathbb{R}^n$, we have

$$\varphi^{\circ}(x;d) = \max\{\langle \xi, d\rangle : \ \xi \in \partial\varphi(x)\}. \tag{19}$$

For a given function $g: U \times \mathscr{V}_0 \subset \mathbb{R}^n \times \mathbb{R}^q \longrightarrow \mathbb{R}$, suppose g satisfies the following assumptions (see [7]):

(i) $g(x, v_0)$ is upper semicontinuous in $(x, v_0) \in U \times \mathscr{V}_0$.

(ii) $g(x, v_0)$ is a Lipschitz function with respect to the first variable $x \in U$, that is, $g(\cdot, v_0)$ is a Lipschitz function for any $v_0 \in \mathscr{V}_0$.

(iii) g is regular with respect to the first variable $x \in U$, that is,

$$g_x^{\circ}(x, v_0; \cdot) = g_x'(x, v_0; \cdot), \tag{20}$$

where $g_x^{\circ}(x, v_0; \cdot)$ is a Clarke generalized directional derivative with respect to the first variable x and $g_x'(x, v_0; \cdot)$ is the directional derivative with respect to the first variable x.

(iv) The *Clarke* subdifferential $\partial_x g(x, v_0)$ with respect to the first variable x is weak * upper semicontinuous in $(x, v_0) \in U \times \mathscr{V}_0$.

Let

$$\psi(x) := \max\{g(x, v_0): \ v_0 \in \mathscr{V}_0\}, \quad \forall x \in \mathbb{R}^n. \tag{21}$$

If $g(x, v_0)$ satisfies Assumptions (i)–(iv), then $\psi(x)$ is a Lipschitz function (see [7]). For a given $\overline{x} \in \mathbb{R}^n$, set

$$\mathscr{V}_0(\overline{x}) := \{v_0 \in \mathscr{V}_0: \ g(\overline{x}, v_0) = \psi(\overline{x})\}. \tag{22}$$

Remark 1. (see [7]). If Assumptions (i)–(iv) are fufilled, $\mathscr{V}_0$ is a convex subset and $g(x, \cdot)$ is a concave on $\mathscr{V}_0$; then,

$$\partial\psi(x) = \{\xi: \ \exists v_0 \in \mathscr{V}_0(x) \ s.t. \ \xi \in \partial_x g(x, v_0)\}, \quad \forall x \in \mathbb{R}^n. \tag{23}$$

Lemma 2 (see [9]). *Let φ, ϕ: $X \subset \mathbb{R}^n \longrightarrow \mathbb{R}$ be a Lipschitz function, $\overline{x} \in X$. Then,*

$$\partial(\varphi + \phi)(\overline{x}) \subset \partial\varphi(\overline{x}) + \partial\phi(\overline{x}). \tag{24}$$

If φ, ϕ are regular at $\overline{x}$, then $\varphi + \phi$ is regular at $\overline{x}$, and $\partial(\varphi + \phi)(\overline{x}) = \partial\varphi(\overline{x}) + \partial\phi(\overline{x})$.

Lemma 3 (alternative theorem, see [10]). *Let $A \subset \mathbb{R}^n$ be a convex set, and $\phi_1(x), \ldots, \phi_m(x)$ are convex on A, if the following system of inequalities*

$$\phi(x) < 0, \quad i = 1, \ldots, m, \ \forall x \in A, \tag{25}$$

has no solution on A, then there exist $\lambda_1, \ldots, \lambda_m \geq 0$, not all zero, such that

$$\sum_{i=1}^{m} \lambda_i \phi_i(x) \geq 0, \quad \forall x \in A. \tag{26}$$

Definition 1 (see [3]). Let $\varepsilon = (\varepsilon_1, \ldots, \varepsilon_l) \in \mathbb{R}_+^l$, $\overline{x} \in \mathscr{F}$.

(i) It is said that $\overline{x}$ is a robust ε−quasi weak efficient solution of the problem (NUMP), iff $\overline{x}$ is an ε−quasi weak efficient solution of the problem (NRMP), that is,

$$(f(x) - f(\overline{x}) + \sqrt{\varepsilon}\,\|x - \overline{x}\|) \notin -\mathbb{R}_{++}^l, \quad \forall x \in \mathscr{F}. \tag{27}$$

(ii) It is called that $\overline{x}$ is a robust ε−quasi efficient solution of the problem (NUMP), iff $\overline{x}$ is an ε−quasi efficient solution of the problem (NRMP), that is,

$$(f(x) - f(\overline{x}) + \sqrt{\varepsilon}\,\|x - \overline{x}\|) \notin -\frac{\mathbb{R}_+^l}{\{0\}}, \quad \forall x \in \mathscr{F}. \tag{28}$$

The following generalized convexity is introduced for the objective and constraint functions (f, g) to the problem (NUMP).

Definition 2. It is said that (f, g) is a pseudoquasi-type-I function at $\overline{x} \in C$, if for any $x \in C$, $\xi_i \in \partial f_i(\overline{x})$, $i = 1, \ldots, l$, $b \in \mathbb{B}$, $\eta_j \in \partial_x g_j(\overline{x}, v_j)$, and $v_j \in \mathscr{V}_j(\overline{x})$, $j = 1, \ldots, m$, there exists $u \in \mathbb{R}^n$, such that

$$\langle \xi_i, u\rangle + \sqrt{\varepsilon_i}\langle b, u\rangle \geq 0 \Longrightarrow f_i(x) - f_i(\overline{x}) + \sqrt{\varepsilon_i}\|x - \overline{x}\| \geq 0, \quad i = 1, \ldots, l, \tag{29}$$

$$g_j(x, v_j) \leq g_j(\overline{x}, v_j) \Longrightarrow \langle \eta_j, u\rangle \leq 0, \quad j = 1, \ldots, m. \tag{30}$$

If equation (29) takes a strictly inequality, i.e.,

$$\langle \xi_i, u\rangle + \sqrt{\varepsilon_i}\langle b, u\rangle \geq 0 \Longrightarrow f_i(x) - f_i(\overline{x}) + \sqrt{\varepsilon_i}\|x - \overline{x} > 0, \quad i = 1, \ldots, l, \tag{31}$$

then (f, g) is called a strictly pseudoquasi-type-I function at $\overline{x} \in C$.

The following is an example to illustrate the existence of the pseudoquasi-type-I function.

Example 1. Let $f_i: \mathbb{R} \longrightarrow \mathbb{R}$, $i = 1, 2$, be given by

$$f_1(x) = \begin{cases} \frac{3}{2}x, & \text{if } x \geq 0, \\ x, & \text{if } x < 0, \end{cases} \qquad f_2(x) = \begin{cases} \frac{4}{3}x, & \text{if } x \geq 0, \\ x, & \text{if } x < 0, \end{cases} \tag{32}$$

and $g: \mathbb{R} \times \mathscr{V} \longrightarrow \mathbb{R}$ be defined as

$$g(x, v) = vx^2,\ x \in \mathbb{R},\ v \in \mathscr{V}\backslash\{0\},\ g(x, 0) = \begin{cases} -\frac{2}{3}x, & \text{if } x < 0, \\ -x, & \text{if } x \geq 0, \end{cases} \tag{33}$$

where $\mathscr{V} = [0, 1]$. Taking $\overline{x} = 0$, $\sqrt{\varepsilon} = (\sqrt{\varepsilon}_1, \sqrt{\varepsilon}_2) = (1, 1)$, by simple calculation, we can obtain that $\partial f_1(\overline{x}) = [1, 3/2]$, $\partial f_2(\overline{x}) = [1, 4/3]$, $\partial_x g(\overline{x}, v) = \{0\}$, $v \in \mathscr{V}\backslash\{0\}$, $\partial_x g(\overline{x}, 0) = [-1, -2/3]$, and $\mathscr{V}(\overline{x}) = [0, 1]\sqrt{2}$. For any $x \in \mathbb{R}$, $\xi_i \in \partial f_i(\overline{x})$, $i = 1, 2$, $b \in \mathbb{B}$, $\eta \in \partial_x g\ (\overline{x}, 0)$, and $v \in \mathscr{V}(\overline{x})$, there exists $0 \leq u \in \mathbb{R}$, such that

$$\langle \xi_1, u\rangle + \sqrt{\varepsilon_1}\langle b, u\rangle = \langle \xi_1, u\rangle + \langle b, u\rangle \geq 0 \Longrightarrow f_1(x) - f_1(\overline{x}) + \sqrt{\varepsilon_1}\|x - \overline{x}\| = f_1(x) + \|x\| \geq 0 \tag{34}$$

$$\langle \xi_2, u\rangle + \sqrt{\varepsilon_2}\langle b, u\rangle = \langle \xi_2, u\rangle + \langle b, u\rangle \geq 0 \Longrightarrow f_2(x) - f_2(\overline{x}) + \sqrt{\varepsilon_2}\|x - \overline{x}\| = f_2(x) + \|x\| \geq 0 \tag{35}$$

$$g(x, v) \leq g(\overline{x}, v) \Longrightarrow 0 \cdot u \leq 0, \quad v \in \mathscr{V}\backslash\{0\}, \tag{36}$$

$$g(x, 0) \leq g(\overline{x}, 0) \Longrightarrow \eta \cdot u \leq 0, \quad v = 0. \tag{37}$$

Hence, (f, g) is a pseudoquasi-type-I function at $\overline{x} = 0$.

3. Optimality Conditions

In this section, we begin with establishing the optimality necessary conditions for a robust ε−quasi weak efficient solution to the problem (NUMP) by using the alternative theorem (Lemma 3).

Theorem 1. *In the problem (NUMP), if $\overline{x} \in \mathscr{F}$ is a robust ε−quasi weak efficient solution of the problem (NUMP), then there exists not all the zero real values $\overline{\lambda}_i \geq 0$, $i = 1, \ldots, l$, $\overline{\mu}_j \geq 0$, $j \in J_1(\overline{x})$, such that*

$$\sum_{i=1}^{l} \overline{\lambda}_i f_i^{\circ}(\overline{x}; d) + \sum_{j \in J_1(\overline{x})} \overline{\mu}_j \psi_j^{\circ}(\overline{x}; d) + \sum_{i=1}^{l} \overline{\lambda}_i \left(\sqrt{\varepsilon}_i \|\cdot - \overline{x}\|\right)^{\circ}(\overline{x}; d) \geq 0, \quad \forall d \in \mathbb{R}^n. \tag{38}$$

Proof. Firstly, we claim that the following system of inequalities:

$$\begin{cases} f_i^{\circ}(\overline{x}, d) + \left(\sqrt{\varepsilon}_i \|\cdot - \overline{x}\|\right)^{\circ}(\overline{x}, d) < 0, & i = 1, \ldots, l, \\ \psi_j^{\circ}(\overline{x}, d) < 0, & \forall j \in J_1(\overline{x}), \end{cases} \tag{39}$$

has no solution $d\prime \in \mathbb{R}^n$. Otherwise, there exists $d \in \mathbb{R}^n$, such that

$$f_i^{\circ}(\overline{x}, d) + \left(\sqrt{\varepsilon}_i \|\cdot - \overline{x}\|\right)^{\circ}(\overline{x}, d) < 0, \quad i = 1, \ldots, l, \qquad \psi_j^{\circ}(\overline{x}, d) < 0, \quad \forall j \in J_1(\overline{x}). \tag{40}$$

Since

$$\limsup_{t \longrightarrow 0^+} \frac{f_i(\overline{x} + t\,d) - f_i(\overline{x})}{t} = \inf_{\overline{\delta}_i^1 > 0} \sup_{0 < t < \overline{\delta}_i^1} \frac{f_i(\overline{x} + t\,d)(\overline{x}, d)}{t}, \tag{41}$$

$$\limsup_{t \longrightarrow 0^+} \frac{\sqrt{\varepsilon}_i \|\overline{x} + t\,d - \overline{x}\| - \sqrt{\varepsilon}_i \|\overline{x} - \overline{x}\|}{t} = \inf_{\overline{\delta}_i^2 > 0} \sup_{0 < t < \overline{\delta}_i^2} \frac{\sqrt{\varepsilon}_i \|\overline{x} + t\,d - \overline{x}\| - \sqrt{\varepsilon}_i \|\overline{x} - \overline{x}\|}{t}, \tag{42}$$

$$i = 1, \ldots, l, \tag{43}$$

we get

$$\begin{aligned}
&\limsup_{t\longrightarrow 0^+}\left(\frac{f_i(\overline{x}+t\,d)+\sqrt{\varepsilon}_i\|\overline{x}+t\,d-\overline{x}\|-f_i(\overline{x})-\sqrt{\varepsilon}_i\|\overline{x}-\overline{x}\|}{t}\right)\\
&\le \limsup_{t\longrightarrow 0^+}\frac{f_i(\overline{x}+t\,d)-f_i(\overline{x})}{t}+\limsup_{t\longrightarrow 0^+}\frac{\sqrt{\varepsilon}_i\|\overline{x}+t\,d-\overline{x}\|-\sqrt{\varepsilon}_i\|\overline{x}-\overline{x}\|}{t}\\
&=\inf_{\overline{\delta}_i^1>0}\sup_{0<t<\overline{\delta}_i^1}\frac{f_i(\overline{x}+t\,d)-f_i(\overline{x})}{t}+\inf_{\overline{\delta}_i^2>0}\sup_{0<t<\overline{\delta}_i^2}\frac{\sqrt{\varepsilon}_i\|\overline{x}+t\,d-\overline{x}\|-\sqrt{\varepsilon}_i\|\overline{x}-\overline{x}\|}{t}\\
&\le \inf_{\overline{\delta}_i^1>0\,\epsilon>0}\sup_{0<t<\overline{\delta}_i^1\,\|h\|<\epsilon}\frac{f_i(\overline{x}+h+t\,d)-f_i(\overline{x}+h)}{t}+ \qquad (44)\\
&\inf_{\overline{\delta}_i^2>0\,\epsilon>0}\sup_{0<t<\overline{\delta}_i^2\,\|h\|<\epsilon}\frac{\sqrt{\varepsilon}_i\|\overline{x}+h+t\,d-\overline{x}\|-\sqrt{\varepsilon}_i\|\overline{x}+h-\overline{x}\|}{t}\\
&=\limsup_{\mathrm{h}\longrightarrow 0,\,\mathrm{t}\longrightarrow 0^+}\frac{f_i(\overline{x}+h+t\,d)-f_i(\overline{x}+h)}{t}+\limsup_{\mathrm{h}\longrightarrow 0,\,\mathrm{t}\longrightarrow 0^+}\frac{\sqrt{\varepsilon}_i\|\overline{x}+h+t\,d-\overline{x}\|-\sqrt{\varepsilon}_i\|\overline{x}+h-\overline{x}\|}{t}\\
&=f_i^{\circ}(\overline{x},d)+\left(\sqrt{\varepsilon}_i\|\cdot-\overline{x}\|\right)^{\circ}(\overline{x},d)<0,\quad i=1,\ldots,l.
\end{aligned}$$

Therefore, there exists $\overline{\delta}_i^*$, for any $0<t<\overline{\delta}_i^*$, and we arrive at

$$f_i(\overline{x}+t\,d)-f_i(\overline{x})+\sqrt{\varepsilon}_i\|\overline{x}+t\,d-\overline{x}\|<0,\quad i=1,\ldots,l. \qquad (45)$$

On the other hand, for any $j\in J_1(\overline{x})$,

$$\begin{aligned}
&\limsup_{t\longrightarrow 0^+}\frac{\psi_j(\overline{x}+t\,d)-\psi_j(\overline{x})}{t}=\inf_{\widetilde{\delta}_j^1>0}\sup_{0<t<\widetilde{\delta}_j^1}\frac{\psi_j(\overline{x}+t\,d)-\psi_j(\overline{x})}{t}\\
&\le \inf_{\widetilde{\delta}_j^1>0\,\varepsilon>0}\sup_{0<t<\widetilde{\delta}_j^1\,\|h\|<\varepsilon}\frac{\psi_j(\overline{x}+h+t\,d)-\psi_j(\overline{x}+h)}{t}\\
&=\limsup_{h\longrightarrow 0,\,t\longrightarrow 0^+}\frac{\psi_j(\overline{x}+h+t\,d)-\psi_j(\overline{x}+h)}{t}=\overset{\circ}{\psi}_j^{\circ}(\overline{x};d)<0.
\end{aligned} \qquad (46)$$

Hence, there exists $\widetilde{\delta}_j^*$, $j\in J_1(\overline{x})$ such that $\psi_j(\overline{x}+t\,d)<\psi_j(\overline{x})=0$, for any $0<t<\widetilde{\delta}_j^*$. In addition, for any $j\in J_2(\overline{x})$, one has $\psi_j(\overline{x})<0$. Noticing that ψ_j is a Lipschitz function, we know that there exists $\widehat{\delta}_j^*>0$, for any $t\in(0,\widehat{\delta}_j^*)$:

$$\psi_j(\overline{x}+t\,d)<0,\ \forall j\in J_2(\overline{x}). \qquad (47)$$

Let $\delta^*=\min(\overline{\delta}^*,\widetilde{\delta}^*,\widehat{\delta}^*)$, where $\overline{\delta}^*=\min_{i\in\{1,\ldots,l\}}\overline{\delta}_i^*$, $\widetilde{\delta}^*=\min_{j\in J_1(\overline{x})}\widetilde{\delta}_j^*$, and $\widehat{\delta}^*=\min_{j\in J_2(\overline{x})}\widehat{\delta}_j^*$. Then, for any $t\in(0,\delta^*)$, it yields that

$$\begin{aligned}
&\overline{x}+t\,d\in\mathscr{F},\ f_i(\overline{x}+t\,d)-f_i(\overline{x})+\sqrt{\varepsilon}_i\|\overline{x}+t\,d-\overline{x}\|<0,\\
&\qquad\qquad i=1,\ldots,l,
\end{aligned} \qquad (48)$$

which contradicts to the fact that $\overline{x}\in\mathscr{F}$ is a robust ε−quasi weak efficient solution of the problem (NUMP).

We conclude from Lemma 1 (ii) that

$$d\longmapsto f_i^{\circ}(\overline{x};d)+\left(\sqrt{\varepsilon}\left\|_i\cdot-\overline{x}\right\|\right)^{\circ}(\overline{x};d),\quad i=1,\ldots,l, \qquad (49)$$

$$\psi_j^{\circ}(\overline{x};d),\quad j\in J_1(\overline{x}) \qquad (50)$$

are convex functions. Again by Lemma 3, it can be known that there exists not all zero real values $\overline{\lambda}_i\ge 0$, $i=1,\ldots,l$, $\overline{\mu}_j\ge 0$, $j\in J_1(\overline{x})$, such that equation (38) holds.

Next, we will examine the optimality necessary conditions of the robust ε−quasi weak efficient solution to the problem (NUMP). For this purpose, we need to introduce the following extended nonsmooth Mangasarian–Fromovitz constrained qualification. □

Definition 3. In the problem (NRMP), let $\overline{x}\in\mathscr{F}$. If

$$\exists d\in\mathbb{R}^n\quad s.t.\ g_{jx}^{\circ}\left(\overline{x},v_j;d\right)<0,\ \forall v_j\in\mathscr{V}_j(\overline{x}),\ j\in J_1(\overline{x}), \qquad (51)$$

then it is called that the problem (NRMP) satisfies extended the nonsmooth Mangasarian–Fromovitz constrained qualification at $\overline{x}$.

Theorem 2. *In the problem (NUMP), suppose that g_j, $j=1,\ldots,m$, satisfy Assumptions (i)–(iv), and for any $x\in\mathbb{R}^n$, $g_j(x,\cdot)$ is a concave function on $\mathscr{V}_j$. If $\overline{x}\in\mathscr{F}$ is a robust ε−quasi weak efficient solution to the problem (NUMP), then there exists $(\overline{\lambda},\overline{\mu},\overline{v})\in\mathbb{R}_+^l\times\mathbb{R}_+^m\times\mathscr{V}$ and $(\overline{\lambda},\overline{\mu})\ne 0$, where $\overline{\lambda}=(\overline{\lambda}_1,\ldots,\overline{\lambda}_l)$, $\overline{\mu}=(\overline{\mu}_1,\ldots,\overline{\mu}_m)$, $\overline{v}=(\overline{v}_1,\ldots,\overline{v}_m)$, and $\overline{v}_j\in\mathscr{V}_j(\overline{x})$, $j=1,\ldots,m$, such that*

$$0\in\sum_{i=1}^{l}\overline{\lambda}_i\partial f_i(\overline{x})+\sum_{j=1}^{m}\overline{\mu}_j\partial_x g_j\left(\overline{x},\overline{v}_j\right)+\sum_{i=1}^{l}\overline{\lambda}_i\sqrt{\varepsilon_i}\mathbb{B}, \qquad (52)$$

$$\overline{\mu}_j g_j\left(\overline{x},\overline{v}_j\right)=0,\quad j=1,\ldots,m. \qquad (53)$$

In addition, if the problem (NRMP) satisfies the extended nonsmooth Mangasarian–Fromovitz constrained qualification at $\overline{x}$, then there exists $\overline{\lambda} \in \mathbb{R}_+^l \backslash \{0\}$ and $\overline{\mu} \in \mathbb{R}_+^m$, $\overline{v}_j \in \mathscr{V}_j(\overline{x})$, $j = 1, \ldots, m$, such that equations (52) and (53) hold.

Proof. Since $\overline{x}$ is a robust ε−quasi weak efficient solution to the problem (NUMP), it yields from Theorem 2 that there exists not all zero real values $\overline{\lambda}_i \geq 0$, $i = 1, \ldots, l$, $\overline{\mu}_j \geq 0$, $j \in J_1(\overline{x})$, such that

$$\sum_{i=1}^{l} \overline{\lambda}_i f_i^{\circ}(\overline{x}; d) + \sum_{j \in J_1(\overline{x})} \overline{\mu}_j \psi_j^{\circ}(\overline{x}; d) + \sum_{i=1}^{l} \overline{\lambda}_i \left(\sqrt{\varepsilon}_i \| \cdot - \overline{x} \|\right)^{\circ}, (\overline{x}; d) \geq 0, \ \forall d \in \mathbb{R}^n. \tag{54}$$

According to Lemma 1 (iii), we know that

$$\begin{aligned} &\sum_{i=1}^{l} \overline{\lambda}_i \max\{\langle \xi_i, d\rangle : \ \xi_i \in \partial f_i(\overline{x})\} \\ &+ \sum_{j \in J_1(\overline{x})} \overline{\mu}_j \max\left\{\langle \eta_j, d\rangle : \ \eta_j \in \partial \psi_j(\overline{x})\right\} \\ &+ \sum_{i=1}^{l} \overline{\lambda}_i \max\{\langle \zeta_i, d\rangle : \ \zeta_i \in \sqrt{\varepsilon}_i \mathbb{B}\} \geq 0, \quad \forall d \in \mathbb{R}^n. \end{aligned} \tag{55}$$

This means that

$$\max_{\xi_i \in \partial f_i(\overline{x})\, \eta_j \in \partial \psi_j(\overline{x})\, \zeta_i \in \sqrt{\varepsilon}_i \mathbb{B}} \left\{ \sum_{i=1}^{l} \overline{\lambda}_i \xi_i + \sum_{j \in J_1(\overline{x})} \overline{\mu}_j \eta_j + \sum_{i=1}^{l} \overline{\lambda}_i \zeta_i, d \right\} \geq 0, \quad \forall d \in \mathbb{B}, \tag{56}$$

this is equivalent to

$$\begin{aligned} &\inf_{d \in \mathbb{B}} \max_{\xi_i \in \partial f_i(\overline{x})\, \eta_j \in \partial \psi_j(\overline{x})\, \zeta_i \in \sqrt{\varepsilon}_i \mathbb{B}} \\ &\cdot \left\{ \sum_{i=1}^{l} \overline{\lambda}_i \xi_i + \sum_{j \in J_1(\overline{x})} \overline{\mu}_j \eta_j + \sum_{i=1}^{l} \overline{\lambda}_i \zeta_i, d \right\} \geq 0. \end{aligned} \tag{57}$$

Noticing that $\partial f_i(\overline{x})$, $\sqrt{\varepsilon}_i \mathbb{B}$, $i = 1, \ldots, l$, $\partial \psi_j(\overline{x})$, $j \in J_1(\overline{x})$, are the nonempty compact convex set in $\mathbb{R}^n$ (by Lemma 1 (i)). Hence, it follows from lop-sided minimax theorem [11] that there exists $\overline{\xi}_i \in \partial f_i(\overline{x})$, $\overline{\zeta}_i \in \sqrt{\varepsilon}_i \mathbb{B}$, $i = 1, \ldots, l$, $\overline{\eta}_j \in \partial \psi_j(\overline{x})$, $j \in J_1(\overline{x})$, such that

$$\begin{aligned} &\inf_{d \in \mathbb{B}} \left\{ \sum_{i=1}^{l} \overline{\lambda}_i \overline{\xi}_i + \sum_{j \in J_1(\overline{x})} \overline{\mu}_j \overline{\eta}_i + \sum_{i=1}^{l} \overline{\lambda}_i \overline{\zeta}_i, d \right\} \\ &= \max_{\xi_i \in \partial f_i(\overline{x})\, \eta_j \in \partial \psi_j(\overline{x})\, \zeta_i \in \sqrt{\varepsilon}_i \mathbb{B}} \\ &\cdot \inf_{d \in \mathbb{B}} \left\{ \sum_{i=1}^{l} \overline{\lambda}_i \xi_i + \sum_{j \in J_1(\overline{x})} \overline{\mu}_j \eta_j + \sum_{i=1}^{l} \overline{\lambda}_i \zeta_i, d \right\} \geq 0. \end{aligned} \tag{58}$$

Again because

$$\begin{aligned} &\inf_{d \in \mathbb{B}} \left\{ \sum_{i=1}^{l} \overline{\lambda}_i \overline{\xi}_i + \sum_{j \in J_1(\overline{x})} \overline{\mu}_j \overline{\eta}_j + \sum_{i=1}^{l} \overline{\lambda}_i \overline{\zeta}_i, d \right\} \\ &= -\left\| \sum_{i=1}^{l} \overline{\lambda}_i \overline{\xi}_i + \sum_{j \in J_1(\overline{x})} \overline{\mu}_j \overline{\eta}_j + \sum_{i=1}^{l} \overline{\lambda}_i \overline{\zeta}_i \right\| \geq 0, \end{aligned} \tag{59}$$

we arrive at

$$\left\| \sum_{i=1}^{l} \overline{\lambda}_i \overline{\xi}_i + \sum_{j \in J_1(\overline{x})} \overline{\mu}_j \overline{\eta}_j + \sum_{i=1}^{l} \overline{\lambda}_i \overline{\zeta}_i \right\| = 0. \tag{60}$$

Therefore,

$$0 \in \sum_{i=1}^{l} \overline{\lambda}_i \partial f_i(\overline{x}) + \sum_{j \in J_1(\overline{x})} \overline{\mu}_j \partial \psi_j(\overline{x}) + \sum_{i=1}^{l} \overline{\lambda}_i \sqrt{\varepsilon_i} \mathbb{B}. \tag{61}$$

In addition, for any $j \in J_2(\overline{x})$, let $\overline{\mu}_j = 0$. Then, from the above equation, we get that

$$0 \in \sum_{i=1}^{l} \overline{\lambda}_i \partial f_i(\overline{x}) + \sum_{j=1}^{m} \overline{\mu}_j \partial \psi_j(\overline{x}) + \sum_{i=1}^{l} \overline{\lambda}_i \sqrt{\varepsilon_i} \mathbb{B}, \tag{62}$$

$$\overline{\mu}_j \psi_j(\overline{x}) = 0, \quad j = 1, \ldots, m. \tag{63}$$

It yields from Remark 1 that there exists $\overline{v}_j \in \mathscr{V}_j(\overline{x})$, $j = 1, \ldots, m$, such that (52) and (53) are true.

On the other hand, if the problem (NRMP) satisfies the extended nonsmooth Mangasarian–Fromovitz constrained qualification at $\overline{x}$ and $\overline{\lambda} = 0$, then there exists $\overline{\mu} \in \mathbb{R}_+^m$, $\overline{v}_j \in \mathscr{V}_j(\overline{x})$, $j \in J_1(\overline{x})$, such that

$$0 \in \sum_{j \in J_1(\overline{x})} \overline{\mu}_j \partial_x g_j\left(\overline{x}, \overline{v}_j\right) = \partial_x \left(\sum_{j \in J_1(\overline{x})} \overline{\mu}_j g_j\left(\overline{x}, \overline{v}_j\right) \right), \tag{64}$$

and the above equation holds according to Lemma 2. Again by Lemma 1 (iii), we have

$$\sum_{j \in J_1(\overline{x})} \overline{\mu}_j g_{jx}^{\circ}\left(\overline{x}, v_j; d\right) \geq 0, \quad \forall d \in \mathbb{R}^n, \tag{65}$$

which contradicts to Definition 3. Hence, this leads to $\overline{\lambda} \in \mathbb{R}_+^l \backslash \{0\}$. □

It is said that equations (52) and (53) are robust optimality necessary conditions of the problem (NUMP). We present the following Theorem 3 which is an optimality sufficient condition for the robust ε-quasi weak efficient solution to the problem (NUMP). □

Theorem 3. *In the problem (NUMP), supposing that $(\overline{x}, \overline{\lambda}, \overline{\mu}, \overline{v}) \in \mathscr{F} \times (\mathbb{R}_+^l \backslash \{0\}) \times \mathbb{R}_+^m \times \mathscr{V}$ satisfies the robust optimality necessary conditions.*

(i) If (f, g) is a pseudoquasi-type-I function at $\overline{x}$, then $\overline{x}$ is a robust ε-quasi weak efficient solution of the problem (NUMP).

(ii) If (f, g) is a strictly pseudoquasi-type-I function at $\overline{x}$, then $\overline{x}$ is a robust ε-quasi efficient solution of the problem (NUMP).

Proof. By the given conditions, it follows that the robust optimality necessary conditions hold at $(\overline{x}, \overline{\lambda}, \overline{\mu}, \overline{v}) \in \mathscr{F} \times (\mathbb{R}^l_+ \backslash \{0\}) \times \mathbb{R}^m_+ \times \mathscr{V}$, that is,

$$0 \in \sum_{i=1}^{l} \overline{\lambda}_i \partial f_i(\overline{x}) + \sum_{j=1}^{m} \overline{\mu}_j \partial_x g_j\left(\overline{x}, \overline{v}_j\right) + \sum_{i=1}^{l} \overline{\lambda}_i \sqrt{\varepsilon_i}\mathbb{B}, \tag{66}$$

$$\overline{\mu}_j g_j\left(\overline{x}, \overline{v}_j\right) = 0, \quad j = 1, \ldots, m. \tag{67}$$

Therefore, there exists $\overline{\xi}_i \in \partial f_i(\overline{x})$, $b \in \mathbb{B}$, $\overline{\eta}_j \in \partial_x g_j(\overline{x}, \overline{v}_j)$, $j = 1, \ldots, m$, such that

$$\sum_{i=1}^{l} \overline{\lambda}_i \overline{\xi}_i + \sum_{j=1}^{m} \overline{\mu}_j \overline{\eta}_j + \sum_{i=1}^{l} \overline{\lambda}_i \sqrt{\varepsilon_i} b = 0. \tag{68}$$

Let us prove conclusion (i). If $\overline{x}$ is not a robust ε-quasi weak efficient solution of the problem (NUMP), then there exists $\hat{x} \in \mathscr{F}$, such that

$$f(\hat{x}) - f(\overline{x}) + \sqrt{\varepsilon}\|\hat{x} - \overline{x}\| \in -\mathbb{R}^l_{++}, \tag{69}$$

that is,

$$f(\hat{x}) - f(\overline{x}) + \sqrt{\varepsilon}\|\hat{x} - \overline{x}\| < 0, \quad i = 1, \ldots, l. \tag{70}$$

On the other hand, in equation (66), if $\overline{\mu}_j \neq 0$, then $g_j(\overline{x}, \overline{v}_j) = 0$, $j = 1, \ldots, m$. Again since $\hat{x} \in \mathscr{F}$, then

$$g_j\left(\hat{x}, \overline{v}_j\right) \leq 0. \tag{71}$$

Hence,

$$g_j\left(\hat{x}, \overline{v}_j\right) \leq 0 = g_j\left(\overline{x}, \overline{v}_j\right). \tag{72}$$

Because (f, g) is a pseudoquasi-type-I function at $\overline{x}$, combining equation (70) with equation (72), we conclude that for $\overline{\xi}_i \in \partial f_i(\overline{x})$, $i = 1, \ldots, l$, $b \in \mathbb{B}$, $\overline{\eta}_j \in \partial_x g_j(\overline{x}, \overline{v}_j)$, $\overline{v}_j \in \mathscr{V}_j(\overline{x})$, $j = 1, \ldots, m$, there exists $u \in \mathbb{R}^n$, such that

$$\langle \overline{\xi}_i, u\rangle + \sqrt{\varepsilon_i}\langle b, u\rangle < 0, \quad i = 1, \ldots, l, \tag{73}$$

$$\langle \overline{\eta}_j, u\rangle \leq 0, \quad \mu_j \neq 0. \tag{74}$$

Noticing that $\overline{\lambda} \in \mathbb{R}^l_+ \backslash \{0\}$, it holds that

$$\sum_{i=1}^{l} \overline{\lambda}_i\left(\overline{\xi}_i + \sqrt{\varepsilon_i} b, u\right) + \sum_{j=1}^{m} \overline{\mu}_j \langle \overline{\eta}_j, u\rangle < 0, \tag{75}$$

which contradicts to equation (74). Therefore, $\overline{x}$ is a robust ε-quasi weak efficient solution of the problem (NUMP).

By the similar arguments, we can prove (ii).

Finally, as the end of this article, we give a concrete example to verify Theorem 3. □

Example 2. Consider the following nonsmooth robust multiobjective programming $(\mathrm{NRMP})_0$ problem:

$$(\mathrm{NRMP})_0 \begin{cases} \min & f = \left(f_1(x), f_2(x)\right), \\ \text{s.t.} & g(x, v) \leq 0, \ v \in \mathscr{V} = [0, 1], \end{cases} \tag{76}$$

where

$$f_1(x) = \begin{cases} \dfrac{5}{2}x, & \text{if } x \geq 0, \\ x, & \text{if } x < 0, \end{cases} \qquad f_2(x) = \begin{cases} \dfrac{5}{3}x, & \text{if } x \geq 0, \\ x, & \text{if } x < 0, \end{cases} \tag{77}$$

and g: $\mathbb{R} \times \mathscr{V} \longrightarrow \mathbb{R}$ is given by

$$g(x, v) = vx^2, \ x \in \mathbb{R}, \ v \in \mathscr{V} \backslash \{0\}, \qquad g(x, 0) = \begin{cases} -\dfrac{1}{3}x, & \text{if } x < 0, \\ -x, & \text{if } x \geq 0. \end{cases} \tag{78}$$

Taking $\overline{x} = 0$ and $\sqrt{\varepsilon} = (\sqrt{\varepsilon}_1, \sqrt{\varepsilon}_2) = (1, 1)$, it is obvious to get that $\overline{x} = 0$ is a robust ε-quasi weak efficient solution of the problem $(\mathrm{NRMP})_0$. It is easy to know that

$$\partial f_1(\overline{x}) = \left[1, \frac{5}{2}\right], \qquad \partial f_2(\overline{x}) = \left[1, \frac{5}{3}\right], \tag{79}$$

$$\partial_x g(\overline{x}, v) = \{0\}, \quad v \in \mathscr{V} \backslash \{0\}, \tag{80}$$

$$\partial_x g(\overline{x}, 0) = \left[-1, -\frac{1}{3}\right], \ \mathscr{V}(\overline{x}) = [0, 1]. \tag{81}$$

For any $x \in \mathbb{R}$, $\xi_i \in \partial f_i(\overline{x})$, $i = 1, 2$, $b \in \mathbb{B}$, $\eta \in \partial_x g(\overline{x}, 0)$, and $v \in \mathscr{V}(\overline{x})$, there exists $0 \leq u \in \mathbb{R}$, such that

$$\langle \xi_1, u\rangle + \sqrt{\varepsilon_1}\langle b, u\rangle = \langle \xi_1, u\rangle + \langle b, u\rangle \geq 0 \Longrightarrow f_1(x) - f_1(\overline{x}) + \sqrt{\varepsilon_1}\|x - \overline{x}\| = f_1(x) + \|x\| \geq 0, \tag{82}$$

$$\langle \xi_2, u\rangle + \sqrt{\varepsilon_2}\langle b, u\rangle = \langle \xi_2, u\rangle + \langle b, u\rangle \geq 0 \Longrightarrow f_2(x) - f_2(\overline{x}) + \sqrt{\varepsilon_2}\|x - \overline{x}\| = f_2(x) + \|x\| \geq 0, \tag{83}$$

$$g(x, v) \leq g(\overline{x}, v) \Longrightarrow 0 \cdot u \leq 0, \quad v \in \mathscr{V} \backslash \{0\}, \tag{84}$$

$$g(x, 0) \leq g(\overline{x}, 0) \Longrightarrow \eta \cdot u \leq 0, \quad v = 0. \tag{85}$$

It is clear that (f, g) is a pseudoquasi-type-I function at $\overline{x}$. Equations (58) and (59) hold for $\lambda_1 = 1$, $\lambda_2 = 0$, $\mu = 0$, and $b = -1$. It yields from Theorem 3 that $\overline{x}$ is a ε-quasi weak efficient solution of the problem $(\mathrm{NRMP})_0$.

4. Conclusions

The optimality conditions of the robust approximate quasi weak efficient solution to a nonsmooth uncertain

multiobjective programming problem (NUMP) are studied by using the robust optimization method in this note. Firstly, we have introduced (f, g)-pseudoquasi-type-I functions to the problem (NUMP), and an example is presented to illustrate its existence. Secondly, under the assumptions that the problem (NUMP) satisfies the extended nonsmooth Mangasarian–Fromovitz constrained qualification and pseudoquasi-type-I convexity, optimality conditions of the robust ε-quasi weak efficient solution are proved.

Data Availability

The data used to support the findings of this study are included within the article.

Conflicts of Interest

The authors declare that they have no conflicts of interest.

Authors' Contributions

All authors contributed equally to the writing of this paper. All authors read and approved the final manuscript.

Acknowledgments

This research was supported by the Natural Science Foundation of China, under Grant no. 11861002; Natural Science Foundation of Ningxia, under Grant no. NZ17112; Key Project of North Minzu University, under Grant no. ZDZX201804; Nonlinear analysis and financial optimization research center of North Minzu University.

References

[1] A. Ben-Tal, L. E. Ghaoui, and A. Nemirovski, *Robust Optimization*, Princeton University Press, Princeton, NY, USA, 2009.

[2] T. D. Chuong and D. S. Kim, "A class of nonsmooth fractional multiobjective optimization problems," *Annals of Operations Research*, vol. 244, no. 2, pp. 367–383, 2016.

[3] M. Fakhar, M. R. Mahyarinia, and J. Zafarani, "On approximate solutions for nonsmooth robust multiobjective optimization problems," *Optimization*, vol. 150, pp. 1–31, 2019.

[4] J. H. Lee and L. Jiao, "On quasi ϵ-solution for robust convex optimization problems," *Optimization Letters*, vol. 10, pp. 1–14, 2016.

[5] X. K. Sun, "Characterizations of robust solution for convex optimization problems with data uncertainty," *Acta Mathematica Scientia*, vol. 37A, no. 2, pp. 257–264, 2017.

[6] X. K. Sun, X. B. Li, X. J. Long et al., "On robust approximate optimal solutions for uncertain convex optimization and applications to multiobjective optimization," *Pacific Journal of Optimization*, vol. 13, no. 4, pp. 621–643, 2017.

[7] G. M. Lee and P. T. Son, "On nonsmooth optimality theorems for robust optimization problems," *Bulletin of the Korean Mathematical Society*, vol. 51, no. 1, pp. 287–301, 2014.

[8] M. Fakhar, M. R. Mahyarinia, and J. Zafarani, "On nonsmooth robust multiobjective optimization under generalized convexity with applications to portfolio optimization," *European Journal of Operational Research*, vol. 265, no. 1, pp. 39–48, 2018.

[9] F. H. Clarke, *Optimization and Nonsmooth Analysis*, Wiley-Interscience, New York, NY, USA, 1983.

[10] O. L. Mangasarian, *Nonlinear Programming*, McGraw-Hill, New York, NY, USA, 1969.

[11] J. P. Aubin and I. V. Ekeland, *Applied Nonlinear Analysis*, John Wiley & Sons, 1984.

Hindawi
Complexity
Volume 2020, Article ID 2906546, 13 pages
https://doi.org/10.1155/2020/2906546

Research Article

Stabilisation of a Flexible Spacecraft Subject to External Disturbance and Uncertainties

Yun Fu,[1] **Yu Liu**,[2] **Lingyan Hu**,[1] **and Lingxi Peng**[3]

[1]*School of Information Engineering, Nanchang University, Nanchang 330031, China*
[2]*School of Automation Science and Engineering, South China University of Technology, Guangzhou 510640, China*
[3]*School of Mechanical and Electrical Engineering, Guangzhou University, Guangzhou 510006, China*

Correspondence should be addressed to Lingxi Peng; scu.peng@gmail.com

Received 1 May 2020; Accepted 18 June 2020; Published 23 July 2020

Academic Editor: Shuping He

This paper addresses the problems of vibration reduction and attitude tracking for a flexible spacecraft subject to external disturbances and uncertainties. Based on Hamilton's principle, flexible spacecraft is modelled by a coupled nonlinear partial differential equation with ordinary differential equations. Adaptive boundary control scheme is adopted to stabilize the vibration displacement of flexible appendage into a small neighbourhood of original position and simultaneously maintain attitude angle within the desired angle region. Two disturbance adaptive laws are constructed to attenuate the effect of unknown external disturbances. The well posedness of the controlled system is proven by using the semigroup theory. The proposed adaptive boundary control scheme can guarantee the uniform boundedness of the closed-loop system. Numerical simulation results illustrate the effectiveness of the proposed control scheme.

1. Introduction

Spacecraft with flexible appendage is playing a key role in the development of the communication industry and remote sensing. To satisfy the space mission requirements, attitude maneuver is the basic operation of spacecraft. In the complex space environment, flexible appendage may vibrate under the effects of external disturbances and attitude maneuver. Flexible appendage generally possesses characteristics of light weight, low damping, and limited energy. These flexible characteristics make the vibration reduction slow down. However, the continuous vibration may reduce the operating efficiency of flexible spacecraft and even result in the destruction of flexible appendage. Hence, it is necessary to design a powerful and efficient controller to reduce the vibration of flexible appendage and simultaneously track the desired attitude.

In recent years, many research studies related to the modeling, vibration suppression, and attitude control of flexible spacecraft have been published. For the sake of control design, the models of flexible spacecraft are discretized in most of these works. Examples of these control schemes include fault tolerant control [1], optimal control [2], and positive position feedback control [3]. In [4], a variable structure control based on pulse-width pulse-frequency technology is designed to suppress the vibration of a flexible spacecraft with parameter uncertainties and input nonlinearity. In [5], using the distributed piezoelectric actuator technology, the authors propose a momentum exchange feedback control to stabilize flexible spacecraft. In [6], H_∞ state feedback control is proposed for a flexible spacecraft in the presence of the multiobjective design requirements. The above control schemes are developed based on the discretization ordinary differential equation (ODE) models. However, model discretization may make the model inaccurate and bring spillover instability in control system although the ODE model provides the convenience in design control and appears brief in form [7, 8].

Compared with the control schemes designed from the ODE model [9–11], boundary control and distributed control are derived from the original partial differential equation (PDE) model, which can control all system modes

and eliminate the drawback of spillover instability. They have been widely used in the vibration reduction of flexible mechanical systems [12–14]. Synchronization control [15], backstepping boundary control [16], and cooperative control [17] are also effective for the distributed parameter system. In [18], the distributed fuzzy controller is adopted for a nonlinear distributed parameter system. It must be noted that distributed control is effective for the distributed parameter system. In [19], the authors design a mixed fuzzy/boundary control to ensure the practical stability of a nonlinear beam system. However, distributed control is more difficult to be implemented than boundary control in practice since it requires many distributed actuators and senors. Hence, boundary control is regarded as a more practical control scheme. In [20, 21], the authors design the restricted boundary controls to stabilize the flexible aerial refueling hose systems in the presence of varying length and speed. In [22], adaptive boundary control is designed to suppress the vibration of the flexible axially moving belt system with high acceleration/deceleration. Boundary barrier-based control is developed to regulate the elastic deformation of a flexible crane system with output constraint in [23]. In [24, 25], output feedback controls are developed to realize the target of vibration reduction for nonlinear flexible strings. For the nonuniform flexible wind turbine tower system, boundary control strategy is developed to reduce vibration via the generator electric torque in [26]. Although the great progress has been acquired for the boundary control design of flexible mechanical systems, the study of adaptive boundary control design for a flexible spacecraft system subject to external disturbances and parameter uncertainties is few. These results motivate us to design an adaptive boundary control scheme for the flexible spacecraft system.

External disturbance exists widely in practical engineering application. Many disturbance rejection technologies have been developed [27–29]. In [30], the signum function is considered to attenuate the impact of external disturbance, where the exact value of the upper bound of external disturbance is known. However, the signum function may bring the chattering in control input and the accurate information of external disturbance is hard to determine in practice. In [31], a common disturbance observer is developed to compensate for the effect of the bounded disturbance with the bounded rate, where the system structure physical parameters are certain. However, the robustness of the disturbance observers proposed in these papers is weak and the structure physical parameters of flexible spacecraft are uncertain. Hence, handling the effect of external disturbances in control design for a flexible spacecraft with uncertain parameters is still challenging. Mathematically, the proof of well posedness is one of the most important aspects of the stability analysis of the distributed parameter system. In [32], using the spectral analysis based on Lyapunov approach, the exponential stability of the Euler–Bernoulli beam system and the behavior of the solution of the closed-loop system are investigated. In [33–35], employing Gelerkin's approximation method, the well posedness of the flexible beam system with the proposed feedback boundary control is discussed. To avoid the complicated and tedious functional calculations, the semigroup theory is used to prove the well posedness of the closed-loop system in this paper.

In this paper, we investigate the vibration reduction and attitude control of a flexible spacecraft with parameter uncertainties. The accurate dynamic model of flexible spacecraft is given by a set of coupled partial differential equation with ordinary differential equations. Two adaptive boundary control laws are designed to ensure the uniformly bounded stability of the closed-loop system. It should be noted that the proposed control scheme is derived from the original infinite dimensional dynamic model without any discretization, which can avoid spillover instability. Combining robust control strategy with two disturbance adaptive laws, the effect of external disturbances is attenuated exponentially in the negative feedback loop. The proposed disturbance rejection method can avoid chattering phenomenon and improve robust of the designed control scheme. The well posedness and uniform boundedness of the closed-loop system are proven under the semigroup theory and Lyapunov stability theory.

The paper is organized as follows. The model of flexible spacecraft is derived in Section 2. Adaptive boundary control scheme with disturbance adaptive laws is designed in Section 3. In Section 4, the well posedness and stability of the closed-loop system are discussed. The results of numerical simulations are given in Section 5. Finally, this paper is concluded in Section 6.

2. Dynamics Analysis

2.1. Dynamic Model. Figure 1 shows a typical model of flexible spacecraft. The model consists of a rigid hub with the radius r, which represents the spacecraft body, and an uniform flexible cantilever beam with the tip mass m, which represents the flexible appendage, such as solar array or any other flexible structure. OXY and oxy are defined as the inertial frame and the frame fixed on the hub, respectively. Denote $w(x,t)$ as the elastic deflection at point x and time t with respect to the oxy frame. Define $\theta(t)$ as the attitude angle. θ_d is defined as the desired attitude. The tracking error is defined as $\theta_e(t) = \theta(t) - \theta_d$. $d_1(t)$ and $d_2(t)$ are the unknown boundary disturbances. $u_1(t)$ and $u_2(t)$ are the control inputs. The structure physical parameters of the flexible spacecraft system are listed as follows: EI is the bending stiffness of the flexible appendage, c is the coefficient of viscous damping, l is the length of the flexible appendage, T is the tension, ρ is the uniform mass per unit length, and I_h denotes the hub inertia.

For the sake of convenience in writing, the following notations are used throughout this paper: $(\cdot) = (\cdot)(x,t)$, $\dot{(\cdot)} = \partial(\cdot)/\partial t$, $\ddot{(\cdot)} = \partial^2(\cdot)/\partial t^2$, $(\cdot)' = \partial(\cdot)/\partial x$, $(\cdot)'' = \partial^2(\cdot)/\partial x^2$, $(\cdot)''' = \partial^3(\cdot)/\partial x^3$, $(\cdot)'''' = \partial^4(\cdot)/\partial x^4$, $(\cdot)^{(n)} = \partial^n(\cdot)/\partial x^n$.

To obtain the PDE model of the flexible spacecraft system, the kinetic energy, potential energy, and virtual work can be expressed as follows:

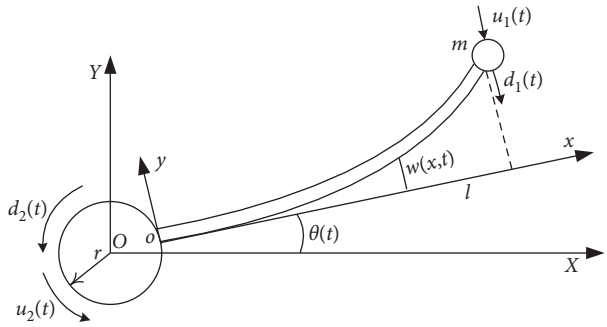

Figure 1: A typical flexible spacecraft system.

$$\begin{aligned}
E_k(t) &= \frac{1}{2}\rho\int_0^l [\dot{w} + (r+x)\dot{\theta}(t)]^2 \mathrm{d}x + \frac{1}{2}I_h\dot{\theta}^2(t) \\
&\quad + \frac{1}{2}m[\dot{w}(l,t) + (r+l)\dot{\theta}(t)]^2, \\
E_p(t) &= \frac{1}{2}T\int_0^l (w')^2 \mathrm{d}x + \frac{1}{2}\mathrm{EI}\int_0^l (w'')^2 \mathrm{d}x, \\
\delta W(t) &= -c\int_0^l [\dot{w} + (r+x)\dot{\theta}(t)]\delta[w + (r+x)\theta(t)]\mathrm{d}x \\
&\quad + [u_1(t) + d_1(t)]\delta[w(l,t) + (r+l)\theta(t)] \\
&\quad + [u_2(t) + d_2(t)]\delta\theta(t).
\end{aligned} \tag{1}$$

Using Hamilton's principle $\int_{t_1}^{t_2}[\delta E_k(t) - \delta E_p(t) + \delta W(t)]\mathrm{d}t = 0$, variational principle, and integration by parts, we can obtain the governing equations of the flexible spacecraft system as

$$\rho\ddot{w} + \mathrm{EI}w'''' - Tw'' + c\dot{w} = -(r+x)[\rho\ddot{\theta}(t) + c\dot{\theta}(t)], \tag{2}$$

$$\begin{aligned}
I_h\ddot{\theta}(t) &= \mathrm{EI}w'''(0,t) - r\mathrm{EI}w'''(0,t) + Tw(l,t) + u_2(t) \\
&\quad + d_2(t),
\end{aligned} \tag{3}$$

and the boundary conditions as

$$\begin{aligned}
m\ddot{w}(l,t) &= -m(r+l)\ddot{\theta}(t) + \mathrm{EI}w'''(l,t) - Tw'(l,t) \\
&\quad + u_1(t) + d_1(t),
\end{aligned} \tag{4}$$

$$w(0,t) = w'(0,t) = w''(l,t) = 0. \tag{5}$$

2.2. Preliminaries. The following lemmas and assumption are proposed for the convenience of control design and stability analysis.

Lemma 1. *Let $w(x,t)$ be the continuously differentiable function with $w(0,t) = 0$; then, the following inequality holds [36]:*

$$w^2(x,t) \le l\int_0^l [w'(x,t)]^2 \mathrm{d}x, \quad \forall t \in [0,\infty). \tag{6}$$

Lemma 2. *For bounded initial conditions, if there exists a C^1 continuous Lyapunov function $V(x) > 0$ satisfying $a_1(\|x\|) \le V(x) \le a_2(\|x\|)$, such that $\dot{V}(x) \le -bV(x) + c$, where a_1, a_2: $R^n \longrightarrow R$ are class $\mathcal{K}$ functions and $b, c > 0$, then the solution $x(t)$ is uniformly bounded [37].*

Assumption 1. For the unknown boundary disturbances $d_1(t)$ and $d_2(t)$, we assume that there exist two positive constants $\overline{d}_1$ and $\overline{d}_2$, such that $d_1(t) \le \overline{d}_1$ and $d_2(t) \le \overline{d}_2$, $\forall t \in [0,\infty)$. In practice, the energy of external disturbances $d_1(t)$ and $d_2(t)$ is finite. Thus, this assumption is reasonable.

3. Control Design

The control objectives of this paper are to reduce the vibration of flexible appendage and simultaneously trace the desired attitude. The block diagram given by Figure 2 describes the design procedure of the control strategy proposed in this paper for a flexible spacecraft system with external disturbances and parameter uncertainties. To stabilize the flexible spacecraft system described by (2)–(5), we design the following two adaptive boundary control laws:

$$\begin{cases}
u_1(t) = -k_0u_a(t) - \widehat{m}[k_1\dot{w}'(l,t) - k_2\dot{w}'''(l,t)] \\
\quad\quad + \widehat{T}w'(l,t) - \widehat{EI}\dot{w}'''(l,t) + u_{d_1}(t), \\
u_2(t) = -k_3\theta_e(t) - k_4S(t) - \gamma_1\widehat{I}_h\dot{\theta}(t) + u_{d_2}(t),
\end{cases} \tag{7}$$

where $\gamma_1, k_0, k_1, k_2, k_3, k_4 > 0$, $\widehat{m}$, $\widehat{T}$, $\widehat{\mathrm{EI}}$, and $\widehat{I}_h$ are the system parameter estimates, and the auxiliary signals $u_a(t)$ and $S(t)$ are given as follows:

$$\begin{cases}
u_a(t) = \dot{w}(l,t) + (r+l)\dot{\theta}(t) + k_1w'(l,t) - k_2w'''(l,t), \\
S(t) = \gamma_1\theta_e(t) + \dot{\theta}(t),
\end{cases} \tag{8}$$

where $u_{d_1}(t)$ and $u_{d_2}(t)$ are two new input signals and are proposed as follows:

$$\begin{cases}
u_{d_1}(t) = -\dfrac{\widehat{d}_1^2(t)}{\widehat{d}_1(t)|u_a(t)| + \tau_1}u_a(t), \\
u_{d_2}(t) = -\dfrac{\widehat{d}_2^2(t)}{\widehat{d}_2(t)|S(t)| + \tau_2}S(t),
\end{cases} \tag{9}$$

in which $\tau_1, \tau_2 > 0$ and $\widehat{d}_1(t)$ and $\widehat{d}_2(t)$ are the estimates of $\overline{d}_1$ and $\overline{d}_2$.

For a flexible spacecraft system with parameter uncertainties, we consider the following adaptive laws to estimate system parameters

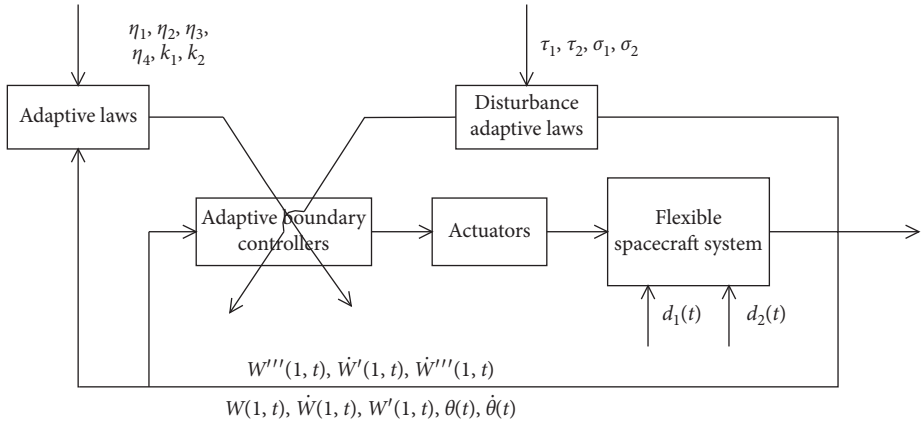

Figure 2: Design procedure of the adaptive boundary control scheme.

$$\begin{cases} \dot{\widehat{m}} = -\eta_1 \widehat{m} + u_a(t)\left[k_1 \dot{w}'(l,t) - k_2 \dot{w}'''(l,t)\right], & \widetilde{m} = \widehat{m} - m, \\ \dot{\widehat{T}} = -\eta_2 \widehat{T} - u_a(t) w'(l,t), & \widetilde{T} = \widehat{T} - T, \\ \dot{\widehat{\mathrm{EI}}} = -\eta_3 \widehat{\mathrm{EI}} + u_a(t) w'''(l,t), & \widetilde{\mathrm{EI}} = \widehat{\mathrm{EI}} - \mathrm{EI}, \\ \dot{\widehat{I}}_h = -\eta_4 \widehat{I}_h + \gamma_1 S(t)\dot{\theta}(t), & \widetilde{I}_h = \widehat{I}_h - I_h, \end{cases} \tag{10}$$

in which $\widetilde{m}$, $\widetilde{T}$, $\widetilde{\mathrm{EI}}$, and $\widetilde{I}_h$ are the estimation errors of system parameters.

The following disturbance adaptive laws are constructed to handle unknown boundary disturbances:

$$\begin{cases} \dot{\widehat{d}}_1(t) = -\sigma_1 \widehat{d}_1(t) + \left|u_a(t)\right|, \\ \widetilde{d}_1(t) = \widehat{d}_1(t) - \overline{d}_1, \end{cases} \tag{11}$$

$$\begin{cases} \dot{\widehat{d}}_2(t) = -\sigma_2 \widehat{d}_2(t) + |S(t)|, \\ \widetilde{d}_2(t) = \widehat{d}_2(t) - \overline{d}_2, \end{cases} \tag{12}$$

where $\widetilde{d}_1(t)$ and $\widetilde{d}_2(t)$ are the estimation errors of $\overline{d}_1$ and $\overline{d}_2$.

Remark 1. All signals in the proposed adaptive boundary control scheme (7) can be measured by sensors or computed by backward difference algorithm. $w(l,t)$, $w'(l,t)$, $w'''(l,t)$, $\theta(t)$, and $\dot{\theta}(t)$ can be directly measured by laser displacement sensor, inclinometer, shear force sensor, rotary encoder, and tachometer, respectively. $\dot{w}'(l,t)$ and $\dot{w}'''(l,t)$ can be computed by using backward difference algorithm based on measured values.

Remark 2. In this paper, different from the traditional control schemes designed from the ODE model, the adaptive boundary control scheme given by (7) is designed directly based on the original PDE model. Therefore, the drawback of spillover instability can be avoided and all system modes can be controlled. Moreover, the proposed boundary scheme (7) is an easier implemented control scheme than distributed control since it only requires the actuators and sensors at the system boundaries.

Remark 3. In practice, the exact values of boundary disturbances and the system structure physical parameters of flexible spacecraft are uncertain. To handle the unknown boundary disturbances, two disturbance adaptive laws (11) and (12) are developed, where we only require to ensure the existence of $\overline{d}_1$ and $\overline{d}_2$ and the chattering can be avoided. Thus, the proposed adaptive boundary control scheme (7) has better robustness than the common disturbance rejection technologies such as the signum function and disturbance observers.

4. Stability Analysis

4.1. Well-Posed Problem. In this part, the well posedness of the closed-loop system given by (2)–(5) is proven by employing the semigroup theory. The Hilbert space is introduced as the functional space. And then the closed-loop system can be rewritten to a first-order evolution equation. This result means that many results of the ordinary differential equation system can be applied in the proposed flexible spacecraft system.

For analyzing the well posedness, we introduce the following new variables:

$$\begin{cases} \widehat{\Phi} = [\widehat{m}, \widehat{T}, \widehat{EI}]^T, \\ \widetilde{\Phi} = [\widetilde{m}, \widetilde{T}, \widetilde{EI}]^T, \\ \Psi = \left[k_1 \dot{w}'(l,t) - k_2 \dot{w}'''(l,t), -w'(l,t), w'''(l,t)\right]^T, \\ z(x,t) = w(x,t) + (r+x)\theta(t), \\ w_e(x,t) = w(x,t) + (r+x)\theta_e(t). \end{cases} \tag{13}$$

The flexible spacecraft system described by (2)–(5) can be transformed as the following closed-loop system:

$$\begin{cases} \rho\ddot{z} + EIz'''' - Tz'' + c\dot{z} = 0, \\ I_h\dot{S}(t) = -k_4 S(t) - \gamma_1\widetilde{I}_h\dot{\theta}(t) - k_3\theta_e(t) + EIz''(0,t) \\ \quad -rEIz'''(0,t) \\ +d_2(t) + u_{d_2}(t) + T[z(l,t) - (r+l)\theta(t)], \\ m\dot{u}_a(t) = -k_0 u_a(t) + d_1(t) + u_{d_1}(t) - \Psi^T\widetilde{\Phi}, \\ \theta(t) = z'(0,t) = \dfrac{1}{r}z(0,t), \\ z''(l,t) = 0. \end{cases} \tag{14}$$

Define the state space as follows:

$$H \triangleq H_L^2(0.l) \times H_L^2(0,l) \times L^2(0,l) \times R^2, \tag{15}$$

where the space L^2 and H_L^2 are defined as

$$L^2(0,l) = \left\{ f\colon [0,l] \longrightarrow R \mid \int_0^l f^2 \mathrm{d}x < \infty \right\},$$

$$H_L^2(0,l) = \left\{ f \in L^2(0,l) \mid \frac{\partial f}{\partial x}, \frac{\partial^2 f}{\partial x^2} \in L_2, f(0) = rf'(0), \right.$$

$$\left. f''(l) = 0 \right\}. \tag{16}$$

The inner product of H is considered as

$$\begin{aligned} \langle Y_1, Y_2 \rangle_H = {} & \frac{\rho}{2}\int_0^l \psi_1\psi_2 \mathrm{d}x + \frac{\mathrm{EI}}{2}\int_0^l (\omega_1'')(\omega_2'')\mathrm{d}x \\ & + \frac{T}{2}\int_0^l [\omega_1' - \omega_1'(0)][\omega_2' - \omega_2'(0)]\mathrm{d}x + \frac{m}{2}u_{a_1}u_{a_2} \\ & + \frac{I_h}{2}S_1S_2 + \frac{k_3}{2\gamma_1^2}[S_1 - \psi_1'(0)][S_2 - \psi_2'(0)] \\ & + \gamma_1\rho\int_0^l (r+x)[(\varphi_1' + \psi_1)(\varphi_2' + \psi_2) \\ & - \varphi_1'\varphi_2' - \psi_1\psi_2]\mathrm{d}x, \end{aligned} \tag{17}$$

where $Y_i = (\omega_i, \varphi_i, \psi_i, u_{a_i}, S_i)^T \in H$, $i = 1, 2$.

We construct a linear operator as

$$A\begin{bmatrix} \omega \\ \varphi \\ \psi \\ u_a \\ S \end{bmatrix} = \begin{bmatrix} \psi \\ \psi \\ \dfrac{T}{\rho}\omega'' - \dfrac{\mathrm{EI}}{\rho}\omega'''' - \dfrac{\gamma}{\rho}\psi \\ -\dfrac{k_0}{m}u_a \\ -\dfrac{k_4}{I_h}S + \zeta \end{bmatrix}, \tag{18}$$

with its domain

$$\begin{aligned} D(A) = \Big\{ & (\omega, \varphi, \psi, u_a, S)^T \in H \mid S = \gamma_1\varphi'(0) + \frac{1}{r}\psi'(0), \\ & u_a = \psi(l) + k_1[\omega'(l) - \omega'(0)] - k_2\omega'''(l)\Big\}, \end{aligned} \tag{19}$$

where

$$\begin{aligned} \zeta = {} & -\frac{k_3}{I_h}\varphi'(0) + \frac{\mathrm{EI}}{I_h}\omega''(0) - \frac{r\mathrm{EI}}{I_h}\omega'''(0) \\ & + \frac{T}{I_h}[\omega(l) - (r+l)\omega'(0)]. \end{aligned} \tag{20}$$

Therefore, the closed-loop system (15) can be rewritten by the following evolutionary equation:

$$\begin{cases} \dfrac{\mathrm{d}Y(t)}{\mathrm{d}t} = AY(t) + F(t), \\ Y(0) = Y_0, \end{cases} \tag{21}$$

where $Y(t) = [z(\cdot,t), w_e(\cdot,t), \dot{z}(\cdot,t), u_a(t), S(t)]^T$, Y_0 is the system initial state, and $F(t)$ is given as follows:

$$F(t) = \begin{bmatrix} 0 \\ 0 \\ 0 \\ \dfrac{1}{m}\left[d_1(t) + u_{d_1}(t) - \Psi^T\widetilde{\Phi}\right] \\ \dfrac{1}{I_h}\left[d_2(t) + u_{d_2}(t) - \dfrac{\gamma_1\widetilde{I}_h}{r}\psi'(0,t)\right] \end{bmatrix}. \tag{22}$$

For any $Y \in H$,

$$\langle Y, AY\rangle_H \leq -M\left[\int_0^l \psi^2 \mathrm{d}x + \int_0^l \left[\omega' - \omega'(0)\right]^2 \mathrm{d}x + \int_0^l (\omega'')^2 \mathrm{d}x + u_a^2 + \int_0^l \varphi^2 \mathrm{d}x + S^2 + \theta_e^2(t)\right] \leq 0, \tag{23}$$

where M is a positive constant. Then, the operator A given by (18) is dissipative in H.

We claim that A^{-1} is compact on H. For any $Q = (q_1, q_2, q_3, q_4, q_5)^T \in H$, consider the solvability of equation $AY = Q$, $Y = (\omega, \varphi, \psi, u_a, S)^T \in D(A)$. From (18), we can obtain the following equation:

$$\begin{cases} \psi(x) = q_1(x), \\ \psi(x) = q_2(x), \\ \dfrac{T}{\rho}\omega''(x) - \dfrac{\mathrm{EI}}{\rho}\omega''''(x) - \dfrac{\gamma}{\rho}\psi(x) = q_3(x), \\ -\dfrac{k_0}{m}u_a = q_4, \\ \dfrac{k_4}{I_h}S + \zeta = q_5, \end{cases} \tag{24}$$

with corresponding boundary conditions

$$\begin{cases} \omega(0) = r\omega'(0), \\ \omega''(l) = 0, \\ S = \gamma_1\varphi'(0) + \dfrac{1}{r}\psi'(0), \\ u_a = \psi(l) + k_1\left[\omega'(l) - \omega'(0)\right] - k_2\omega'''(l). \end{cases} \tag{25}$$

Solving (24) leads to

$$\begin{cases} \omega(x) = \dfrac{e^{-bx}}{\mathrm{EI}}\displaystyle\int_0^x e^{2bg}\int_0^g e^{-b\varsigma}\int_0^\varsigma\int_0^p \left[\rho q_3(s) + \gamma q_1(s)\right] \\ \quad \mathrm{d}s\mathrm{d}p\mathrm{d}\varsigma\mathrm{d}g + a_1 + a_2x + a_3e^{-bx} + a_4e^{bx}, \\ \varphi(x) = \omega(x) - (r+x)\theta_d, \\ \psi(x) = q_2(x), \\ u_a = \dfrac{-m}{k_0}q_4, \\ S = \dfrac{I_h}{k_4}q_5 - \dfrac{I_h}{k_4}\zeta, \end{cases} \tag{26}$$

where $b = \sqrt{T/\mathrm{EI}}$, $a_i, i = 1, \ldots, 4$, are the constants and their values are uniquely determined by the boundary conditions (25) and ζ can be computed by $\varphi'(0), \omega(l), \omega'(0), \omega''(0)$, and $\omega'''(0)$. Thus, we can obtain that A^{-1} is a compact operator using Sobolev embedding theorem.

Under Assumption 1, using (9), (11), and (12), we can conclude that $F(t)$ is locally Lipschitz continuous. Thus, the closed-loop system is well posed [38]. Finally, if $Y_0 \in H$, the closed-loop system has a unique solution, which can be expressed as

$$Y = \Theta(t)Y_0 + \int_0^t \Theta(t-s)F(s)\mathrm{d}s, \tag{27}$$

where $\Theta(t)$ is the semigroup associated with A.

4.2. Uniform Boundedness. Consider the candidate Lyapunov function as

$$E(t) = E_1(t) + E_2(t) + E_3(t) + E_4(t), \tag{28}$$

where the energy term $E_1(t)$, auxiliary term $E_2(t)$, small crossing term $E_3(t)$, and estimation error term $E_4(t)$ are proposed as

$$\begin{cases} E_1(t) = \dfrac{\rho}{2}\displaystyle\int_0^l \left[\dot{w} + (r+x)\dot{\theta}\right]^2 \mathrm{d}x + \frac{T}{2}\int_0^l (w')^2 \mathrm{d}x \\ \quad + \dfrac{\mathrm{EI}}{2}\displaystyle\int_0^l (w'')^2 \mathrm{d}x, \\ E_2(t) = \dfrac{m}{2}u_a^2(t) + \dfrac{k_3}{2}\theta_e^2(t) + \dfrac{I_h}{2}S^2(t), \\ E_3(t) = \gamma_1\rho\displaystyle\int_0^l (r+x)\left[w' + \theta_e(t)\right]\left[\dot{w} + (r+x)\dot{\theta}(t)\right]\mathrm{d}x, \\ E_4(t) = \dfrac{1}{2}\left(\tilde{m}^2 + \tilde{T}^2 + \tilde{\mathrm{EI}}^2 + \tilde{I_h}^2\right) + \dfrac{1}{2}\left[\tilde{d}_1^2(t) + \tilde{d}_2^2(t)\right]. \end{cases} \tag{29}$$

Using Young's inequality for $E_3(t)$ yields

$$\begin{aligned} \left|E_3(t)\right| &= \gamma_1\rho\left|\int_0^l (r+x)\left[w' + \theta_e(t)\right]\left[\dot{w} + (r+x)\dot{\theta}\right]\mathrm{d}x\right| \\ &\leq \frac{\gamma_1\rho(r+l)}{2}\int_0^l (w')^2 \mathrm{d}x + \frac{\gamma_1\rho(r+l)}{\delta_1}\theta_e^2(t) \\ &\quad + \gamma_1\rho(r+l)\left(\frac{1}{2} + \delta_1\right)\int_0^l \left[\dot{w} + (r+x)\dot{\theta}\right]^2 \mathrm{d}x \\ &\leq \lambda\left[E_1(t) + E_2(t)\right], \end{aligned} \tag{30}$$

where δ_1, $\lambda = \gamma_1(r+l)\max\{\rho/T, 1 + 2\delta_1, 2\rho/\delta_1 k_3\} > 0$.

From (30), we can obtain

$$-\lambda\left[E_1(t) + E_2(t)\right] \leq E_3(t) \leq \lambda\left[E_1(t) + E_2(t)\right]. \tag{31}$$

Therefore, we further obtain

$$0 < \vartheta_1 \left[E_1(t) + E_2(t) + E_4(t)\right] \le E(t) \le \vartheta_2 \left[E_1(t) + E_2(t) + E_4(t)\right], \tag{32}$$

where $\vartheta_1 = 1 - \gamma_1 (r+l)\max\{\rho/T, 1+2\delta_1, 2\rho/\delta_1 k_3\} > 0$ and $\vartheta_1 = 1 - \gamma_1 (r+l)\max\{\rho/T, 1+2\delta_1, 2\rho/\delta_1 k_3\} > 1$.

The following lemma is proposed as a useful tool to obtain our main results.

Lemma 3. *The time derivative of the candidate Lyapunov function $E(t)$ has an upper bound as*

$$\dot{E}(t) \le -\vartheta E(t) + \varepsilon, \tag{33}$$

where ϑ and ε are two positive constants.

Proof. See Appendix A.

According to the above proposed lemmas, the stability theorem of the closed-loop flexible spacecraft system can be given as follows. □

Theorem 1. *For a flexible spacecraft system described by (2)–(5), under the proposed adaptive boundary control scheme (7), Assumption 1, and the bounded initial conditions, it can be obtained that the closed-loop flexible spacecraft system is uniformly bounded. The elastic deflection $w(x,t)$ and tracking error $\theta_e(t)$ remain in the compact sets Ω and Ω_e given by*

$$\Omega = \left\{ w(x,t) \in R \,|\, |w(x,t)| \le \sqrt{\frac{\lambda_1}{\vartheta_1}\left[E(0) + \frac{\varepsilon}{\vartheta}\right]}, \quad \forall (x,t) \in [0,l] \times [0,\infty) \right\},$$

$$\Omega_e = \left\{ \theta_e(t) \in R \,|\, |\theta_e(t)| \le \sqrt{\frac{\lambda_2}{\vartheta_1}\left[E(0) + \frac{\varepsilon}{\vartheta}\right]}, \quad \forall t \in [0,\infty) \right\}. \tag{34}$$

Proof. See Appendix B. □

5. Simulation

In order to demonstrate the feasibility and effectiveness of the proposed control scheme, the simulation is carried out employing the finite difference method. Let the initial conditions of the flexible spacecraft system be $w(x,0) = 0.6x$, $\dot{w}(x,0) = 0$, $\forall x \in [0,l]$, $\theta(0) = 0.4$, and $\dot{\theta}(0) = 0$. The system parameters are listed as follows: $\rho = 8$ kg/m, $l = 10$ m, $r = 0.5$ m, $m = 5$ kg, EI $= 120$ Nm^2, $T = 10$ N, $I_h = 300$ Ns/m, and $c = 0.0001$ kg/ms. The external boundary disturbances are given as

$$\begin{cases} d_1(t) = \sin(0.1\pi t) + \sin(0.2\pi t), \\ d_2(t) = \cos(0.1\pi t). \end{cases} \tag{35}$$

The elastic deflection and attitude angle of the flexible spacecraft system without control are shown in Figures 3 and 4,

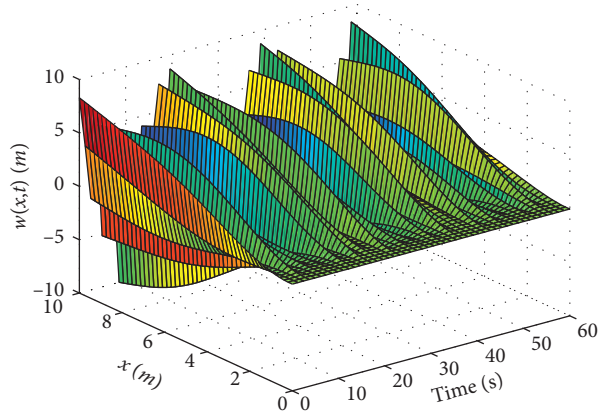

Figure 3: Deflection of the spacecraft without control.

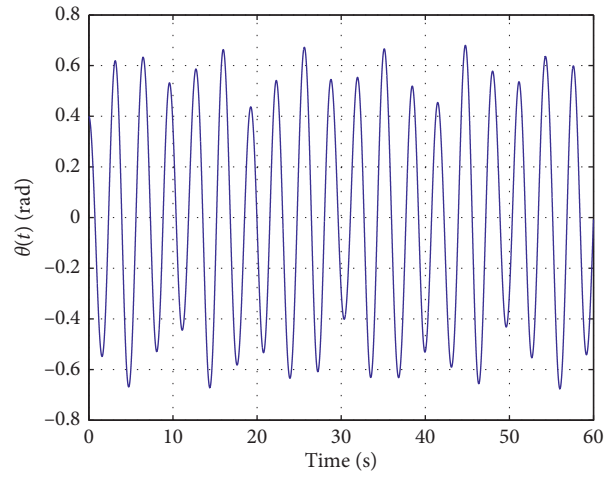

Figure 4: Attitude angle of the spacecraft without control.

respectively. Figures 5 and 6 display the deflection and attitude angle of the flexible spacecraft with the proposed adaptive boundary control scheme (7), respectively. Corresponding control inputs are described by Figure 7, where the control parameters are selected as follows: $k_0 = 10$, $k_1 = 1$, $k_2 = 12$, $k_3 = 6000$, and $k_4 = 100$. In addition, the estimates of upper bounds of boundary disturbances are shown in Figure 8. Figure 9 depicts the estimates of system parameters.

From Figures 3 and 4, it can be observed that the deflection $w(x,t)$ is quite large and the attitude angle (s) widely exceeds the desired attitude $\theta_d = 0.2$ (rad). From Figures 5 and 6, it is clear that the proposed adaptive boundary control scheme (7) can reduce effectively the deflection of flexible appendage and track the desired attitude after 20 s. These imply that great performances of tracking attitude and vibration reduction can be obtained based on the designed control scheme. From Figure 8, the control scheme proposed in this paper can stabilize the flexible spacecraft system in spite that the estimation error values of upper bounds of boundary disturbances cannot converge completely to zero. It can conclude from Figure 9 that the estimates of system

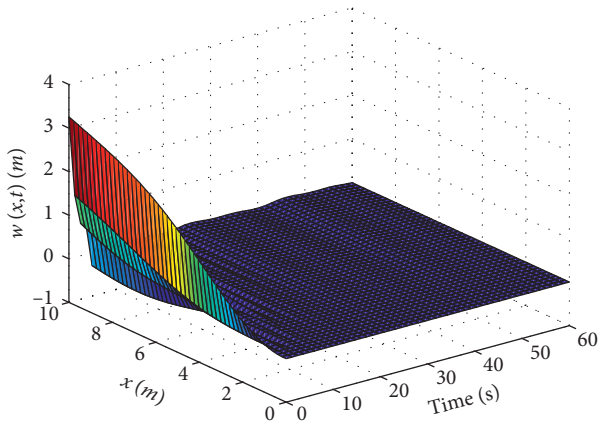

Figure 5: Deflection of the spacecraft with adaptive boundary control.

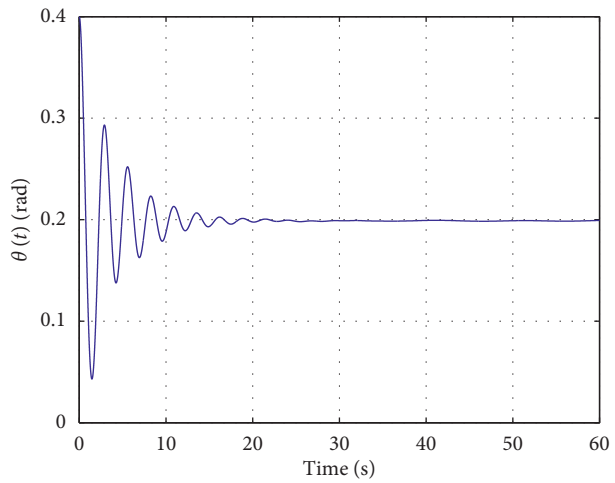

Figure 6: Attitude angle of the spacecraft with adaptive boundary control.

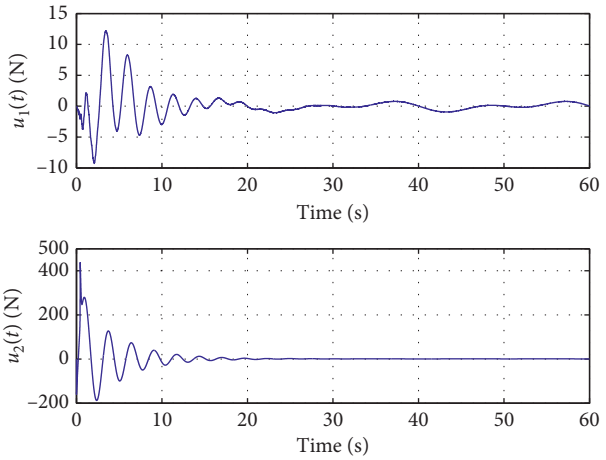

Figure 7: Control inputs.

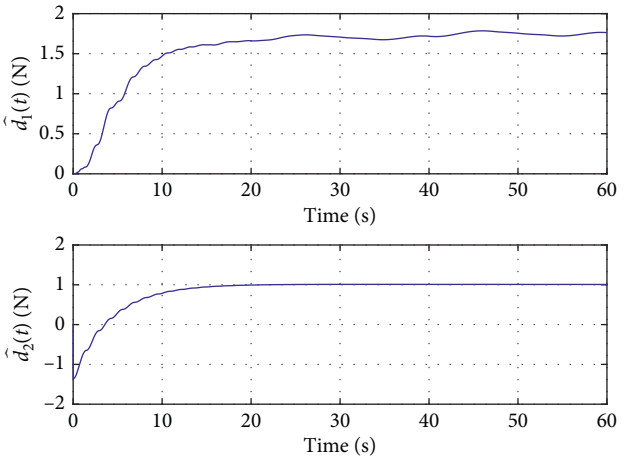

Figure 8: Estimates of $\overline{d}_1$ and $\overline{d}_2$.

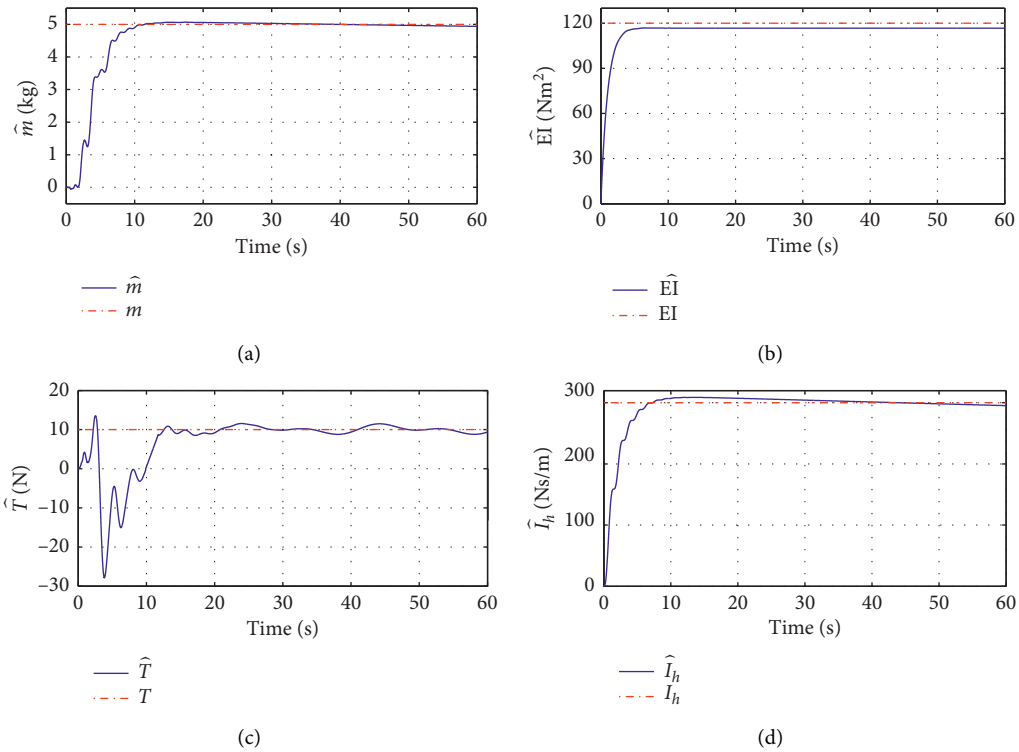

Figure 9: Estimates of system parameters.

parameters converge to the neighborhood of their true values.

6. Conclusion

In this paper, the control problems of vibration suppression and tracking attitude for a flexible spacecraft system subject to external disturbances and parameter uncertainties have been addressed. We have designed an adaptive boundary control scheme (7) to reduce the elastic deflection of flexible appendage and guarantee the convergence of the tracking error of attitude angle. Two disturbance adaptive laws (11) and (12) and adaptive laws (10) have been developed to eliminate the impacts of unknown boundary disturbances and parameter uncertainties. The well posedness and uniform boundedness of the closed-loop system have been proven. The simulation results have illustrated the effectiveness of the proposed control scheme.

It is worth mentioning that the proposed control scheme can avoid the problem of spillover instability and control all system modes since it is designed based on the original PDE model. In addition, the proposed control scheme is relatively practical control strategy since it is easy to be implemented by sensors and actuators embedded at the system boundaries. The proposed adaptive boundary scheme has great robustness for the unknown external disturbance. In future, we will investigate the other advanced control schemes such as fuzzy control and active disturbance rejection control to stabilize the flexible spacecraft system studied in this paper.

Appendix

Proof of Lemma 3:

Taking the time derivative of (28) results in

$$\dot{E}(t) = \dot{E}_1(t) + \dot{E}_2(t) + \dot{E}_3(t) + \dot{E}_4(t). \tag{A.1}$$

Differentiating $E_1(t)$ and then substituting the governing equation (3), we have

$$\dot{E}_1(t) = A_1 + A_2 + A_3, \tag{A.2}$$

where A_1, A_2, and A_3 are defined as

$$\begin{cases} A_1 = T\int_0^l \dot{w}' w' \mathrm{d}x, \\ A_2 = \mathrm{EI}\dot{w}'' w'' \mathrm{d}x, \\ A_3 = \int_0^l [\dot{w} + (r+x)\dot{\theta}(t)][Tw'' - \mathrm{EI}w''''] \mathrm{d}x \\ \quad -c\int_0^l [\dot{w} + (r+x)\dot{\theta}(t)]^2 \mathrm{d}x. \end{cases} \tag{A.3}$$

Applying integration by parts for A_1 and A_2 leads to

$$\begin{aligned} A_1 &= T\left[\dot{w}w'|_{x=0}^{l} - \int_0^l \dot{w}w''\mathrm{d}x\right] \\ &= -T\int_0^l \dot{w}w''\mathrm{d}x + Tw'(l,t)\dot{w}(l,t), \end{aligned} \tag{A.4}$$

$$\begin{aligned} A_2 &= \mathrm{EI}\left[\dot{w}'w''|_{x=0}^{l} - \int_0^l \dot{w}'w'''\mathrm{d}x\right] \\ &= \mathrm{EI}\left[\dot{w}'w''|_{x=0}^{l} - \dot{w}w'''|_{x=0}^{l} + \int_0^l \dot{w}w''''\mathrm{d}x\right] \\ &= \mathrm{EI}\int_0^l \dot{w}w''''\mathrm{d}x - \mathrm{EI}\dot{w}(l,t)w'''(l,t). \end{aligned} \tag{A.5}$$

Substituting (A.4) and (A.5) into (A.2) yields

$$\begin{aligned} \dot{E}_1(t) = &-c\int_0^l [\dot{w} + (r+x)\dot{\theta}(t)]^2\mathrm{d}x \\ &+ [\dot{w}(l,t) + (r+l)\dot{\theta}(t)][Tw'(l,t) - \mathrm{EI}w'''(l,t)] \\ &+ \dot{\theta}(t)[r\mathrm{EI}w'''(0,t) - \mathrm{EI}w''(0,t) - Tw(l,t)]. \end{aligned} \tag{A.6}$$

Differentiating $E_2(t)$ with respect to time t and substituting (7) yields

$$\begin{aligned} \dot{E}_2(t) = &-k_0u_a^2(t) - k_4S^2(t) - \gamma_1k_3\theta_e^2(t) - \gamma_1\widetilde{I}_hS(t)\dot{\theta}(t) \\ &+ u_a(t)\left[u_{d_1}(t) + d_1(t)\right] + S(t)\left[u_{d_2}(t) + d_2(t)\right] \\ &+ S(t)[Tw(l,t) + \mathrm{EI}w''(0,t) - r\mathrm{EI}w'''(0,t)] \\ &+ u_a(t)\Big[\widetilde{T}w\imath(l,t) - \widetilde{\mathrm{E}}\widetilde{\mathrm{I}}w'''(l,t) - \widetilde{m}\big(k_1\dot{w}'(l,t) \\ &- k_2\dot{w}'''(l,t)\big)\Big]. \end{aligned} \tag{A.7}$$

Differentiating $E_3(t)$, we have

$$\begin{aligned} \dot{E}_3(t) = &\gamma_1\rho\int_0^l (r+x)\left[\dot{w}' + \dot{\theta}(t)\right][\dot{w} + (r+x)\dot{\theta}(t)]\mathrm{d}x \\ &+ \gamma_1\rho\int_0^l (r+x)[w' + \theta_e(t)][\ddot{w} + (r+x)\ddot{\theta}(t)]\mathrm{d}x. \end{aligned} \tag{A.8}$$

Utilizing integration by parts derives

$$\begin{aligned} &\gamma_1\rho\int_0^l (r+x)\left[\dot{w}' + \dot{\theta}(t)\right][\dot{w} + (r+x)\dot{\theta}(t)]\mathrm{d}x \\ &= \frac{\gamma_1\rho(r+l)}{2}[\dot{w}(l,t) + (r+l)\dot{\theta}(t)]^2 - \frac{\gamma_1\rho r^3}{2}\dot{\theta}^2(t) \\ &\quad - \frac{\gamma_1\rho}{2}\int_0^l [\dot{w} + (r+x)\dot{\theta}(t)]^2\mathrm{d}x. \end{aligned} \tag{A.9}$$

Substituting the governing equation (3), we obtain

$$\begin{aligned} &\gamma_1\rho\int_0^l (r+x)[w' + \theta_e(t)] \\ &\quad\cdot [\ddot{w} + (r+x)\ddot{\theta}(t)]\mathrm{d}x = I_1 + I_2 + I_3 + I_4, \end{aligned} \tag{A.10}$$

in which

$$\begin{cases} I_1 = \gamma_1T\int_0^l (r+x)ww''\mathrm{d}x, \\ I_2 = -\gamma_1\mathrm{EI}\int_0^l (r+x)ww''''\mathrm{d}x, \\ I_3 = -\gamma_1c\int_0^l (r+x)w[\dot{w} + (r+x)\dot{\theta}(t)]\mathrm{d}x, \\ I_4 = \gamma_1\int_0^l (r+x)\theta_e(t)[Tw'' - \mathrm{EI}w''''']\mathrm{d}x \\ \quad -c\gamma_1\theta_e(t)\int_0^l (r+x)[\dot{w} + (r+x)\dot{\theta}(t)]\mathrm{d}x. \end{cases} \tag{A.11}$$

Using integration by parts for I_1 and I_2 and applying (7) yield

$$I_1 = -\frac{\gamma_1T}{2}\int_0^l (w')^2\mathrm{d}x + \frac{\gamma_1T(r+l)}{2}[w'(l,t)]^2, \tag{A.12}$$

$$\begin{aligned} I_2 = &-\frac{3\gamma_1EI}{2}\int_0^l (w'')^2\mathrm{d}x - \frac{\gamma_1\mathrm{EI}(r+l)}{2}[w''(0,t)]^2 \\ &- \gamma_1(r+l)\mathrm{EI}w'(l,t)w'''(l,t). \end{aligned} \tag{A.13}$$

Apply triangle inequality and Lemma 1 for I_3 results in

$$I_3 \le \frac{c\gamma_1(r+l)}{2}\left[l\int_0^l (w)'^2\mathrm{d}x + \int_0^l [\dot{w} + (r+x)\dot{\theta}(t)]^2\mathrm{d}x\right]. \tag{A.14}$$

By using integration by parts and Lemma 1, we derive

$$\begin{aligned} I_4 \le &\gamma_1c\delta_4\int_0^l [\dot{w} + (r+x)\dot{\theta}(t)]^2\mathrm{d}x + \gamma_1T(r+l)\delta_2[w'(l,t)]^2 \\ &+ \gamma_1\theta_e(t)[r\mathrm{EI}w'''(0,t) - \mathrm{EI}w''(0,t) - Tw(l,t)] \\ &+ \left(\frac{\gamma_1T(r+l)}{\delta_2} + \frac{\gamma_1\mathrm{EI}(r+l)}{\delta_3} + \frac{\gamma_1c}{\delta_4}\right)\theta_e^2(t) \\ &+ \gamma_1\mathrm{EI}(r+l)\delta_3[w'''(l,t)]^2, \end{aligned} \tag{A.15}$$

where $\delta_2, \delta_3, \delta_4 > 0$.

Combining with (A.12)–(A.15), we have

$$\begin{aligned}\dot{E}_3(t) \le & -\left(\frac{\gamma_1\rho}{2}-\frac{\gamma_1(r+l)c}{2}-\gamma_1 c\delta_4\right)\int_0^l [\dot{w}+(r+x)\dot{\theta}(t)]^2 \mathrm{d}x \\ & -\frac{3\gamma_1 \mathrm{EI}}{2}\int_0^l (w'')^2 \mathrm{d}x-\left(\frac{\gamma_1 T}{2}-\frac{\gamma_1(r+l)c}{2}\right)\int_0^l (w')^2 \mathrm{d}x \\ & +\gamma_1 \mathrm{EI}(r+l)[w'''(l,t)]^2+\frac{\gamma_1\rho(r+l)}{2} \\ & \cdot [\dot{w}(l,t)+(r+l)\dot{\theta}(t)]^2 \\ & +\gamma_1(r+l)\left[T(1+2\delta_2)[w'(l,t)]^2\right. \\ & \left.-\mathrm{EI}w'(l,t)w'''(l,t)\right] \\ & +\gamma_1\theta_e(t)[r\mathrm{EI}w'''(0,t)-\mathrm{EI}w''(0,t)-Tw(l,t)] \\ & +\left(\frac{\gamma_1 T(r+l)}{\delta_2}+\frac{\gamma_1 \mathrm{EI}(r+l)}{\delta_2}+\frac{\gamma_1 c}{\delta_4}\right)\theta_e^2(t).\end{aligned} \tag{A.16}$$

Substituting (10) into the fourth term of (A.1) and utilizing triangle inequality lead to

$$\begin{aligned}\dot{E}_4(t) \le & -\frac{\eta_1}{2}\tilde{m}^2-\frac{\eta_2}{2}\tilde{T}^2-\frac{\eta_3}{2}\tilde{\mathrm{EI}}^2-\frac{\eta_4}{2}\tilde{I}_h^2-\frac{\sigma_1}{2}\tilde{d}_1^{\,2}(t)-\frac{\sigma_2}{2}\tilde{d}_2^{\,2}(t) \\ & +\frac{\eta_1}{2}m^2+\frac{\eta_2}{2}T^2+\frac{\eta_3}{2}\mathrm{EI}^2+\frac{\eta_4}{2}I_h^2+\frac{\sigma_1}{2}\overline{d}_1^{\,2}+\frac{\sigma_2}{2}\overline{d}_2^{\,2} \\ & +\tilde{d}_1(t)|u_a(t)|+\tilde{d}_2(t)|S(t)|-\gamma_1\tilde{I}_h S(t)\dot{\theta}(t) \\ & +u_a(t)\left[\tilde{T}w'(l,t)-\tilde{m}\left(k_1\dot{w}'(l,t)-k_2\dot{w}'''(l,t)\right)\right. \\ & \left.-\tilde{\mathrm{EI}}w'''(l,t)\right].\end{aligned} \tag{A.17}$$

Substituting (A.6), (A.7), (A.16), and (A.17) into (A.1), we have

$$\begin{aligned}\dot{E}(t) \le & -\nu_1\int_0^l [\dot{w}+(r+x)\dot{\theta}(t)]^2 \mathrm{d}x-\gamma_1\nu_2\int_0^l (w')^2 \mathrm{d}x \\ & -\frac{3\gamma_1 \mathrm{EI}}{2}\int_0^l (w'')^2 \mathrm{d}x-\nu_3 u_a^2(t)-k_4 S^2(t)-\gamma_1\nu_4\theta_e^2(t) \\ & -\nu_5[\dot{w}(l,t)+(r+l)\dot{\theta}(t)]^2-\nu_6[w'''(l,t)]^2 \\ & -\nu_7[w'(l,t)]^2-\frac{\sigma_1}{2}\tilde{d}_1^{\,2}(t)-\frac{\sigma_2}{2}\tilde{d}_2^{\,2}(t)-\frac{\eta_1}{2}\tilde{m}^2 \\ & -\frac{\eta_2}{2}\tilde{T}^2-\frac{\eta_3}{2}\tilde{\mathrm{EI}}^2-\frac{\eta_4}{2}\tilde{I}_h^2+\frac{\eta_1}{2}m^2+\frac{\eta_2}{2}T^2+\frac{\eta_3}{2}\mathrm{EI}^2 \\ & +\frac{\eta_4}{2}I_h^2+\frac{\sigma_1}{2}\overline{d}_1^{\,2}+\frac{\sigma_2}{2}\overline{d}_2^{\,2}+\tau_1+\tau_2 \\ \le & -\vartheta_3[E_1(t)+E_2(t)+E_4(t)]+\varepsilon,\end{aligned} \tag{A.18}$$

where the proper parameters γ_1, k_i ($i=0,1,2,3,4$), and δ_j ($j=1,\ldots,6$) are chosen to satisfy the following conditions:

$$\begin{cases}\nu_1=c+\dfrac{\gamma_1\rho}{2}-\dfrac{\gamma_1(r+l)c}{2}-\gamma_1 c\delta_4>0, \\ \nu_2=T-(r+l)c>0, \\ \nu_3=k_0-\dfrac{T}{2k_1}>0, \\ \nu_4=k_3-\dfrac{T(r+l)}{\delta_2}-\dfrac{\mathrm{EI}(r+l)}{\delta_3}-\dfrac{c}{\delta_4}>0, \\ \nu_5=\dfrac{T}{2k_1}-\dfrac{\gamma_1\rho(r+l)}{2}-\dfrac{|k_2T-k_1\mathrm{EI}|}{k_1\delta_5}>0, \\ \nu_6=\dfrac{Tk_1}{2}-|k_2T-\gamma_1(r+l)\mathrm{EI}|\delta_6-\gamma_1(r+l)T(1+2\delta_2)>0, \\ \nu_7=\dfrac{Tk_2^2}{2k_1}-\dfrac{|k_2T-k_1\mathrm{EI}|\delta_5}{k_1}-\gamma_1(r+l)\mathrm{EI}\delta_3 \\ \quad -\dfrac{|k_2T-\gamma_1(r+l)\mathrm{EI}|}{\delta_6}>0, \\ \vartheta_3=\min\left\{\dfrac{2\nu_1}{\rho},\dfrac{\gamma_1\nu_2}{T},3\gamma_1,\dfrac{2k_4}{I_h},\dfrac{2\nu_3}{m},\dfrac{2\gamma_1\nu_4}{k_3},\eta_1,\eta_2,\eta_3,\right. \\ \quad \left.\eta_4,\sigma_1,\sigma_2\right\}>0, \\ \varepsilon=\dfrac{\eta_1}{2}m^2+\dfrac{\eta_2}{2}T^2+\dfrac{\eta_3}{2}\mathrm{EI}^2+\dfrac{\eta_4}{2}I_h^2+\dfrac{\sigma_1}{2}\overline{d}_1^{\,2}+\dfrac{\sigma_2}{2}\overline{d}_2^{\,2}+\tau_1+\tau_2.\end{cases} \tag{A.19}$$

According to (32) and (A.18), we further obtain

$$\dot{E}(t) \le -\vartheta E(t)+\varepsilon, \tag{A.20}$$

where $\vartheta=\vartheta_3/\vartheta_2>0$.

Proof of Theorem 1:

From Lemma 3, multiplying both sides of (33) by $e^{\vartheta t}$ yields

$$\frac{\partial\left(E(t)e^{\vartheta t}\right)}{\partial t} \le \varepsilon e^{\vartheta t}. \tag{B.1}$$

Integrating the above inequality, we have

$$E(t) \le \left[E(0)-\frac{\varepsilon}{\vartheta}\right]e^{-\vartheta t}+\frac{\varepsilon}{\vartheta} \le E(0)e^{-\vartheta t}+\frac{\varepsilon}{\vartheta}. \tag{B.2}$$

$E(0)$ is bounded since the system initial conditions is bounded. Inequality (B.2) implies that $E(t)$ is bounded.

Applying Lemma 1, (29), and (32) results in

$$\begin{cases} w^2(x,t) \le l\int_l^0 (w')^2 \mathrm{d}x \le \varrho_1 E_1(t) \le \dfrac{\varrho_1}{\vartheta_1} E(t), \\ \theta_e^2(t) \le \varrho_2 E_2(t) \le \dfrac{\varrho_2}{\vartheta_1} E(t), \\ \tilde{m}^2, \tilde{\mathrm{EI}}^2, \tilde{T}^2, \tilde{I_h}^2 \le 2E_4(t) \le \dfrac{2}{\vartheta_1} E(t), \\ \tilde{d}_1^2(t), \tilde{d}_2^2(t) \le 2E_4(t) \le \dfrac{2}{\vartheta_1} E(t), \end{cases} \tag{B.3}$$

where $\varrho_1 = 2l/T > 0$ and $\varrho_2 = 2/k_3$.

Substituting (B.2) into (B.3) leads to

$$\begin{cases} |w(x,t)| \le \sqrt{\dfrac{\varrho_1}{\vartheta_1}} \sqrt{\left[E(0) - \dfrac{\varepsilon}{\vartheta}\right] e^{-\vartheta t} + \dfrac{\varepsilon}{\vartheta}} \\ \le \sqrt{\dfrac{\varrho_1}{\vartheta_1}\left[E(0) + \dfrac{\varepsilon}{\vartheta}\right]}, \quad \forall 0 \le x \le l, \forall t \ge 0, \\ |\theta_e(t)| \le \sqrt{\dfrac{\varrho_2}{\vartheta_1}} \sqrt{\left[E(0) - \dfrac{\varepsilon}{\vartheta}\right] e^{-\vartheta t} + \dfrac{\varepsilon}{\vartheta}} \\ \le \sqrt{\dfrac{\varrho_2}{\vartheta_1}\left[E(0) + \dfrac{\varepsilon}{\vartheta}\right]}, \quad \forall t \ge 0, \\ |\tilde{m}|, |\tilde{\mathrm{EI}}|, |\tilde{T}|, |\tilde{I_h}|, |\tilde{d}_1(t)|, |\tilde{d}_2(t)| \\ \le \sqrt{\dfrac{2}{\vartheta_1}} \sqrt{\left[E(0) - \dfrac{\varepsilon}{\vartheta}\right] e^{-\vartheta t} + \dfrac{\varepsilon}{\vartheta}}, \\ \le \sqrt{\dfrac{2}{\vartheta_1}\left[E(0) + \dfrac{\varepsilon}{\vartheta}\right]}, \quad \forall t \ge 0. \end{cases} \tag{B.4}$$

According to Lemma 2, we can get that the closed-loop system is uniformly bounded. The error signals $\tilde{m}$, $\tilde{\mathrm{EI}}$, $\tilde{T}$, $\tilde{I_h}$, $\tilde{d}_1(t)$, and $\tilde{d}_2(t)$ are uniformly bounded. $w(x,t)$ and $\theta_e(t)$ remain in the compact sets.

Data Availability

The data used to support the findings of this study are available from the corresponding author upon request.

Conflicts of Interest

The authors declare that they have no conflicts of interest.

Acknowledgments

This work was supported in part by the National Natural Science Foundation of China (61203060, 61673181, and 81960327), Science and Technology Planning Project of Guangdong Province under Grant (2019A050510015), and Science and Technology Department of Jiangxi Province of China (20192BAB207029).

References

[1] B. Li, Q. Hu, Y. Yu, and G. Ma, "Observer-based fault-tolerant attitude control for rigid spacecraft," *IEEE Transactions on Aerospace and Electronic Systems*, vol. 53, no. 5, pp. 2572–2582, 2017.

[2] R. Chai, A. Savvaris, A. Tsourdos, S. Chai, and Y. Xia, "Optimal tracking guidance for aeroassisted spacecraft reconnaissance mission based on receding horizon control," *IEEE Transactions on Aerospace and Electronic Systems*, vol. 54, no. 4, pp. 1575–1588, 2018.

[3] N. Qi, Q. Yuan, Y. Liu, M. Huo, and S. Cao, "Consensus vibration control for large flexible structures of spacecraft with modified positive position feedback control," *IEEE Transactions on Control Systems Technology*, vol. 27, no. 4, pp. 1712–1719, 2019.

[4] Q. Hu and G. Ma, "Variable structure control and active vibration suppression of flexible spacecraft during attitude maneuver," *Aerospace Science And Technology*, vol. 9, no. 4, pp. 307–317, 2005.

[5] Z. Li and P. M. Bainum, "Vibration control of flexible spacecraft integrating a momentum exchange controller and a distributed piezoelectric actuator," *Journal of Sound and Vibration*, vol. 177, no. 4, pp. 539–553, 1994.

[6] H. J. Gao, X. Yang, and P. Shi, "Multi-objective robust, H_∞ control of spacecraft rendezvous," *IEEE Transactions on Control Systems Technology*, vol. 17, no. 4, pp. 794–802, 2009.

[7] M. J. Balas, "Active control of flexible systems," *Journal of Optimization Theory and Applications*, vol. 25, no. 3, pp. 415–436, 1978.

[8] W. He and S. Zhang, "Control design for nonlinear flexible wings of a robotic aircraft," *IEEE Transactions on Control Systems Technology*, vol. 25, no. 1, pp. 351–357, 2017.

[9] C. Ren and S. P. He, "Positiveness and observer-based finite-time control for a class of Markov jump systems with some complex environment parameters," *Complexity*, vol. 2018, Article ID 5365493, 13 pages, 2018.

[10] S. P. He, Q. Ai, C. C. Ren, J. Dong, and F. Liu, "Finite-time resilient controller design of a class of uncertain nonlinear systems with time-delays under asynchronous switching," *IEEE Transactions on Systems, Man, and Cybernetics: Systems*, vol. 49, no. 2, pp. 281–286, 2018.

[11] S. He, H. Fang, M. Zhang, F. Liu, and Z. Ding, "Adaptive optimal control for a class of nonlinear systems: the online policy iteration approach," *IEEE Transactions on Neural Networks and Learning Systems*, vol. 31, no. 2, pp. 549–558, 2020.

[12] Z. J. Zhao and C. K. Ahn, "Boundary output constrained control for a flexible beam system with prescribed Performance," *IEEE Transactions on Systems, Man, and Cybernetics: Systems*, pp. 1–9, 2019.

[13] B. Xu and P. Zhang, "Composite learning sliding mode control of flexible-link manipulator," *Complexity*, vol. 2017, Article ID 9430259, 6 pages, 2017.

[14] H.-N. Wu, H.-D. Wang, and L. Guo, "Disturbance rejection fuzzy control for nonlinear parabolic PDE systems via multiple observers," *IEEE Transactions on Fuzzy Systems*, vol. 24, no. 6, pp. 1334–1348, 2016.

[15] M. A. Demetriou, "Adaptive and optimal synchronization control of networked positive real infinite dimensional systems with virtual leader," *International Journal of Adaptive Control and Signal Processing*, vol. 32, no. 10, pp. 1403–1416, 2018.

[16] Z. Liu, J. Liu, and W. He, "Robust adaptive fault tolerant control for a linear cascaded ODE-beam system," *Automatica*, vol. 98, pp. 42–50, 2018.

[17] T. Endo, F. Matsuno, and Y. Jia, "Boundary cooperative control by flexible Timoshenko arms," *Automatica*, vol. 81, pp. 377–389, 2017.

[18] L. P. Jose, M. Rakhshan, M. M. Mardani et al., "Distributed saturated control for a class of semilinear PDE systems: an SOS spproach," *IEEE Transactions on Fuzzy Systems*, vol. 26, no. 2, pp. 749–760, 2018.

[19] H.-N. Wu and S. Feng, "Mixed fuzzy/boundary control design for nonlinear coupled systems of ODE and boundary-disturbed uncertain beam," *IEEE Transactions on Fuzzy Systems*, vol. 26, no. 6, pp. 3379–3390, 2018.

[20] Z. Liu, J. Liu, and W. He, "Modeling and vibration control of a flexible aerial refueling hose with variable lengths and input constraint," *Automatica*, vol. 77, pp. 302–310, 2017.

[21] Z. J. Liu, X. Y. He, Z. J. Zhao, C. K. Ahn, and H. X. Li, "Vibration control for spatial aerial refueling hoses with bounded actuators," *IEEE Transactions on Industrial Electronics*, 2020, In press.

[22] Y. Liu, Z. Zhao, and W. He, "Boundary control of an axially moving accelerated/decelerated belt system," *International Journal of Robust and Nonlinear Control*, vol. 26, no. 17, pp. 3849–3866, 2016.

[23] W. He, S. Zhang, and S. S. Ge, "Adaptive control of a flexible crane system with the boundary output constraint," *IEEE Transactions on Industrial Electronics*, vol. 61, no. 8, pp. 4126–4133, 2014.

[24] Z. J. Zhao, X. Y. He, Z. Ren, and G. Wen, "Boundary adaptive robust control of a flexible riser system with input nonlinearities," *IEEE Transactions on Systems, Man, and Cybernetics: Systems*, vol. 49, no. 10, pp. 1971–1980, 2018.

[25] Z. J. Zhao, X. Y. He, Z. Ren, and G. Wen, "Output feedback stabilization for an axially moving system," *IEEE Transactions on Systems, Man, and Cybernetics: Systems*, vol. 49, no. 12, pp. 2374–2383, 2018.

[26] X. Tong, X. Zhao, and S. Zhao, "Load reduction of a monopile wind turbine tower using optimal tuned mass dampers," *International Journal of Control*, vol. 90, no. 7, pp. 1283–1298, 2017.

[27] W. He, T. T. Meng, X. Y. He et al., "Iterative learning control for a flapping wing micro aerial vehicle under distributed disturbances," *IEEE Transactions on Cybernetics*, vol. 49, no. 4, pp. 1524–1535, 2018.

[28] Z. J. Zhao, X. Y. He, and C. K. Ahn, "Boundary disturbance observer-based control of a vibrating single-link flexible manipulator," *IEEE Transactions on Systems, Man, and Cybernetics: Systems*, 2019, In press.

[29] Z. Zhao, C. K. Ahn, and H.-X. Li, "Boundary antidisturbance control of a spatially nonlinear flexible string system," *IEEE Transactions on Industrial Electronics*, vol. 67, no. 6, pp. 4846–4856, 2020.

[30] L. J. Yang, Z. J. Liu, and S. Zhang, "Single parameter adaptive control of unknown nonlinear systems with tracking error constraints," *Complexity*, vol. 2018, Article ID 6457354, 19 pages, 2018.

[31] W. He, X. Y. He, and S. S. Ge, "Vibration control of flexible marine riser systems with input saturation," *IEEE/ASME Transactions on Mechatronics*, vol. 21, no. 1, pp. 254–265, 2016.

[32] Y. Liu, F. Guo, X. Y. He, and Q. Hui, "Boundary control for an axially oving system with input restriction based on disturbance observers," *IEEE Transactions on Systems, Man, and Cybernetics: Systems*, vol. 49, no. 11, pp. 2242–2253, 2018.

[33] W. Kang and B.-Z. Guo, "Stabilisation of unstable cascaded heat partial differential equation system subject to boundary disturbance," *IET Control Theory & Applications*, vol. 10, no. 9, pp. 1027–1039, 2016.

[34] Z. J. Zhao, C. K. Ahn, and X. H. Li, "Dead zone compensation and adaptive vibration control of uncertain spatial flexible riser systems," *IEEE/ASME Transactions on Mechatronics*, 2020, In press.

[35] F.-F. Jin and B.-Z. Guo, "Lyapunov approach to output feedback stabilization for the Euler-Bernoulli beam equation with boundary input disturbance," *Automatica*, vol. 52, pp. 95–102, 2015.

[36] C. D. Rahn, *Mechatronic Control of Distributed Noise and Vibration*, Springer, New York, NY, USA, 2001.

[37] W. He, Y. Dong, and C. Sun, "Adaptive neural impedance control of a robotic manipulator with input saturation," *IEEE Transactions on Systems, Man, and Cybernetics: Systems*, vol. 46, no. 3, pp. 334–344, 2016.

[38] A. Pazy, *Semigroups of Linear Operators and Applications to Partial Differential Equations*, Springer-Verlag, New York, NY, USA, 1983.

Hindawi
Complexity
Volume 2020, Article ID 3491845, 11 pages
https://doi.org/10.1155/2020/3491845

Research Article

Constant Force PID Control for Robotic Manipulator Based on Fuzzy Neural Network Algorithm

Zhu Dachang,[1] **Du Baolin**,[1] **Zhu Puchen**,[2] **and Chen Shouyan**[1]

[1]*School of Mechanical and Electrical Engineering, Guangzhou University, Guangzhou 510006, China*
[2]*School of Automation, Guangdong University of Technology, Guangzhou 510006, China*

Correspondence should be addressed to Zhu Dachang; zdc98998@gzhu.edu.cn

Received 13 April 2020; Accepted 14 May 2020; Published 17 July 2020

Academic Editor: Shuping He

The increased demand for robotic manipulator has driven the development of industrial manufacturing. In particular, the trajectory tracking and contact constant force control of the robotic manipulator for the working environment under contact condition has become popular because of its high precision and quality operation. However, the two factors are opposite, that is to say, to maintain constant force control, it is necessary to make limited adjustment to the trajectory. It is difficult for the traditional PID controller because of the complexity parameters and nonlinear characteristics. In order to overcome this issue, a PID controller based on fuzzy neural network algorithm is developed in this paper for tracking the trajectory and contact constant force simultaneously. Firstly, the kinetic and potential energy is calculated, and the Lagrange function is constructed for a two-link robotic manipulator. Furthermore, a precise dynamic model is built for analyzing. Secondly, fuzzy neural network algorithm is proposed, and two kinds of turning parameters are derived for trajectory tracking and contact constant force control. Finally, numerical simulation results are reported to demonstrate the effectiveness of the proposed method.

1. Introduction

Nowadays, the increased involvement of robotic manipulators in various industrial manufacturing facilities, such as precision assembly, and polishing in the field of ceramic sanitary ware or aircraft engine, precision surgery, and automobile manufacturing lead to new and innovative developments in the domain of dynamic modeling of mechanisms and control [1–3]. According to the working conditions of the robotic manipulators, there are two types: contract and noncontact. The vital features of the contact working condition are highly precise trajectory tracking capabilities; at the same time, it should have the ability to adjust the contact force/twist flexible [4, 5]. Along with the complexity and nonlinearity issues, the robotic manipulator suffered from various uncertainties, external disturbances, payload variations, and parameter variations during their operations [6, 7]. Therefore, it is not possible for the traditional proportional-integral-derivative (PID) controllers to provide effective control for trajectory tracking and constant force/twist control simultaneously.

According to the given value $r(t)$ and the actual output value $c(t)$, the traditional PID control combines the deviation $e(t) = r(t) - c(t)$ by proportion (P), integration (I), and differentiation (D) to form the control quantity. The control law is given by

$$\begin{aligned} u(t) &= K_p\left[e(t) + \frac{1}{T_i}\int_0^t e(t)\mathrm{d}t + T_d\frac{\mathrm{d}e(t)}{\mathrm{d}t}\right] \\ &= K_p e(t) + K_i\int_0^t e(t)\mathrm{d}t + K_d\frac{\mathrm{d}e(t)}{\mathrm{d}t}, \end{aligned} \tag{1}$$

where K_p is proportionality coefficient, T_i is integral time constant, T_d is differential time constant, and$K_i = K_p/T_i$is integral coefficient and $K_d = K_p \cdot T_d$ is differential coefficient. The parameter selection of a traditional PID controller must take into account the dynamic and static performance requirements. By using the method of closed-loop response,

a heuristic tuning method of PID parameters is proposed by Ziegler and Nichols in the 1940s.

In recent times, an overwhelming development in the terrain of advantage PID control schemes for parameters tuning has encouraged various control engineers to work in this developing field. Differential evolution (DE), genetic algorithm (GA), and particle swarm optimization (PSO) were used to determine the optimal gains of the position domain PID controller, and three distinct fitness functions were also used to quantify the contour tracking performance of each solution set in [8]. In order to expand the robustness and adaptive capabilities of conventional PID controller, a neural network- (NN-) based PID controller which is tuned when the controller is operating in an online mode for high-performance magnet synchronous motor position control was proposed by Kumar et al. [9], and the training algorithm for the PID controller gain initialization based on the minimum norm least square solution was also proposed. For the last few years, several works have been cited on the intelligent algorithm as well as online policy iterative approach, adaptive optimal control, sliding mode control, and neural network control for different processes or plants such as uncertain nonlinear systems [10, 11], autonomous under water vehicle (AUV) [12], mobile robot [13], permanent magnet synchronous motor drivers [14], and many others [15–19].

Recently, real-time trajectory optimization of robotic manipulators has received a lot of attention and research due to the increasing demand to improve movement speed, accuracy, and lower energy consumption when executing tasks. Several authors have been working toward intelligent PID control techniques of trajectory tracking for robotic manipulators, such as global asymptotic saturated PID control [20], fuzzy PID for enhanced position control in surgery robot [21], mobile robot [22–25], and flexible joint robot [26]. However, trajectory tracking is not the only factor to ensure the accuracy of the operation during the contact working conditions of the robotic manipulator, such as high precision flexible assembly, surface polishing, and location of clamp in minimally invasive surgery (shown in Figure 1).

With the changes of the pressure, temperature, friction, and wear of the contact surface, the contact force/twist between the robot and the work piece will also change. Although the robotic manipulator can run accurately according to the present trajectory, the machining quality or assembly quality on the contact surface will decline. By using a modified hybrid computed torque method based on the principle of orthogonalization, Sanchez presented an improving force tracking control structure to reduce the number of sensors with a velocity observer [27]. Cortesao proposed double active observer architecture to tackle precise force control in the presence of heart motion, and one controls the desired interaction force, and the other one is responsible for compensating heart motion autonomously [28]. An adaptive fuzzy backstepping position tracking control scheme was proposed for multirobot manipulator systems, and extra terms were also added to the control signals to consider the force tracking problem by utilizing the properties of internal forces in [29]. Accurate and robust force/twist control is still a great challenge for robot-environment contact applications, such as in drilling operations [30], polishing [31–33], welding [34], and surgical tasks [35].

In general, the traditional PID controller helps in eliminating the steady state error. However, this controller does not provide effective control in presence of nonlinearities and uncertainties. Moreover, motivated by the research studies carried out in [36, 37]. We proposed in this paper fuzzy neural network proportion-integration-differentiation (FNN-PID) constant force/twist control of the robotic manipulator for contact working conditions. The main contributions of the current paper are summarized as follows:

(1) By using Lagrange energy function, the precise dynamic model of two-link robotic manipulator is built. Compared with the literature [38], it completely represents the relationship between actuated torque and displacement and velocity and acceleration in joint space.

(2) For the contact working condition, the change of contact force will reduce the machining quality, so it is important to keep the contact constant force during manufacturing process. However, constant contact force and trajectory tracking are opposite to each other. In order to tune PID controller parameters quickly and effectively, a fuzzy neural network algorithm is proposed for two kinds functions of PID controller, that is, trajectory tracking and limited change online while contact constant force control.

This paper is organized in the following manner. Section 2 presents the precise dynamic modeling method, and the precise dynamic model of two types of planar robotic manipulator with RR (revolute joint) and RP (prismatic joint) are derived. Section 3 describes the PID controller with fuzzy neural network, and its stability is analyzed. Section 4 discusses the relationship between the contact force/twist with the trajectory according to the contact working conditions, and numerial simulation results are reported to demonstrate the effectiveness of the proposed method. Finally, conclusions are given in Section 5.

2. Dynamic Modeling of Two-Link Robot

The dynamic mathematical model for a rigid planar robotic manipulator having two links and a contact surface and the external force acted on the surface, as shown in Figure 2. According to the coordinate system $\{o - xy\}$, it consists of two links having link length l_1 and l_2 with their center of mass m_1 and m_2 lying at the middle of links, respectively. The length of center of mass are p_1 and p_2, respectively.

Different from the literature [39], the Lagrange method is used to build the precise dynamic model of two-link robotic manipulator with their nominal values as listed in Table 1.

The location coordinates and the square of velocity of $1^{\#}$ center of mass can be derived as follows:

(a) (b) (c)

Figure 1: Constant working conditions. (a) High precision flexible assembly; (b) minimally invasive surgery; (c) complexity surface polishing.

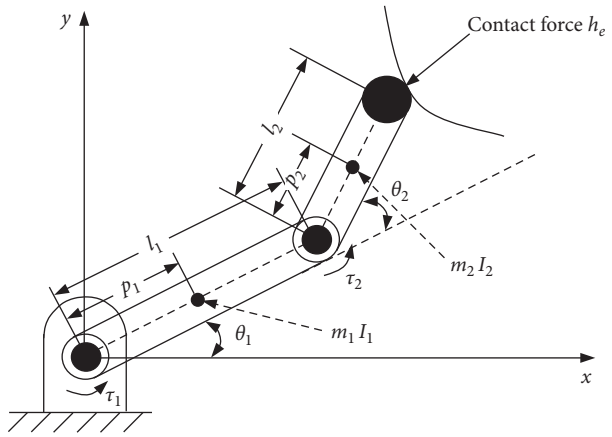

Figure 2: Two-link robotic manipulator plant with contact force at tip.

Table 1: Variables description of two-link robotic manipulator [39].

Description	Nominal value	Description	Nominal value
Center of mass link 1: m_1 (kg)	0.1	Center of mass link 2: m_2 (kg)	0.1
Length of link 1: l_1 (m)	0.8	Length of link 2: l_2 (m)	0.4
Length of center of mass link 1: p_1 (m)	0.4	Length of center of mass link 2: p_2 (m)	0.2
Centroid inertia of link 1: I_1 (kgm^2)	0.064	Centroid inertia of link 2: I_2 (kgm^2)	0.016
Joint variable of link 1: θ_1 (rad)	—	Joint variable of link 2: θ_2 (rad)	—
Torque of link 1: τ_1 (Nm)	—	Torque of link 2: τ_2 (Nm)	—

$$\begin{aligned} x_1 &= p_1 \sin\theta_1, \\ y_1 &= p_1 \cos\theta_1, \\ \dot{x}_1^2 + \dot{y}_1^2 &= \left(p_1\dot{\theta}_1\right)^2. \end{aligned} \tag{2}$$

The location coordinates and the square of velocity of 1# center of mass can also be derived as follows:

$$\begin{aligned} x_2 &= l_1 \sin\theta_1 + p_2 \sin(\theta_1 + \theta_2), \\ y_2 &= l_1 \cos\theta_1 + p_2 \cos(\theta_1 + \theta_2), \\ \dot{x}_2^2 + \dot{y}_2^2 &= l_1^2\dot{\theta}_1^2 + p_2^2\left(\dot{\theta}_1 + \dot{\theta}_2\right)^2 + 2l_1p_2\left(\dot{\theta}_1^2 + \dot{\theta}_1\dot{\theta}_2\right)\cos\theta_2. \end{aligned} \tag{3}$$

The total kinetic energy of the two-link robotic manipulator is

$$\begin{aligned} E_k = E_{k1} + E_{k2} &= \frac{1}{2}m_1p_1^2\dot{\theta}_1^2 + \frac{1}{2}m_2l_1^2\dot{\theta}_1^2 + \frac{1}{2}m_2p_2^2\left(\dot{\theta}_1 + \dot{\theta}_2\right)^2 \\ &+ m_2l_1p_2\left(\dot{\theta}_1^2 + \dot{\theta}_1\dot{\theta}_2\right)\cos\theta_2. \end{aligned} \tag{4}$$

The total potential energy of the two-link robotic manipulator is

$$\begin{aligned} E_p = E_{p1} + E_{p2} &= m_1gp_1\cos\theta_1 \\ &+ m_2g\left(l_1\cos\theta_1 + p_2\cos(\theta_1 + \theta_2)\right). \end{aligned} \tag{5}$$

The Lagrange function is constructed as follows:

$$L = E_k - E_p. \tag{6}$$

The dynamic equation of the two-link robotic manipulator can be calculated by

$$\tau_i = \frac{d}{dt}\frac{\partial L}{\partial \dot{\theta}_i} - \frac{\partial L}{\partial \theta_i}, \quad i = 1, 2. \tag{7}$$

The torque of joint 1 τ_1 can be derived as follows:

$$\begin{aligned}\frac{\partial L}{\partial \dot{\theta}_1} &= \left(m_1 p_1^2 + m_2 l_1^2\right)\dot{\theta}_1 + m_2 l_1 p_2\left(2\dot{\theta}_1 + \dot{\theta}_2\right)c_2 \\ &\quad + m_2 p_2^2\left(\dot{\theta}_1 + \dot{\theta}_2\right), \\ \frac{\partial L}{\partial \theta_1} &= -m_1 g p_1 s_1 - m_2 g\left(l_1 s_1 + p_2 s_{12}\right), \\ \tau_1 &= \frac{\mathrm{d}}{\mathrm{d}t}\frac{\partial L}{\partial \dot{\theta}_1} - \frac{\partial L}{\partial \theta_1} = D_{11}\ddot{\theta}_1 + D_{12}\ddot{\theta}_2 + D_{112}\dot{\theta}_1\dot{\theta}_2 \\ &\quad + D_{122}\dot{\theta}_2^2 + D_1,\end{aligned} \tag{8}$$

where $s_1 = \sin\theta_1$, $c_1 = \cos\theta_1$, $s_{12} = \sin(\theta_1 + \theta_2)$, and

$$\begin{cases} D_{11} = m_1 p_1^2 + m_2 p_2^2 + m_2 l_1^2 + 2m_2 l_1 p_2 c_2, \\ D_{12} = m_2 p_2^2 + m_2 l_1 p_2 c_2, \\ D_{112} = -2m_2 l_1 p_2 s_2, \\ D_{122} = -m_2 l_1 p_2 s_2, \\ D_1 = \left(m_1 p_1 + m_2 l_1\right) g s_1 + m_2 p_2 g s_{12}. \end{cases} \tag{9}$$

Meanwhile, the torque of joint 2 τ_2 can be also derived as

$$\tau_2 = \frac{\mathrm{d}}{\mathrm{d}t}\frac{\partial L}{\partial \dot{\theta}_2} - \frac{\partial L}{\partial \theta_2} = D_{21}\ddot{\theta}_1 + D_{22}\ddot{\theta}_2 + D_{212}\dot{\theta}_1\dot{\theta}_2 + D_{211}\dot{\theta}_2^2 + D_2, \tag{10}$$

where

$$\begin{cases} D_{21} = m_1 p_2^2 + m_2 l_1 p_2 c_2, \\ D_{22} = m_2 p_2^2, \\ D_{212} = 0, \\ D_{211} = m_2 l_1 p_2 s_2, \\ D_2 = m_2 p_2 g s_{12}. \end{cases} \tag{11}$$

Combined (8) with (10), the robotic plant can be rewritten with the following mathematical model:

$$\begin{bmatrix} D_{11} & D_{12} \\ D_{21} & D_{22} \end{bmatrix}\begin{bmatrix} \ddot{\theta}_1 \\ \ddot{\theta}_2 \end{bmatrix} + \begin{bmatrix} D_{112} \\ D_{212} \end{bmatrix}\begin{bmatrix} \dot{\theta}_1\dot{\theta}_2 \\ \dot{\theta}_2\dot{\theta}_1 \end{bmatrix} + \begin{bmatrix} D_{211} \\ D_{122} \end{bmatrix}\begin{bmatrix} \dot{\theta}_2^2 \\ \dot{\theta}_1^2 \end{bmatrix} + \begin{bmatrix} D_1 \\ D_2 \end{bmatrix} = \begin{bmatrix} \tau_1 \\ \tau_2 \end{bmatrix}. \tag{12}$$

Comparing with the literature [39], (12) completely represents the relationship between actuated torque and displacement and velocity and acceleration in joint space. The issues with D_{11} and D_{22} represent the moment of inertia caused by the acceleration of joint 1 and joint 2, respectively. The issues with D_{12} and D_{21} represent the moment of inertia of the acceleration coupling between two joints. The issues with D_{122} and D_{211} represent the coupling moment term of the centripetal force caused by the velocity between two joints. The issues with D_{112} and D_{212} represent the coupling moment term of the Coriolis force between two joints. D_1 and D_2 represent the gravity moment term. Considering the effect of centroid inertia, (12) can be modified by

$$\begin{aligned} D'_{11} &= I_1 + I_2 + D_{11}, \\ D'_{12} &= I_2 + D_{12}, \\ D'_{21} &= I_2 + D_{21}, \\ D'_{22} &= I_2 + D_{22}. \end{aligned} \tag{13}$$

Furthermore, to consider the effect of contact force act on the end-effector, right side of (12) can be replaced by

$$\tau' = \tau - J^T(q)h_e, \tag{14}$$

where h_e is the force and moment vector applied by the end-effector in the working environment, and $J^T(q)$ is the velocity Jacobian matrix, which yields to

$$J(q) = \begin{bmatrix} -l_1 s_1 - l_2 s_{12} & -l_2 s_{12}, \\ l_1 c_1 + l_2 c_{12} & l_2 c_{12}. \end{bmatrix} \tag{15}$$

3. PID Controller with Fuzzy Neural Network Algorithm

In order to design a fuzzy neural network PID (FNN-PID) controller for trajectory tracking and constant force control of the robotic manipulator, it is essential to derive the absolute error and the rate change of the external force act on the end-effector as the inputs for the fuzzy controller, which are calculated as

$$\begin{aligned} \Delta e_1 &= r(t) - y(t), \\ \Delta e_2 &= c(t) - \tau(t), \end{aligned} \tag{16}$$

where Δe_1 is the error of trajectory tracking, $r(t)$ is the given planning trajectory, $y(t)$ is output trajectory at time t, Δe_2 is the error of contact force, $c(t)$ is the given contact constant force, and $\tau(t)$ is the output contact force. A block diagram illustrating the proposed FNN-PID controller is shown in Figure 3.

The fuzzy control algorithm comprises the following three units: fuzzification, fuzzy rules, and defuzzification:

(1) Fuzzification: it takes e and ec as input language variables and K_p, K_I, and K_D as output language variables. The fuzzy subset of input and output variables are expressed as negative big (NB), negative middle (NM), negative small (NS), zero (ZO), positive small (PS), positive middle (PM), and positive big (PB). The domain of e and ec is $\{-3\ 3\}$, and the domain of K_p, K_I, and K_D are $\{-0.3\ 0.3\}$, $\{-0.06\ 0.06\}$, and $\{3\ 3\}$, respectively. The

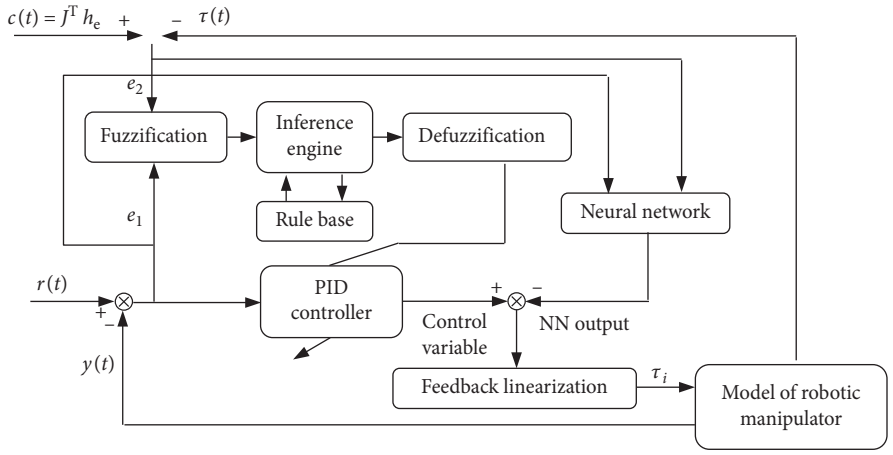

Figure 3: Block diagram of the proposed fuzzy PID with NN.

membership function for the proposed fuzzy algorithm is shown in Figure 4.

(2) Fuzzy rules: fuzzy rules were designed for tuning the gain control parameters of the PID controller (the same rules for trajectory tracking and constant force) as follows:

(i) When the error is large, in order to maintain a rapid response and make the absolute or errors reduce with the maximum speed, K_p should be bigger and K_I and K_D should be smaller. As the error decreases, to prevent an excessively large overshoot, K_D should be added, and K_p and K_I should be decreased uniformly.

(ii) When the system is over the steady state and the error is increasing, in order to decrease the overshoot, K_D should be bigger and K_I and K_D should be smaller.

(iii) When the system is tending toward a steady state, K_P should be assigned a bigger value in order to enhance the response speed and access the steady state quickly. K_D should be added to decrease the overshoot and K_I should be reduced to avoid the oscillations caused by integral overshoot.

(iv) When the overshoot of the system is negative and the error is increasing, K_D should be assigned a bigger value. When the error reaches the maximum and the system tends toward a steady state, K_D should be decreased and K_P and K_I should be increased.

Forty-nine fuzzy rules are obtained for the proposed fuzzy algorithm as follows:

Rule one: *if (e is NB) and (ec is NB) then ($K_P$is PB), ($K_I$is NB), and ($K_D$is PS)*

Rule two: *if (e is NB) and (ec is NM) then ($K_P$is PB), ($K_I$is NB), and ($K_D$is NS)*

Rule three: *if (e is NB) and (ec is NS) then ($K_P$is PM), ($K_I$is NM), and ($K_D$is NB)*

.....

Fuzzy rule setting for K_p, K_I, and K_D is given by Table 2.

(3) Defuzzification: defuzzification was performed to extract the values from all of the rules given above, where the number of rules was transformed into the number of variables by using a membership function. A center of gravity method is employed for defuzzification in this paper [40].

Furthermore, in order to accelerate the trajectory tracking and constant force control by the fuzzy PID controller, the NN is utilized in the proposed method previously.

Neural network function solves nonlinear problems, which change into linear ones, by mapping the low-dimension original space to the high-dimension feature space and approximating any continuous function with the weighted sum of multiple basis functions. The neural network structure is shown in Figure 5.

In the network structure, $X = [r(t), c(t)]^T$ is the input, $Y = [y(t), \tau(t)]^T$ is the output, $H = [h_1, h_2, \cdots, h_m]^T$ is the vector of radial basis, and h_j is usually the Gauss function:

$$h_j = \exp\left(-\frac{\left\|X - C_j\right\|^2}{2b_j^2}\right), \quad X = [r(t), c(t)]^T, \tag{17}$$

where $C_j = [c_{j1}, c_{j2}, \cdots, c_{jn}]^T$ is the center vector of the nth node and $B = [b_1, b_2, \cdots, b_m]^T$ is the width of the basis vector; the weight vector of network is selected as $W = [w_1, w_2, \ldots, w_m]^T$.

The output of the neural network is given by

$$Y_m(t) = w_1 h_1 + w_2 h_2 + \cdots + w_m h_m. \tag{18}$$

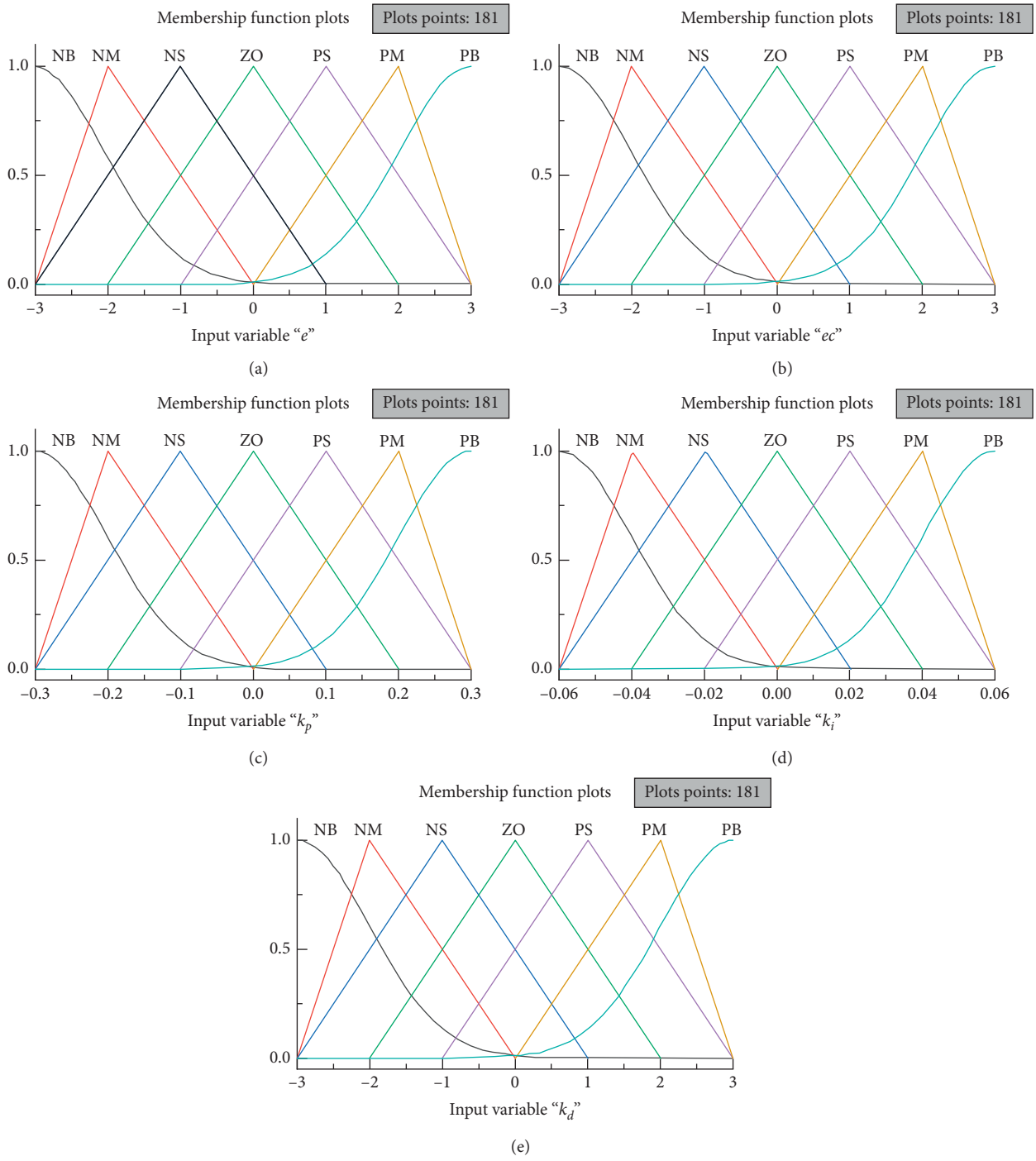

Figure 4: Fuzzy membership function.

The optimization objective function is given by

$$F = \frac{1}{2}\left(Y(t) - Y_m(t)\right)^2 = \frac{1}{2}\left(u(t)\right)^2. \tag{19}$$

According to the gradient descent method, the iteration algorithm of the neural network parameters is satisfied as follows:

Table 2: Fuzzy rule setting for K_p, K_I, and K_D.

e, ec	NB	NM	NS	ZO	PS	PM	PB
NB	PB/NB/PS	PB/NB/NS	PM/NM/NB	PM/NM/NB	PS/NS/NB	ZO/ZO/NM	ZO/ZO/PS
NM	PB/NB/PS	PB/NB/NS	PM/NM/NB	PS/NS/NM	PS/NS/NM	ZO/ZO/NS	NS/ZO/ZO
NS	PM/NM/ZO	PM/NM/NS	PS/NS/NM	PS/NS/NM	ZO/ZO/NS	NS/PS/NS	NS/PS/ZO
ZO	PM/NM/ZO	PM/NM/NS	PS/NS/NS	ZO/ZO/NS	NS/PS/NS	NM/PM/NS	NM/PM/ZO
PS	PS/NM/ZO	PS/NS/ZO	ZO/ZO/ZO	NS/PS/ZO	NS/PS/ZO	NM/PM/ZO	NM/PB/ZO
PM	PS/ZO/PB	ZO/ZO/NS	NS/PS/PS	NM/PS/PS	NM/PM/PS	NM/PB/PS	NB/PB/PB
PB	ZO/ZO/PB	ZO/ZO/PM	NM/PS/PM	NM/PM/PM	NM/PM/PS	NB/PB/PS	NB/PB/PB

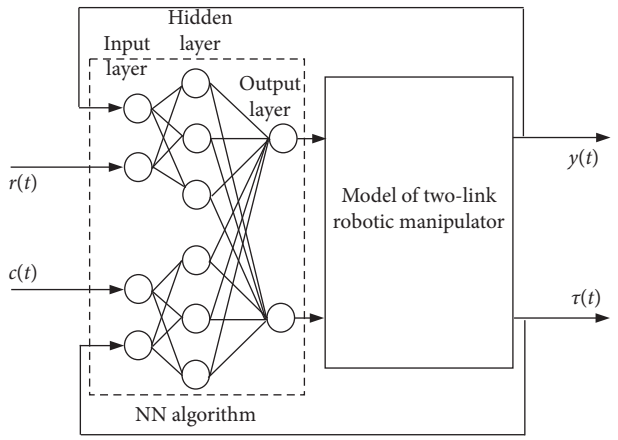

Figure 5: Structure diagram of NN algorithm for two-link robotic manipulator.

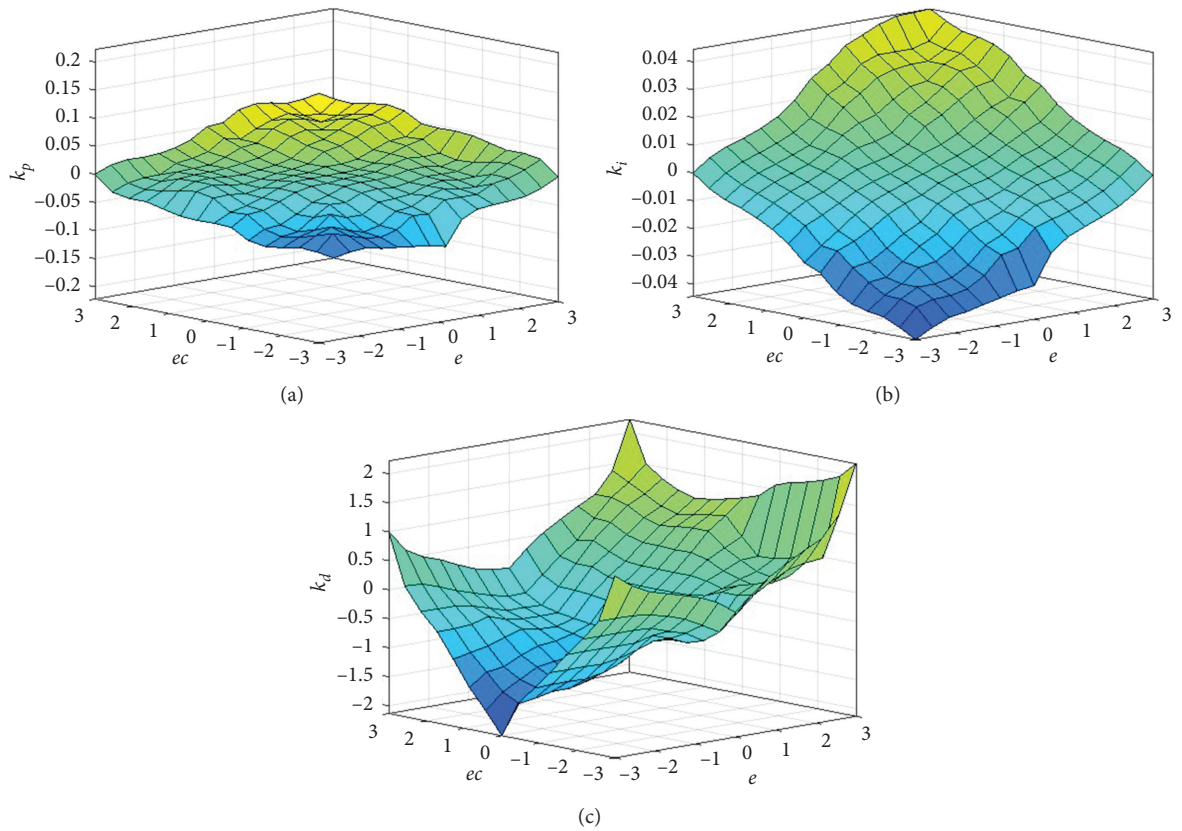

Figure 6: Surface schematic representations for K_P, K_I, and K_D.

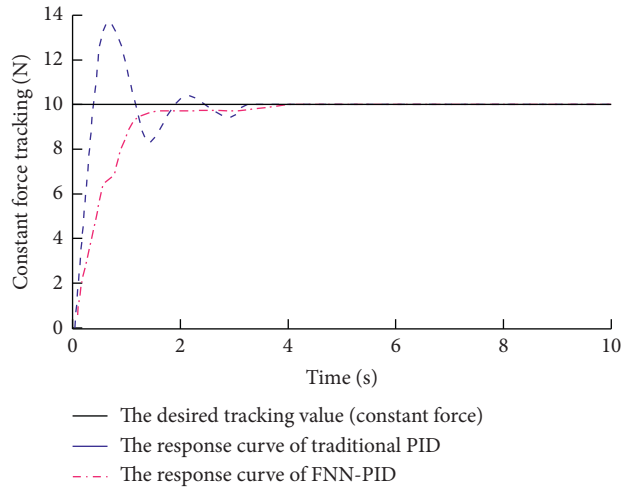

Figure 7: Comparison of response curves of two control strategies.

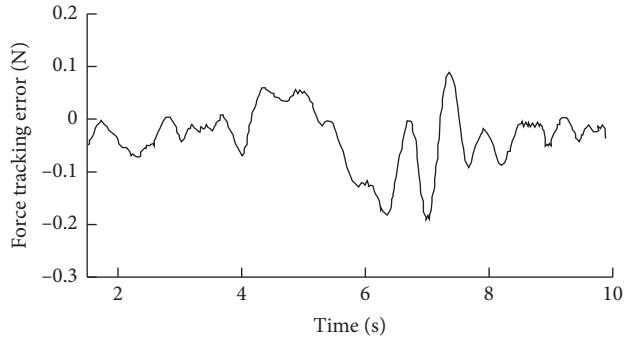

Figure 8: The constant force tracking error.

$$w_j(k) = w_j(k-1) + \eta u(t) h_j + \alpha\left(w_j(k-1) - w_j(k-2)\right),$$

$$\Delta b_j = u(t) w_j h_j \frac{\left\|X - C_j\right\|^2}{b_j^3},$$

$$b_j(k) = b_j(k-1) + \eta \Delta b_j + \alpha\left(b_j(k-1) - b_j(k-2)\right),$$

$$\Delta c_{ji} = u(t) w_j \frac{x_j - c_{ji}}{b_j^2},$$

$$c_{ji}(k) = c_{ji}(k-1) + \eta \Delta c_{ji} + \alpha\left(c_{ji}(k-1) - c_{ji}(k-2)\right), \tag{20}$$

where η is the learning rate and α is the momentum factor.

Regarding the sensitivity of the output to input changes, the algorithm is given as follows:

$$\frac{\partial Y}{\partial u} = \sum_{j=1}^{m} w_j h_j \frac{c_{ji} - \Delta u}{b_j^2}. \tag{21}$$

4. Simulation and Discussion

In this section, numerical simulation is conducted to demonstrate the performance of the proposed controller. The initialization parameters are determined as $\eta = 0.25$ and $\alpha = 0.04$. The initial value of the weight vector, the node center, and the width value of the basis function are shown as follows:

$$W = [-0.6132, -0.9216, 0.1835, 0.6783, -0.2210, -0.3275]^T,$$

$$B = [1.5039, 0.3736, 2.6521, 2.4361, 0.2505, 1.5362]^T,$$

$$C = \begin{bmatrix} 0.5862 & 0.6302 & -0.8965 & -2.0464 & -1.8435 & 1.6532 \\ -1.0356 & -0.2987 & 1.0536 & 0.5626 & 2.3748 & 0.5032 \\ -2.1452 & -0.2098 & 1.8364 & 2.6869 & 1.0592 & 2.1782 \end{bmatrix}^T. \tag{22}$$

Surface schematic representations of the gain control parameters comprising K_P, K_I, and K_D are shown in Figure 6.

The contact constant force is loaded as $10N$, and the response curves of two control strategies are shown in Figure 7. The constant force traction error in the stability interval (1.5–10 s) is shown in Figure 8. As shown in Figures 7 and 8, the response time of the complete tracking process in 1.5 s and the maximum traction error is 0.22 N. The parameters of the FNN-PID controller are self-adjusted; therefore, the response speed improved and the constant force tracking process is more stable.

While maintaining constant force control, simulation comparisons of the displacement trajectory tracking

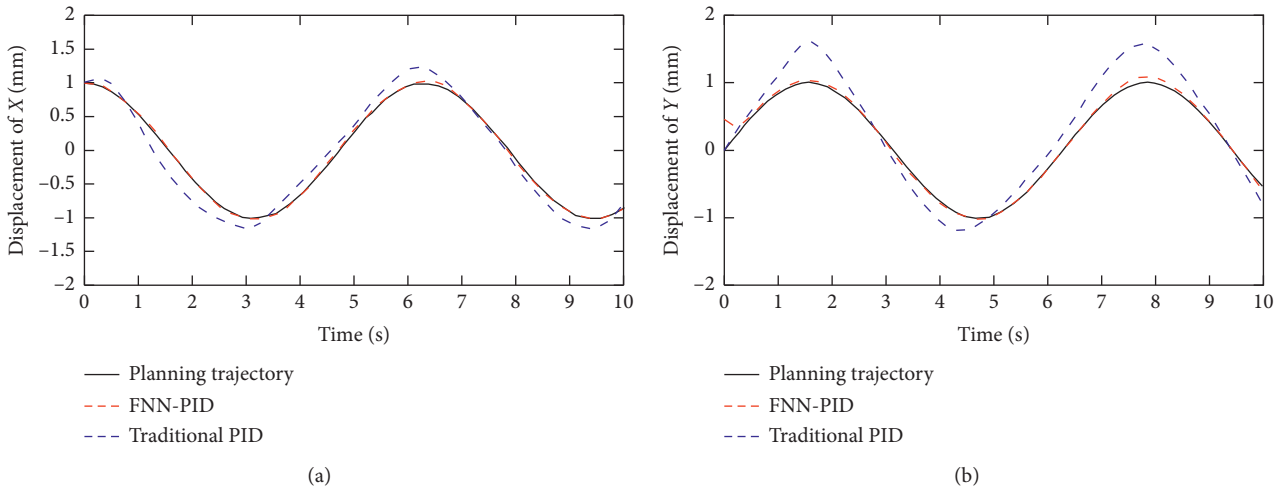

Figure 9: Displacement tracking of (a) x direction; (b) y direction.

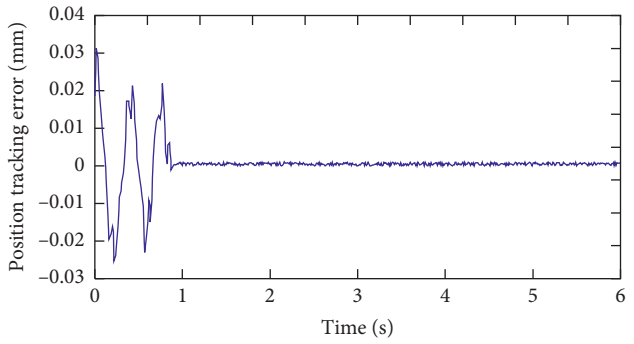

Figure 10: Position tracking errors of the end-effector of two-link robotic manipulator.

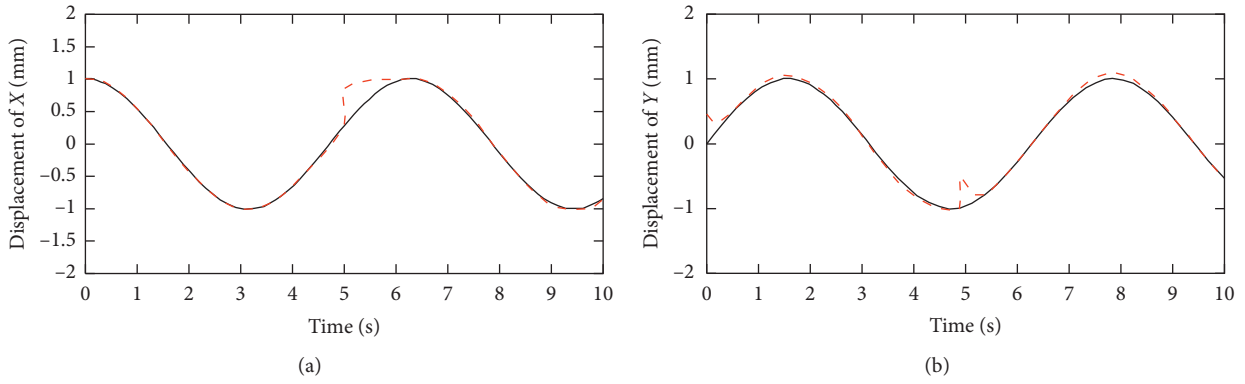

Figure 11: Displacement tracking (a) x direction and (b) y direction with external disturbance.

performance are derived. Displacement of the directions of x and y of the end-effector is shown in Figures 9(a) and 9(b), respectively, and the trajectory tracking errors of the end-effector are derived and shown as Figure 10. It shows that the maximum error is 0.03 mm, and the error is close to balance position and keeps stabilities after 0.8 s.

In order to test the dynamic characteristics of the proposed system, step function is used as an external disturbance at 5 s, and the displacement tracking of directions x and y is shown in Figure 11.

It shows that the tracking performance is convergence behind 0.85 s for x direction and 0.25 s for y direction,

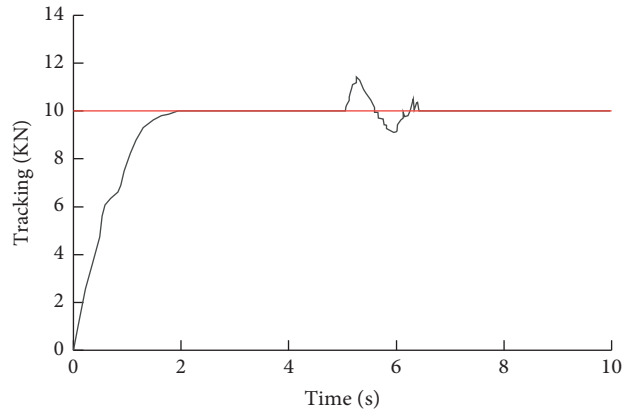

Figure 12: Constant force tracking with external disturbance.

respectively. Furthermore, the constant force tracking is also adjusted convergence with external disturbance, as shown in Figure 12.

5. Conclusions

The framework of the fuzzy-neural-network PID (FNN-PID) control of the robotic manipulator has been presented in this article. By using Lagrange energy function, a precise dynamic model of two-link robotic manipulator is built, and the relationship among actuated torque, displacement, velocity, and acceleration in joint space is presented. In order to tune PID controller parameters quickly and effectively, a fuzzy neural network algorithm is proposed for two kinds of PID controller, that is, trajectory tracking and limited change online while in contact with constant force control. Numerical simulations are conducted and analyzed to illustrate the effectiveness of the proposed method.

Data Availability

The data used to support the findings of this study are available from the corresponding author upon request.

Conflicts of Interest

The authors declare that they have no conflicts of interest.

Acknowledgments

The authors are grateful for the financial support from the National Natural Science Foundation of China (Grant no. 51165009) and Innovation School Project of Education Department of Guangdong Province, China (Grant nos. 2017KZDXM060 and 2018KCXTD023).

References

[1] I. Rodriguez, K. Nottensteiner, D. Leidner, M. Durner, F. Stulp, and A. Albu-Schaffer, "Pattern recognition for knowledge transfer in robotic assembly sequence planning," *IEEE Robotics and Automation Letters*, vol. 5, no. 2, pp. 3666–3673, 2020.

[2] K. Numakura, Y. Muto, M. Saito, S. Narita, T. Inoue, and T. Habuchi, "Robot-assisted laparoscopic pyeloplasty for ureteropelvic junction obstruction with duplex system," *Urology Case Reports*, vol. 30, Article ID 101138, 2020.

[3] Y. F. Dong, T. Y. Ren, K. Hu, D. Wu, and K. Chen, "Contact force detection and control for robotic polishing based on joint torque sensors," *International Journal of Advanced Manufacturing Technology*, vol. 107, no. 5-6, pp. 2745–2756, 2020.

[4] T. Ozaki, T. Sujuki, T. Furuhashi, S. Okuma, and Y. Uchikawa, "Trajectory control of robotic manipulators using neural networks," *IEEE Transaction on Industrial Electronics*, vol. 38, no. 3, pp. 195–202, 1999.

[5] V. A. Mut, J. F. Postigo, R. O. Carelli, and B. Kuchen, "Robust hybrid motion-force control algorithm for robot manipulators," *International Journal of Engineering*, vol. 13, no. 3, pp. 233–242, 2000.

[6] T.-H. S. Li and Y.-C. Huang, "MIMO adaptive fuzzy terminal sliding-mode controller for robotic manipulators," *Information Sciences*, vol. 180, no. 23, pp. 4641–4660, 2010.

[7] M.-D. Tran and H.-J. Kang, "Adaptive terminal sliding mode control of uncertain robotic manipulators based on local approximation of a dynamic system," *Neurocomputing*, vol. 228, pp. 231–240, 2017.

[8] P. Ouyang and V. Pano, "Comparative study of DE, PSO and GA for position domain PID controller tuning," *Algorithms*, vol. 8, no. 3, pp. 697–711, 2015.

[9] V. Kumar, P. Gaur, and A. P. Mittal, "ANN based self tuned PID like adaptive controller design for high performance PMSM position control," *Expert Systems with Applications*, vol. 41, no. 17, pp. 7995–8002, 2014.

[10] S. He, H. Fang, M. Zhang, F. Liu, X. Luan, and Z. Ding, "Online policy iterative-based H∞ optimization algorithm for a class of nonlinear systems," *Information Sciences*, vol. 495, pp. 1–13, 2019.

[11] S. He, H. Fang, M. Zhang, F. Liu, and Z. Ding, "Adaptive optimal control for a class of nonlinear systems: the online policy iteration approach," *IEEE Transactions on Neural Networks and Learning Systems*, vol. 31, no. 2, pp. 549–558, 2020.

[12] M. H. Khodayari and S. Balochian, "Modeling and control of autonomous underwater vehicle (AUV) in heading and depth attitude via self-adaptive fuzzy PID controller," *Journal of Marine Science and Technology*, vol. 20, no. 3, pp. 559–578, 2015.

[13] F. G. Rossomando and C. M. Soria, "Identification and control of nonlinear dynamics of a mobile robot in discrete time using an adaptive technique based on neural PID," *Neural Computing and Applications*, vol. 26, no. 5, pp. 1179–1191, 2015.

[14] J. -W. Jung, V. Q. Leu, T. D. Do, E. -K. Kim, and H. H. Choi, "Adaptive PID speed control design for permanent magnet synchronous motor drives," *IEEE Transactions on Power Electronics*, vol. 30, no. 2, pp. 900–908, 2015.

[15] X. Zhou, C. Yang, and T. Cai, "A model reference adaptive control/PID compound scheme on disturbance rejection for an aerial initially stabilized platform," *Journal of Sensors*, vol. 2016, Article ID 7964727, 11 pages, 2016.

[16] A. S. W. P. Annal and S. Kanthalakshmi, "An adaptive PID control algorithm for nonlinear process with uncertain dynamics," *International Journal of Automation and Control*, vol. 11, no. 3, pp. 262–273, 2017.

[17] C. C. Ren and S. P. He, "Finite-time stabilization for positive Markovian jumping neural networks," *UNSP*, vol. 365, Article ID 124631, 2020.

[18] P. Pei, Z. C. Pei, Z. Y. Tang, and H. Gu, "Position tracking control o PMSM based on fuzzy PID-variable structure adaptive control," *Mathematical Problems in Engineering*, vol. 2018, Article ID 5794067, 15 pages, 2018.

[19] Z. Pan, D. Li, K. Yang, and H. Deng, "Multi-robot obstacle avoidance based on the improved artificial potential field and PID adaptive tracking control algorithm," *Robotica*, vol. 37, no. 11, pp. 1883–1903, 2019.

[20] Y. X. Su, P. C. Muller, and C. H. Zheng, "Global asymptotic saturated PID control for robot manipulator (vol 18, pg 1280, 2010)," *IEEE Transactions on Control Systems Technology*, vol. 23, no. 1, p. 412, 2015.

[21] S. J. Song, Y. Moon, D. H. Lee, C. B. Ahn, Y. Jo, and J. Choi, "Comparative study of fuzzy PID control algorithms for enhanced position control in laparoscopic surgery robot," *Journal of Medical and Biological Engineering*, vol. 35, no. 1, pp. 34–44, 2015.

[22] J. M. Seok, "Type-2 fuzzy self-tuning PID controller design and steering angle control for mobile robot turning," *The Journal of Korea Navigation Institute*, vol. 20, no. 3, pp. 226–231, 2016.

[23] K. S. Chia and X. Y. Yap, "A portable PID control learning tool by means of a mobile robot," *International Journal of Online Engineering (iJOE)*, vol. 12, no. 6, pp. 54–57, 2016.

[24] S. Wang, X. Yin, P. Li, M. Zhang, and X. Wang, "Trajectory tracking control for mobile robots using reinforcement learning and PID," *Iranian Journal of Science and Technology, Transactions of Electrical Engineering*, vol. 44, p. 1031, 2019.

[25] A. K. khalaji, "PID-based target tracking control of a tractor-trailer mobile robot," *Proceedings of the Institution of Mechanical Engineers, Part C: Journal of Mechanical Engineering Science*, vol. 233, no. 13, pp. 4776–4787, 2019.

[26] J. Ju, Y. Zhao, C. Zhang, and Y. Liu, "Vibration suppression of a flexible-joint robot based on parameter identification and fuzzy PID control," *Algorithms*, vol. 11, no. 11, p. 189, 2018.

[27] P. Sanchez-Sanchez and M. A. Arteaga-Perez, "Improving force tracking control performance in cooperative robots," *International Journal of Advanced Robotic Systems*, vol. 14, no. 4, Article ID 1729881417708969, 2017.

[28] R. Cortesao and M. Dominici, "Robot force control on a beating heart," *IEEE/ASME Transactions on Mechatronics*, vol. 22, no. 4, pp. 1736–1743, 2017.

[29] B. Baigzadehnoe, Z. Rahmani, A. Khosravi, and B. Rezaie, "On position/force tracking control problem of cooperative robot manipulators using adaptive fuzzy backstepping approach," *ISA Transactions*, vol. 70, pp. 432–446, 2017.

[30] D. G. G. Rosa, J. F. S. Feiteira, A. M. Lopes, and P. A. F. de Abreu, "Analysis and implementation of a force control strategy for drilling operations with an industrial robot," *Journal of the Brazilian Society of Mechanical Sciences and Engineering*, vol. 39, no. 11, pp. 4749–4756, 2017.

[31] A. E. K. Mohammad, J. Hong, and D. Wang, "Design of a force-controlled end-effector with low-inertia effect for robotic polishing using macro-mini robot approach," *Robotics and Computer-Integrated Manufacturing*, vol. 49, pp. 54–65, 2018.

[32] J. E. Solanes, L. Gracia, P. Munoz-Benavent, J. V. Miro, C. Perez-Vidal, and J. Tornero, "Robust hybrid position-force control for robotic surface polishing," *Journal of Manufacturing Science and Engineering-Transactions of the ASME*, vol. 141, no. 1, Article ID 011013, 2019.

[33] Y. Ding, X. Min, W. Fu, and Z. Liang, "Research and application on force control of industrial robot polishing concave curved surfaces," *Proceedings of the Institution of Mechanical Engineers, Part B: Journal of Engineering Manufacture*, vol. 233, no. 6, pp. 1674–1686, 2019.

[34] Y. Gan, J. Duan, M. Chen, and X. Dai, "Multi-robot trajectory planning and position/force coordination control in complex welding tasks," *Applied Sciences*, vol. 9, no. 5, p. 924, 2019.

[35] T. Osa, N. Sugita, and M. Mitsuishi, "Online trajectory planning and force control for automation of surgical tasks," *IEEE Transactions on Automation Science and Engineering*, vol. 15, no. 2, pp. 675–691, 2018.

[36] T. Zhang, M. Xiao, Y. B. Zou, and J. D. Xiao, "Robotic constant-force grinding control with a press-and-release model and model-based reinforcement learning," *International Journal of Advanced Manufacturing Technology*, vol. 106, no. 1-2, pp. 589–602, 2020.

[37] T. Zhang and X. Liang, "Disturbance observer-based robot end constant contact force-tracking control," *Complexity*, vol. 2019, Article ID 5802453, 20 pages, 2019.

[38] S. Richa, B. Shubhendu, G. Prerna, and J. Deepak, "A switching-based collaborative fractional order fuzzy logic controllers for robotic manipulators," *Applied Mathematical Modelling*, vol. 73, pp. 228–246, 2019.

[39] M. Vijay, C. Himanshu, R. Asha, and S. Vijander, "An expert 2DOF fractional order fuzz PID controller for nonlinear systems," *Neural Computing and Applications*, vol. 31, pp. 4253–4270, 2019.

[40] H. Sadeghi, H. Motameni, A. Ebrahimnejad, and J. Vahidi, "Morphology of composition functions in Persian sentences through a newly proposed classified fuzzy method and center of gravity defuzzification method," *Journal of Intelligent & Fuzzy Systems*, vol. 36, no. 6, pp. 5463–5473, 2019.

Hindawi
Complexity
Volume 2020, Article ID 9438285, 13 pages
https://doi.org/10.1155/2020/9438285

WILEY | Hindawi

Research Article

The Small-Signal Stability of Offshore Wind Power Transmission Inspired by Particle Swarm Optimization

Jiening Li,[1] Hanqi Huang,[1] Xiaoning Chen,[2] Lingxi Peng,[1,3] Liang Wang,[4] and Ping Luo[5]

[1]*School of Mechanical and Electrical Engineering, Guangzhou University, Guangzhou 510006, China*
[2]*School of Mathematics and Information Science, Guangzhou University, Guangzhou 510006, China*
[3]*Data Recovery Key Laboratory of Sichuan Province, Neijiang Normal University, Sichuan 641100, China*
[4]*School of Public Administration, Guangzhou University, Guangzhou 510006, China*
[5]*School of Economics and Statistics, Guangzhou University, Guangzhou 510006, China*

Correspondence should be addressed to Lingxi Peng; scu.peng@gmail.com, Liang Wang; wl_1998@gzhu.edu.cn, and Ping Luo; 514923134@qq.com

Received 6 May 2020; Accepted 22 May 2020; Published 15 July 2020

Academic Editor: Shuping He

Voltage source converter-high-voltage direct current (VSC-HVDC) is the mainstream technology of the offshore wind power transmission, which has been rapidly developed in recent years. The small-signal stability problem is closely related to offshore wind power grid-connected safety, but the present study is relatively small. This paper established a mathematical model of the doubly fed induction generator (DFIG) integrated into the IEEE9 system via VSC-HVDC in detail, and small-signal stability analysis of offshore wind farm (OWF) grid connection is specially studied under different positions and capacities. By selecting two load nodes and two generator nodes in the system for experiments, the optimal location and capacity of offshore wind power connection are obtained by comparing the four schemes. In order to improve the weak damping of the power system, this paper presents a method to determine the parameters of the power system stabilizer (PSS) based on the particle swarm optimization (PSO) algorithm combined with different inertia weight functions. The optimal position of the controller connected to the grid is obtained from the analysis of modal control theory. The results show that, after joining the PSS control, the system damping ratio significantly increases. Finally, the proposed measures are verified by MATLAB/Simulink simulation. The results show that the system oscillation can be significantly reduced by adding PSS, and the small-signal stability of offshore wind power grid connection can be improved.

1. Introduction

Offshore wind power, as a clean and sustainable technology, has been developed rapidly in recent years [1]. At present, the total installed capacity in Europe is increasing every year, among which the UK and Germany dominate the offshore wind power industry [2]. According to Wind Europe's High Scenario, it is estimated that the offshore wind energy capacity in Europe will reach 99 GW by 2030 [3]. Nowadays, the mainstream transmission technology is VSC-HVDC [4–6]. Compared to other traditional transmission modes, it has the advantages of independent control of the active and reactive power output, smaller power loss, and lower voltage drop [7–10].

Small-signal stability analysis is to study the dynamic response characteristics of the power system after small disturbances (including random fluctuations in power generation or consumption) and to evaluate their ability to suppress oscillations [11]. It is of great significance to promote the development of wind power and improve the safe stability of the system, which needs urgent attention [12]. However, there are few studies on the small-signal stability analysis of the offshore wind power grid connected by VSC-HVDC transmission at present. Based on the small-signal stability problem of the offshore wind power system transmitted by VSC-HVDC, the damping control of the system is increased by introducing PID regulation at the converter station. The modeling method does not consider

the aerodynamic model, and the selection of PID parameters based on eigenvalues has limitations [13]. Small-signal stability analysis method from the perspective of voltage and frequency is discussed in [14, 15]. In [14], the variability of wind power was considered as the interference source of the system and used Prony analysis and swing-based frequency response metric to study the influence of the small signal on the large offshore wind power system. However, the whole system modeling process has not been described in detail but is focused on analysis. In [15], the model of the offshore AC network for point-to-point VSC-HVDC transmission is deduced in detail, and the droop gain boundary under the stable operation is determined by eigenvalue analysis. A low-pass filter was introduced to improve the system damping, but the effect of different grid-connected positions and capacity on the small signal of the system was not considered. At present, neural networks [16, 17], deep learning, and machine learning methods have been widely used in various fields, and remarkable results have been achieved [18, 19].

To improve the stability of the system under the small signal and large signal, the PSO algorithm is used to optimize the parameters of the DFIG controller. However, the PSO algorithm will fall into local optimum, and more controller equations increase the dimension of the state matrix, which will slow down the fast operation of the system [20]. In these studies, although scholars have studied the small-signal stability of offshore wind power grid connection in different fields, it is still in the exploratory stage to change the grid-connected position and capacity of offshore wind farms for small-signal stability analysis and to apply damping control.

Aiming at the problem of small-signal stability of the offshore wind power grid-connected system, this paper firstly establishes a complete VSC-HVDC transmission offshore wind power grid-connected mathematical model and then analyzes the impact of OWFs on the small-signal stability of the system under different positions and capacities. Secondly, PSS is introduced for damping control. The optimal position of the PSS connected to the power grid is determined by modal control theory, and the parameters of the controller are determined by the PSO algorithm combined with different inertia weight functions. Finally, the correctness of the established model and the effectiveness of the proposed control measures are verified by MATLAB/Simulink simulation.

2. Modeling of Offshore Wind Power Transmitted by VSC-HVDC

This paper uses the typical offshore wind power grid connection system [21] for reference, and the designed system topology is shown in Figure 1. The OWFs are composed of 10 2-MW DFIGs, and they are equivalent to a DFIG representation according to the aggregated model [22]. The wind turbine (WT) runs on the low-speed (LS) shaft, the generator runs on the high-speed (HS) shaft, and the gearbox connects the two to act as the booster. Each 690 V DFIG is connected to 10 kV bus through the boost transformer X_{T0} and then sent to 110 kV bus through the boost transformer X_{T1} and the transmission line X_{T1}. VSC1 and VSC2 are converter stations, which play the roles of the rectifier and the inverter, respectively. The HVDC plays the role of power transmission. In addition, there are resistance-capacitance (RC) filters and phase reactors, whose influence on the system is ignored in this paper. The VSC-HVDC outlet u_{s2} is connected to the 230 kV 3-machine, 9-bus test system [23] via the boost transformer X_{T2} and the transmission line X_{L2}, which is represented by IEEE9.

2.1. Aerodynamic Model. WT is driven by the wind, which is converted into mechanical energy through three blades. The equations of the aerodynamic model [24] are given by

$$\begin{aligned} C_{\mathrm{P}} &= 0.22\left(\frac{116}{\lambda_i} - 0.4\beta - 5\right)e^{-12.5/\lambda_i}, \\ \frac{1}{\lambda_i} &= \frac{1}{\lambda + 0.08\beta^2} - \frac{0.035}{\beta^3 + 1}, \\ T_{\mathrm{t}} &= \frac{P_{\mathrm{t}}}{\omega_{\mathrm{t}}} = \frac{\rho\pi r^2 C_{\mathrm{P}} v^3}{2\omega_{\mathrm{t}}}, \end{aligned} \tag{1}$$

where C_{p} is the coefficient of wind energy utilization; β is the pitch angle; λ is the tip speed ratio ($\lambda = \omega_{\mathrm{t}} r/v$); ω_{t} is the mechanical angular velocity of the WT; r is the radius of the wind wheel; v is the wind speed; P_{t} is the mechanical power output by the WT; T_{t} is the mechanical torque; and ρ is the air density.

2.2. Shafting Model. In order to ensure the accuracy of calculation, this paper selects the two-mass block shafting model. The mathematical model of the shafting model [25] is as follows:

$$\begin{cases} 2H_{\mathrm{t}}\dfrac{\mathrm{d}\omega_{\mathrm{t}}}{\mathrm{d}t} = T_{\mathrm{t}} - K\theta - D\left(\omega_{\mathrm{t}} - (1-s)\omega_{\mathrm{s}}\right), \\ \dfrac{\mathrm{d}\theta}{\mathrm{d}t} = \omega_{\mathrm{b}}\left(\omega_{\mathrm{t}} - (1-s)\omega_{\mathrm{s}}\right), \\ -2H_{\mathrm{g}}\omega_{\mathrm{s}}\dfrac{\mathrm{d}s}{\mathrm{d}t} = K\theta + D\left(\omega_{\mathrm{t}} - (1-s)\omega_{\mathrm{s}}\right) - T_{\mathrm{e}}, \end{cases} \tag{2}$$

where H_{t} and H_{g} are the inherent inertial time constants of the WT and the generator; T_{t} and T_{e} are the mechanical torque of the WT and the electromagnetic torque of the generator; K and D are the stiffness and damping coefficients of the shaft; θ is the shaft torsional angle; ω_{t} and ω_{r} are the speeds of the rotor of the WT and the generator; ω_{s} is the stator speed of the generator; and ω_{b} is the base value of rotational speed.

2.3. Pitch Angle Control Model. To ensure the smooth power output of the OWFs, the pitch angle [26] needs to be controlled. The equations are given by

$$\begin{cases} \dfrac{\mathrm{d}\beta}{\mathrm{d}t} = \dfrac{1}{T_\beta}\left(\beta_{\mathrm{ref}} - \beta\right), \\ \beta_{\mathrm{ref}} = K_{\mathrm{p0}}\dfrac{\mathrm{d}\omega_t}{\mathrm{d}t} + K_{10}\Delta\omega_{\mathrm{t}}, \end{cases} \tag{3}$$

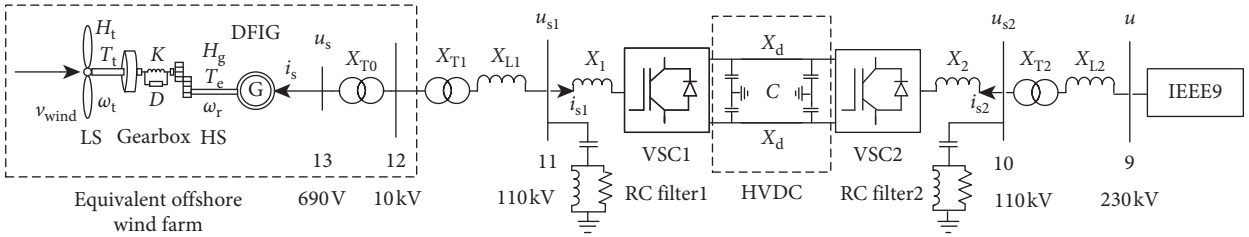

Figure 1: The topology of the whole system.

where T_β is the inertial time constant of the pitch angle control model; β_{ref} and ω_{t_ref} are the reference values of the pitch angle and the WT speed; and K_{p0} and K_{I0} are the proportional and integral coefficients of the controller.

2.4. DFIG Model. Currently, DFIG is the most widely used WT. Ignoring the electromagnetic transient process of stator winding, the mathematical model of the DFIG [27] is as follows:

$$\begin{cases} \dfrac{de'_d}{dt} = -\dfrac{1}{T'_0}e'_d + s\omega_s e'_q - \dfrac{(X_s - X'_s)}{T'_0}i_{qs} - \dfrac{\omega_s L_m}{L_{rr}}u_{qr}, \\ \dfrac{de'_q}{dt} - s\omega_s e'_d - \dfrac{1}{T'_0}e'_q + \dfrac{(X_s - X'_s)}{T'_0}i_{ds} + \dfrac{\omega_s L_m}{L_{rr}}u_{dr}, \\ u_{dr} = R_r i_{dr} + T'_b\dfrac{di_{dr}}{dt} - s\omega_s T'_b i_{qr}, \\ u_{qr} = R_r i_{qr} + T'_b\dfrac{di_{qr}}{dt} + s\omega_s\left(T'_a u_{qs} + T'_b i_{dr}\right), \\ i_{ds} = \dfrac{1}{L_{ss}}u_{qs} - \dfrac{L_m}{L_{ss}}i_{dr}, \\ i_{qs} = -\dfrac{L_m}{L_{ss}}i_{qr}, \end{cases} \tag{4}$$

where $T'_0 = L_{rr}/R_r$; $T'_a = L_m/L_{ss}$; $T'_b = L_{rr} - L_m/L_{ss}$; $X_s = \omega_s L_{ss}$; $L_{ss} = L_s + L_m$; and $L_{rr} = L_r + L_m$ are the sum of self-inductance of the stator and the rotor; R_s and R_r are the resistances of the stator and the rotor; L_m is the mutual inductance between the stator and the rotor; X_s is the reactance of the stator; $e'_d = -(\omega_s L_m/L_{rr})\psi_{qr}$; $e'_q = (\omega_s L_m/L_{rr})\psi_{dr}$; $X'_s = \omega_s/L_{rr}$ $(L_{ss}L_{rr} - L_m)$; e'_d and e'_q are the d- and q-axis components of the transient voltages; X'_s is the transient resistance of the stator; and ψ_{dr} and ψ_{qr} are the d- and q-axis components of the rotor flux, respectively. i_{ds}, i_{qs}, i_{dr}, and i_{qr} are the d- and q-axis components of the stator and rotor currents, respectively. Let the stator flux ψ_s always reunite with the d-axis; then, $u_{ds} = 0$ and $u_{qs} = \psi_s$. u_{ds}, u_{qs}, u_{dr}, and u_{qr} are the voltages of the stator and the rotor.

The active and the reactive power output of OWFs are

$$\begin{cases} P_e = \dfrac{3}{2}\left[\dfrac{R_r\left(P_s^2 + Q_s^2\right)}{T'^2_a u_s^2} + \dfrac{2R_r Q_s}{T'^2_a L_{ss}} + (1 - s\omega)P_s + \dfrac{R_r u_s^2}{L_m^2}\right], \\ Q_e = \dfrac{3}{2}\left[-s\omega T'_b\left(\dfrac{P_s^2 + Q_s^2}{T'^2_a u_s^2} + \dfrac{2Q_s}{T'^2_a L_{ss}} + \dfrac{u_s^2}{L_m^2}\right) + (1 - s\omega_s)Q_s - \dfrac{s\omega_s u_s^2}{L_{ss}}\right]. \end{cases} \tag{5}$$

2.5. VSC-HVDC Model. According to the relationship between the three-phase stationary coordinate system and the d and q synchronous rotating coordinate system, after the Park transformation, the 7-order mathematical model [13, 21] can be obtained as follows:

$$\begin{cases} L_1\dfrac{di_{1d}}{dt} = -R_1 i_{1d} - \omega_1 L_1 i_{1q} + u_{sd1} - K_1 u_{d1}\cos\delta_1, \\ L_1\dfrac{di_{1q}}{dt} = -R_1 i_{1q} + \omega_1 L_1 i_{1d} + u_{sq1} - K_1 u_{d1}\sin\delta_1, \\ L_2\dfrac{di_{2d}}{dt} = -R_2 i_{2d} - \omega_2 L_2 i_{2q} + u_{sd2} - K_2 u_{d2}\cos\delta_2, \\ L_2\dfrac{di_{2d}}{dt} = -R_2 i_{2q} - \omega_2 L_2 i_{2d} + u_{sq2} - K_2 u_{d2}\sin\delta_2, \\ C\dfrac{du_{d1}}{dt} = \dfrac{3K_1}{2}\left(i_{1d}\cos\delta_1 + i_{1q}\sin\delta_1\right) - i_d, \\ C\dfrac{du_{d2}}{dt} = \dfrac{3K_2}{2}\left(i_{2q}\cos\delta_2 + i_{2q}\sin\delta_2\right) - i_d, \\ L_d\dfrac{di}{dt} = u_{d1} - u_{d2} - R_d i_d, \end{cases} \tag{6}$$

where the physical quantities corresponding to the rectifier and the inverter station are denoted by subscripts "1" and "2," respectively. i_{1d}, i_{1q}, i_{2d}, and i_{2q} represent the current components of the AC network; u_{sd1}, u_{sq1}, u_{sd}, and u_{sq2} represent the voltage components of the AC network; u_{d1}, u_{q1}, u_{d2}, and u_{q2} represent the voltage components between buses of the DC system; and K_1 and K_2 are the voltage utilization coefficients of the DC system. δ_1 and δ_2 are the deviation angles between the voltage of the converter station

and the bus voltage of the AC system; ω_1 and ω_2 are the fundamental angular frequencies of the AC system. i_d is the DC current transmitted by the high-voltage transmission line.

2.6. System Interface Model. Position the stator voltage u_s on the d-axis, and the voltage vector between the DFIG and the rectifier station is shown in Figure 2.

Its mathematical relationship is

$$\begin{bmatrix} u_{sd1} \\ u_{sq1} \end{bmatrix} = \begin{bmatrix} u_{ds} \\ u_{qs} \end{bmatrix} + \begin{bmatrix} 0 & -X_{TL1} \\ X_{TL1} & 0 \end{bmatrix} \begin{bmatrix} i_{ds} \\ i_{qs} \end{bmatrix}, \tag{7}$$

where X_{TL1} is the total impedance of line 1; X_{T0} is the equivalent transformer impedance of OWFs; and X_{T1} and X_{L1} are the transformer and the circuit impedance of line 1.

Position the terminal voltage u of the power system on the x-axis, and the vector between the inverter station and the power system is shown in Figure 3.

Its mathematical relationship is

$$\begin{bmatrix} u_{sd2} \\ u_{sq2} \end{bmatrix} = \begin{bmatrix} \cos\varphi \\ -\sin\varphi \end{bmatrix} u - \begin{bmatrix} 0 & -X_{TL2} \\ X_{TL2} & 0 \end{bmatrix} \begin{bmatrix} i_{2d} \\ i_{2q} \end{bmatrix}. \tag{8}$$

2.7. Complete Model. All the equations of DFIG and VSC-HVDC are combined and linearized near the stable value:

$$\begin{bmatrix} \dfrac{d\Delta x_{10}}{dt} \\ 0 \end{bmatrix} = \begin{bmatrix} \tilde{A} & \tilde{B} \\ \tilde{C} & \tilde{D} \end{bmatrix} \begin{bmatrix} \Delta x_{10} \\ \Delta y_{10} \end{bmatrix}, \tag{9}$$

where $x_{10} = [\omega_t\ \theta\ s\ \beta\ e_d'\ e_q'\ i_{1d}\ i_{1q}\ i_{2d}\ i_{2q}\ u_{1d}\ u_{2d}\ i_d]^T$ and $y_{10} = \begin{bmatrix} i_{ds} & i_{qs} \end{bmatrix}^T$.

The offshore wind power transmitted by VSC-HVDC is integrated into the IEEE9 system, as shown in Figure 4. The small-signal equation of the system is

$$\frac{d\Delta x}{dt} = A\Delta x, \tag{10}$$

where $x = \begin{bmatrix} x_1 & x_2 & x_3 & x_{10} \end{bmatrix}^T$; $x_1 = \begin{bmatrix} \delta_1 & \omega_1 \end{bmatrix}^T$; $x_2 = \begin{bmatrix} \delta_2 & \omega_2 & e_{q2}' & e_{d2}' & e_{fq2} & v_{R2} & v_{M2} \end{bmatrix}^T$; and $x_3 = \begin{bmatrix} \delta_3 & \omega_3 & e_{q3}' & e_{d3}' & e_{fq3} & v_{R3} & v_{M3} \end{bmatrix}^T$.

After deducing the complete small-signal stability model of offshore wind power transmitted by VSC-HVDC, it is necessary to do further research on the influence of small-signal stability on the system of offshore wind power in different positions and capacities.

3. Small-Signal Stability Analyses

This section will combine with the concrete example of the offshore wind power grid-connected position and capacity for small-signal stability analysis. Firstly, the parameters of each subsystem are initialized, which are detailed in Appendix and then the state of OWFs is found before incorporation into the system. Finally, two load nodes and two generator nodes are chosen, and the influence of the offshore wind power grid connection is analyzed in detail.

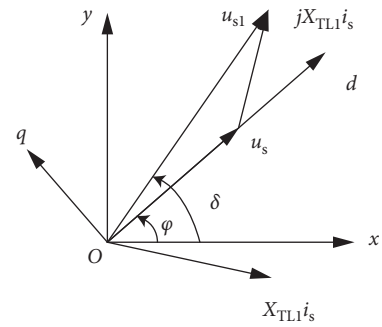

Figure 2: The voltage vector between the DFIG and the rectifier station.

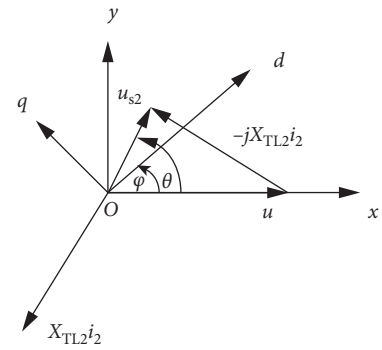

Figure 3: The voltage vector between the inverter station and the power system.

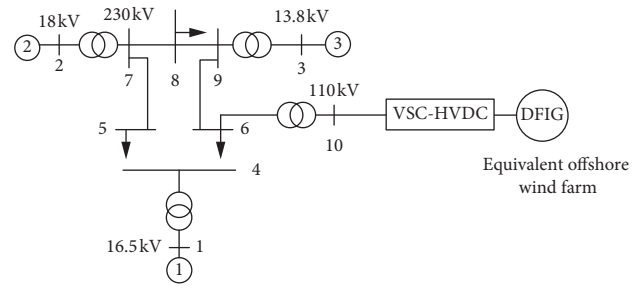

Figure 4: Schematic diagram of the equivalent offshore wind farm connected to the IEEE9 system by VSC-HVDC.

3.1. Eigenvalue Analysis. When the OWFs are added at node 6 and the active power output is 0.5 pu, the eigenvalues of the system are shown in Table 1. It can be seen from Table 1 that the real part of the eigenvalues is all negative, which are on the left side of the imaginary axis, indicating that the original power system is running in a stable state.

$\lambda_{7,8}$, $\lambda_{10,11}$, $\lambda_{12,13}$, and $\lambda_{16,17}$ are related to the generator rotational speed ($\Delta\omega_1$, $\Delta\omega_2$, and $\Delta\omega_3$) and the rotational speed difference Δs of wind generator 10, respectively, belonging to the electromechanical oscillation mode.

Table 1: Eigenvalues of the system during stable state.

Number	Eigenvalue	Number	Eigenvalue
λ_1	-99.9360	λ_2	-74.4198
λ_3	-52.7251	λ_4	-51.3813
λ_5	-31.1510	λ_6	-28.8327
$\lambda_{7,8}$	$-2.6655 \pm 18.2668i$	λ_9	-12.9409
$\lambda_{10,11}$	$-0.6959 \pm 12.8937i$	$\lambda_{12,13}$	$-0.1431 \pm 8.6461i$
$\lambda_{14,15}$	$-4.7160 \pm 8.0754i$	$\lambda_{16,17}$	$-0.1222 \pm 4.0611i$
$\lambda_{18,19}$	$-4.4655 \pm 3.1380i$	$\lambda_{20,21}$	-5.4943
λ_{21}	-4.1027	λ_{22}	-0.4476
$\lambda_{23,24}$	$-0.8287 \pm 0.9010i$	$\lambda_{25,26}$	$-0.3560 \pm 0.5849i$
λ_{27}	-0.0290	$\lambda_{28,29}$	$-0.0291 \pm 0.0502i$

3.2. Damping Ratio Analysis. Damping ratio [28] can reflect the speed and the characteristics of oscillation attenuation. The expression is given by

$$\zeta = -\frac{\sigma}{\sqrt{\sigma^2 + \omega^2}}, \tag{11}$$

where σ and ω are the real and the imaginary part of the eigenvalue, respectively.

In the actual power system, it is generally required that the damping ratio of the electromechanical oscillation mode should be above 0.05, and then the operating state of the system could be accepted. However, this principle is not unchanged. If the mode of fluctuation is not large when the system operation mode changes, it is acceptable to have such a low damping ratio (for example, 0.03) [28].

By changing different active power outputs and grid-connected positions of OWFs, the damping ratio curve in various cases can be obtained as shown in Figure 5.

4. Control Measures

In order to improve the weak damping instability of the system, it is necessary to add a controller to the system for auxiliary regulation. Firstly, PSS needs to be modeled, and the speed difference is used as the feedback signal to be added to the system voltage equation. Secondly, the optimal position of the PSS is determined by the detailed analysis of modal control theory.

Finally, the PSO algorithm is introduced, and the objective function is established according to the research content of this paper. The parameters of PSS controllers are determined with different inertia weight functions.

4.1. PSS Model. The main function of the PSS is to increase damping or suppress low-frequency oscillation of the power system [29]. The mathematical expression of the PSS is

$$\begin{cases} \dfrac{\mathrm{d}\Delta V_1}{\mathrm{d}t} = \dfrac{K_{\mathrm{gain}}}{T_6}\Delta\omega - \dfrac{1}{T_6}\Delta V_1, \\ \dfrac{\mathrm{d}\Delta V_2}{\mathrm{d}t} = \dfrac{K_{\mathrm{gain}}}{T_6}\Delta\omega - \dfrac{1}{T_6}\Delta V_1 - \dfrac{1}{T_5}\Delta V_2, \\ \dfrac{\mathrm{d}\Delta V_3}{\mathrm{d}t} = \dfrac{K_{\mathrm{gain}}T_1}{T_2T_6}\Delta\omega - \dfrac{T_1}{T_2T_6}\Delta V_1 - \dfrac{T_1 - T_5}{T_2T_5}\Delta V_2 - \Delta V_3, \\ \dfrac{\mathrm{d}\Delta V_S}{\mathrm{d}t} = \dfrac{K_{\mathrm{gain}}T_1T_3}{T_2T_4T_6}\Delta\omega - \dfrac{T_1T_3}{T_2T_4T_6}\Delta V_1 - \dfrac{T_3(T_1 - T_5)}{T_2T_4T_5}\Delta V_2 - \dfrac{T_3 - T_2}{T_2T_4}\Delta V_3 - \dfrac{1}{T_4}\Delta V_S, \end{cases} \tag{12}$$

where the generator speed difference $V_{IS} = \omega\text{-}\omega_t$ is selected as the input signal. V_S is the output signal, which serves as the auxiliary input signal of the stator voltage equation Δu_{qi} ($i = 1,2,3$) of the IEEE9 system. K_{gain} is the gain of the amplification link; T_6 is the time constant of the measurement link. T_5 is the time constant of the filtering link. T_1, T_3, T_2, and T_4 are the lead and lag time constants of two phase compensation links, respectively.

If the PSS is added to IEEE9 system generator 2, the voltage equation needs to be

$$\begin{cases} \Delta u_{d2} = \Delta e'_d - R_{a2}\Delta i_{d2} + X'_{q2}\Delta i_{q2}, \\ \Delta u_{q2} = \Delta e'_q - R_{a2}\Delta i_{q2} + X'_{d2}\Delta i_{d2} + \Delta V_S. \end{cases} \tag{13}$$

4.2. PSS Grid-Connected Position Selection. When OWFs integrate into load node 6 and in normal operation, the changes of the electromechanical oscillation mode are shown in Table 2.

As can be seen from Table 2, in the eigenvectors of the first and fourth modes, the modulus value of Δs is the largest, but the directions of each component are basically the same, indicating that the influence of each generator on the mode is similar. In the second mode, the modulus value of $\Delta\omega_3$ and Δs is larger and opposite to the direction of other components (the average argument is about -154.57°), indicating that the oscillation mainly exists in generators 3, 10 and generators 1, 2. The oscillation frequency $f = 8.65/(2\pi) = 1.3767$ Hz, belonging to the local oscillation mode. In the

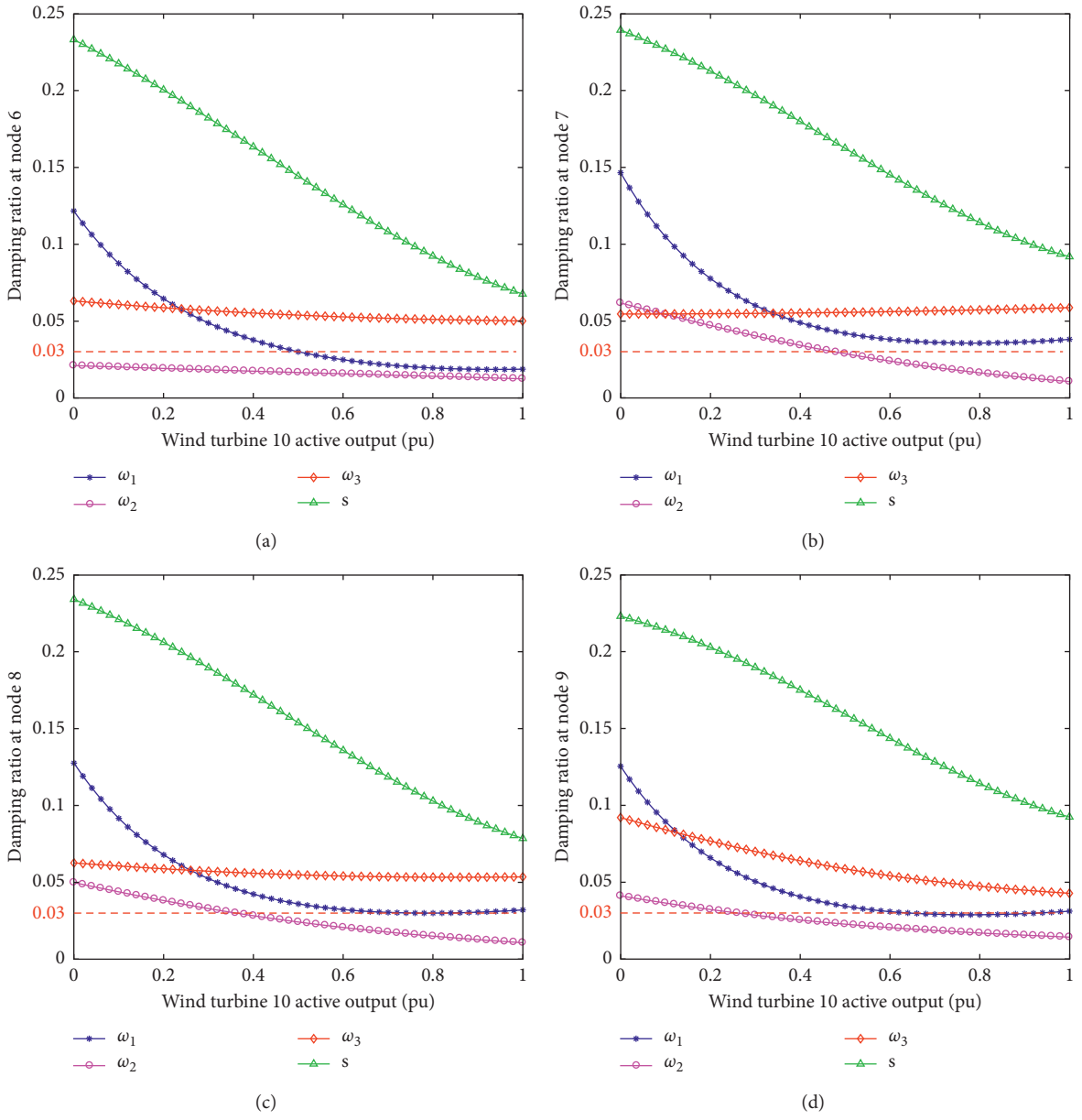

Figure 5: The damping ratio of OWF grid connection.

Table 2: Corresponding components of generator speed in the right eigenvector.

Generator	$\lambda_{7,8}$		$\lambda_{10,11}$		$\lambda_{12,13}$		$\lambda_{16,17}$	
	Modulus value (pu)	Argument (°)	Modulus value (pu)	Argument (°)	Modulus value (pu)	Argument (°)	Modulus value (pu)	Argument (°)
1	0.0000	−65.65	0.0002	−158.19	0.0009	−108.95	0.0007	−73.93
2	0.0001	−50.39	0.0012	−150.94	**0.0024**	69.35	0.0006	−81.42
3	0.0003	−57.68	**0.0040**	26.21	0.0013	72.60	0.0005	−81.49
10	**0.0115**	−42.98	**0.0046**	23.87	**0.0025**	72.36	**0.0021**	−78.95

third mode, the modulus values of $\Delta\omega_2$ and Δs are larger and are basically opposite to $\Delta\omega_1$ in the direction (the argument is −108.95°), indicating that the oscillation mainly exists in generators 2, 10 and generator 1. The oscillation frequency $f = 12.89/(2\pi) = 2.0515$ Hz, belonging to the local oscillation mode.

In the participation vector, if the generator speed component is positive and the value is large, it indicates that

the generator is the best candidate position for installing the PSS, which can significantly increase the damping of the mode. For increasing system damping, it is better to apply control on a larger capacity generator [30].

The local oscillation modes $\lambda_{10,11}$ and $\lambda_{12,13}$ are specifically analyzed. The components of the participation vector corresponding to the rotation speed of each generator are shown in Table 3.

As can be seen from Table 3, for the participation vector of local mode $\lambda_{10,11}$, the value of generator 3 is the largest and that of generator 10 is the smallest, indicating that the control is mainly applied in generator 3, and the damping of the system can be significantly increased. Similarly, for the participation vector of local mode $\lambda_{12,13}$, the value of generator 2 is the largest and that of generator 10 is the smallest, indicating that fine effects can be achieved by applying control on generator 2.

Furthermore, compared with the capacity of generators 2 and 3, the active power of generator 2 (1.63 pu) is larger than that of generator 3 (0.85 pu), so the damping control of generator 2 can achieve better suppression of the oscillation effect.

4.3. PSO Algorithm Based on Different Inertia Weight Functions. The updating formulas of particle velocity and position are as follows:

$$\begin{aligned} v_{iD}^{k+1} &= \omega v_{iD}^{k} + c_1 r_1\left(p_{iD}^{k} - x_{iD}^{k}\right) + c_2 r_2\left(p_{gD}^{k} - x_{gD}^{k}\right), \\ x_{iD}^{k+1} &= x_{iD}^{k} + v_{iD}^{k+1}, \end{aligned} \tag{14}$$

where k represents the number of iterations; v_{iD}^{k} and x_{iD}^{k} represent the velocity and position of the i-th particle in the D-dimensional space, and the value range is $[v_{\mathrm{lb}}, v_{\mathrm{ub}}]$ and $[x_{\mathrm{lb}}, x_{\mathrm{ub}}]$; and c_1 and c_2 refer to the individual learning factors and the group learning factors, and $c_1 = c_2 = 2$ is taken in this paper. r_1 and r_2 are random numbers between 0 and 1; p_{iD}^{k} and p_{gD}^{k} represent the individual optimal position and the global optimal position of the i-th and g-th particle in the D-dimensional space; and ω represents the inertia weight.

The inertia weight ω indicates the ability to retain existing velocity. The larger the value is, the stronger the global optimization is. On the contrary, the smaller the value is, the better the local optimization is. In order to weigh the global optimization and local optimization, Shi. Y summarized a new method of calculating weights, linear decreasing inertia weights (LDIW) [31], which is specifically expressed as

$$\omega 1(k) = \omega_{\mathrm{start}} - \left(\omega_{\mathrm{start}} - \omega_{\mathrm{end}}\right)\frac{k}{T_{\max}}, \tag{15}$$

where ω_{start} is the inertia weight in the initial state; ω_{end} is the inertia weight at the end of the iteration; k is the number of iterations; and $T_{\max}$ is the maximum number of iterations. It is generally believed that $\omega_{\mathrm{start}} = 0.9$ and $\omega_{\mathrm{end}} = 0.4$ in which the algorithm performs best. In addition to LDIW, the common inertia weight functions [32] are as follows:

Table 3: Components of the participation vector corresponding to the rotation speed of each generator.

Generator	1	2	3	10
$\lambda_{10,11}$	0.0099	0.1914	**1.0000**	**0.0264**
$\lambda_{12,13}$	0.3700	**1.0000**	0.1220	**0.0143**

$$\begin{aligned} \omega 2(k) &= \omega_{\mathrm{start}} - \left(\omega_{\mathrm{start}} - \omega_{\mathrm{end}}\right)\left(\frac{k}{T_{\max}}\right)^2, \\ \omega 3(k) &= \omega_{\mathrm{start}} + \left(\omega_{\mathrm{start}} - \omega_{\mathrm{end}}\right)\left[\frac{2k}{T_{\max}} - \left(\frac{k}{T_{\max}}\right)^2\right], \\ \omega 4(k) &= \omega_{\mathrm{end}}\left(\frac{\omega_{\mathrm{start}}}{\omega_{\mathrm{end}}}\right)^{1/\left(1+k/T_{\max}\right)}. \end{aligned} \tag{16}$$

4.4. Determination of Optimization Objective Function. In order to improve the weak damping of the system, it is very important to determine the optimal target. As can be seen from Figure 5, when OWFs first join the system, the damping ratio is relatively large. With the increase of the active power output, most damping ratios show a downward trend, and some electromechanical oscillation modes even have weakly damped unstable states. In order to improve the low-frequency oscillation, when generator 10 active output is 1.0 pu, the minimum damping ratio of each generator is selected as the optimal target, and then the maximum value of this target in the iterative process can be obtained by the PSO algorithm. If the optimization target is larger than 0.03, the variation curve of damping ratio can be ensured to be in a stable running state. The mathematical expressions of fitness function are as follows:

$$\begin{aligned} D_n &= \min\left(\zeta_{ni}\right), \\ \mathrm{fitness} &= \max\left(D_n\right), \end{aligned} \tag{17}$$

where ξ_{ni} $(i = 1,2,3,4)$ is the damping ratio of the component related to the rotation speed of generators 1, 2, 3, and 10 during the n-th iteration process.

According to the research of this topic, the steps of the PSO algorithm are as follows:

(1) Initialize particle swarm size, velocity, and position. Particle specifically refers to PSS parameters.

(2) Take the small-signal stability program as a subfunction, and then optimize the designed objective function to obtain the individual and the global optimal fitness value of the particle.

(3) Compare the fitness value of each generation particle. If the current fitness value is better, update the previously recorded optimal fitness value with the current fitness value, and update the previously recorded optimal position with the current position. If not, leave the value unchanged.

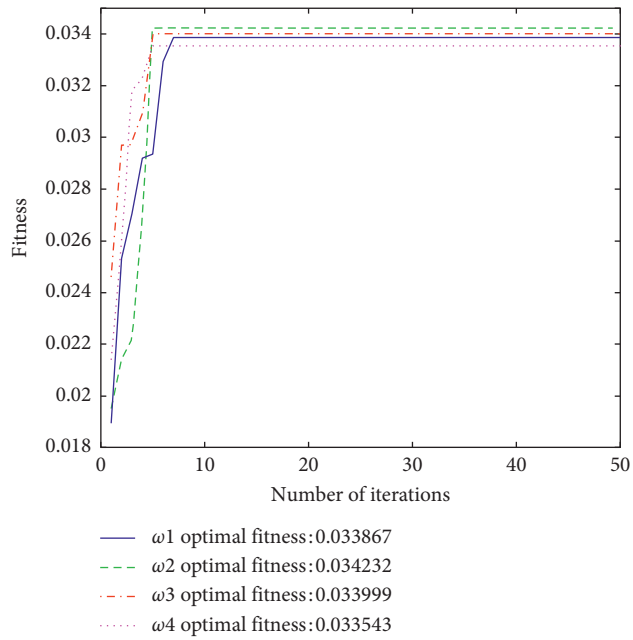

Figure 6: Fitness curves under different inertia weights.

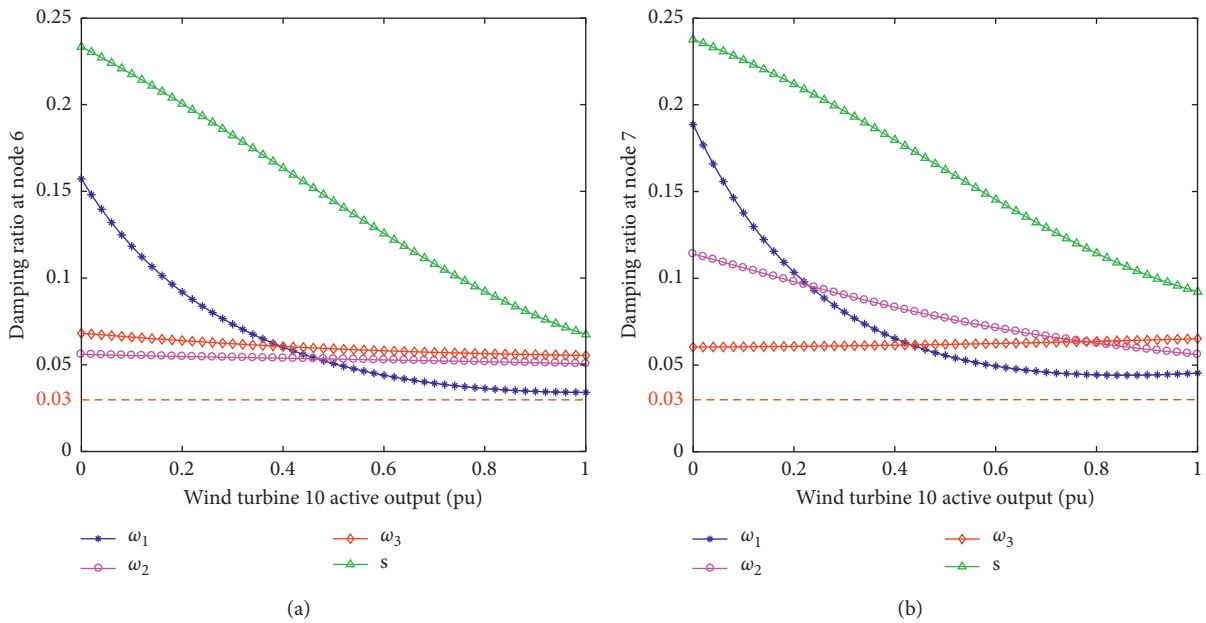

Figure 7: Continued.

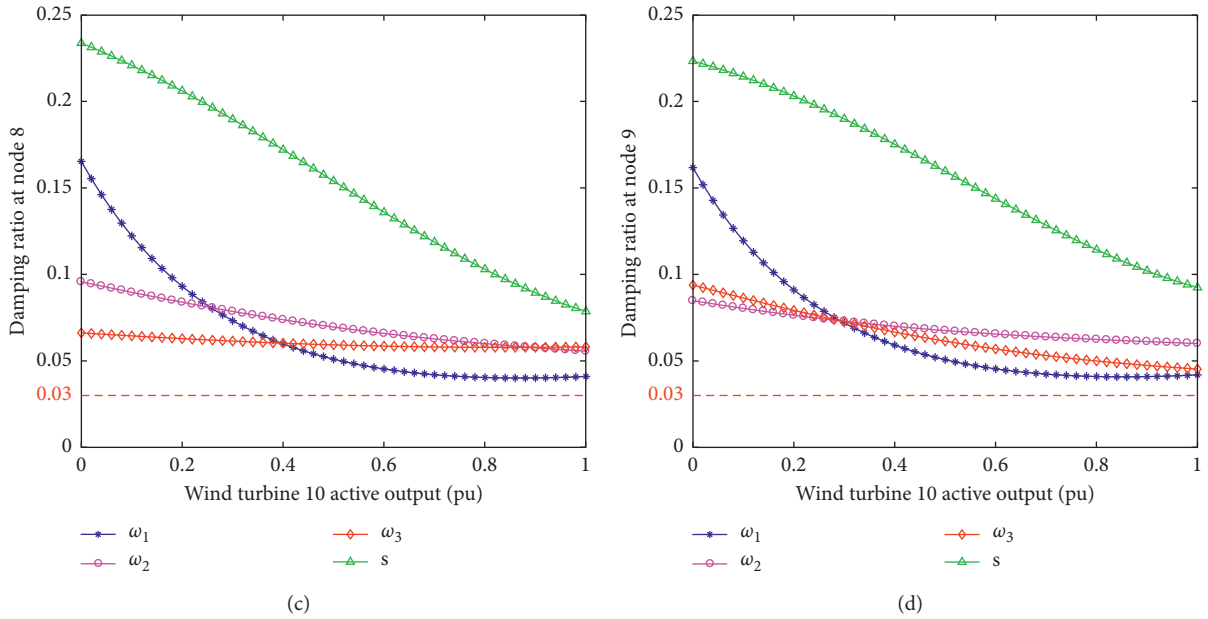

Figure 7: Curve of damping ratio change after the PSS is added into generator 2.

(4) Update the position and velocity of each particle.

(5) Determine whether the current fitness value reaches the given standard or reaches the upper limit of the number of iterations. If yes, the program ends. If not, return to (2) and continue to execute the loop body.

4.5. Effect of Applying PSS Control. According to the analysis of Section 4.3, PSS installed in generator 2 works well. Under different inertial weights, the fitness curve can be obtained by solving the function for many times and taking the mean value, as shown in Figure 6.

It can be seen from Figure 6 that the deviation of the optimal fitness obtained under the four inertia weights is small. The optimal fitness of the inertia weight $\omega 2$ is 0.034232, the effect of $\omega 1$ and $\omega 3$ is similar, and the worst is $\omega 4$. Based on $\omega 2$, the control parameters are deeply optimized, and the optimized parameters of each controller are $K_{\text{gain}} = 10$, $T_1 = 0.66$, $T_2 = 0.25$, $T_3 = 0.45$, $T_4 = 0.15$, $T_5 = 4.5$, and $T_6 = 1.25$. By substituting the PSS parameters into the original state matrix and changing the position and capacity of the offshore wind power into the power system, the effect can be obtained, as shown in Figure 7.

As can be seen from Figure 7, after adding the PSS to generator 2, each damping ratio is improved correspondingly, and the curves are all above 0.03, indicating that the system works stably. The variation trend of each damping ratio is basically the same as that without the PSS, and the damping ratio of generator 2 rotation speed is significantly increased. Furthermore, it can be verified that the theoretical analysis is reasonable, and generator 2 is the best place to add the PSS.

5. Simulink Simulation

Through theoretical analysis and programming experiments, the control measures of offshore wind power grid connection have been obtained. However, how the actual power system operates and whether the controller PSS achieves the desired effect need to be verified by simulation. The circuit in Figure 1 was built on MATLAB/Simulink. By applying the small signal (wind speed disturbance and system fault), the proposed control measures are verified and analyzed.

5.1. Wind Speed Disturbance. Assuming the initial wind speed of the OWFs is 10 m/s, a step signal generator disturbs the wind speed to 12 m/s at 1.8 s. The dynamic response effect of the system before and after adding PSS control to generator 2 is shown in Figure 8.

From the PSS2 control in Figures 8(a) and 8(c), it can be clearly seen that the power of the system fluctuates within a small range after applying the wind speed disturbance, and the system runs stably again at 3.3 s. The process has gone through 1.5 s; it can be seen from Figure 8(a) that, after the addition of PSS2, the electromagnetic torque of synchronous generator 1 is stabilized more quickly, and the oscillation amplitude is effectively suppressed. Figure 8(b) is the voltage curve of synchronous generator 1, and the effect of adding PSS2 is small. It can be seen from Figure 8(c) that the amplitude of the synchronous generator 1 active power is significantly reduced after the addition of PSS2. Figure 8(d) shows the DC curve of HVDC. By comparison, the amplitude of the oscillation is reduced when PSS2 is applied. The amplitude of the voltage stability will drop slightly without PSS2 control, which is also the adverse effect of wind speed disturbance. Figures 8(e) and 8(f) show the active and reactive power of VSC1. It can be seen that, after the addition of the damping controller, the oscillation of the system is better improved. In summary, when the OWFs are disturbed by wind speed, adding PSS2 will improve the small-signal stability of the whole system.

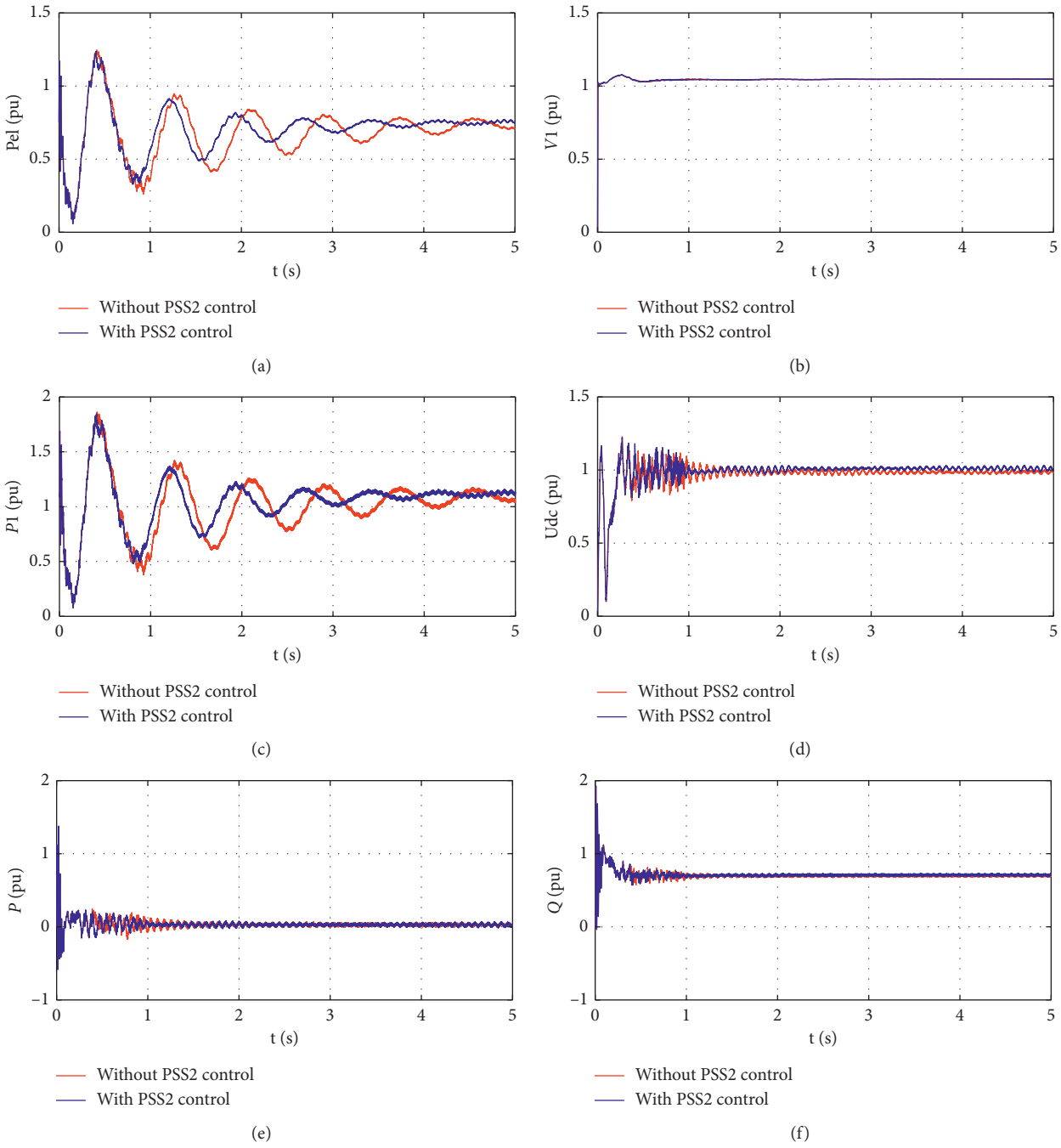

Figure 8: Dynamic response of the system before and after adding PSS2 in the case of wind speed disturbance. (a) The electromagnetic torque of synchronous generator 1. (b) The voltage of synchronous generator 1. (c) The active power of synchronous generator 1. (d) The direct current voltage of HVDC. (e) The active power of VSC1. (f) The reactive power of VSC1.

5.2. System Fault. In order to simulate the actual system fault, a three-phase short circuit was applied to the transmission line incorporated into node 8 at 1.5 s, and the fault duration is 0.12 s. The dynamic response of the system controlled by PSS2 is shown in Figure 9.

It can be seen from Figures 9(a) and 9(f) that, after applying a three-phase short-circuit fault, the state of the system changes obviously. The system recovers at 2.8 s, and the adjustment process goes through 1.3 s; Figure 9(a) is the electromagnetic torque curve of synchronous generator 1, and the oscillation of the system is significantly reduced after the addition of PSS2. Figure 9(b) shows the voltage curve of synchronous generator 1, and the effect of adding or not adding PSS2 is small. It can be seen from Figure 9(c) that the amplitude of the synchronous generator 1 active power is remarkably suppressed after the addition of PSS2.

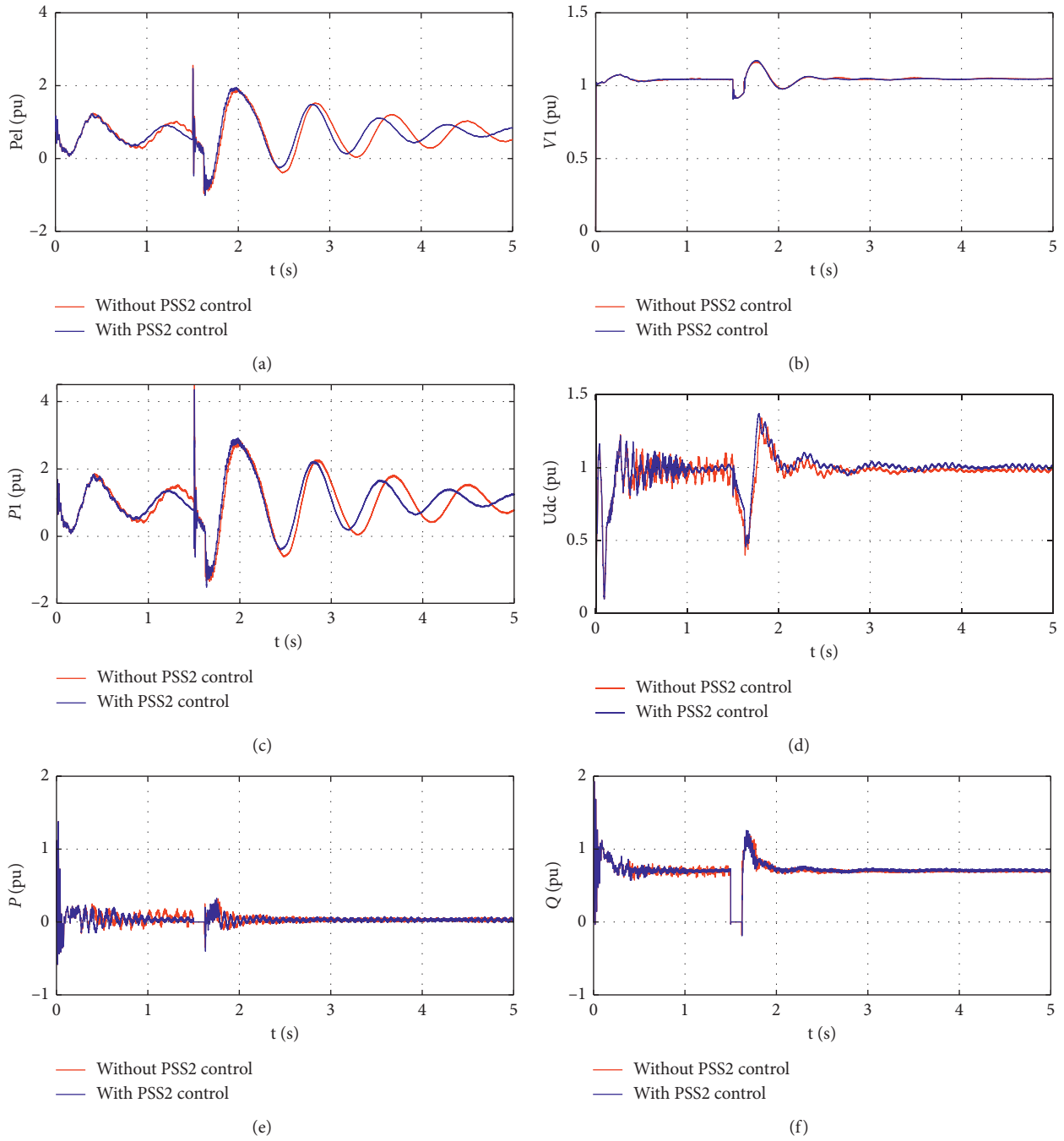

Figure 9: Dynamic response of the system before and after adding PSS2 in the case of the three-phase short-circuit fault. (a) The electromagnetic torque of synchronous generator 1. (b) The voltage of synchronous generator 1. (c) The active power of synchronous generator 1. (d) The direct current voltage of HVDC. (e) The active power of VSC1. (f) The reactive power of VSC1.

Figure 9(d)shows the DC curve of HVDC. It can be seen that the DC voltage fluctuation amplitude is reduced, and the system reaches stability more quickly. Figures 9(e) and 9(f) show the active and reactive power of VSC1. It can be seen that, after the damping controller is added, the oscillation of the system is better improved. In summary, when the onshore power system is disturbed by the fault, adding PSS2 improves the small-signal stability of the whole system.

6. Conclusions

Based on the establishment of a complete mathematical model, the influence of offshore wind power on the system at different positions and capacities is analyzed in detail according to the damping characteristics. The experimental results show that most of the damping ratios are decreasing, and some of the electromechanical oscillation modes will show weak damping instability. By comparing the

experimental results of two load nodes and two generator nodes, the optimal location and capacity of offshore wind farms are obtained. In order to improve the weak damping of the power system, the optimal positions of the PSS in the power grid are obtained through the modal control. PSO algorithm combining with different inertia weight functions is presented to determine the parameters of the PSS. Finally, the whole system model is built on MATLAB/Simulink platform, and the influence of PSS control on the system is compared and analyzed by applying wind speed disturbance and system fault. The simulation results show that the dynamic response of the system is obviously improved, the oscillation amplitude is significantly reduced, and the accuracy of the proposed control strategy is verified.

Appendix

DFIG parameters of offshore wind farms:

$r = 40$ m; $\rho = 1.242$ kg m^3; $v_0 = 10.45$ m s^{-1}; $R_r = 0.0073$ pu; $R_s = 0.0076$ pu; $L_r = 0.0884$ pu; $L_s = 0.1248$ pu; $L_m = 1.8365$ pu; $\omega_{t0} = 1.1055$ rad s^{-1}; $s_0 = -0.003$; $\beta_0 = 0$ rad; $K_{p0} = 0.1$ pu; $K_{I0} = 20$ s^{-1}; $T_\beta = 10$ s; $H_t = 3$ s; $H_g = 0.05$ s; $K = 10$ pu·rad^{-1}; and $D = 0.5$ pu·rad^{-1}.

VSC-HVDC parameters:

$R_1 = R_2 = 0.075$ pu; $L_1 = L_2 = 0.016$ pu; $\omega_1 = \omega_2 = 1$ pu; $\boldsymbol{\delta}_1 = \boldsymbol{\delta}_2 = 10^\circ$; $K_1 = K_2 = 0.1$; $R_d = 1.0425$ pu; $L_d = 0.0119$ pu; and $C = 0.1733$ pu.

System interface parameters:

$X_{T0} = 0.015$ pu; $X_{T1} = 0.016$ pu; $X_{L1} = 0.02$ pu; $X_{T2} = 0.061$ pu; and $X_{L2} = 0.014$ pu.

Data Availability

All data generated or analyzed during this study are included in this article.

Conflicts of Interest

The authors declare no conflicts of interest.

Acknowledgments

This paper was carefully guided by Professor Ru Yang of Guangzhou University and was supported by the National Natural Science Foundation of China under Grant nos. 61772147 and 61100150, the University Innovation Team Construction Project of Guangdong Province under Grant no. 2015KCXTD014, Guangdong Province Philosophy and Social Science Foundation under Grant no. GD19CSH03, the key Project of Science and Technology Plan of Guangdong Province under Grant No. 2020b1010010014 and Open Research Fund Program of Data Recovery Key Laboratory of Sichuan Province. Here, the authors express their sincere gratitude.

References

[1] I. Pineda, K. Ruby, A. Ho, A. Mbistrova, and G. Corbetta, *"The European Offshore Wind Industry—Key Trends and Statistics 2015*, European Wind Energy Association, Brussels, Belgium, 2016.

[2] C. Walsh, L. Miró, F. Selot, D. Fraile, and G. Brindley, *"Offshore Wind in Europe – Key Trends and Statistics 2018*, Wind Europe, Brussels, Belgium, 2019.

[3] P. Tardieu, L. Velde, A. Nghiem, and I. Pineda, *Wind Energy in Europe: Scenarios for 2030*, Wind Europe, Brussels, Belgium, 2017.

[4] L. Shen, M. Barnes, R. Preece, and J. Milanović, "Frequency stabilisation using VSC-HVDC," in *Proceedings of the 2016 IEEE Power and Energy Society General Meeting (PESGM)*, pp. 1–5, Boston, MA, USA, 2016.

[5] L. Yan, S. Wei, C. Yong-Ning, W. Lin-Jun, and L. Wei, "Research on offshore wind farm VSC-HVDC transmission system fault ride through issue," in *Proceedings of the 2014 International Conference on Power System Technology*, pp. 2190–2195, Chengdu, China, 2014.

[6] K. Asimenia, Q. Wu, and H. Zhao, "Review of VSC HVDC connection for offshore wind power integration," *Renewable and Sustainable Energy Reviews*, vol. 59, pp. 1405–1414, 2016.

[7] M. Edrah, K. L. Lo, O. Anaya-Lara, and A. Elansari, "Impact of DFIG based offshore wind farms connected through VSC-HVDC link on power system stability," in *Proceedings of the 11th IET International Conference on AC and DC Power Transmission*, pp. 1–7, Birmingham, UK, 2015.

[8] Q. Fu, W. Du, J. Cao, and H. F. Wang, ""VSC-based HVDC power transmission for the large-scale offshore wind power—a survey," in *Proceedings of the International Conference on Renewable Power Generation (RPG 2015)*, pp. 1–6, Beijing, China, 2015.

[9] S. Lu and Z. Xu, "A novel control strategy of VSC-HVDC for offshore platforms," in *Proceedings of the 12th IET International Conference on AC and DC Power Transmission (ACDC 2016)*, pp. 1–6, Beijing China, 2016.

[10] Y. Guo, H. Gao, Q. Wu, H. Zhao, J. Ostergaard, and M. Shahidehpour, "Enhanced voltage control of VSC-HVDC-Connected offshore wind farms based on model predictive control," *IEEE Transactions on Sustainable Energy*, vol. 9, no. 1, pp. 474–487, 2018.

[11] J. Machowski, J. Bialek, and J. Bumby, *Power System Dynamics: Stability and Control*, Wiley, New York, NY, USA, 2nd edition, 2008.

[12] H. Huang, C. Mao, J. Lu, and D. Wang, "Small-signal modelling and analysis of wind turbine with direct drive permanent magnet synchronous generator connected to power grid," *IET Renewable Power Generation*, vol. 6, no. 1, pp. 48–58, 2012.

[13] Y. Yang and G. Li, "The small signal stability control of offshore wind farm based on VSC-HVDC," *Transactions of China Elect Rotechnical Society*, vol. 31, no. 13, pp. 101–110, 2016.

[14] A. Sajadi, S. Zhao, K. Clark, and K. A. Loparo, "Small-signal stability analysis of large-scale power systems in response to variability of offshore wind power plants," *IEEE Systems Journal*, vol. 13, no. 3, pp. 1–10, 2018.

[15] M. Raza, E. Prieto-Araujo, and O. Gomis-Bellmunt, "Small-signal stability analysis of offshore AC network having multiple VSC-HVDC systems," *IEEE Transactions on Power Delivery*, vol. 33, no. 2, pp. 830–839, 2018.

[16] C. Wang, H. Fang, and S. He, "Adaptive optimal controller design for a class of LDI-based neural network systems with

input time-delays," *Neurocomputing*, vol. 385, pp. 292–299, 2020.

[17] S. He, H. Fang, M. Zhang, F. Liu, and Z. Ding, "Adaptive optimal control for a class of nonlinear systems: the online policy iteration approach," *IEEE Transactions on Neural Networks and Learning Systems*, vol. 31, no. 2, pp. 549–558, 2020.

[18] S. He, H. Fang, M. Zhang, F. Liu, X. Luan, and Z. Ding, "Online policy iterative-based H∞ optimization algorithm for a class of nonlinear systems," *Information Sciences*, vol. 495, pp. 1–13, 2019.

[19] S. He, M. Zhang, H. Fang, F. Liu, X. Luan, and Z. Ding, "Reinforcement learning and adaptive optimization of a class of Markov jump systems with completely unknown dynamic information," *Neural Computing and Applications*, 2019.

[20] F. Wu, X.-P. Zhang, K. Godfrey, and P. Ju, "Small signal stability analysis and optimal control of a wind turbine with doubly fed induction generator," *IET Generation, Transmission & Distribution*, vol. 1, no. 5, pp. 751–760, 2007.

[21] G. Tang, *HVDC Transmission Technology Based on Voltage Source Converter*, China Electric Power Press, Beijing, China, 2010.

[22] C. Qin and Y. Yu, "Small signal stability region of power systems with DFIG in injection space," *Journal of Modern Power Systems and Clean Energy*, vol. 1, no. 2, pp. 127–133, 2013.

[23] Z. Li, X. Zhang, Y. Deng, and B. He, "Studies of transient stability of wind power acess grid system," *J of China Three Gorges Univ. (Natural Sciences)*, vol. 38, no. 2, pp. 47–50, 2016.

[24] B. Mehta, P. Bhatt, and V. Pandya, "Small signal stability analysis of power systems with DFIG based wind power penetration," *International Journal of Electrical Power & Energy Systems*, vol. 58, pp. 64–74, 2018.

[25] E. Prasanthi and K. N. Shubhanga, "Stability analysis of a grid connected DFIG based WECS with two-mass shaft modeling," in *Proceedings of the 2016 IEEE Annual India Conference (INDICON)*, pp. 1–6, Bangalore, India, 2016.

[26] S. Feng, D. Liu, X. Yang, and X. Xiang, "The impact of wind power inverse-peaking characteristics on power system low frequency oscillation," in *Proceedings of the 2012 China International Conference on Electricity Distribution*, pp. 1–4, Shanghai, China, 2012.

[27] H. Huang, *Research on Small-Signal Stability of Wind and Photovoltaic Power Generation System*, Ph.D. dissertation, Department Electronical Engineering, HUST University, Wuhan, China, 2012.

[28] X. Wang, W. Fang, and Z. Du, *Modern Power System Analysis*, Science Press, Beijing, China, 2003.

[29] K. Thanpisit and I. Ngamroo, "Power oscillation damping control by PSS and DFIG wind turbine under multiple operating conditions," *Turkish Journal of Electrical Engineering & Computer Sciences*, vol. 25, pp. 4354–4368, 2017.

[30] D. Gautam and V. Vittal, "Impact of DFIG based wind turbine generators on transient and small signal stability of power systems,," in *Proceedings of the 2009 IEEE Power & Energy Society General Meeting*, pp. 1–6, Calgary, Canada, 2009.

[31] J. Xin, G. Chen, and Y. Hai, "A particle swarm optimizer with multi-stage linearly-decreasing inertia weight,," in *Proceedings of the 2009 International Joint Conference on Computational Sciences and Optimization*, pp. 505–508, Sanya, China, 2009.

[32] L. Yu, F. Shi, H. Wang, and F. Hu, *Analysis of 30 Cases of Intelligent Algorithms in MATLAB*, Beihang University Press, Beijing, China, 2011.

Hindawi
Complexity
Volume 2020, Article ID 5686413, 13 pages
https://doi.org/10.1155/2020/5686413

Research Article

Differential Games of Rechargeable Wireless Sensor Networks against Malicious Programs Based on SILRD Propagation Model

Guiyun Liu, Baihao Peng, Xiaojing Zhong, and Xuejing Lan

School of Mechanical and Electric Engineering, Guangzhou University, Guangzhou 510006, China

Correspondence should be addressed to Baihao Peng; 2111807063@e.gzhu.edu.cn

Received 2 May 2020; Revised 4 June 2020; Accepted 10 June 2020; Published 3 July 2020

Academic Editor: Shuping He

Based on the traditional propagation model, this paper innovatively divides nodes into high- and low-energy states through introducing Low-energy (L) state and presents a whole new propagation model which is more suitable for WSNs (wireless sensor networks) against malicious programs, namely, SILRD (Susceptible, Infected, Low-energy, Recovered, Dead) model. In this paper, nodes are divided into five states according to the residual energy and infection level, and the differential equations are constructed to describe the evolution of nodes. At the same time, aiming at the exhaustion of WSNs' energy, this paper introduces charging as a method to supplement the energy. Furthermore, we regard the confrontation between WSNs and malicious programs as a kind of game and find the optimal strategies by using the Pontryagin Maximum Principle. It is found that charging as a defense mechanism can inhibit the spread of malicious programs and reduce overall costs. Meanwhile, the superiority of bang-bang control on the SILRD model is highlighted by comparing with square control.

1. Introduction

WSNs consist of a series of energy-limited nodes with monitoring, receiving, transmitting, and other functions that act as connections between surrounding environment and control centers or computers for further process. As WSNs have gradually penetrated into every aspect of our daily life, they have become an indispensable part of us, including environmental monitoring, medical care, and vehicle tracking [1].

However, the shortcomings of WSNs are increasingly exposed, such as vulnerability to malicious programs and limited battery capacity. Due to the similarity of transmission mechanism, the propagation of malicious programs in WSNs can be modeled by imitating the theory of epidemiology. After decades of research studies of the initial SIR (Susceptible, Infected, Removed) model proposed by Kephart and White [2], the epidemiological model has been fully developed [3–6].

Many scholars are also devoted to the study of malicious programs' propagation mechanism in WSNs. In order to better protect against worm theft of security-critical information, Haixia Peng et al. proposed a reliability-oriented local-area model, which considers the topology of WSNs [7]. Based on the actual scenario, Akansha Singh et al. proposed a mathematical model that considered the influence of node distribution density and different communication radius on worm propagation [8]. Mohammad Sayad Haghighi et al. proposed a dynamic propagation model with the consideration of geospatial limitation [9]. Shakya [10] and Bahi et al. [11] have even considered the spatial correlations in WSNs. Bo Qu and Wang added nodal degree into the model as a factor affecting the infection rates [12]. The sleep and work interleaving policy was incorporated in a multiworm propagation model proposed by [13]. Tang also introduced sleep pattern to enhance the defense of WSNs [14]. In mobile WSNs, the operations of providing pulse immunization to susceptible nodes can well resist the propagation of malware [15]. Compared with static defensive measures, mobile patching is more effective in suppressing the spread of mobile sensor worms [16]. Nicola Roberto Zema et al. also

used a mobile approach to repair WSNs [17]. By adding time delay to the propagation model, Neha Keshri et al. found it could reduce the damage to nodes [18]. Many scholars have considered the energy problem of WSNs, for example, Lei Mo et al. introduced a mobile charger to add energy to the networks [19]. However, it is not difficult to find that the nodal energy is basically not taken into account in the classification criteria of different states of nodes. One of the highlights of this paper is that the energy of nodes has been put forward and divided into high- and low-energy state further. At the same time, the SILRD (Susceptible, Infected, Low-energy, Recovered, Dead) model is proposed in this paper according to the nodal states.

As it is a problem of antagonism against malicious programs, some of the scholars also used game theory to get the optimal strategy in the nonlinear system. By reducing the transmission range to suppress the spread of malicious programs, M. H. R. Khouza-ni et al. obtained the optimal transmission range by constructing the optimal control model [20] and also considered bandwidth consumption and invasion risk as an optimal problem [21]. Mohamed S. Abdalzaher and Osamu Muta proposed a Stackelberg game approach to improve the defense mechanisms of WSNs against the spectrum sensing data falsification attack [22]. As a study of nonlinear systems, Chenglong Wang et al. studied the problem of online adaptive optimal controller with input time delays [23]. Shuping He et al. proposed a scheme of online $H\infty$ control laws for nonlinear systems [24]. Chengcheng Ren et al. designed a suitable distributed controller [25] and a suitable finite-time stabilizable controller [26] to guarantee the positiveness and stabilization of the closed-loop systems. As an inseparable part of game theory, differential game has advantages in dealing with dynamic problems. Miao and Li exploited differential game to construct the optimal problem between network systems and attackers [27]. Miao figured out the optimum between throughput and energy efficiency [28]. Dong HAO and Kouichi SAKURAI defined a game called PUE attack game between attackers and secondary users [29]. Ding et al. constructed a differential game between two types of nodes in WSNs [30]. In addition to various game theories, Shuping He et al. also used reinforcement learning [31] and policy iteration algorithm [32] to solve the problem of optimal control. Differential game can also solve different kinds of problems: multiagent collision prevention [33], multipath routing optimization [34], optimal storage capacities [35], and minimization of transmission cost [36]. At the same time, linear programming can also be used to find the optimal solution [37]. In this paper, the optimal dynamic game strategies between the malicious programs and WSNs are obtained by using Pontryagin's Maximum Principle.

Our contributions are summarized below.

First, an improvement on the basic epidemiological model has been proposed. Considering the energy storage of WSNs, the low-energy state to further satisfy the feature of WSNs has been introduced. In the actual situation, nodes will consume their energy as a result of daily work, and they will definitely undergo a process from full energy to low energy. Meanwhile, since the attack of some malicious programs will be embodied in the faster consumption of energy, the introduction of low-energy state can reflect the attack degree to some extent.

Second, the effect of rechargeable factor on WSNs has been considered. In order to maintain the normal function of WSNs, the rechargeable factor is introduced. As one of the main defects of WSNs, limited energy has been restricted the lifetime of WSNs, for nodes, which are infected by a certain kind of malicious programs, can consume energy quickly. Thus, the influence of malicious programs can be suppressed by charging. As the number of low-energy nodes decreases, the cost of WSNs' operation increases by deploying UAVs. Therefore, this paper will reveal the balance between the two. At the same time, the validity of the control method in the SILRD model is further explained.

The rest of our paper is organized as follows. In Section 2, SILRD model with low-energy state has been proposed. At the same time, the influence of rechargeable factors on WSNs is considered and the corresponding differential equations are formulated. In Section 3, differential game has been used to figure out optimal strategies applied by WSNs and malicious programs. In Section 4, the evolution of nodal states, the flow of nodal energy, and the games between WSNs and malicious programs will be revealed by simulation. In Section 5, a conclusion of the full paper is presented here.

2. SILRD Model with WSNs

In WSNs, the total number of identical and static nodes is N and they are distributed randomly in a flat area with S (m^2). Each node is equipped with an antenna for messaging and a receiver for wireless charging. The maximum radius of node's transmission is r (m). In this section, the SILRD model will be proposed, and the differential equations will dynamically reflect the transition of nodal states.

2.1. Nodal States in WSNs. At the same time, charging is happening all the time in WSNs. This model assumes the attack from only one type of malicious program, that is, the recovered nodes will not be repeatedly infected. Each node transmits information to their surrounding nodes, which will relay the information to remote computer or control center step by step. Malicious programs propagate through information transmission between nodes. Once infected with malicious programs, the nodes will consume their energy at a faster rate.

Based on the traditional model, the SILRD model further considers energy level of each nodes and classifies nodes into the following five states:

Susceptible (S): a node in the Susceptible state is extremely vulnerable to malicious programs because of its lack of defenses. Energy consumption level of these nodes is normal.

Infected (I): a node in the Infected state has a rapid increase in energy consumption due to the successful infection of malicious programs. If infected nodes are not patched or charged in time, they will die of exhaustion.

Low-energy (L): nodes in the Low-power state are those that are infected with malicious programs or that consume energy normally. These nodes are characterized by low-energy level so that they cannot maintain normal work, including data transmission between nodes.

Recovered (R): a node in the Recovered state is immune to malicious programs. Particularly, charging and patching occur at the same time. In other words, nodes in recovered state are possessing not only immunity but also a high-energy level.

Dead (D): a node in the Dead state is completely dysfunctional. Even charging such a node cannot restore it. Meanwhile, this part of nodes due to total loss of energy is unable to infect its neighbors.

In this paper, $S(t)$, $I(t)$, $R(t)$, $L(t)$, and $D(t)$ are the ratio of susceptible, infected, recovered, low-energy, and dead nodes at time t, respectively. The sum of these five ratios is equal to 1. Thus, the following equation must be satisfied:

$$S(t) + I(t) + R(t) + D(t) + L(t) = 1. \quad (1)$$

2.2. Transitions between Nodal States in SILRD Model. Before the game started, only susceptible nodes and infected nodes existed in WSNs, and their sum is equal to N. Furthermore, the death of nodes because of hardware damage or environmental factors have not been considered in this paper.

The transmission range of each node is πr^2 (m^2). The density of susceptible nodes in WSNs is $(S(t)/S)$. For an infected node, the number of susceptible nodes around which it can infect is $(\pi r^2 S(t)/S)$. Therefore, in whole WSNs, the number of susceptible nodes infected by malicious programs is $\pi r^2 I(t) S(t)/S$.

In this model, the number of sensor nodes does not increase. Before WSNs were not infected by malicious programs, nodes in WSNs normally collect different kinds of environmental information and transmit the processed messages to their surrounding nodes. Malicious programs are artificially implanted into WSNs. Besides destroying the functionality of nodes, malicious programs can eavesdrop on information through transmission between nodes. In the absence of rechargeable devices, nodes will eventually shut down as the power runs out.

It is necessary to charge WSNs because of the consumption of electricity caused by normal work and the attack by malicious programs. Infected nodes spread malicious programs to neighbors with a certain probability. Susceptible nodes which receive malicious programs and get infectivity will become infected nodes. Some susceptible nodes have not been infected by malicious programs during their lifetime and remain in the normal working state. This part of the nodes will be transferred directly from the susceptible state to low-energy state without recharging by UAVs (Unmanned Aerial Vehicles) or the other MCs (Moving Chargers). Some susceptible nodes will gain immunity to this type of malicious programs in time by receiving and installing patches from the UAVs. The rest of susceptible nodes will keep staying into the normal state. Specifically, two simple schematic diagrams of the scene of the SILRD model have also been portrayed, and the states evolutions of nodes covered during the UAV movement are clearly visible, as depicted in Figure 1.

The transmission capacity of malicious programs directly determines the number of nodes transmit from the susceptible state to infected state. Infected nodes dissipate their own energy by enhancing the frequency of information acquisition and the strength of communication with surrounding nodes. With the increasing damage degree of malicious programs, nodes will enter into the dead state at a faster speed. At the same time, malicious programs can also choose not to continue to attack the infected nodes, and these infected nodes are only infectious but not destructive. However, if the patches carried by UAVs are timely and successfully installed early, the nodes will safely convert to the recovered state.

Nodes in the recovered state are not only immune to the malicious programs but also in a high-energy level. Nodes that move from susceptible and infected states to recovered states are in high-energy level, and UAVs only need to transmit patches without charging them. On the contrary, nodes in the low-energy state need to be charged and patched at the same time to transform to the recovered state, even if the nodes in the recovered state shift to the low-energy state without energy replenishment due to normal consumption.

Some of the nodes in the low-energy state are immune, while others are not. Nodes in the low-energy state will exhaust quickly, and the effect of malicious programs on nodes transmitting from the low-energy state to dead state has been ignored. The flow diagram of the SILRD propagation model is shown in Figure 2.

The transition probability from the susceptible state to infected state due to being infected by malicious programs is P_{SI}. The probability of the susceptible nodes moves from the high-energy level to low-energy level due to normal operation is P_{SL}. Probability of susceptible nodes being patched by UAVs is P_{SR}. The probability that infected nodes will be repaired while still at high-energy level is P_{IR}. The probability that infected nodes are destroyed by malicious programs and squander energy until exhaustion is P_{ID}. Malicious programs in some infected nodes stop destroying, at this time, these infected nodes can work normally with probability P_{IL} at the low-energy state. The probability of nodes at the low-energy level being successfully charged and patched by UAVs before they run out of energy is P_{LR}. The probability of immune nodes entering the low-energy level due to daily collection and transmission is P_{RL}. Finally, the probability of death due to exhaustion at the low-energy level is P_{LD}. The rate of change in each state is formulated from

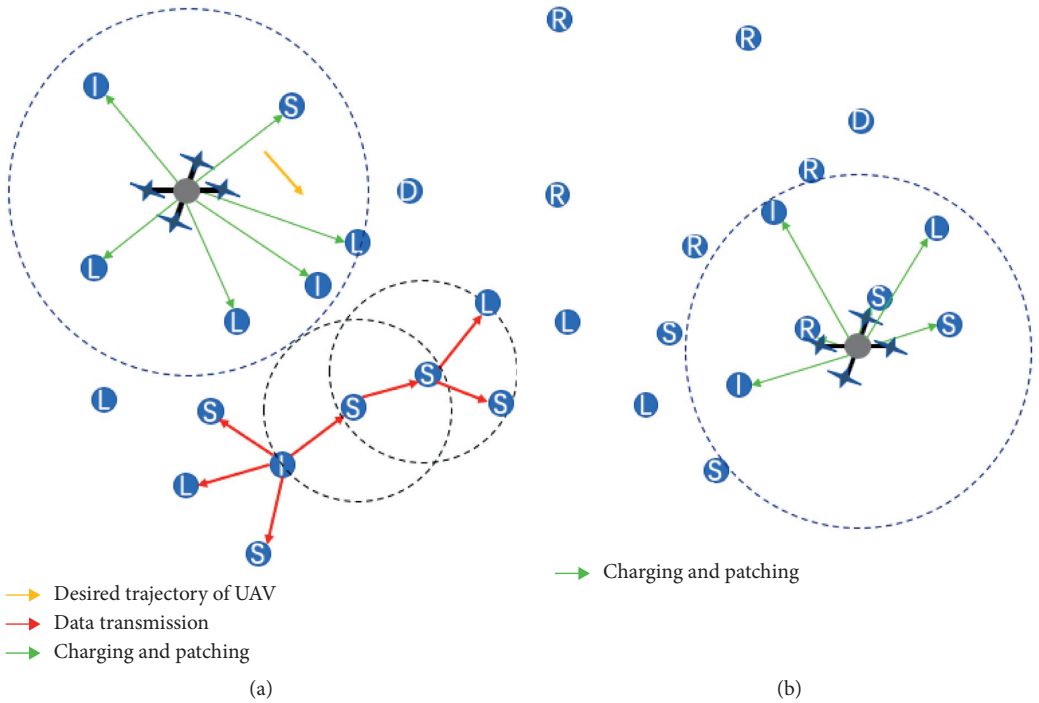

Figure 1: Evolution of nodal states in UAV coverage area. (a) The location of the UAV at a certain moment and the nodal states before UAV moves. (b) The evolution of Nodal states as a result of the UAV moving with the desired trajectory from the original position.

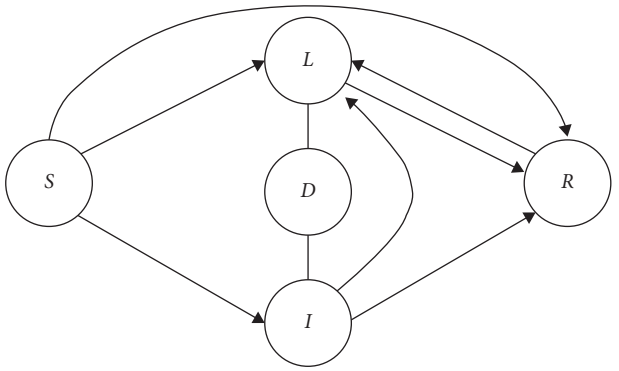

Figure 2: The flow diagram of the propagation model. The letters in the circle represent the corresponding state of the node. Arrows indicate the direction of transition between node states.

$$\frac{dS(t)}{dt} = -P_{SI}\pi r^2 \frac{S(t)I(t)}{S} - P_{SR}S(t) - P_{SL}S(t), \quad (2)$$

$$\frac{dI(t)}{dt} = P_{SI}\pi r^2 \frac{S(t)I(t)}{S} - P_{IR}I(t) - P_{IL}I(t) - P_{ID}I(t), \quad (3)$$

$$\frac{dL(t)}{dt} = P_{IL}I(t) + P_{SL}S(t) - P_{LR}L(t) - P_{LD}L(t) + P_{RL}R(t), \quad (4)$$

$$\frac{dR(t)}{dt} = P_{IR}I(t) + P_{SR}S(t) + P_{LR}L(t) - P_{RL}R(t), \quad (5)$$

$$\frac{dD(t)}{dt} = P_{LD}L(t) + P_{ID}I(t). \quad (6)$$

2.3. The Introduction of Control Variables. In this paper, the damage caused by malicious programs to WSNs is mainly reflected in the conversion process from the infected state to dead state. At the same time, the propagation ability of malicious programs depends not only on the transmission frequency between nodes but also on themselves. Therefore, attack modes of malicious programs include the destruction of WSNs and their propagation.

The defense measures of WSNs are embodied in charging and patching various nodes. Charging nodes in different types of states by UAVs can not only prolong the lifespan of WSNs but also mitigate the damage from malicious programs to some degree. Patching a node can make it immune to the corresponding malicious programs. Thus, the defense patterns of WSNs are manifested in the supplement of node electricity and the provision of relevant patches.

According to the effects of the attack and defense measures on nodal states, two hypotheses have been proposed. One is that P_{SI} and P_{ID} are controlled by malicious programs to some degree. The higher the attack level of the malicious programs, the higher these two probabilities. The other is that P_{SR}, P_{IR}, and P_{LR} are controlled by WSNs to some degree. Similarly, the higher the defense level of WSNs, the higher the probability of all three.

To further formulate this five transition probabilities, equation (7) has been put forward:

$$\begin{cases} P_{\mathrm{SI}} = \dfrac{A_{\mathrm{SI}} L_{\mathrm{SI}}}{A_{\mathrm{SImax}} + A_{\mathrm{SImin}}}, \\ P_{\mathrm{ID}} = \dfrac{A_{\mathrm{ID}} L_{\mathrm{ID}}}{A_{\mathrm{IDmax}} + A_{\mathrm{IDmin}}}, \\ P_{\mathrm{SR}} = \dfrac{D_{\mathrm{SR}} L_{\mathrm{SR}}}{D_{\mathrm{SRmax}} + D_{\mathrm{SRmin}}}, \\ P_{\mathrm{IR}} = \dfrac{D_{\mathrm{IR}} L_{\mathrm{IR}}}{D_{\mathrm{IRmax}} + D_{\mathrm{IRmin}}}, \\ P_{\mathrm{LR}} = \dfrac{D_{\mathrm{LR}} L_{\mathrm{LR}}}{D_{\mathrm{LRmax}} + D_{\mathrm{LRmin}}}, \end{cases} \tag{7}$$

where A_{SI} and A_{ID} represent the control levels of malicious programs, while L_{SI} and L_{IL} represent the probability of successful attack by malicious programs. In the same way, D_{SR}, D_{LR}, and D_{IR} represent the control level of WSNs, while L_{SR}, L_{IR}, and L_{LR} represent the probability of successful defense. A_{SImin} and A_{SImax} represent the minimum and maximum values of malicious program's control level, respectively, so do the other counterparts in equation (7).

The success rates of infection and suppression are all on a scale of 0 to 1, as shown below:

$$L_{\mathrm{SI}}, L_{\mathrm{ID}}, L_{\mathrm{SR}}, L_{\mathrm{IR}}, L_{\mathrm{LR}} \in [0, 1]. \tag{8}$$

3. Optimal Dynamic Game Strategies for the Malicious Programs and WSNs

As an important branch of game theory, differential game is the theory which both parties can make decisions freely proposed by Isaac in solving the pursuit evasion problem in 1965 [38]. Differential game refers to the game played by multiple players in a continuous time system. At the same time, players in the system try to optimize their independent and ambivalent goals and finally obtain the optimal strategies of the players over time. Generally speaking, differential game is a theory to study the decision-making process of two or more players when their controls are applied to a dynamical system described by differential equations. In the differential game, figuring out a saddle point is the same thing as finding out Nash equilibrium. In this section, the cost of the game is formulated by further description of the flow diagram, and the optimal dynamic strategies of both sides of the game are constructed according to Pontryagin's Maximum Principle.

3.1. Payoff Function in the Attack-Defense Game. In this paper, the zero-sum noncooperative differential game between malicious programs and WSNs has been discussed. The goal of malicious programs is to maximize the payoff while the networks want to minimize it. After analysis by Pontriagin's Maximum Principle, the optimal attack strategy for malicious programs has been obtained, and WSNs also have the corresponding optimal countermeasures.

Definition 1. Given a fixed duration T, $\nu(t) = (A_{\mathrm{SI}}(t), A_{\mathrm{ID}}(t))$ is a strategy set of malicious programs at time t. Identically, $\mu(t) = (D_{\mathrm{SR}}(t), D_{\mathrm{IR}}(t), D_{\mathrm{LR}}(t))$ is a strategy set of WSNs at time t.

In addition to the costs cause by malicious programs' attack, WSNs themselves will generate a variety of costs with time.

Nodes in the infected state, by destroying the transmission mechanism between nodes, lose plenty of their own energy and bring to a certain cost. Moreover, such nodes also cause unexpected losses through eavesdropping on WSNs. Although nodes in the low-energy state do not have the ability to propagate malicious programs, they cannot work normally due to the low-energy level, which will definitely engender much losses. As a result of complete loss of function of the dead node, topological structure of WSNs will be disrupted. In the reconstruction of the new transmission mechanism, it is bound to incur additional costs. Multiple UAVs charge or patch corresponding nodes by carrying patches and energy to some area of WSNs. During the flight of the UAVs, a part of electricity will be consumed, and it will be consumed in the process of SWIPT (simultaneous wireless information and power transfer) of UAVs.

While malicious programs create networks' losses, WSNs' own defense measures will make up for this losses. The purpose of malicious programs is to make them as greater as possible, whereas WSNs do the opposite, thus forming two sides of the game.

By patching susceptible nodes, they will be immune to some malicious programs, which ensures normal operation of WSNs in the future. The infected node returns to the normal state, which not only reduces the loss that should have occurred but also guarantees the normal operation for a period of time. In addition to the low-energy levels, nodes in the low-energy state are likely to contain more malicious programs. Therefore, it should not only be replenished with energy but also be patched to make it immune.

The risk posed by infected nodes spreading malicious programs is $C_I I(t)$ at time t, where C_I is a cost coefficient and $C_I \geq 0$. The consumption caused by using UAVs to repair nodes while replenishing the node energy is $C_{\mathrm{LR}} P_{\mathrm{LR}} L(t)$ at time t, where $C_{\mathrm{LR}} \geq 0$. The cost of losing some functions due to nodes at low-energy levels is $C_L L(t)$ at time t, where $C_L \geq 0$. Loss of WSNs' failure due to nodes death is $C_D D(t)$ at time t, where $C_D \geq 0$. Nodes have positive benefits $C_R R(t)$ at time t due to having immunity, where $C_R \geq 0$. The costs of patching susceptible and infected nodes are $C_{\mathrm{SR}} P_{\mathrm{SR}} S(t)$ and $C_{\mathrm{IR}} P_{\mathrm{IR}} I(t)$ at time t, respectively, where $C_{\mathrm{SR}} \geq 0$ and $C_{\mathrm{IR}} \geq 0$. Nodes in the susceptible state have $C_S S(t)$ benefit from working normally at time t, where $C_S \geq 0$. At the terminal moment, susceptible and recovered nodes will bring future benefits, so $C_{S_f} S(t_f)$ and $C_{R_f} R(t_f)$ will be used to measure these benefits, where $C_{S_f} \leq 0$ and $C_{R_f} \leq 0$. Conversely, nodes in the infected, low-energy, and dead states will continue to affect the networks. $C_{I_f} I(t_f)$,

$C_{L_f}L(t_f)$, and $C_{D_f}D(t_f)$ will be used to describe these costs, where $C_{I_f} \geq 0$, $C_{L_f} \geq 0$, and $C_{D_f} \geq 0$.

The payoff function of this game is shown in

$$J(\mu(t), \nu(t)) = \int_{t_0}^{t_f} \{-C_S S(t) + [C_I + C_{\mathrm{IL}}P_{\mathrm{IL}} + C_{\mathrm{PATCH}}P_{\mathrm{IR}}]I(t) - C_R R(t) + C_D D(t) + [C_{\mathrm{LR}}P_{\mathrm{LR}} + C_L]L(t) + C_{\mathrm{PATCH}}P_{\mathrm{SR}}S(t)\}\mathrm{d}t + C_{S_f}S(t_f) + C_{I_f}I(t_f) + C_{\mathrm{PATCH}}P_{\mathrm{SR}}S(t)\mathrm{d}t + C_{S_f}S(t_f) + C_{I_f}I(t_f). \tag{9}$$

According to the payoff function, we have ϕ to determine terminal constraint of the game, as depicted in the following equation:

$$\phi = C_{S_f}S(t_f) + C_{I_f}I(t_f) + C_{L_f}L(t_f) + C_{R_f}R(t_f) + C_{D_f}D(t_f). \tag{10}$$

3.2. Optimal Dynamic Strategies in the Attack-Defense Game

Theorem 1. *In the Attack-Defense game in the SILRD model, the optimal dynamic strategies of malicious programs and WSNs are*

$$A_{SI}^* = \begin{cases} A_{\mathrm{SImax}}, & \beta_{SI} > 0, \\ \text{unknown}, & \beta_{SI} = 0, \\ A_{\mathrm{SImin}}, & \beta_{\mathrm{SI}} < 0, \end{cases}$$

$$A_{\mathrm{ID}}^* = \begin{cases} A_{\mathrm{IDmax}}, & \beta_{\mathrm{ID}} > 0, \\ \text{unknown}, & \beta_{\mathrm{ID}} = 0, \\ A_{\mathrm{IDmin}}, & \beta_{\mathrm{ID}} < 0, \end{cases}$$

$$D_{\mathrm{SR}}^* = \begin{cases} D_{\mathrm{SRmin}}, & \beta_{\mathrm{SR}} > 0 \\ \text{unknown}, & \beta_{\mathrm{SR}} = 0, \\ D_{\mathrm{SRmax}}, & \beta_{\mathrm{SR}} < 0, \end{cases} \tag{11}$$

$$D_{\mathrm{IR}}^* = \begin{cases} D_{\mathrm{IRmin}}, & \beta_{\mathrm{IR}} > 0, \\ \text{unknown}, & \beta_{\mathrm{IR}} = 0, \\ D_{\mathrm{IRmax}}, & \beta_{\mathrm{IR}} < 0, \end{cases}$$

$$D_{\mathrm{LR}}^* = \begin{cases} D_{\mathrm{LRmin}}, & \beta_{\mathrm{LR}} > 0, \\ \text{unknown}, & \beta_{\mathrm{LR}} = 0, \\ D_{\mathrm{LRmax}}, & \beta_{\mathrm{LR}} < 0, \end{cases}$$

where β_{SI}, β_{ID}, β_{SR}, β_{IR}, and β_{LR} satisfy the following equation:

$$\beta_{\mathrm{SI}} = \frac{[\lambda_I(t) - \lambda_S(t)]\pi r^2 L_{\mathrm{SI}}(S(t)I(t)/S)}{A_{\mathrm{SImax}} + A_{\mathrm{SImin}}},$$

$$\beta_{\mathrm{ID}} = \frac{[\lambda_D(t) - \lambda_I(t)]L_{\mathrm{ID}}I(t)}{A_{\mathrm{IDmax}} + A_{\mathrm{IDmin}}},$$

$$\beta_{\mathrm{SR}} = \frac{[\lambda_R(t) - \lambda_S(t) + C_{\mathrm{PATCH}}]L_{\mathrm{SR}}S(t)}{D_{\mathrm{SRmax}} + D_{\mathrm{SRmin}}}, \tag{12}$$

$$\beta_{\mathrm{IR}} = \frac{[\lambda_R(t) - \lambda_I(t) + C_{\mathrm{PATCH}}]L_{\mathrm{IR}}I(t)}{D_{\mathrm{IRmax}} + D_{\mathrm{IRmin}}},$$

$$\beta_{\mathrm{LR}} = \frac{[\lambda_R(t) - \lambda_L(t) + C_{\mathrm{LR}}]L_{\mathrm{LR}}L(t)}{D_{\mathrm{LRmax}} + D_{\mathrm{LRmin}}}.$$

Proof. According to (2)–(6) and (8), we can construct the Hamiltonian function as shown below:

$$H = \lambda_S(t)\frac{S(t)}{\mathrm{d}t} + \lambda_I(t)\frac{I(t)}{\mathrm{d}t} + \lambda_L(t)\frac{L(t)}{\mathrm{d}t} + \lambda_R(t)\frac{R(t)}{\mathrm{d}t} + \lambda_D(t)\frac{D(t)}{\mathrm{d}t} - C_S S(t) + C_I I(t) - C_R R(t) + C_L L(t) + C_D D(t) - C_{\mathrm{LR}}P_{\mathrm{LR}}L(t) - C_{\mathrm{IR}}P_{\mathrm{IR}}I(t) + C_{\mathrm{SR}}P_{\mathrm{SR}}S(t). \tag{13}$$

From state functions (2)–(6) and payoff function (8), the following characteristics have been found out:

1 The five state functions and the payoff function are all continuous in time

2 The control variables are all bounded and continuous in the state functions and payoff function

Thus, there must exist a saddle point $(\mu^*(t), \nu^*(t))$ that meets (14) according to [39]:

$$J(\mu^*(t), \nu(t)) \leq J(\mu^*(t), \nu^*(t)) \leq J(\mu^*(t), \nu^*(t)), \tag{14}$$

where $J(\mu^*(t), \nu(t))$ represents the cost incurred when only the optimal strategy is selected by WSNs. $J(\mu^*(t), \nu(t))$ also

denotes that only malicious programs choose the optimal strategy. $J(\mu^*(t), \nu(t))$ indicates that not only the networks choose the optimal strategy but also malicious programs choose the optimal strategy.

According to [40] and the characteristics of this model, there must be a V satisfying

$$V = \max_{\nu(t)}\min_{\mu(t)} J(\mu(t), \nu(t)) = \min_{\mu(t)}\max_{\nu(t)} J(\mu(t), \nu(t)) = J(\mu^*(t), \nu^*(t)), \tag{15}$$

where $\max_{\nu(t)}\min_{\mu(t)} J(\mu(t), \nu(t))$ represents the cost incurred by WSNs in selecting the optimal strategy after the malicious programs makes optimal decision, while $\min_{\mu(t)}\max_{\nu(t)} J(\mu(t), \nu(t))$ denotes the cost incurred when the order of two sides is switched.

The following co-state differential equations (16)–(20) determine the co-state variables $\lambda_S(t)$, $\lambda_I(t)$, $\lambda_R(t)$, $\lambda_L(t)$, and $\lambda_D(t)$, which are all time dependent:

$$\frac{d\lambda_S(t)}{dt} = -\frac{dH}{dS(t)} = \frac{[\lambda_S(t) - \lambda_I(t)]\pi r^2 I^*(t) A_{SI}^* L_{SI}}{(A_{SImax} + A_{SImin})S} + C_S - \frac{C_{PATCH} D_{SR}^* L_{SR}}{D_{SRmax} + D_{SRmin}} + [\lambda_S(t) - \lambda_L(t)]P_{SL} + \frac{[\lambda_S(t) - \lambda_R(t)]D_{SR}^* L_{SR}}{D_{SRmax} + D_{SRmin}}, \tag{16}$$

$$\frac{d\lambda_S(t)}{dt} = -\frac{dH}{dI(t)} = \frac{[\lambda_S(t) - \lambda_I(t)]\pi r^2 S^*(t) A_{SI}^* L_{SI}}{(A_{SImax} + A_{SImin})S} - C_I + \frac{[\lambda_I(t) - \lambda_R(t)]D_{IR}^* L_{IR}}{D_{IRmax} + D_{IRmin}} - \frac{C_{PATCH} D_{IR}^* L_{IR}}{D_{IRmax} + D_{IRmin}} + [\lambda_I(t) - \lambda_L(t)]P_{IL} + (\lambda_I(t) - \lambda_D(t))A_{ID}^* L_{ID}, \tag{17}$$

$$\frac{d\lambda_L^*(t)}{dt} = -\frac{dH}{dL(t)} = \frac{[\lambda_L(t) - \lambda_R(t)]D_{LR}^* L_{LR}}{D_{LRmax} + D_{LRmin}} + [\lambda_L(t) - \lambda_D(t)]P_{LD} - C_L - \frac{C_{LR} D_{LR}^* L_{LR}}{D_{LRmax} + D_{LRmin}}, \tag{18}$$

$$\frac{d\lambda_R^*(t)}{dt} = -\frac{dH}{dR(t)} = [\lambda_L(t) - \lambda_R(t)]P_{RL} + C_R, \tag{19}$$

$$\frac{d\lambda_D^*(t)}{dt} = -\frac{dH}{dD(t)} = -C_D. \tag{20}$$

Meanwhile, the terminal value of the co-state variables satisfies

$$\begin{cases} \lambda_S(t_f) = \dfrac{d\phi}{dS(t)} = C_{S_f}, \\ \lambda_I(t_f) = \dfrac{d\phi}{dI(t)} = C_{I_f}, \\ \lambda_L(t_f) = \dfrac{d\phi}{dL(t)} = C_{L_f}, \\ \lambda_R(t_f) = \dfrac{d\phi}{dR(t)} = C_{R_f}, \\ \lambda_D(t_f) = \dfrac{d\phi}{dD(t)} = C_{D_f}. \end{cases} \tag{21}$$

According to Pontryagin's Maximum Principle, when $([\lambda_I(t) - \lambda_S(t)]\pi r^2 L_{SI}(S(t)I(t)/S)/A_{SImax} + A_{SImin})$ is greater than 0, the malicious programs will choose the maximum control A_{SImax} in order to make the cost as large as possible. On the contrary, supposing $([\lambda_I(t) - \lambda_S(t)]\pi r^2 L_{SI}(S(t)I(t)/S)/A_{SImax} + A_{SImin})$ is less than 0, the malicious programs will choose the minimum control A_{SImax} to maximize the cost. Similarly, when $[\lambda_D(t) - \lambda_I(t)]L_{ID}I(t)/(A_{IDmax} + A_{IDmin})$ is greater than 0, the malicious programs will choose A_{IDmax}, and the malicious programs will choose A_{IDmin} if $[\lambda_D(t) - \lambda_I(t)]L_{ID}I(t)/(A_{IDmax} + A_{IDmin})$ is less than 0.

For WSNs, in case $[\lambda_R(t) - \lambda_S(t) + C_{PATCH}]L_{SR}S(t)/(D_{SRmax} + D_{SRmin})$is greater than 0, it will adopt the minimum control D_{SRmin} to make the cost as small as possible. Maximum control D_{SRmax} is taken to minimize the cost, when $[\lambda_R(t) - \lambda_S(t) + C_{PATCH}]L_{SR}S(t)/(D_{SRmax} + D_{SRmin})$is less than 0. In terms of restoration measures for infected nodes, if $[\lambda_R(t) - \lambda_I(t) + C_{PATCH}]L_{IR}I(t)/(D_{IRmax} + D_{IRmin})$is greater than 0, WSNs will choose the minimum control D_{IRmin}, while WSNs will choose the maximum control D_{IRmax} when $[\lambda_R(t) - \lambda_I(t) + C_{PATCH}]L_{IR}I(t)/(D_{IRmax} + D_{IRmin})$ is less than 0. WSNs also takes similar measures to nodes moving from the low-energy state to recovered state. The node will take the maximum control D_{LRmax} supposing $[\lambda_R(t) - \lambda_L(t) + C_{LR}]L_{LR}L(t)/(D_{LRmax} + D_{LRmin})$is less than 0, while the node will take the minimum control D_{LRmin} if $[\lambda_R(t) - \lambda_L(t) + C_{LR}]L_{LR}L(t)/(D_{LRmax} + D_{LRmin})$is greater than 0. □

4. Simulation

In this chapter, two parts are discussed. In the first part, based on the dynamic strategy, charging factor is further analyzed to illustrate its advantages. The second part will compare and analyze with other control combinations to highlight the points of bang-bang control. In these two parts, simulations are verified on MATLAB R2017 B and the memory specification of the computer is 8 GB 1600 MHz DDR3.

In our assumptions, nodes are distributed at random in a two-dimensional region with an area of 10,000 m^2. The maximum transmission radius of a node is 10 m, and the neighbor nodes must exist within the maximum transmission range of the nodes. UAVs will perform nodes' patching and wireless charging operations together. At the beginning of the game, most of the nodes are in the susceptible state, and the rest are in the infected state. The maximum value of all control levels is assumed to be 1, and the minimum value is assumed to be 0. The parameters are set as shown in Table 1. According to the Pontriagin Maximum Principle, the algorithm of the Attack-Defense Game based on the SILRD model will be briefly explained in the form of pseudocode in Algorithm 1.

4.1. Dynamic Strategies in the Game between WSNs and Malicious Programs. This section will focus on the evolution on different nodes, control rules, and overall costs. At the same time, it is worth noting that this section will compare the case of no energy input.

4.1.1. The Variation Trend of Nodal States. Here, the variation trend of each state quantity over time under two cases will be compared. In particular, similar state quantities are contrasted in one simulation diagram for further analysis. Each state quantity curve is constructed from 100 sample points. The number of each type of nodes is evolved based on (2)–(6). The difference between Figures 2 and 3 is whether or not charging involved.

It can be seen from the comparison between Figure 3(a) and Figure 3(b) that, in the SILRD model proposed in this paper, energy input, namely, charging, has little influence on the number of susceptible nodes and infected nodes because charging does not directly affect such high-energy nodes.

Although the curves of the same type of nodes are similar in both cases, there exist numerical difference. The number of recovered nodes increased to 17.1% with energy input, up by 6% compared with the case of no energy input, and low-energy and death nodes decreased by 1.8% and 4.1%.

4.1.2. Comparison of Dynamic Optimal Control. Here, the reason for the evolution of states' quantities will be investigated, that is, the change of control levels of both sides in the game. When $T = 0$, the initial value of each controls is assumed to be 1. The malicious programs select the strategy according to (9) and (10), and WSNs choose according to (11)–(13).

Malicious programs stopped propagation on the third day because the peak of infection has been arrived. Even so, the damage from malicious programs continued until the end of the game, that is, the malicious programs have not been cleaned up.

Similarly, WSNs stopped patching infected and susceptible nodes on the second day of the game, as depicted in Figures 4 and 5. Because malicious programs are no longer spreading, patching vulnerable nodes is not cost effective. The same applies to infected nodes. Even if the malicious programs still exist, it costs more to patch them, so it stops.

The difference between Figures 4 and 5 is that the former adds control over energy input to the networks. As can be seen from Figures 3(a) and 4, after the number of recovered nodes reaches a peak, WSNs stop the repair of low-energy nodes to suspend the cost of charging and patching.

4.1.3. Cost Comparison. The costs of four cases will be compared over here. Due to the impact of the dynamic strategies' end-values, only the cost simulation diagram when $T < 100$ will be shown and will explain in detail. The costs are all constructed according to equation (8).As can be seen from Figure 6, without taking the terminal cost ($T = 100$) into account, strategies with energy inputs can actually reduce cost than strategies without them. Therefore, it is not always good to charge, and sometimes it is more cost effective to use the networks' residual energy. In the first ten days, the difference between charging and noncharging strategies is nonsignificant. However, with the development of the iteration, the gap continues to expand. From the comparison of costs, the strategies with charging are cost-saving than those without charging. Thus, the benefits of charging can cover the costs of it. It is worth noting that when the charging power is slightly reduced to about 50%, the cost will decrease rapidly. And then as the power continues to drop to about 10%, the cost, at 43 days, exceeds the cost at full power.

However, the ranking of costs will change after the end values are taken into account. At this point, the cost order from high to low is strategies with 10% power charging (-5.9344×10^4), strategies with full-power charging (-9.9543×10^4), strategies without charging (-1.7139×10^5), and strategies with 50% power charging (-1.7772×10^5). Therefore, the maximum charging power is not necessary when WSNs are evenly replenished. Because larger power means more nodes are converted to the high-energy state, but costs are also rising. There must exist a number of tradeoffs that are lower than both full-power operation and no energy input, such as the 50% power in this paper.

4.2. Comparison of Differential Hybrid Control Strategies. In this section, four combination control strategies are discussed. In the above, both the control of patching and charging belong to bang-bang control. In order to highlight the advantages of bang-bang control in the SILRD model, this paper compares it with another common control method which only needs to expand the corresponding

Table 1: Experimental parameters.

Parameter	Description	Value
L_{SI}	Probability of nodes converting from the susceptible state to infected state	0.1
L_{ID}	Probability of nodes converting from the infected state to dead state	0.05
L_{SR}	Probability of nodes converting from the susceptible state to recovered state	0.2
P_{IL}	Probability of nodes converting from the infected state to low-energy state	0.005
L_{LR}	Probability of nodes converting from the low-energy state to recovered state	0.2
P_{SL}	Probability of nodes converting from the susceptible state to low-energy state	0.005
P_{LD}	Probability of nodes converting from the low-energy state to dead state	0.005
P_{RL}	Probability of nodes converting from the recovered state to low-energy state	0.005
C_{SR}	Cost of nodes converting from the susceptible state to recovered state	5
C_{IR}	Cost of nodes converting from the infected state to recovered state	7
C_S	Cost of nodes in the susceptible state	12
C_D	Cost of nodes in the dead state	20
C_I	Cost of nodes in the infected state	12
C_R	Cost of nodes in the recovered state	15
C_L	Cost of nodes in the low-energy state	15
C_{LR}	Cost of nodes converting from the low-energy state to recovered state	10
$S(0)$	The ratio of the initial number of susceptible nodes	95%
$I(0)$	The ratio of the initial number of infected nodes	5%
$L(0)$	The ratio of the initial number of low-energy nodes	0%
$R(0)$	The ratio of the initial number of recovered nodes	0%
$D(0)$	The ratio of the initial number of dead nodes	0%

(1) Initialize all coefficients;
(2) Define $\alpha(t) = \{S(t), I(t), L(t), R(t), D(t)\}$;
(3) Define $\beta(t) = \{\lambda_S(t), \lambda_I(t), \lambda_L(t), \lambda_R(t), \lambda_D(t)\}$;
(4) Define $\gamma(t) = \{\mu(t), \nu(t)\}$;
(5) **if** $t = 0$ **then**
(6) Substitute $\alpha(0)$ and $\gamma(0)$ into (2)–(6);
(7) Substitute $\alpha(0)$, $\beta(0)$ and $\gamma(0)$ into (17)–(21);
(8) end if
(9) **for** $t = 1$ to T **do**
(10) Substitute $\alpha(t)$ and $\gamma(t)$ into (2)–(6);
(11) Substitute $\alpha(t), \beta(t)$ and $\gamma(t)$ into (17)–(21);
(12) Substitute $\alpha(t+1)$ and $\beta(t+1)$ into (9)–(13);
(13) **end for**

Algorithm 1: Attack-Defense Game based on the SILRD Model.

control into second term, that is, replace D_{SR} with D_{SR}^2, D_{IR} with D_{IR}^2, and D_{LR} with D_{LR}^2. It is worth noting that the payoff function describing the game under square control does not change. According to the proof conditions of the Maximum Principle in [38], there still exist a pair of saddle points $(\mu^*(t), \nu^*(t))$ at this time, so the proofs will not be described here again.

For the convenience of the following description, this kind of control is named as square control in this paper. Bang-bang control and square control will alternate between charging process and patching process to form four different control combinations.

4.2.1. The Variation Trend of Nodal States. In particular, similar state quantities are contrasted in one simulation diagram for further analysis.

The trend of the number of susceptible nodes under four strategies is basically similar, as depicted in Figure 7(a). The number of susceptible nodes decayed most slowly when square control was only used to patch high-energy nodes. When the square control is used for charging low-energy nodes, the curves are fairly close. Therefore, if the aim of the network is to keep the number of susceptible nodes as high as possible, the bang-bang control can be applied to patching high-energy nodes and square control for charging and patching low-energy nodes.

As can be seen from Figure 7(b), if only the square control is used in WSNs, the number of infections will reach a very high peak at about 13%. Applying square control to patching high-energy nodes is more effective at suppressing the spread of malicious programs than just only using bang-bang control and its peak value is about 5.6%.

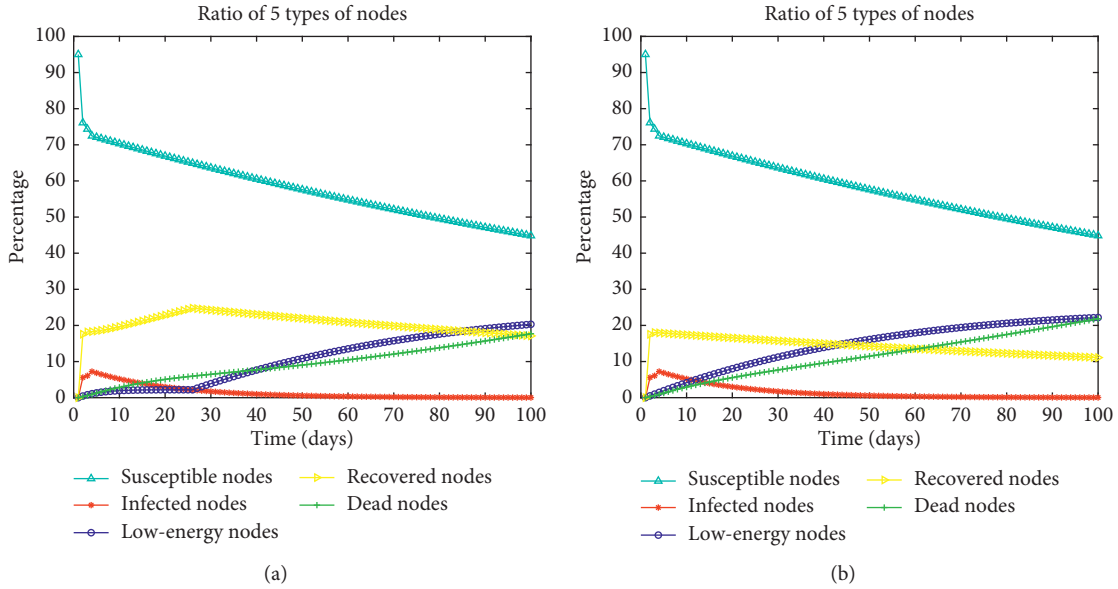

Figure 3: Evolution of five types of nodes. In order to emphasize the impact of charging, this experiment takes charging as a research factor. (a) The evolution of nodes under the condition of charging (i.e., with energy inputs). (b) The evolution of nodes under the condition of no charging (i.e., without energy input).

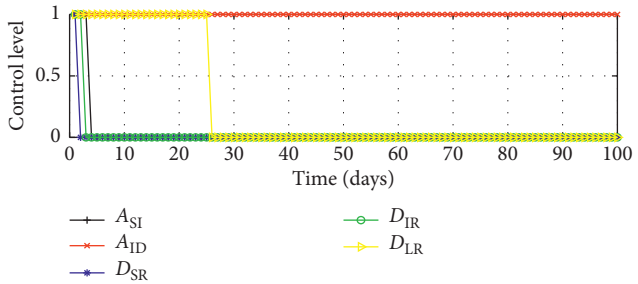

Figure 4: Optimal dynamic control with charging factors. This figure shows how the five control variables change over 100 days.

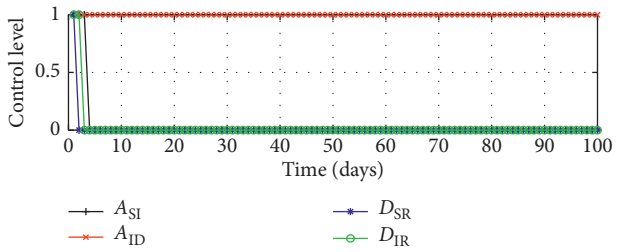

Figure 5: Optimal dynamic control without charging factors. The difference (Figure 4) is the change of the five control variables in the absence of UAVs within 100 days.

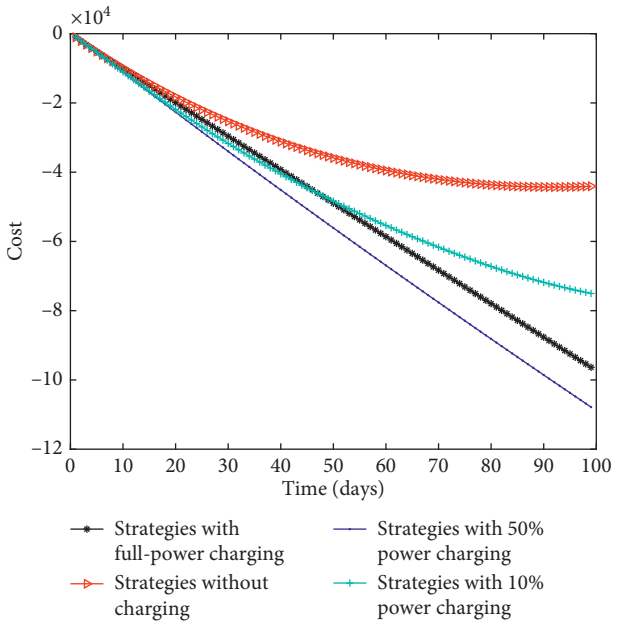

Figure 6: Cost comparison on four cases. The four cases differ in the level of charging power. The corresponding charging power levels of the curve from top to bottom are 0%, 10%, 100%, and 50%.

As can be seen from the comparison between Figures 7(c) and 7(d), when bang-bang control is only applied in WSNs, the number of low-energy nodes and recovered nodes are significantly changed. In Figures 7(c) and 7(d), the other three control combinations' evolution areas similarly. In other words, applying bang-bang control to charging and patching is more effective in suppressing low-energy nodes and boosting the number of recovered nodes. In particular, when only bang-bang control is applied, the peak value of recovered nodes can reach 25%.

All control combinations had lower mortality rates, as depicted in Figure 7(e). In the first six days, there was little difference in mortality among the combinations. For the first 41 days, applying bang-bang control and square control, respectively, to patching and charging had the lowest

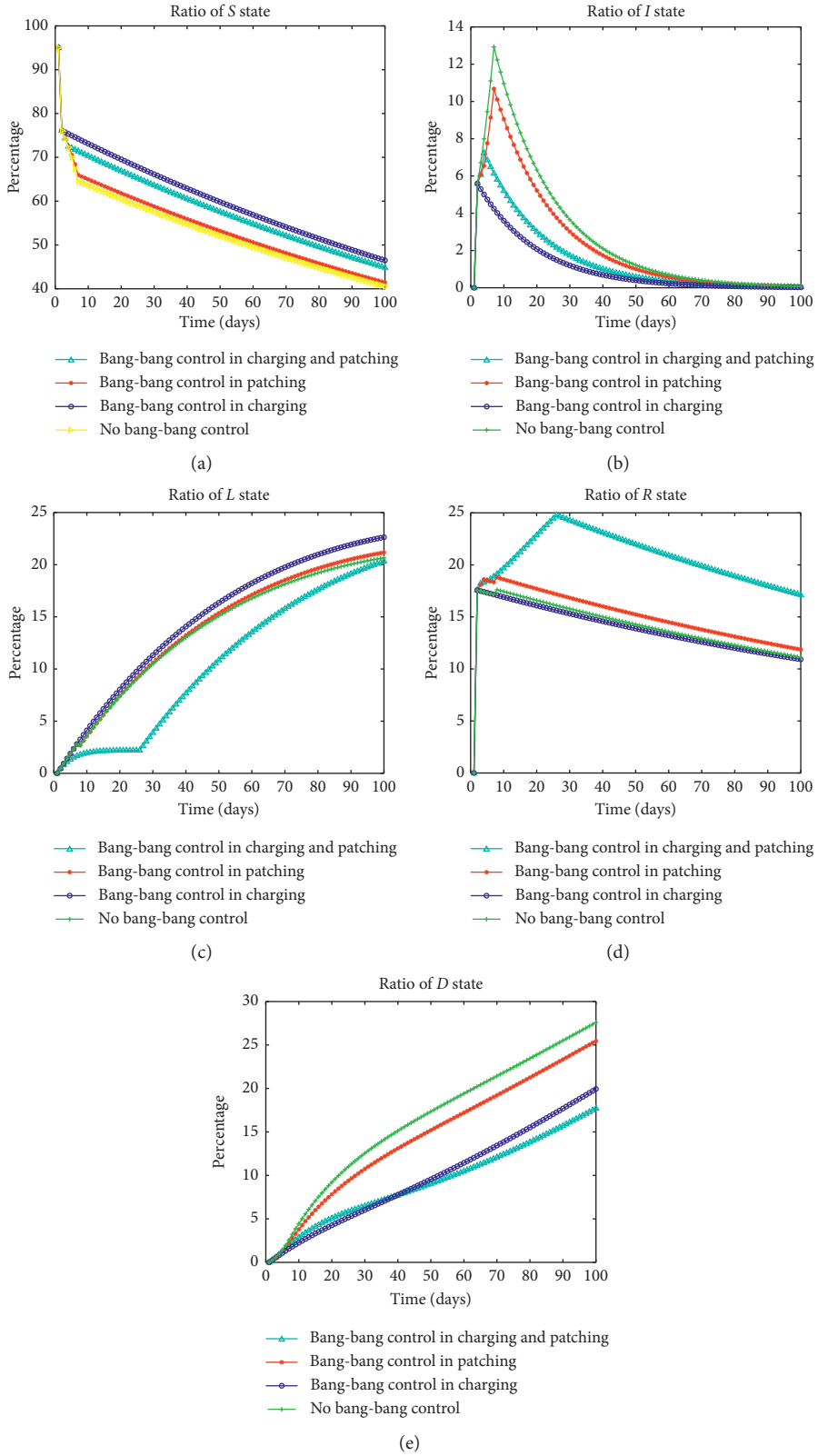

Figure 7: Evolution of five types of nodes under four control combinations. Unlike the previous section, the research factor considered in Section 4.2.1 is the control combination applied to charging and patching. This section considers the control combination of bang-bang control and square control. If bang-bang control is only applied to patching on high-energy nodes, then square control is applied to charging and patching on low-energy nodes. Similarly, if bang-bang control is used to low-energy nodes, then high-energy nodes use square control. If UAVs do not use bang-bang control, then they adopt square control. (a) The number of S-nodes. (b) The number of I-nodes. (c) The number of L-nodes. (d) The number of R-nodes. (e) The number of D-nodes.

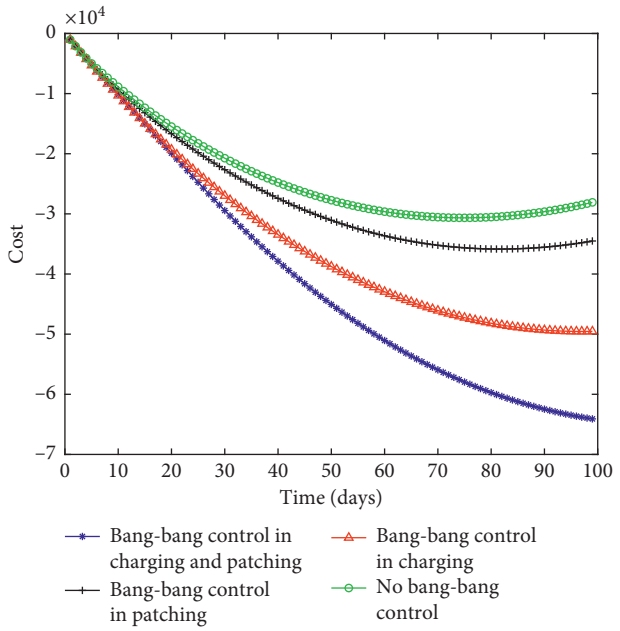

Figure 8: Cost comparison based on four control combinations. The four combinations are consistent with the four in Figure 7. The advantages of the combinations are further explained by comparing the costs incurred by them.

mortality. Starting at day 42, the combinations with bang-bang control only had a lower mortality.

4.2.2. Cost Comparison. In this part, the costs of the control combinations will be compared. The combination with the highest cost is the one with only the square control, as can be seen from Figure 8. The lowest-cost combination is the one with only the bang-bang control. At the same time, further analysis shows that bang-bang control can be applied to the charging process to reduce the cost effectively.

The reason bang-bang control produces lower costs is because of the jump property of the control. Specifically, when generating revenue, the jump from the minimum control level to the maximum level can quickly yield. Similarly, a jump from the maximum level to minimum can quickly reduce losses.

5. Conclusion

By using residual energy of nodes as one of the classification criteria, not only the flows of energy between nodes are revealed but also the attack patterns of malicious programs can be further described. The idea of charging, though just pro forma, can be used as a way to fend off malicious programs and reduce mortality of nodes. Meanwhile, the relationship between charging power and game cost has been further revealed in this paper. The advantages of bang-bang control in WSNs against malicious programs are demonstrated. When the cost of patching or charging becomes too high, the bang-bang control rule can quickly jump from maximum to minimum.

When considering the process of charging nodes, this paper assumes that charging and patching are carried out simultaneously. However, there may be a delay between the two process. Further analysis shows the way of charging may be affected by various random factors, such as light, wind speed, and human factors. The model would be more precise and practical if more practical conditions were considered. Incorporating more realistic elements into the model is a promising direction for future work.

Data Availability

The data used to support the findings of this study are included within the article, such as the cover area of the WSNs, the maximum transmission radius of nodes, the initial values of the number of sensor nodes, the transition probabilities among five nodal states, and the cost coefficients.

Conflicts of Interest

The authors declare that they have no conflicts of interest.

References

[1] J. Yick, B. Mukherjee, and D. Ghosal, "Wireless sensor network survey," *Computer Networks*, vol. 52, no. 12, pp. 2292–2330, 2008.

[2] W. O. Kermack and A. G. McKendrick, "Contribution to the mathematical theory of epidemics," *Proceedings of the Royal Society*, vol. 115, no. 772, pp. 700–721, 1927.

[3] L. P. Feng, L. P. Song, Q. S. Zhao, and H. B. Wang, "Modeling and stability analysis of worm propagation in wireless sensor network," *Mathematical Problems in Engineering*, vol. 2015, Article ID 129598, 8 pages, 2015.

[4] R. P. Ojha, P. K. Srivastava, and G. Sanyal, "Improving wireless sensor networks performance through epidemic model," *International Journal of Electronics*, vol. 106, no. 6, pp. 862–879, 2019.

[5] O. A. Toutonji, S.-M. Yoo, and M. Park, "Stability analysis of VEISV propagation modeling for network worm attack," *Applied Mathematical Modelling*, vol. 36, no. 6, pp. 2751–2761, 2012.

[6] K. M. Bimal and N. Keshri, "Mathematical model on the transmission of worms in wireless sensor network," *Applied Mathematical Modelling*, vol. 37, no. 6, pp. 4103–4111, 2013.

[7] H. X. Peng, H. Zhao, Y. G. Bi, and S. Z. Si, "A reliability-oriented local-area model for large-scale wireless sensor networks," *Mathematical Problems in Engineering*, vol. 2015, Article ID 923692, 17 pages, 2015.

[8] A. Singh, A. K. Awasthi, K. Singh, and P. K. Srivastava, "Modeling and analysis of worm propagation in wireless sensor networks," *Wireless Personal Communications*, vol. 98, no. 3, pp. 2535–2551, 2018.

[9] M. S. Haghighi, S. Wen, Y. Xiang, B. Quinn, and W. L. Zhou, "On the race of worms and patches: modeling the spread of information in wireless sensor networks," *IEEE Transactions on Information Forensics and Security*, vol. 11, no. 12, pp. 2854–2865, 2016.

[10] R. K. Shakya, "Modified si epidemic model for combating virus spread in spatially correlated wireless sensor networks," http://arxiv.org/abs/1801.04744v1.

[11] J. M. Bahi, C. Guyeux, M. Hakem, and A. Makhoul, "Epidemiological approach for data survivability in unattended

wireless sensor networks," *Journal of Network and Computer Applications*, vol. 46, pp. 374–383, 2014.

[12] B. Qu and H. Wang, "SIS epidemic spreading with correlated heterogeneous infection rates," *Physica A: Statistical Mechanics and Its Applications*, vol. 472, pp. 13–24, 2017.

[13] X. Wang, Q. Li, and Y. Li, "EiSIRS: a formal model to analyze the dynamics of worm propagation in wireless sensor networks," *Journal of Combinatorial Optimization*, vol. 20, no. 1, pp. 47–62, 2010.

[14] S. Tang, "A modified SI epidemic model for combating virus spread in wireless sensor networks," *International Journal of Wireless Information Networks*, vol. 18, no. 4, pp. 319–326, 2011.

[15] S. Shen, H. Zhou, S. Feng, J. Liu, and Q. Cao, "SNIRD: disclosing rules of malware spread in heterogeneous wireless sensor networks," *IEEE Access*, vol. 7, pp. 92881–92892, 2019.

[16] T. Wang, Q. Wu, S. Wen et al., "Propagation modeling and defending of a mobile sensor worm in wireless sensor and actuator networks," *Sensors*, vol. 17, no. 1, pp. 1–17, 2017.

[17] N. R. Zema, E. Natalizio, G. Ruggeri, M. Poss, and A. Molinaro, "MeDrone: on the use of a medical drone to heal a sensor network infected by a malicious epidemic," *Ad Hoc Networks*, vol. 50, pp. 115–127, 2016.

[18] N. keshri and B. K. Mishra, "Two time-delay dynamic model on the transmission of malicious signals in wireless sensor network," *Chaos, Solitons & Fractals*, vol. 68, pp. 151–158, 2014.

[19] L. Mo, P. C. You, X. H. Cao, Y. Q. Song, and J. M. Chen, "Decentralized multi-charger coordination for wireless rechargeable sensor networks," in *Proceedings of the IEEE IEEE 20th International Conference on High Performance Computing and Communications*, pp. 1–8, Nanjing, China, 2015.

[20] M. H. R. Khouzani, E. Altman, and S. Sarkar, "Optimal quarantining of wireless malware through reception gain control," *IEEE Transactions on Automatic Control*, vol. 57, no. 1, pp. 49–61, 2012.

[21] M. H. R. Khouzani, S. Sarkar, and E. Altman, "Maximum damage malware attack in mobile wireless networks," *IEEE/ACM Transactions on Networking*, vol. 20, no. 5, pp. 1347–1360, 2012.

[22] M. S. Abdalzaher and O. Muta, "Employing game theory and tdma protocol to enhance security and manage power consumption in wsns-based cognitive radio," http://arxiv.org/abs/1908.06844.

[23] C. Wang, H. Fang, and S. He, "Adaptive optimal controller design for a class of LDI-based neural network systems with input time-delays," *Neurocomputing*, vol. 385, pp. 292–299, 2020.

[24] S. He, H. Fang, M. Zhang, F. Liu, X. Luan, and Z. Ding, "Online policy iterative-based H∞ optimization algorithm for a class of nonlinear systems," *Information Sciences*, vol. 495, no. 25, pp. 1–13, 2019.

[25] C. Ren, R. Nie, and S. He, "Finite-time positiveness and distributed control of lipschitz nonlinear multi-agent systems," *Journal of the Franklin Institute*, vol. 356, no. 15, pp. 8080–8092, 2019.

[26] C. C. Ren and S. P. He, "Finite-time stabilization for positive Markovian jumping neural networks," *Applied Mathematics and Computation*, vol. 365, Article ID 123631, 2020.

[27] M. Li and L. Shuai, "A differential game-theoretic approach for the intrusion prevention systems and attackers in wireless networks," *Wireless Personal Communications*, vol. 103, no. 3, pp. 1993–2003, 2018.

[28] X. N. Miao, X. W. Zhou, and H. Y. Wu, "A cooperative differential game model based on network throughput and energy efficiency in wireless networks," *Optimization Letters*, vol. 6, no. 1, pp. 65–68, 2012.

[29] H. Dong and K. SAKURAI, "A differential game approach to mitigating primary user emulation attacks in cognitive radio network," in *Proceedings of the 26th International Conference on Advanced Computing, Networking, and Informatics*, pp. 495–502, Fukuoka, Japan, 2012.

[30] Y. Ding, X.-w. Zhou, Z.-m. Cheng, and F.-h. Lin, "A security differential game model for sensor networks in context of the internet of things," *Wireless Personal Communications*, vol. 72, no. 1, pp. 375–388, 2013.

[31] S. He, M. Zhang, H. Fang, F. Liu, X. Luan, and Z. Ding, "Reinforcement learning and adaptive optimization of a class of markov jump systems with completely unknown dynamic information," *Neural Computing and Applications*, 2019.

[32] S. He, H. Fang, M. Zhang, F. Liu, and Z. Ding, "Adaptive optimal control for a class of nonlinear systems: the online policy iteration approach," *IEEE Transactions on Neural Networks and Learning Systems*, vol. 31, no. 2, pp. 549–558, 2020.

[33] T. Mylvaganam, M. Sassano, and A. Astolfi, "A differential game approach to multi-agent collision avoidance," *IEEE Transactions on Automatic Control*, vol. 62, no. 8, pp. 4229–4235, 2017.

[34] J. Hu and Y. Xie, "A stochastic differential game theoretic study of multipath routing in heterogeneous wireless networks," *Wireless Personal Communications*, vol. 80, no. 3, pp. 971–991, 2015.

[35] B. Gao, X. Liu, C. Wu, and Y. Tang, "Game-theoretic energy management with storage capacity optimization in the smart grids," *Journal of Modern Power Systems and Clean Energy*, vol. 6, no. 4, pp. 656–667, 2018.

[36] J. Hu, Q. Qian, A. Fang, S. Wu, and Y. Xie, "Optimal data transmission strategy for healthcare-based wireless sensor networks: a stochastic differential game approach," *Wireless Personal Communications*, vol. 89, no. 4, pp. 1295–1313, 2016.

[37] L. Mo, A. Kritikakou, and S. He, "Energy-aware multiple mobile chargers coordination for wireless rechargeable sensor networks," *IEEE Internet of Things Journal*, vol. 6, no. 5, pp. 8202–8214, 2019.

[38] R. Isaacs, *Differential Game*, Wiley, New York, NY, USA, 1965.

[39] F. Avner, *"Differential Games," in Handbook of Game Theory*, Elsevier, Amsterdam, Netherlands, 1994.

[40] A. Bressan, "Noncooperative differential games," *Milan Journal of Mathematics*, vol. 79, no. 2, pp. 357–427, 2011.

Hindawi
Complexity
Volume 2020, Article ID 3297203, 8 pages
https://doi.org/10.1155/2020/3297203

Research Article

The Dissolved Oxygen Sensor Design Based on Ultrasonic Self-Adaption and Self-Cleaning

Zhong Xiao,[1] Jingtong Wang,[2] Chen Yi,[3] Zairong Wang,[4] and Liang Wang[5]

[1]*School of Mechanical and Electrical Engineering, Guangzhou University, Guangzhou 510006, China*
[2]*School of Mathematics and Statistics, Hunan University of Technology and Business, Changsha 410205, China*
[3]*School of Business Administration, Guangzhou University, Guangzhou 510006, China*
[4]*Data Recovery Key Laboratory of Sichuan Province, Neijiang Normal University, Neijiang, Sichuan 641100, China*
[5]*School of Public Administration, Guangzhou University, Guangzhou 510006, China*

Correspondence should be addressed to Jingtong Wang; jingtong_wang@126.com

Received 6 May 2020; Revised 5 June 2020; Accepted 8 June 2020; Published 3 July 2020

Academic Editor: Shuping He

Dissolved oxygen sensor is the key of dissolved oxygen measurement and it is usually implemented by electrochemical method, which measures dissolved oxygen content by the diffusion rate of molecular oxygen through film. However, the film on the electrochemical sensor probe is most likely to be blocked up by the waterborne contaminant, which may reduce the service life of the sensor and the indirect influence on the sensor's current. This is caused by changes of water temperature, which may lead to the decline in the accuracy of the sensor's output. This paper suggests a new method to implement the intelligent dissolved oxygen sensor. Our method mainly aims at ultrasonic automatic cleaning, automatic adjustment, and adaptation for the changes of temperature, which can not only regularly clean the dissolved oxygen sensor probe but also automatically calibrate the instruments based on the changes of temperature by combining software and hardware. The experiments show that the ultrasonic cleaning technology can not only increase the service life of the sensor by cleaning the film on the probe safely and effectively but also improve the accuracy of the sensor's output. Our method also has the advantages of simple structure, high accuracy of measurement, long service life, convenience, and stability, which is suitable for application and popularization.

1. Introduction

Dissolved oxygen [1] is not only a main parameter to characterization of water environment quality but also an essential condition for the survival of higher aquatic animals such as fish. The dissolved oxygen measurement is of great significance for the environmental monitoring and the development of aquaculture.

The common methods of dissolved oxygen measurement are iodimetry [2, 3], current measurement (Clark dissolved oxygen electrode) [4, 5], fiber-optic fluorescence quenching [6–8], and so on. Iodimetry is a classical method of dissolved oxygen measurement with high accuracy, but since it is time-consuming and laborious, it is unsuitable for online monitoring. Fiber-optic fluorescence quenching has complex manufacturing process and high manufacturing cost, so it is less used at present. Current measurement is an electrochemical method that obtains the dissolved oxygen content by measuring the current of dissolved oxygen sensor. Since the sensor solves the online measurement problem of dissolved oxygen and it is simple, fast, and not easy to be affected by chromaticity of water, turbidity of water, and impurities, it is widely used in water quality environmental measurement. Liu et al. proposed the measuring instrument of dissolved oxygen based on MSP430 [9]. Li et al. set forward the AVR in Detection of Dissolved Oxygen [10], Dong and Zhan designed an automatic control system based on ZigBee technology for the oxyty in fresh water cultivation [11]. The design conducted effective researches on the principle, structure, and system of the online measurement of dissolved oxygen. Nowadays, neural network [12, 13], self-adaptive methods, machine learning, and deep learning

have been successfully applied in various fields and achieved significant results [14–16].

However, the probe of dissolved oxygen sensor is easy to be blocked up by algae and phytoplankton in water, which leads it to not be able to continuously work for a long time and it cannot be used in projects, and the change of water temperature can easily increase the output current of the probe and indirectly affects the accuracy of measurement. In order to solve the above problems and improve the accuracy of measurement, this paper suggests a new design of dissolved oxygen sensor based on ultrasonic self-adaption and self-cleaning. This novel dissolved oxygen sensor with cleaning mechanism and automatic calibration solves the problem of pollution and blockage, which leads to the continuous decrement of the sensitivity of probe, improves the accuracy of measurement, and produces a barrier-free dissolved oxygen sensor with long service life and high precision.

2. Structure of System

2.1. Overall Structure of Measurement System. The dissolved oxygen sensor is an advanced intelligent sensor, which has an important component of the dissolved oxygen measurement system. The dissolved oxygen measurement system is shown in Figure 1. It includes some intelligent dissolved oxygen sensors with remote communication function, a cloud server, and some intelligent terminals such as mobile phones. Among them, the intelligent dissolved oxygen sensors measure the water temperature and the dissolved oxygen content, upload data, automatically clean the probe, and adapt to temperature for calibration. The cloud server stores the data uploaded by intelligent dissolved oxygen sensors and the control command of intelligent terminals. The intelligent terminals monitor the status of water temperature and dissolved oxygen in real time, dynamically display the historical curve, and send the control commands such as cleaning and calibration.

2.2. Circuit Composition. The main functions of an intelligent dissolved oxygen sensor are to measure the water temperature, measure the dissolved oxygen content, calibrate the system, and clean the probe automatically. Its structure is shown in Figure 2. It is composed of an embedded microcontroller (MCU), a one-wire digital temperature sensor, a primary battery dissolved oxygen sensor, an operational amplifier circuit, a relay module group, an ultrasonic power supply, an ultrasonic transducer, a system power supply, and the GPRS/4G module.

The MCU requires a certain amount of IO, enough timers and interrupts, an analog-to-digital converter (ADC), a one-wire interface, an universal asynchronous serial interface, and other universal interfaces, as well as a watchdog timer and strong anti-interference ability. It is suitable to choose STM32 series products of Italian French Semiconductor Company, PIC series products of Microchip Company, or relevant compatible microcontroller products as MCU.

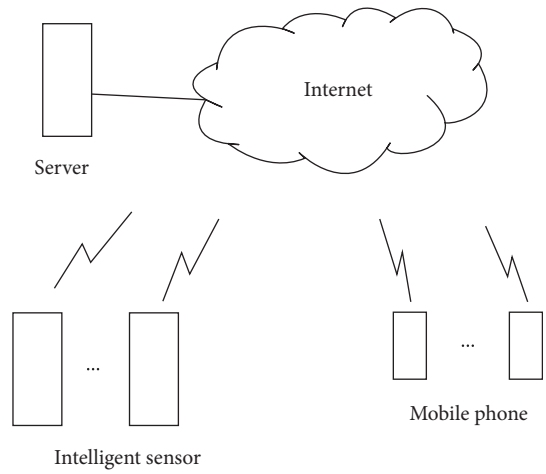

Figure 1: System structure.

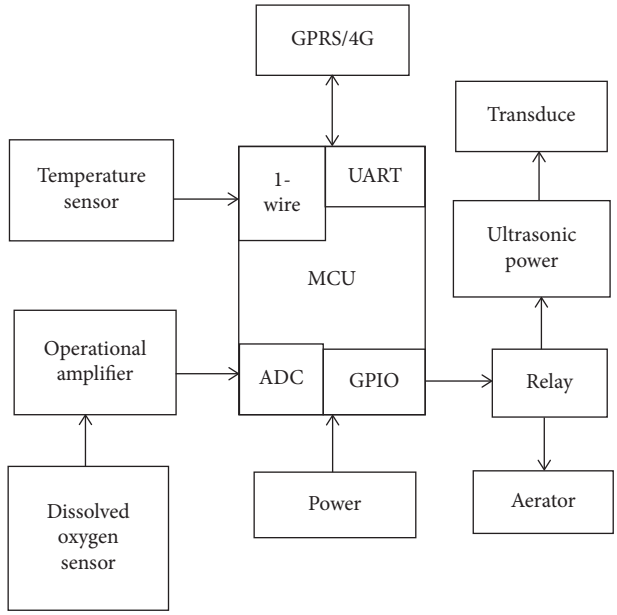

Figure 2: The composition of our sensor.

The operational amplifying circuit is applied to amplify the millivolt level voltage signal output by the dissolved oxygen sensor almost 100 times and complete the measurement with the ADC in MCU. Since most of the ADC in MCU is 10-bit precision or 12-bit precision, the products that are not satisfied with such settings need the higher measurement precision in order to add 16-bit or 24-bit special ADC module in the back end of operational amplifier circuit such as AD7705, MAX195, AD7710, and ADuC845.

DS18B20 [17–19] can be used as the temperature sensor, which is flexible and portable and has high precision. It can provide temperature in the range of −55°C~125°C with precision of ±0.5°C. DS18B20 uses one-wire interface, which is simple to connect with MCU and convenient to be applied.

The relay module group is applied to control the ultrasonic power supply and submersible pump in order to automatically clean the probe.

GPRS/4G module is applied to connect the cloud server remotely and build a communication channel for the establishment of intelligent aquaculture Internet of things system and the implementation of remote monitoring of intelligent terminals.

2.3. Dissolved Oxygen Sensor. The intelligent dissolved oxygen sensor is the front end of the measurement system. Its quality, service life, and accuracy are the basis of water environment monitoring and aquaculture development. A good design ensures the safety, the accuracy, the stability, and a long service life of the measurement system.

In general, coated primary battery electrode or polarographic electrode is used as the electrode of dissolved oxygen sensor, so the sensor is essentially an oxygen battery, with oxygen as its cathode and lead as its anode. The sensor's cathode is usually made of silver wire, which is filled with electrolyte inside and covered with coating outside for isolation, since oxygen needs to be discharged by metal. The molecular oxygen in water enters the sensor through the permeable film and meets the electrode, which leads to the oxidation-reduction reaction; then the cathode of the electrode outputs the microlevel current. The reaction formulas that take place in battery are as follows:

Cathode: $O_2 + 2H_2O + 4e^- \longrightarrow 4OH^-$

Anode: $2Pb + 4OH- \longrightarrow 2Pb(OH)2 + 4e-$

Total chemical equation: $O_2 + 2Pb + 2H_2O \longrightarrow 2Pb(OH)_2$

The coated oxygen sensor is a current element. In the coated oxygen sensor, the current outputted by the electrode is proportional to the oxygen consumption, and the rate of oxygen passing through the film is also proportional to the pressure on the film. Since oxygen is consumed rapidly at the cathode, it can be assumed that there is no pressure on the film, which will lead to the diffusion of oxygen, and that the force through the film and the pressure on the film both force the oxygen to reach the electrode rapidly. If the pressure outside the probe increases, more dissolved oxygen will diffuse through the film and more current will be generated. Otherwise, the current decreases, which can be described by the diffusion current model. The related formula is as follows:

$$i = \frac{n * F * A * D}{L} c. \quad (1)$$

In this formula, n is the number of electrons in electrode reaction, F is the Faraday constant, A is the surface area of the cathode, D is the coefficient of oxygen diffusion, L is the distance from the outer surface of the permeable film to the surface of the cathode, and C is the partial pressure of oxygen. According to Faraday's law, when the material and structure of battery are determined, the current generated by the diffusion of molecular oxygen through the film to the electrode is proportional to the partial pressure of oxygen at certain temperatures, which can be expressed as linear element: $i = k * c$.

3. Mechanical Structure of Intelligent Sensor

Intelligent sensor is a digital measurement system rather than a common sensor element. It has the rational and perfect design including MCU, conditioning circuit, communication circuit, measurement mechanism, and cleaning mechanism. It is not only convenient in output control and function enhancement but also has a short learning curve. The mechanical structure of intelligent sensor is shown in Figure 3. The sensor system floats on the surface of water; the upper part of it (above the surface) and the lower part of it (below the surface) are both in the shape of cylinders, and the middle part of it is in the shape of a disc (floating on the surface). The groove in the center of the upper part is embedded with a dissolved oxygen probe, and the cavity around it is used to contain the water which is pumped up by the submersible pump and needs to be measured. One side of the lower edge of the middle part is the water inlet which is connected with a small submersible pump, and another side is the lower water outlet, while the upper water outlet is on the upper part. The upper water outlet with a large opening is the main water outlet, and the lower water outlet with a small opening is the auxiliary water outlet. The flow direction of water is also shown in Figure 3. The purpose of this design is to provide water for the probe, while the water flows in a suitable speed, and prepare for air calibration (see Section 4) by stopping the submersible pump, draining the water, and exposing the dissolved oxygen probe to the air. The temperature sensor which is inserted into the bottom shell of the upper part is used to measure the temperature of the water in cavity.

The middle part is designed as a disc in order to float on the water and store enough flowing water to be measured. The lower part is used to put the ultrasonic transducer and the ultrasonic power supply and they are both set below the water line. Such setting has two advantages: firstly, the temperature below the water line is lower than the temperature above, which is convenient for the heat dissipation of the ultrasonic power supply; secondly, the weight of the ultrasonic transducer and the ultrasonic power supply is large enough to be used as the counterweight of the system in order to prevent the system structure from overturning. However, there is a difficulty in manufacture that it is hard to ensure the features of waterproofing and sealing in ultrasonic transducer and ultrasonic power supply shell.

4. The Design of Automatic Cleaning

The effect of the permeable film on the probe is to make the molecular oxygen in water permeate through it from the outside under the push of dissolved partial pressure and react with the electrode in the probe to generate current, while water, organic matter, and other macromolecules are blocked outside the film at the same time. Due to the selective feature of the film, the organic matter will be stuck on the surface of the film and lead to the film pollution, which is the main factor that limits the sensor to continuous work for a long time. Therefore, the effective cleaning of the permeable film is a good way to extend the sensor's service life.

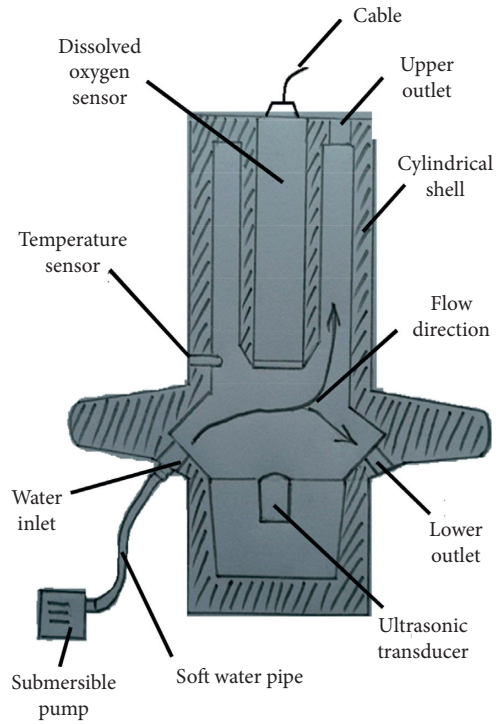

Figure 3: Sensor and self-cleaning device.

Common cleaning methods include biological cleaning, chemical cleaning, and physical cleaning.

Biological cleaning is to remove the contaminants on the film with the help of microorganisms, enzymes, and other biological active agents. Its weakness is that the cleaning takes a long time and it is prone to secondary pollution after cleaning. Chemical cleaning is to soak and clean the film with a cleaning solution added with a suitable chemical agent. Its weakness is that the cleaning is time-consuming, laborious, and unsafe. Both of the above cleaning methods can improve the permeability of the film, but there is also a possibility that they introduce new contaminants and damage the film. Otherwise, they are complex in operation and have low reliability.

Physical cleaning includes mechanical method and ultrasonic method. Mechanical methods, such as manual wiping, water washing, and automatic wiping mechanism, have several disadvantages such as difficult cleaning operation, poor cleaning effect, and high damage rate since the thickness of the probe film is usually 20–40 μm.

Ultrasonic cleaning is to use the cavitation effect of ultrasonic to break down the adsorption of the dirt and the surface of the cleaning parts and destroy the dirt layer. The cavitation effect is that the micro bubble (cavitation core) in the liquid vibrates under the periodic action of ultrasonic, so the micro bubble in the liquid will expand rapidly and then suddenly close. At the moment of bubble closing, the strong shock wave and the high-temperature and high-speed micro jet will be generated, and the shock wave will hit on the interface between solid and liquid. In addition, the high-temperature and high-speed micro jet will hit on the surface of the film. It will destroy the insoluble dirt, wash the particles and organic substances away, and make them separate and disperse in the liquid, so as to achieve the purpose of cleaning.

Cui et al., combined with the application of the technology of ultrasonic cleaning and the research of relative influencing factors, looked forward to the development's direction of ultrasonic cleaning technology [20, 21]; Huang and Mo investigated the film pollution and the cleaning statue of water source polluted by suspended growth MBR and two kinds of adherent growth MBR [22]; the results showed that the ultrasonic cleaning can significantly improve the performance of the film with high surface viscosity polluted by adherent growth MBR. The previously mentioned researches show that the ultrasonic cleaning technology will be suitable for the cleaning of the film of the dissolved oxygen sensor probe if the cleaning mechanism is designed reasonably and the working parameters are selected appropriately.

In this design, the ultrasonic cleaning mechanism is located at the bottom of the sensor system, with the transducer facing up and facing the vertical probe, which means that the ultrasonic cleaning mechanism is especially designed for the cleaning. In the process of the cleaning, the submersible pump keeps working normally and the cavity is full of water, which is used as cleaning fluid. After the repeated experiments, this paper finds that it can ensure the probe's nondestructive cleaning and long-term use when the working frequency is 28 kHz, the transducer is 50 W, the cleaning period is four times a day, and the cleaning time is 20 seconds.

The flow chart of regular automatic cleaning is shown in Figure 4. The concentration polarization of the electrolyte in the sensor is caused by ultrasonic wave; that is, the concentration of the electrolyte near the two electrodes is obviously higher than the electrolyte itself; the electrode potential of the anode or cathode of the sensor deviates from the equal potential produced by the concentration of the electrolyte itself, which causes the output current of the sensor to change greatly and the result of measurement to increase suddenly, so the system cannot normally measure the dissolved oxygen content. Therefore, the system stops data sampling in the process of cleaning and after the process of cleaning in order to prevent the collection of the error data with large deviation.

5. Temperature Compensation Design

The temperature compensation of an instrument is to correct the final parameters (indirect parameters), which are easily affected by the temperature.

The measurement of dissolved oxygen is a relative measuring method, which obtains the dissolved oxygen content by linear calculation through measuring the output current of the sensor. Due to the limitation of thickness of the film, the electrolyte concentration, the purity of lead silver metal, and the manufacturing level, the output current of each sensor probe is different. Therefore, zero calibration and span calibration should be carried out before measurement, that is, calibrating the instrument's current value of the zero point and the saturation point under a certain

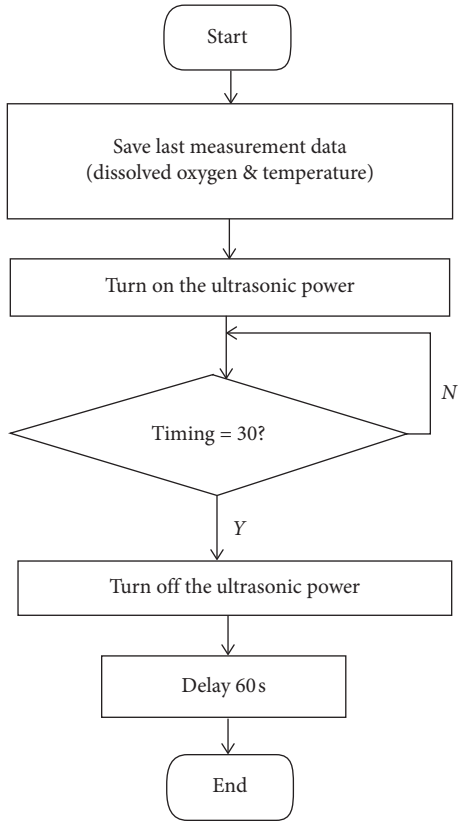

Figure 4: The self-cleaning and self-adaption.

temperature t. Since the current value of zero point corresponds to the zero dissolved oxygen value and the current value of saturation point corresponds to the saturated dissolved oxygen value under temperature t and there is a linear relationship between the dissolved oxygen content and the output current of the electrode when the temperature is constant, the two-point calibration can determine the coefficient of linear relationship between current and dissolved oxygen k_t, and the mapping relationship between current and dissolved oxygen at temperature t is established. For example, if the dissolved oxygen sensor system is calibrated at 20°C, $i = k_{20}c$ can be used for accurate calculation to obtain the accurate dissolved oxygen content when the water is at 20°C.

Figure 5 is a comparison of the relationship between dissolved oxygen saturation and temperature under ordinary temperature, salinity of 0°C, and standard atmospheric pressure. Since the relationship between dissolved oxygen saturation and temperature is not linear just like the example above, k_{20} cannot be used to calculate the dissolved oxygen content when the temperature rises to 22°C or falls to 18°C. The calibration line has different slopes at different temperatures. Since the linear relationship between the electrode current and oxygen partial pressure is based on environmental temperature, if the temperature of water changes, the output current will increase or decrease. For example, with the increment of temperature, the oxygen penetration coefficient of the film will increase and the diffusion coefficient of dissolved oxygen in the electrolyte solution will increase,

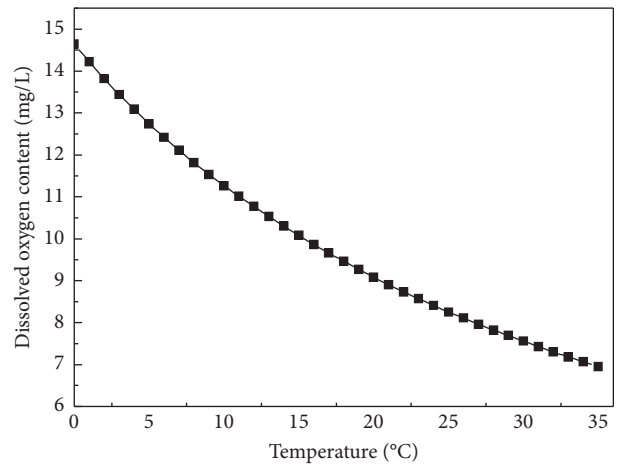

Figure 5: The comparison of temperature and saturated dissolved oxygen (atmospheric pressure, 0.1 MPa).

so the permeability of dissolved oxygen will increase, which leads to the increment of the reaction speed of electrode and the change of the signal of current, so the indirect measurement results of dissolved oxygen content will also increase. At the same time, the oxygen partial pressure may remain or change very little, so the dissolved oxygen content will remain and the change of temperature will change the probe's current output and lead to an inaccurate measurement. Therefore, the probe should be compensated based on temperature.

Ding et al. put forward a compensation and correction method for intelligent dissolved oxygen sensor [23]. Zhang and Shao studied the characteristics of the temperature of dissolved oxygen sensor [24], analyzed the temperature compensation of oxygen electrode, and designed a software compensation method. The accuracy of dissolved oxygen measurement can be significantly improved when the difference between the calibration temperature and the water temperature is small. However, the software temperature compensation may miscalculate the dissolved oxygen content when the difference is large enough (±8°C). Moreover, the third-order polynomial which is used to fit the slope of the temperature saturated dissolved oxygen degree may cause too heavy burden of MCU, which is inconvenient and impractical. Therefore, it is necessary to study and design a new and advanced temperature compensation method to improve the accuracy of dissolved oxygen measurement.

In this paper, a method combining software temperature compensation with real-time recalibration is suggested. In this new method, the linear temperature compensation model is used when the temperature difference is tiny, and the real-time recalibration is used when temperature difference is large, which means that the measured water temperature is within the range of ±2°C of the calibration temperature. At first, it uses the formulation $D = K * T + b$ to correct the saturated solubility, and then it uses the formulation $i = k_t * c$ to indirectly calculate the dissolved oxygen content (partial pressure of dissolved oxygen). If the water temperature is outside the range of ±2°C of the calibration temperature, it needs to recalibrate and calibrate the

instrument at a new temperature to determine new k_t. On one hand, since the zero calibration of the instrument is generally determined by anaerobic water before the product leaving factory and is hardly affected by the temperature, the recalibration can be ignored. On the other hand, there are four kinds of span calibration: classical chemical method, air calibration method, water calibration method, and electrolytic oxygen calibration method, and air calibration method and water calibration method are usually used in online measurement. In this paper, air calibration method is selected to be implemented.

Air calibration method is also known as air calibration for water's saturated vapor. When the water is saturated by air at a certain temperature, the partial pressure of dissolved oxygen is equal to the partial pressure of oxygen in the air on the surface of water, so the rate of oxygen entering the water from the air is equal to the rate of oxygen escaping from the water to the air. Therefore, no matter whether the electrode is immersed in water or placed in the air, it can produce the same current, and the method that is based on it is known as air calibration method. The air calibration method is easy to implement and is able to measure at high accuracy, so it is one of the best methods for on-site calibration.

The air calibration process of the sensor is shown in Figure 6. It turns off the submersible pump at first and then drains the water and waits for 60 seconds, measures the temperature and current by adjusting the slope of the dissolved oxygen instrument based on Figure 6, and recalibrates the dissolved oxygen electrode at last.

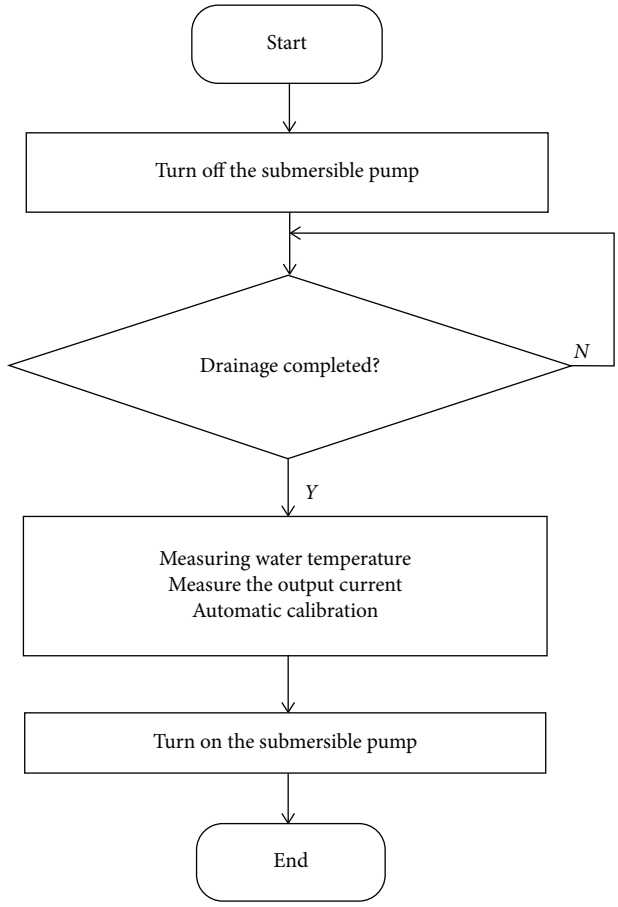

Figure 6: The automatic calibration.

6. Experiment and Discussion

There are two different aquaculture ponds selected for experiments below. The experiments mainly focus on two aspects of the probe. Experiment 1 was used to reveal the effect of ultrasonic cleaning on the durability of the probe. Experiment 2 was used to reveal the influence of the new temperature compensation technology on the accuracy of the measurement.

6.1. Experiment 1. There is an outdoor soil pond as aquaculture pond which is sunny and rich in algae. The main way to increase dissolved oxygen content is to naturally add oxygen, and the auxiliary way is to add oxygen by aerator. The aquaculture organism is *Penaeus vannamei*. The temperature of water is usually $25 \pm 3^{\circ}$C. The measurement time each day is from 15:00 to 17:00 and the experiment lasts for 90 days. Among them, *A* corresponds to the results measured by iodimetry, *B* corresponds to the results measured by the probe which is periodically ultrasonic cleaned, and *C* corresponds to the results measured by the probe which is never cleaned. The results are shown in Figures 7 and 8.

The results show that the *C*-type probe's relative error increases and its result of measurement decreases with the passing of time. In the 30th day, the *C*-type probe's relative error has reached 30.3%, which means that this probe can no longer be used for measurement. However,

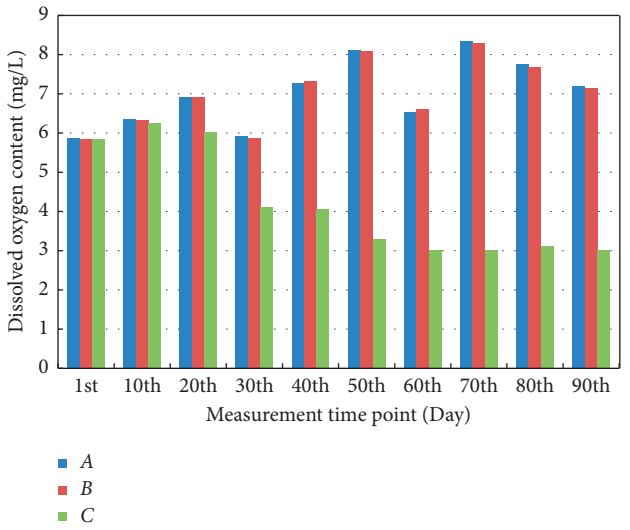

Figure 7: Measurement results of ultrasonic cleaning probe and noncleaning probe.

the *B*-type probe can continuously work for more than 90 days and its relative error is still less than 1%. In practice, the sensor with *B*-type probe has already continuously worked for more than one year; it still does not need to replace the film or the electrolyte and its attenuation of output is less than 5%.

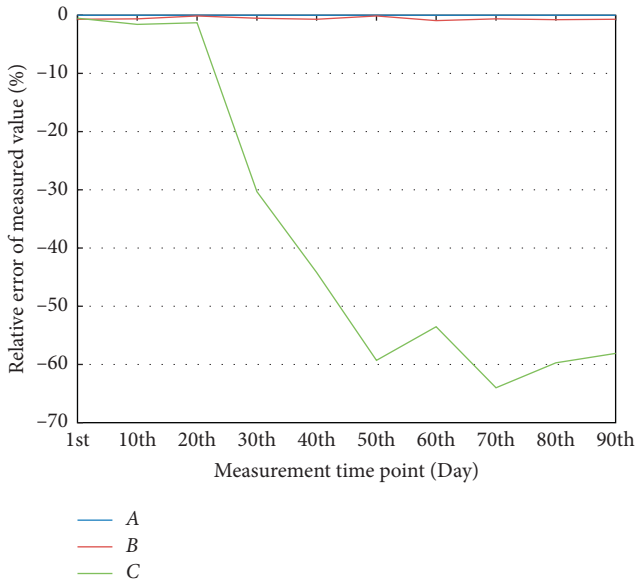

Figure 8: Relative errors with *A* of ultrasonic cleaning probe and noncleaning probe.

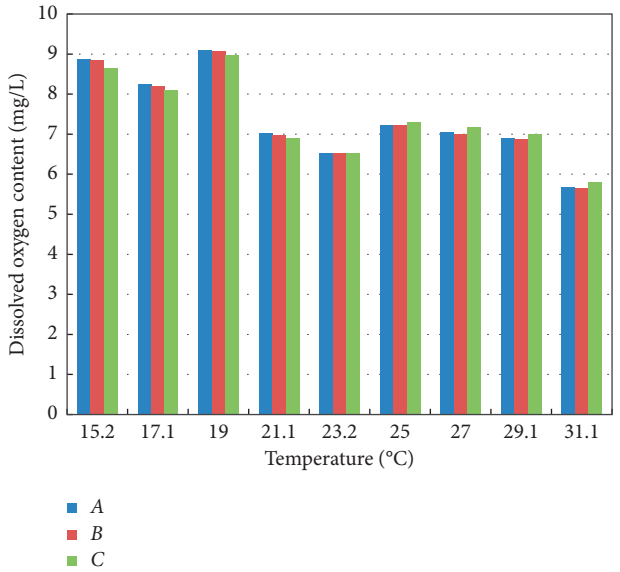

Figure 9: Measurement results of old and new temperature compensation probes.

6.2. Experiment 2. There is an indoor factory-built cement pond as aquaculture pond. Its pond is paved with micropore oxygenating pipe. There are little algae in the water and the main way to increase dissolved oxygen content is to artificially add oxygen. The aquaculture organism is gentian grouper. The temperature of water changes in real time and the measurement time each day is from 8:00 to 18:00. Among them, *A* corresponds to the results measured by iodimetry, *B* corresponds to the results measured by the probe with software temperature compensation and real-time calibration, and *C* corresponds to the results measured by the probe which is only calibrated at 23°C. The results are shown in Figures 9 and 10.

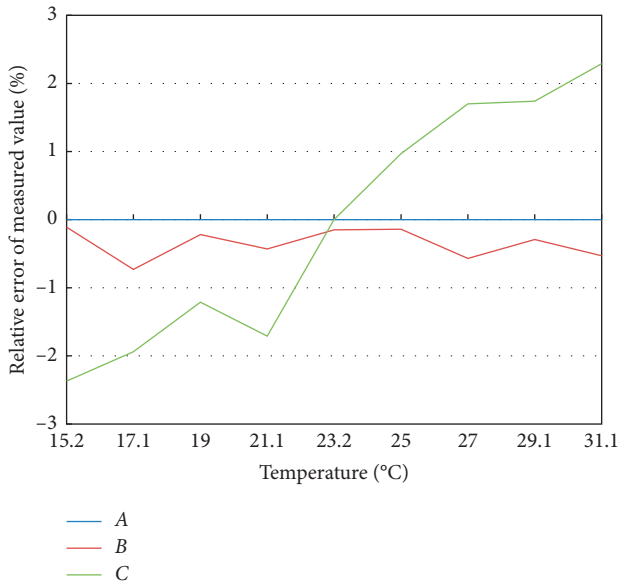

Figure 10: Relative errors with *A* of old and new temperature compensation probes.

The results show that the *C*-type probe's relative error increases with the temperature deviation of 23°C (calibrated temperature) and its relative error reaches 2.38% at the maximum, though it retains the software temperature compensation. Meanwhile the *B*-type probe's relative error is less than 1%, which means that it has a very good accuracy on measurement.

7. Conclusion

The research shows that the new dissolved oxygen measurement system developed by MCU can reasonably solve the problem of probe cleaning after applying ultrasonic cleaning technology, since, compared with other cleaning technologies, ultrasonic cleaning technology has the advantages of higher cleaning rate, less residue, shorter cleaning time, and better cleaning effect, and it greatly prolongs the service life of the sensor. The application of software temperature compensation and real-time air calibration can significantly improve the accuracy of the measurement, achieve the continuity, stability, reliability, and accuracy in dissolved oxygen measurement in water quality environmental monitoring, and provide important data for scientific aquaculture in aquaculture industry. At present, there are about 100 sets of measuring instruments implemented in many shrimp pond farms in Beihai, Qinzhou, Fangcheng, Haikou, Sanya, Zhongshan, and Shanwei of Guangdong Province, and all of them have worked continuously for more than one year. The introduced GPRS/4G module can effectively establish the big data of water quality monitoring and aquaculture industry and the new self-cleaning self-adaptive dissolved oxygen sensor system will provide higher-quality services for water-quality monitoring and aquaculture industry.

Data Availability

The data used to support the findings of this study are included within the article.

Conflicts of Interest

The authors declare that no conflicts of interest exist. Submitting authors are responsible for coauthors declaring their interests.

Acknowledgments

The authors thank the National Natural Science Foundation of China under Grants nos. 61772147 and 61100150, the University Innovation Team Construction Project of Guangdong Province under Grant no. 2015KCXTD014, the Major Scientific Research Project of Provincial Education Department of Chinese Hunan under Grant no. 19A271, Guangdong Province Natural Science Foundation of Major Basic Research and Cultivation Project under Grant 2015A030308016, the Collaborative Innovation Major Projects of Bureau of Education of Guangzhou City under Grant 1201610005, the Guangdong Province Natural Science Foundation of Major Basic Research and Cultivation Project under Grant 2015A030308016, the Open Subject Project of State Key Laboratory of Cryptography Science and Technology under Grant MMKFKT201913, and the National Cryptography Development Fund under Grant MMJJ20170117 for their support.

References

[1] Z. H. Chen, H. S. Xu, X. Liu et al., "Distribution characteristics of bottom dissolved oxygen and mechanism of hypoxia in reservoir in southern China," *Water Resources Protection*, vol. 32, pp. 108–114, 2016.

[2] X. M. Xia, "Study on the determination of dissolved oxygen in water by iodinimetric method," *China High Tech Enterprise*, no. 36, pp. 30-31, 2014.

[3] W. D. An and L. Y. Tao, "Evaluation of the uncertainty of measurement for the determination of dissolved oxygen content in water by iodinimetric method," *Chemical Analysis and Metrology*, vol. 12, no. 6, pp. 5–7, 2003.

[4] G. Q. Wang, *Study on Dissolved Oxygen Detecting and the Preparation Iron Porphyrin LB Films Electrode*, Jilin University, Changchun, China, 2016.

[5] A. M. An, L. C. Qi, Y. M. Chou et al., "The study on soft sensor with BP neural network and its application to dissolved oxygen concentration," *Computer and Applied Chemistry*, vol. 33, no. 1, pp. 100–104, 2016.

[6] J. L. Fu, "Discussion on calibration method of fluorescence quenching method dissolved oxygen meter," *Chemical Analysis and Metrology*, vol. 23, no. 1, pp. 83–85, 2014.

[7] W. Y. Dai and L. Sun, "The measurement methods of dissolved oxygen in water," *Anhui Agronomy Bulletin*, vol. 13, no. 19, pp. 77–79, 2007.

[8] J. Wang, *Reaserch on Remote Monitor System for Water-Dissolved Oxygen*, Yanshan University, Qinhuangdao, China, 2010.

[9] Q. Liu, Y. Q. Zou, and H. Y. Hang, "Measuring instrumment of dissolved oxygen based on MSP430," *Instrument Technology and Sensor*, no. 9, pp. 33–35, 2009.

[10] Z. X. Li, X. Yang, and T. Z. Li, "Application of AVR in detection of dissolved oxygen in fish pond," *Hubei Agricultural Science*, vol. 49, no. 7, pp. 1712-1713, 2010.

[11] F. W. Dong and Z. Y. Zhan, "The design of automatic control system based on ZigBee technology for the oxyty in fresh water cultivation," *Agricultural Network Information*, no. 8, pp. 125–129, 2008.

[12] C. Wang, H. Fang, and S. He, "Adaptive optimal controller design for a class of LDI-based neural network systems with input time-delays," *Neurocomputing*, vol. 385, pp. 292–299, 2020.

[13] S. He, H. Fang, M. Zhang, F. Liu, and Z. Ding, "Adaptive optimal control for a class of nonlinear systems: the online policy iteration approach," *IEEE Transactions on Neural Networks and Learning Systems*, vol. 31, no. 2, pp. 549–558, 2020.

[14] H. Deng, L. Peng, L. Peng, J. Zhang, C. Fang, and H. Liu, "An intelligent aerator algorithm inspired-by deep learning," *Mathematical Biosciences and Engineering*, vol. 16, no. 4, pp. 2990–3002, 2019.

[15] S. He, H. Fang, M. Zhang, F. Liu, X. Luan, and Z. Ding, "Online policy iterative-based H∞ optimization algorithm for a class of nonlinear systems," *Information Sciences*, vol. 495, pp. 1–13, 2019.

[16] S. He, M. Zhang, H. Fang, F. Liu, X. Luan, and Z. Ding, "Reinforcement learning and adaptive optimization of a class of Markov jump systems with completely unknown dynamic information," *Neural Computing and Applications*, 2019.

[17] Y. M. Zhu and W. M. Ding, "Online measurement method for dissolved oxygen," *Electronic Measurement Technology*, vol. 32, no. 7, pp. 122–124, 2009.

[18] Z. C. Duan and X. K. Jiang, "Hans-held water temperature inspection instrument based on 1-wire interface," *Water Conservancy Technology and Economy*, vol. 15, no. 4, pp. 355–357, 2009.

[19] T. Luo and B. Y. Wang, "Design of remote monitoring for the water temperature control system of fry," *Light Industry Technology*, vol. 4, pp. 93-94, 2017.

[20] Y. J. Cui, O. Li, and D. Wang, "Advances in membrane fouling ultrasonic cleaning technology," *Cleaning World*, vol. 32, no. 6, pp. 37–40, 2016.

[21] Y. Kang, J. Xu, and Y. Q. Jia, "Principle and development status of ultrasonic cleaning membrane fouling," *Cleaning World*, vol. 28, no. 11, pp. 33–36, 2013.

[22] X. Huang and L. Mo, "Characteristics of membrane fouling and its cleaning in membrane bioreactors for water purification," *China Water Supply and Drainage*, vol. 19, no. 5, pp. 8–12, 2003.

[23] Q. S. Ding, D. K. Ma, and D. L. Li, "Research and application on compensation and calibration methods for smart sensor of dissolved oxygen," *Journal of Shandong Agricultural University (Natural Science)*, vol. 42, no. 4, pp. 567–571, 2011.

[24] G. H. Zhang and H. H. Shao, "Temperature dependence and compensation for the dissolved oxygen probe," *Chinese Journal of Sensors and Actuators*, vol. 19, no. 2, pp. 323–327, 2006.

Hindawi
Complexity
Volume 2020, Article ID 9535818, 8 pages
https://doi.org/10.1155/2020/9535818

Research Article

Two-Round Diagnosability Measures for Multiprocessor Systems

Jiarong Liang,[1] **Qian Zhang**,[1] **and Changzhen Li**[2]

[1]*School of Computer, Electronics and Information, and with Guangxi Key Laboratory of Multimedia Communications and Network Technology, Guangxi University, Nanning 530004, China*
[2]*School of Public Policy and Management, Guangxi University, Nanning 530004, China*

Correspondence should be addressed to Changzhen Li; 19960126@gxu.edu.cn

Received 19 April 2020; Accepted 19 May 2020; Published 24 June 2020

Academic Editor: Shuping He

In a multiprocessor system, as a key measure index for evaluating its reliability, diagnosability has attracted lots of attentions. Traditional diagnosability and conditional diagnosability have already been widely discussed. However, the existing diagnosability measures are not sufficiently comprehensive to address a large number of faulty nodes in a system. This article introduces a novel concept of diagnosability, called two-round diagnosability, which means that all faulty nodes can be identified by at most a one-round replacement (repairing the faulty nodes). The characterization of two-round t-diagnosable systems is provided; moreover, several important properties are also presented. Based on the abovementioned theories, for the n-dimensional hypercube (Q_n), we show that its two-round diagnosability is $(n^2 + n/2)$, which is $(n + 1/2)$ times its classic diagnosability. Furthermore, a fault diagnosis algorithm is proposed to identify each node in the system under the PMC model. For Q_n, we prove that the proposed algorithm is the time complexity of $O(n2^n)$.

1. Introduction

With the growth of the large scale integration technology, a huge number of multiprocessors are integrated to a multiprocessor computer system. It is not difficult to predict that, in such a system, some faulty processors (nodes) will be produced. To make sure that the system works properly, the designers should consider the problem that the system needs to have the ability to diagnose itself faulty processors such that they can be repaired or replaced with the new fault-free processors. In dealing with the problem of fault diagnosis for multiprocessor systems, two approaches are used: one is the system-level approach and another is the logic-circuit-level approach. Since the system-level approach is helpful for user-transparent reconfiguration, automatic, and recovery in the multiprocessor system while the logic-circuit approach is not, the designers prefer to design the system into a system-level fault-diagnosis system. In 1967, Preparata et al. proposed an automatic diagnosis procedure in multiprocessor systems, which is known as the first system-level diagnosis approach [1, 2]. This model proposed by Preparata et al. [1] is called the Preparata, Metze, and Chien (PMC) model. In theory, a digraph $G = (V, E)$ can usually be used to denote a PMC model, where for two processors i and j, $(i, j) \in E$ if and only if processor u is tested processor i. For each testing edge (i, j), we can use 1 or 0 to denote their test result $\sigma(i, j)$, where $\sigma(i, j) = 1$ implies that i judges j to be faulty and $\sigma(i, j) = 0$ implies that i judges j to be fault-free.

There are several fundamental system-level diagnosis strategies: t-diagnosis, t/s-diagnosis $(s \geq t)$ and conditional t-diagnosis. Suppose that a system S has at most t faulty nodes, if each node in the system can be diagnosed correctly as either fault-free or faulty, then the system is called a t-diagnosable system; some research results on a t-diagnosable system can be found in [1–4], etc. In theory, the t-diagnosis approach is a key measurement for the reliability of considered network system. Besides, the t-diagnosis approach is desirable to be applied to the areas being related to network control, for example, in the research on reinforcement learning and adaptive optimization, we know that the neural network is often used to represent actor network and chosen as a optimal control policy [5]. Before an adaptive optimal controller is designed, it is necessary and important to test whether the nodes (neurons) in the neural network are fault-free or faulty by the t-diagnosis approach. For a system having at most t faulty nodes, if it can

determine a set with the size s $(s \leq t)$ that contains all its faulty nodes, then it is t/s-diagnosable. Numerous studies have been reported on a t/s-diagnosable system, such as [6–12].

In a system, denoted by $G = (V, E)$, with at most t faulty nodes, a subset $V_i \subset V$ with $|V_i| \leq t$ is called a conditional faulty set if there does not exist a node v such that $N(v) \subset V_i$, where $N(v)$ is a set consisting of all v's neighbors. If for any two conditional faulty sets V_1 and V_2 with $V_1 \neq V_2$, $\sigma(V_1) \cap \sigma(V_2) = \phi$, where $\sigma(V_i)$ is the set of syndromes produced by V_i, then the system is called conditionally t-diagnosable. Lots of efforts are made to study the conditionally t-diagnosable system, see [13–22].

It is worth mentioning that the above three strategies are one-round diagnosis strategies, whose diagnosabilities are usually not too large. For instance, Q_n is shown to be n-diagnosable and its t/t-diagnosability and conditional diagnosability are n and $(2n-2)/(2n-2)$, respectively, based on the PMC model. However, when the size of the faulty node set is larger than the diagnosability of the above diagnosis strategies, the above diagnosable systems can do little for the diagnosis. Therefore, to address the issue that a system has a large number of faulty nodes, Chen et al. introduced a novel strategy, called by t/k-diagnosis, for the star network [23], where $1 \leq k \leq t$. A t/k-diagnosable system guarantees to identify at least k faulty nodes only if as long as the size of the set consisting of faulty nodes in it does not exceed t. Although a t/k-diagnosis has a large diagnosability, it takes much longer to repair faulty nodes, which leads to low efficiency. Therefore, it provides strong motivation for the study of a diagnosis strategy that can reach a balance between improving the diagnosability and being highly efficient. This paper presents a novel diagnosis approach, called by two-round t-diagnosis. Using the two-round t-diagnosis approach, the system can guarantee that each faulty node can be diagnosed by at most a one-round replacement (repairing the faulty nodes).

A simple introduction on this paper's remainder is as follows. Some related notations and definitions are presented as the preliminaries in Section 2. In Section 3, two-round t-diagnosable systems are characterized and several important properties are also presented. In Section 4, the properties of a two-round t-diagnosable system is applied for computing the two-round t-diagnosability of Q_n. In Section 5, a fast two-round diagnosis algorithm, whose time complexity is $O(n2^n)$, is proposed for Q_n. Section 6 draws the conclusions.

2. Preliminaries

In the section, we introduce some necessary notations and definitions that are frequently used in the rest of the paper.

Under the PMC model, for a system given by graph $G = (V, E)$, let $\Gamma x = \{y \mid (x, y) \in E \text{ and } x, y \in V\}$ and $\Gamma^{-1}x = \{y \mid (y, x) \in E \text{ and } x, y \in V\}$. Similarly, for any subset $X \subset V$, $\Gamma X = \cup_{x \in X} \Gamma x - X$ and $\Gamma^{-1} X = \cup_{x \in X} \Gamma^{-1} x - X$. In particular, if G is undirected, then $\Gamma x = \Gamma x^{-1} = N(x)$ and $\Gamma X = \Gamma X^{-1} = N(X)$, where $X \subset V$.

Definition 1. Suppose that $G = (V, E)$ is a graph and has k connected components, say $C_1, C_2, \ldots, C_k$. Then, $C_{\text{sub}}(G) = \{C_1, C_2, \ldots, C_k\}$ is called a connected subgraph set of G. In particular, if G is connected, then $C_{\text{sub}}(G) = \{G\}$. Additionally, let $\max\{C_{\text{sub}}(G)\} = C_i$, where $|V(C_i)| \geq |V(C_j)|$ for each $C_j \in C_{\text{sub}}(G)$.

Definition 2. Let $G = (V, E)$ denote a graph and $X \subset V$. Then, $G[X] = (X, \overline{E})$ is called the induced subgraph by X, where $\overline{E} = \{(u, v) \mid (u, v) \in E, u, v \in X\}$.

Definition 3. Let $G = (V, E)$ denote a graph, let $Card_k(C_{\text{sub}}(G)) = \{C \mid C \in C_{\text{sub}}(G) \text{ and } |V(C)| = k\}$ be the set of connected subgraphs with k nodes in G.

For instance, for graph G shown in Figure 1, $C_{\text{sub}}(G) = \{C_1, C_2\}$, where $C_1 = G[\{v_2, v_3, v_6\}]$, $C_2 = G[\{v_1, v_4, v_5, v_7\}]$, $Card_3(C_{\text{sub}}(G)) = G[\{v_2, v_3, v_6\}]$, and $Card_4(C_{\text{sub}}(G)) = G[\{v_1, v_4, v_5, v_7\}]$.

Definition 4. Let $G = (V, E)$ denote a system, $M \subset V$. For a given syndrome σ, if the following conditions are satisfied, then $M \subset V$ is said to be an allowable fault set (AFS):

(1) $\sigma(x, y) = 0$, for any $x, y \in V - M$

(2) $\sigma(x, y) = 1$, for any $x \in V - M$ and $y \in M$

Lemma 1. *Suppose that $G = (V, E)$ is a system and σ is a given syndrome. Let $F_1, F_2 \subseteq V$ be two AFSs, then $F_1 \cup F_2$ is also an AFS.*

Proof. To the contrary, assume that $F_1 \cup F_2$ is not an AFS; then, there exists at least one condition in Definition 4, which is not true.

If condition (1) is not true, then $\exists x, y \in V - (F_1 \cup F_2)$ such that $\sigma(x, y) = 1$, a condition to F_1 and F_2 are two AFS.

If condition (2) is not true, then $\exists x \in V - (F_1 \cup F_2)$ and $y \in F_1 \cup F_2$, where $(x, y) \in E$ such that $\sigma(x, y) = 0$. If $y \in F_1$, then F_1 is not an AFS; if $y \in F_2$, then F_2 is not an AFS, which contradicts the hypothesis. □

Lemma 2. *For a given syndrome σ on the system $G = (V, E)$, suppose that G has k AFSs for σ, say $F_1, F_2, \ldots, F_k \subseteq V$, then, $\cap_{i=1}^{k} F_i$ is the fault set of the system.*

Proof. Let $F_c = \cap_{i=1}^{k} F_i$. Let F be the maximal fault set, which exactly consists of all faulty nodes. We will show that F is an AFS for σ. To this end, let $(u, v) \in E$. $u, v \in V - F$ implies that u and v are fault-free nodes, and then $\sigma(u, v) = 0$. Hence, condition (1) holds for F. For condition (2), $u \in V - F$ and $v \in F$ implies that u is a fault-free node and v is a faulty node and then that $\sigma(x, y) = 1$. Hence, condition (2) holds for F. Then, F is an AFS for σ. According to the assumption, we have that $F \in \{F_1, F_2, \ldots, F_k\}$. So, $F_c = \cap_{i=1}^{k} F_i \subseteq F$. □

Definition 5. Let $G = (V, E)$ be a system, t an integer, $X \subseteq V$ with $0 < |X| < t$. Suppose that $X_1, X_2 \subseteq V - X$ with $|X_1 \cup X| \leq t$ and $|X_2 \cup X| \leq t$ are two different subsets. (X_1, X_2) is called a pair of distinguishable subsets of $V - X$ if there exists an edge from X to $X_1 \Delta X_2$.

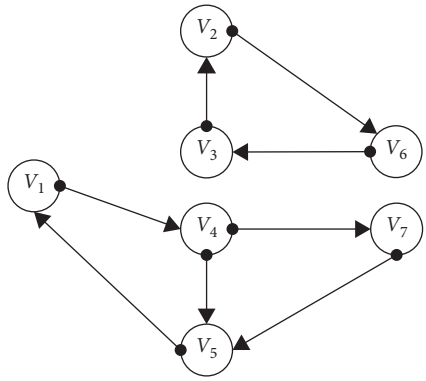

Figure 1: A graph with 7 nodes.

According to Definition 5, the following results are true. In the system $G = (V, E)$, if $X \subseteq V$ with $|X| < k$, any two subsets $X_1 \subseteq V - X$ with $|X_1 \cup X| \leq t$, $X_2 \subseteq V - X$ with $|X_2 \cup X| \leq t$, and (X_1, X_2) is a pair of distinguishable subsets in $V - X$, then the system can determine the fault set, provided that G has less than k faulty nodes and all faulty nodes in X have been repaired or replaced with additional fault-free nodes.

Lemma 3. *Suppose that that the undirected graph $G = (V, E)$ has less than t faulty nodes and $G\prime \subset G$ with $|V(G')| \geq t + 1$ is connected. If each result in G' is 0, then $G\prime$ does not have faulty nodes.*

Proof. To the contrary, let $G' \subset G$ with $|V(G')| \geq t + 1$ be connected, in which each result in it is 0 and there is a faulty node, say u. Then, it is clear that each node in $N_{G'}(u)$ is faulty. Similarly, each node in $N_{G'}(N_{G'}(u))$ is 1 faulty. As a result, each node $V(G')$ is faulty. Note that $|V(G')| \geq t + 1$; this implies that the number of fault nodes in G' exceeds t, a contradiction. Therefore, each node in $V(G')$ is fault-free. □

3. Two-Round t-Diagnosable Systems

At the beginning of the section, the concept of a two-round t-diagnosable system is presented as follows.

Definition 6. A system is two-round t-diagnosable if, for given syndrome σ, after repairing or replacing the faulty nodes identified by one-round diagnosis, the system can diagnose the remaining faulty nodes without replacement, provided that the system has less than $t + 1$ faulty nodes.

According to Definition 6, we can obtain the following necessary conditions for a two-round t-diagnosable system.

Theorem 1. *Let $G = (V, E)$ represent a system. Then, G is two-round t-diagnosable if and only if for any a subset $Y \subseteq V$ with $|Y| \leq t$ and any two distinct subsets $Y_1, Y_2 \subseteq V - Y$, where $|Y \cup Y_1| \leq t$, $|Y \cup Y_2| \leq t$, and $Y_1 \cap Y_2 = \phi$, there exists at least an edge from $V - Y_1 - Y_2$ to $Y_1 \Delta Y_2$.*

Proof.

Necessity: since for any $Y \subseteq V$ with $|Y| = t$, the result is trivial, next, we show that the result is true for the case of $|Y| < t$. To the contrary, suppose that there exists a subset $Y \subseteq V$, where $|Y| < t$ and distinct subsets $Y_1, Y_2 \subseteq V - Y$ with $|Y \cup Y_1| \leq t$, $|Y \cup Y_2| \leq t$, $Y_1 \cap Y_2 = \phi$, such that there are no edges from $V - Y_1 - Y_2$ to $Y_1 \Delta Y_2$. Without loss of generality, suppose that each node in Y is faulty and G has more than $|Y|$ faulty nodes. Define a syndrome σ as follows. Let $x, y \in V$ with $(x, y) \in E$:

(1) If $x, y \in V - Y - Y_1 - Y_2$, then $\sigma(x, y) = 0$
(2) If $x \in V - Y - Y_1 - Y_2$ and $y \in Y$, then $\sigma(x, y) = 1$
(3) If $x \in Y_1 - Y_2$ and $y \in Y_2 - Y_1$, then $\sigma(x, y) = 1$
(4) If $x \in Y_2 - Y_1$ and $y \in Y_1 - Y_2$, then $\sigma(x, y) = 1$
(5) The remaining test results are arbitrary

Both $(Y \cup Y_1)$ and $(Y \cup Y_2)$ are allowable sets for syndrome σ. Suppose that $F_1, F_2, \ldots, F_k \subseteq V$ are all the allowable fault sets for σ. Let $F_c = \cap_{i=1}^{k} F_i$; F_c is a fault set of G and $F_c \subseteq Y$, which implies that the fault set Y_1 identified by the first-round diagnosis is a subset of Y. Let $G\prime$ denote the system after replacing the nodes of Y_1, and σ is a syndrome obtained by performing a test task on $G\prime$. Since there are no edges from $V - Y_1 - Y_2$ to $Y_1 \Delta Y_2$, then $\sigma(x, y) = \sigma(x, y) = 1$ for $x \in Y_1 - Y_2$, $y \in Y_2 - Y_1$, and $\sigma(x, y) = \sigma(x, y) = 1$ for $x \in Y_2 - Y_1$, $y \in Y_1 - Y_2$. Hence, both Y_1 and Y_2 are AFSs for σ, which is a contradiction to the hypothesis that $G = (V, E)$ is two-round t-diagnosable.

Sufficiency: for a syndrome σ, let F_c be the intersection of all AFSs for σ. According to Lemma 2, F_c is a fault set, where $|F_c| \leq t$. If $|F_c| = t$, then each system has been diagnosed by syndrome σ, which implies that G is two-round t-diagnosable. If $|F_c| < t$, then let $G\prime$ denote the system for which all the nodes in F_c are repaired or replaced with additional fault-free nodes from G. Then, the number of faulty nodes in $G\prime$ will not be more than $t - |F_c|$, and these faulty nodes belong to $V - F_c$. Let σ denote a syndrome obtained by performing the test task to $G\prime$. We claim that the fault set $Y_1 \subseteq V - F_c$ of $G\prime$ where $|Y_1| \leq t - |F_c|$ can be determined by σ. In contrast, there exists another nonempty allowable subset $Y_2 \subseteq V - F_c$ of $G\prime$, where $|Y_2| \leq t - |F_c|$ for σ, and we derive a contradiction. Consider the following situations.

Case 1: there is an edge (x, y) from $V - F_c - Y_1 - Y_2$ to $Y_1 \Delta Y_2$. Without loss of generality, let $y \in Y_1$. Since Y_2 is an allowable subset of $V - F_c$ for σ, $\sigma(x, y) = 0$. On the contrary, since Y_1 is a fault subset of $V - F_c$ for σ, $\sigma(x, y) = 1$ is a contradiction.

Case 2: there are no edges from $V - F_c - Y_1 - Y_2$ to $Y_1 \Delta Y_2$. According to this assumption, there exists an edge (x, y) from F_c to $Y_1 \Delta Y_2$. Without loss of generality, suppose that $y \in Y_1 - Y_2$. Since Y_2 is an allowable set for σ, $\sigma(x, y) = 0$. On the contrary, since Y_1 is a fault set of $G\prime$, $\sigma(x, y) = 1$ is a contradiction. Hence, G is two-round t-diagnosable.

According to the proof of Theorem 1, the two corollaries described as follows are obvious. □

Corollary 1. *A system $G = (V, E)$ is two-round t-diagnosable if for any subset $Y \subseteq V$ with $|Y| < t$, and for any distinct disjoint*

subsets $Y_1, Y_2 \subseteq V - Y$, where $|Y \cup Y_1| \leq t$ and $|Y \cup Y_2| \leq t$, and (Y_1, Y_2) is a pair of distinguishable subsets of $V - Y$.

Definition 7. Let S be a network system. The maximum nonnegative integer t that guarantees S to be two-round t-diagnosable is called the two-round diagnosability of S.

For convenience, it is necessary to introduce a notation $\Gamma_2^{-1}v = \Gamma^{-1}v \cup \Gamma^{-1}(\Gamma^{-1}v) - \{v\}$ for the coming corollary, where $G = (V, E)$ is a system, $v \in V$.

Corollary 2. *For the system $G = (V, E)$, let $\alpha = \min\{|\Gamma_2^{-1}v| \mid v \in V\} + 1$. Then, the system is not two-round α-diagnosable.*

Proof. Let $v \in V$ be a node such that $\alpha = |\Gamma_2^{-1}v| + 1$. Consider the case such that $F = \Gamma_2^{-1}v \cup \{v\}$ is a fault set that consists of exactly all faulty nodes in the system. Note that $|F| = \alpha$. Define a syndrome σ as follows. Let $x, y \in V$ with $(x, y) \in E$ (see Figure 2):

(i) If $x, y \in V - \Gamma_2^{-1}v - \{v\}$, then $\sigma(x, y) = 0$

(ii) If $x \in V - \Gamma_2^{-1}v - \{v\}$ and $y \in \Gamma^{-1}(\Gamma^{-1}v) - \{v\}$, then $\sigma(x, y) = 1$ (before replacement)

(iii) If $x \in \Gamma^{-1}(\Gamma^{-1}v) - \{v\}$ and $y \in V - \Gamma_2^{-1}v - \{v\}$, then $\sigma(x, y) = 0$

(iv) If $x \in \Gamma^{-1}(\Gamma^{-1}v) - \{v\}$ and $y \in \Gamma^{-1}v$, then $\sigma(x, y) = 1$

(v) If $x \in \Gamma^{-1}v$, then $\sigma(v, x) = 1$

(vi) If $x \in \Gamma^{-1}(\Gamma^{-1}v) - \{v\}$, then $\sigma(v, x) = 0$

(vii) If $x \in \Gamma^{-1}v$, then $\sigma(v, x) = 1$

(viii) If $x \in \Gamma^{-1}(\Gamma^{-1}v) - \{v\}$, then $\sigma(v, x) = 1$ (before replacement)

(ix) The other test results are arbitrary

For σ, the nodes of subset $\Gamma^{-1}(\Gamma^{-1}v) - \{v\}$ can be identified correctly as faulty, which implies that the nodes of subset $\Gamma^{-1}v \cup \{v\}$ cannot be identified by syndrome σ. After the faulty nodes of subset $\Gamma^{-1}(\Gamma^{-1}v) - \{v\}$ are repaired, there exist no edges from fault-free nodes to v, and the test results from v to faulty (fault-free) nodes are 1 (0), which implies that we cannot judge the state of node v. Therefore, to identify the state of node v, we need a second replacement. So, the system is not two-round α-diagnosable. □

4. Two-Round Diagnosability of Hypercube Networks

Q_n is a regular graph with 2^n nodes and $n2^n$ edges. Each node in Q_n can be denoted by an n-bit binary string. $(x, y) \in E(Q_n)$ if and only if there is exactly different one bit position between x and y. Figure 3 is an illustration of a 4-dimensional hypercube network Q_4.

Lemma 4 (see [17]). *Let $X \subset V(Q_n)$ with $|Y| = s$ and $0 > s \leq n + 1$. Then, the size of the neighbor set of Y is more than $(sn - s(s + 1)/2)$.*

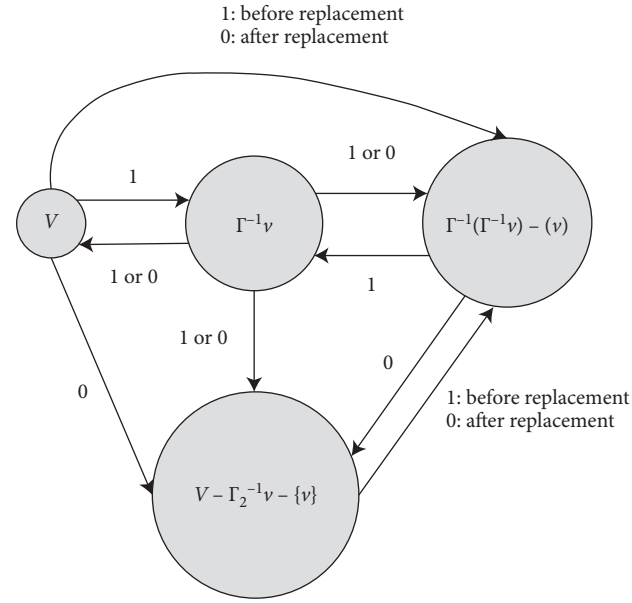

Figure 2: A syndrome of Corollary 2.

Lemma 5. *For Q_n $(n \geq 5)$, let $S = \{v_i \mid v_i \in V(Q_n), 1 \leq i \leq n, |\cap_{i=1}^{n} N(v_i)| = 1\}$. Then, $|N(S)| = (n^2 - n/2) + 1$.*

Proof. We use $\text{add}(v)$ to denote v' address. Suppose that $\cap_{i=1}^{n} N(v_i) = \{v_0\}$ and $\text{add}(v_0) = a_1 a_2 \cdots a_n$. According to the definition of Q_n, without loss of generality, assume that $\text{add}(v_1) = \overline{a_1} a_2 \cdots a_n$, $\text{add}(v_2) = a_1 \overline{a_2} \cdots a_n, \ldots, \text{add}(v_n) = a_1 a_2 \cdots \overline{a_n}$. For some i, we have that $N(v_i) = \{\overline{a_1} a_2 \cdots \overline{a}\, i \cdots a_n, a_1 \overline{a_2} a_3 \cdots \overline{a_i} \cdots a_n, \ldots, a_1 a_2 \cdots \overline{a_i} \cdots \overline{a_n}\}$. Then, $N(v_i) \cap N(v_j) = \{v_0, u\}$, where $\text{add}(u) = a_1 a_2 \cdots \overline{a_i} \cdots \overline{a_j} \cdots a_n$ and $1 \leq i, j \leq n, i \neq j$. So, $|N(S)| = n(n-1) - C_n^{\ 2} + 1 = n^2 - (n(n+1)/2) + 1 = (n^2 - n/2) + 1$.

According to Lemmas 4 and 5, for an n-dimensional hypercube and a subset $S \subseteq V$, where $|S| = n + 1$, if $\exists v \in S$ with $N(v) \subseteq S$, then $|N(S)| = (n^2 - n/2)$. □

Lemma 6 (see [19]). *Suppose that Q_n is modelled by a graph $G(V, E)$ $(n \geq 5)$. Let $S \subset V$ with $n \leq |S| \leq 2(n-1) - 1$. If $G[V - S]$ is disconnected and $C_{sub}(G[V - S]) = \{C_1, C_2, \ldots, C_m\}$, then the following conditions hold:*

(i) $\Sigma_{i=0}^{1} i|Card_i(C_{sub}((G[V - S])))| \leq 1$

(ii) There is unique $C_i \in C_{sub}(G[V - S])$, where $|V(C_i)| \geq 2$

Lemma 7 (see [24]). *Suppose that Q_5 is modelled by a graph $G(V, E)$. Let $S \subset V$ with $\leq 5k - (k(k+1)/2)$ $(1 \leq k \leq 4)$. If $G[V - S]$ is disconnected and $C_{sub}(G[V - S]) = \{C_1, C_2, \ldots, C_m\}$, then the following conditions hold:*

(i) $\Sigma_{i=0}^{k-1} i|Card_i(C_{sub}(G[V - S]))| \leq k - 1$

(ii) There is unique $C_i \in C_{sub}(G[V - S])$, where $|V(C_i)| \geq k$

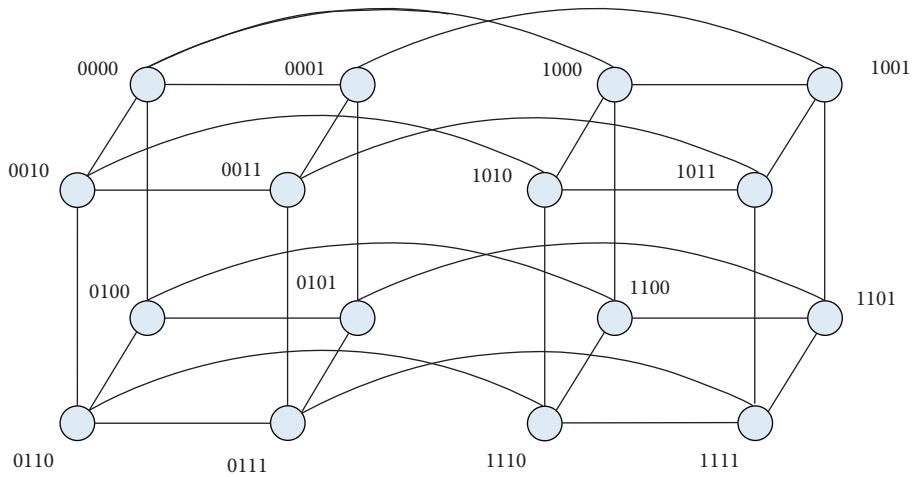

Figure 3: A 4-dimensional hypercube.

Lemma 8 *Let $x > 0$ and $y > 0$ are two integers. Then, $(x + y) \leq 1 + xy$.*

Proof. Consider the function $g(x, y) = (1 + xy) - (x + y)$. It is obvious that $g(x, y) = (x - 1)(y - 1)$. Since $x \geq 1$ and $y \geq 1$, then $g(x, y) \geq 0$, which implies that $(x + y) \leq 1 + xy$. □

Lemma 9 (see [24]). *Suppose that Q_n is modelled by a graph $G(V, E)$ $(n \geq 5)$. Let $S \subset V$ with $|S| \leq kn - (k(k + 1)/2)$ $(1 \leq k \leq n - 1)$. If $G[V - S]$ is disconnected and $C_{sub}(G[V - S]) = \{C_1, C_2, \ldots, C_m\}$, then the following conditions are true:*

(i) $\Sigma_{i=0}^{k-1} i|Card_i(C_{sub}(G[V - S]))| \leq k - 1$

(ii) There is unique $C_i \in C_{sub}(G[V - S])$, where $|V(C_i)| \geq k$

Lemma 10 (see [24]). *Suppose that Q_5 is modelled by a graph $G(V, E)$. Let $S \subset V$ with $|S| \leq 9$. If $G[V - S]$ is disconnected and $C_{sub}(G[V - S]) = \{C_1, C_2, \ldots, C_m\}$, then the following conditions are true:*

(i) $\Sigma_{i=0}^{k-1} i|Card_i(C_{sub}(G[V - S]))| \leq 4$

(ii) There is unique $C_i \in C_{sub}(G[V - S])$, where $|V(C_i)| \geq 5$

Lemma 11 (see [24, 25]). *Suppose that Q_n is modelled by a graph $G(V, E)$ $(n \geq 5)$. Let $S \subset V$ with $|S| \leq n^2 - (n(n + 1)/2) - 1$. If $G[V - S]$ is disconnected and $C_{sub}(G[V - S]) = \{C_1, C_2, \ldots, C_m\}$, then the two conditions as follows are true:*

(i) $\Sigma_{i=0}^{n-1} i|Card_i(C_{sub}(G[V - S]))| \leq n - 2$

(ii) There is unique $C_i \in C_{sub}(G[V - S])$, where $|V(C_i)| \geq n$

With the above preliminaries, we shall discuss the two-round diagnosability of Q_n.

Theorem 2. *An n-dimensional $(n \geq 6)$ hypercube given by $G = (V, E)$ is not two-round $(n^2 + n/2) + 1$-diagnosable.*

Proof. Note that, for each node $v \in V$, we have $|\Gamma_2^{-1}v \cup \{v\}| = (n^2 + n/2) + 1$ by Lemma 5. According to Corollary 2, it is easily determined that an n-dimensional hypercube is not two-round $(n^2 + n/2) + 1$-diagnosable. □

Theorem 3. *An n-dimensional $(n \geq 6)$ hypercube given by $G = (V, E)$ is two-round $(n^2 + n/2)$-diagnosable.*

Proof. Let $X \subseteq V$ be a subset of V, where $|X| < (n^2 + n/2)$. According to Theorem 1, we will show that, for any two distinct subsets $S_1, S_2 \subseteq V - X$, where $|X \cup S_1| \leq (n^2 + n/2)$, $|X \cup S_2| \leq (n^2 + n/2)$, and $S_1 \cap S_2 = \phi$, there exists at least an edge from $V - S_1 - S_2$ to $S_1 \Delta S_2$. Without loss of generality, let $S_1 - S_2 \neq \phi$.

Now, consider the two situations:

Case 1: $|X| \geq (n^2 - n/2)$.

Note that $|S_1| < (n^2 + n/2) - |X| \leq (n^2 + n/2) - (n^2 - n/2) = n$ and $|S_2| < (n^2 + n/2) - |X| \leq (n^2 + n/2) - (n^2 - n/2) = n$, which implies that $|(S_1 - S_2)| < n$. Let $k = |(S_1 - S_2)|$; then, $1 \leq k < n$. According to Lemma 4, we have that $N(S_1 - S_2) \geq kn - (k(k + 1)/2) + 1$. Since $f(k) = kn - (k(k + 1)/2) + 1$ is an increasing function for $k \in [1, n - (1/2)]$, $f(k) \geq f(1) = n$, which implies that $|S_1 - S_2| = f(k) > n > |S_2|$. Hence, there exists at least an edge from $V - S_1 - S_2$ to $S_1 - S_2$.

Case 2: $|X| < (n^2 - n/2)$.

To the contrary, assume that $\exists S_1, S_2 \subseteq V - X$ with $|X \cup S_1| \leq (n^2 + n/2)$, $|X \cup S_2| \leq (n^2 + n/2)$, and $S_1 \cap S_2 = \phi$, but that there are no edges from $V - S_1 - S_2$ to $S_1 \Delta S_2$. Next, we derive a contradiction. According to Lemma 11, we know that the system can be divided into three parts by a subset X (shown in Figure 4). Note that A is the largest component of $G[V - X]$, where $|A| \geq 2^n - ((n^2 - n/2) - 1) - (n - 1) = 2^n + 2 - (n^2 + n/2)$, and B is the union of the remaining components of $G[V - X]$, where $|B| \leq n - 1$. Since $|B| \leq n - 1$ and Q_n is a

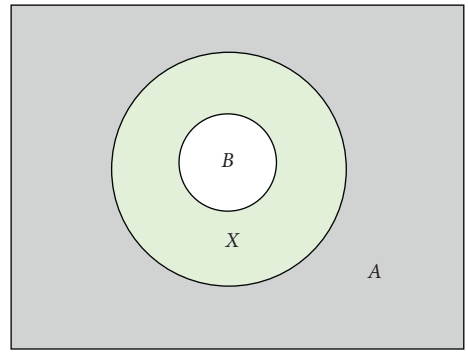

Figure 4: System divided into A, B, and X by subset X.

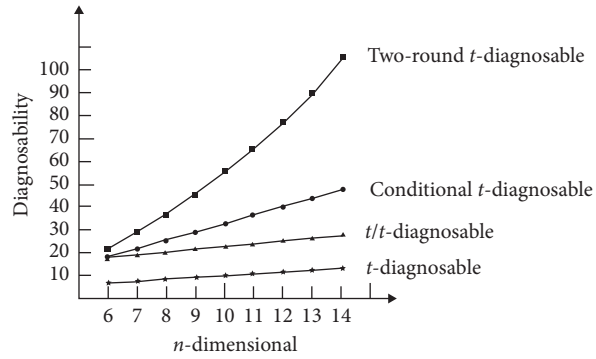

Figure 5: Comparison of the diagnosabilities of Q_n between the traditional diagnosis approach and the two-round diagnosis approach.

n-regular graph, $S_1 \cap B = \phi$. A similar argument can be used to obtain that $S_2 \cap B = \phi$. Hence, $S_1 \subseteq A$, and $S_2 \subseteq A$.

Note that $|A - S_1 \cup S_2| = |A| - |S_1| - |S_2| \geq 2^n - |X| - |S_1| - |S_2| - (n-1) \geq 2^n - (3/2)(n^2 + n/2) - (n-1) > 0$ $(n \geq 6)$, and A is a component of $V - S$. This property implies that $N(S_1 \Delta S_2) \cap A \neq \phi$, which is a contradiction.

In summary, we conclude that Q_n $(n \geq 6)$ is two-round $(n^2 + n/2)$-diagnosable. □

As we know, Q_n is n-diagnosable, $(2n - 2/2n - 2)$-diagnosable, and conditionally $4n - 7$-diagnosable. A previous study has shown that Q_n is also two-round $(n^2 + n/2)$-diagnosable. Figure 5 gives an intuitive comparison between these diagnosabilities for Q_n.

5. A Fault Diagnosis Algorithm of Two Round t-Diagnosable Hypercubes

In Section 4, we observed that an n-dimensional hypercube (Q_n) was two-round $(n^2 + n/2)$-diagnosable. Then, identifying all faults with at most a one-round replacement remains an open question. This section presents a fast identification algorithm to address this issue (Algorithm 1. The completeness of the identification algorithm is demonstrated, provided that the system has less than $t + 1$ faulty nodes $(t \leq (n^2 - n/2) - 1)$. The fast identification algorithm is described in detail in Algorithm 2.

Algorithm 1 is applied to each node of Q_n with at most t faulty nodes $(t \leq (n^2 - n/2) - 1)$. According to Lemmas 9 and 11, the unique set S can be output by Algorithm DFS, where $|S| \geq t + 1$.

Theorem 4. *The time complexity of the fast identification algorithm is $O(N \log_2 N)$, where $N = 2^n$.*

Proof. For the sake of convenience, let F denote a set exactly consisting of faulty nodes in the system, L the largest component of the induced subgraph by $V - F$, and S a set consisting of all remaining small components in the induced subgraph by $V - F$. When $u_i \in L$), Step 1 takes an amount of time equal to $O(N \log_2 N)$. When the $(u_i) \in S \cup F$, Step 1 takes an amount of time equal to $O((n^2 + n/2) + N \log_2 N) = O(N \log_2 N)$. Hence, Step 1 takes an amount of time equal to $O(N \log_2 N)$. Step 2 and Step 3 take an amount of time equal to $O(N)$. So, the total time for Fast Identification is $O(N \log_2 N)$.

According to Lemmas 9 and 11, the completeness of the fast identification algorithm is obvious, provided that Q_n has no more than $(n^2 - n/2) - 1$ faulty nodes. Note that Q_n is two-round $(n^2 + n/2)$-diagnosable. Then, there is a question of whether our algorithm is suitable for the scenario in which there are $t((n^2 - n/2) \leq t \leq (n^2 + n/2))$ faults in the system. We perform a simulation to evaluate the system; in the following simulation, we assume that Q_n has $(n^2 + n/2)$

Input:
(i) An undirected graph $G = (V, E)$ with $|V| = N$ representing a network system of interest and a network node $x \in V$. Let $S = \{x\}$.
Output:
A subset $S \subseteq V$.
(1) DFS(v):
for each $u \in N(x)$,
if $\sigma(y, x) = \sigma(x, y) = 0$,
$S = S \cup \{y\}$ and DFS(y).
(2) Output the node set S.

Algorithm 1: Depth-first search.

Input:
An undirected graph $G = (V, E)$ with $|V| = 2^n$, a positive integer t $(t \leq (n^2 - n/2) - 1)$ and a syndrome σ.
(i) **Output:**
A fault set A, a fault-free node set B and a second-round fault set C, where $A \cup B \cup C = V$.
(1) Let $S_i = \varnothing$ $(1 \leq i \leq 2^n)$ and $B = A = C = \varnothing$.
For any $u_i \in V - \cup_{j=1}^{i} S_i$ $(1 \leq i \leq 2^n)$, perform DAS(u_i); S_i DAS(u_i).
while $|S_i| \geq t + 1$, let $B = B \cup S_i$, and $A = A \cup N(B)$.
(2) While $V = B \cup A$, output B and A. Otherwise, go to Step 3.
(3) While $|A| \geq t$, let $B = V - A$, output B and A.
Otherwise, repair the faulty nodes in A and execute
Best (A, B, C) until $B \cup A \cup C = V$. Additionally, output subsets B, A, and C.
Best (A, B, C):
For any $v \in V - A - B$, if $\sigma(u, v) = 1$ $(u \in A \cup B)$, then $C = C \cup \{v\}$; otherwise, $B = B \cup \{v\}$.

Algorithm 2: Fast identification.

Table 1: Number of faulty nodes identified by the two-round algorithm applied to an n-dimensional hypercube.

n	7	8	9	10	11	12
Faults	28	36	45	66	78	91
Identified faults	28	36	45	66	78	91

faulty nodes, and each node of the system may be faulty with the same probability. We run our algorithm 1000 times. Table 1 gives the corresponding experimental results.

The simulation shows that our algorithm is suitable for Q_n, provided that it has no more than $(n^2 + n/2)$ faulty nodes. □

6. Conclusion

In this article, we introduce a novel diagnosis strategy called the two-round diagnosis strategy that implies that each node can be determined by at most a one-round replacement. A necessary and sufficient condition of the system being two-round t-diagnosable is presented. Additionally, several important properties of this system are described. Using the theory of a two-round t-diagnosable system, we show that Q_n is two-round $(n^2 + n/2)$-diagnosable. Compared to the traditional diagnosis strategy, the two-round diagnosability of Q_n is $(n + 1/2)$ times as large as n, the classic diagnosability of Q_n. Furthermore, an $O(n2^n)$ algorithm is provided to identify faulty nodes for Q_n. The conditionally t-diagnosable network systems are a lass of typical nonlinear systems, in which the state (syndrome) of a node impacted these nodes in its surrounding area. Recent years, there are some studies to analyze nonlinear systems by using online policy iterative optimization algorithms [20, 26]. The combination of these algorithms and our algorithm will be a try to obtain an optimal fault set for considered conditionally t-diagnosable network system; this is one of our studies in the future.

Data Availability

The data used to support the findings of this study are included within the article.

Conflicts of Interest

The authors declare that there are no conflicts of interest regarding the publication of this paper.

Acknowledgments

This work was supported in part by the Natural Science Foundation of China under Grant nos. 61862003 and 61761006 and Natural Science Foundation of the Guangxi Zhuang Autonomous Region of China under Grant no. 2018GXNSFDA281052.

References

[1] F. P. Preparata, G. Metze, and R. T. Chien, "On the connection assignment problem of diagnosable systems," *IEEE Transactions on Electronic Computers*, vol. 16, no. 6, pp. 848–854, 1967.

[2] X. Li, J. Fan, C.-K. Lin, and X. Jia, "Diagnosability evaluation of the data center network DCell," *The Computer Journal*, vol. 61, no. 1, pp. 129–143, 2018.

[3] J. Fan and X. Jia, "Edge-pancyclicity and path-embeddability of bijective connection graphs," *Information Sciences*, vol. 178, no. 2, pp. 340–351, 2008.

[4] J. Fan, X. Jia, X. Liu, S. Zhang, and J. Yu, "Efficient unicast in bijective connection networks with the restricted faulty node set," *Information Sciences*, vol. 181, no. 11, pp. 2303–2315, 2011.

[5] S. He, H. Fang, M. Zhang, F. Liu, and Z. Ding, "Adaptive optimal control for a class of nonlinear systems: the online policy iteration approach," *IEEE Transactions on Neural Networks and Learning Systems*, vol. 31, no. 2, pp. 549–558, 2020.

[6] J. Liang and Q. Zhang, "The t/s-diagnosability of hypercube networks under the PMC and comparison models," *IEEE Access*, vol. 5, no. 1, pp. 5340–5346, 2017.

[7] L.-C. Ye, J.-R. Liang, and H.-X. Lin, "A fast pessimistic diagnosis algorithm for hypercube-like networks under the comparison model," *IEEE Transactions on Computers*, vol. 65, no. 9, pp. 2884–2888, 2016.

[8] M. Xie, J. Liang, and X. Xiong, "The strong local diagnosability of a hypercube network with missing edges," *Complexity*, vol. 2018, Article ID 5745628, 10 pages, 2018.

[9] J. Liang, Q. Zhang, and H. Li, "Structural properties and t/s-diagnosis for star networks based on the PMC model," *IEEE Access*, vol. 5, no. 11, pp. 26175–26183, 2017.

[10] W. Yang, H. Lin, and C. Qin, "On the t/k-diagnosability of BC networks," *Applied Mathematics and Computation*, vol. 225, no. 12, pp. 366–371, 2013.

[11] W. Yang, H. Li, and X. Guo, "A kind of conditional fault tolerance of (n, k)-star graphs," *Information Processing Letters*, vol. 110, no. 22, pp. 1007–1011, 2010.

[12] X. Yang, "A fast diagnosis algorithm for hypercube multiprocessor systems under the pessimistic one-step diagnosis," *Journal of Parallel and Distributed Computing*, vol. 64, no. 3, pp. 537–553, 2004.

[13] D.-R. Duh, C.-H. Chen, and K.-N. Chang, "A fast pessimistic diagnosis algorithm for generalized hypercube multicomputer systems," *The Journal of Supercomputing*, vol. 61, no. 3, pp. 605–618, 2012.

[14] B. Cheng, J. Fan, X. Jia, and J. Jia, "Parallel construction of independent spanning trees and an application in diagnosis on Möbius cubes," *The Journal of Supercomputing*, vol. 65, no. 3, pp. 1279–1301, 2013.

[15] L. Xu, S. Zhou, and G. Lian, "Conditional diagnosability of multiprocessor systems based on complete-transposition graphs," *Discrete Applied Mathematics*, vol. 247, pp. 367–379, 2018.

[16] S. He, M. Zhang, H. Fang, F. Liu, X. Luan, and Z. Ding, "Adaptive optimization and reinforcement learning of stochastic Markov jump systems with completely unknown dynamic information," *Neural Computing and Applications*, vol. 31, 2019.

[17] W. Liu, J. Fan, X. Jia, and S. Zhang, "The spined cube: a new hypercube variant with smaller diameter," *Information Processing Letters*, vol. 111, no. 12, pp. 561–567, 2011.

[18] G.-H. Hsu and J. J. M. Tan, "A local diagnosability measure for multiprocessor systems," *IEEE Transactions on Parallel and Distributed Systems*, vol. 18, no. 5, pp. 598–607, 2007.

[19] P. L. Lai, J. J. M. Tan, C. P. Chang, and L. H. Hsu, "Conditional diagnosability measures for large multiprocessor systems," *IEEE Transactions on Computers*, vol. 54, no. 2, pp. 165–175, 2005.

[20] S. He, H. Fang, M. Zhang, F. Liu, X. Luan, and Z. Ding, "Online policy iterative-based H_∞ optimization algorithm for a class of nonlinear systems," *Information Sciences*, vol. 495, pp. 1–13, 2019.

[21] J. Zheng, S. Latifi, E. Regentova, K. Luo, and X. Wu, "Diagnosability of star graphs under the comparison diagnosis model," *Information Processing Letters*, vol. 93, no. 1, pp. 29–36, 2005.

[22] S. Zhou, S. Song, X. Yang, and L. Chen, "On conditional fault tolerance and diagnosability of hierarchical cubic networks," *Theoretical Computer Science*, vol. 609, no. 9, pp. 421–433, 2016.

[23] S. Chen, L. Lin, L. Xu, and D. Wang, "The t/k-diagnosability of star graph networks," *IEEE Transactions on Computers*, vol. 62, no. 2, pp. 547–555, 2015.

[24] X. Wang, D. J. Evans, and G. M. Megson, "On the maximal connected component of a hypercube with faulty vertices III," *International Journal of Computer Mathematics*, vol. 83, no. 1, pp. 27–37, 2006.

[25] L. H. Hsu, E. Cheng, L. Lipták, J. J. M. Tan, C.-K. Lin, and T.-Y. Ho, "Component connectivity of the hypercubes," *International Journal of Computer Mathematics*, vol. 89, no. 2, pp. 137–145, 2012.

[26] D. Liu and Q. Wei, "Policy iteration adaptive dynamic programming algorithm for discrete-time nonlinear systems," *IEEE Transactions on Neural Networks and Learning Systems*, vol. 25, no. 3, pp. 621–634, 2014.

Hindawi
Complexity
Volume 2020, Article ID 1628023, 11 pages
https://doi.org/10.1155/2020/1628023

Research Article

Joint Channel Allocation and Power Control Based on Long Short-Term Memory Deep Q Network in Cognitive Radio Networks

Zifeng Ye,[1,2] Yonghua Wang ,[1] and Pin Wan[1,3]

[1]*School of Automation, Guangdong University of Technology, Guangzhou 510006, China*
[2]*School of Electronics and Communication Engineering, Sun Yat-Sen University, Guangzhou 510006, China*
[3]*Hubei Key Laboratory of Intelligent Wireless Communications, South-Central University for Nationalities, Wuhan 430074, China*

Correspondence should be addressed to Yonghua Wang; sjzwyh@163.com

Received 18 April 2020; Accepted 19 May 2020; Published 11 June 2020

Academic Editor: Shuping He

Efficient spectrum resource management in cognitive radio networks (CRNs) is a promising method that improves the utilization of spectrum resource. In particular, the power control and channel allocation are of top priorities in spectrum resource management. Nevertheless, the joint design of power control and channel allocation is an NP-hard problem and the research is still in the preliminary stage. In this paper, we propose a novel joint approach based on long short-term memory deep Q network (LSTM-DQN). Our objective is to obtain the channel allocation schemes of the access points (APs) and the power control strategies of the secondary users (SUs). Specifically, the received signal strength information (RSSI) collected by the microbase stations is used as the input of LSTM-DQN. In this way, the collection of RSSI can be shared between users. After the training is completed, the APs are capable of selecting channels with small interference while the SUs may access the authorized channels in an underlay operation mode without knowing any knowledge about the primary users (PUs). Experimental results show that the channels are allocated to the APs with a lower probability of collision. Moreover, the SUs can adjust their power control strategies quickly to avoid the harmful interference to the PUs when the environment parameters change randomly. Consequently, the overall performance of CRNs and the utilization of spectrum resources are improved significantly compared to existing popular solutions.

1. Introduction

Cognitive radio networks (CRNs), also known as cognitive wireless networks (CWNs), are formed when cognitive radio devices are organically connected through cognitive base stations. Spectrum resource management is one of the basic tasks of CRNs, which aims to achieve high unitization of the spectrum resource through dividing it into a group of channels or resource blocks and designing proper management strategies. Faced with the increasing demand for mobile data capacity, channel allocation and power control play a key role in spectrum resource management [1, 2].

Spectrum resource management is to determine the most suitable channels for secondary users (SUs) without affecting the communication of primary users (PUs), based on the analysis of available channels. Currently, optimization and game theory have been widely used in spectrum management. In [3], spectrum sharing was made according to interference temperature and radio frequency (RF) power per unit of bandwidth measured in the receiving antenna. The optimal solution can be obtained by particle swarm optimization (PSO) algorithm, if the objective function was convex. In addition, simulated annealing (SA) is applied to prevent falling into suboptimal solutions. Three improved algorithms of PSO, namely, binary PSO, sociocognitive PSO, and derivation zero algorithm were proposed and the throughput of SU links was compared under the interference constraints in [4]. The spectrum access algorithm, proposed

in [5], improved the throughput and spectrum sensing ability of the network system by formulating a Lagrange dual optimization problem and derived the optimal power allocation strategy and target detection probability. In the research of spectrum resource management based on game theory, the core idea is to obtain the equilibrium of optimal distribution of spectrum resources among SUs. In [6], the double auction model from microeconomic theory was used in TV band transactions between TV broadcasting companies and wireless regional area network (WRAN) service providers. For WRAN service providers, spectrum bidding and pricing problems were formulated as a noncooperative game model and obtained the Nash equilibrium. Tehrani and Uysal [7] proposed a sealed bid first-price auction model, aiming to maximize the revenue of service provider and the satisfaction of SUs under incomplete spectrum sensing conditions. Tan et al. [8] considered cooperative and noncooperative spectrum access schemes based on threshold policy. Experimental results showed that, in noncooperative cases, the optimal scheme met the Nash equilibrium.

Existing work using the optimal control or game theory often assumes that users in the wireless networks have obtained the complete environmental state information. However, such information is difficult, if not impossible to obtain in complex and dynamic scenarios, so in many cases, a solution has to be given based on partial environmental information. Inspired by the emerging artificial intelligence, reinforcement learning and neural network provide us a new tool to tackle challenges in CRNs [9–12]. Deep reinforcement learning (DRL) has used the model free feature of reinforcement learning (RL) and the ability of deep learning (DL) to process data in spectrum resource management. The potential advantages of applying DRL to spectrum resource management are threefold. First, the optimal solution for decision-making problems can be obtained through trial and error, and the cycle of manual spectrum planning is greatly reduced. So, CRNs can learn and obtain efficient spectrum resource management solutions. Second, it is possible to simulate the complex real-loop scenario that is difficult to model mathematically and constantly accumulate new experiences to adapt to various extreme situations. Third, real-time effective monitoring of dynamic environment, mining the potentially important data and information, and improving the performance of CRNs can be achieved. These advantages boost a few research works [13–17]. For instance, Wan and Cohen [14] proposed a distributed dynamic spectrum access algorithm based on deep multiuser reinforcement learning, aiming at maximizing network utility in multichannel wireless networks. At each time slot, each SU mapped its current state into the spectrum access action by using the trained deep Q network (DQN). Experimental results showed that, in some observable environments, SUs were able to learn out good control strategies to ensure network performance without using online acknowledgement (ACK) signals. Liu et al. [16] adopted a multiagent DQN technology, which further optimized the learning process by combining the DQN algorithm with transfer learning so that SUs of the new access network could obtain more experience and knowledge.

In spite of the aforementioned research work, spectrum resource management based on DRL is still in its infancy stage. Existing results revealed that the state information of the channels has a high degree of self-correlation [18, 19]. However, this property may have a considerable time interval from the current state. There is still a large gap in the study of this problem. Considering the extraordinary network structure of long short-term memory, it is possible to explore such self-correlation and make a better estimate of the state of the channels. Motivated by the limitations of the current state-of-the-art and the joint design problem of channel allocation and power control for spectrum resource management, this paper proposes a long short-term memory deep Q network- (LSTM-DQN-) based joint channel allocation and power control algorithm, which helps to achieve spectrum utilization flexibility by sharing the received signal strength information (RSSI) among users. Additionally, we consider that PUs may have multiple alternative power control strategies rather than a single strategy and choose the appropriate one dynamically according to the changing environment. The evaluations show that the adjacent access points (APs) access available channels without conflict, whereas SUs maximize the power control strategies to avoid harmful interference to PUs.

The remainder of this paper is organized as follows. Section 2 introduces the system model and formulates the problem to be solved. The implementation of the proposed algorithm is discussed in Section 3. Section 4 describes the simulation experiments and result analysis, and finally, the conclusion and future work are presented in Section 5.

2. Preliminaries

2.1. System Model. The channel allocation problem is raised due to huge number of wireless devices accessing limited spectrum space. In such problem, there is no one-to-one connection between channels and APs. The main challenges are adjacent channel interference (ACI) and co-channel interference (CCI). For the joint optimization of channel allocation and power control, it is necessary to consider not only the transmit power of primary and secondary users but also the selection of channels at different access points and their possible conflicts to each other.

The system model we focus in this paper is shown in Figure 1. There are 5 APs deployed in the scenario, and each AP serves several primary and secondary users distributed randomly within its communication range. We allow overlapping between APs. For instance, the service range of AP1 and AP2 overlap with each other, and so do AP3 and AP4. In contrast, AP5 is independent of others. Within the service range of each AP, the PUs always transmit data on their authorized channels, whereas SUs are only allowed to access channels without affecting the communication of PUs. The base station in the middle is mainly responsible for the communication of PUs. Meanwhile, microcells assist SUs to control the transmit power. These microcells collect the RSSI of primary and secondary users, package the collected information into packets occupying a few bytes,

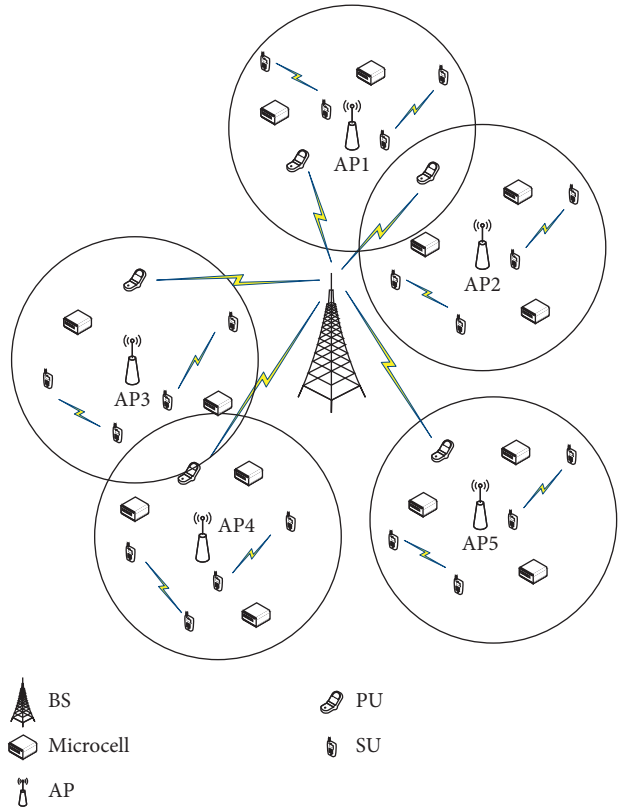

Figure 1: The system model of CRNs.

and then send them to SUs through a dedicated control channel. It is assumed that each PU adjusts the transmitting power according to its own control strategy and always transmits data on its authorized channel. Both PUs and SUs are ignorant of others' power control strategy. To be more specific, PUs are never concerned about the existence of SUs. Therefore, SUs need to learn appropriate transmit power strategies through utilizing the RSSI, as to accomplish their own transmission tasks.

2.2. Problem Formulation. In the joint optimization of channel allocation and power control, the first thing to determine is whether to allow the same channel to be selected between different APs. In this paper, this is not allowed, i.e., we consider the case of no channel conflicts. Based on such assumption, the transmit power and control strategies of primary and secondary users are then determined. Table 1 specifies the symbols used in this paper.

The set of APs is denoted as $\mathscr{P}$, and the set of available channels is $\mathscr{C}$. Each AP can only use one channel. The channel matrix is $\rho: \mathscr{C} \times \mathscr{P} \longrightarrow [0,1]$ in which each element is defined by

$$\rho(c,p) = \begin{cases} 1, & \text{if AP } p \text{ occupies channel } c, \\ 0, & \text{otherwises,} \end{cases} \tag{1}$$

where $c \in \{1,2,\ldots,|\mathscr{C}|\}$, $p \in \{1,2,\ldots,|\mathscr{P}|\}$.

Accordingly, we define $\Omega_{|\mathscr{P}|\times|\mathscr{P}|}$ as the interference matrix, and each element is defined by the following formula:

$$\Omega_{p,q} = \begin{cases} 1, & \text{adjacent AP } p, q \text{ occupy the same channel,} \\ 0, & \text{otherwise.} \end{cases} \tag{2}$$

In order to measure the service quality, the SINR of primary and secondary users need to be defined. We assume that the users are able to communicate only if the relevant adjacent APs access the channel successfully. Let the SINR of PU i in AP p at time t be written as follows:

$$\mathrm{SINR}_{i,p}(t) = \frac{\left(1-\Omega_{p,q}\right)h_{ii}^{p}(t)P_{i,p}(t)}{\sum_{j}h_{ji}^{p}(t)P_{j,p}(t)+\delta_{i,p}(t)}. \tag{3}$$

Similarly, the SINR of SU j in AP p at time t is

$$\mathrm{SINR}_{j,p}(t) = \frac{\left(1-\Omega_{p,q}\right)h_{jj}^{p}(t)P_{j,p}(t)}{h_{ij}^{p}(t)P_{i,p}(t)+\sum_{j\neq k}h_{kj}^{p}(t)P_{k,p}(t)+\delta_{j,p}(t)}. \tag{4}$$

In multichannel scenarios, both the available channels and the channel gain change with time. Therefore, the problem becomes dynamic, and thus more complicated. The throughput of a single SU j in AP p at time t is

$$T_{j,p}(t) = W\log_2\left(1+\mathrm{SINR}_{j,p}(t)\right). \tag{5}$$

The objective is to maximize the total throughput of all SUs, which is denoted as follows:

Table 1: Notation of definitions.

Symbol	Definition
$P_{i,p}(t)$	The transmit power of the ith PU in AP p at time t
$P_{j,p}(t)$	The transmit power of the jth SU in AP p at time t
$h_{ii}^{p}(t)$	The channel gain of AP p from the ith PU transmitter to the ith PU receiver at time t
$h_{jj}^{p}(t)$	The channel gain of AP p from the jth SU transmitter to the jth SU receiver at time t
$h_{ji}^{p}(t)$	The channel gain of AP p from the jth SU transmitter to the ith PU receiver at time t
$h_{ij}^{p}(t)$	The channel gain of AP p from the ith PU transmitter to the jth SU receiver at time t
$h_{kj}^{p}(t)$	The channel gain of AP p from the kth SU transmitter to the jth SU receiver (j is not equal to k) at time t
$\delta_{i,p}(t)$	The noise power received by the ith PU of AP p at time t
$\delta_{j,p}(t)$	The noise power received by the jth SU of AP p at time t
$\mu_{i,p}$	The SINR threshold required by the PU
$\mu_{j,p}$	The SINR threshold required by the SU
M_p	The number of PUs in the area served by AP p
N_p	The number of SUs in the area served by AP p
$d_{il,p}(t)$	The distance from the ith PU in AP p to the microcells at time t
$d_{jl,p}(t)$	The distance from the jth SU in AP p to the microcells at time t

$$\begin{aligned} \max \quad & \sum_{p}\sum_{j=1}^{N} T_{j,p}(t) \\ \text{s.t.} \quad & \text{(I)}\mathrm{SINR}_{i,p}(t) \geq \mu_{i,p}, \quad \forall i,t \\ & \text{(II)}\mathrm{SINR}_{j,p}(t) \geq \mu_{j,p}, \quad \exists j,t \\ & \text{(III)}P_{i,p}(t) \geq \sum_{j} P_{j,p}(t). \end{aligned} \tag{6}$$

3. Deep Reinforcement Learning-Based Framework

Due to the widespread application of CRNs, the network structure is becoming more and more complex. It is difficult to establish a corresponding mathematical model to simulate a highly complex network environment. The model-free RL can effectively solve this problem. In recent years, DRL has shown excellent ability in dealing with complex problems and data operations. Therefore, this paper focuses on the application of DRL in spectrum resource management, especially the joint optimization of power control and channel allocation to improve the robustness and adaptability of CRNs.

3.1. Description of RL. The model-free learning is one type of method through continuous interaction with the virtual environment in RL. In general, RL constructs the problem as a Markov decision process (MDP). At every moment t, the agent can observe the current state of the environment $s \in S$ and then select an action $a \in A$. After the action is executed, the environment state is transitioned with a certain probability $P_{ss'}(a)$ to a new state $s' \in S$. Meanwhile, the environment will feed back a reward value $r \in R$ to the agent. The schematic diagram is shown in Figure 2. In a word, RL aims to find the best strategy by maximizing the cumulative reward value through a limited number of steps [9].

Using RL to solve the joint design problem in CRNs, an array (S, A, R) should be defined in advance, where S represents the set of environmental states, A is the set of SU actions, and R: $S \times A \longrightarrow \Re$ denotes the reward obtained when taking the next action in the current state.

3.1.1. State Space. There are 5 APs deployed in the network environment, with several primary and secondary users around each AP. The SUs can only obtain incomplete environmental information at APs to implement their transmission tasks. Assuming that L microcells are responsible for collecting the RSSI of primary and secondary users in the service area of each AP, a total of 5 L microcells are distributed in the whole network environment. We adopt a discretized-time model. According to the nonfree space propagation [20], the RSSI collected by the microcells in the area served by the AP p at time slot t is denoted by the following equation:

$$\mathbf{S_p}(t) = \left[s_{1,p}(t), s_{2,p}(t), \ldots, s_{L,p}(t)\right]^{T}, \tag{7}$$

where $s_{l,p}(t)$ is defined by

$$s_{l,p}(t) = \sum_{i=1}^{M_p} P_{i,p}(t)\left[\frac{d_{il,p}(t)}{d_0(t)}\right]^{-\tau} + \sum_{j=1}^{N_p} P_{j,p}(t)\left[\frac{d_{jl,p}(t)}{d_0(t)}\right]^{-\tau} + \Delta(t). \tag{8}$$

Therefore, the RSSI of these 5 APs is integrated and used as the input layer of LSTM-DQN, namely,

$$\mathbf{Input}(t) = \left[\mathbf{S}_1(t), \mathbf{S}_2(t), \mathbf{S}_3(t), \mathbf{S}_4(t), \mathbf{S}_5(t)\right]. \tag{9}$$

3.1.2. Action Space. We add the set of SU transmit power into the action space, and the action of all SUs in AP p at time t is

$$\mathbf{A_p}(t) = \left[P_{1,p}(t), P_{2,p}(t), \ldots, P_{N,p}(t)\right]^{T}, \tag{10}$$

where $P_{j,p}(t)$ represents the transmit power of the SU j in AP p.

Therefore, the action value of all APs in the whole network environment is

$$\mathbf{Action}(t) = \left[\mathbf{A}_1(t), \mathbf{A}_2(t), \mathbf{A}_3(t), \mathbf{A}_4(t), \mathbf{A}_5(t)\right]. \tag{11}$$

3.1.3. Reward Function. For the problem of channel allocation and power control, it is firstly necessary to consider

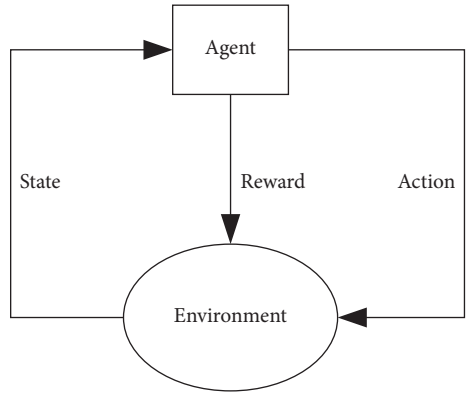

Figure 2: The interaction model of RL.

that the channels are selected by APs without conflict. Specifically, APs 1 and 2 choose different channels, 3 and 4 choose different channels, and 5 can choose any channel. Only after the APs successfully select the channels can the users perform data transmission. It should be considered that both primary and secondary users in each AP meet the service quality requirements and do not exceed the threshold. According to the constraint conditions, the reward at AP p is defined by the following equation:

$$R_p(t) = \begin{cases} \sum_j \mathrm{SINR}_{j,p}, & I_{11}, \\ -\sum_i \mathrm{SINR}_{i,p}, & I_{22}, \\ -\left(\sum_i \mathrm{SINR}_{i,p} + \sum_j \mathrm{SINR}_{j,p}\right), & \text{otherwise}, \end{cases} \tag{12}$$

where the constraints are given as follows: I_{11}: AP p access the available channel, $\forall \mathrm{SINR}_i \geq \mu_i$, $\exists \mathrm{SINR}_j \geq \mu_j$ and $\forall P_i \geq \sum_j P_j$ and I_{22}: AP p accesses the available channel, $\mathrm{SINR}_i \leq \mu_i$, $\quad i \in \{1, 2, \ldots, N\}$.

The reward function of the whole network system is

$$R(t) = \frac{\sum_p R_p(t)}{|\mathscr{P}|}, \tag{13}$$

which represents the mean value of rewards obtained by all APs.

3.2. Power Control Strategy of PUs. We consider that the PUs can adjust their transmit power according to the specified control strategy and always transmit data on the authorized channels. The typical power control strategy proposed in [21] is

$$P_i(k+1) = D\left(\frac{\mu_i P_i(k)}{\mathrm{SINR}_i(k)}\right), \tag{14}$$

where the value of $D(x)$ is no less than the minimum value of x according to the predefined range of the discretization threshold.

We also adopt the more intelligent strategy proposed in [22] as follows:

$$P_i(t+1) = \begin{cases} P_i(t) + \Delta P, & \mathrm{SINR}_i(t) \leq \mu_i \text{ and } \mathrm{SINR}_i'(t) \geq \mu_i, \\ P_i(t) - \Delta P, & \mathrm{SINR}_i(t) \geq \mu_i \text{ and } \mathrm{SINR}_i'(t) \geq \mu_i, \\ P_i(t), & \text{otherwise}, \end{cases} \tag{15}$$

where $\mathrm{SINR}_i'(t) = h_{ii}(t)P_i(t+1)/[\sum_{j\neq 1} h_{ji}(t)P_i(t) + \delta_i(t)]$, which represents the SINR of the PU i at the predicted time $t+1$.

When a PU conducts the intelligent control strategy of equation (15), according to the current SINR at time t and the predicted SINR at time $t+1$, it only needs to adjust its own transmit power only once. Therefore, the advantage of this intelligent strategy lies in that it can reduce the extra energy consumption caused by frequent power switching. At the same time, it comprehensively considers the trend estimation to determine whether the PU should adjust its transmit power and has the ability of spectrum prediction.

In order to cope with the complexity of network environment, PUs may have multiple alternative power control strategies rather than a single strategy and choose the appropriate one according to the actual situation. Equation (14) is denoted as power control strategy 1 of the PU, and equation (15) is strategy 2. We will discuss and analyse these strategies in detail in the experiments in Section 5.

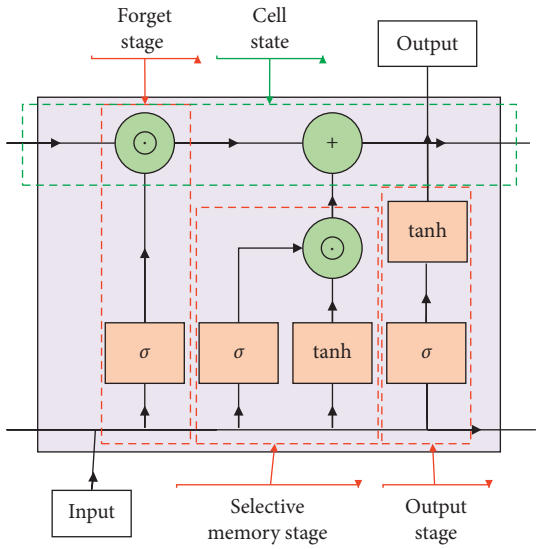

Figure 3: The unit of LSTM.

3.3. LSTM-DQN-Based Joint Channel Allocation and Power Control Algorithm. LSTM is a special recurrent neural network (RNN) [23]. As shown in Figure 3, the unit of LSTM mainly includes the forget stage, selective memory stage, and output stage, which is realized through the forget gate, input gate, and output gate, respectively. The core of LSTM is to control the cell state through these three interactive gate states. It can catch the important but implicit knowledge for a long time and discard the unnecessary message. Therefore, it shows excellent performance in solving the problem of gradient disappearance or gradient explosion in the process of long sequence training.

On one hand, it is verified that the state information of the channels has a high degree of self-correlation, which may have a considerably long time interval from the current state [24]. On the other hand, there is great potential to improve the probability of successfully access the channels owing to the unique network structure of LSTM because LSTM can effectively capture valuable knowledge that is not obvious. To track the implicit correlation over a long period of time, we combine LSTM with DQN (as shown in Figure 4) to integrate the collected partial known information and obtain better control strategies through offline learning. Once the training phase is completed, the users only need to communicate with the central unit by slightly adjusting the weight of the neural network. At each moment, the APs select the available channels and the SUs choose the optimal transmit power according to the trained DQN. The specific algorithm is shown in Algorithm 1.

4. Performance Evaluation

In this section, we evaluate the performance of our proposed algorithm through simulation-based experiments.

4.1. Experiment Settings. In our simulated scenarios, there is a circular area with a radius of 1,000 m. 3 available channels are provided for 5 APs. AP 1 has overlap with AP 2, and AP 3 has overlap with AP 4. AP 5 is independent of others. There are 10 microcells in the service range of each AP, where 1 PU and 2 SUs contend for accessing the spectrum resources. Thus, the whole network environment includes one base station, 50 microcells, 5 PUs, and 10 SUs. Specifically, the transmission power range of the PU is $\{0.0, 5.0, 10.0, \ldots 30.0\}$ mW, and the transmit power range of SU is $\{0.0, 1.0, 2.0, \ldots 12.0\}$ mW. The white noise is 0.1 mW. The SINR thresholds for primary and secondary users are 1.0 dB and 0.5 dB, respectively. According to the path loss rule of nonfree space, the channel model is now considered as the 2-ray ground reflection model of wireless propagation, and the channel gain expression is

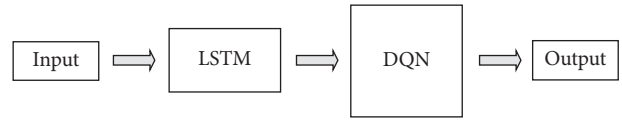

Figure 4: The structure of LSTM-DQN.

$$g = \frac{G_t G_r h_t^2 h_r^2}{d^\tau}, \tag{16}$$

where path loss index $\tau = 4$, G_t and G_r are the gain of the transmitter and receiver, respectively, and h_t and h_r are the heights of the transmit and receive antennas, respectively [20]. In order to simulate the complex change of the environment, the number of each iteration is now set to 40,000. Furthermore, the position of primary and secondary users in the environment as well as the channel gain are randomly initialized every 10,000 iterations.

The LSTM-DQN is constructed with 5 hidden layers. The first hidden layer is the LSTM layer, and the middle 4 hidden layers are the full connection layer. The number of neurons in the full connection layer is 256, 128, 128, and 256, respectively. The activation function of the second, third, and fourth hidden layers adopt ReLUs function, and the activation function of the fifth hidden layer is tanh function. Besides, Adam algorithm is used to update the weight of the neural network. The size of the training samples is set to 128. The initial exploration probability of greedy algorithm is 0.8 and linearly decreases to 0 with the number of iterations. Moreover, the memory bank has a capacity of 1,000, whereas training is not started until the capacity reaches 500 or more.

For the dynamic and the complexity of the application environment, we consider the PUs take different power control strategies. One case is in which the PUs take single control strategy 2. Another one is that each time the environmental parameters are updated, the power control strategy of 1 or 2 is chosen randomly by PUs. The proposed joint algorithm based on LSTM-DQN will be compared with two benchmark algorithms: the original DQN-based algorithm and priority memory combined with DQN- (PM-DQN-) based algorithm.

4.2. Simulation Results. Figure 5 shows the loss function of different algorithms when the PUs adopt control strategy 2,

(1) Initialization: the capacity O of memory D, the transmit power of PU and SU is $P_{i,p}(t), P_{j,p}(t)$ respectively, the channel interference matrix $\Omega_{|\mathscr{P}|\times|\mathscr{P}|}$, LSTM-estimates LSTM-DQN Q weight $\theta = \theta_0$, targets LSTM-DQN $\widehat{Q}$ weight $\widehat{\theta} = \theta_0$
(2) **For** episode = 1 to E **do**
(3) According to the initial state **Input**(0), SUs randomly select actions **Action**(0) with ε probability, otherwise choose actions **Action**(0) = $\max_a Q(\textbf{Input}(0), a; \theta)$ with $1 - \varepsilon$ probability
(4) **For** $t = 1$ to T **do**
(5) The PUs update the transmit power according to their own power control strategies
(6) SUs select actions **Action**(t) with ε_t probability, otherwise select the action **Action**$(t) = \max_a Q(\textbf{Input}(t), a; \theta)$
(7) Obtain rewards $R(t)$ and the next state **Input**$(t+1)$
(8) Save empirical data $d(t) \equiv \{\textbf{Input}(t), \textbf{Action}(t), R(t), \textbf{Input}(t+1)\}$ to memory D
(9) **If** $t > O/2$ **then**
(10) Select training sample $d(l)$ randomly from D
(11) Calculate $\widehat{Q}(l) = R(l) + \gamma \max_{a'} \widehat{Q}(\textbf{Input}(l+1), a'; \widehat{\theta})$
(12) Use the gradient descent method to minimize the loss function $[\widehat{Q}(l) - (\textbf{Input}(l+1), a'; \widehat{\theta})]^2$ and update parameters θ
(13) **End If**
(14) **End For**
(15) Reset environment parameters randomly
(16) **End For**

Algorithm 1: The joint design algorithm of LSTM-DQN.

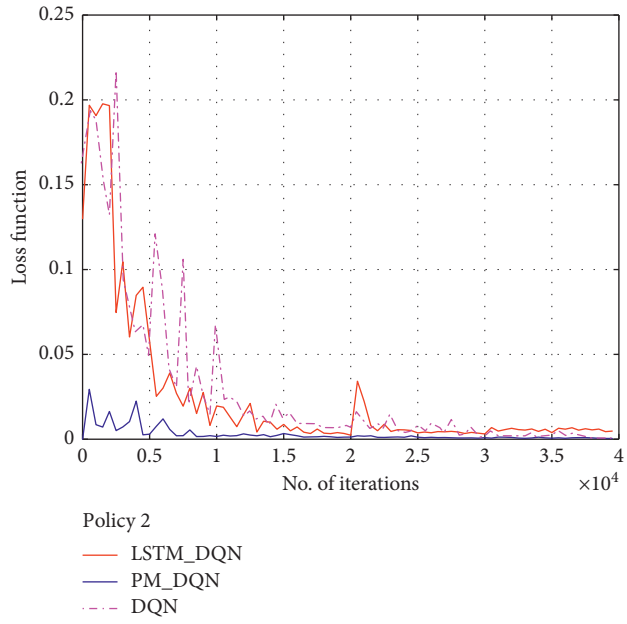

Figure 5: Relationship between the number of iterations and loss function (policy 2).

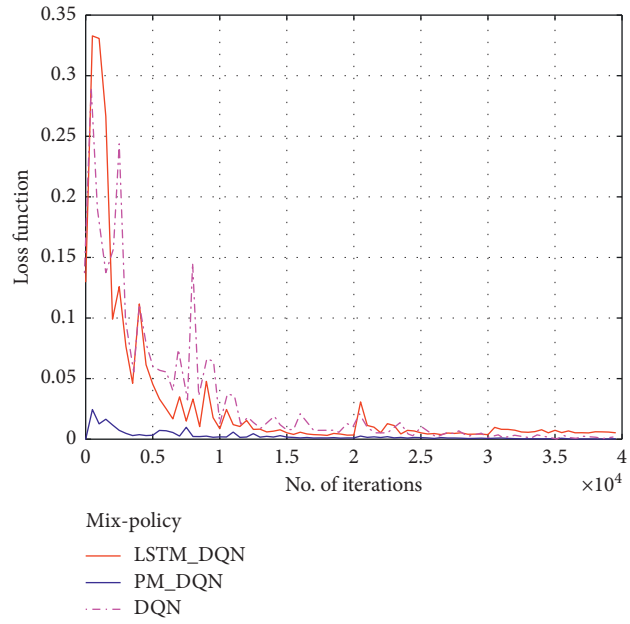

Figure 6: Relationship between the number of iterations and loss function (mix-policy).

and Figure 6 plots the loss function when the PUs employ mixed control strategies. It can be seen that all of algorithms meet convergence after iterative learning. Our LSTM-DQN algorithm has a large instantaneous fluctuation when the environmental parameters change, which is slightly better than the benchmark. On the other hand, the algorithm based on PM-DQN has less fluctuation. This is because the PM greatly accelerates the convergence rate of the loss function by cutting off the correlation, whereas the LSTM needs to correlate the past experience so that the loss function does not converge to the minimum value quickly. Nevertheless, it is meaningful for the joint problem of channel allocation and power control without Markov property. We will explain from other aspects below.

Figures 7 and 8 describe the comparison of the cumulative rewards when the PUs adopt a single and mixed control strategies, respectively. It can be seen from the results that the reward of the benchmark algorithm is always decreasing, whereas the cumulative rewards of our LSTM-DQN and the algorithm based on PM-DQN are relatively stable. Moreover, the reward of LSTM-DQN is higher. It is worth noting that the cumulative reward of LSTM-DQN is close to or slightly higher than the horizontal line of 0, which indicates that the channel allocation and power control

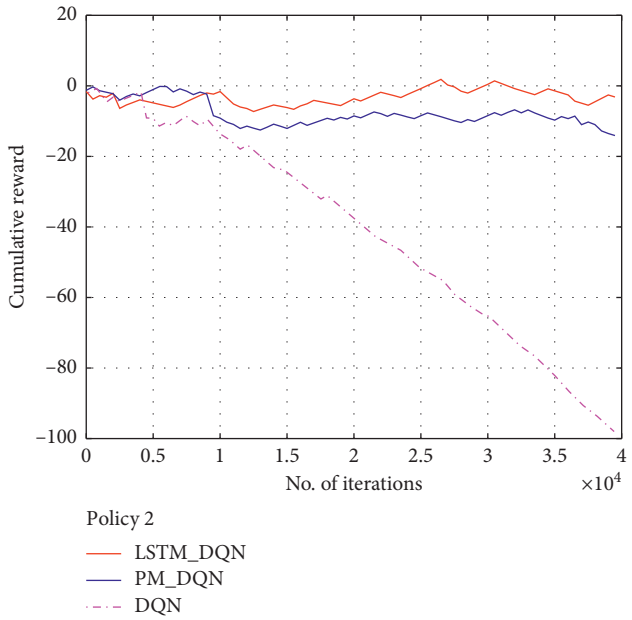

Figure 7: Relationship between the number of iterations and reward function (policy 2).

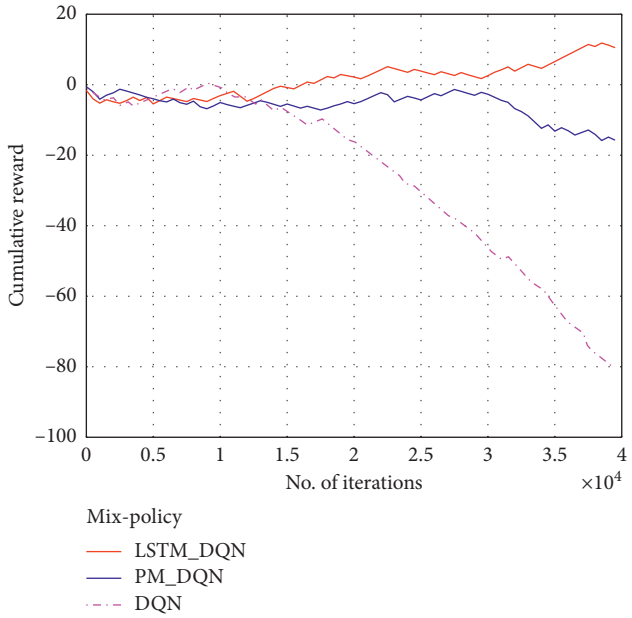

Figure 8: Relationship between the number of iterations and reward function (mix-policy).

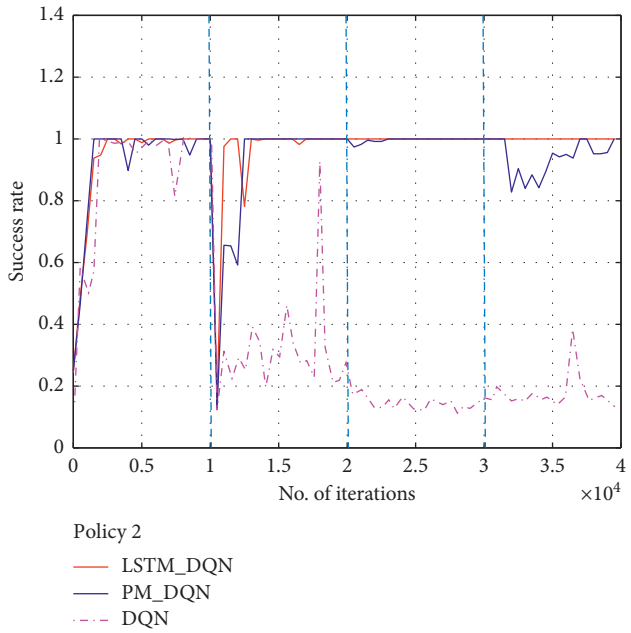

Figure 9: Relationship between the number of iterations and success rate (policy 2).

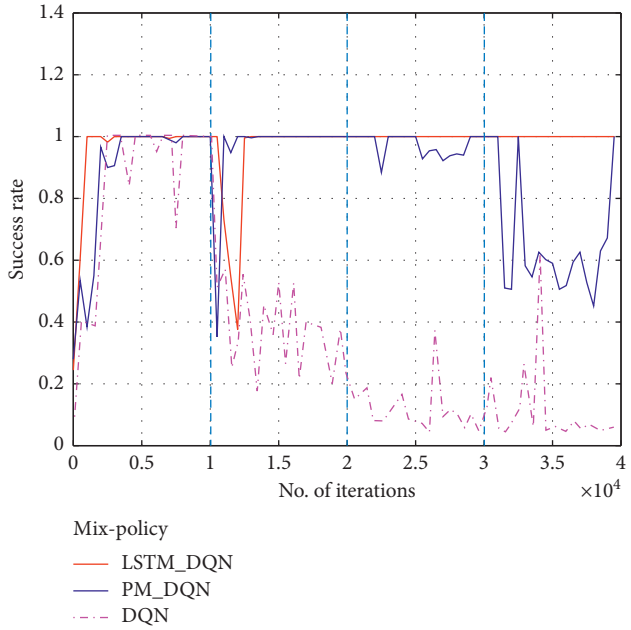

Figure 10: Relationship between the number of iterations and success rate (mix-policy).

scheme still have room for further improvement in the future work.

Figures 9 and 10 are evaluated in terms of the switching success rate. Once the user is able to access the channel and successfully complete the transmission task within 20 switches, it is deemed to a successful experience. It can be concluded from the simulation results that our LSTM-DQN can ensure the maximum success rate and adjust the strategy rapidly when the environment parameters are updated randomly. Moreover, when the PU adopts the mixed strategy, the proposed algorithm can still show excellent robustness and desirable generalization ability.

Figures 11 and 12 depict the comparison of handover steps. We observe that regardless of the control strategies adopted by the PUs, and the proposed algorithm guarantees that the optimal strategy can be found after an average of one

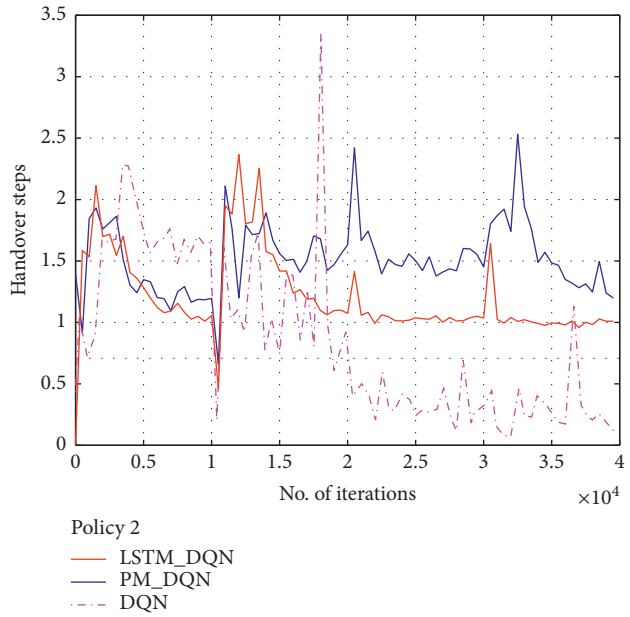

Figure 11: Relationship between the number of iterations and handover steps (policy 2).

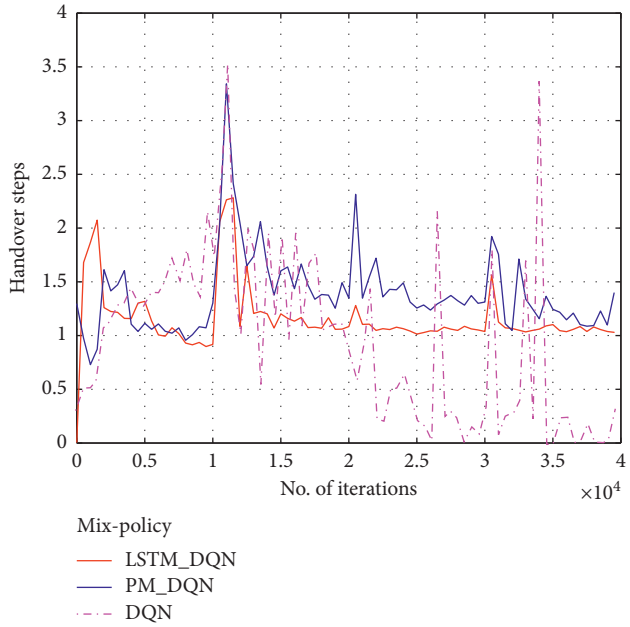

Figure 12: Relationship between the number of iterations and handover steps (mix-policy).

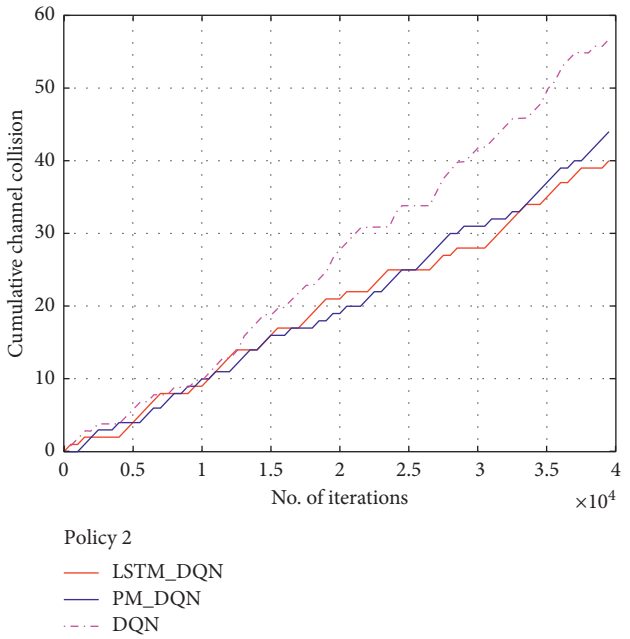

Figure 13: Relationship between the number of iterations and channel collision (policy 2).

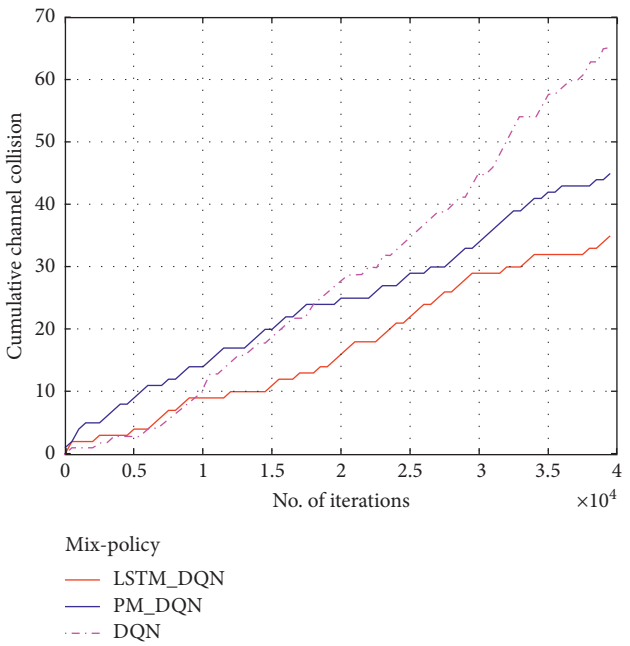

Figure 14: Relationship between the number of iterations and channel collision (mix-policy).

handover. It helps reduce the energy consumption and greatly improve the sensitivity of the users, which can react to the change of the real-time environment more quickly. Moreover, when the environmental parameters update, the proposed algorithm shows the anti-interference performance and generalization ability.

We then analyse the channel cumulative conflicts shown in Figures 13 and 14. When the PUs take the single control strategy, the proposed algorithm and the algorithm based on PM-DQN perform closely. In the situation that PUs employ the mixed strategy, LSTM-DQN-based algorithm can further reduce channel conflict. It shows that the proposed algorithm has a good potential in dealing with complex conditions.

5. Conclusion and Future Work

Aiming at the joint design problem of channel allocation and power control in CRNs, this paper proposed a novel

algorithm based on LSTM-DQN. We analysed the feasibility and implementation process of the proposed algorithm. Through simulation-based experiments, the advantages of LSTM-DQN-based algorithm were discussed and illustrated from the aspects of loss function, reward function, success rate, handover steps, and channel cumulative conflict. Specially, our proposed method outperformed other two DQN-based competitors.

Our future work will involve using real data to verify the feasibility of the algorithm. Moreover, various factors of the environment, e.g., mobility of users, can be taken into account, as to further study the large-scale spectrum resource management problems.

Data Availability

The data used to support the findings of this study are currently under embargo while the research findings are commercialized. Requests for data, 12 months after publication of this article, will be considered by the corresponding author.

Conflicts of Interest

The authors declare that there are no conflicts of interest.

Acknowledgments

This work was supported in part by the National Natural Science Foundation of China (Grant no. 61971147), Special Funds from Central Finance to support the development of local universities (Grant nos. 400170044 and 400180004), Foundation of National & Local Joint Engineering Research Center of Intelligent Manufacturing Cyber-Physical Systems, and Guangdong Provincial Key Laboratory of Cyber-Physical Systems (Grant no. 008).

References

[1] J. Chapin and W. Lehr, "Cognitive radios for dynamic spectrum access - the path to market success for dynamic spectrum access technology," *IEEE Communications Magazine*, vol. 45, no. 5, pp. 96–103, 2007.

[2] S. Srinivasa and S. Jafar, "Cognitive radios for dynamic spectrum access-the throughput potential of cognitive radio: a theoretical perspective," *IEEE Communications Magazine*, vol. 45, no. 5, pp. 73–79, 2007.

[3] M. Tang, C. Long, and X. Guan, "Nonconvex dynamic spectrum allocation for cognitive radio networks via particle swarm optimization and simulated annealing," *Computer Networks*, vol. 56, no. 11, pp. 2690–2699, 2012.

[4] A. Martínez-Vargas and Á. G. Andrade, "Comparing particle swarm optimization variants for a cognitive radio network," *Applied Soft Computing*, vol. 13, no. 2, pp. 1222–1234, 2013.

[5] S. Stotas and A. Nallanathan, "On the throughput and spectrum sensing enhancement of opportunistic spectrum access cognitive radio networks," *IEEE Transactions on Wireless Communications*, vol. 11, no. 1, pp. 97–107, 2012.

[6] D. Niyato, E. Hossain, and Z. Zhu Han, "Dynamic spectrum access in IEEE 802.22-based cognitive wireless networks: a game theoretic model for competitive spectrum bidding and pricing," *IEEE Wireless Communications*, vol. 16, no. 2, pp. 16–23, 2009.

[7] M. N. Tehrani and M. Uysal, "Auction based spectrum trading for cognitive radio networks," *IEEE Communications Letters*, vol. 17, no. 6, pp. 1168–1171, 2013.

[8] S.-S. Tan, J. Zeidler, and B. Rao, "Opportunistic spectrum access for cognitive radio networks with multiple secondary users," *IEEE Transactions on Wireless Communications*, vol. 12, no. 12, pp. 6214–6227, 2013.

[9] R. S. Sutton and A. G. Barto, "Reinforcement learning," *Journal of Cognitive Neuroscience*, vol. 11, no. 1, pp. 126–134, 1999.

[10] V. Mnih, K. Kavukcuoglu, D. Silver et al., "Human-level control through deep reinforcement learning," *Nature*, vol. 518, no. 7540, pp. 529–533, 2015.

[11] Y. Rusu, K. G. Vamvoudakis, and H. Modares, "Safe reinforcement learning for dynamical games," *International Journal of Robust and Nonlinear Control*, vol. 30, no. 9, pp. 2706–3726, 2020.

[12] Y. Wang, Z. Ye, and P. Wan, "A survey of dynamic spectrum allocation based on reinforcement learning algorithms in cognitive radio networks," *Artificial Intelligence Review*, vol. 51, no. 3, pp. 493–506, 2019.

[13] Y. Zhao, S. Zhang, Y. Zhang, P. Wan, and S. Wang, "A cooperative spectrum sensing method based on signal decomposition and *k*-medoids algorithm," *International Journal of Sensor Networks*, vol. 29, no. 3, pp. 171–180, 2019.

[14] O. Wan and K. Cohen, "Deep multi-user reinforcement learning for distributed dynamic spectrum access," *IEEE Transactions on Wireless Communications*, vol. 18, no. 1, pp. 310–323, 2019.

[15] S. He, M. Zhang, H. Fang, F. Liu, X. Luan, and Z. Ding, "Reinforcement learning and adaptive optimization of a class of Markov jump systems with completely unknown dynamic information," *Neural Computing and Applications*, 2019.

[16] J. Liu, V. Koivunen, S. R. Kulkarni et al., "Reinforcement learning based distributed multiagent sensing policy for cognitive radio networks,," in *Proceedings of the 2011 IEEE International Symposium on Dynamic Spectrum Access Networks (DySPAN)*, pp. 642–646, Aachen, Germany, May 2011.

[17] C. Wang, H. Fang, and S. He, "Adaptive optimal controller design for a class of LDI-based neural network systems with input time-delays," *Neurocomputing*, vol. 385, pp. 292–299, 2020.

[18] D. Willkomm, S. Machiraju, J. Bolot et al., "Primary users in cellular networks: a large-scale measurement study,," in *Proceedings of the 2008 3rd IEEE Symposium on New Frontiers in Dynamic Spectrum Access Networks*, pp. 1–11, Chicago, IL, USA, October 2008.

[19] X. Xing, T. Jing, W. Cheng, Y. Huo, and X. Cheng, "Spectrum prediction in cognitive radio networks," *IEEE Wireless Communications*, vol. 20, no. 2, pp. 90–96, 2013.

[20] T. S. Huo, *Wireless Communications: Principles and Practice*, Prentice-Hall, Englewood Cliffs, NJ, USA, 2002.

[21] S. A. Grandhi, J. Zander, and R. Yates, "Constrained power control," *Wireless Personal Communications*, vol. 1, no. 4, pp. 257–270, 1994.

[22] X. Li, J. Fang, W. Cheng et al., "Intelligent power control for spectrum sharing in cognitive radios: a deep reinforcement learning approach," *IEEE Access*, vol. 6, no. 25, pp. 463–473, 2018.

[23] M. Hausknecht and P. Stone, "Deep recurrent Q-learning for partially observable MDPs," in *Proceedings of the 2015 AAAI Fall Symposium Series*, pp. 29–37, Arlington, Virginia, 2015.

[24] M. Malajner, K. Benkic, P. Planinsic et al., "The accuracy of propagation models for distance measurement between WSN node," in *Proceedings of the 2009 16th International Conference on Systems, Signals and Image Processing*, pp. 1–4, Chalkida, Greece, June 2009.

Hindawi
Complexity
Volume 2020, Article ID 2394948, 16 pages
https://doi.org/10.1155/2020/2394948

Research Article

Credit Risk Assessment for Small and Microsized Enterprises Using Kernel Feature Selection-Based Multiple Criteria Linear Optimization Classifier: Evidence from China

Yimeng Wang and Yunqi Zhang

Business School, Central University of Finance and Economics, Beijing 100089, China

Correspondence should be addressed to Yimeng Wang; wangym0129@163.com

Received 26 April 2020; Accepted 20 May 2020; Published 8 June 2020

Guest Editor: Guangchen Zhang

Credit risk assessment has gained increasing marked attention in the recent years by researchers, financial institutions, and banks, especially for small and microsized enterprises. Evidence shows that the core of small and microsized enterprises' credit risk assessment is to construct a scientific credit risk indicator system, and the key is to establish an effective credit risk prediction model. Therefore, we analyze the factors that influence the credit risk of Chinese small and microsized enterprises and then construct a comprehensive credit risk indicator system by adding behaviour information, supervision information, and policy information. Furthermore, we improve the multiple criteria linear optimization classifier (MCLOC) by introducing the one-norm kernel feature selection and thereby establish the kernel feature selection-based multiple criteria linear optimization classifier (KFS-MCLOC). As for experiments, we use real business data from a Chinese commercial bank to test the performance of these models. The results show that (1) the proposed KFS-MCLOC has greater advantages in predictive accuracy, interpretability, and stability than other models; (2) the KFS-MCLOC selects 10 features from 53 original features and gives selected features their weight automatically; (3) the features selected by the KFS-MCLOC are further verified and compared by the features selected by the logistic regression model with stepwise parameter, and the indicators of "quick ratio; net operating cash flow; enterprises' abnormal times of water, electricity, and tax fee; overdue days of enterprises' loans; and mortgage and pledge status" are proved to be the most influencing credit risk factors.

1. Introduction

Nowadays, faced with the challenges of economic globalization, credit risk assessment of small and microsized enterprises has attracted more and more considerable attention from financial market investors, financial regulators, and national governments. The main purpose of credit risk assessment is to measure the possibility of enterprises' default through qualitative analysis and quantitative calculation of factors that may lead to credit risk and to provide the basis for credit decision-making and risk prevention of banks. In reality, a small increase in the level of bad credit level of enterprises will lead to huge losses to financial institutions [1]. Thus, if we can accurately evaluate the credit risk of an enterprise, it will not only promote the improvement of the enterprise's own risk management level, but also help the bank to effectively prevent the enterprise's default risk, thereby effectively improving the operation efficiency of the whole capital market.

Small and microsized enterprises have been recognized as the predominant type of business units in most Asian economies. In the recent years, small and microsized enterprises have played an increasingly important role in promoting economic growth, increasing employment opportunities, and creating industries. For example, according to the Ministry of Commerce of China, small and microsized enterprises contribute 60% of GDP, provide 80% of urban employment opportunities, and introduce 75% of new products, accounting for 65% of patents and inventions. Thus, the important role played by Chinese small and microsized enterprises can be seen obviously.

Therefore, it is necessary to establish a credit risk indicator system and a credit risk assessment model, especially for small and microsized enterprises.

However, the construction of the small and microsized enterprises' credit risk indicator system is different from that of the large enterprises. For instance, the financial information of small and microsized enterprises is incomplete and opaque, thereby cannot objectively and truly reflect the comprehensive credit risk status of SMEs. So, it is far from enough to only use financial information, whereas it is mainly used by large enterprises. How to build a comprehensive credit risk indicator system by including some behavior variables, supervision variables, and other novel related variables becomes the main focus in today's SMEs' credit risk assessment. Moreover, the improvements and optimization of models can further increase the predictive accuracy to better help enterprises and financial institutions with their risk management and risk prevention.

Recently, many researchers have paid great attention to improve the algorithm of the credit risk assessment models, including statistical models, intelligent models, and optimization models. Evidence indicates that the models used nowadays are more advanced and complicated than before, and these models are also proved to be more effective than before. For instance, Zhang et al. proposed a sparse multicriteria optimization classifier to deal with credit risk assessment. The results showed that the proposed model is more efficient and has better interpretability as well as generalization power [2]. Zhang et al. presented an improved sequential minimal optimization learning algorithm named FV-SMO by using the credit data from the Chinese Banking Regulatory Commission. The experimental results demonstrated that FV-SMO performed much better in saving the computational cost and increasing predictive accuracy compared with the other five state-of-the-art classification methods in enterprises' credit risk assessment [3]. However, few of them study how to carry out feature selection and classification simultaneously.

In this paper, firstly, we construct a credit risk indicator system especially for Chinese SMEs, which contains six parts, that is, basic information, financial information, actual controllers' information, behavior information, supervision information, and policy information. Secondly, we improve the MCLOC from two aspects. Firstly, the one-norm of feature kernel weight vector is introduced into the objective function of MCLOC for feature selection and data dimensionality reduction. Secondly, the kernel feature selection is introduced, and the importance of each feature is expressed by the weight of the kernel feature. The empirical results show that the KFS-MCLOC not only shows high accuracy in predictive performance, but also has great advantages in the feature selection process. The experimental results are shown as follows. Firstly, the proposed KFS-MCLOC has greater advantages in predictive accuracy, interpretability, and stability than other models. Secondly, the KFS-MCLOC selects 10 features from 53 original features and gives selected features their weight automatically. Thirdly, the features selected by the KFS-MCLOC are further compared with the features selected by the logistic regression model with stepwise parameter, and the comparison results show that the indicators of "quick ratio; net operating cash flow; abnormal times of water, electricity, and tax fee; overdue days of enterprises' loans; and mortgage and pledge status" are proved to be the most influencing risk factors.

The remaining sections are structured as follows. Section 2 provides an introduction to credit risk assessment, feature selection, and sparse learning and classification models, with reviews and comparison of the related literatures. Section 3 proposes a new model—kernel feature selection-based multiple criteria linear optimization classifier (KFS-MCLOC). Section 4 presents the experimental design, including the Chinese small and microsized enterprises' credit risk indicator system, dataset description and preprocessing, parameter setting, and models' evaluation criteria, whilst Section 5 describes and analyzes the experimental results. Finally, Section 6 is devoted to the conclusions as well as future work.

2. Literature Review and Related Works

At present, the research studies on credit risk assessment of small and microsized enterprises in academia and practice mainly focus on two aspects: one is the design of the credit risk indicator system; the other is the construction of the credit risk prediction model. In this section, we review and discuss the credit risk indicator system, feature selection methods, and credit risk assessment models by using examples from the past literature.

2.1. Credit Risk and Credit Risk Assessment. Credit risk assessment is emerging as an important concerning topic nowadays. Recently, it has played a more and more important role in assessing the credit worthiness of individuals and enterprises. Generally, the enterprises' credit risk refers to the risk associated with financing problems [3]. Credit risk can not only lead to creditors' economic losses, but also lead to business failure (or corporate distress or bankruptcy or corporate failure). Therefore, how to avoid the credit risk crisis of small and microsized enterprises has been a main focus in the recent years. The purpose of enterprises' credit risk assessment is to distinguish enterprises from good ones to bad ones by various methods, which is essentially a binary classification problem. Recently, the binary classification problem has become the focus of research in the fields of statistics, machine learning, and optimization algorithms, and various methods including logistic regression, SVM, ANN, and MCLPC have been applied to solve this problem.

2.2. Credit Risk Assessment Models

2.2.1. Statistical Models. Originally, credit risk was evaluated by experts' experience and then evolved into the 5Cs theory. With the development of statistical technology, statistical methods were applied to predict the enterprises' credit risk. In 1936, Fisher first established a discriminant analysis to discriminate between the two groups of applicants, which is a very classical statistical method [4]. Later on, Altman proposed a famous Z-score model, which is based on the discriminate analysis model [5]. After that, Orgler applied

linear regression into credit risk evaluation aiming at differentiating between "good" and "bad" credit applicants for commercial banks in practical credit-scoring applications [6]. However, linear regression has strict linear assumption and many other restrictions. Wiginton proposed the logistic regression model for bankruptcy prediction [7]. Since logistic regression has no linear requirement and is easy to understand and interpret, this method is widely used to solve credit risk assessment problems in real business practice. However, for most statistical methods, the shortcomings are obvious, such as they cannot deal effectively with high-dimensional data, they have some assumptions, and their computation time is too long.

2.2.2. Artificial Intelligence Models. In the recent years, with the development of machine learning and the wide use of big data, more and more sophisticated intelligence approaches emerge which are widely applied to enterprises' credit risk prediction, such as neural networks [8–10], genetic algorithms [11,12], and decision trees [13–16]. The literature shows that the intelligent techniques performed better in credit risk assessment than traditional statistical methods [17], and artificial intelligence methods proved to have higher computation accuracy, less computation time, and lower computation cost. Nevertheless, the higher predictive accuracy of artificial intelligence models is often associated with lower interpretive power and longer training time. So, despite the advantages of using intelligent methods, there are still some challenges. For example, most artificial intelligence methods, such as ANN methods, are "black box" methods, whose output result cannot directly interpret the credit risk evaluation result. However, whether the results can be explained is of great importance in practice since most rejected credit applicants will ask for the reasons for refusal. Lu et al. believed that it is very important to determine the importance of each variable by decision rule generation tools before using a black box for prediction [18].

2.2.3. Optimization Models. Besides conventional statistical techniques and artificial intelligence techniques, more attention has been paid to the collaborative use of optimization methods and data mining methods. For example, the SVM, which was first proposed by Cortes and Vapnik, can achieve a higher generalization power and promising results relative to other classification techniques in credit risk modelling [19]. Subsequently, many researchers used improved SVM based on optimizing theory for enterprises' credit risk assessment. Yao et al. proposed a novel two-stage model which is based on the least square support vector machine, and the results showed that this model yields better performance than that of the other statistical models [20].

Moreover, similar to the idea of SVM, mathematical programming optimization techniques such as linear programming, quadratic programming, integer programming, and multicriteria linear programming, which are also based on the optimizing and data mining methods, are widely used in credit risk assessment. Meanwhile, the literature shows that the mathematical programming techniques are shown to have higher predictive accuracy and better explanatory power. In the early 20th century, Shi et al. proposed a compromise solution-based MCLPC model by using behavior analysis of credit cardholders [21]. Maldonado et al. proposed a mixed-integer linear programming model for simultaneous classification and feature selection. The experimental results showed the effectiveness of this method in terms of predictive performance [22]. In addition, some other researchers also solved the linear and nonlinear problems through optimization methods [23,24].

2.3. Feature Selection and Sparse Learning. Feature selection is a necessary step to select features from a large number of data when using classification algorithms to build credit risk assessment models because the quality of data will significantly affect the performance of almost all algorithms. In most cases, it is highly possible that the real-world data contain many irrelevant and redundant features, whereas an appropriate feature selection method can reduce high feature dimension and remove irrelevant features and redundant features [12]. Ala'raj and Abbod's experimental results proved that choosing an optimal subset of features can improve prediction accuracy of the classifiers when constructing the hybrid model [25]. Zhang et al. also indicated that feature selection process was of great importance in reducing the computation time and increasing predictive accuracy [26].

Generally, the two most commonly used feature selection methods are filter and wrapper [27]. However, these two methods can only improve the predictive accuracy, but cannot automatically find out the most important features. To improve the interpretation ability, some researchers proposed to solve this problem by the sparse method, among which zero-norm and one-norm are more typical data sparse methods. Generally, zero-norm regularization is considered as a good method in theory. However, since zero-norm is a nonconvex discontinuous function, the corresponding mathematical problems are difficult to solve and domain knowledge is needed to control the value of superparameters, so it is not suitable for large-scale high-dimensional data problems. However, because of its convexity, one-norm can be directly used in the case of sparse features. In general, these sparse methods are difficult to integrate into kernel functions of high-dimensional feature space. More recently, many researchers have studied the sparse method; for instance, Sun used sparse nonnegative matrix factorizations for reducing the data dimensionality, and the empirical results showed that the NMF-SVM model has the relatively good predictive performance [28]. Mei proposed a sparse coding with sparse dictionaries (K-SVD method) for enterprises' credit risk prediction, and the empirical results demonstrated that this method shows a superior predictive performance [17].

3. Research Methodology

3.1. Multiple Criteria Linear Optimization Classifier (MCLOC). For a binary classification problem and given dataset $D = \{(\mathbf{x}_1, y_1), \ldots, (\mathbf{x}_n, y_n)\}$ with a feature set $X = (X_1, \ldots, X_d)^T$, each input point $\mathbf{x}_i (\mathbf{x}_i \in R^d)$ belongs to

the class label y_i where $y_i \in \{-1, 1\}$, d is the dimensionality of the input space, and n is the sample size.

According to these research works [29–31], two measures can be used to make a separation between the positive class and the negative class for solving a two-class classification problem. One measure is the overlapping degree of deviation from the separating hyperplane, and another is the distance between input points and the separating hyperplane, respectively. Thus, in the case of linearly separable data, a multiple criteria linear optimization classifier (MCLOC) model can be denoted as

$$\begin{aligned} \min_{w,b,\alpha,\beta} \quad & C\sum_{i=1}^{n}\alpha_i - \sum_{i=1}^{n}\beta_i \\ \text{s.t.} \quad & y_i\left(\mathbf{w}^T\mathbf{x}_i - b\right) = \beta_i - \alpha_i, \quad \alpha_i \geq 0, \beta_i \geq 0, \\ & i = 1, \ldots, n, \end{aligned} \tag{1}$$

where α_i ($\alpha_i \geq 0$, $\alpha = (\alpha_1, \ldots, \alpha_n)^T$) is the distance at which an input point $\mathbf{x}_i$ deviates from the separating hyperplane $\mathbf{w}^T\mathbf{x}_i = b$, $\beta_i (\beta_i \geq 0, \beta = (\beta_1, \ldots, \beta_n)^T)$ is the distance where the input point $\mathbf{x}_i$ departs from the decision hyperplane, the penalty constant $C(C > 0)$ is used to tradeoff the overlapping degree $\sum_{i=1}^{n}\alpha_i$ and the separation degree $\sum_{i=1}^{n}\beta_i$, the weight vector $\mathbf{w}(\mathbf{w} = (w_1, \ldots, w_d)^T)$ consists of the weights of different features, and the scalar $b(b \in R)$ is the unrestricted variable.

3.2. Multiple Criteria Quadratic Optimization Classifier (MCQOC). For the MCOC model in (1), the function $\|\mathbf{w}\|_2^2$ regarding the weight vector $\mathbf{w}$ with a penalty factor $D(D > 0)$, which determines the complexity of the classifier model, is also added to the objective function of the classification problem. Besides, the linear sum of errors is replaced by the squared sum. Thus, we get a multiple criteria quadratic optimization classifier (MCQOC) with the quadratic objective function and the linear constraints, which can be denoted as

$$\begin{aligned} \min_{w,b,\alpha,\beta} \quad & D\|\mathbf{w}\|_2^2 + C\sum_{i=1}^{n}\alpha_i^2 - \sum_{i=1}^{n}\beta_i \\ \text{s.t.} \quad & y_i\left(\mathbf{w}^T\mathbf{x}_i - b\right) = \beta_i - \alpha_i, \quad \alpha_i, \beta_i \geq 0, \\ & i = 1, \ldots, n. \end{aligned} \tag{2}$$

Based on the constraints in the MCOC model in (2), we can calculate the intercept $b(b \in \mathbb{R})$, and the separating hyperplane regarding the weight vector $\mathbf{w}(\mathbf{w} \in \mathbb{R}^d)$ is defined as

$$\mathbf{w}^T\mathbf{x} - b = 0, \tag{3}$$

where $\mathbf{x}$ is any input point from the independent test set.

Thus, for a new input point $\mathbf{x}$, its class label y can be predicted by the following decision function:

$$f(\mathbf{x}) = \operatorname{sign}\left(\mathbf{w}^T\mathbf{x} - b\right). \tag{4}$$

Thus, the input point $\mathbf{x}$ is classified as the positive class ($y = 1$) if $\mathbf{w}^T\mathbf{x} \geq b$. Otherwise, the input point $\mathbf{x}$ is classified as the negative one ($y = -1$).

In general, there are three main characteristics that make the multiple criteria optimization classifier (MCOC) more popular than some other traditional classifier models. Firstly, either the principle of MCOC or the algorithm of MCOC is relatively easy to interpret in practice. Secondly, MCOC gains a perfect generalization power as well as an excellent classification accuracy rate since it can correctly find the best balance between minimizing the overlapping degree and maximizing the total distance departed from the boundary. Thirdly, it is shown that since it is very easy and simple to implement the MCOC classifier and adjust its parameters, the performance of the model can be improved considerably. Besides, for the multiclass classification problem, the above MCOC model can be changed into multiple one versus one and one versus the rest classifiers.

3.3. The KFS-MCLOC Model. Nonlinear separable data often appear in the real business world, especially when classifying the credit status of SMEs. Traditionally, a basis function $\phi(\cdot)$ can be used to transform the nonlinear problem into a linear problem by mapping the input points from the input space to the new high-dimensional feature space, where data are linearly separable. For any input point $\mathbf{x}_j$ from the training set D, the weight vector $\mathbf{w}$ is expressed as a linear combination with respect to the instance coefficient vector $\lambda(\lambda = (\lambda_1, \ldots, \lambda_n)^T)$ and class label $\mathbf{y}$, and we have

$$\mathbf{w} = \sum_{j=1}^{n}\lambda_j y_j \phi\left(x_j\right). \tag{5}$$

Then, for any two input points $\mathbf{x}_i$ and $\mathbf{x}_j$ from the training set D, their dot product $\phi(\mathbf{x}_i)^T\phi(\mathbf{x}_j)$ with respect to the basis function $\phi(\cdot)$ can be replaced with the kernel function $K(\mathbf{x}_i, \mathbf{x}_j)$. Therefore, the separating hyperplane is reformulated as

$$\sum_{j=1}^{n}\lambda_j y_j K\left(\mathbf{x}_j, \mathbf{x}\right) = b. \tag{6}$$

Here, for any two input points $\mathbf{x}_i$ and $\mathbf{x}_j$ from the training set D, their dot product $\phi(x_{i,m})^T\phi(x_{j,m})$ with respect to the $m$thdimension is replaced by the mth dimensional kernel $k_m(x_{i,m}, x_{j,m})$. Let the feature kernel weight vector be $\mu(\mu = (\mu_1, \ldots, \mu_d)^T)$, then the total kernel function $K(\mathbf{x}_j, \mathbf{x}_i)$ is further defined as the linear combination of $k_m(x_{i,m}, x_{j,m})$ and the kernel weight of $\mu_m (\mu_m \in R)$. Thus, we have

$$K\left(\mathbf{x}_j, \mathbf{x}_i\right) = \sum_{m=1}^{d}\mu_m k_m\left(x_{j,m}, x_{i,m}\right). \tag{7}$$

For the purpose of dimensionality reduction, the one-norm of the feature kernel weight vector μ with the sparsity factor S can be introduced to the MCLOC model in (1). At the same time, the kernel feature selection is realized by applying the total kernel function to the MCLOC model in (1), so the kernel feature selection-based MCLOC (KFS-MCLOC) model can be written as

$$\begin{aligned} \min_{\mu,b,\alpha,\beta} \quad & S\|\boldsymbol{\mu}\|_1 + C\sum_{y_i=-1}\alpha_i - \sum_{i=1}^{n}\beta_i \\ \text{s.t.} \quad & y_i\left[\sum_{j=1}^{n} y_j \sum_{m=1}^{d} \mu_m k_m\left(x_{j,m}, x_{i,m}\right) - b\right] = \beta_i - \alpha_i, \quad 0 \le \beta_i, 0 \le \alpha_i \le C, \mu_m \in \mathbb{R}, \\ & \qquad\qquad i, j = 1, \ldots, n. \end{aligned} \tag{8}$$

Owing to the discontinuity of the one-norm of the feature kernel weight vector μ in the objective function in the KFS-MCLOC model in (8), let $|\mu_m| \le t_m (t_m \ge 0)$, and we have the final KFS-MCLOC model with the form

$$\begin{aligned} \min_{\mu,b,\alpha,\beta} \quad & S\sum_{m=1}^{d} t_m + C\sum_{i=1}^{n}\alpha_i - \sum_{i=1}^{n}\beta_i \\ \text{s.t.} \quad & y_i\left[\sum_{j=1}^{n} y_j \sum_{m=1}^{d} \mu_m k_m\left(x_{j,m}, x_{i,m}\right) - b\right] = \beta_i - \alpha_i, 0 \le \beta_i, 0 \le \alpha_i \le C, -t_m \le \mu_m \le t_m, 0 \le t_m \le S, \\ & \qquad\qquad i, j = 1, \ldots, n, \\ & \qquad\qquad m = 1, \ldots, d. \end{aligned} \tag{9}$$

As shown in (9), the feature kernel weight μ_m represents the importance of each feature. The larger the μ_m, the higher the importance of the feature in the mth dimension. And then, the mth feature should be held in the feature space. Otherwise, the feature is redundant which can be removed from the feature space. In this way, the high-dimensional feature vector can be transformed to a low-dimensional feature vector by the feature kernel weight vector in the total kernel function, which can make it efficient for the model to make later calculation.

For any input point $\mathbf{x}$, its class label can be determined by the following decision function:

$$f(x) = \operatorname{sign}\left[\sum_{j=1}^{n} y_j \sum_{m=1}^{d} \mu_m k_m\left(x_{j,m}, x_{i,m}\right) - b\right], \tag{10}$$

where for any input point $\mathbf{x}_i$ with $\alpha_i = 0$ and $\beta_i > 0$, the intercept b can be obtained by $b = \sum_{j=1}^{n} y_j \sum_{m=1}^{d} \mu_m k_m(x_{j,m}, x_{i,m})$, based on the optimal feature kernel weight vector μ.

Finally, for two input points $\mathbf{x}_i$ and $\mathbf{x}_j$, the RBF kernel function regarding the mth feature is defined as

$$k_m\left(x_{j,m}, x_{i,m}\right) = \exp\left(-\frac{\left(x_{j,m} - x_{i,m}\right)^2}{2\sigma^2}\right), \tag{11}$$

where the parameter σ is specified by the user.

3.4. Algorithmic Design of KFS-MCLOC. The overall process of the experimental design of KFS-MCLOC is shown in Figure 1.

This process can be divided into several stages as follows:

Stage 1. Data Preprocessing. We will use the Binning method and the min-max normalization method to normalize the original dataset

Stage 2. Data Partitioning. We will divide the dataset into the training subset and the test subset, and we will use the five-fold cross-validation method for the training process

Stage 3. Parameter Setting. We will use grid-search method for parameter setting

Stage 4. Two-Stage KFS-MCLOC Model and Other Models. We will test KFS-MCLOC, logistic regression, SVM, neural networks, MCLOC, and MCQOC with the test set to get the predictive results

Stage 5. Predictive Results and Performance Evaluation of Models. We will use seven performance criteria, including the total accuracy, F_1 score, MCC, KS score, AUC, type-I accuracy, and type-II accuracy, to evaluate six models' predictive performance

Stage 6. Feature Importance Analysis. We will use importance analysis and the reduction rate to make an in-depth analysis of the selected features

4. Empirical Design for Small and Microsized Enterprises' Credit Risk Assessment

In this section, we use the proposed KFS-MCLOC and other classifiers for small and microsized enterprises' credit risk assessment, and this section includes four parts, that is, Chinese small and microsized enterprises' credit risk indicator system, data description and data preprocessing, parameter setting, and performance evaluation criteria.

4.1. Design of Small and Microsized Enterprises' Credit Risk Indicator System. In this experiment, the dependent variable is defined by whether it is in credit risk status. If the enterprise is in credit risk status, then the indicator will be equal to 1; otherwise, the indicator will be equal to 0.

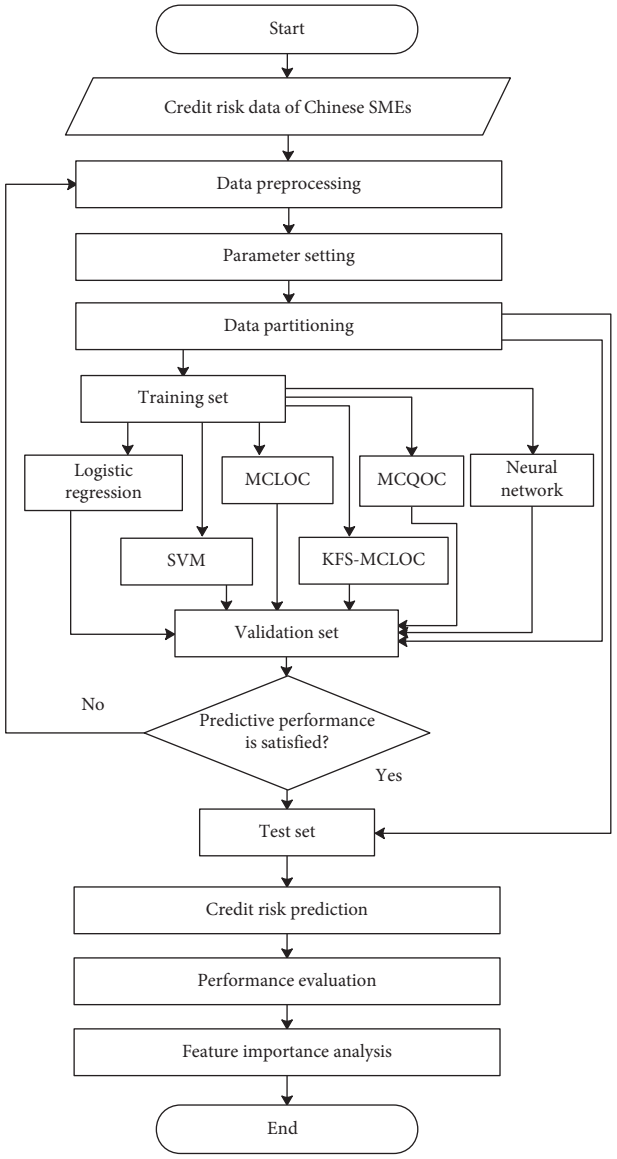

Figure 1: The overall process of the KFS-MCLOC algorithm for small and microsized enterprises' credit risk assessment.

Meanwhile, as for independent variables, a total of 53 credit risk indicators are selected as initial input variables. Based on the characteristics of small and microsized enterprises, we construct a multidimensional and multilevel credit risk indicator system especially for Chinese small and microsized enterprises, and these variables are picked based not only on the financial experts' suggestions but also on the past classical and influential literature [32]. On the whole, the credit risk indicators in this paper can be broadly classified into six overall dimensions: basic information, enterprises' financial information, the actual controller's information, behavior information, supervision and evaluation information, and policy information.

First of all, the basic information of the enterprise directly reflects the most basic situation of the enterprise and reflects the basic quality of the enterprise itself. In general, the higher the quality of the enterprise itself, the less the credit risk of the enterprise will be. Experience shows that the size and the ownership structure of the enterprises are very essential for credit risk assessment. Moreover, the industry to which the enterprise belongs also has a great influence on whether the enterprise will go bankrupt in the future. This is because some industries are largely affected by macroeconomic factors such as national policies, which may lead to unstable operating conditions to enterprise. The description of enterprises' basic information is shown in Table 1.

In the second level, the financial information is an indispensable link in the construction of the credit risk indicator system. The literature shows that the financial information of the enterprise must be fully considered when constructing the enterprise credit evaluation index system. Hence, we select commonly used financial indicators (solvency, profitability, operating capacity, and growth capacity) to reflect the financial situation of the enterprise and select the cash flow-related indicators to reflect the capital turnover of the enterprise. The description of small and microsized enterprises' financial information is shown in Table 2.

As for the third level, we focus on the information about small and microsized enterprises' actual controllers. It is of great importance since the management right and ownership of small and microsized enterprises are usually highly concentrated in the hands of the actual controller, which means that the actual controller has the absolute power to influence the decision-making and the future development direction of the enterprise. Simon found that managerial ability plays a much higher role in predicting credit rating performance than other indicators [33]. Karabag found the great impact of top management actions and the quality of human resources about enterprises' failures [34]. In terms of the existing literature, we find that some indicators are frequently chosen, for instance, marital status, educational background, age, gender, daily behavior, and their credit status. In this paper, the actual controller's information includes the basic information, behaviour information, and supervision information. The description of the actual controller's information is shown in Table 3.

In terms of the fourth level, we focus on the small and microsized enterprises' behaviour information. Under the "Internet Plus" and "Big Data Era," enterprises' behaviour records are increasingly being concerned by the government, financial institutions, and counterparts. Since the influence of enterprises' behaviour becomes more and more extensive, researchers pay more attention to the enterprises' daily behaviour. In fact, nowadays, the relationship between the expected behaviour of enterprises and their past social relations as well as their past behaviour rules is far more important than that of their financial information. For instance, Wang et al. proved that besides conventional hard information, soft information like behaviour information also enters into the lending decision process [35]. Therefore, we add the behaviour information to supplement the content of the credit risk indicator system. The description of behaviour information is shown in Table 4.

As for the fifth level, since supervision information reflects the past production, operation, and credit status of the enterprise, it can help the government to better supervise enterprises and help banks to better prevent the default risk. Therefore, supervision information is necessary. The

Table 1: Small and microsized enterprises' basic information.

Variable	Variable name	Variable definition
X_1	Registered capital	The amount of registered capital
X_2	The size of enterprises	Micro 1, small 2
X_3	The size of employees	The number of the enterprises' employees
X_4	Years of establishment	1 plus years since the enterprises' started to incorporate
X_5	The nature of enterprises	Private 1, collective 2, foreign commercial 3, Hong Kong, Macao, and Taiwan 4, state owned 5.
X_6	Industry of enterprise	Manufacturing 1, wholesale and retail 2, electricity and thermal 3, transportation 4, water conservancy 5, agriculture and forestry 6, construction 7, resident service 8, and mining 9

Table 2: Small and microsized enterprises' financial information.

Variable	Category	Variable name
X_7	Solvency	Asset-liability ratio
X_8		Current ratio
X_9		Quick ratio
X_{10}		Interest coverage ratio
X_{11}		Operating cash flow liability ratio
X_{12}	Profitability	Return on total asset
X_{13}		Gross profit margin
X_{14}		Return on sales
X_{15}		Return on total assets
X_{16}		Return on equity
X_{17}	Operating capacity	Inventory turnover ratio
X_{18}		Account receivable turnover
X_{19}		Total asset turnover
X_{20}	Growth capacity	Sales growth rate
X_{21}		Profit growth rate
X_{22}		The growth rate of total assets
X_{23}	Cash flow information	Capital accumulation rate
X_{24}		Net cash flow from operating activities
X_{25}		Net cash flow

Table 3: Actual controller's information.

Variable	Category	Variable name	Variable definition
X_{26}	Actual controller's basic information	Family status	Married 1, unmarried 2, divorce 3
X_{27}		Educational background	High school 1, secondary school 2, college 3, university 4
X_{28}		Gender	Male 1, female 2
X_{29}		Age	The age of the actual controller
X_{30}	Actual controller's behaviour information	Managerial experience	Number of year that the actual controller engaged in management
X_{31}		Number of self-owned enterprises	Number of enterprises owned by the actual controller
X_{32}		Accumulated overdue repayment	Accumulated overdue repayment times of the actual controller in the bank in the past two years
X_{33}		Financial situation of actual controller	Amount of deposit owned by the actual controller
X_{34}	Actual controller's supervision information	Whether there are bad tax records and illegal behaviours	Yes 1, no 0
X_{35}		Positive comments	Number of positive comments of actual controller
X_{36}		Negative comments	Number of negative comments of actual controller

description of supervision and evaluation information is shown in Table 5.

Finally, in the macrolevel, policy information can largely influence the future development direction of the enterprises. In general, enterprises which are in line with national industrial policies or bank's own policy are more likely to get credit support from banks; on the contrary, banks will be more cautious. The basic description of policy information is shown in Table 6.

Table 4: Small and microsized enterprises' behaviour information.

Variable	Variable name	Variable definition
X_{37}	Whether the wages of employees in the past 12 months can be paid on time	Yes 1, no 0
X_{38}	Employees provided with insurance	The proportion of employees provided with insurance
X_{39}	Whether water, electricity, and tax fees are abnormal in the past 12 months	Abnormal times of water, electricity, and tax in the past 12 months
X_{40}	Change of manager in the past three years	The number of the changes of the general manager in the past three years
X_{41}	Whether has credit business with the bank	Yes 1, no 0
X_{42}	Overdue enterprise loans	Overdue days of enterprises' loans
X_{43}	Whether affiliated enterprises is abnormal	Yes 1, no 0
X_{44}	Mortgage and pledge status	Whether the mortgage and pledge of enterprises is abnormal
X_{45}	Whether the guarantee enterprise is abnormal	Yes 1, no 0

Table 5: Supervision and evaluation information.

Variable	Category	Variable name	Variable definition
X_{46}	Abnormal information of business operation	Business exceptions	Number of business exceptions
X_{47}		Administrative sanction	Number of administrative sanction
X_{48}	Judicial litigation information	Civil judgment document	Number of civil judgment document
X_{49}		Abnormal tax payment	Number of abnormal tax payment
X_{50}	Evaluation information	Positive comments	Number of positive comments
X_{51}		Negative comments	Number of negative comments

Table 6: Policy information.

Variable	Variable name	Variable definition
X_{52}	Whether the enterprise complies with the preferential policies of the bank	Yes 1, no 0
X_{53}	Whether the enterprise conforms to the industry preferential policies	Yes 1, no 0

4.2. Data Description and Data Preprocessing

4.2.1. Data Description. The data we use in this paper come from a Chinese commercial bank. This dataset comprises 188 small and microsized enterprises, in which 130 enterprises are regarded as "not in credit risk status (normal)" while 58 of them are regarded as "in credit risk status (default)." The enterprises we choose cover various industries, such as industrial enterprises, agricultural enterprises, and marine enterprises. Moreover, the nature of enterprises also covers many types, such as private, joint venture, and foreign capital. In terms of data type, this dataset includes various types of variables, such as binary data (male/female), character data (bank's historical credit rating), and numerical data (financial ratios). Therefore, the enterprises' data chosen in this paper are relatively representative.

4.2.2. Data Preprocessing. In reality, irrelevant and redundant features will not only reduce the predictive performance of a classification model but also increase the computational complexity [36]. Generally, data will be firstly preprocessed before going to the model by converting the initial data to standard form data. In this paper, the "Binning" and "min-max normalization" are used as data preprocessing methods. The process of using the min-max normalization method is shown as follows:

$$X' = \frac{X - X_{\min}}{X_{\max} - X_{\min}}, \tag{12}$$

where $X_{\min}$ represents the minimum value of X and $X_{\max}$ represents the maximum value of X.

In order to ensure the typicality of sample data extraction, we adopt the stratified random sampling method to collect samples from the training set. Through the stratified random sampling method, 70 normal enterprises and 30 default enterprises are selected from the total samples as training samples. The remaining 60 normal enterprises and 28 default enterprises are used as test samples. The distribution of the sample is shown in Table 7.

In addition, Stone proved that the cross-validation method is an effective method to test the strength of the predictive power of models [37]. Since the K-fold cross-validation is applied due to its properties of being simple, easy, and using all data for training and validation [38], we use a five-fold cross-validation for each of the aforementioned classifiers on the training subset in each iterative process. After that, we can obtain the final predictive accuracy by using the average of the five groups' results. Furthermore, an iterative process on the predefined

Table 7: Distribution of samples.

Sample set	Number of total enterprise	Number of normal enterprise	Number of default enterprise	Proportion of normal enterprise (%)	Proportion of default enterprise (%)
Total sample set	188	130	58	69.15	30.85
Training set	100	70	30	70	30.00
Test set	88	60	28	68.18	31.82

parametric set will be used to find the best parameter. At last, the predictive performance of each classifier will be reported for comparison in order to get the best classification accuracy.

4.3. Parameter Setting. Based on the given training set, we employ the 5-fold cross-validation method to train KFS-MCLOC, SVM, neural networks, MCLOC, and MCQOC, and then they are tested by using the independent test. In the process of training these classifiers, some discrete sets corresponding with different parameters are predefined. As for neural networks, we define a two-dimensional grid corresponding with various numbers of hidden layers and nodes in each hidden layer to search the optimal network structure. That is, the number of hidden layers took values from 1 to 3, while the number of nodes in each hidden layer varies from 10 to 50 with the stride 2. For the SVM classifier, the optimal penalty factor C is selected from the set {1, 2, 5, 10, 20, 50, 100, 200, 500, 1000}, whereas the range of the parameter σ is set to {0.01, 0.05, 0.1, 0.2, 0.5, 1, 2, 5, 10, 20, 50, 100} for the RBF kernel function. For MCLOC, MCQOC, and KFS-MCLOC, the penalty factor C and the shrinkage factor S for feature selection are uniformly defined as the set {1, 2, 5, 10, 20, 50, 100, 200, 500, 1000}. Meanwhile, the domain of the parameter σ for the RBF kernel function is set to the set {0.01, 0.05, 0.1, 0.2, 0.5, 1, 2, 5, 10, 20, 50, 100}. Furthermore, all of the experiments are carried out using the MATLAB 8.1 platform.

4.4. Performance Evaluation Criteria. In this paper, we use seven criteria to evaluate the performance of six classifiers, which includes total accuracy, type-I accuracy, type-II accuracy, F_1 score, MCC, and KS score.

4.4.1. Total Accuracy. Total accuracy is one of the most popular performance evaluation criteria which is defined as the correct predicted samples divided by the total sample, and it is computed as

$$\text{total accuracy} = \frac{\text{TP} + \text{TN}}{\text{TP} + \text{TN} + \text{FP} + \text{FN}}, \tag{13}$$

where TP refers to the number of the correct classification of the good creditor as the good creditor; FN refers to the number of the wrong classification of the poor creditor as the good creditor; TN refers to the number of the correct classification of the poor creditor as the poor creditor; and FP refers to the number of the wrong classification of the good creditor as the poor creditor.

4.4.2. Type-I Accuracy or Type-I Error. Type-I error is known as the false negative rate, and type-I accuracy is known as the true positive rate, which are, respectively, computed as

$$\begin{gathered}\text{type} - \text{I error} = \frac{\text{FN}}{\text{TP} + \text{FN}}, \\ \text{type} - \text{I accuracy} = 1 - \text{type} - \text{II error}.\end{gathered} \tag{14}$$

4.4.3. Type-II Accuracy or Type-II Error. Type-II error is known as the false positive rate, and type-II accuracy is known as the true negative rate, which are, respectively, computed as

$$\begin{gathered}\text{type} - \text{II error} = \frac{\text{FN}}{\text{TP} + \text{FN}}, \\ \text{type} - \text{II accuracy} = 1 - \text{type} - \text{II error}.\end{gathered} \tag{15}$$

4.4.4. F_1 Score. F_1 score is commonly used to measure the predictive accuracy of the binary classification model in statistics, and it is computed as

$$F_1 \text{ score} = \frac{2 \times \text{TP}}{2 \times \text{TP} + \text{FN} + \text{FP}}. \tag{16}$$

4.4.5. Matthew's Correlation Coefficient (MCC). MCC is usually used to judge the correlation relationship between two groups of data, and it is computed as

$$\text{MCC} = \frac{\text{TP} \times \text{TN} - \text{FP} \times \text{FN}}{[(\text{TP} + \text{FN}) \times (\text{TP} + \text{FP}) \times (\text{TN} + \text{FP}) \times (\text{TN} + \text{FN})]^{1/2}}. \tag{17}$$

4.4.6. Kolmogorov–Smirnov Score (KS Score). KS score is widely used in evaluating the discriminatory ability of the model between positive and negative samples because it is sensitive to the difference of position and shape between two kinds of empirical cumulative distribution functions. The higher the KS score, the better the performance of the model. The KS score is computed as

$$\text{KS score} = \max(|\text{TP} - \text{FP}|). \tag{18}$$

4.4.7. AUC. AUC is regarded as a widely used measure for model performance evaluation. As a numerical value which ranges from 0 to 1, AUC can evaluate the classifier

intuitively. The evaluation criterion is that the larger the AUC value, the better the evaluation performance of the model.

5. Results and Discussion

5.1. Optimal Parameter Setting. In this paper, we study the effect of different parameters on the classification performance of SVM, MCLOC, MCQOC, KFS-MCLOC, and ANN, respectively. By running the grid search and 5-fold cross-validation against the training data, the best parameters are found for SVM with $C = 100$ and $\sigma = 10$, MCLOC with $C = 5$, and MCQOC with $C = 10$. As for KFS-MCLOC, its optimal parameters are, respectively, 20 for the shrinkage factor S for feature selection, 200 for the penalty factor C, and 0.2 for the bandwidth σ of the RBF kernel function. For the neural network classifier, the optimal network topological structure is composed of 1 hidden layer with 44 nodes in addition to input and output layers.

5.2. Model Evaluation of Predictive Results. As for Chinese small and microsized enterprises' credit risk assessment, we use the five-fold cross-validation method to train the training subsets of the proposed KFS-MCLOC and the other five models, respectively, and then provide each predictive result. In this paper, we totally use seven evaluation criteria, including total accuracy (TA), type-I accuracy, type-II accuracy, F_1 score, MCC, KS score, and AUC to measure the performance of six models.

As shown in Table 8, we can find that the performance of KFS-MCLOC is significantly better than that of the other classifiers. The total accuracy of KFS-MCLOC is 93.63%, which is the highest, indicating that KFS-MCLOC has the best overall predictive performance. As for the F_1 score, only KFS-MCLOC's F_1 score exceeds 0.9, which is 0.91. In comparison, the other five models' F_1 scores are all below 0.9, i.e., SVM (0.82), neural networks (0.77), logistic regression (0.75), MCQOC (0.74), and MCLOC (0.72). In terms of MCC, KFS-MCLOC also has an absolute advantage (0.87), which is much higher than the other classifiers.

In order to compare the predictive ability of each model more clearly, we draw an ROC curve. Figure 2 shows that the ROC curve of KFS-MCLOC is on the far left, which means that it is far better than MCLOC and MCQOC. This indicates that the predictive performance of the MCLOC can be largely improved by introducing the one-norm kernel feature selection. In addition, the ROC curves of neural networks and SVM almost overlap, and both are slightly better than logistic regression in most cases.

Moreover, compared with the ROC curve, since AUC has a specific value, it can intuitively show the classification performance of the model. Therefore, we make a supplementary comparison of the results through AUC. As shown in Table 8, the AUC of KFS-MCLOC is the highest, which is 0.93, and MCLOC performed the worst, which is 0.79.

In addition, experience shows that when the negative sample has a greater influence on the judgment of results, the KS score can better reflect the distinguishing ability of the model than AUC. Figure 3 shows the comparison of KS score among six classifiers. We can see in Table 8 that the KS score of KFS-MCLOC is also the largest (0.85), while the KS score of logistic regression is the lowest (0.61). This result fully demonstrates that unbalanced data have a negative impact on the classification performance of traditional classifiers, which also proves the conclusion of Galar et al.'s research, in which they said that when faced with unbalanced distribution of classes, the performance of traditional classifiers was often disappointing [39].

However, in real business practice, the banks are more concentrated on the type-II error since the cost of the type-II error is much higher than the cost of the type-I error. Table 9 shows the type-I accuracy, type-I error, type-II error accuracy, and type-II error of the six models.

In order to display the results more intuitively, we draw the histograms of type-I accuracy and type-II accuracy of six classifiers, respectively (Figure 4). From the comparison results of type-I accuracy, SVM performs the best (94.64%). However, from the comparison results of type-II accuracy, KFS-MCLOC performs the best (98.57%), followed by logistic regression (85.71%); and the worst is MCLOC (68.57%), which is almost 30% lower than KFS-MCLOC.

Table 8: Predictive results of six models based on five evaluation criteria.

Model	TA (%)	F_1 score	AUC	KS score	MCC
Logistic regression	82.05	0.75	0.82	0.61	0.63
Neural networks	85.68	0.77	0.83	0.72	0.67
MCLOC	82.73	0.72	0.79	0.75	0.6
MCQOC	84.32	0.74	0.8	0.68	0.63
SVM	89.09	0.82	0.87	0.8	0.74
KFS-MCLOC	93.63	0.91	0.93	0.85	0.87

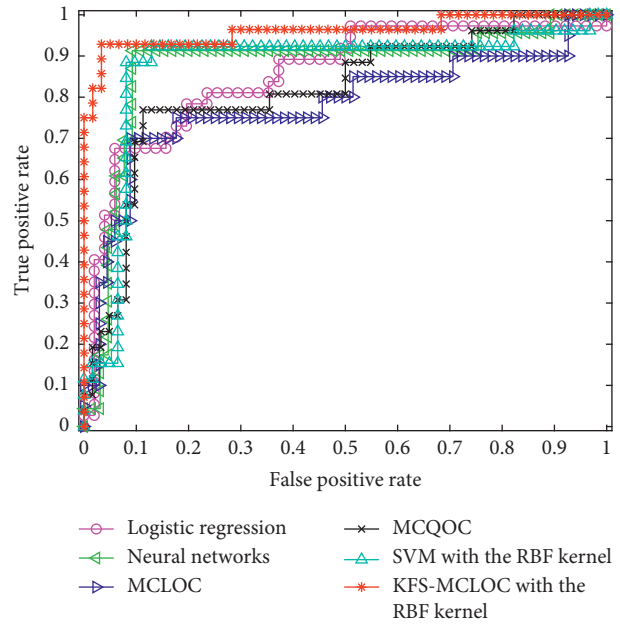

Figure 2: ROC curve of six models.

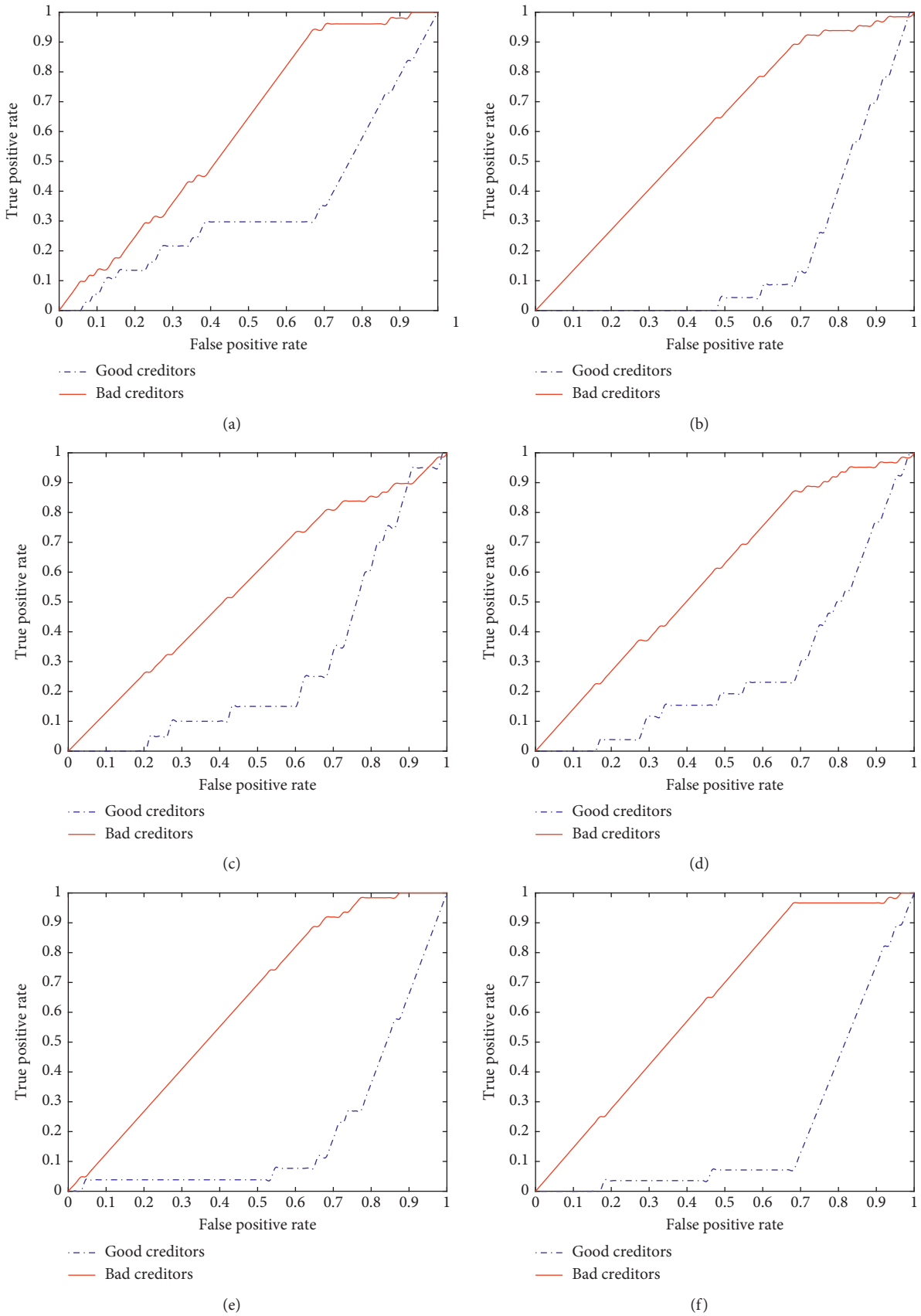

Figure 3: KS curves of six models. (a) Logistic regression. (b) Neural networks. (c) MCLOC. (d) MCQOC. (e) SVM. (f) KFS-MCLOC.

Table 9: Predictive results of six models based on four evaluation criteria.

Model	Type-I accuracy (%)	Type-I error (%)	Type-II accuracy (%)	Type-II error (%)
Logistic regression	80.33	19.67	85.71	14.29
Neural networks	91.67	8.33	72.86	27.14
MCLOC	89.33	10.67	68.57	31.43
MCQOC	90.67	9.33	70.71	29.29
SVM	94.67	5.33	77.14	22.86
KFS-MCLOC	91.33	8.67	98.57	1.43

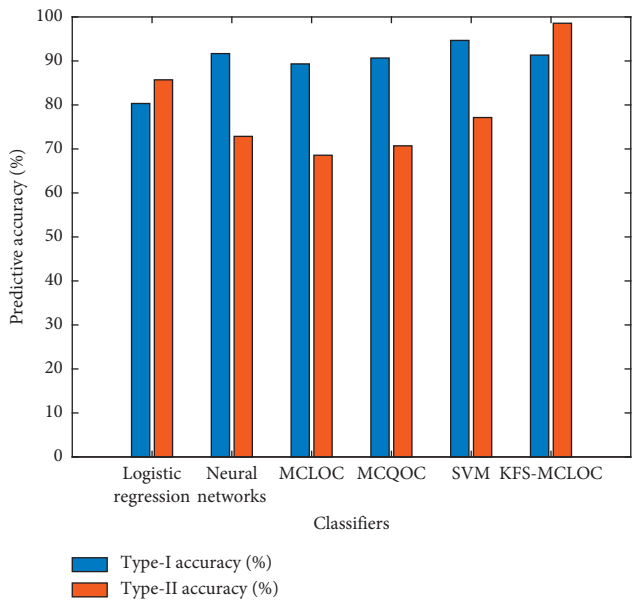

Figure 4: Type-I accuracy and type-II accuracy of six models.

In conclusion, there are three main findings: firstly, in the comparison of the results of total accuracy, type-II accuracy, AUC, KS score, F_1 score, and MCC, KFS-MCLOC's performance is significantly better than that of the other models, i.e., logistic regression, SVM, neural networks, MCLOC, and MCQOC, except for type-I accuracy, in which KFS-MCLOC's performance is slightly worse than that of SVM. Secondly, SVM has almost the second-best predictive performance among the six models. Thirdly, the predictive performance of MCLOC is the worst, which fully shows that it is very necessary to improve the algorithm of MCLOC.

5.3. The Analysis and Discussion of Feature Selection Results

5.3.1. Reduction Rate Analysis. Generally, the purpose of dimension reduction or attribute reduction is to solve the problem of too many features in the original feature set. Obviously, the computational complexity of the model will be greatly reduced and the calculation efficiency of the model will be greatly improved, by reducing the number of original features in the feature space. Furthermore, a proper feature reduction can ensure that the final predictive results from the reduced data are basically consistent with the predictive results obtained from the original data set.

In this paper, the sparse kernel method is used to filter the original feature set, which can reduce the attributes and ensure the accuracy of the predictive results simultaneously. Among them, the reduction rate is an important indicator, i.e.,

$$\text{reduction rate} = \frac{\text{total features} - \text{used features}}{\text{total features}} \times 100\%. \tag{19}$$

In general, the less the number of features in credit risk indicators is, the more the explainable power of small and microsized enterprises' credit risk assessment will be. The comparison of reduction rates of six classifiers is listed in Table 10.

Normally, the fewer the selected features, the higher the reduction rate and the stronger the explanatory power of the selected features. As shown in Table 10, KFS-MCLOC selects 10 most important features from 53 original features, with a reduction rate of 81.13%; while other models (logistic regression, SVM, neural networks, MCLOC, and MCQOC) are with a reduction rate of 0%.

5.3.2. Feature Importance Analysis. The 10 selected features and their weights are shown in Figure 5 and are described in brief as follows: X_9(−2.04%), X_{24}(−19.76%), X_{30}(−2.52%), X_{34}(7.95%), X_{37}(−7.21%), X_{39}(21.42%), X_{42}(10.14%), X_{44}(−13.09%), X_{45}(10.06%), and X_{47}(5.81%).

In order to make a more specific analysis, we combine and classify the name, category, positive/negative impact, and weight proportion of the features selected by KFS-MCLOC, which is shown in Table 11 in detail.

Specifically, from the perspective of the categories of the selected features, they cover the financial information, basic information of the actual controller's information, behavioural information, and supervision information. Among them, the number of features belonging to behavioural information is the largest, accounting for more than 50% of all indicators. In terms of contribution degree, the sum of the three features ("abnormal times of water, electricity, and tax in the past 12 months," "net operation cash flow," and "mortgage and pledge status") importance weights exceeds 50% and plays a decisive role. Among which, two features belong to behaviour information and one feature belongs to financial information. As for the influence direction of selected features, we can see that there are 5 selected features that have positive influence and five selected features that have negative influence.

5.3.3. Further Verification of Selected Features. In order to further verify the rationality of the important features

Table 10: Reduction rate of six models.

Model	Selected features	Number of selected features	Reduction rate (%)
Logistic regression	$X_1, \ldots, X_{53}$	53	0
SVM	$X_1, \ldots, X_{53}$	53	0
Neural networks	$X_1, \ldots, X_{53}$	53	0
MCLOC	$X_1, \ldots, X_{53}$	53	0
MCQOC	$X_1, \ldots, X_{53}$	53	0
KFS-MCLOC	$X_9, X_{24}, X_{30}, X_{34}, X_{37}, X_{39}, X_{42}, X_{44}, X_{45}, X_{47}$	10	81.13

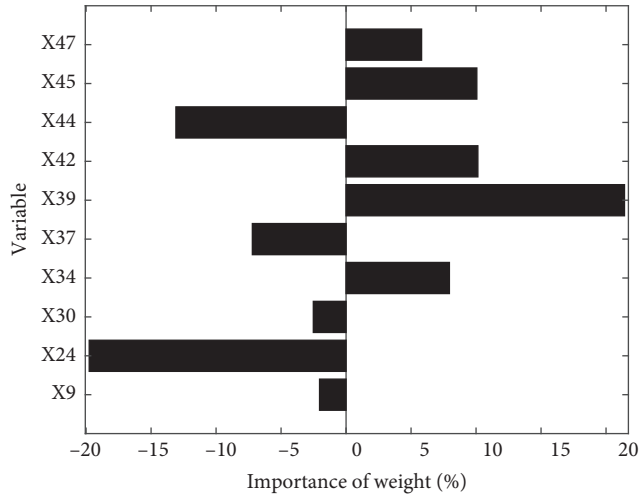

Figure 5: The 10 features selected by KFS-MCLOC and their importance weights.

Table 11: Feature selection results by KFS-MCLOC.

Variable	Variable name	Category	Positive/ negative	Weight
X_9	Quick ratio	Enterprises' financial information	Negative	−2.04%
X_{24}	Operating net cash flow	Enterprises' financial information	Negative	−19.76%
X_{30}	Actual controller's management experience	Actual controller's information	Negative	−2.52%
X_{34}	Whether the actual controller has any record of tax default and illegal behaviour	Actual controller's information	Positive	7.95%
X_{37}	Whether the wages of employees in the past 12 months can be paid on time	Enterprises' behaviour information	Negative	−7.21%
X_{39}	Abnormal times of water, electricity, and tax in the past 12 months	Enterprises' behaviour information	Positive	21.42%
X_{42}	Overdue days of enterprises' loans	Enterprises' behaviour information	Positive	10.14%
X_{44}	Mortgage and pledge status	Enterprises' behaviour information	Negative	−13.09%
X_{45}	Whether the guarantee enterprise is abnormal	Enterprises' behaviour information	Positive	10.06%
X_{47}	Number of administrative punishments	Enterprises' supervision information	Positive	5.81%

selected by KFS-MCLOC, we choose the logistic regression model with stepwise parameter to screen the original 53 features. At the significance level of 5%, logistic regression with stepwise parameter selects 8 important features which are shown in Table 12.

As we can see from Table 12, according to the categories of selected features, most of the selected features belong to small and microsized enterprises' behaviour information, which again proves that the behaviour information plays an important role in SME's credit risk assessment. In addition,

Table 12: Feature selection results by logistic regression with stepwise parameter.

Variable	Variable name	Category	Coefficient	p value
X_9	Quick ratio	Enterprises' financial information	−0.3168	0.0014
X_{20}	Interest coverage ratio	Enterprises' financial information	−0.2924	0.0076
X_{24}	Operating net cash flow	Enterprises' financial information	−0.2401	0.0198
X_{32}	Accumulated overdue repayment of actual controller	Actual controller's information	−0.3426	≤ 0.001
X_{39}	Abnormal times of water, electricity, and tax in the past 12 months	Enterprises' behaviour information	1.2816	≤ 0.001
X_{42}	Overdue days of enterprises' loans	Enterprises' behaviour information	0.2164	0.0248
X_{44}	Mortgage and pledge status	Enterprises' behaviour information	−0.271	≤ 0.001
X_{46}	Number of administrative punishments	Enterprises' supervision information	0.345	0.0006

by comparing the features selected by KFS-MCLOC and features selected by the logistic regression model, it is found that there is no significant difference between them. It can be shown that five indicators including "quick ratio, net operating cash flow, abnormal times of water, electricity, and taxes in the past 12 months, overdue days of enterprises' loans, and mortgage and pledge status" are selected by both KFS-MCLOC and the logistic regression model. To some extent, this result further proves the effectiveness and correctness of the KFS-MCLOC model in feature selection. Furthermore, it should be worth noting that although both models can select important features, KFS-MCLOC can automatically give importance weight to each selected feature, whereas the logistic regression model is relatively weak in this respect. From this point of view, KFS-MCLOC has more advantages in feature selection process.

In addition, combined with the results of Tables 11 and 12, we make a more in-depth discussion on the indicators selected by both KFS-MCLOC and logistic regression with stepwise parameters, as follows.

Firstly, "quick ratio" is considered to be the ability of quick assets to pay current liabilities and is an important index to measure the short-term solvency of enterprises. The higher the "quick ratio" is, the stronger the short-term solvency is and the less likely the enterprise is to have credit risk.

Secondly, "net operating cash flow" is proved to be one of the most important factors, and its importance weight is relatively high. This is probably because small and microsized enterprises have a small scale of assets and a single type of production and operation, which lessen their external financing channels. Once they face short-term financing pressure or fall into production difficulties, it is usually difficult to get the support of external funds. In this case, the internal capital generated by the production and operation of small and microsized enterprises is particularly important. Therefore, through operating cash flow, we can analyze the rationality of enterprise capital operation and judge the ability of enterprise to repay loans, and thereby assess the enterprises' credit risk status.

Thirdly, "abnormal times of water, electricity, and tax fees in the past 12 months" can well illustrate the daily operating status of enterprises' credit risk. Because, if the enterprise cannot pay the water, electricity, and tax fees on time, it means that there may be a high probability of problems in the operation of the enterprise at this stage. Therefore, it can be preliminarily judged that the probability of enterprises' credit risk will increase, which needs to be paid attention.

Fourthly, "overdue days of enterprises' loans" is a very important signal to judge small and microsized enterprises' risk status. The longer the overdue days of enterprises' loans are, the greater the risk of operation of the enterprise is, the less the cash flow is, and the greater the credit risk of the enterprise is. Moreover, "overdue days of enterprises' loans" is the precursor index for the determination of the high risk of enterprises.

Finally, "mortgage and pledge status" is also a very significant indicator. In general, the higher the value of the mortgage, the less the risk the enterprise will have. At present, since the financial information and operation information between banks and small and microsized enterprises are seriously asymmetric, the "mortgage and pledge status" is shown to be a particularly important factor. By increasing mortgage and pledge, credit risk can be effectively mitigated, thus reducing the occurrence of nonperforming loans.

6. Conclusions

Credit risk assessment has always been an important research topic in the fields of accounting, finance, and business. At the same time, it has become a hot research field of statistical learning, artificial intelligence, and optimization algorithm in the recent years. Nowadays, enterprises' credit risk analysis is gradually forming its own theoretical system and research framework. A good credit risk assessment model for enterprises has important practical significance on improving the awareness of credit risk, preventing the credit crisis, and avoiding the bankruptcy liquidation.

Based on the credit data of small and microsized enterprises of a Chinese commercial bank, we design a credit risk indicator system, especially for small and microsized enterprises, including basic information, financial information, actual controllers' information, behaviour information, supervision information, and policy information. As for model construction, we improve the MCLOC by introducing the one-norm kernel feature selection and thereby establish the KFS-MCLOC. In order to test the effectiveness of the KFS-MCLOC, we use total accuracy, F_1 score, MCC, KS score, and AUC to compare models' predictive performance. The empirical result shows that the KFS-MCLOC

model performs better than the other models in almost all aspects by using a real-world credit dataset from a Chinese commercial bank. Secondly, the KFS-MCLOC selects 10 features from 53 original features and gives selected features their weight automatically. Thirdly, the features selected by KFS-MCLOC are further verified and compared by the features selected by logistic regression with stepwise parameter, and the indicators of "quick ratio; net operating cash flow; enterprises' abnormal times of water, electricity, and taxes fee; overdue days of enterprises' loans; and mortgage and pledge status" are proved to be the most influencing credit risk factors. This finding is meaningful for banks and regulatory institutions because these key indicators can be regarded as important credit risk factors and should be paid more attention in practice in the future. In theory, this study provides a useful idea and reference for enriching and developing the credit risk indicator system for Chinese small and microsized enterprises. In practice, this paper also has practical contribution since the effectiveness of the KFS-MCLOC model has been validated by a real-world credit dataset from a Chinese commercial bank.

6.1. Contribution. In general, the contributions of this paper are as follows. Firstly, we construct a comprehensive multi-dimensional credit risk indicator system especially for small and microsized enterprises by adding enterprises' behaviour information, supervision information, and policy information. Secondly, we test the evaluation performance of the model based on the real credit dataset of Chinese small and microsized enterprises. The empirical results show that the KFS-MCLOC model has great advantages in predictive accuracy and stability, which means that the model is suitable for evaluating the credit risk of small and microsized enterprises in the real business world. Thirdly, in the financial field, all credit decisions are required to be interpretable. The proposed KFS-MCLOC model can automatically select the most important indicators and determine their importance weights, which is very effective in solving the "black box" problem, so as to help the credit personnel make effective understandable and traceable decisions.

6.2. Limitations and Future Works. In this section, we conclude the limitations of the proposed model, and put forward the corresponding future works. At first, since the sample size in this paper is relatively small, in the future, a large dataset with a more complex data structure should be explored to further validate the proposed model. In addition, dynamic data changing is a relatively new research problem, and more attention should be paid to it in the future. Finally, although the KFS-MCLOC is shown to be relatively effective in small and microsized enterprises' credit risk assessment, "expert technology" could also be added to the model for a higher predictive accuracy.

Data Availability

The data used to support the findings of this study are available from the corresponding author upon request.

Conflicts of Interest

The authors declare that there are no conflicts of interest in connection with the work submitted.

References

[1] N. Gulsoy and S. Kulluk, "A data mining application in credit scoring processes of small and medium enterprises commercial corporate customers," *Wiley Interdisciplinary Reviews-data Mining And Knowledge Discovery*, vol. 9, no. 3, p. e1299, 2019.

[2] Z. Zhang, J. He, G. Gao, and Y. Tian, "Sparse multi-criteria optimization classifier for credit risk evaluation," *Soft Computing*, vol. 23, no. 9, pp. 3053–3066, 2019.

[3] Q. Zhang, J. Wang, A. Lu, S. Wang, and J. Ma, "An improved SMO algorithm for financial credit risk assessment - evidence from China's banking," *Neurocomputing*, vol. 272, pp. 314–325, 2018.

[4] A. R. Fisher, "The use of multiple measurements in taxonomic problems," *Annals of Eugenics*, vol. 7, no. 2, pp. 179–188, 1936.

[5] E. I. Altman, "Financial ratios, discriminant analysis and the prediction of corporate bankruptcy," *The Journal of Finance*, vol. 23, no. 4, pp. 589–609, 1968.

[6] Y. E. Orgler, "A credit scoring model for commercial loans," *Journal of Money, Credit and Banking*, vol. 2, no. 4, pp. 435–445, 1970.

[7] J. C. Wiginton, "A note on the comparison of logit and discriminant models of consumer credit behavior," *The Journal of Financial and Quantitative Analysis*, vol. 15, no. 3, pp. 757–770, 1980.

[8] A. Zakaryazad and E. Duman, "A profit-driven Artificial Neural Network (ANN) with applications to fraud detection and direct marketing," *Neurocomputing*, vol. 175, pp. 121–131, 2016.

[9] Z. Zhao, S. Xu, B. H. Kang, M. M. J. Kabir, Y. Liu, and R. Wasinger, "Investigation and improvement of multi-layer perceptron neural networks for credit scoring," *Expert Systems with Applications*, vol. 42, no. 7, pp. 3508–3516, 2015.

[10] X. Huang, X. Liu, and Y. Ren, "Enterprise credit risk evaluation based on neural network algorithm," *Cognitive Systems Research*, vol. 52, pp. 317–324, 2018.

[11] V. Kozeny, "Genetic algorithms for credit scoring: alternative fitness function performance comparison," *Expert Systems with Applications*, vol. 42, no. 6, pp. 2998–3004, 2015.

[12] S. Oreski, D. Oreski, and G. Oreski, "Hybrid system with genetic algorithm and artificial neural networks and its application to retail credit risk assessment," *Expert Systems with Applications*, vol. 39, no. 16, pp. 12605–12617, 2012.

[13] Y. Xia, C. Liu, Y. Li, and N. Liu, "A boosted decision tree approach using Bayesian hyper-parameter optimization for credit scoring," *Expert Systems with Applications*, vol. 78, pp. 225–241, 2017.

[14] C. Qiu, L. Jiang, and C. Li, "Randomly selected decision tree for test-cost sensitive learning," *Applied Soft Computing*, vol. 53, pp. 27–33, 2017.

[15] Y. Li, G. Chi, and Z. Zhang, "Decision tree for credit scoring and discovery of significant features: an empirical analysis based on Chinese microfinance for farmers," *Filomat*, vol. 32, no. 5, pp. 1513–1521, 2018.

[16] J. Sun, J. Lang, H. Fujita, and H. Li, "Imbalanced enterprise credit evaluation with DTE-SBD: decision tree ensemble based on SMOTE and bagging with differentiated sampling rates," *Information Sciences*, vol. 425, pp. 76–91, 2018.

[17] X. Mei, "Sparse coding with sparse dictionaries for credit risk classification," in *Proceedings of the International Conference on Progress in Informatics and Computing*, pp. 23–26, Shanghai, China, December 2016.

[18] W. Lu, Z. Li, and J. Chu, "Adaptive ensemble undersampling-boost: a novel learning framework for imbalanced data," *Journal of Systems and Software*, vol. 132, pp. 272–282, 2017.

[19] C. Cortes and V. Vapnik, "Support-vector networks," *Machine Learning*, vol. 20, no. 3, pp. 273–297, 1995.

[20] X. Yao, J. Crook, and G. Andreeva, "Enhancing two-stage modelling methodology for loss given default with support vector machines," *European Journal Of Operational Research*, vol. 263, no. 2, pp. 679–689, 2017.

[21] Y. Shi, M. Wise, M. Luo, and Y. Lin, "Data mining in credit card portfolio management: a multiple criteria decision-making approach," in *Proceedings of the Multiple Criteria Decision Making in the New Millennium*, pp. 427–436, Berlin, Germany, July 2001.

[22] S. Maldonado, C. Bravo, J. Pérez, and J. Perez, "Integrated framework for profit-based feature selection and SVM classification in credit scoring," *Decision Support Systems*, vol. 104, pp. 113–121, 2017.

[23] S. He, H. Fang, M. Zhang, F. Liu, and Z. Ding, "Adaptive optimal control for a class of nonlinear systems: the online policy iteration approach," *IEEE Transactions on Neural Networks and Learning Systems*, vol. 31, no. 2, pp. 549–558, 2020.

[24] S. He, H. Fang, M. Zhang, F. Liu, X. Luan, and Z. Ding, "Online policy iterative-based H∞ optimization algorithm for a class of nonlinear systems," *Information Sciences*, vol. 495, pp. 1–13, 2019.

[25] M. Ala'raj and M. F. Abbod, "A new hybrid ensemble credit scoring model based on classifiers consensus system approach," *Expert Systems with Applications*, vol. 64, pp. 36–55, 2016.

[26] W. Zhang, H. He, and S. Zhang, "A novel multi-stage hybrid model with enhanced multi-population niche genetic algorithm: an application in credit scoring," *Expert Systems with Applications*, vol. 121, pp. 221–232, 2019.

[27] A. Jain and D. Zongker, "Feature selection: evaluation, application, and small sample performance," *IEEE Transactions on Pattern Analysis and Machine Intelligence*, vol. 19, no. 2, pp. 153–158, 1997.

[28] H. Sun, Z. Chen, and J. Chen, "Credit risk analysis using sparse non-negative matrix factorizations," in *Proceeding of the Information Science and Control Engineering*, pp. 181–184, Shanghai, China, April 2015.

[29] N. Freed and F. Glover, "Simple but powerful goal programming models for discriminant problems," *European Journal of Operational Research*, vol. 7, no. 1, pp. 44–60, 1981.

[30] Y. Shi, "Multiple criteria optimization-based data mining methods and applications: a systematic survey," *Knowledge and Information Systems*, vol. 24, no. 3, pp. 369–391, 2010.

[31] Z. Zhang, G. Gao, J. Yue, Y. Duan, and Y. Shi, "Multi-criteria optimization classifier using fuzzification, kernel and penalty factors for predicting protein interaction hot spots," *Applied Soft Computing*, vol. 18, pp. 115–125, 2014.

[32] F. Barboza, H. Kimura, and E. Altman, "Machine learning models and bankruptcy prediction," *Expert Systems with Applications*, vol. 83, pp. 405–417, 2017.

[33] S. Cornée, "The relevance of soft information for predicting small business credit default: evidence from a social bank," *Journal of Small Business Management*, vol. 57, no. 3, pp. 699–719, 2019.

[34] S. F. Karabag, "Factors impacting firm failure and technological development: a study of three emerging-economy firms," *Journal of Business Research*, vol. 98, pp. 462–474, 2019.

[35] Z. Wang, C. Jiang, H. Zhao, and Y. Ding, "Mining semantic soft factors for credit risk evaluation in Peer-to-Peer lending," *Journal of Management Information Systems*, vol. 37, no. 1, pp. 282–308, 2020.

[36] H. He, W. Zhang, and S. Zhang, "A novel ensemble method for credit scoring: adaption of different imbalance ratios," *Expert Systems with Applications*, vol. 98, pp. 105–117, 2018.

[37] M. Stone, "Cross-validatory choice and assessment of statistical predictions," *Journal of the Royal Statistical Society: Series B (Methodological)*, vol. 36, no. 2, pp. 111–133, 1974.

[38] Y. Zhang, S. Wang, P. Phillips, and G. Ji, "Binary PSO with mutation operator for feature selection using decision tree applied to spam detection," *Knowledge-Based Systems*, vol. 64, pp. 22–31, 2014.

[39] D. D. Galar, R. Villarejo, C. A. Johansson, U. Kumar, and L. F. B. Muro, "Hybrid models for PHM deployment techniques in railway," in *Proceedings of the Tenth International Conference on Condition Monitoring and Machinery Failure Prevention Technologies*, pp. 1047–1056, Krakóv, Poland, June 2013.